COASTAL AND ESTUARINE STUDIES

Mixing in Estuaries and Coastal Seas

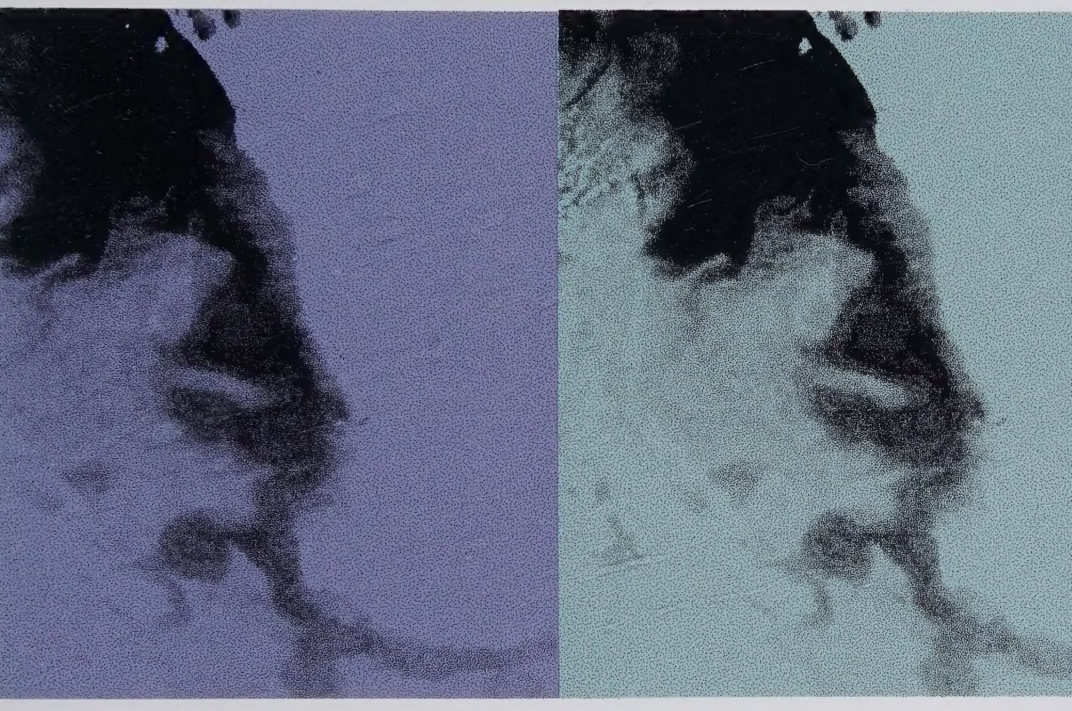

Charitha Pattiaratchi, Editor

American Geophysical Union

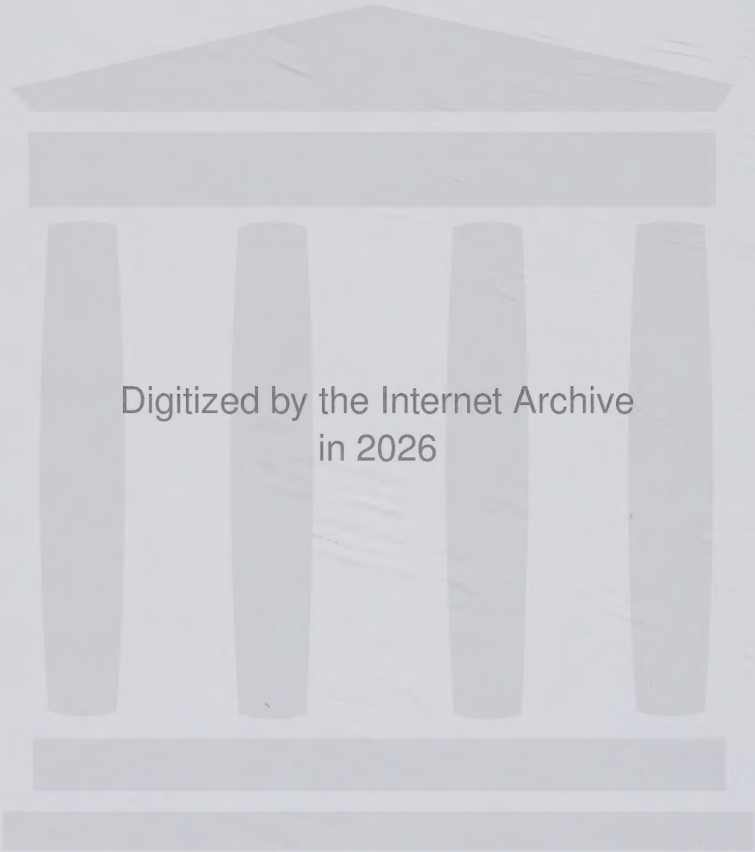
Digitized by the Internet Archive
in 2026

https://archive.org/details/mixinginestuarie0050unse

Thompson

Coastal and Estuarine Studies

Series Editors:
Malcolm J. Bowman Christopher N.K. Mooers

Coastal and Estuarine Studies

50

Charitha Pattiaratchi (Ed.)

Mixing in Estuaries and Coastal Seas

American Geophysical Union

Washington, DC

Series Editors
Malcolm J. Bowman
Marine Sciences Research Center, State University of New York
Stony Brook, N.Y. 11794, USA

Christopher N.K. Mooers
Division of Applied Marine Physics
RSMAS/University of Miami
4600 Rickenbacker Cswy.
Miami, FL 33149-1098, USA

Editor
Charitha B. Pattiaratchi
University of Western Australia
Nedlands, W.A. 60009 Australia

Library of Congress Cataloging-in-Publication Data

Mixing in estuaries and coastal seas / Charitha Pattiaratchi, editor.
p. cm. — (Coastal and estuarine studies ; 50)
"Papers . . . presented at the 6th International Biennial Conference on Physics of Estuaries and Coastal Seas, held in Margaret River, Western Australia, in December 1992"—Pref.
Includes bibliographical references.
ISBN 0-87590-264-2
1. Estuarine oceanography—Congresses. 2. Coasts—Congresses. 3. Ocean mixing—Congresses. I. Pattiaratchi, Charitha, 1957– . II. International Conference on Physics of Estuaries and Coastal Seas (6th : 1992 : Margaret River, Augusta–Margaret River Shire. W.A.) III. Series.
GC96.5.M59 1996
551.46'09—dc20 96-175
CIP

ISSN 0733-9569

ISBN 0-87590-264-2

Copyright 1996 by the American Geophysical Union, 2000 Florida Avenue, NW, Washington, DC 20009, U.S.A.

Figures, tables, and short excerpts may be reprinted in scientific books and journals if the source is properly cited.

Authorization to photocopy items for internal or personal use, or the internal or personal use of specific clients, is granted by the American Geophysical Union for libraries and other users registered with the Copyright Clearance Center (CCC) Transactional Reporting Service, provided that the base fee of $1.00 per copy plus $0.10 per page is paid directly to CCC, 222 Rosewood Dr., Danvers, MA 01923. 0733-9569/96/$01.50 + .35.

This consent does not extend to other kinds of copying, such as copying for creating new collective works or for resale. The reproduction of multiple copies and the use of full articles or the use of extracts, including figures and tables, for commercial purposes requires permission from AGU.

Printed in the United States of America.

CONTENTS

PREFACE xi

PART I: INTRODUCTION

1 **Introduction**
C. Pattiaratchi 1

PART II: INNER CONTINENTAL SHELF PROCESSES

2 **The Response of Stratified Shelf Waters to the Leeuwin Current and Wind Forcing: Winter Observations off Perth, Western Australia**
D. Mills, N. D'Adamo, A. Wyllie and A. Pearce 5

3 **Measurements of the Wave, Current and Sea Level Dynamics of an Exposed Coastal Site**
K. Black, M. Rosenberg, G. Symonds, R. Simons, C. Pattiaratchi, and P. Nielsen 29

4 **The Lagrangian Barycentric Method to Compute 2D and 3D Long Term Dispersion in Tidal Environments**
J. C. Salomon, P. Garreau and M. Breton 59

5 **Modelling Oil Slick Trajectories in Spencer Gulf, South Australia**
P. J. Bills, D. W. F. Standingford and B. J. Noye 77

6 **Tide-Induced Residual Currents Generated by the Stokes Layer in the Rotating Tidal Basin**
H. Yasuda 95

7 **Wave and Dispersion Studies in Shallow Water Using Side-Scan Sonar**
S. A. Thorpe, A. Graham and A. Hall 110

8 **Detailed Cross-Frontal Structure of a Tidal Front in the Kii Channel, Japan**
T. Yanagi, T. Yamamoto, T. Ishimaru and T. Saino 135

PART III: SHELF-ESTUARY EXCHANGE PROCESSES

9 **A Field Investigation of Water Exchange Between a Small Coastal Embayment and an Adjacent Shelf**
P. E. Holloway 145

10 **A Note on the Influence of a Deep Ship Channel on Estuarine-Shelf Exchange in a Broad, Shallow Estuary**
W. W. Schroeder, J. R. Pennock and W. J. Wiseman Jr. 159

11 **Tidal and Low Frequency Flushing of a Coastal Lagoon Using a Flexible Grid Model**
N. P. Smith.....171

12 **Circulation and Transport in Sarasota Bay, Florida: The Effect of Tidal Inlets on Estuarine Circulation and Flushing Quality**
Y. P. Sheng, S. Peene and E. Yassuda.....184

PART IV: ESTUARINE PROCESSES

13 **Internal Tidal Asymmetry in Channel Flows: Origins and Consequences**
D. A. Jay and J. D. Musiak.....211

14 **Relative Contributions of Interfacial and Bed Generated Mixing to the Estuarine Energy Balance**
R. E. Lewis 250

15 **Short Salt Wedges and the Limit of No Salt Wedge**
J. B. Hinwood 267

16 **A Spring-Neap Flushing Box Model**
Z. Z. Ibrahim.....278

17 **Studies on Transport Times and Water Quality in the Weser Estuary (Germany)**
I. Grabemann, H. Kühle, B. Kunze, and A. Müller 291

PART V: SEDIMENT PROCESSES

18 **Modelling Suspended Sediment Dynamics in Tidally Stirred and Periodically Stratified Waters: Progress and Pitfalls**
S. E. Jones, C. F. Jago and J. H. Simpson.....302

19 **Bottom Friction Reduction in Turbid Estuaries**
B. King and E. Wolanski 325

20 **Tidal Dynamics and Sediment Transport in a Shallow Macrotidal Estuary**
G. Lessa 338

21 **Net Transport of Fine Sediment in a Homogeneous Tidal Channel**
J. van de Kreeke 361

22 **Seasonal Variability of Mobile Mud Deposits in the Tamar Estuary**
R. J. Uncles, M. L. Barton and J. A. Stephens 374

23 **Dry Season Hydrodynamics and Sediment Transport in a Mangrove Creek**
P. Larcombe and P. V. Ridd 388

24 **Uniform Bottom Shear Stress and Equilibrium Hyposometry of Intertidal Flats**
C. T. Friedrichs and D. G. Aubrey 405

PART VI: OCEAN OUTFALLS

25 **Dispersion of Effluent from Sydney's New Deepwater Outfalls. Part 1: Ocean processes**
R. S. Lee and T. R. Pritchard.....430

26 **Dispersion of Effluent from Sydney's New Deepwater Outfalls. Part 2: Observations of Plume Behaviour: Winter and Summer Examples**
T. R. Pritchard, R. S. Lee and A. Davison 439

27 **Monte Carlo Simulation of Sydney Deepwater Outfalls**
T. Webb and D. Cox *453*

28 **Study of Thermal Discharge with Satellite and Airborne Data**
S. Onishi.....*467*

PART VII: THEORETICAL STUDIES

29 **Distortion and Dispersion: Dilution of Solutes in Coastal Waters**
R. Smith 479

30 **Capillarity Correction to Periodic Solutions of the Shallow Flow Approximation**
D. A. Barry, S. J. Barry and J.-Y. Parlange.....496

LIST OF CONTRIBUTORS 511

PREFACE

Continental shelves, coastal seas and estuaries contain many valuable resources for economic, social, tourist and recreational activity. The majority of the world's largest cities are located on the coastline. For example, 86% of the total Australian population is located in the coastal zone. Almost 75% of the global harvest of fisheries comes from coastal areas. However, it is also the region into which anthropogenic wastes are discharged, leading to degradation of the environment. As we become more aware of the consequences of these discharges, and develop new management strategies to avoid detrimental effects in estuaries and coastal regions, it is clear that an understanding of mixing processes plays a very important role in dispersion of introduced contaminants.

This volume consists of 30 papers, each dealing with different aspects of mixing processes in the marine environment. The following topics are covered: inner continental shelf processes, shelf-estuary interactions, estuarine processes, sediment transport processes, ocean outfalls, and theoretical studies. The majority of the papers include results of field experiments with some degree of integration with numerical and/or analytical models. A wide variety of environments from different countries are presented. These include micro- and macro-tidal environments, areas influenced by major oceanic current systems, enclosed and semi-enclosed embayments, and mangrove environments.

All papers included in this volume are based on presentations at the 6th International Biennial Conference on Physics of Estuaries and Coastal Seas, held in Margaret River, Western Australia, in December 1992. The theme of the conference was "Mixing Processes in Estuaries and Coastal Seas." Previous conferences in this series have been held in Hamburg, Miami, Qingdao, Monterey, and Gregynog, and each of these conferences, except Qingdao, has resulted in a volume in the Coastal and Estuaries Studies series. The aim of these conferences is to promote the exchange of information and interaction between physical oceanographers and coastal engineers. The Margaret River venue provided a very relaxed, informal atmosphere in which papers were presented in plenary session followed by a generous time for discussion. This stimulated a rich exchange of ideas many of which are reflected in the contents of the final papers included here.

I would like to take this opportunity to acknowledge the contributions made by several individuals and organisations which resulted in a successful conference at Margaret River and the subsequent preparation of this volume. The contributors whose research is presented here are thanked for their patience, as well as the numerous (more than 70) external reviewers for their comments on the manuscripts, which ensured a high scientific quality in the papers included in this volume. The international steering committee for the conference consisted of Jörg Imberger (Centre for Water Research, The University of Western Australia); Ralph Cheng (U.S. Geological Survey); David Prandle (Proudman Oceanographic Laboratory, UK); and David Aubrey (Woods Hole Oceanographic Institution, USA). I am very grateful for the support and advice of these individuals as well as

from Co van de Kreeke (University of Miami). Financial assistance, which was vital for this endeavor, was provided by: Department of Industry Technology and Commerce (Australia); CSIRO Division of Oceanography; Steedman Science and Engineering Pty Ltd (now WNI Science and Engineering): ALCOA Australia; Environmental Protection Authority (WA); American Geophysical Union; and the Centre for Water Research, The University of Western Australia. Malcolm Bowman (State University of New York at Stony Brook) is thanked for his support and encouragement in the preparation of the volume. My deepest appreciation goes to Lorraine Dorn, who initially contributed to the organisation of the conference correspondence and the preparation of the volume of extended abstracts and then painstakingly undertook the task of producing the complete camera-ready copy of the manuscript; without her dedicated efforts this volume would not have materialised. Finally, I would like to thank my family: Gabi, Nafyn and Tesni for their patience and understanding during my extended absences from home which was necessary to complete this volume.

Charitha Pattiaratchi
Centre for Water Research
University of Western Australia
Nedlands, Western Australia

1

Introduction

C. Pattiaratchi

The biennial *Physics of Estuaries and coastal seas* series of conferences began in 1978 with the first conference in Hamburg (Sündermann and Holtz, 1980). Subsequent conferences were held in Miami (van de Kreeke, 1986), Qingdao, Monterey (Cheng, 1990) and Gregynog (Prandle, 1992). This volume is a collection of papers presented at the 6th conference held in Margaret River, Western Australia in December 1992. The aim of these conferences is to promote the exchange of information and the interaction between physical oceanographers and coastal engineers. The 6th conference held at the Margaret River Hotel, was attended by 88 people representing ten countries (Australia, UK, USA, Japan, Germany, France, Malaysia, New Zealand, Canada, The Netherlands) and 44 oral papers (all in plenary session) and 15 poster papers were presented.

The theme of the 5th conference was *Mixing processes in estuaries and coastal seas* and papers included in this volume have been divided into 7 sections: introduction; inner continental shelf processes; shelf-estuary processes; estuarine processes; sediment processes; ocean outfalls; and, theoretical studies. A short summary of papers included in each of these sections are presented below. Each paper has been refereed by at least two external reviewers who were asked to judge the papers to a 'Journal' standard.

Inner Continental Shelf Processes

Processes on the inner continental shelf are important as the ultimate fate of anthropogenic materials is determined by these processes. In this section 7 papers are included in a mix of field, numerical and analytical approaches. Mills *et al.* describe the oceanographic processes on the continental shelf offshore Perth, Western Australia during winter. Field and remotely sensed data are used to document changes in the density structure due to wind stress, freshwater inputs and meanders of the Leeuwin Current. Black *et al.* use field observations from Bass Strait, south-eastern Australia to investigate tidal dynamics, local wind forcing, factors effecting vertical mixing and sediment transport processes. Saloman *et al.* describe a Lagrangian technique, the barycentric method, to predict the long-term transport of conservative tracers in tidally

Mixing in Estuaries and Coastal Seas
Coastal and Estuarine Studies Volume 50, Pages 1-4
Copyright 1996 by the American Geophysical Union

dominated areas and in particular, in the English Channel. Bills *et al.* develop an oil slick model and compare the model output with an actual oil spill in Spencer Gulf, South Australia. An analytical approach is used by Yasuda to investigate the generation of residual currents due to the non-linear effects in the presence of the Stokes layer and earth's rotation. Thorpe *et al.* present examples of using high frequency sonar to measure wave characteristics in the nearshore zone, investigate surface convergence patterns associated with Langmuir circulation and to estimate the diffusion of floating particles. Yanagi *et al.* use high resolution CTD and ADCP data to investigate the three dimensional structure of a tidal front in the Kii Channel, Japan.

Shelf-Estuary Processes

Exchange processes between estuaries/embayments with offshore waters are of vital importance as the residence time of material in an estuary depends on these processes. There are four papers in this section. Holloway presents current data from Jervis Bay, a low tidal energy embayment located in eastern Australia, which provide evidence for the generation of internal Kelvin waves within the embayment forced by coastally trapped waves. It is shown that these low frequency oscillations enhance the flushing of embayments. Schroeder *et al.* analyse satellite imagery and field data from Mobile Bay, Alabama to show that during cold-air outbreaks in the Gulf Mexico and under low discharge conditions, warm salinity water is present at the landward end of the Bay due to upwelling. Smith develops a model to examine tidal and low frequency flushing of the Indian River lagoon system in Florida. Sheng *et al.* use a numerical model and field observations to investigate circulation and flushing characteristics of Sarasota Bay system and in particular, the effects of re-opening an inlet to the system.

Estuarine Processes

The mixing and transport processes of conservative material within estuaries directly effect water quality and the 5 papers in this section describe studies using field data from different estuaries around the world as well as numerical and laboratory techniques. Jay and Musiak describe how non-linear shallow water processes generate barotropic tidal asymmetry leading to flood- or ebb-dominant currents as well as an internal tidal asymmetry. Field data from the Columbia River (USA) Estuary are used to show that internal tidal asymmetry play a dominant role in the salt and sediment balance in narrow stratified estuaries. Lewis uses field data from the Tees Estuary (UK) to examine variations in the potential energy anomaly over a tidal cycle and to determine the relative contribution of bed and interfacial generated mixing. Hinwood re-analyses the laboratory data of Keulegan to investigate conditions which allow the development of a salt wedge in an estuarine channel. The application of a simple box model to investigate flushing characteristics of the Klang Estuary, Malaysia is described by Ibrahim whilst Grabemann

et al. report on the transit times of conservative material and its effects on water quality in the Weser Estuary, Germany.

Sediment Processes

Sediment transport processes are important for the morphological changes in estuaries and coastal seas. They also play a major role in water quality both in terms of determining turbidity levels (hence light propagation) and providing a transport mechanism for contaminants (nutrients, heavy metals etc) which attach themselves to the sediment particles. In this section, 7 papers are presented and all except one paper deal with sediment transport processes in estuaries. Jones *et al.* incorporate dynamics of suspended particulate matter in a one-dimensional hydrodynamic model and together with field measurements obtained from the North Sea, describe the processes controlling the concentration of suspended particulate matter under different conditions. King and Wolanksi, using a numerical model, demonstrate that the presence of fluid mud within estuaries may reduce the bottom friction coefficient. Lessa report on the results of a field experiment undertaken in Louisa Creek, a shallow macrotidal estuary located along the central Queensland coast (Australia), to investigate morphodynamics of the estuary. van de Kreeke shows that the interaction between the M_2 tide and its harmonic M_4 leads to a divergence in the sediment transport directions within an estuary. Uncles *et al.* discuss the results of field measurements of suspended particulate matter in the Tamar Estuary (UK) on spring-neap and seasonal time scales and show that there is a seasonal change in the longitudinal distribution of unconsolidated sediment along the estuary. Larcombe and Ridd report on field measurements of bedload and suspended sediment fluxes in Gordon Creek, a meso tidal creek and mangrove swamp system in north-eastern Australia. The distribution of horizontal surface area with respect to elevation on tidal flats, defined as hypsometry, is shown by Friedrichs and Aubrey to be determined by the relative dominance of tidal- or wave-bottom shear stress.

Ocean Outfalls

The effects of municipal and industrial discharges into the coastal zone has received much attention over the years. As a result of increased urban development these discharges have increased and major studies have been undertaken in many cities to investigate the effects of increased discharges on the coastal environment. One of the most publicised examples of wastewater discharges to the coastal zone has been that of Sydney where primary treated domestic wastewater was discharged at the shoreline for a number of years. To alleviate problems associated with these discharges, new deepwater outfalls have been constructed and commissioned in the early 90's. Three out of the four papers in this section describe the performance of these new deepwater outfalls. The papers by Lee and Pritchard and Pritchard *et al.* are a two part paper in which the first (Lee and Pritchard) discuss the processes on the Sydney continental shelf which influence the

dispersion patterns of the discharges whilst in the second paper, Pritchard *et al.* report on the results of field experiments undertaken with a radioactive tracer. Webb and Cox discuss results of Monte Carlo simulations of the Sydney outfalls. Onishi present a method in which the centre line of a thermal discharge plume from a power station may be determined from remotely sensed data.

Theoretical Studies

The two papers in this section present analytical solutions to investigate coastal phenomena. Smith describes the influence of Earth's rotation and the aspect ratio of the tidal ellipse on shear dispersion and demonstrates the affects of tidal frequency, time-scale of vertical mixing, Coriolis parameter and tidal ellipse aspect ratio on the dilution of solutes in tidal waters. Barry *et al.* investigate the behaviour of the water level in a coastal aquifer using a model that includes the effects of the capillarity fringe.

Conclusions

The collection of papers presented in this book reflect the current philosophy of research on mixing processes in estuaries and coastal seas. Many investigators now use a combination of field, numerical analytical and laboratory techniques to identify the dominant processes which control horizontal and vertical mixing processes as well as transport of conservative and non-conservative materials. All of these approaches are included in this volume. With the current thrust of research being in water quality issues and their effects on the environment, this book should provide a very good overview of the current work on mixing and exchange processes in estuaries and coastal seas.

References

Cheng, R. T. Residual currents and long-term transport. Lecture Notes on Coastal and Estuarine Studies, 38. Springer-Verlag, 544 pp., 1990.

Kreeke van de, J. Physics of shallow estuaries and bays. Lecture Notes on Coastal and Estuarine Studies, 16. Springer-Verlag, 280pp., 1986.

Prandle, D. Dynamics and exchanges in estuaries and the coastal zone. Coastal and Estuarine Studies, 40, American Geophysical Union, Washington DC, 647pp., 1992.

Sündermann J. and Holtz K.-P. (eds), Mathematical modelling of estuarine physics. Lecture Notes on Coastal and Estuarine Studies, 1. Springer-Verlag, 265pp., 1980.

2

The Response of Stratified Shelf Waters to the Leeuwin Current and Wind Forcing: Winter Observations off Perth, Western Australia

D. Mills, N. D'Adamo, A. Wyllie and A. Pearce

Abstract

Winter observations of the dynamic response and transport of stratified shelf waters off Perth, Western Australia are presented and discussed. These observations comprise cross shelf temperature, salinity and density structure measurements, wind and current time-series data, and satellite imagery from August 1991. Leeuwin Current water was identified over the outer shelf and slope as a thick buoyant layer which was 4°C warmer than nearshore water. Density generally decreased with distance offshore. The data reveal the responsiveness of the cross shelf density structure to meso-scale fluctuations of the Leeuwin Current, wind stress, and buoyancy fluxes due to surface heat transfer and freshwater inputs. In particular, two contrasting cross shelf density structures, separated in time by a typical winter wind cycle, are shown. In one case, cross shelf transport of coastal water was facilitated and in another it was inhibited. Southward and onshore wind stress assisted the shoreward migration of warm, buoyant Leeuwin Current water in a surface layer, and the associated cross shelf flushing of denser coastal waters in a bottom layer. In contrast, the circulation of meso-scale meanders of the Leeuwin Current is anti-cyclonic and we present a case of one such meander that forced northward flow over the shelf under weak wind conditions. In this case the mid shelf isopycnals were steeply-inclined due to upwelling, the relaxation of the density structure was opposed and cross shelf exchange was therefore inhibited. The satellite imagery revealed strongly coloured plumes of discharged estuarine water, which could be

Mixing in Estuaries and Coastal Seas
Coastal and Estuarine Studies Volume 50, Pages 5-28
Copyright 1996 by the American Geophysical Union

traced over distances of order 100 km along the shelf. From the hydrographic data we inferred that the estuarine outflows, initially low in salinity and buoyant, underwent mixing with denser inner shelf water and eventually became negatively buoyant relative to warmer, more saline outer shelf water.

Introduction

Current oceanographical studies of circulation and mixing processes over the continental shelf off Perth, Western Australia (Hearn, 1991; Pattiaratchi and Backhaus, 1992) are motivated by the need to understand transport pathways of anthropogenic wastes discharged to the nearshore marine environment in order to assess the long-term ecological effects of these discharges (Environmental Protection Authority, 1990, Simpson *et al.*, 1993).

This paper investigates the hydrodynamics and transport characteristics of the Perth coastal waters with reference to an August 1991 winter data set comprising *in situ* measurements and concurrent satellite imagery. These data are used to describe the cross shelf physical structure extending from shallow inshore waters (< 1 km offshore, 10 m depth) to beyond the continental shelf (85 km offshore) and to document variations in the density structure of the nearshore region (to the 35 m contour) at daily intervals over a typical winter meteorological cycle.

In winter, the Leeuwin Current advects warm water along the outer shelf and slope and enhances the cross shelf temperature and density gradients off Perth (e.g. Smith *et al.* 1991). Our data illustrate the influence of the Leeuwin Current and wind forcing on the response of the density structure over the shelf, the transport pathways of estuarine plumes, and the exchange between nearshore and offshore waters.

During August 1991 nutrient-rich water draining from rural catchments was stained by tannins during runoff and was then discharged via estuaries to the shelf. This enabled us to use water colour as well as salinity and temperature to interpret the mixing and advection of these discharges over the shelf. It also helped us to trace cross shelf transport and exchange between nearshore and offshore waters under several meteorological and oceanographical forcing conditions.

In winter, the monthly averaged wind stress vector is predominantly onshore with alternating periods (a few days in duration) of northward and southward longshore wind stress (Steedman and Craig, 1983, Breckling, 1989). Shallow (< 20 m) nearshore waters off the Perth region are strongly wind-driven (Steedman and Associates, 1981, Hearn, 1991, D'Adamo, 1992) and undergo corresponding longshore reversals in current direction. Since this may favour longer residence times of nearshore waters, it is important to consider the role and significance of cross shelf transport as a flushing mechanism for nearshore waters.

The Study Area and its Winter Characteristics

The continental margin off the coast of metropolitan Perth (Figure 1) has four zones: (1) a nearshore inner shelf zone of shallow (< 20 m) basins, lagoons and channels, partially enclosed by reefs and islands (2) a gently sloping mid shelf, approximately 30 km wide, extending from the outer reefs to the 50 m isobath (3) a more inclined outer shelf, deepening from 50 m to 300 m over a distance of 30 km, and (4) a continental slope. Depth contours beyond the inner shelf are generally smooth and shore-parallel, except around Rottnest Island which extends across the mid shelf, and a deep submarine canyon which cuts across the continental slope.

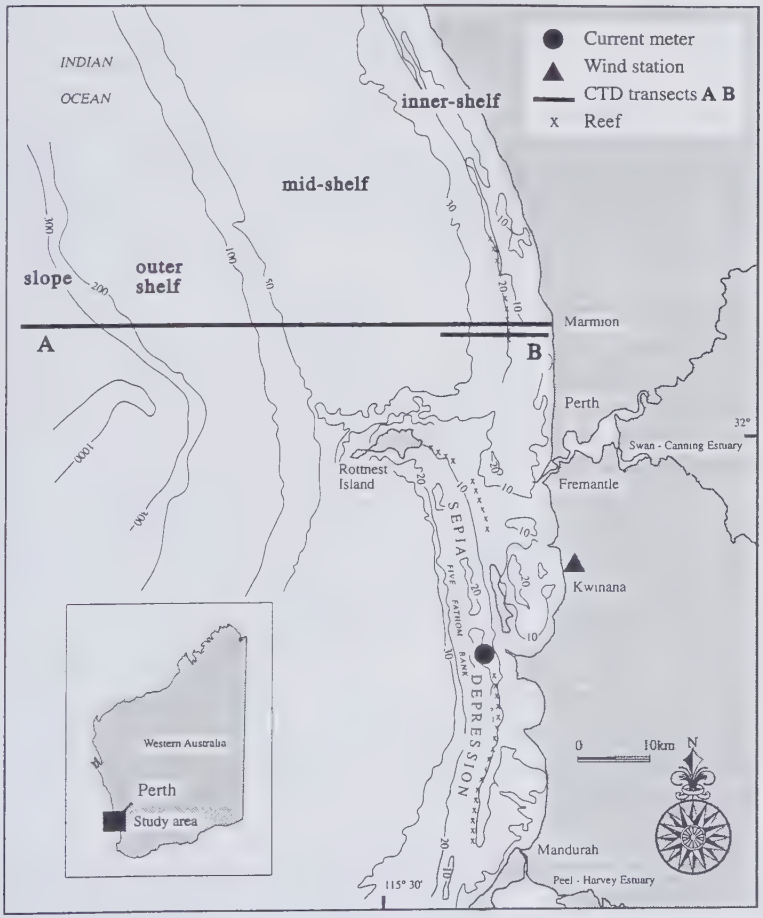

Figure 1. Bathymetry of the study area and the locations of main hydrographic lines and instruments.

The Leeuwin Current (e.g. Church *et al.* 1989, Smith *et al.* 1991) is a poleward surface flow of warm tropical water which is driven along the edge of the western continental shelf of Australia by a steric height gradient. The current intensifies in autumn and early winter when the opposing mean wind stress is weaker. Drifting buoy tracks (e.g. Cresswell and Golding, 1980) and satellite imagery (e.g. Legeckis and Cresswell, 1981, Pearce and Griffiths, 1991) show the common occurrence of mesoscale jets, undulations and meanders of the Leeuwin Current. The warm core meanders have strong anticyclonic circulation around their offshore frontal boundaries and are separated by intervening cold cyclonic gyres. The meanders may grow in offshore amplitude to more than 200 km, before pinching off to form detached eddies. On the landward side of some meanders, northward recirculating flow adjacent to the shelf has been documented by Pearce and Griffiths (1991). Pearce *et al.* (1985), Cresswell *et al.* (1989) and Pearce and Church (submitted) have shown that the mid and outer shelf off Perth is influenced by the Leeuwin Current.

In winter, weather systems passing over southwest Australia from the Indian Ocean consist of high pressure anticyclones, separated by cold fronts. Wind records from the study area show cycles, typically of 7-8 days, with episodic north-west to south-west winter gales associated with cold fronts, followed by longer periods of moderating and weak winds swinging through the south, east and north with the passing of high pressure systems (Steedman and Craig, 1983, Breckling, 1989).

The nearshore currents on the open shelf have typical speeds of order 0.1 ms^{-1} (Steedman and Craig, 1983). They are primarily wind-driven and bathymetrically controlled, with secondary influences from along shelf pressure gradients and baroclinic effects. In winter, current reversals occur typically at intervals of 3-5 days, in association with major wind shifts. The resultant monthly mean alongshore current component in winter is of order 0.01 ms^{-1} (Steedman and Associates, 1981).

The water level regime of south-western Australia has been summarised by Hearn (1991). The astronomical tides are mainly diurnal with an annual mean range of 0.5 m. Tidal currents are of order 0.01 ms^{-1}, with tidal excursions of order 1 km. Lower frequency oscillations in the coastal sea level are caused by barometric pressure, wind and oceanographic forcings, which together lead to elevation changes up to 0.5 m over a typical time period of 7 days. These oscillations are in part a direct sea-level response to variations in the barometric pressure and the associated wind stress fields (e.g. Harrison, 1983). They may also be due to the propagation of coastally-trapped waves (as suggested by Hamon (1966), Provis and Radok (1979) and Fandry *et al.* (1984)).

In winter, freshwater is discharged from the mouths of the Swan-Canning estuary (at Fremantle) and the Peel-Harvey estuary (at Mandurah) as plumes which may be transported along shelf for up to 100 km (Wyllie *et al.*, 1992, Simpson *et al.*, 1993). The volumes of freshwater discharge show strong interannual variation (Finlayson and McMahon, 1988) however they are not of sufficient magnitude to overcome the dominance of temperature on the density structure at shelf-scales.

Environmental Data - August 1991

Conductivity-temperature-depth (CTD) transect lines occupied during the period August 13-22, 1991 and the locations of a moored current meter and a wind station are shown in Figure 1. Vertical CTD profiles were taken from less than 1 km off the coast at Marmion to 85 km offshore (Transect A) on August 14 and 21. Transect B, approximately 16 km long, and extending offshore from the coast at Marmion to the 35 m contour, was monitored on August 13, 15, 16, 18, 20 and 22.

A CSIRO/Yeo-Kal Model 606 CTD meter was used for vertical profiling to a maximum depth of 300 m. A vector-averaging Neil Brown Acoustic Current Meter (ACM-2) measured inner shelf currents at mid-depth in a 20 m water column. Wind data (at 12 m) were gathered with Unidata sensors and logging system near the coast at Kwinana, approximately 20 km south of Perth. LANDSAT Thematic Mapper (TM) and NOAA AVHRR satellite images were acquired and processed using methods discussed in Wyllie *et al.* (1992) to complement the *in situ* measurements.

Time-series of meteorological, water level and nearshore currents for the period August 1-23, leading up to and including the duration of the oceanographic survey, are shown in Figure 2 and may be described as follows:

Wind:

Winter gale conditions prevailed from August 1-4. For 8 days leading up to the survey (August 5-12) and for the first two days of the survey (August 13-14) winds were variable and generally less than 5 ms^{-1}. From August 15-17 the wind swung through north to west, and freshened. August 18 saw the passage of a cold front and the onset of another winter gale, with west to south-west winds which reached a maximum speed of 14 ms^{-1} at 1800 hrs on August 19. The wind then subsided to about 7 ms^{-1} (south-west) by August 21. It swung to the south and south-east and weakened further to 3 ms^{-1} by August 23. These wind data are also presented in Figure 3(a) as a progressive vector plot, to illustrate the classical synoptic meteorological winter cycle (Breckling, 1989) experienced in the Perth region during the period of the oceanographic survey.

Barometric Pressure:

The barometric pressure time-series (Bureau of Meteorology, Perth) for August 1991 shows the passage of high and low pressure systems over the Perth region with periods of order 7 days. These pressure systems drive the mesoscale wind field and influence the water level.

Water Level:

The water level time-series at Fremantle (Department of Marine & Harbours) exhibited tidal variations characteristic of south-western Australia, i.e. diurnal components were dominant with an August spring tide range of about 0.8 m. Longer period oscillations (including energetic time scales of order 7 days) were also evident.

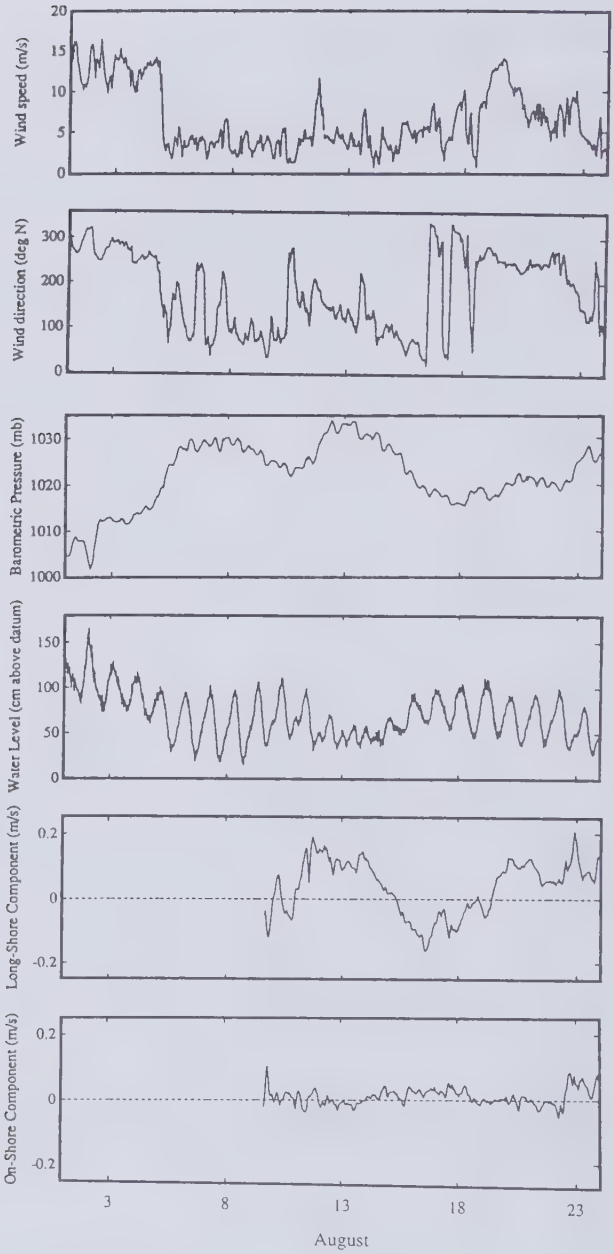

Figure 2. Time-series of wind at 12 m height at Kwinana, barometric pressure at Perth, water level at Fremantle, and mid-depth current in Sepia Depression for the period August 1-23, 1991.

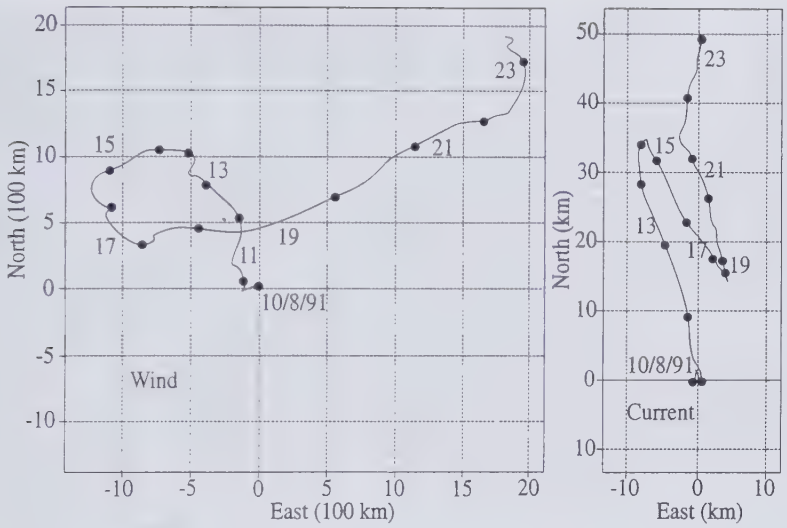

Figure 3. Progressive vector plots of (a) wind (12m) at Kwinana and (b) mid-depth current in Sepia Depression for the period August 10-23, 1991.

Current:

Near-shore currents measured at mid depth in the Sepia Depression (20 m) had a mean speed of 0.09 ms^{-1}. Current direction was predominantly longshore with alternating northward and southward current runs of about 3 days duration and about 30 km horizontally, subject to bathymetric constraints. As can be seen from the progressive vector diagrams of wind and current (Figures 3(a) and 3(b)) long-shore current reversals at this site responded rapidly to major reversals in the long-shore wind component.

Streamflow data and runoff calculations for ungauged catchment areas were combined to estimate freshwater flux to the coastal waters. The Swan-Canning estuary (pers. comm. F Davies, Water Authority of WA, G Bott, WADEP) and the Peel-Harvey estuary (pers. comm. D Deeley, Waterways Commission) each had mean August 1991 freshwater discharge rates to the ocean of about 60-70 $m^3 s^{-1}$.

Cross shelf Structure - August 14, 1991

Vertical profiles of water temperature, salinity and density were measured across the shelf and slope (Transect A, Figure 1) on August 14, 1991. The cross shelf structure of water properties was used, together with wind and current time-series data and satellite imagery, to interpret the dynamical response of the shelf waters to meteorological and oceanographical forcings.

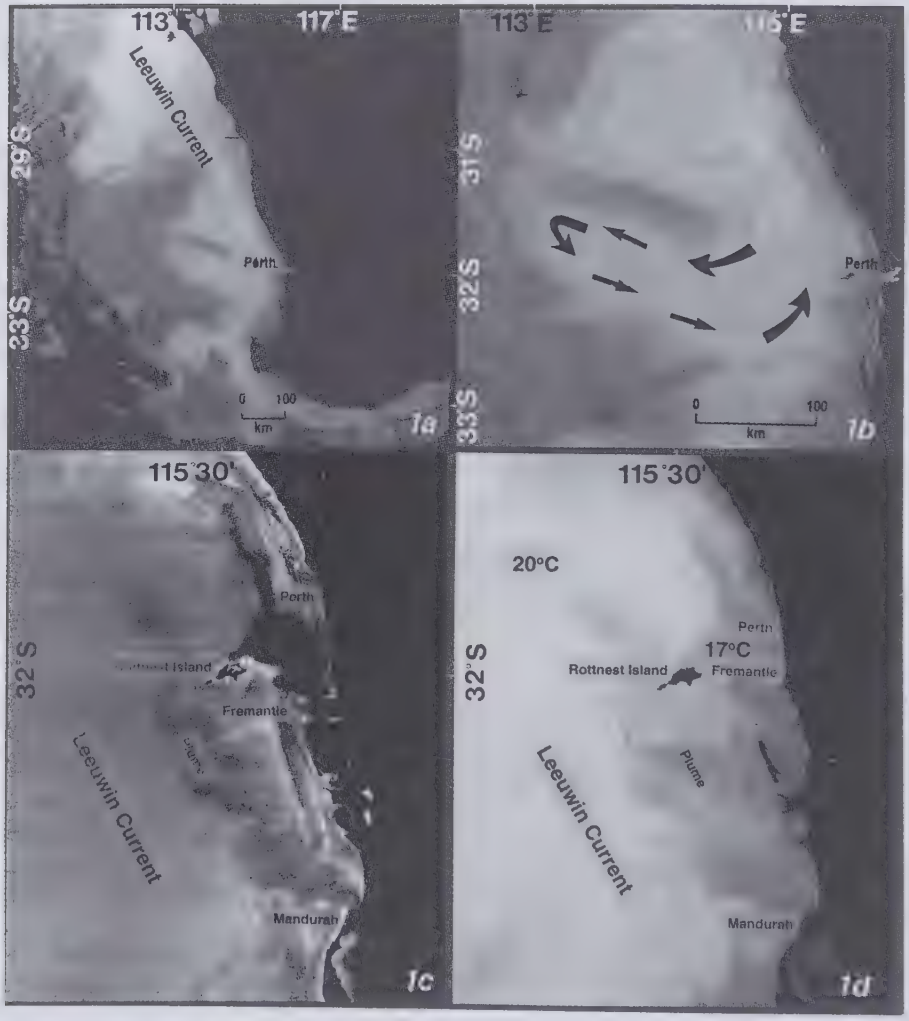

Plate 1(a) NOAA AVHRR imagery (sea surface temperature) for August 15, 1991 showing mesoscale features of the Leeuwin Current off the West Australian coastline.

Plate 1(b) NOAA AVHRR imagery (sea surface temperature) for August 15, 1991 showing mesoscale meanders and jets of the Leeuwin Current in relation to the study area.

Plate 1(c) LANDSAT Thematic Mapper (TM) imagery of the study area for August 14, TM bands 1,2,3 - (Blue, Green, Red).

Plate 1(d) LANDSAT Thematic Mapper (TM) imagery of the study area for August 14, TM band 6 - Thermal Structure.

Mesoscale Oceanographic Conditions

Cloud-free NOAA AVHRR imagery for August 15 (Plates 1(a) and (b)) shows two mesoscale, warm-core meanders of the Leeuwin Current extending to about 200 km seaward of the shelf break between the latitudes 30 and 33°S. Offshore, beyond the shelf, these meanders were separated by an elongated cold water gyre. Inshore of this gyre, over the shelf and slope, the meanders were linked together by a short poleward jet (Pearce and Griffiths, 1991) of the Leeuwin Current.

The southern meander was situated directly seaward of the study area and extended 80-100 km in a longshelf direction. The presence of smaller-scale billows on its western and southern fronts suggest that there was strong cross-frontal shear and anticlockwise circulation about the meander. CTD profiles were obtained from outer shelf and slope stations located within (the eastern side of) this meander. The salinity, temperature and density contours from these stations (Figure 4) indicated a depth scale for the meander of about 150 m. The NOAA imagery was used to estimate a horizontal density difference of 1.2 kg m^{-3} (ΔT~ 5°C) in 20 km across the offshore front of the meander. Hence the baroclinic shear differential was estimated from the thermal wind equation (e.g. Gill, 1982) to have been of order 1 ms^{-1}.

Shelf-scale Oceanographic Conditions

Plates 1(c) and 1(d) show the visible and thermal band LANDSAT images of continental shelf and slope waters off Perth for August 14, 1991. The thermal band image reveals a sea-surface temperature differential across the shelf of about 3°C, with warmer water (offshore) and cooler water (near the coast) separated by a distinct front. The warmest water (~20°C) was located at the eastern margin of the Leeuwin Current meander discussed above. The image also shows a tongue-like incursion of Leeuwin Current water across the mid shelf, north of Rottnest Island, and as a result of this the temperature front approached to within 15 km of the coast.

Plate 1(b) suggests that some of the anticlockwise flow returning shoreward on the southern side of the meander was subsequently recirculated northward over the outer shelf, while the remainder was diverted south as a continuation of the Leeuwin Current. Such behaviour was clearly identified by Pearce and Griffiths (1991) for a similar meander.

Plate 1(c), the visible band image, reveals the extent and trajectory of plumes emanating from the Peel-Harvey and the Swan-Canning estuaries. These plumes were strongly coloured by tannins, dissolved during freshwater runoff from the catchments. Upon discharge from the estuary mouths at Fremantle and Mandurah, the plumes initially spread offshore (to the west-north-west). Further away from their respective sources, they moved in a long shelf (northward) direction. Reference to Plate 1(d) shows that the plumes were bounded offshore by the temperature front. In the case of the Peel-Harvey plume this occurred near the mid shelf break. In the case of the Swan-Canning plume, it occurred within 15 km of the coast. These images indicate that plumes can transport estuarine water alongshelf up to 100 km away from source.

Physical Structure over the Outer Shelf and Slope - August 14, 1991

As shown in Figure 4, a warm, well-mixed, 140 m deep surface layer was situated over the outer shelf and slope. This has been identified in Section 4.1 as the eastern edge of an anti-clockwise circulating meander of the Leeuwin Current. Beneath this surface layer was a zone of strong vertical density stratification ($\Delta\rho$ =1.6 kg m^{-3}). At 245 m depth the density, salinity and temperature contours were horizontal, the salinity was maximum (35.85 pss) and the water properties were characteristic of South Indian Central Water, as reported by Rochford (1969). Above this level the isopycnals inclined upward toward the continental margin. The horizontal extent of this isopycnal deformation was about 30 km. This scales with the baroclinic Rossby radius (R = NH/f) calculated for the shelf slope, where the buoyancy frequency, N ~ 10^{-2} s^{-1}, the total depth, H ~ 300 m and the Coriolis parameter, f ~ -7.7 x 10^{-5} s^{-1}. The density structure therefore suggests upwelling supported by vertical shear flow to the north above a level of 245 m depth.

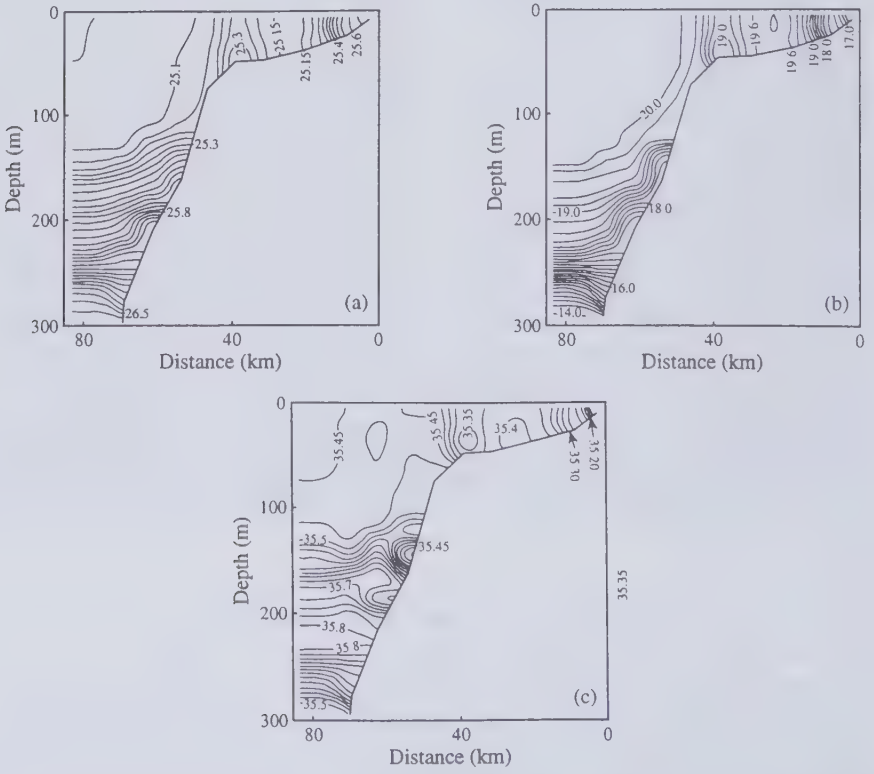

Figure 4. Cross shelf hydrographic section along Transect A from Marmion to 85 km offshore on August 14, 1991, showing (a) density structure (sigma-t contour interval 0.05 kg m^{-3}), (b) temperature structure (contour interval 0.2°C), and (c) salinity structure (contour interval 0.025psu).

Estimates of the baroclinic shear associated with an inclined density structure can be obtained from the thermal wind equation (e.g. Gill, 1982) as

$$\Delta v \sim -g\, \Delta\rho\, \Delta z/(\rho\, f\, \Delta x) \qquad (1)$$

where $\Delta v/\Delta z$ characterises the vertical gradient of the current component that is perpendicular to the density section, $\Delta\rho/\Delta x$ characterises the horizontal density gradient, g (= 9.8 ms^{-2}) is the gravitational acceleration, ρ (= 1025 kg m^{-3}) is a reference density and f (= -7.7×10^{-5} s^{-1}) is the Coriolis parameter. Applied to the upwelled density structure over the outer shelf and slope (where $\Delta\rho/\Delta x = 0.9 \times 10^{-5}$ kg m^{-4}, Δz = 100 m) equation (1) yields a northward flow of about 0.15 ms^{-1} near the base of the upper mixed layer (relative to an assumed level of no motion at 245 m).

Physical Structure over the Mid Shelf - August 14, 1991

The physical structure across the mid shelf (Transect A, Figure 4) exhibited a significant horizontal density differential (about 0.5 kg m^{-3}) and steeply-inclined density contours. Inner shelf waters, of lower temperature and salinity, were generally denser than surface waters over the outer shelf. The mid shelf structure of August 14 comprised the following main features:

(a) a steep density front ($\Delta\rho$ = 0.12 kg m^{-3}) situated at the mid shelf break, which delineated the warm, buoyant surface layer (the Leeuwin Current meander) from mid shelf waters; (b) a dense core of cooler, fresher water (local maximum σ_t = 25.34 kg m^{-3}) centred at the 50 m depth contour and partially overlain by lighter water, both from inshore and offshore; (c) a less dense mid shelf water mass with properties very similar to Leeuwin Current water; (d) a region of strong horizontal temperature and density gradient located about 15 km offshore, separating cooler, fresher coastal water from warmer water of off-shore origin.

The main features of the cross shelf hydrographic structure, listed above, can be identified by inspection of the LANDSAT imagery. Plate 1(c) shows that the darkly coloured estuarine plume from Mandurah travelled in an along shelf direction and intersected Transect A at the 50 m depth contour. The dense but slightly fresh core found at this location in the cross shelf structure was therefore identified as diluted plume water from the Peel-Harvey estuary, about one week after discharge and 80 km from its source. The initially buoyant, estuarine plume had mixed with cool, dense inner shelf water, reducing its salinity deficit, and had eventually become more dense than the warmer, outer shelf Leeuwin Current water.

The less dense, warm water mass on the mid shelf was identified from the satellite imagery as part of the tongue-like incursion of Leeuwin Current water, north of Rottnest Island. This warm water tongue was situated between the Peel-Harvey plume (to seaward) and coastal water (to shoreward). The shore-parallel Swan-Canning estuary plume was located immediately inshore of a sharp horizontal

temperature gradient zone (Plates 1(c) and 1(d)) which was identified but not finely resolved in the hydrographic structure of August 14.

The general picture across the mid shelf is therefore one of adjacent water masses of different density, including estuarine plumes, coastal waters and the Leeuwin Current. Contours were steeply inclined, with strong horizontal gradients and opposing density fronts. These local variations and slope reversals were associated with differential longshore advection, causing interleaving of distinct water masses, as also inferred from the LANDSAT imagery. Figure 5 provides a schematic representation of the LANDSAT images and the hydrographic section along Transect A for August 14.

For the 9 day period preceding this cruise, the mean wind speed was 3.7 ms^{-1} and winds seldom exceeded 5 ms^{-1} (Figure 2). D'Adamo (1992) showed that complete vertical mixing of mid shelf waters by such weak winds was unlikely under winter hydrographic conditions. The internal Rossby radius of deformation for the mid shelf ($\Delta\rho$ = 0.5 kg m^{-3}, H = 50 m) was about 5 km, much smaller than the width of the mid shelf itself. The steeply inclined density structure has therefore been interpreted as an upwelling response consistent with northward flow over the shelf, as recorded by the inshore current meter and indicated by the northward advection of estuarine plumes over the mid shelf.

Simple along shelf momentum balance calculations involving wind stress, along shelf pressure gradient and bottom stress suggest that a 5 ms^{-1} southerly wind opposed by an along shelf sea-surface gradient of order 10^{-7}, typical for the region in winter (Smith *et al.* 1991) would not be able to drive northerly flow of about 0.1 ms^{-1} over the mid shelf. It is therefore proposed that the offshore Leeuwin Current meander was mainly responsible for forcing the northward flow over the shelf and slope for several days prior to August 14. This forcing opposed gravitational relaxation of the inclined density structure and inhibited cross shelf transport. This probably occurred over a long shelf distance of about 100 km, commensurate with the dimension of the meander. The satellite imagery shows that the dense Peel-Harvey plume was constrained to travel along the mid shelf for a similar distance.

It is not possible at present to estimate the frequency and duration of events such as described in this section. However, Pearce and Griffiths (1991) showed that mesoscale features of the Leeuwin Current are common and that they tend to migrate only slowly. Smith *et al.* (1991) noted some mesoscale reversals in the long shelf pressure gradient off the Western Australian continental shelf and suggested that they may have been caused by the presence of mesoscale meanders and eddies of the Leeuwin Current.

Cross shelf Structure - August 21, 1991

The physical structure across the shelf and slope (Transect A) was again measured on August 21, 1991 and is discussed here with reference to complementary satellite imagery and available time-series data. This structure was in sharp contrast to that of August 14, 1991.

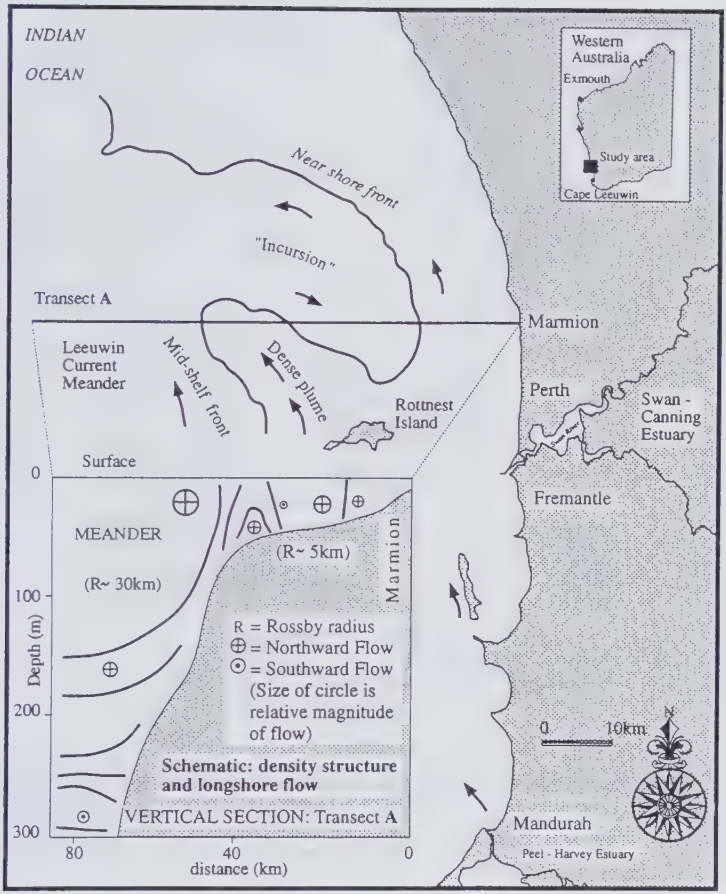

Figure 5. Schematic of the inferred flow structure for August 14, 1991, in the vicinity of Transect A, derived from Landsat TM imagery and the hydrographic section.

Mesoscale Oceanographic Conditions

A comparison of NOAA AVHRR images for August 15 and August 22 shows (Figure 6) that a significant change occurred during this period in the offshore mesoscale features associated with the Leeuwin Current. In particular, the two well-developed meanders migrated southward, and by August 22, the short Leeuwin Current jet linking the meanders was situated directly off the study area (Transect A). Hence, it is suggested that the northward flow over the outer shelf on August 14 had given way to southward flow a week later.

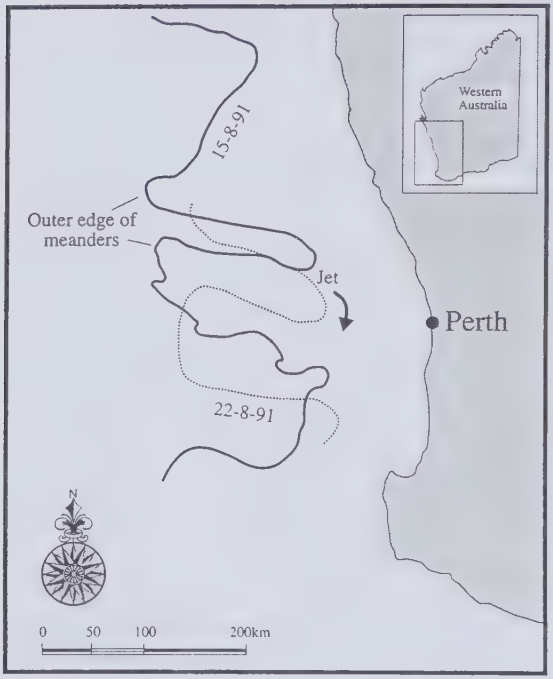

Figure 6. Outer edge of the mesoscale meanders and jets of the Leeuwin Current, showing southward migration over the period August 15-22, 1991. Data from NOAA AVHRR satellite imagery.

Meteorological Conditions

This period also saw the passage of cold fronts, which brought first northerly and then strong onshore winds for several days (see Figures 2 and 3). These winds became more southerly and moderated as the next high pressure system approached.

Physical Structure over the Outer Shelf and Slope - August 21, 1991

A warm well-mixed surface layer (the Leeuwin Current) overlaying a vertically stratified zone was again found on August 21, as shown in Figure 7. However, the structure was different to that of August 14 in that the contours of the pycnocline either deepened or remained nearly horizontal as they approached the outer shelf and slope. The upwelled structure of August 14 was gone, and replaced by an apparently downwelled structure on August 21. The onset of downwelling would

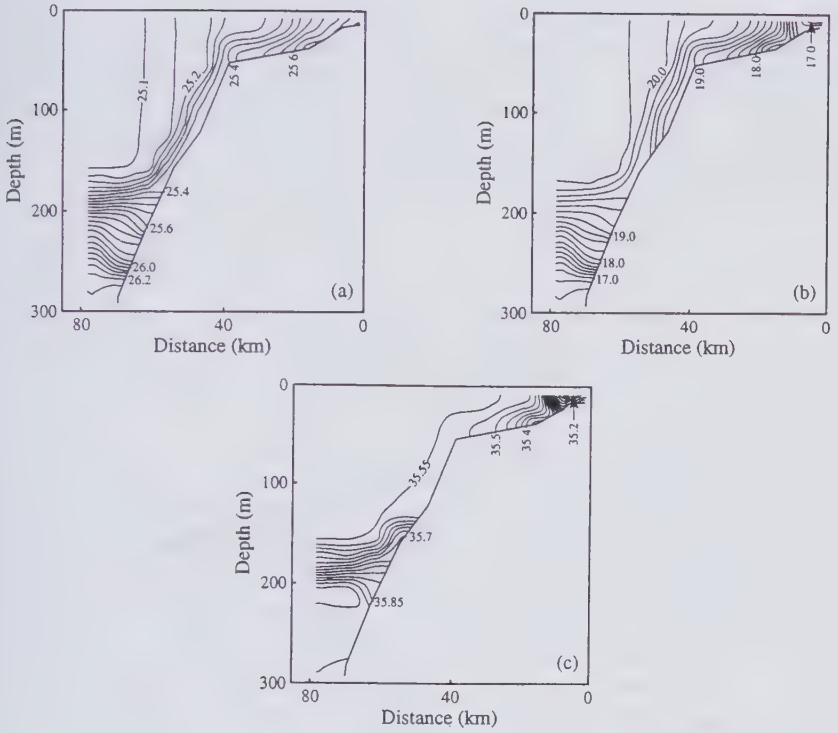

Figure 7. Cross shelf hydrographic section along Transect A from Marmion to 85 km offshore on August 21, 1991, showing (a) density structure (sigma-t contour interval 0.05 kg m^{-3}), (b) temperature structure (contour interval 0.2°C), and (c) salinity structure (contour interval 0.025 psu)

require a southward flow. Hence, the evidence presented above for a reversal from northward to southward flow over the outer shelf during this period is consistent with the observed change in the density structure.

Figure 7 also reveals a narrow zone of steeply inclined temperature, salinity and density contours adjacent to the outer shelf. This represents a baroclinically-enhanced leakage of cool, relatively fresh (but dense) water off the mid shelf, and would again be consistent with southward flow, downwelling and offshore Ekman transport in a bottom boundary layer.

Physical Structure over the Mid Shelf - August 21, 1991

By August 21 cooler, fresher, denser coastal water had moved off-shore across the mid shelf beneath warmer water (see Figure 7). The thermocline, halocline and

pycnocline were well-defined and horizontal at a depth of about 25 m delineating an upper mixed layer of constant thickness from a lower mixed layer thickening offshore. The horizontal salinity difference in the upper layer was small, indicating that Leeuwin Current water had moved shoreward and cooled, but had undergone minimal mixing with coastal water. In contrast, the lower layer exhibited a marked offshore salinity gradient, possibly the result of entrainment from the upper layer.

Discussion of Factors Leading to the Changed Structure of August 21

It has been shown that the structure across the mid shelf changed markedly over the period August 14-21, from a steeply inclined structure with strong cross shelf gradients and small vertical stratification to a distinctly two-layered structure. In this section we discuss a range of factors and processes which could have caused the observed structural change.

Interestingly, the steeply-inclined structure of August 14 occurred under very weak wind conditions, whereas the vertically-layered structure of August 21 formed under stronger wind conditions. From this we make two deductions. Firstly, wind-induced vertical mixing was unlikely to have been primarily responsible for the change in the vertical density structure across the mid shelf, although it may have contributed to the well-mixed nature of the upper layer (Figure 7). Secondly, the change of structure was unlikely to have been primarily due to a baroclinic relaxation, which normally occurs when there has been a reduction in energy available for vertical mixing. The horizontal length scale for baroclinic relaxation is the internal Rossby radius of deformation, which has already been shown to be much smaller than the mid shelf width. However the layered structure of August 21 extended right across the mid shelf.

Enhanced differential cooling, a reduction in freshwater flux, or a change to the density of outer shelf waters are factors which could have led to an increase in density differential across the mid shelf and hence to a change in the hydrographic structure. However the density differential would need to have increased by an order of magnitude for the internal Rossby radius of deformation to scale with the mid shelf width. Comparison of Figures 4 and 7 shows that this did not happen. It is therefore concluded that the observed change in structure was not primarily in response to a rapid increase in the density differential over the mid shelf.

The onset of a southward current over the mid and outer shelf during the period August 14-21 could possibly explain the development of the two-layered density structure over the mid shelf. In the absence of outer shelf current meter data, there are two pieces of evidence which suggest a reversion to a southward current: (a) comparison of NOAA satellite images from the beginning and end of the period show (Figure 6) that the short Leeuwin Current jet conveying southward flow between the two meanders had itself migrated southward, to be situated directly off Transect A; and (b) comparison of the density distributions for August 14 and August 21 shows the onset of a downwelling structure at about 200 m depth over the continental slope that is consistent with a southward flowing Leeuwin Current.

Southward flow would have induced secondary cross shelf circulation with shoreward transport above a compensating offshore Ekman transport near the sea bed. This circulation would have facilitated an exchange between buoyant Leeuwin Current water (moving landward in a surface layer) and dense coastal water (moving seaward across the mid shelf in a lower layer) over distances much greater than the local baroclinic Rossby radius of deformation. The following calculations were made to further examine this hypothesis. The Pollard, Rhines and Thompson (1973) expression for the mixed layer depth of a rotating, stratified fluid may be used to estimate the bottom shear velocity (u*) required to achieve a specified bottom mixed layer depth (h_{max}):

$$u^* = (Nf)^{1/2} h_{max}/2^{3/4} \quad (2)$$

At the 50 m depth contour the observed bottom layer depth for August 21 was 25 m. For a value of N ~ 10^{-2} s^{-1}, equation (2) gives u^* ~ 10^{-2} ms^{-1}, which would require a current speed ~ 0.2 ms^{-1}. A southward current with this bottom shear stress would lead to an offshore bottom Ekman flux of $\tau/\rho f = (u^*)^2/f$ ~ -1.5 m^2 s^{-1}. Dividing bottom Ekman flux by bottom mixed-layer thickness gives an offshore velocity estimate for the bottom layer of 0.06 ms^{-1}. For a midshelf width of ~ 20 km, this suggests an advective timescale for bottom water to traverse the mid shelf of about 4 days, which seems reasonable, given that the change in observed structure across the mid shelf occurred in less than 1 week.

Southward and then strong onshore wind stress, and an associated peak in coastal sea level (Figures 2 and 3) occurred in the week between the cross shelf transects. It is suggested that these forcings would also have driven onshore movement of warmer surface water and offshore underflow of denser coastal water. This will be further examined below.

Response of the Inner shelf Physical Structure to Forcings

The two contrasting cross shelf structures discussed above were separated by 7 days. More closely spaced CTD measurements of the inner shelf physical structure from the coast at Marmion to the 35 m depth contour (Transect B, Figure 1) were undertaken on August 13, 15, 16, 18, 20 and 22. These data are briefly examined here for three reasons: (a) they highlight the presence and mobility of a major nearshore temperature/density front; (b) they better resolve the transition between inner shelf and mid shelf density structure; (c) they indicate when the major change in cross shelf density structure was initiated.

The major near-shore density front was dominated by a sharp temperature gradient and formed the boundary between warm Leeuwin Current water, transported across the shelf, and coastal water. The coastal water was generally cooler, slightly less saline and more dense than the offshore waters. Plumes from the Swan-Canning estuary were sometimes detected as small surface cores in the density structures

along Transect B. These plumes overflowed the coastal waters, however they were generally less buoyant than the Leeuwin Current water to seaward of the major front. The cross shelf migration of the major near-shore front is now described and its response is discussed with reference to the history of wind forcing, the coastal water level and the near-shore flow.

Northward Nearshore Flow

On August 13 the front was near vertical, and located at the 30 m depth contour, 16 km offshore (Figure 8(a)). A similar inclination of density contours and location of the front was noted (Figure 4) in the cross shelf transect of August 14, under repeated conditions of northward nearshore flow and weak winds.

North to South Nearshore Flow Reversal

On August 15 the surface expression of the front was found to be within 8 km of the coast (Figure 8(b)). The front was less steeply-inclined than on the preceding two days, but still extended from top to bottom of the water column, meeting the seabed at the 30 m depth contour. The longshore wind component and the nearshore current slowed and reversed direction on August 15. Warm water was found 8 km closer to the coast along Transect B.

Southward Nearshore Flow

The southward nearshore current strengthened from August 15 to 16 under the influence of a strengthening southward wind stress component. CTD data from the August 16 transect (Figure 8(c)) shows that the surface front had moved a further 2 km onshore.

South to North Flow Reversal and Strong Onshore Wind

Figure 8(d) shows that by August 18 a marked structural change had occurred. The surface front had moved to within about 2 km of the coast. Further offshore the front had been depressed to a horizontal density interface 25 m below the water surface, delineating a lower layer of relatively cool, less saline water which extended offshore beyond the 35 m depth contour from a warm upper layer. August 18 saw the cessation of northwesterly winds and the commencement of strong onshore winds (Figure 3). The southward near-shore current decelerated rapidly prior to reversal (on August 19) from southward to northward flow. The recent history of southward and strong onshore wind stress, and the associated rise in coastal sea level (Figure 3) appears to have combined to force onshore movement of warmer surface water and offshore underflow of denser coastal water.

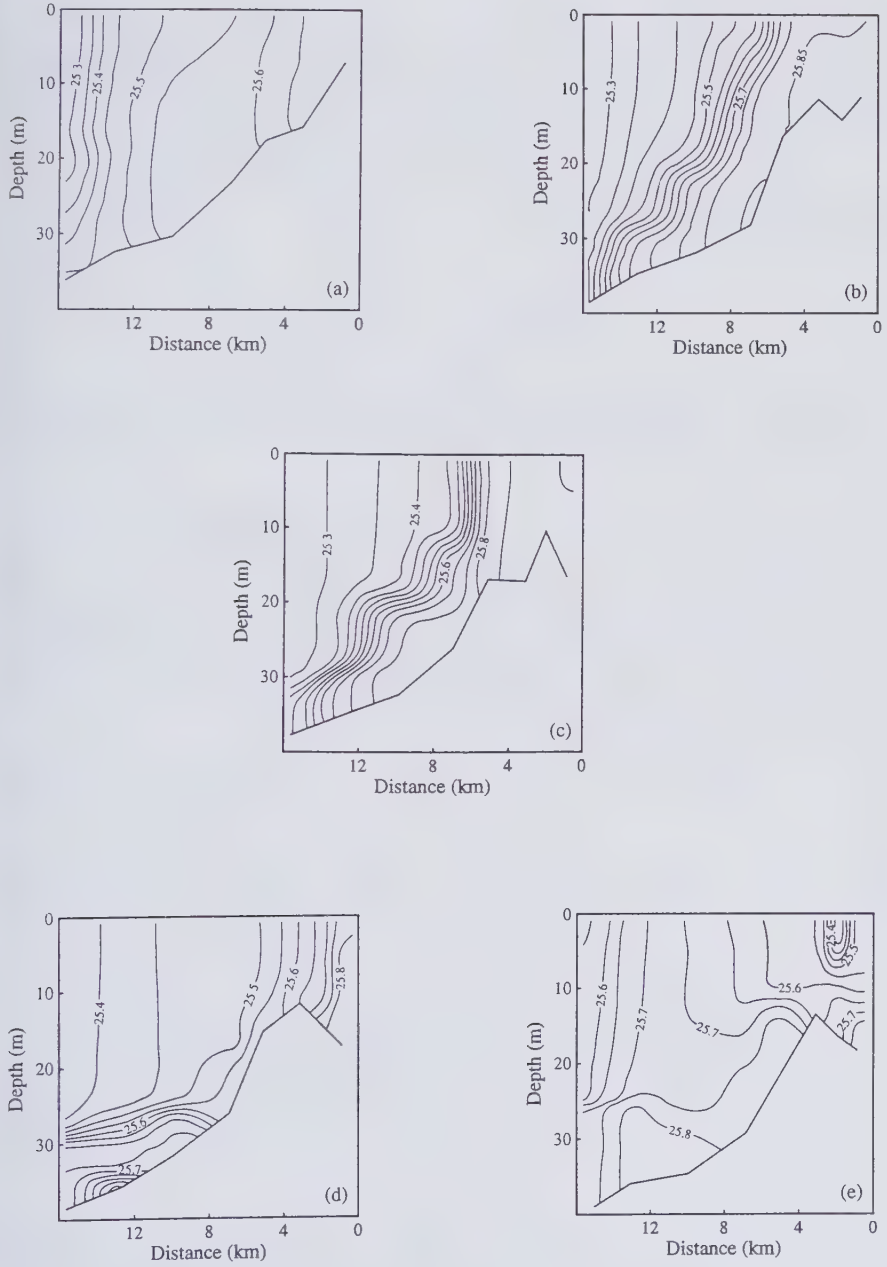

Figure 8. Cross shelf density sections (sigma-t contour intervals 0.05 kg m^{-3}) along Transect B from Marmion to 16 km off-shore, for (a) August 13, (b) August 15, (c) August 16, (d) August 18, and (e) August 22, 1991.

In addition to the coastal downwelling process just described, wind mixing would also have contributed to producing the observed structure. An estimate of mixing to 20 m depth was calculated from the theory of Pollard, Rhines and Thompson (1973) for the 10 hour, 8 ms^{-1} wind event (August 17/18) that preceded the CTD measurements. However the salinity and temperature properties of the density interface at 25 m depth remained essentially the same as for the near shore front on preceding days, suggesting that coastal downwelling was the principal process involved in the structural change.

Northward Nearshore Flow and Onshore Wind Stress

By August 20, the wind was still onshore, but with a clear northward component, and the nearshore current was to the north at about 0.1 ms^{-1} (Figure 3). The surface front had moved offshore more than 10 km (water depth >30 m) beyond the outer profile station occupied on that day.

The cross shelf structure measured along Transect A on August 21 has been documented in section 5. The near-shore zone of the transect (to the 20 m contour, ~10 km offshore) possessed considerably lower salinity due to northward advection of the Swan-Canning estuary plume. Further off the coast, a well defined horizontal density interface at about 25 m depth extended from 10 km offshore (30 m depth contour) across the mid shelf to the mid shelf break. This is reminiscent of the feature formed by coastal downwelling on August 18.

By August 22 the wind was swinging to northward and the nearshore current was also to the north. Figure 8(e) reveals that the surface front was located 14 km offshore (35 m contour). It was essentially vertical down to 22 m, at which depth it became horizontal and extended offshore. This suggests that the lower layer was still present over the mid shelf. Nearer to the shore is cooler, low salinity water associated with a newly introduced northward flowing Swan River plume. This generated a buoyant structure in the coastal zone, but it was not buoyant enough to override Leeuwin Current water.

Based on the chronology of the front outlined in this section, it is likely that the lower layer cross shelf transport of coastal water was initiated on August 17 or 18. A cross shelf advection of 25 km in 3-4 days equates to a cross shelf velocity of order 0.05 ms^{-1}.

Conclusions

This paper shows that mesoscale features of the Leeuwin Current, such as meanders and jets, may significantly influence the response of adjacent continental shelf waters. A well-developed anticlockwise circulating meander of the Leeuwin Current

was situated off the Perth shelf for several days prior to our measurement period. Winds had been very light and variable for the preceding 10 days. The cross shelf hydrographic structure of August 14 revealed a transverse baroclinic upwelling response of the pycnocline between 140-240 m depth over the outer shelf. Estimates of the vertical shear required to support this upwelled density structure were derived from the thermal wind equation. On this basis a northward flow of about 0.15 ms^{-1} at the eastern edge of the Leeuwin Current meander was inferred. Pearce and Griffiths (1991) have previously documented northward recirculating flow on the landward side of such meanders. Light, variable winds over the preceding 10 days were considered too weak to have induced the observed upwelling response over the outer shelf, which we attributed to the recirculating flow of the offshore meander. The mid shelf structure of August 14 was characterised by steeply-inclined density contours and marked horizontal density gradients, with density decreasing in the offshore direction. The preceding period of light winds suggests that upwelling, rather than vertical wind mixing was responsible for the perturbed mid shelf density structure.

Strongly coloured plumes of discharged estuarine water were revealed by the satellite imagery. These plumes could be traced over distances up to 100 km long shelf. From the hydrographic data we inferred that the estuarine outflows, initially low in salinity and buoyant, underwent mixing with denser inner shelf water and eventually became negatively buoyant relative to warmer, more saline outer shelf water. The upwelled density structure of August 14 inhibited cross shelf transport of these relatively dense plumes which were advected northward along the shelf and remained shoreward of steeply-inclined density fronts marking the eastern edge of the Leeuwin Current meander. Under these conditions, the plumes mixed slowly, showing low rates of dilution.

Between August 14 and 21, significant changes occurred both in oceanographical and meteorological conditions. By the end of this period the two well-developed Leeuwin Current meanders had migrated southward and the short section of Leeuwin Current jet flow linking the meanders was situated directly off the study area. Hence it is suggested that the northward flow adjacent to the Perth shelf on August 14 had given way to southward flow a week later. Longshore wind stress was southward from August 15-17 and this was followed by onshore wind stress from August 18-21. The movement of a major density front was tracked across the inner shelf during this week. By August 18 it had approached to within 2 km of the coast, and had undergone coastal downwelling, which led to the formation of a dense lower layer of cooler, less saline water, extending offshore beyond the 35 m depth contour.

By August 21 the cross shelf density structure displayed depression of the pycnocline over the outer shelf and slope, and a two-layer vertical structure which extended across the mid shelf. The formation of the two-layer mid shelf structure was indicative of cross shelf exchange, with warm, offshore water moving landward in the surface layer and cooler, fresher water moving seaward in the bottom layer. The estimated time scale of about 4 days for establishment of the two-layer density

structure, observed over the mid shelf on August 21, was consistent with the observed formation of the lower layer on August 18.

The vertically-stratified mid shelf structure of August 21 evolved in the presence of strong wind forcing, whereas the steeply-inclined structure of August 14 evolved in the presence of weak wind forcing. We have discussed various mechanisms in an attempt to explain the observed changes in mid shelf structure and the cross shelf transport of coastal water. Neither vertical wind mixing nor baroclinic relaxation appear to be primary mechanisms. However downwelling associated with a poleward Leeuwin Current jet flow (Thompson, 1987, Smith *et al.*, 1991), Ekman adjustment over the mid shelf in response to southward wind stress (Csanady, 1982) and direct shoreward wind-driven surface advection due to strong onshore winds appear to have been primary contributors to the observed changes. In the presence of the density differential across the shelf, these mechanisms would explain the observed two-layer structure.

Acknowledgements Many people helped in gathering and processing the data. In particular we wish to thank Mr Andrew Sanders (WADEP) and Mr Bob Griffith (CSIRO) for their assistance in instrument preparation, deployment. and data processing. The Department of Marine and Harbours provided a vessel and crew. The Remote Sensing Applications Centre, Department of Land Administration provided facilities for the processing of satellite imagery. The Centre for Water Research (CWR) at the University of Western Australia kindly provided software for processing and contouring CTD data. Mr Don Wallace and Mr Grant Ryan (Department of Marine and Harbours) supplied water level and wave data for August 1991. Mr Greg May (Water Authority of Western Australia) and Mr David Deeley (Waterways Commission) assisted with the provision of streamflow data. Dr Ken Rayner and Mr Peter Mountford (WADEP) gave advice and assistance with meteorological data. Dr Peter Craig and Professor David Wilkinson are particularly thanked for providing useful comments on an early draft of the paper.

References

Breckling, J. The analysis of directional time series: Applications to wind speed and direction. In *Lecture Notes in Statistics* - 61. Springer-Verlag. 231pp, 1989.

Church, J.A., G.R. Cresswell and J.S. Godfrey. The Leeuwin Current. In *Poleward Flows along Eastern Ocean Boundaries*, edited by S. Neshyba, C.N.K. Mooers and R.L. Smith, 379 pp, Springer-Verlag New York Inc., 1989.

Cresswell, G.R. The trapping of two drifting buoys by an ocean eddy. *Deep Sea Res.* 24, 1203-1209, 1977.

Cresswell, G.R. and T.J. Golding, Observations of a south-flowing current in the south-eastern Indian Ocean. *Deep-Sea Res.* 27A:449-466, 1980.

Cresswell, G.R. The Leeuwin Current - observations and recent models. In *The Leeuwin Current: an influence on the coastal climate and marine life of Western Australia*, edited by A.F. Pearce and D.I. Walker). *J. Roy. Soc.* WA 74:1-14, 1991.

Csanady, G.T. *Circulation in the Coastal Ocean.* D. Reidel Publishing Company, Dordrecht, 279 pp., 1982.

D'Adamo, N. Hydrodynamics and recommendations for further studies in Cockburn Sound and adjacent waters. Technical series 41. *Environmental Protection Authority*, Perth, Western Australia, 100pp., 1992

Environmental Protection Authority. Proposed Beenyup wastewater treatment plant and ocean outfall duplication into Marmion Marine Park. Bulletin 393 *Environmental Protection Authority*, Perth, Western Australia, 16pp., 1990.

Fandry, C.F., Leslie, L.M. and R.K. Steedman, Kelvin-type coastal surges generated by tropical cyclones. *J. Phys. Ocean.* 14, 582-593, 1984.

Finlayson, B.L. and T.A. McMahon, Australia vs the World, a comparative analysis of streamflow characteristics. In *Fluvial Geomorphology of Australia*, edited by R.F. Warner, pp. 17-40, Academic Press, 1988.

Gill, A.E. *Atmosphere-Ocean Dynamics*. Academic Press, New York. 662 pp, 1982.

Hamon, B.V. Geostrophic currents in the south-eastern Indian Ocean. *Aust. J. Mar. Freshw. Res.* 16, 255-272, 1965.

Hamon, B.V. Continental Shelf waves and the effects of atmospheric pressure and wind stress on sea level. *J. Geophys. Res*. 71, 2883-2893, 1966.

Harrison, G.E. Low frequency sea level oscillations along the Western Australian coastline. M.E. Thesis, University of Western Australia, 1983.

Hearn, C.J. A review of past studies of the hydrodynamics of Cockburn sound and surrounding waters with an appraisal of physical processes and recommendations for future data collection and modelling. Report to the Environmental Protection Authority, Perth, Western Australia, 75pp, 1991.

Legeckis, R. and G.R. Cresswell, Satellite observations of sea-surface temperature fronts off the coast of western and southern Australia. *Deep Sea Res.*, 28, 297-306, 1981.

Pattiaratchi, C.B. and J. Backhaus, Circulation patterns on the continental shelf off Perth, Western Australia. Application of a 3D baroclinic model. *Proceedings of the Sixth International Conference on Physics of Estuaries and Coastal Seas*, Margaret River, Western Australia, 8-10 December 1992, 231-234, 1992.

Pearce, A.F. and J.A. Church (submitted) A coastal heat and salt budget using seasonal temperature and salinity data off Perth, Western Austrtalia, submitted to Continental Shelf Research.

Pearce, A.F. and R.W. Griffiths The Mesoscale structure of the Leeuwin Current. *J. Geophys Res.* C96:16739-16757, 1991.

Pearce, A.F. and Phillips, 1990 Oceanic processes, Puerulus settlement and recruitment of the Western Rock Lobster *Panulirus cygnus*. Boden Research Conference on Interdisciplinary Approaches to Dispersal and Recruitment Processes in the Marine Environment, Thredbo

Pearce,A.F., R.E. Johannes, C.R. Manning, D.W. Rimmer and D.F. Smith. Hydrology and nutrient data off Marmion, Perth, 1979-1982. CSIRO Marine Laboratories Report 167, 1985.

Pollard, R.T., P.B. Rhines and R.O.R.Y. Thompson. The deepening of the wind-mixed layer, *Geophys. Fluid Dynamics*, **3**, 381-404, 1973.

Provis, D.G. and R. Radok. Sea level oscillations along the Australian coast. Aust. J. Mar. Freshw. Res. 30 295-301, 1979.

Rochford, D. Seasonal variations in the Indian Ocean along 110°E. 1. Hydrological structure of the upper 500m. *Aust. J. Mar. Freshw. Res.*, 20, 7-30, 1969.

Simpson, J.E. Gravity currents in the laboratory, atmosphere, and ocean. *Ann. Rev. Fluid Mech.* 14, 213-234, 1982.

Simpson, C.J., J.S. Burt, J.L. Cary, N. D'Adamo, R.J. Masini and D.A. Mills Southern Metropolitan Coastal Waters Study (1991-1994) Progress Report August 1993. Technical Series 53. *Environmental Protection Authority of Western Australia*, Perth, Western Australia. 65pp, 1993.

Smith, R.L., A. Huyer, J.S. Godfrey and J.A. Church, The Leeuwin Current off Western Australia, 1986-1987. *J. Phys. Oceanogr.* 21: 323-345, 1991.

Steedman, R.K. and Associates, Cape Peron wastewater ocean outlet effluent dispersion studies, Unpublished report prepared for Binnie and Partners, 1981.

Steedman, R.K. and P.D. Craig, Wind-driven circulation of Cockburn Sound. *Aust. J. Mar. Freshw. Res.* 34, 187-212, 1983.

Thompson, R.O.R.Y. Continental shelf-scale model of the Leeuwin Current. *J. Mar. Res.* 45, 813-827, 1987.

Wyllie, A., A. Buchanan, N. D'Adamo, D. Mills and A. Pearce. The use of Landsat Thematic Mapper and NOAA AVHRR for environmental investigations of the Perth metropolitan coastal waters. *Proceedings, 6th Australasian Remote Sensing Conference*, 2-6 Nov, 1992, Wellington, New Zealand, 3, 203-208, 1992.

3

Measurements of the Wave, Current and Sea Level Dynamics of an Exposed Coastal Site

K. Black, M. Rosenberg, G. Symonds, R. Simons, C. Pattiaratchi, and P. Nielsen

Abstract

Field studies were undertaken at a coastal location (Bass Strait) to investigate the interaction of waves and currents and to establish relationships between nearshore and offshore wave parameters, including friction in mixed wave/current environments. The area is characterised by moderate tidal currents (maximum spring flow of about 0.18 ms^{-1}) and wave energy (H_s and T_s of about 2 m and 10 s respectively).

Wave-recording electromagnetic current meters were deployed along a 13 km shore-normal transect at 3 sites of depth 20, 40 and 50 m. Six week deployments during winter and summer were made with current meters at up to four levels above the bed at each site. At the inshore site, suspended sediment monitors and a video camera were deployed on a frame lowered to the sea bed. The underwater video camera was used to specify the sediment threshold and the changing nature of the bedforms. In addition, to determine the bed roughness along the cross-shelf transect, the sea bed was observed using ship-borne video at 23 sites 400-800 m apart. Bed characteristics were also observed at an additional 103 sites in the surrounding regions. The fall velocity and grain size of the bed sediments from these sites were determined using settling tube analyses.

The interaction of waves and currents and the frequency attenuation of the wave spectrum with distance below the surface is considered to be responsible for a belt of coarser sands and larger bedforms identified at 30-45 m depth. The sediments were

Mixing in Estuaries and Coastal Seas
Coastal and Estuarine Studies Volume 50, Pages 29-58
Copyright 1996 by the American Geophysical Union

finer and the bedform heights were smaller both shorewards and offshore of this region. A thermocline was common in summer and up to 4 °C temperature differences were observed between the bed and near the surface in 40 m depth. Using multiple regression, 68% of the temperature gradient could be explained by 3 variables; air temperature, wind stress and wave orbital amplitude. Near the bed, 98% of the temperature variation over the 6-week measurement period could be explained by temperatures at a site to the west plus the longshore, cross-shore and vertical temperature gradients. The vertical gradient was the most important. Wind-induced stirring eliminated the thermocline and caused the bottom layer temperature to rise sharply as upper level water mixed with the lower layer.

The dynamics of the coastal environment and the changing magnitude with depth of the various current components is considered. Wave refraction diagrams and velocity profile measurements are used to examine the interaction of the waves and currents, including their joint effect on the development of bed roughness and near-bed shear stress during storms.

Introduction

Shelf sediment transport and hydrodynamic research has progressed rapidly in the last 30 years. The use of better measurement techniques (Sternberg and Creager, 1965; Cachione and Drake, 1979), the collection of more data sets (Wiberg and Smith, 1983; Amos *et al.*, 1988) and improved theoretical development (Grant and Madsen, 1979) have resulted in a greater understanding of wave/current interaction in natural environments and of the relationship between sediment transport and local hydrodynamics. Independent of the fine-scale studies, wind-forced motion (Gordon, 1982), coastal-trapped waves (Middleton and Viera, 1991) and geostrophic response (Burrage *et al.*, 1991) have been investigated on many continental shelves around the world.

With these developments, however, the need for detailed and comprehensive field measurements remains. In particular, measurements are needed to validate wave/current interaction formulae in natural conditions and to allow for feedback due to the response of the sea bed in a non-steady environment (Black and McShane, 1990). In natural conditions, adjustments of the sea bed may occur rapidly with changing current and wave conditions. The dependence of vertical shear on vertical eddy viscosity or bed shear stress can be a crucial balance which may help to determine net sediment transport at the bed and dispersal on the continental shelf.

Typically, the most dynamic region lies above the mud depositional limit at about 50 m (Smith and Hopkins, 1972). In this zone, the wave/current interaction becomes more important as the depth decreases and the temporal response of the sea bed equally becomes more dynamic.

We established two field measurement programs, in winter and summer, to record the horizontal and vertical circulation and sediment dynamics between the 20 and 50 m contours of the continental shelf in east Gippsland, in southern Australia. The

region is exposed to ocean wave attack and experiences both tidal and low frequency currents due to winds, barometric pressure and coastal-trapped waves. Sediments in the east Gippsland region are sandy and mobile above the 45 m contour. As such, the measurements presented in this paper are generally applicable to many open coastlines worldwide.

A number of similar studies have been undertaken (see the summary in Cachione and Drake, 1990 for example). However, few studies have been able to record currents both horizontally across the shelf and at various vertical levels above the bed while simultaneously measuring suspended sediment concentration, and sediment mobility with underwater video, in conjunction with a regional bedform and grain size survey. The measurements were unified in a 3-dimensional numerical hydrodynamic model which helped to specify the relationships between continental shelf hydrodynamics and the nature and scale of bed sediment transport.

A simultaneous investigation of the biological characteristics of the region (Parry *et al.*, 1990) provided the basis for a broad environmental assessment and established the foundation for linked studies of continental shelf hydrodynamics, dispersal and the ecology of the region.

Detailed descriptions of the data from the physical field program are presented in Black *et al.* (1991a,b; 1992). The adaptation of numerical models of the hydrodynamics and dispersal are described by Black and Hatton (1992). In this paper, we present the scope of the field study and examine the dynamics of the continental shelf. A number of topics are considered including the wave refraction, bed friction and the link between bedform character and depth across the continental shelf. This paper serves to summarise the interesting features of the data sets. More detailed studies of particular aspects of the data are being undertaken, and these will form the basis of future publications.

Study Region and Field Site

The rectangular-shaped study region lies offshore of Ninety Mile Beach in East Gippsland, Victoria, along 75 km of coastline between Lakes Entrance in the west and Pearl Point in the east, and extending 30 km offshore (Figure 1a). The coastline, popular for recreational use, consists of fairly straight sandy beach, backed by dunes, with the only major headland at Cape Conran in the east. Estuaries are found within the region at Lake Tyers and also at Marlo where the Snowy River flows into the sea. Immediately to the west is the entrance to the very large system of estuarine waterways known collectively as the Gippsland Lakes (Figure 1a).

The continental shelf to the southwest widens at the entrance to Bass Strait, while to the southeast, the continental slope drops abruptly towards the Tasman Abyssal Plain. Within the study region, the bathymetry drops smoothly from the coast to a broad platform lying between 40-55 m depth. This platform narrows to the east, with steeper bathymetry found to the southeast of the region. Near the measurement sites, the depth contours are approximately shore parallel.

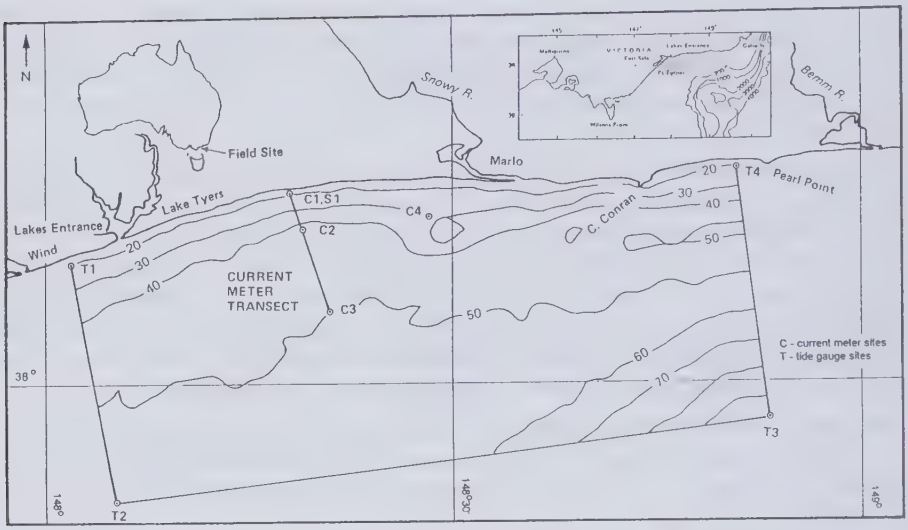

Figure 1a. Field site location in southern Australia, showing details of bathymetry within the study region, and in the surrounding region of eastern Bass Strait.

Field Measurements

Tidal and Current Measurements

Three current meter and four tide gauge stations were monitored during two 6-week deployments in the winter of 1990 and the summer of 1991 (Figures 1a and 1b). These were denoted as the A and B series respectively. The instrument layout was designed to specify the (i) tidal behaviour (ii) sea level response to coastal currents (iii) cross-shelf gradient in current and (iv) the influence of wave action on the circulation. Placed in intermediate water depths on the continental shelf, the instruments measured tidal and coastal currents, wave orbital motion, sea levels, temperatures and conductivity. The last two specified the salinity.

Tide gauges were deployed at the corners of the approximately rectangular study region (Sites T1-T4) (Figure 1a). Up to 4 vector-averaging current meters at different elevations above the sea bed were placed at each of the 3 current meter sites (C1-C3) in approximate depths of 20, 40 and 50 m respectively (Figure 1b). One additional tide gauge was placed at Site C3 during the 1990 data collection period, and an additional current meter was deployed in October 1990 within the study region at Site C4 (Figure 1a). The winter and summer series are denoted in the site name by a preceding A or B. The distance of the meter above the sea bed is included in the name after a "slash". Thus, measurements from Site C1, winter series at 3 m above the bed are denoted as AC1/3.

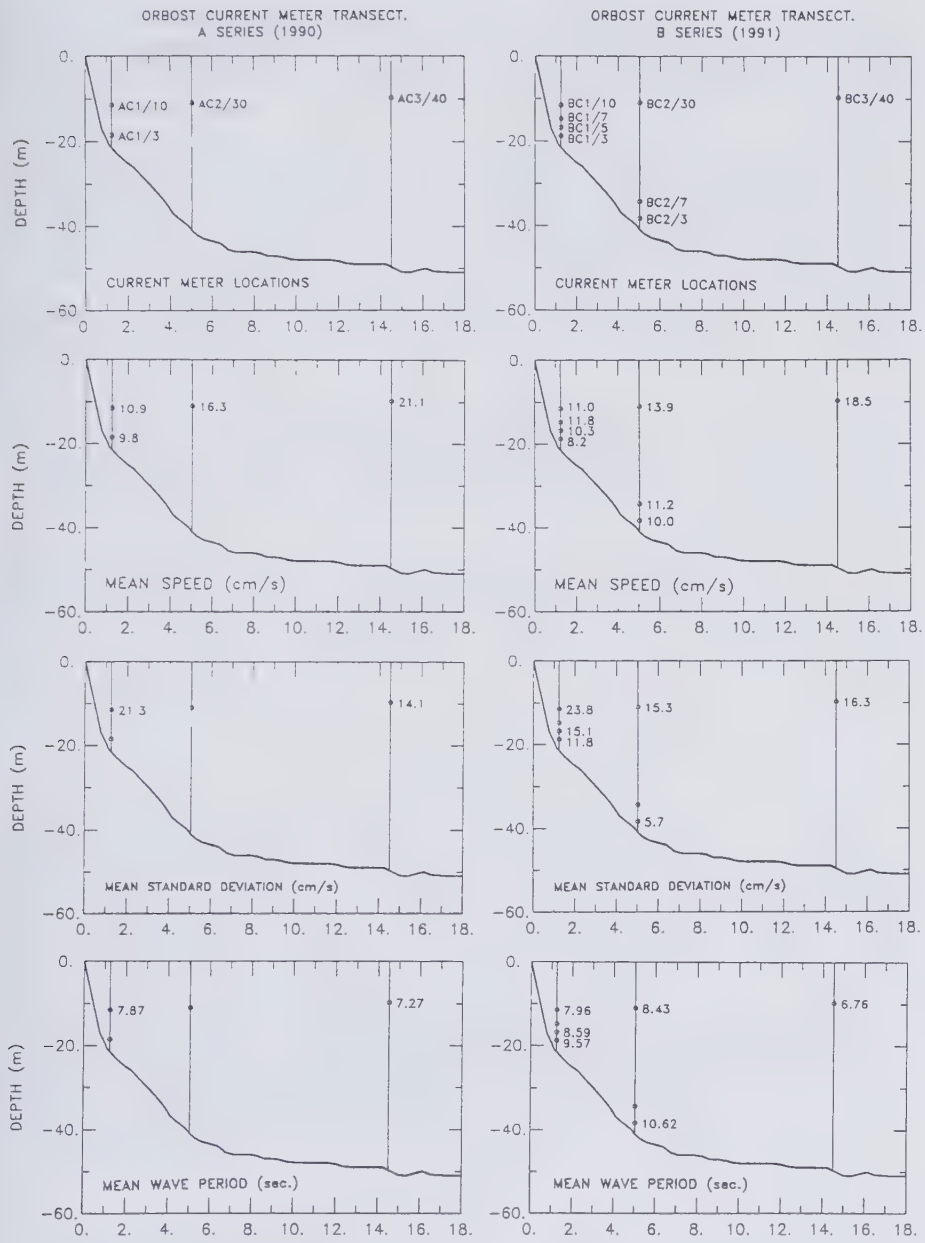

Figure 1b. Instrument positions, mean current speeds (record averages), mean of the standard deviation of the bursts, mean wave period during the A (winter) and B (summer) series.

Tides were recorded with Aanderaa WLR5 and one TG3A high-resolution digital quartz pressure sensors. The current meters were vector-averaging Neil Brown acoustic or S4 electromagnetic instruments, suitable for locations with surface waves.

The instruments were mostly deployed in vertical mooring strings (Figure 1b). The two offshore tide gauges were within 1.5 m of the bed on the mooring and buoyancy was large to ensure rigidity and low tilt. The two tide gauges nearest the coast were placed in frames mounted on the bed.

Waves

Wave orbital motion was recorded with the S4 electromagnetic current meters operating in burst mode. Instantaneous currents measured at 0.5 second intervals were averaged over 2 second periods during measurement bursts of up to 9 mins, a sufficient time to sample most of the variability due to wave groupiness. The bursts were at intervals of up to 6 hours.

The current meter transect lies within a region of relatively subtle bathymetric variability in the longshore direction. The effect of wave refraction on the measurements was small and relatively uniform in the longshore direction (see below).

In situ Suspended Sediment Measurements

Suspended sediment concentration and the sediment threshold were monitored in situ during both the A and B deployments at Site C1 at 20 m depth. A self-contained underwater unit (SEDCAM) was developed which housed a video camera for observations of bed mobility, and either one or two optical backscatterance sensors (OBS, Downing, 1984) to measure suspended sediment concentrations. These instruments were suspended on a frame above the sea bed to minimise the interference to flow at bed level. Nearby current meters measured both the wave orbital motion, and the lower frequency coastal and tidal currents. Internal timing circuitry allowed the OBS sensors and video camera to record in "bursts", over deployment periods of up to 6 weeks. The calibration of the OBS sensors is detailed by Black *et al.* (1991b).

Sediment Sampling Program

Surficial sediment samples were collected and analysed from 126 sites in the study region (Figures 2a and 2b). To specify the on/offshore variation in grain size and the nature of the sea bed, 23 of the samples were taken at closely spaced intervals along the 13 km shore-normal current meter transect in depths from 20 m to 50 m (Figures

2c and 2d). Sediment grain sizes, fall velocities and grain size distributions were determined using settling tube analysis for the sands and gravels (George and Black, 1989, 1991). Mud contents (< 63 micron) were usually much less than 5% by weight throughout the region. As such, grain size analyses of the mud fractions were not undertaken.

The nature of the sea bed and the size of bedforms (height and wavelength) were obtained from underwater video observations taken throughout the region (Figures 3 and 4). The video was attached to a metal frame lowered to the bed and output was viewed on a ship-borne television receiver. Bedform profiles were observed on a graduated scale board placed in the field of view. A computer frame grabber provided hard copies of the bedform profiles for analysis (Figure 4).

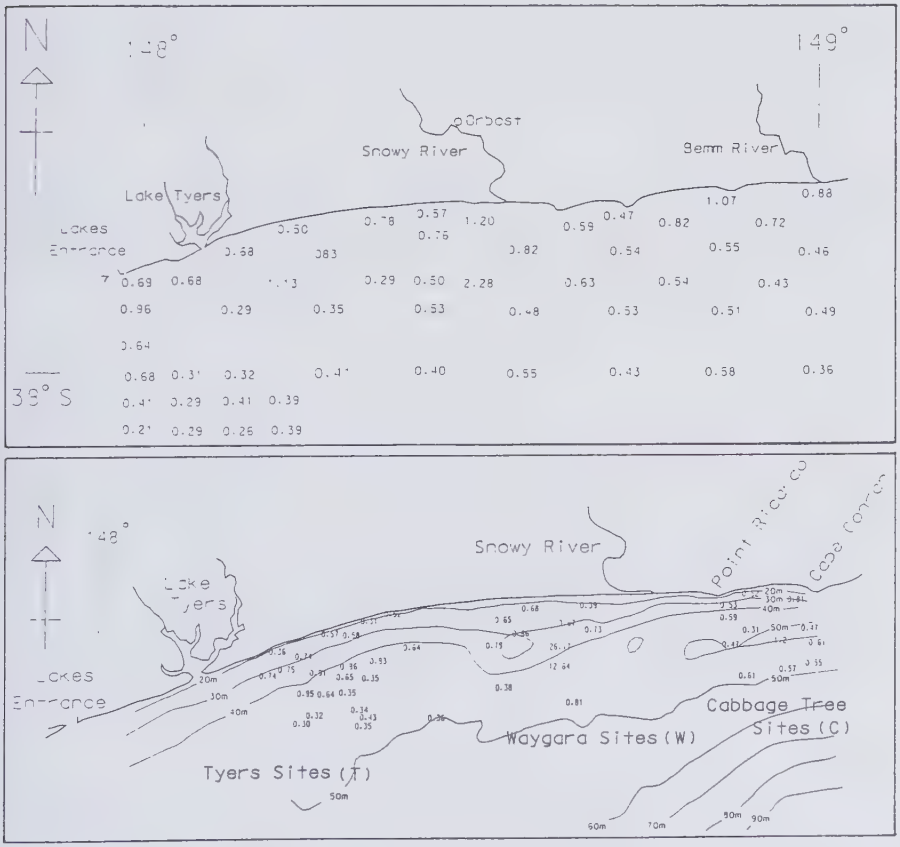

Figure 2a and b. Median grain sizes (mm) over the study region during two surveys.

(c) 1st Survey

	BEDFORM TYPE	MEAN BEDFORM HEIGHT (Δ)(cm)	MEAN BEDFORM WAVELENGTH(λ)(cm)	BEDFORM ROUGHNESS LENGTH $\left(\frac{\Delta^2}{2\lambda}\right)$	SEA DEPTH (m)	MEDIAN GRAINSIZE (mm)
C1 - 08T1 -	≈	5.3	37.5	0.37	20	0.52
08T2 -	≈	4.6	41.3	0.26	23	0.57
08T3 -	≈	2.6	36.0	0.094	25	0.62
08T4 -	≈	4.3	40.8	0.23	26	0.65
08T5 -	≈	3.8	36.9	0.20	28	0.70
08T6 -	≈	4.5	31.0	0.36	30	0.76
08T7 -	≈	5.6	48.0	0.33	33	0.37
08T8 -	≈	8.5	117.5	0.31	36	0.81
08T9 -	≈	5.1	62.5	0.21	38	0.85
08T10 -	≈	6.9	58.3	0.41	40	0.71
C2 - 08T11 -	≈	6.5	76.6	0.28	41	0.64
08T15 -	≈	3.0	9.5	0.47	45	0.26
08T16 -	≈	1.0	5.0	0.10	46	0.42
08T17 -	≈	1.0	5.0	0.10	47	0.37
08T18 -	⌒	F	F	F	48	0.34
08T19 -	⌒	F	F	F	49	0.31
08T20 -	∴	F	F	F	49	0.33
08T21 -	∴	F	F	F	49	0.29
08T22 -	∴	F	F	F	50	0.29
08T23 -	∴	F	F	F	50	0.28
08T24 -	∴	F	F	F	50	0.28
08T25 -	∴	F	F	F	50	0.28
C3 - 08T26 -	∴	F	F	F	51	0.36

(d) 2nd Survey

	BEDFORM TYPE	MEAN BEDFORM HEIGHT(Δ)(cm)	MEAN BEDFORM WAVELENGTH(λ)(cm)	BEDFORM ROUGHNESS LENGTH $\left(\frac{\Delta^2}{2\lambda}\right)$
C1 - 08T1 -	≈	4.8	35.6	0.32
08T2 -	≈	3.8	36.7	0.20
08T3 -	≈	3.4	38.4	0.15
08T4 -	≈	1.3	32.5	0.026
08T5 -	≈	3.2	40.1	0.13
08T6 -	∴	F	F	F
08T7 -	≈	8.3	100.0	0.34
08T8 -	≈	10.0	100.0	0.45
08T9 -	⌒	F	F	F
08T10 -	∴	F	F	F
C2 - 08T11 -	∴	F	F	F

Figure 2c and d. Bed type, bedform wavelength and height, bottom roughness length, depth and median grain size along the cross-shelf transect from Site C1 to C3. The two surveys were conducted on 10 June, 1990 and 11 February, 1991.

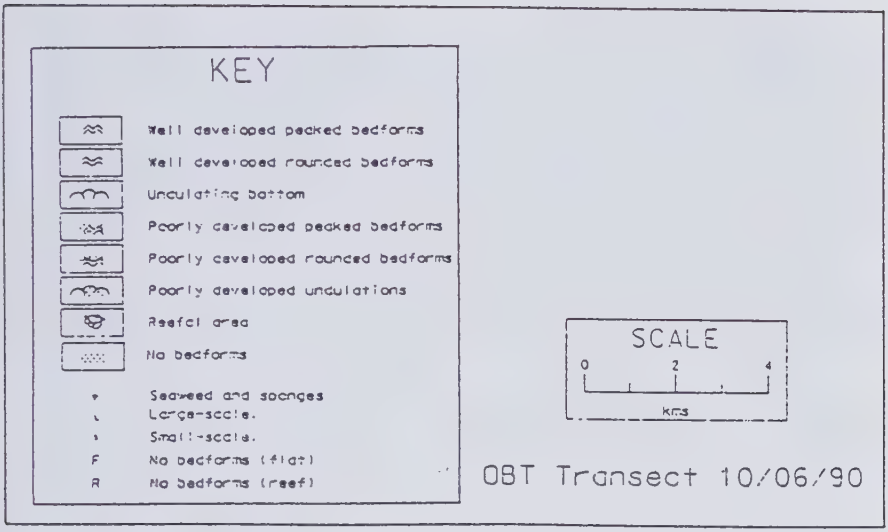

Figure 2c and d (Continued). Bed type, bedform wavelength and height, bottom roughness length, depth and median grain size along the cross-shelf transect from Site C1 to C3. The two surveys were conducted on 10 June, 1990 and 11 February, 1991.

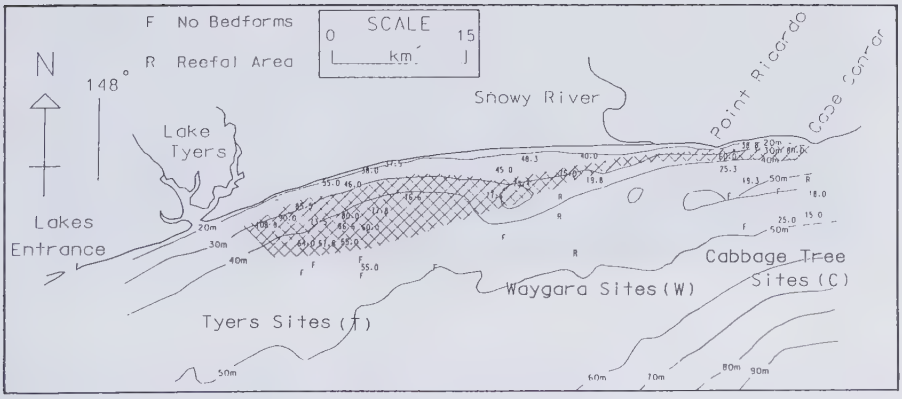

Figure 3. Bedform wavelength (cm). The hatched region shows the band of longer bedforms between the 30 and 42 m contours.

Figure 4. The sea bed at Site OBT3 in 25 m depth.

Results

Winds

Spatial variability in the wind was noted between the different stations. This was examined by comparing observations from the closest permanent anemometers at Lakes Entrance, Wilson's Promontory, East Sale and Gabo Island (Figure 1). The town of Lakes Entrance is located on a coastal plain backed by a 60 m high ridge so that the anemometer is sheltered from northerly winds. The Wilson's Promontory and Gabo Island gauges are exposed, but distant, while the East Sale site is 30 km inland.

Regression analyses showed that the inland East Sale winds were slower than the coastal stations (Table 1). Both the east/west and north/south winds at Lakes Entrance were slower than the other two coastal stations. The coherence between the stations was generally low (minimum correlation coefficient r = 0.38 and maximum r = 0.74) (Table 1) but a good correlation between currents and the Lakes Entrance winds was obtained (see below).

TABLE 1. Regression of Wilson's Promontory (WP), East Sale (ES) and Gabo Island (GI) wind against Lakes Entrance wind (LE). The gradient (a), intercept (b) and correlation coefficient of the best fit equation is given for each case. The east/west (E/W) and north/south (N/S) components were treated separately.

Sites	Dirn	a	b	r
WP-LE	E/W	1.32	2.65	0.71
	N/S	0.73	-1.12	0.38
ES-LE	E/W	0.52	0.13	0.74
	N/S	0.23	0.12	0.46
GI-LE	E/W	0.88	0.63	0.60
	N/S	0.85	-1.15	0.42

Currents

Record-duration mean current speeds (no consideration of direction) increased in strength with offshore distance at 10 m below the surface. Speeds nearer the bed, however, were very similar at Sites C1 and C2 (Figure 1b). Temporally, mean speeds were very similar during the winter and summer deployments, being 0.11 ms^{-1} in both deployments at 10 m below the surface at nearshore Site C1 and 0.19-0.21 ms^{-1} at offshore site C3 (Figure 1b).

A tidal constituent analysis of each sea level and velocity time series was undertaken using the procedure of Foreman (1977). Residual (or non-tidal) velocities were obtained by subtracting the tidal constituents from the measured data series. Spring tidal range (M_2+S_2) was 0.95 m and the dominant tidal constituents combined to generate currents of about 0.12 ms^{-1} at the nearshore site and 0.18 ms^{-1} offshore. The amplitude of the K_1 diurnal component was approximately equal to the M_2. Maximum tidal currents occurred after mid-tide and were directed longshore.

Maximum residual currents were larger than the tidal currents being up to about 0.35 ms^{-1} (Figure 5). The residual currents were directed to the east more than 90% of the time at all levels and all sites. Current reversals were much more common in summer (Figure 5), in response to the greater number of winds from the east (see below).

Vector-averaged currents were calculated by averaging the orthogonal velocity components over the record duration. With a finite number of cycles in the record (Figure 5), some trend can result when the number of periods resolved is not exact. This may result in a spurious component in the vector-averaged currents which may be particularly evident when the current is small.

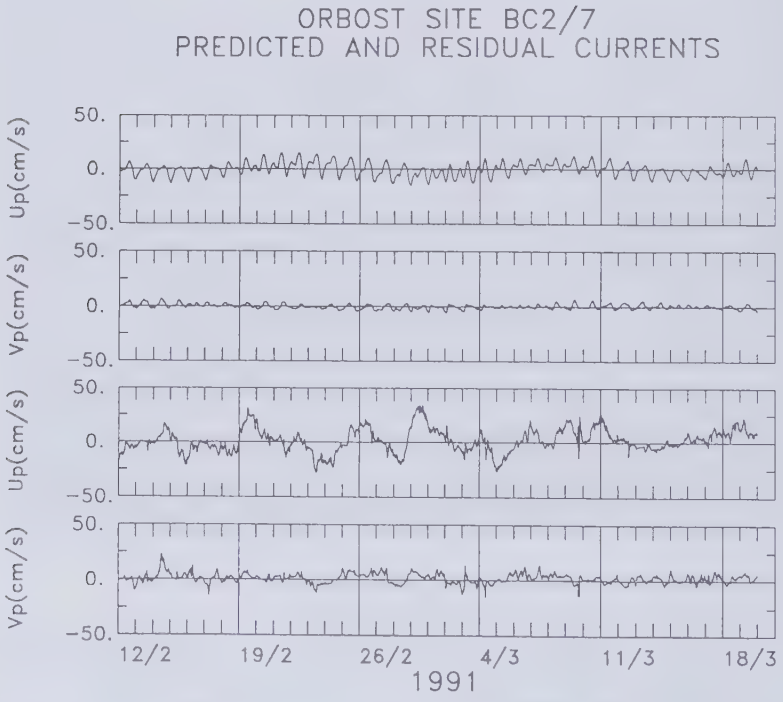

Figure 5. East/west (U) and north/south (V) components of the tidal and residual currents at Site BC2/7 during February and March 1991.

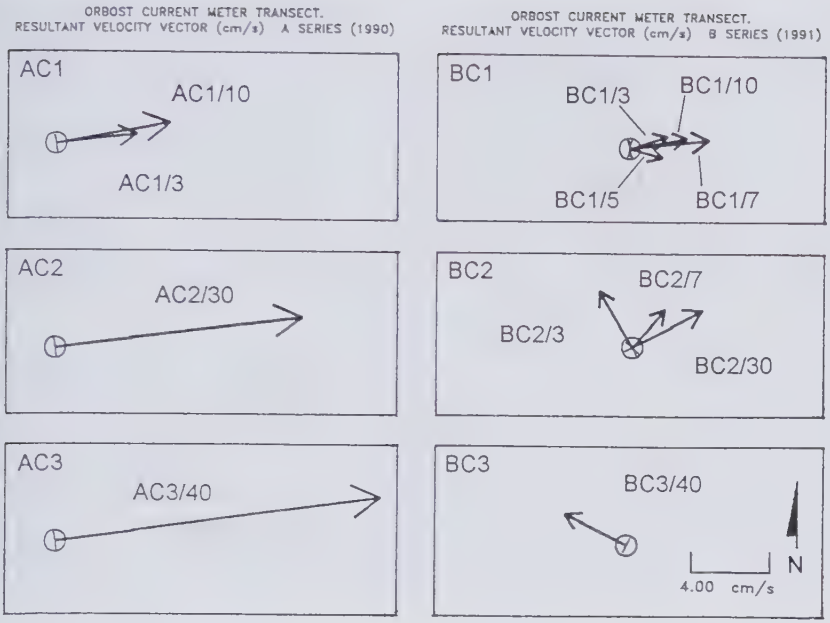

Figure 6. Net vector-averaged currents over the measurement periods during the A and B series.

With more flow reversals in summer, the vector averages of current velocity were very different in summer and winter. Net excursions at offshore Site C3 were large and directed east during winter and west during summer. The cross-shelf variability was also seasonal. In winter, the residual at all sites was directed approximately to the east (longshore), while the net directions varied with depth and cross-shelf position in summer (Figure 6). In summer, the net current direction rotated anti-clockwise across the shelf, from east at BC1 to west at BC3.

At Site BC2/3 the dominant direction was to the north-west, while 4 m higher in the water column at Site BC3/7 the net direction was to the north-east. The currents 10 m below the surface at BC2/30 were directed east-north-east while offshore the currents were directed west-north-west. All of these vectors include significant onshore components.

Up/downwelling

As no vertical current measurements were made, the following discussion relies on inferences from the horizontal flow, assuming a volume continuity requirement at the coastal boundary. In addition, numerical model simulations indicated down-welling (not shown), particularly during onshore winds (Black and Hatton, 1992).

Very small rotations (less than 5°) between the bed and the surface were evident during winter (Figure 6). If the rotation is not an artefact of the averaging errors noted above, it could be due to the greater deflection to the left of the faster flowing surface layers under the prevailing westerly winds. The orientation of currents in winter was similar at all levels and across the shelf, indicating that the prevailing easterly currents were in pseudo-geostrophic balance with a cross shelf sea gradient spanning the measurement transect (see below).

In summer, net currents varied in strength and orientation, while net circulation was more strongly onshore during summer than during winter (Figure 6). In fact, the residual at Site BC2 had a shoreward component at all measured levels. The rotation with depth was variable at site BC1 and anti-clockwise at BC2.

The measured variability in vertical current structure indicates that vertical shear through the depth may be difficult to quantify. Near a natural coastline, an empirical specification of the velocity profile is not readily available, particularly as the profile is a function of offshore distance (Mofjeld, 1988). One implication of the importance of 3-dimensional structure on the Gippsland shelf was noted by Black and Hatton (1992) who showed that the dispersal patterns predicted by 2-dimensional numerical simulations were very different to those from the 3-dimensional version of the same numerical model. The latter model spread the material over a far wider region across the shelf.

Waves

A zero down-crossing analysis furnished wave periods and orbital velocities on a wave-by-wave basis over each 9 minute measurement burst. The standard deviation of the velocities during each burst provided an additional estimate of wave orbital motion. The principal component of the wave direction was obtained by fitting a linear curve to the scatter plot at east/west (U) and north/south (V) velocity components. The gradient indicated wave direction. A third-order polynomial curve fit (to interpolate the data along the principal direction) was applied to find the zero crossings and corresponding wave periods.

The wave energy is depicted by the standard deviation of the measurement bursts at the level of each instrument. The bursts were 1 or 2 minutes in the winter (A series) and 9 minutes in summer. Thus, the uncertainty in estimates of orbital motion due to wave groupiness may be fairly large in the winter series. To examine the cross-shelf transformation in wave height, a wave recording current meter was established at 10 m below the surface at each of the 3 current mooring locations C1, C2 and C3 (Figure 1).

The standard deviation of the measurements increases towards shore due to shoaling (Figure 1b). In the vertical, the period increases towards the bed due to the greater attenuation of high frequency components of the spectrum with distance below the surface (Figure 1b). As such, the period at the bed is larger at Site C2 in 40 m depth than at Site C1 in 20 m depth (Figure 1b). This result has important implications for

the size of bedforms across the shelf (see below). There appears to be a small increase in period from C3 to C1 (towards shore) at the common level of 10 m below the surface (Figure 1b), although the result is probably not statistically significant. This may be associated with a greater increase in the amplitude of the low frequency components as the waves shoal.

The numerical wave shoaling and refraction model of Black and Rosenberg (1992) was applied to examine wave refraction along the measurement transect. A number of different offshore wave angles were chosen in accordance with the variation in the field measurements. A 15 s period was treated which was representative of the longest observed waves.

Common wave directions for the region were from the south-south-west (towards 30°T) and south-south-east (towards 330°T). Figure 7 shows the refraction results at these angles. A small amount of shoaling and refraction occurs. At 330°T, the height increases by 12% and the angle changes by 3° (Figure 7). At 30°T, the height varies by 3% and the angle by 14°. Applying these predicted height increases using linear theory, the expected orbital velocities at 10 m below the surface at Site C1 are 1.64 and 1.50 times the offshore value at C3. This coincides with measured ratios of the average wave standard deviations (Figure 1b) of 1.50 and 1.46 for the A and B series respectively. Frictional dissipation would account for the discrepancy.

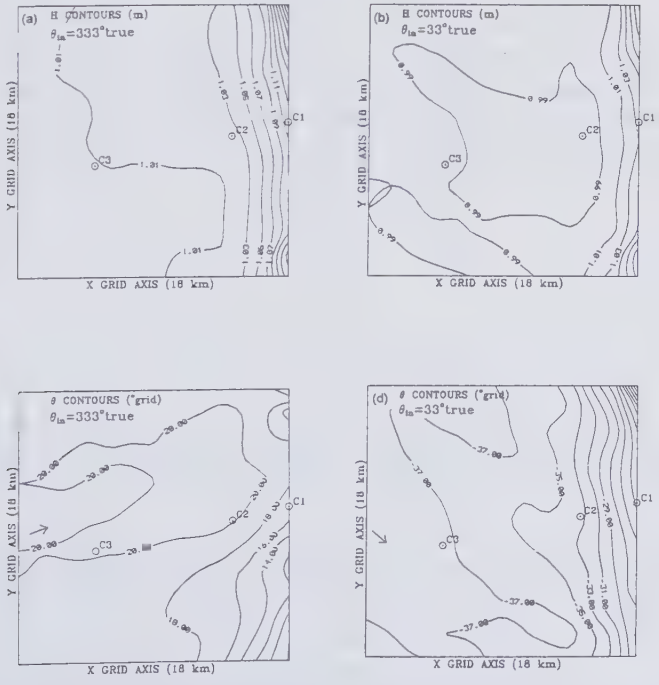

Figure 7. Refraction diagrams showing the wave height and angle contours for waves of 15 s period and 1 m height (a) heading towards 333°T and (b) towards 33°T.

Local Wind Forcing of Currents and Coastal-trapped Waves

Middleton and Viera (1991) have demonstrated that the source of low frequency (3-14 day) currents in this region is winds within Bass Strait and coastal-trapped waves incident from the Great Australian Bight. Using numerical techniques, Middleton and Black (1994) found that coastal-trapped waves dominate the low frequency energy at the western entrance to Bass Strait, but the relative importance of local winds increases to the east. Local winds and coastal-trapped waves were shown to typically generate currents on the east Gippsland shelf with approximately equal magnitude. Black *et al.* (1993) identified a similar partition in the response of sea levels recorded at a Victorian coastal site in central Bass Strait. Thus, we can expect correlation analyses to local wind to explain approximately 50% of the variance in the low frequency currents.

Jones (1980) found that wind and current were correlated with r = 0.49 at a site offshore of our transect. We found a higher correlation between wind and longshore currents at all levels and sites, but a poor correlation to cross-shore currents. Thus,

$$U = aW_x + bW_y + c$$

$$V = dW_x + eW_y + f \qquad (1)$$

where U and V are the longshore and cross-shore current velocities respectively, W_x and W_y are the components of wind velocity along 80°T and 350°T respectively and a,b,c,d,e,f are regression coefficients. The goodness of fit is given by r^2. A wind "stress" (with a unit drag coefficient) was tested in one case, i.e.,

$$W_{xstrv} = W_x |W|$$

$$W_{ystr} = W_y |W| \qquad (2)$$

Currents at BC1/7 (at 7m above the bed), BC2/7 (at 7m) and BC3/40 (at 40 m) in 20, 40 and 50 m depth respectively were analysed.

The lag between current and wind was obtained from the cross correlation in the time domain of the dominant, most correlated variables, i.e. longshore wind and longshore current. The currents lagged the local Lakes Entrance winds by 3 hours (Table 2).

Linear regression showed that up to 64% of the variance in the residual longshore current was attributable to the measured wind. The on/offshore component was poorly correlated with wind in every case.

The more distant Wilson's Promontory measurements generally predicted the currents better than the local Lakes Entrance wind. The worst correlation was obtained with records from Gabo Island, located to the east of the field site. Thus, the relevant wind forcing evidently occurs to the west of the site within Bass Strait.

TABLE 2. Wind and current regression analysis. Results of a regression to the equation, (U,V) = $aW_x + bW_y + c$ where U and V are the longshore and cross-shore current velocities respectively, W_x and W_y are the components of wind velocity along 80°T and 350°T respectively, a,b,c are regression coefficients. For the cases marked *, the wind stress component was used where $W_{xstr} = W_x |W|$ and $W_{ystr} = W_y |W|$. The goodness of fit is given by r^2. Three wind records were considered: Wilson's Promontory (WP), Gabo Island (GI) and Lakes Entrance (LE). The lag is the time (hours) time that the current lags the wind. The current axes were rotated by 1, 5 and 28° anti-clockwise at Sites C1, C2 and C3 respectively onto the principal residual current axis.

WP		a	b	c	r^2	lag
BC1/7	U	0.87	-0.10	3.21	0.53	6
	V	-0.04	0.09	0.89	0.04	
BC2/7	U	0.89	-0.02	0.40	0.63	6
	V	0.07	0.07	1.56	0.03	
BC2/7	U*	0.055	0.003	0.810	0.64	6
	V*	0.005	-0.005	1.597	0.03	
BC3/40	U	1.45	0.32	-2.05	0.50	9
	V	-0.02	-0.13	1.61	0.00	

GI		a	b	c	r^2	lag
BC1/7	U	1.07	-0.70	4.23	0.35	0
	V	0.01	0.06	0.82	0.02	
BC2/7	U	1.16	-0.72	1.38	0.46	0
	V	0.07	-0.08	1.65	0.01	
BC3/40	U	1.90	-0.80	-0.34	0.37	-3
	V	-0.72	0.17	1.64	0.00	

LE		a	b	c	r^2	lag
BC1/7	U	1.57	0.30	4.82	0.49	3
	V	-0.05	0.02	0.65	0.01	
BC2/7	U	1.58	0.07	2.42	0.53	3
	V	0.18	-0.18	1.85	0.07	
BC3/40	U	2.64	0.71	-1.50	0.41	3
	V	0.25	-0.67	3.07	0.04	

The currents in the longshore direction were from 0.87% to 2.64% of the wind speed, depending on the wind chosen and the vertical position of the current meter. The currents at Site BC2/7 were 1.58% of the local winds, but only 0.89% of the stronger winds at Wilson's Promontory.

The variability between wind stations suggests that none of the wind records will be individually fully representative of the wind blowing over water at all locations in the

region. Quite possibly, more of the velocity variance is attributable to wind, but the wind measurements at the sites considered are not able to adequately represent the combination of actual conditions over the region and the more remote wind forcing within Bass Strait.

Site C2 in 40 m depth was the most highly correlated with wind while the offshore and inshore sites showed less correlation. At the shallowest site, the reduced correlation may be explained by increased land effects on the wind, wave/current interaction in the bed friction term or the presence of more energy nearshore due to remote coastal-trapped waves. The results offshore are strictly not comparable because time series measured near (or within) the upper boundary layer had to be used for the regression (Site BC3/40), compared with the deeper deployments used for the inshore analyses. Surface boundary effects will be more pronounced at BC3/40 located 10 m below the surface.

A wind measurement, although locally accurate, may not be a reliable indicator of currents. For example, Hsu (1986) suggested a simple dimensional relation between the wind velocity over the sea and over land,

$$W_{sea} = 1.62 + 1.17W_{land} \qquad (3)$$

When calibrating the numerical model of the region, we found that the Lakes Entrance wind had to be multiplied by 1.07 for the model to match the measured currents. However, this factor is dependent on the selected bed roughness because the dominant balance in the momentum equation is between bed roughness and wind stress once a pseudo-steady state is reached. In an open coast environment where roughness varies spatially and temporally and the roughness depends on the wave/current interaction, the best which can be achieved is to determine the appropriate factor for the wind, given a roughness condition. The solution is not unique if there are uncertainties in the bed roughness estimate.

With a factor of 1.07 applied to the regression coefficients in Table 2, the longshore currents at Sites BC1 and BC2 (at 0.35d and 0.18d respectively for water depth d) were 1.7% of the longshore Lakes Entrance wind speed. This result is in general agreement with the commonly-adopted assumption that the vertically-averaged current is about 2% of the wind speed. The lower value at our sites may be related to a local large bed frictional resistance (see below). Higher in the water column at Site BC3, the longshore current at 10 m below the surface was 2.8% of the wind speed.

A better correlation to wind may also be obtained if the inertia in the currents is considered. However, the lag between wind and current was short (about 3 hours) and the currents decayed quickly after the wind diminished. Black and McShane (1990) found at a nearby site in 20 m depth that this rapid decay was associated with high friction due to the presence of waves.

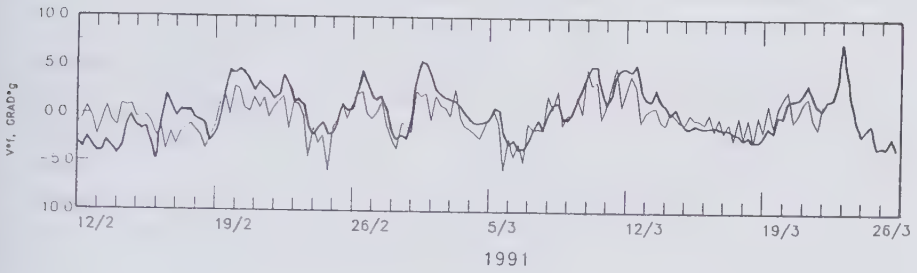

Figure 8. Comparison of the Coriolis and cross-shelf gradient terms in the geostrophic balance (see text).

Notably, the prediction using the wind stress rather than the wind velocity estimated the flow velocity peaks better (not shown), although the correlation for the two cases was similar ($r^2 = 0.63$ and 0.64, Table 2).

Geostrophy

The cross-shelf sea gradient was highly correlated with the longshore residual currents and the two were evidently in geostrophic balance. The Coriolis and cross-shelf sea gradient terms in the momentum balance, fV and $g\ \partial\zeta/\partial y$, are compared in Figure 8. V is the residual velocity at Site BC3/40 and the sea level gradient was calculated between nearshore and offshore tide gauge stations BT4 and BT3. The other terms are the Coriolis parameter f, gravitational acceleration g and sea level ζ. Considering that no allowance has been made for vertical or horizontal variations in velocity (including longshore differences in response to the changing width of the shelf), the correlation is very good.

Temperature

The temperature structure on the shelf was very different in the winter and summer seasons, the latter being characterised by more rapid temperature changes and a greater variability in vertical structure.

To depict spatial variability, temperatures at the 4 widely-spaced tide gauge stations (T1 to T4) are presented in Figure 9. The linear trend in both winter and summer is a seasonal response. Differential heating as a function of depth causes temperatures to be colder near the coast than offshore during winter, and hotter during summer. The winter temperatures are characterised by small variations (both inshore and offshore) with 1-3 day periods (Figure 9a). However, large oscillations exceeding 4°C occurring in less than 24 hours typify the summer records (Figure 9b).

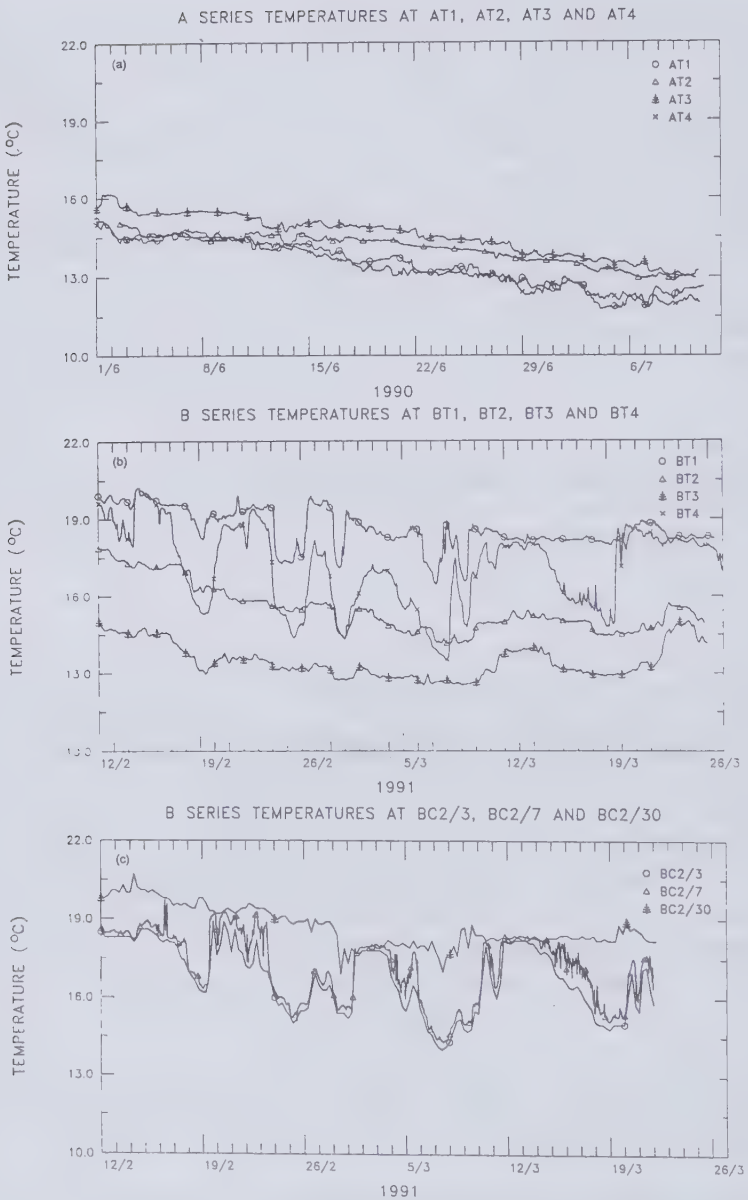

Figure 9. (a) Temperatures measured near the sea bed at Sites T1 to T4 during the winter deployment. (b) Temperatures measured near the sea bed at Sites T1 to T4 during the summer deployment (c) Vertical temperature structure at Site BC2 during the summer deployment.

The vertical variation of temperature at Site BC2 shows a well-mixed layer extending more than 7 m from the bed (Figure 9c). The upper levels were often

warmer by up to 4°C, although a thermocline was not a permanent feature. Vertically well mixed conditions recurred about every 10 days, suggesting a correlation with the weather which has most energy at 10-14 day periods.

Regression analyses were undertaken to isolate the processes responsible for (i) temperature variations at Site BC2/3 and (ii) the factors determining vertical temperature differences over the 27 m of water column between BC2/30 and BC2/3. In the first case, nearby temperatures and temperature gradients were employed as independent variables and therefore served to identify the relative importance of horizontal advection (both longshore and on/offshore) and vertical advection or mixing. The second used physical input variables only, i.e. wind stress, air temperature and wave conditions. This regression therefore shows the physical processes responsible for creating and dissipating vertical temperature stratification on the continental shelf. A complete heat budget was considered but no improved prediction over the regression analysis was achieved.

Factors Which Account for Near-bed Temperature Changes

Table 3a gives the regression coefficients for the prediction of temperature at Site BC2/3 (T_{23}). Up to 97% of the variance in the measured temperatures can be predicted knowing the temperature (T_1) at site BT1 to the west (which accounts for 44% of the variance), the longshore temperature gradient (T_{long}) between nearshore sites BT4 and BT1 (which accounts for 42%), the cross-shore temperature gradient (T_{cross}) between sites BT2 and BT1 (which accounts for 5%) and the vertical temperature gradient (T_{up}) between Sites BC2/30 and BC2/3 (which accounts for 65%). Thus, the variation in temperature is primarily accounted for by vertical mixing and longshore horizontal advection. Cross shelf advection is relatively unimportant. Thus, in accordance with the current observations, cross-shelf transport (related to upwelling and downwelling) plays a minor role compared to the longshore advection. The final regression equation (Figure 10a; Table 3a) was,

$$T_{23} = 0.73\,T_1 + 13204\,T_{long} - 17910\,T_{cross} - 19.38\,T_{up} + 6.52 \quad (4)$$

where T_{long}, T_{cross} and T_{up} are temperature gradients (units°C/m, divided by the distance between measurement sites). A zero lag was applied to all variables, primarily because the advection commences everywhere almost simultaneously, in response to the wind and other forcing, at the spatial scales (maximum 70 km) being considered.

To confirm the results, a simple horizontal advection model was developed which used the measured currents from the transect and measured horizontal temperature gradients from the tide stations to predict the changing temperatures recorded along the transect.

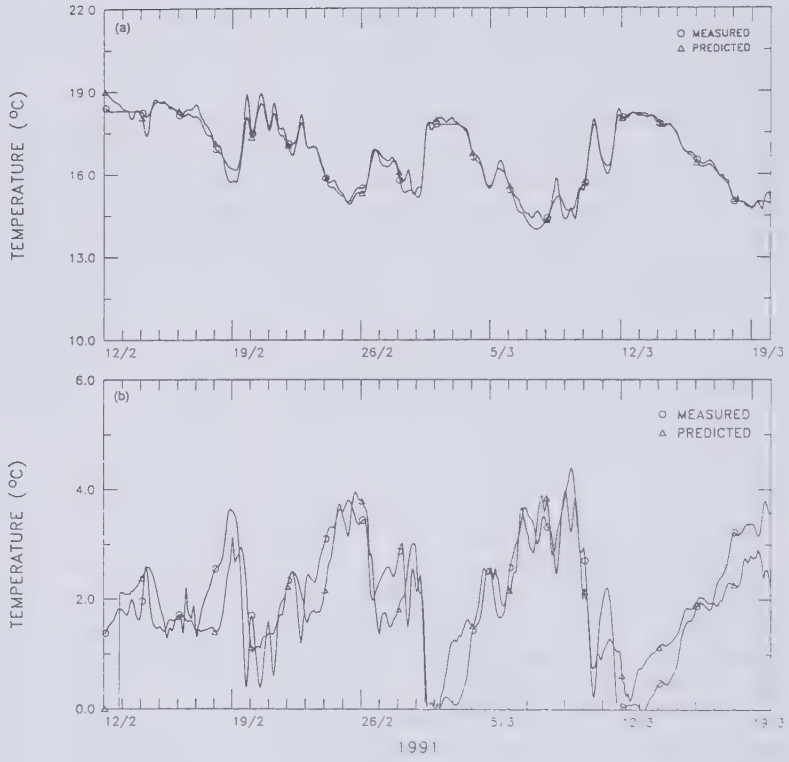

Figure 10. (a) Predicted and measured temperature at Site BC2/3. (b) Predicted and measured temperature difference between BC2/30 at 30 m above the bed and BC2/3 at 2.7 m above the bed in 40 m depth.

Horizontal advection alone was unable to explain the sharp temperature changes over short time periods.

The large horizontal gradients in the near-bed temperatures appear to be primarily related to local water depth. Water depths were 15, 19, 54 and 110 m at Sites BT1, BT4, BT2 and BT3 respectively, which coincides with the ranking of mean temperatures at the sites (Figure 9). Satellite sea-surface temperature observations commonly show intrusion from the east of hotter water coming from a southbound current on the east Australian coast (Edwards, 1990). In this case, temperatures decrease to the west. Our data, however, shows the opposite pattern with hottest bottom water at the western end of the region in summer. The above analyses indicate that local thermal heating and better stirring in shallower depths is a likely explanation (rather than intrusion from the east) for the large alongshore and cross-shore spatial gradients in summer.

TABLE 3A. Regression of temperature at Site BC2/3 against the temperature at BT! and the horizontal and vertical temperature gradients.

Case	T_1	T_{long}	T_{cross}	T_{up}	Constant	R^2
1	1.065	-	-	-	-3.12	0.44
2	0.812	37918	-	-	2.50	0.65
3	0.867	34716	-13848	-	2.76	0.70
4	0.735	13204	-17910	-19.46	6.52	0.97
5	1.110	-	-18799	-	-2.13	0.53
6	0.749	-	-	-21.54	4.34	0.85
7	-	-	-	-25.96	18.62	0.65
8	-	50697	-	-	17.94	0.42
9	-	-	-14521	-	18.14	0.05

Factors Associated with Vertical Temperature Gradients

The factors determining the vertical temperature difference between BC2/30 and BC2/3 (T_{dif}) are now considered. In this case, 68% of the variance in T_{dif} could be predicted knowing environmental factors alone (Figure 9b). The air temperature at east Sale (T_{sale}) accounted for 55% of the variance (Table 3b). (Unfortunately these temperatures were recorded over land but were the nearest available measurements.) The U and V wind stress (U_{str} and V_{str}) together accounted for 37% of the variance, while orbital motion (SDv) as determined by the on/offshore standard deviation of the measurement bursts accounted for 11%. The wind stresses were calculated with the formula of Wu (1982) for the drag coefficient.

Thus, much of the temperature stratification can be predicted from the air temperature alone. Wind is the next most important variable, while waves have little impact. However, wind and waves are correlated. (Of course, coefficients from multiple regressions are less reliable when processes are correlated.)

The air temperature plays two roles. First, the stratification forms when the air temperature exceeds water temperature and is reduced when surface waters are cooled by lower air temperatures. Second, low temperature will be correlated with storm events which means that temperature may be a surrogate for storm-induced mixing. The final regression equation (Figure 10b; Table 3b) was,

$$T_{dif} = 0.21\ T_{sale} - 0.61\ U_{str} - 1.11\ V_{str} - 0.15\ SD_v - 1.62 \qquad (5)$$

Lags applied are given in Table 3b. Notably, the factor which establishes the stratification (T_{sale}) has a positive regression coefficient, while the mixing factors have negative coefficients.

TABLE 3B. Regression of vertical temperature difference between BC2/30 and BC2/3 and the physical forcing factors.

Case	Air temp at East Sale	U_{str}	V_{str}	SD_V	Constant	R^2
1	0.259	-	-	-	-2.53	0.56
2	-	-0.657	-2.354	-	2.08	0.37
3	-	-	-	-10.77	3.28	0.11
4	0.211	-0.608	-1.105	-0.149	-1.62	0.68
Lag (hrs)	10	20	16	12	-	-

We have chosen to include physical environmental factors only in the regression. The above analysis suggests that other factors such as horizontal advection are important also. However, 68% of the variance can be predicted from the physical forcing alone without consideration of the wider spatial structure. Major terrestrial flooding occurred just prior to the A series deployments and resulted in lower salinity and conductivity at nearshore sites. No similar major events occurred during the period used for the above regression analysis, although rainfall over the catchment and river inputs may have been a useful additional variable.

Sea Bed Description

A wide variability in bed type was observed with bedforms and mobile sediment typically occurring in depths less than about 40 m (Figures 2 and 3). Bed sediments were dominantly well sorted medium to coarse shelly sands, with an overall tendency for an offshore increase in colonisation by marine growth (Figures 2a and 2b). The coarsest sediments extended in a distinctive longshore band between the 30-42 m contours. Where a mud fraction was present, it was typically less than 5% by weight (George and Black, 1989, 1991). Areas of rocky reef also occur. At ~20 m water depth on the current meter transect, the bed was composed of clean sand with a median grain size of 0.52 mm (Figure 2c).

Most of the bedforms were symmetrical wave generated ripples. Sharp crested braided bedforms were observed in 20 m water depth, with typical wavelengths and wave heights of 40 cm and 4 cm respectively. Larger parallel bedforms (with wavelengths and heights of up to 120 and 11 cm respectively) were observed in deeper water to a depth of ~43 m, at which point well defined parallel bedforms disappeared.

Thus, the two major features of the bedform patterns were a distinct boundary around 42-45 m where bedforms no longer occurred, and the presence of a band of higher and longer bedforms in a distended shore-parallel band of coarser sediment between the 30-42 m contours.

The 42-45 m limit clearly coincides with a continental shelf mud depositional limit discussed by Jones and Davies (1983) (among others). The limit is the depth at which the wave orbital velocities during storms no longer exceed the sediment threshold. Notably, the location of the limit was at about 42 m during the first survey of the cross-shelf transect, but had moved shoreward during the second survey (Figures 2c and 2d) when no bedforms were observed at depths below about 36 m.

The second observation, that bedform wavelength is a maximum offshore, is evidently a result of differential attenuation of the surface wave spectrum with distance below the surface. The elimination of high frequency components causes near-bed wave periods to be largest offshore, and longer bedforms result. Although a mechanism is not obvious because the wave energy at the bed is much less at Site C2 than inshore at Site C1 (Figure 1b), the coarser grain size may also be associated with the same process of high frequency attenuation. The grain size measurements suggest that winnowing has occurred between the 30 and 42 m contours.

Onshore cross-shelf transport associated with the tidal and other currents appears to be more pronounced at Site C2 than Site C1 (Figure 6) and mean current speeds are also greater (Figure 1b). In addition, the depth filtering of the spectrum eliminates the high frequency (local storm) sea, leaving the lower frequency components which must be shoaling. This spectrum is similar to the swell condition associated with onshore transport of sediment on beaches. Currents are faster under the crests than the troughs of shoaling swell waves, and a net onshore sediment transport should result. Because of the attenuation of the wave energy with depth, the fine sediments should be preferentially winnowed and carried shoreward by this process. While these processes could explain the grain size changes, other factors such as Stoke's drift and phase lags between sediment suspension and wave orbital motion are likely to be important.

Vertical Velocity Profile and Bed Roughness

The velocity profile in the bottom boundary is normally assumed to be logarithmic,

$$U = 5.75\, U_* \log_{10}(z/z_o) \qquad (6)$$

where U is velocity at z (m) above the bed, U_* the friction velocity and z_o the roughness length. U_* and z_o can be obtained from a measured velocity profile using linear regression to fit to eqn (6). However, some difficulties related to (i) small timing differences between the instruments (ii) possible errors in the instrument elevation due to uncertainty in the exact orientation of the mooring weights when dropped to the sea bed (iii) vertical temperature stratification which, if present, causes the profile gradient to be no longer solely related to bed roughness.

We considered the profiles from BC1 (levels BC1/3, BC1/10) and BC2 (levels BC2/3, BC2/5 and BC2/7). Temperature stratification within the bottom 10 m of the water column was minimal (see above) and found not to be correlated with z_o predicted from the profile. However, z_o was highly correlated with vertical

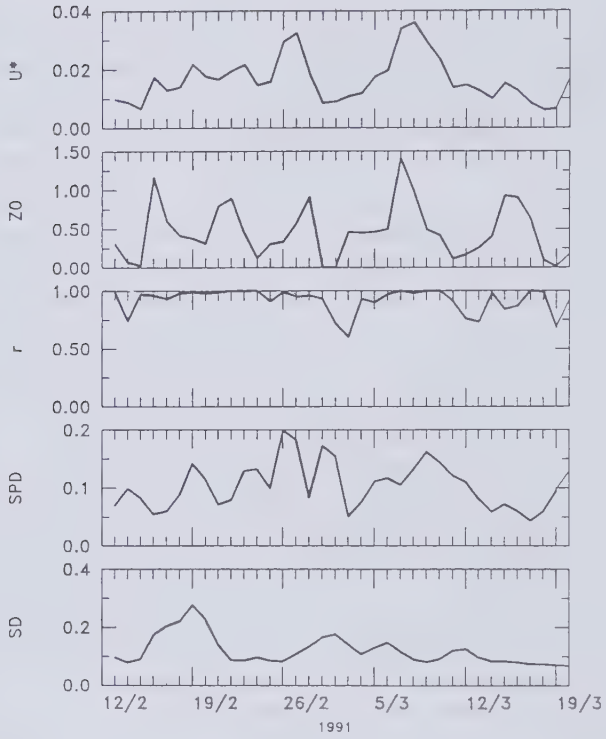

Figure 11. Logarithmic profile regression analysis to find the friction velocity ($U*$), roughness length (z_o) and correlation coefficient (r). The current speed (SPD) at 4.7 m above the bed and the standard deviation of the measurement bursts (SD) are also shown. All variables were running mean averaged over 48 hours and the daily values were treated.

temperature gradient when the measurements from BC2/30 were included in the regression at Site BC2. BC2/30 was typically above the thermocline. Thus, the bottom three meters only were used.

The timing errors made it difficult to ensure that the profiles were instantaneous. In addition, scatter around the logarithmic profile occurred due to the unsteady conditions. Thus to consider the general response of the profile to the bed roughness, we averaged measured speeds at each level over 48-hours and treated values at daily intervals. This gave a view of the averaged current and the lower frequency response of the bottom boundary layer to changing weather and bed conditions. The correlation to the logarithmic profile was found to increase as the averaging period was lengthened.

To examine the error resulting from a poor estimate of the instrument elevations, we fitted the data to eqn (6) with the most likely and the extremes of the possible elevations.

In 20 m depth at BC1, the predicted friction velocities were about 0.02 ms^{-1} and roughness lengths were about 0.5 m (Figure 11). The median of the cases where the regression gave a positive gradient and when the 48-hour averaged current speed at 5 m above the bed exceeded 0.1 ms^{-1} was z_{om} = 0.40 m. This is a very high value. However, z_o remained high even when the instruments were assumed to be 0.5 m lower than expected. Moreover, the temperature stratification and z_o showed no significant correlation. Thus, although very large, these values appear to be representative of the site. In 40 m depth at BC2, z_o was smaller but high values still occurred. The median (as above) was z_{om} = 0.067 m.

There remains a degree of uncertainty as only 2 or 3 levels were sampled. However, while the inshore values appear to be large and a number of possible errors exist, the high value may be justified. At a similar site in 20 m depth in eastern Victoria, Black and McShane (1990) demonstrated that the roughness length in a wave/current environment may be up to 300 times the value obtained from the bedforms alone using the simple formula,

$$z_o = H^2/2L \qquad (7)$$

where H is the bedform height and L the length. The result was subsequently confirmed by Simons *et al.* (1989) who examined a variety of wave/current friction formulae and equally concluded that high roughness lengths are predicted by the wave/current theories and were evidently present in natural conditions.

At Site BC1 using eqn (7), the measured bedforms indicate z_o = 0.002-0.003 m. A factor of 300 applied to these values gives z_o = 0.6-0.9 m, which is at the upper limit of the values independently obtained from the velocity profiles.

Summary and Discussion

Field measurements were made to simultaneously record the currents, sea levels, bed mobility, suspended load and to characterise the sea bed on an exposed continental shelf. Data were recorded during both summer and winter and large differences between the two sets of records were noted.

The processes operating in the region can be summarised as follows. Tidal currents with typical magnitudes of 0.1-0.2 ms^{-1} were directed longshore. Residual currents responded to seasonal fluctuations in wind. Currents in winter were directed east for most of the measurement period, while reversals were common in summer. Temperature stratification both horizontally and vertically was much more common in summer. Bottom temperatures could be explained primarily by vertical mixing across the thermocline and longshore temperature gradients. Vertical temperature differences were explained by air temperature variations and wind stress. Cross shelf

advection (and upwelling and downwelling) was secondary to longshore advection, as indicated by the current measurements and the temperature structure on the shelf.

Larger bedforms in a distended shore-parallel band of coarser sediments was identified between the 30-42 m contours. The offshore limit coincided with a mud depositional limit where wave motion is too weak to move sediments at these depths. Wave orbital measurements indicated that depth filtering of the high frequency components of the spectrum may explain the presence of the longer bedforms at depths greater than 30 m. The observed coarser sediments within the band may be a result of the shoaling of these low frequency components. The fines may have been carried shoreward due to the faster currents under the crest than under the trough of shoaling swell, although other factors also need to be considered.

Large roughness lengths of 0.4 m and 0.067 m in 20 m and 40 m depth respectively were obtained from the velocity profiles. These values are in agreement with results obtained from earlier studies using measurements from 20 m depth off the Gippsland coastline.

Acknowledgment. This work was funded by the Environment Protection Authority (Victoria), and the Australian Research Council. Our thanks to the crew of the "Sarda" (Marine Science Laboratories) and the "Bianca" (Lakes Entrance) for field support, and to the Lakes Entrance Fishing Co-operative. Thanks also to David Hatton for assistance with data preparation.

References

Amos, C.L., A.J. Bowen, D.A. Huntley, and C.F.M. Lewis, Ripple generation under the combined influences of waves and currents on the Canadian continental shelf. *Cont. Shelf Res.* , 8(10), 1129-1153, 1988.

Black, K.P. and P.E. McShane, Influence of surface gravity waves on wind-driven circulation in intermediate depths on an exposed coast. *Aust. J. Mar. Freshw. Res.* 41, 353-363, 1990.

Black, K.P. and M.A. Rosenberg, Natural stability of beaches around a large bay. *J. Coastal Res.* 8(2), 385-397, 1992.

Black, K., M. Rosenberg, D. Hatton, R. Colman, G. Symonds, G., R. Simons, C. Pattiaratchi and P. Nielsen, Hydrodynamic and sediment dynamic measurements in eastern Bass Strait. In *Hydrodynamic measurements: field data collection and analysis.* Working Paper No. 20, Volume 1, Victorian Institute of Marine Sciences, 1991a.

Black, K., M. Rosenberg, G. Symonds, R. Simons, C. Pattiaratchi, and P. Nielsen, Hydrodynamic and sediment dynamic measurements in eastern Bass Strait. In *In situ sediment transport measurements: field data collection and analysis.* Working Paper No. 22, Volume 3, Victorian Institute of Marine Sciences, 1991b.

Black, K., A. Tunks, M. Rosenberg, R. Colman, A. George, G. Parry, N. Coleman, G. Symonds, R. Simons, C. Pattiaratchi, and P. Nielsen, Hydrodynamic and sediment dynamic measurements in eastern Bass Strait. In *Sea bed description and sediment size analysis.* Working Paper No. 21, Volume 2, Victorian Institute of Marine Sciences, 1992.

Black, K.P. and D.N. Hatton, Hydrodynamic and sediment dynamic measurements in eastern Bass Strait. In*Two and three-dimensional numerical hydrodynamic and dispersal models*. Technical Report No. 17, Volume 4, Victorian Institute of Marine Sciences, 1992.

Black, K., D. Hatton, and M. Rosenberg, Locally and externally-driven dynamics of a large semi-enclosed bay in southern Australia. *J. Coastal Res.* 9(2), 509-538, 1993.

Burrage, D.M., J.A. Church and C.R. Steinberg, Linear systems analysis of momentum on the continental shelf and slope of the central Great Barrier Reef. *J. Geophys. Res.*. 96(C), 22 169-22 190, 1991.

Cachione, D.A. and D.E. Drake, A new instrument system to investigate sediment dynamics on continental shelves. *Mar. Geol.*, 30, 299-312, 1979.

Cachione, D.A. and D.E. Drake, Shelf sediment transport: An overview with applications to the northern California continental shelf. In *The Sea*, edited by LeMehaute and Hanes, Wiley Interscience, Volume 9, Part B, 21, 729-774, 1990.

Downing, J.P. Suspended sediment transport on a dissipative beach. *Proc. 19th Intnl Conf. on Coastal Engineering* (ASCE) p. 1765-1781, 1984.

Edwards, R.J. Upwellings could hold clues to fish patterns. *Australian Fisheries,* 49(1), 1990.

Foreman, M.G.G. Manual for tidal heights analysis and prediction. Pacific *Marine Science Report No. 77-10*, Institute of Ocean Sciences, Patricia Bay, Victoria, B.C. Canada, 1977.

George, A.D. and K.P. Black, Settling tube analysis of sediment samples from Eastern Bass Strait and adjacent beaches. Report prepared for Marine Science Laboratories by the *Victorian Institute of Marine Sciences*, September 1989, 1989.

George, A.D. and K.P. Black, Settling tube analysis of sediment samples from Eastern Bass Strait. Report prepared for Marine Science Laboratories by the *Victorian Institute of Marine Sciences*, May 1991, 1991.

Gordon, R.L. Coastal ocean current response to storm winds. *J. Geophys. Res.* 87(C3), 1939-1951, 1982.

Grant, W.D. and O.S. Madsen, Combined wave and current interaction with rough bottom. *J. Geophys. Res.* 84, 1797-1808, 1979.

Hsu, S.A. Correction of land-based wind data for offshore applications. *J. Phys. Oceanogr.* 16, 390-394, 1986.

Jones, I.S.F. Tidal and wind-driven currents in Bass Strait. *Aust. J. Mar. & Freshw. Res.* 31, 109-117, 1980.

Jones, H.A. and P.J. Davies, Superficial sediments of the Tasmanian continental shelf and part of Bass Strait. Bureau Mineral Resources, *Geology and Geophysics Bulletin 218*. Australian Government Publication, ACT. 25 p, 1983.

Middleton, J.F. and F. Viera, The forcing of low frequency motions within Bass Strait. *J. Phys. Oceanogr,* 21, 695-708, 1991.

Middleton, J.F. and K.P. Black, The low frequency circulation in and around Bass Strait: a numerical study. *Cont.. Shelf Res.* in press, 1994.

Mofjeld, H.O. Depth dependence of bottom stress and quadratic drag coefficient for barotropic pressure-driven currents. *J. Phys. Oceanogr.* 18, 1658-1669, 1988.

Parry, G.D., S.J. Campbell and D.K. Hobday, Marine resources off East Gippsland, southeastern Australia. *Technical Report No. 72*, Marine Science Laboratories, Queenscliff, Victoria, Australia, 1990.

Simons, R.R., A.G. Kyriacou and K.P. Black, Predicting wave-current interactions at Mallacoota Bay. *9th Australasian Conference on Coastal and Ocean Engineering,* Adelaide. Australian Institution of Engineers. p. 297-301, 1989.

Smith, J.D. and T.S. Hopkins, Sediment transport on the continental shelf off of Washington and Oregon in light of recent current measurements. In, *Shelf sediment Transport: Process and Pattern,* edited by Swift D.J.P., *et al.* Dowden, Hutchison and Ross, Stroudsburg, Pa. p. 143-180, 1972.

Sternberg, R.W. and J.S. Creager, An instrument system to measure boundary layer conditions on the sea floor. *Mar. Geol.* 3, 475-482, 1965.

Wiberg, P.L. and J.D. Smith, A comparison of field data and theoretical models for wave current interactions at the bed on the continental shelf. *Cont. Shelf Res.*, 2, 147-162, 1983.

Wu, J. Wind stress coefficients over sea surface from breeze to hurricant. *J. Geophys. Res,* 87, 9704-6, 1982.

4

The Lagrangian Barycentric Method to Compute 2D and 3D Long Term Dispersion in Tidal Environments

J. C. Salomon, P. Garreau and M. Breton

Abstract

In macro-tidal coastal seas, long term movement of water and conservation tracers, cannot be described using Eulerian residual currents. Although Lagrangian residual velocities have proven difficult to use as they are perceived to be time dependent, they must be introduced. A method is presented for elaborating Lagrangian residual current fields which eliminates this time dependency without any smoothing effect. The small spatial structures are well defined and direct calculation of long term transport and dispersion can be made without introducing any parasite diffusion. The method has been generalized to real tides, variable wind fields and the three spatial dimensions. This was applied to the English Channel.

Introduction

In some marine environments with very strong tides, such as the Northwestern European continental shelf, meso-scale currents are dominant and suppress other components with different time scales. Amongst these, the synoptic or macro-scale components are particularly difficult to measure because they are often one or two orders of magnitude less than the former and are highly dependent on weather conditions. However, they are of considerable interest, being responsible for the slow movement of all dissolved substances, micro-organisms or eggs and larvae, which are swept along and dispersed over hundreds or thousands of kilometres.

Mixing in Estuaries and Coastal Seas
Coastal and Estuarine Studies Volume 50, Pages 59-76
Copyright 1996 by the American Geophysical Union

Over the past few years, with the increasing interest shown for questions concerning the environment and zoning, coastal physical oceanography has focused on this point. Following Longuet Higgins's (1969) introduction of the idea of mass transport velocity, showing that this was the sum of the Eulerian residual current and Stoke's drift, various important studies have confirmed that water mass displacement can not be understood purely from the Eulerian concept. The Lagrangian concept of long term particle trajectories and residual current had to be introduced. This was done by Zimmerman (1979) and many authors then tried to determine its mathematical relation with Eulerian residual currents, such as Cheng *et al.* (1986) and Feng (1987 and 1990). They demonstrated the existence of a third current component, Lagrangian drift, which depends on the moment of particles' departure.

These fundamental mathematical developments are based on a hypothesis of slight non-linearity of physical systems. In the opposite case, numerical solutions to this problem were sought: Orbi and Salomon (1988), Salomon *et al.* (1988 and 1991), Foreman *et al.* (1991).

When currents and their spatial gradients are particularly intense, for example, in the English Channel's case, the non unicity of Lagrangian residual currents, even for an entirely periodic tide, creates problems for its use. Therefore, the authors have tried to resolve this difficulty by introducing a new spatial reference: the barycentric system, enabling a single current field to be obtained without averaging the Lagrangian drift.

This method, which had been only partially explained in two-dimensional space (Orbi and Salomon, 1988; Salomon *et al.*, 1988 and 1991) is extended here to three-dimensional space.

Methods

Instantaneous Currents Model

Let us consider a numerical tidal current model solving the Navier Stokes equations in the three-dimensional, non-linear form, or a two-dimensional model solving the same equations integrated on the vertical (called Saint-Venant's equations).

The choice of a numerical method is of little importance, however, because the model should then be used to calculate trajectories of imaginary particles, the meshes must be small enough to enable accurate computations of trajectories and of their residual components which are often one or two orders of magnitude lower than the tidal excursion, L. This requirement is general to all numerical methods which approximate derivatives by differences (or integrals by sums), for which a characteristic length scale should preferably be described by about 10 points (Vreugdenhil and Voogt, 1975). Here, after some tests it was concluded that 6 discretization intervals were an acceptable lower limit to obtain a correct evaluation of the residual movement.

The mesh size can then be easily defined. Let u be the current velocity, assumed to be sinusoid, of angular velocity ω :

$$u = u_o \sin(\omega t - \varphi)$$

$$L = \int_{\frac{T}{2}} u\,dt = \frac{2u_o}{\omega}$$

hence $$\Delta x \leq \frac{u_o}{3\omega}$$

For a semi-diurnal tide, comes $\Delta x \leq 2\,000\ u_o$ as average tidal velocities are of the order of 1 ms^{-1}, the tidal model mesh size must be about 1 to 2 km, to avoid the risk of incorrect calculation of the residual component near coasts and reliefs.

It was also observed that a regular spatial mesh, while not absolutely necessary (Foreman *et al.*, 1991), made calculation of trajectories easier.

Confronted with the spectrum of sea movements, this sort of model has a cut-off frequency which depends on the numerical scheme quality but corresponds to a wave length (λ_c) of about three times the mesh size.

According to the Lam *et al.* (1984) relation, this cut-off wave length corresponds to a grid dispersion coefficient (K_G) on the order of:

$$K_G = 5\ 10^{-4}\ \lambda_c^{1.2} \qquad \text{(in m.k.s. units)}$$

i.e. $$K_G = 18.7\ 10^{-4}\ \Delta x^{1.2}$$

or again

$K_G \approx 7\ m^2\ s^{-1}$ if $\Delta x = 1$ km

$\approx 17\ m^2\ s^{-1}$ if $\Delta x = 2$ km

$\approx 28\ m^2\ s^{-1}$ if $\Delta x = 3$ km

By using a model whose mesh and numerical diffusion coefficient comply with the relations above, the advective structures whose size is greater than $3\Delta x$ may be correctly described, and smaller gyres expressed as dispersion.

Therefore, the objective is to determine a residual current field to directly describe long term movements without modifying the cut-off frequency of the tidal model.

Lagrangian Residual Currents

Let us first consider the currents generated by a periodic tide (not necessarily sinusoidal) of period T, a wind field that can be spatially variable, yet constant over time, and no density gradient.

From any given initial situation, the model is activated until a stationary situation is reached, and is then used to calculate trajectories over the following two tidal cycles.

For various particles, each relating to a point of departure (x_o) and a moment of departure (t_o), numerical calculation of Lagrangian residual velocity is made, defined as follows:

$$\vec{V}_{rl}(x_o, t_o) = \vec{V}_{rl}(\alpha) = \int_{t_o}^{t_o+T} \vec{V}(\alpha, t)dt$$

This operation is repeated for a large number of points spread over the entire field, for instance within each mesh and for several moments of departure (t_o) spaced out over the next-to-last tidal cycle mentioned above.

Both theory (Cheng *et al.*, 1986) and numerical experience (Orbi and Salomon, 1988; Foreman *et al.*, 1991) demonstrate that, for each departure point (x_o) a series of different values of $\vec{V}_{rl}(x_o, t)$ which correspond to the various t values (Figure 1) are thus obtained.

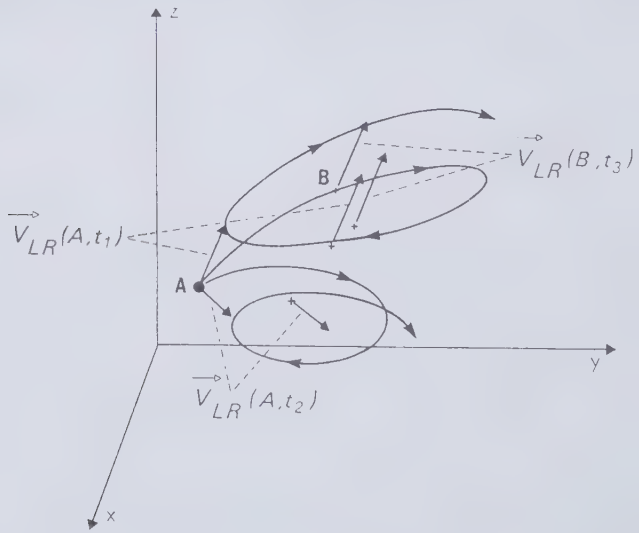

Figure 1. Kinematic representation of the Lagrangian residual velocity field in barycentric coordinates: x_i (i = 0 ; 1) are different points of departure of particles; G (x_i, t_i) are the centers of gravity of the particles trajectories starting from point x_i at time t_i.

Following Foreman *et al.* (1991), averaging these vectors over time may be attempted to obtain a single value:

$$\overline{\vec{V}_{rl}(x_o)} = \frac{1}{T}\int_T \vec{V}_{rl}(x_o, t)dt$$

Clearly, by proceeding in this way, part of the movement spectrum from the calculated current field is removed, which then has to be compensated for by increasing dispersion terms. Thus, the formalism of Reynold's stress on the meso-scale, introduced by Ronday (1976) is approximated.

However, this correction attempt is not satisfactory, since the advective components which were to be eliminated, represent a water and mass flux in a direction determined by the tide, whereas a diffusion term represents a flux in the direction of the concentration gradient.

An alternative solution was sought by introducing barycentric coordinates.

Barycentric Coordinates

The basic idea of this method is that each water particle will make only one long term displacement. Therefore, it has only one residual velocity. The difficulty run into above was due to the fact that residual displacements were assigned to geographical points, which are not characteristic of a particle, unless they are combined with a notion of time: only the (x_o, t_o), pair characterizes a particle. So, another single parameter, being the equivalent of the (x_o, t_o) pair was sought.

Following up on the ideas of Miche (1944) concerning surface waves, an ideal parameter to characterize a particle could be its position at rest, i.e., its position in the case of a tidal movement whose amplitude would be infinitely small.

In fact, for obvious practical reasons, this position is extremely hard to determine numerically and will be initially replaced by the position of the particle's centre of gravity during the tidal cycle under consideration.

Thus, along with the calculation of each particle's Lagrangian residual velocity, the average position of the particle will be calculated simultaneously: $G(x_o, t_o)$

$$G(x_o t_o) = x_o + \frac{1}{T}\int_{t_o}^{t_o+T}\left(\int_{t_o}^{t} V(\alpha, t')dt'\right)dt$$

The Lagrangian residual velocity is now allocated to this center of gravity (the barycenter).

This reference modification corresponds to a displacement of each of the beam vectors and $\vec{V}_{rl}(x_o, t)$ becomes separated and approximately distributed along the edges of an ellipsoid centred on point x_o (points G (x_o, t_o) and $G(x_o, t_1)$ on Figure 1).

Gathering at the same point or immediately beside it, other $\vec{V}_{rl}$ vectors are observed which in fact involve the same water mass, but were determined by releasing particles at other moments, and other locations distributed along the same particle trajectory (point x_1 at time t_1, on Figure 1).

On the contrary, particles released at the same point of departure x_o, but at time t_1 (different from t_o) will undergo a distinct trajectory and probably a different residual velocity.

This last vector will be allocated to a different center of gravity $G(x_o, t_1)$ (on Figure 1).

Finally, it has been numerically verified (Orbi and Salomon, 1988), that vectors gathering in the same area were nearly identical. However, small discordances may be observed in some places which we initially attributed to inaccuracies in the construction of tidal trajectories, but may also be related to the chaotic part of the movement set out by Ridderinkhof and Zimmerman (1992). Without solving the question, probably because our computations are limited to only one tidal cycle, these discrepancies were always found to be very small and could easily be included in the dispersive part of the movement.

The current field thus obtained could be used as it is, to calculate displacements or residence time, with the precaution of effecting a transposition between true three-dimensional space and the new coordinate system. Thus, a particle released at x_o, at the moment t_o, would undergo a spatial translation, and a series of particles successively released at the same x_o spot, would be apart from each other in the new reference. Each is placed at the centre of gravity of the movement defined during a tidal cycle. An inverse conversion then has to be made to return to true space.

As this velocity field is stationary, it might be non-divergent, but because of its kinematic elaboration which does not explicitly involve the notion of mass conservation, this is not absolutely true everywhere. This basic property especially fails near capes where the particle's average position may be quite different from its position at rest. However, for some practical applications dealing with water movements, transit times or fluxes, of water or dissolved chemicals, if the velocity field has been carefully constructed (using accurate tidal velocities, a large number of particles, correct spatial integration etc.) the velocity field may already be fit for use.

For other applications, such as computation of long term transport and mixing of conservative substances, some precautions must be taken to avoid unrealistic apparent local increases or decreases in concentrations which would result from a violation of the conservation of mass.

Two initial possibilities could be either using the conventional advection-dispersion equation in its non-conservative form, or employing a Lagrangian particle tracking technique.

A third possibility, preferable to this study, will be to slightly correct the current field obtained as explained above, to make it non-divergent. Advantage is taken of this operation to try to effect the transformation between the centre of gravity reference and that of the position of particles at rest.

It is then possible to proceed in two successive stages:

- first, the correction of two-dimensional currents (integrated on the vertical coordinate) thus minimizing the quantity $\nabla.(\bar{V}_{rl(x,y)}H_{(x,y)})$, using an iterative procedure, for instance,
- then, for a 3D calculation, horizontal velocities may be corrected in the same way, then vertical velocities deducted using the continuity equation.

At the outcome of this last operation, a single Lagrangian residual velocity field is finally obtained, very close to the previous one, yet non-divergent, thus enabling the advection-dispersion equation to be solved by a conservative numerical method, such as those relating to the control volume approach.

The ideal velocity field we are seeking, which involves the position of particles at rest is unique, by definition. The one we obtain here is clearly not, at least because of its numerical representation, but it is very close to it, and after this last step of correction, conservative.

Calculating Advection-Dispersion

Not only are Lagrangian residual velocities interesting for describing and understanding phenomena linked to long term circulation patterns, but they present another major advantage in enabling a direct calculation, over long time durations of the displacement and mixing of a dissolved substance.

Let us consider the usual expression of the advection-dispersion equation:

$$\frac{\partial C}{\partial t} + \vec{V} \cdot \vec{\nabla} C - [K]\nabla^2 C = 0 \qquad (1)$$

with C being a concentration

[K] is the tensor of turbulent diffusion and $\overline{V}$ the instantaneous velocity.

This can also be written:

$$\frac{DC}{Dt} - [K]\nabla^2 C = 0 \qquad (2)$$

DC/Dt representing the concentration variation along a trajectory, which can be directly calculated here in Lagrangian residual velocity field, with a time step equal to a tidal period.

Since the spatial reference is distorted by the barycentric transformation, the turbulent diffusion term [K] will have slightly different meaning than its usual one, when used throughout the tidal cycle, in Eulerian coordinates. Intra-tidal deformation of the water mass is absent from the calculations based on these residuals and this has to be compensated for by increasing [K]. The deformation of the water mass being generally an order of magnitude lower than the tidal oscillation, one may expect this correction to be small. This will be later verified numerically.

It must be noted that C is by no means a field of average values over a tidal cycle, which in this case would correspond to very high [K] values; C is an instantaneous value field which corresponds to the [K] tensor values which are very close (if not exactly identical) to those in a calculation based on tidal current fields (i.e. of about 10 $m^2 s^{-1}$ in horizontal directions and some 10^{-1} $m^2 s^{-1}$ in the vertical direction (see, for example Fisher *et al.*, 1979).

As hoped (see above), the method thus complies with fine spatial structures (dimension $>3\Delta x$) and enables steep gradients to be represented.

It can also be noted that, for reasons of numerical stability, at least, the integration time step is not necessarily equal to one tidal period. We can easily reduce it and thus either solve the equation (2) with a smaller time step, or solve an equation identical to (1), with $\vec{V}_{rl}$ replacing $\vec{V}$. The only limit of the time step will be due to the numerical scheme used. Since the numerical methods' performances generally depend on $\vec{V}$, through Péclet's number or Courant's number, using $\vec{V}_{rl}$ will enable a time step from 10 to 100 times above that used with instantaneous velocities. Thus carrying out these calculations over very long periods will not be very costly.

Variation of Tidal Amplitude

Up to this point, it was assumed that the tide was perfectly periodic, including only M_2, M_4, M_6. Since this is not true, one possibility to extend the method to real tides would be to consider each elementary component of the tidal spectrum separately, as did Foreman *et al.* (1991), and calculate the residual currents related to each one, then add them together. However, their composition is not linear, and when the related currents-amplitude is a few tens of centimeters per second, which is the case in the Channel near capes and islands, quite poor results can be expected.

In fact, on the northwest European continental shelf, the main tide components are M_2 and S_2, whose combination gives a semi-diurnal tide (here called D_2) whose amplitude varies every 15 days between the sum and the difference of M_2 and S_2. It was therefore considered to be preferable to make Lagrangian residual current calculation for a few specific D_2 amplitudes (spring, average, neap) and then interpolate among these results for any other D_2 amplitude. If possible, this unique tidal constituent which sums up the different semi-diurnal components will be imposed along oceanic boundaries of the model, where higher order terms are very weak, and these will be generated within the field, according to hydrodynamic equations.

In practice, this degree of sophistication will often be unnecessary. As trajectories or diffusion calculations are carried out over long periods (a few months or years), just one D_2 tide, whose amplitude is equal to the quadratic average of true tides, is sufficient.

Wind Effect

Wind stress on the water surface is an important driving force of water masses, having no true periodicity. To use the present method, therefore, the wind's continuous evolution in time has to be replaced by a succession of conditions assumed to be stationary, then calculating the Lagrangian residual currents for each of these phases.

Hence, we have to look for the system's dynamic memory, i.e. the duration over which an initial condition of the water mass remains perceptible, after external conditions have changed. This may be worked out doing combined simulations of the tide and suddenly varying wind fields. For the north-west European continental shelf, we found that this lapse time is 4 days (Salomon *et al.*, 1993). This may be considered as a cut-off frequency of the hydraulic system, which is unable to follow atmospheric events of shorter duration, in detail. As a consequence, the true evolution of weather conditions will be assimilated into a succession of stationary wind fields and the Lagrange current calculation explained above performed for each one.

In practice, to limit the amount of calculation due to the fact that an infinite number of meteorological situations can be thus defined, the Lagrangian residual current calculation could be run on only a finite number of these, and interpolation made among the values to find solutions which correspond to any non calculated meteorological situation. In the latter case, complete Lagrangian residual current calculation is replaced by a simple spatial interpolation.

Results and Discussions

Two-Dimensional Application

a) Residual current calculation

The method (Figure 2) was applied to the entire Western European continental shelf (Figure 3). The results presented here are limited to the English Channel.

The two-dimensional meso-scale numerical model is of the finite difference type with a regular mesh and resolution of one mile, using the A.D.I. method of solution.

The method has been widely described in literature (see Leenderstee, 1970) and will not be reproduced here (also see Salomon and Breton, 1991). Similarly, Orbi and

Salomon (1988) and Salomon *et al.* (1988), describe the Lagrangian residual current construction method in barycentric coordinates.

The results obtained for the Channel isles region are shown in Figures 4a and 4b for average tide and no wind.

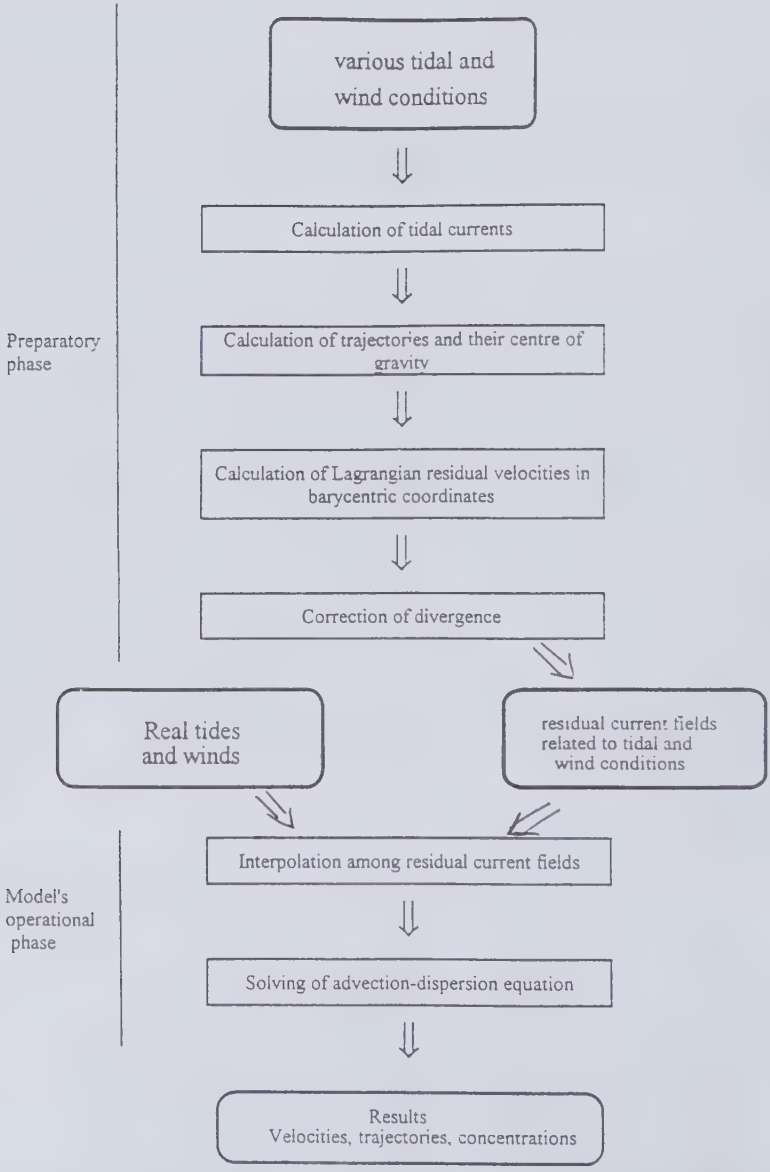
various tidal and wind conditions
Calculation of tidal currents
Preparatory phase
Calculation of trajectories and their centre of gravity
Calculation of Lagrangian residual velocities in barycentric coordinates
Correction of divergence
Real tides and winds
residual current fields related to tidal and wind conditions
Interpolation among residual current fields
Model's operational phase
Solving of advection-dispersion equation
Results
Velocities, trajectories, concentrations

Figure 2. Flow chart for calculation of currents and dissolved substance dispersion using the barycentric method

Figure 3. Location map

Figure 4a shows a field of Eulerian residual velocities, as could be obtained using several thousand current-meters. Many gyre structures can be seen, for example around the La Hague cape and Alderney Island, created by topographical unevenness. A general current can also be observed, turned toward La Hague Cape, in the south-west - north-east direction almost on the map's diagonal, as well as a northerly current along the continent. The mass transport velocity (Figure 4b) shows very similar spatial structures but their intensity can be quite different at times.

The Lagrangian current expressed in barycentric coordinates (Figure 4c) reveals largely different structures which are sometimes total opposites. The general northeasterly current no longer exists, highly intensive cyclonic gyres appear above shoals and around the Channel Islands which were not present in Eulerian representations. The northerly current along the coastline is now replaced by a southerly current. The quantitative importance of Lagrangian drifts can be noted in this application.

The field of Lagrangian residual velocities, corrected for divergence (Figure 4d) differs little from the original. All the structures already appearing in Figure 4c, can also be seen on Figure 4d, and currents are slightly less regular since local topographical variations create equivalent differences in velocity. It must be remembered that the depths input into the model have not been smoothed at all. As expected, the largest differences were found along the coastline near capes (for instance along La Hague Cape), over one to two meshes in width. On this site, the zero flux condition perpendicular to the coastline perceptibly modifies the longitudinal velocity component.

Similar calculations of residual currents were made all over the Channel for an average tide and eight wind stress directions, regularly spaced by 45°, as well as for no wind (Salomon and Breton, 1993). Wind stress was 7.2 x 10^{-2} Pa.

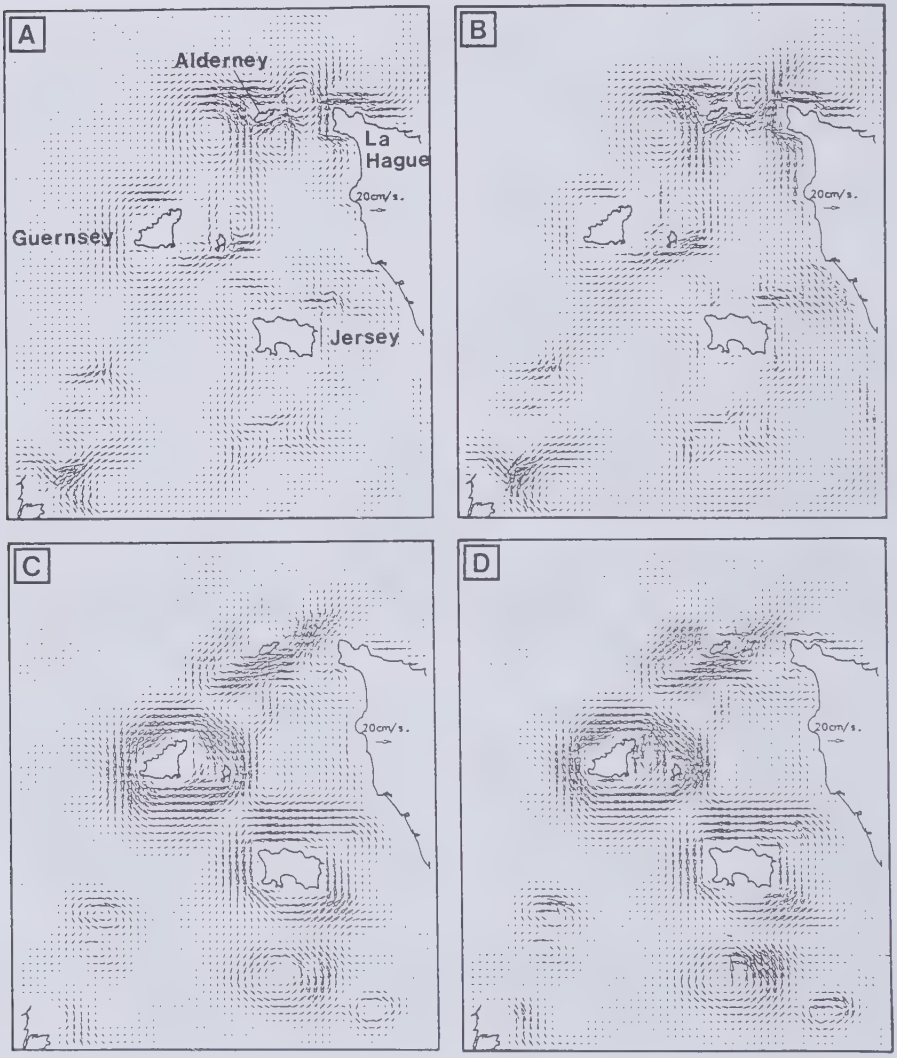

Figure 4: a: Eulerian residual currents ;
b: mass transport velocities
c: raw Lagrangian residual velocities in barycentric coordinates
d: Lagrangian residual velocities corrected for divergence

Figure 5 shows variation of the residual current intensity on a spot located near the Strait of Dover, as it can be calculated by interpolation-extrapolation using these nine numerical values. The Figure is simple for this specific case. Approximate symmetry can be observed between winds from the northern and southern sectors. A north wind of approximately 2 m s^{-1} cancels out the 8 cm s^{-1} residual current created by the tide.

By performing this interpolation calculation for each mesh in the model, Lagrangian residual current field corresponding to every meteorological situation can be constructed.

Figure 6 shows this result for a situation with an average tide and a 6 m s^{-1} wind from the southwest, which approximately makes up the average quadratic wind on the Western European continental shelf.

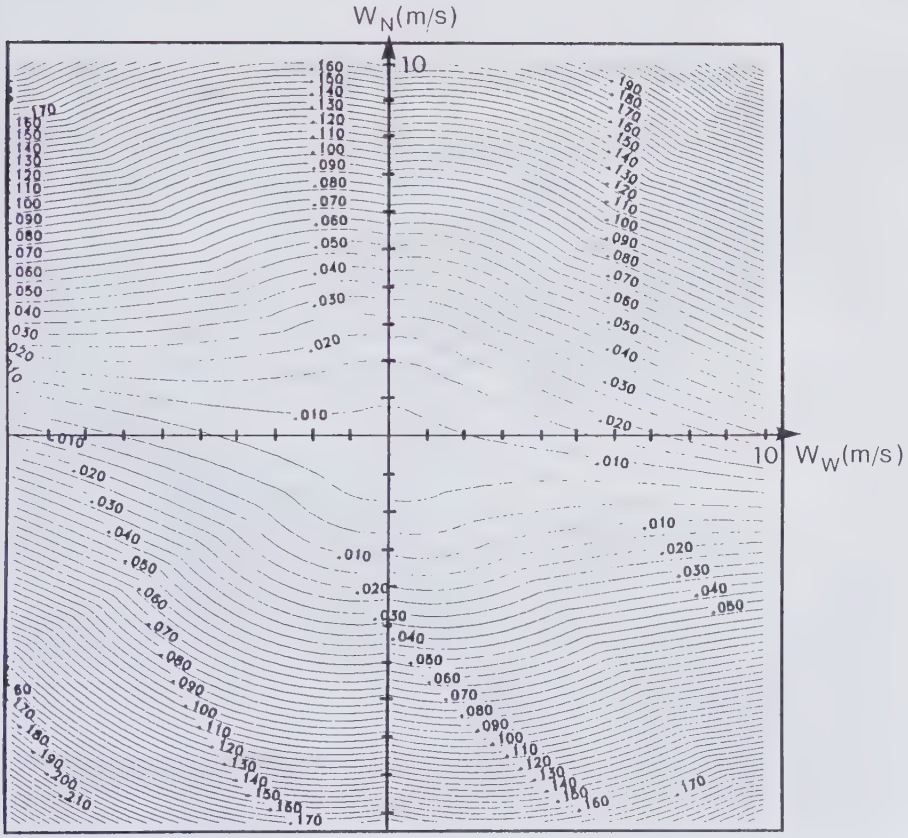

Figure 5. Intensity of Lagrangian residual current, depending on direction and force of wind for a specific point, near the Strait of Dover. W_N and W_E are north and east components of the wind velocity.

b) Long term dispersion calculation

The dispersion of an almost conservative radioactive chemical element was calculated: that of antimony^{125}, discharged at La Hague Cape by a nuclear fuel reprocessing plant.

The advection-dispersion equation was solved in the conservative form:

$$\frac{\partial(HC)}{\partial t} + \nabla.(HC\,\bar{V}_{rl}) - H[K]\nabla^2 C = 0$$

The numerical diagram combines Kurihara-type time discretization (Roache, 1982) and Quick-type spatial discretization (Léonard, 1981). The dispersion tensor is limited to a single element, spatially variable according to Elder's formula (1959):

$$K = \beta\, V\, H$$

The β coefficient is known to be about 0.25 in constant flows.

Two series of tests were run:

- an initial calculation was made using the single field of currents in Figure 6. The time needed to achieve an equilibrium, is about 18 months. Very good correlation between measurements and calculations was obtained (Salomon *et al.*, 1991) for a value of 0.7. The dispersion coefficient then lies between 10 and 50 $m^2\ s^{-1}$, depending on location.

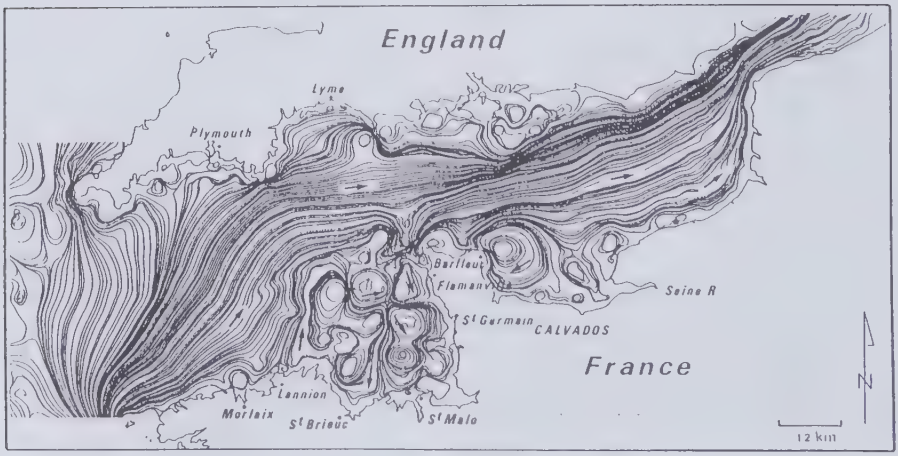

Figure 6. Residual Lagrangian trajectories through the English Channel, for average tide and wind.

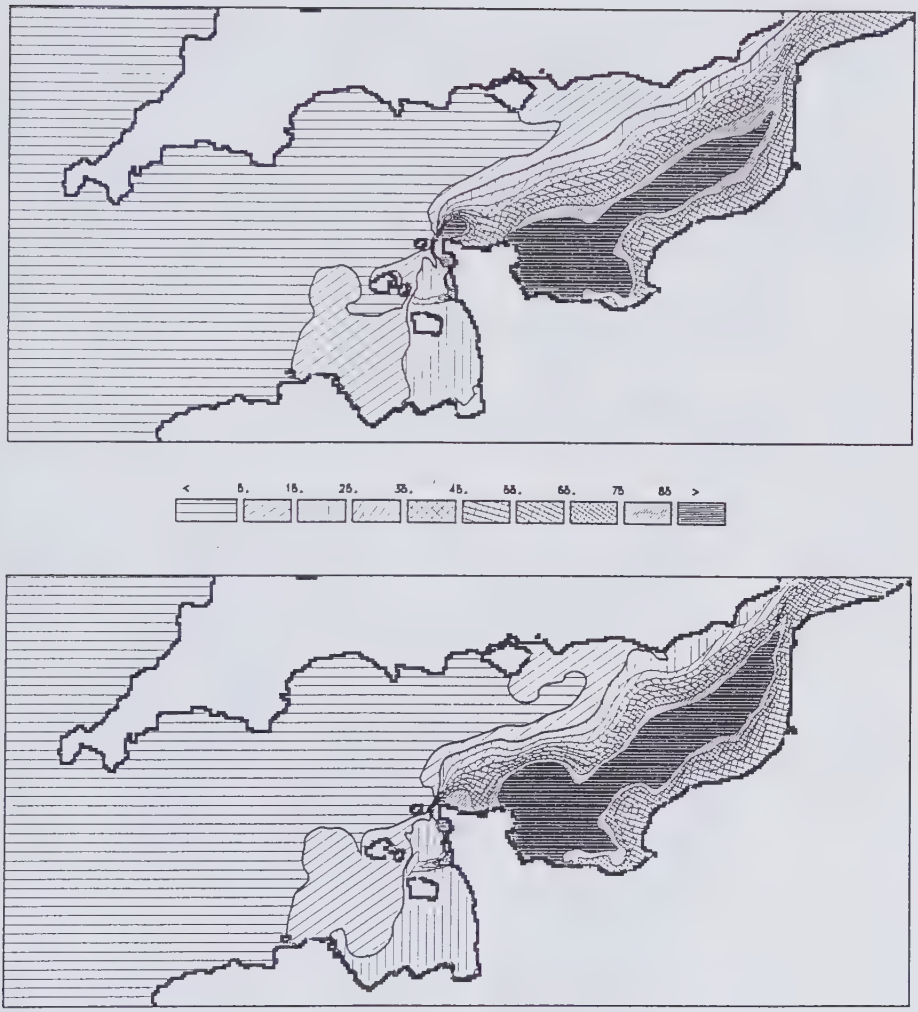

Figure 7. ^{125}Antimony distribution in the Channel
a: Computed with a unique residual velocity field.
b: Computed with a sequence of 3.5 days averaged wind stress situations.

It was thus verified that a single Lagrangian residual velocity field enables the use of a dispersion coefficient of the same order of magnitude, although a bit higher (0.7, instead of 0.25), as that which would been used with instantaneous tidal velocities.

- A second series of simulations were run using a succession of residual current fields, each corresponding to meteorological situations, averaged over a duration of half a week.

The best result obtained here, illustrated by the example in Figure 7, was for a coefficient of $\beta = 0.3$. The value of K then lies between 10 and 20 $m^2 s^{-1}$. This is the proof that all the operations for extracting long term current components did not introduce any parasite diffusion.

In the preceding application, part of the time variability residual current field was lost because only annual mean winds were used, leading to a slight overestimation of the dispersion coefficient. By inputting wind fields averaged twice a week, the model can operate just as it does with real wind fields and instantaneous currents.

2) Three-dimensional Application

Barycentric method results, extended over the vertical dimension are given for the Strait of Dover area (Figure 8). The numerical technique of the tidal model was presented in Lazure and Salomon (1991) and was used here in unchanged form.

Figure 8 shows several vertical cross-sections of the Lagrangian residual currents in the case of no wind. Highest velocities, oriented toward the North Sea, can be seen in the center of the Strait, especially above sand banks. There, lowest depth values correspond to highest velocities. On the contrary, along the coast, in similar water depths, velocities are much lower and in some places, oriented toward the English Channel.

Dispersion calculation of fresh water inputs in the Channel were conducted in three dimensions, using these Lagrangian residual velocity fields, for different wind situations. Although *in situ* validations were not conducted in detail, results appeared to be very coherent with what is known about salinity distribution in the region, the most interesting aspects of the method being its educational and economical aspects.

Conclusion

The calculation method for Lagrangian currents in barycentric coordinates was developed for shallow macrotidal seas.

The model demonstrates that it is possible to remove the paradox in Lagrangian drifts and obtain a single residual current field for given external conditions. By not smoothing the velocities, we avoid the input of any artificial dispersion. The cut-off frequency of the tidal model is preserved and a precise description of long term currents including small-sized spatial structures is obtained.

These current fields can then be used for direct calculation of transport and mixing of dissolved substances (or micro-organisms) over a very long term, in compliance with high-gradient patterns. This calculation is fast and quite inexpensive.

The Channel application demonstrated the method's interest and a possible way to extend it to non periodic tides and variable wind conditions.

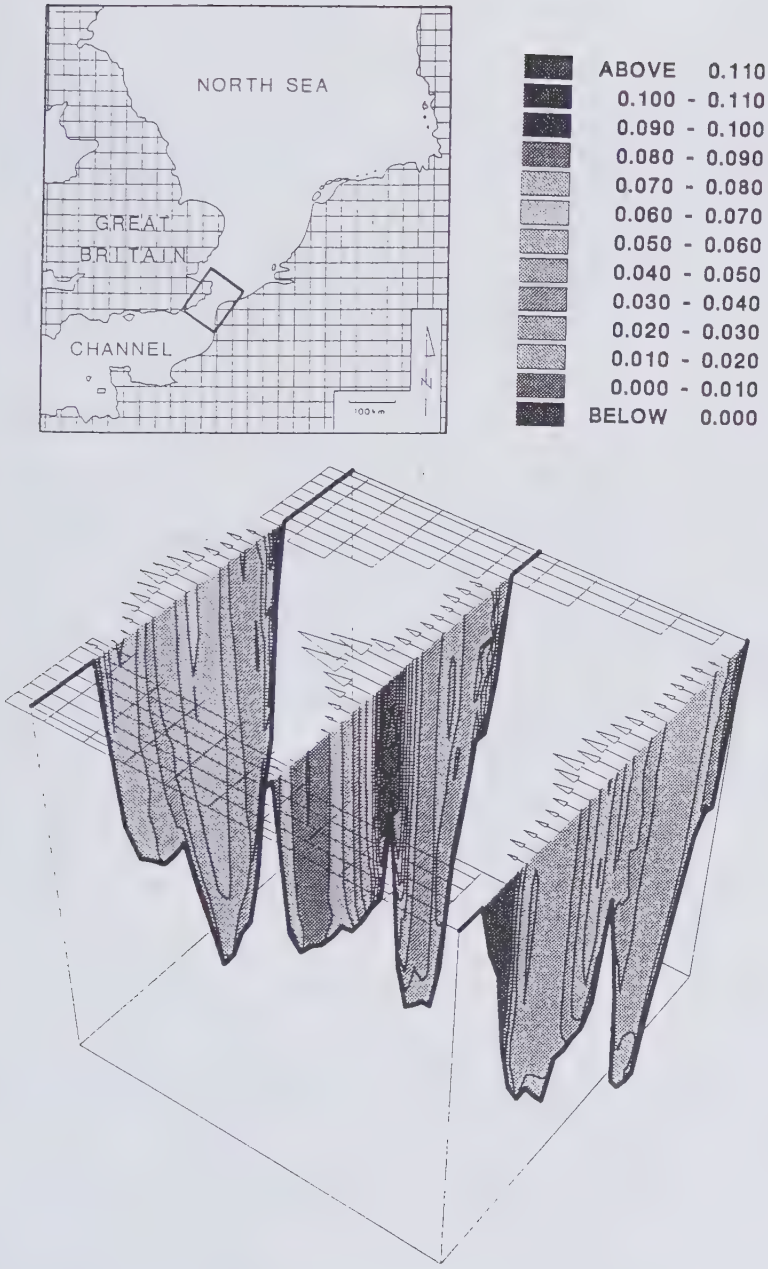

Figure 8. Vertical cross-sections of the 3d. Lagrangian residual currents in the Strait of Dover for no wind and average tide.

References

Cheng R.T., Feng S. and Xi P. On Lagrangian residual ellipse. In *Physics of Small Bays and Estuaries*, edited by J. Van de Kreeke, 102-113. Lecture notes on Coastal and Estuarine Studies, Springer-Verlag, Berlin, 1986.

Feng S.. A three-dimensional weakly non linear model of tide-induced Lagrangian residual current and mass-transport, with an application to the Bohai Sea. In *Three dimensional Models of Marine and Estuarine Dynamics,* edited by J.C.J. Nihoul and B.P. Jamart, 471-488, Elsevier Oceanography Series, Amsterdam, 1987.

Feng S. On the Lagrangian Residual velocity and the mass-transport in a multi-frequency oscillatory system. In *Coastal and Estuarine studies*, edited by R. T. Cheng, 38, 34-48. . Residual currents and long-term transport. Springer Verlag, 1990.

Fisher H.B., List E.J., Imberger J., Brooks N.H. *Mixing in inland and coastal waters*. Academic Press. New York, 483 p, 1979..

Foreman M., Baptista A., Walters R. Tidal model studies of particle trajectories around a shallow coastal bank. *Atmosphere Ocean* 30,43-69, 1992.

Lam D.C.L., Murthy C.R., Simpson R.B. Effluent transport and diffusion models for the coastal zone. Lectures notes on coastal and estuarine studies. Springer Verlag, 1984.

Lazure P. and Salomon J.C. Coupled 2D and 3D modelling of coastal hydrodynamics. *Oceanologica Acta*, 14, 73-180, 1991.

Leendertsee J.J. and Gritton E.C. *A water quality simulation model for well mixed estuaries*. Vol. II. The New York city Rand Institute. Technical report R-708-NYC, 1971.

Leonard B.P. A survey of finite differences with upwinding for numerical modelling of the incompressible corrective diffusion equation. In *Computational techniques in transient and turbulent flows*, Pineridge Press, 2, 1-36, 1981.

Longuet-Higgins M.S. On the transport of mass by time-varying ocean currents, *Deep Sea Research*, 16, 431-447, 1969.

Miche M. Mouvements ondulartoires de la mer en profondeur constante ou décroissante. *Annales des Ponts et Chaussées*, 2, 1944.

Orbi A. and Salomon J.C. Dynamique de marée dans le golfe Normand-Breton. *Oceanologica Acta*, 11, 55-64, 1988.

Ridderinkhof H., Zimmerman J.T.F. Chaotic stirring in a tidal system. *Science*, 258, 1107-1111, 1992.

Roache P. *Computational fluid dynamics*. Hermosa Publishers, Albuquerque, 446 p, 1982.

Ronday F. Modèles hydrodynamiques, modélisation des systèmes marins, projet mer, rapport final. Services du 1er Ministre, Bruxelles, Vol 3, 270, 1976.

Salomon J.C., Guegueniat P., Orbi A., Baron Y. A Lagrangian model for long term tidally induced transport and mixing. Verification by artificial radionuclide concentrations, 384-394. In *Radionuclides : a tool for oceanography*. Elsevier Applied Science, 1988.

Salomon J.C. and Breton M. Courants résiduels de marée dans la Manche. *Oceanologica Acta*, 11, 47-53, 1991.

Salomon J.C., Guegueniat P., Breton M. Mathematical of ^{125}Sb transport and disffusion in the Channel. In *Radionuclides in the Study of Marine Processes* edited by P. Kershaw and D. Woodhead, 74-83. Elsevier Applied Science, 1991.

Salomon J.C. and Breton M. An atlas of long term currents in the Channel. *Oceanologica Acta*, 16, 439-448 1993.

Salomon J.C., Breton M., Guéguéniat. Computed residual flow through the Strait of Dover. *Oceanologica Acta* , 16, 449-455, 1993.

Vreugdenhil C.B. and Voogt J. Hydrodynamic transport phenomena in estuaries and coastal waters: Scope of mathematical models. Symposium on modeling techniques. San Francisco, California. A.S.C.E., 690-708, 1975.

Zimmerman J.T.F. On the Euler-Lagrange transformation and the Stocke's drift in the presence of oscillatory and residual currents. *Deep Sea Research*, 26, 505-520, 1979.

5

Modelling Oil Slick Trajectories in Spencer Gulf, South Australia

P. J. Bills, D. W. F. Standingford and B. J. Noye

Abstract

This paper reports the application of the advection-diffusion equation in hindcasting the movement of an oil spill which occurred during rough weather at Port Bonython in Spencer Gulf, South Australia, in late August 1992. A fine-grid model tracks the slick in the immediate vicinity of the spill and then a medium sized grid (with elements five times the linear dimension of the fine-grid elements) tracks the slick to landfall. Slick size is renormalised periodically and adjusted in accordance with the formulae that describe the dimension of a spill during given phases of slick evolution. Slick shape is determined by the advection-diffusion model. Tidal forcing at the open boundary of the fine-grid model is obtained from runs of the medium-grid model, which in turn uses tidal forcing information from a coarse-grid model. The elements of the coarse-grid model have linear dimension fifteen times those of the fine grid. Wind forcing for the trajectory models is obtained from a half-hourly time series supplied by the Australian Bureau of Meteorology for the duration of the spill.

Introduction

The efforts of tidal modellers are increasingly being directed towards applications of their programs to environmental problems. Concern for the degraded state of the planet's environment provides a natural impetus for this. On one hand the models can be applied to problems associated with the management of finite resources, such as the studies into the movement of prawn larvae that are being conducted by Noye *et al.* (1992) in Spencer Gulf, South Australia (inset, Figure 1).

Mixing in Estuaries and Coastal Seas
Coastal and Estuarine Studies Volume 50, Pages 77-94
Copyright 1996 by the American Geophysical Union

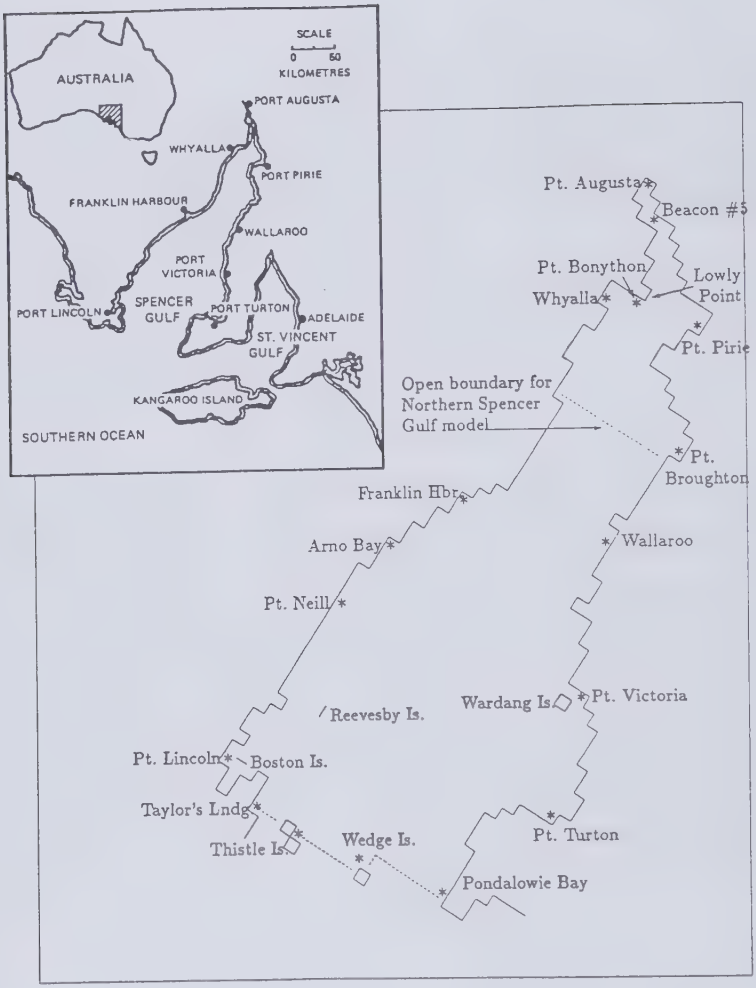

Figure 1. Locality map for Spencer Gulf and the corresponding coarse-grid model. Model location of tidal observation stations is indicated by *. The location of the open boundary for the medium-grid Northern Spencer Gulf model is marked.

On the other hand the models can be applied to mitigate the impact of pollution of various types in the marine environment. In this paper we examine the performance of an oil slick trajectory model (Standingford, 1992) which was designed for the immediate vicinity of Port Bonython, a hydrocarbons pre-processing facility on Spencer Gulf, South Australia. Initially it was intended that the performance of the

model be compared with that of a parametric oil slick trajectory model developed in the early 1980's as part of an Environmental Impact Study that preceded the construction of the Port. Some controlled releases of diesel were made at that time and observations of these have been published by SANTOS Ltd. (1981a,b).

However, in strong winds on 30th August 1992, 296 tonnes of ship's fuel oil were accidentally spilled into Spencer Gulf at Port Bonython when the tug "*Turmoil*" collided with the 95000 D.W.T. tanker "*ERA*". The spill was the largest in South Australian history and caused enormous public concern. In spite of concerted attempts to contain and disperse the slick at sea, an estimated 20 tonnes of oil made landfall, enough to cause the death of hundreds of seabirds. The landfall site, south of Port Pirie, is abundant in mangroves and possible long term damage to fisheries and prawn nurseries there is being studied. The events of the spill served to underline the need for a model capable of accurately predicting a slick's trajectory so that maximum resources can be directed to the containment and subsequent reclamation or dispersal of the oil at sea.

According to the World Almanac (1991) more than one trillion gallons of oil have been accidentally released into the global environment in the last 25 years. Attempts to model these spills have received a significant boost with the development of stable and accurate three-dimensional tidal models and new powerful computer hardware on which they run. A growing literature is developing on the subject. For example, Lardner *et al.* (1988) have developed a pollutant transport model using the advection-diffusion equation and have applied it to the simulation of a 5000-barrel oil spill in the Arabian Gulf. They consider the processes of surface spreading, weathering and both horizontal and vertical dispersion. They also describe attempts to model the sub-surface plume of an oil slick and predict that significant proportions of a spill can eventually reside beneath the surface if the oil remains at sea for sufficient time. They also comment that as much as 1.5 million tons of oil is spilled per decade in the Arabian Gulf! A more recent estimate of the amount of oil spilled the Arabian Gulf is 20,000-40,000 tons a year (Al-Rabeh, 1993).

Al-Rabeh *et al.* (1989), among others, use an alternative approach in which the Lagrangian movement of discrete packets of oil is used, to which is added a stochastic method of simulating the eddy diffusion, in order to model the movement of a slick. In addition to including advection and turbulent diffusion, the processes of surface spreading, vertical dispersion (due to wind-driven wave action), evaporation and emulsification are also included. Al-Rabeh and Gunay (1992a,b) generalise this work to include the dispersion of a range of passive pollutants in the offshore Safaniya area of the Arabian Gulf.

The present paper records our first attempts to model the trajectory of the relatively small Port Bonython slick. Thus far the work has not proceeded to include the modelling of the sub-surface plume, evaporation or emulsification. The results, however, show that the observed trajectory of the slick in the vicinity of Port Bonython is faithfully reproduced.

The Hydrodynamic Model

The movement of the oil slick was determined using tidal and wind-driven currents generated by a three-dimensional hydrodynamic-numeric model.

This model consists of the σ-transformed barotropic tidal equations with wind forcing, and is given in Noye and Bills (1992). Only aspects of the hydrodynamic formulation directly relevant to the present application will be included here.

The equations are closed by using a prescribed form for the vertical eddy viscosity coefficient $N\eta$. The form used is

$$N_\eta(x,y,\eta,t) = \alpha + \beta F(\eta) H \sqrt{U^2 + V^2}, \qquad (1)$$

where

η is the transformed vertical coordinate, such that $\eta = 0$ represents the transformed sea surface and $\eta = 1$ represents the transformed sea floor,

α is a minimum absolute value for $N\eta$; the value 0.0001 m^2s^{-1} is used,

$F(\eta)$ is the prescribed variation of the vertical eddy viscosity coefficient in the η direction; the form

$$F(\eta) = A\eta^2 + B\eta + C$$

is used, where $A = -4N_{max} + 2b + 2s$, $B = 4N_{max} - b - 3s$, $C = s$; $s = F(0)$, $N_{max} = F(0.5) = 1.0$ and $b = F(1.0)$ are the surface, mid-depth and bottom values used, respectively,

β is a dimensionless constant, determined numerically as the value which minimizes errors between observed and predicted tidal flows; the value $\beta = 0.0050$ is used.

H is total depth, and

U,V are the depth-averaged velocity components.

It is assumed that the horizontal components S_x ,S_y of surface stress are proportional to the η-gradient of surface current in the following way:

$$S_x = -\frac{\rho}{H}\left(N_\eta \frac{\partial u}{\partial \eta}\right)\Big|_{\eta=0} \text{ and } S_y = -\frac{\rho}{H}\left(N_\eta \frac{\partial v}{\partial \eta}\right)\Big|_{\eta=0}, \qquad (2)$$

in which ρ is the density of seawater, assumed constant at 1027 kgm^{-3} and u,v are the depth-dependent components of current velocity. The surface stress components may also be expressed in terms of the wind velocity field using the following quadratic law:

$$S_x = \rho_a C_{10} u_{10} \sqrt{(u_{10})^2 + (v_{10})^2} \text{ and } S_y = \rho_a C_{10} V_{10} \sqrt{(u_{10})^2 + (v_{10})^2}\ , \qquad (3)$$

where

ρ_a is the density of air (assumed constant at 1.225 kgm^{-3}),

(u_{10}, v_{10}) are the horizontal components of wind velocity recorded 10 m above mean sea level (MSL), and

C_{10} is a dimensionless drag coefficient which depends on wind speed according to some empirical formula; the relation proposed by Wu (1982), viz.

$$C_{10} = \left(0.8 + 0.065\sqrt{(u_{10})^2 + (v_{10})^2}\right) \times 10^{-3} \quad (4)$$

for light to hurricane force winds is used.

At the open boundaries of the model tidal elevation is specified as the sum of the contributions of the four dominant tidal constituents, two of which are diurnal (O_1, K_1) and two semi-diurnal (M_2, S_2). A Sommerfeld-type radiation condition is used, viz.

$$\frac{\partial \zeta_b}{\partial t} + C\frac{\partial \zeta_b}{\partial n} = 0, \quad (5)$$

where phase speed C is calculated in the Orlanski (1976) manner, n is measured in the outward normal direction, and external meteorological and tidal forcing are specified through the open boundary elevation ζ_b.

The Advection-Diffusion Equation

For the present study the oil slick is regarded as residing in the surface layer. It advects with the water surface as a result of wind and tidal forcing and undergoes horizontal diffusion. The mass of a real oil slick diminishes with time due to vertical dispersion through the water column and the evaporation of lighter fractions, but these factors are not included here. The governing equation adopted is the well known two-dimensional advection-diffusion equation:

$$\frac{\partial C}{\partial t} + u_s\frac{\partial C}{\partial x} + v_s\frac{\partial C}{\partial y} = \alpha_x\frac{\partial^2 C}{\partial x^2} + \alpha_y\frac{\partial^2 C}{\partial y^2}$$

where C(x,y,t) is the mass concentration of oil at position (x,y) at time t. The velocities u_s and v_s are the surface velocities in the x and y directions, respectively. These values are computed as the model simulation proceeds. It is intended that the model be available for on-line simulations for predicting the movement of a slick, so for that reason the advection-diffusion equation is solved concurrently with the tidal/wind simulation. The terms u_s ($\partial C/\partial x$) and v_s ($\partial C/\partial y$) model the advection of

the oil with the surface currents. The terms $\alpha_x (\partial^2 C/\partial x^2)$ and $\alpha_y (\partial^2 C/\partial y^2)$ model the eddy diffusion of the oil on the sea surface; without these terms, which contribute a random spreading of the oil in all directions, the spatially centred differencing used for the advective terms tends to break the oil up as though it were a solid. The constants α_x and α_y are the horizontal eddy diffusion coefficients in the x and y directions. The value 80 $m^2 s^{-1}$ is used, based on field studies done in the Northern Spencer Gulf region by Holloway (1974) (see also Noye, 1984).

The Finite Difference Scheme

The finite difference approximations used for the equations of the hydrodynamic model can be found in Noye and Bills (1990, 1992) and in Bills (1991).

The Arakawa C lattice is used for both the tidal and advection-diffusion models, with mass concentration C defined at the grid point used for elevation ζ (Figure 2).

Using time and space-centred finite difference approximations for both first and second derivatives, an explicit approximation for mass concentration at time level (n+2) and position i can be developed in terms of values of mass concentration at time levels (n+1) and n, and values of surface velocity at time level (n+1). The second order spatial derivatives are differenced on a grid with uniform spacing Δx and Δy in the x and y directions, in the manner

$$\left[\frac{\partial^2 C}{\partial x^2}\right]_i^{n+1} \simeq \frac{1}{(2\Delta x)^2}\left[C_{i+1}^{n+1} - C_i^{n+2} - C_i^n + C_{i-1}^{n+1}\right]$$

where a term $2C_i^{n+1}$ has here been split between time levels (n+2) and n as $\left(C_i^n + C_i^{n+2}\right)$ in order to achieve numerical stability for the overall scheme. The finite difference formula obtained is as follows :

$$C_i^{n+2} \simeq \left(1 + 2d_x + 2d_y\right)^{-1} \left\{ C_i^n + 2d_x\left(C_{i+1}^{n+1} - C_i^n + C_{+1}^{n+1}\right) \right.$$

$$+ 2d_y\left(C_{i_1}^{n+1} - C_i^n + C_{i_2}^{n+1}\right)$$

$$\left. - C_{x\,i}^{\,n+1}\left(C_{i+1}^{n+1} - C_{i-1}^{n+1}\right) - C_{y\,i}^{\,n+1}\left(C_{i_1}^{n+1} - C_{i_2}^{n+1}\right) \right\}$$

where $C_{x\,i}^{\,n+1}$ and $C_{y\,i}^{\,n+1}$ are Courant numbers defined by

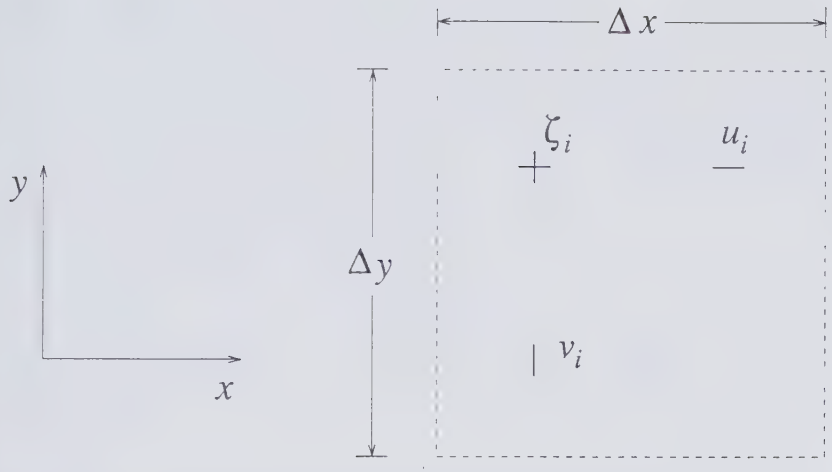

Figure 2. The basic grid element contains 3 grid points, one for elevation ζ and mass concentration C, and one each for the u and v velocity components.

$$C_{x_i}^{n+1} = \frac{\{u_s\}_i^{n+1}\Delta t}{\Delta x}, C_{y_i}^{n+1} = \frac{\{v_s\}_i^{n+1}\Delta t}{\Delta y}$$

and d_x and d_y are diffusion numbers defined by

$$d_x = \frac{\alpha_x \Delta t}{(\Delta x)^2}\ ,\ d_y = \frac{\alpha_y \Delta t}{(\Delta y)^2}$$

where Δt is the uniform spacing in time. Subscript i_1 refers to the element "above" the element i in Figure 2 and i_2 refers to the element "below"; subscript (i-1) refers to the element on the left, (i+1) to the element on the right. The velocity quantities $\{u_s\}_i^{n+1}$ and $\{v_s\}_i^{n+1}$ are averaged values given at the mass concentration gridpoints. I'Anson (1989) has shown that the above relation is stable for $d_x = d_y = d \leq 1/4$. Non-negative answers are obtained if $C_{x_i}^{n+1} = C_{y_i}^{n+1} = C_r$ such that $-2d \leq C_r \leq 2d$, but this sufficiency condition is not necessary and is overly strong in practice.

Phase Formulae and Slick Size

The oil is introduced into the model at the rate at which it was spilled into the environment. Contours of mass concentration are obtained from the predictions of the advection-diffusion procedure. A method for approximating the boundary of the slick from these contours is then required. Fay (1969) provides empirical formulae

upon which to base estimates of the size of a slick as a function of time, given the initial slick volume V. Hoult (1972) and Stolzenbach *et al.* (1977) give useful discussions of these formulae. Slick evolution is divided into three characteristic phases which highlight dominant spreading and retarding forces on the slick:

1. *Gravity-Inertia Phase*

   Average radius of slick ~ $[g\,(\rho_w - \rho_{oil})/\rho_w]^{1/4}\, V^{1/4}\, t^{1/2}$

2. *Gravity-Viscous Phase*

   Radius ~ $[g\,(\rho_w - \rho_{oil})/\rho_w]^{1/6}\, \nu^{-1/12}\, V^{1/3}\, t^{1/4}$

3. *Surface Tension-Viscous Phase*

   Radius ~ $\sigma^{1/2} \left(\rho_w^2 \nu\right)^{-1/4} t^{3/4}$

where g is the acceleration due to gravity, ρ_w is the density of water and ρ_{oil} the density of oil, ν is the kinematic viscosity of water and σ is the net surface tension force.

Having estimated the size of the slick from the above formulae, the position and shape of the slick is that which corresponds to the contours of highest oil concentration given by the advection-diffusion procedure (see Figure 3).

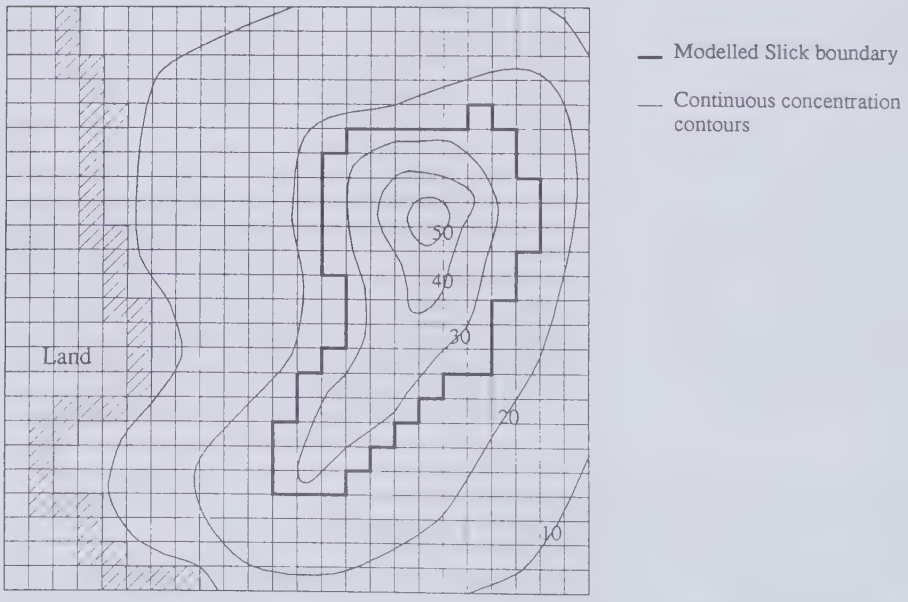

Figure 3. If the empirical formula indicates the slick occupies 100 gridsquares, the extent of the modelled slick is taken to be the 100 gridsquares of highest oil concentration.

Tidal Forcing

For the immediate vicinity of Port Bonython, a 1500 element fine-grid hydrodynamic model - denoted PtB - has been developed (Figure 4) with element dimensions 381 $\times$ 381m^2. The spilled oil is released continuously into this model and the slick is tracked until it is about to leave the model through its north-eastern open boundary. At this point the location of the slick is transferred to a 930 element medium-grid model of Northern Spencer Gulf (element dimensions: 1905 $\times$ 1905 m^2 based on the depth-averaged tidal flat Northern Spencer Gulf (NSG) model of Bills and Noye (1992). The three-dimensional NSG model developed here, however, does not take into account the wetting and drying of tidal flats - mean sea level depths for the model are given a minimum value of 2m in order to prevent elements drying. The slick is tracked within the medium-grid model until it reaches landfall on the eastern coast of Spencer Gulf.

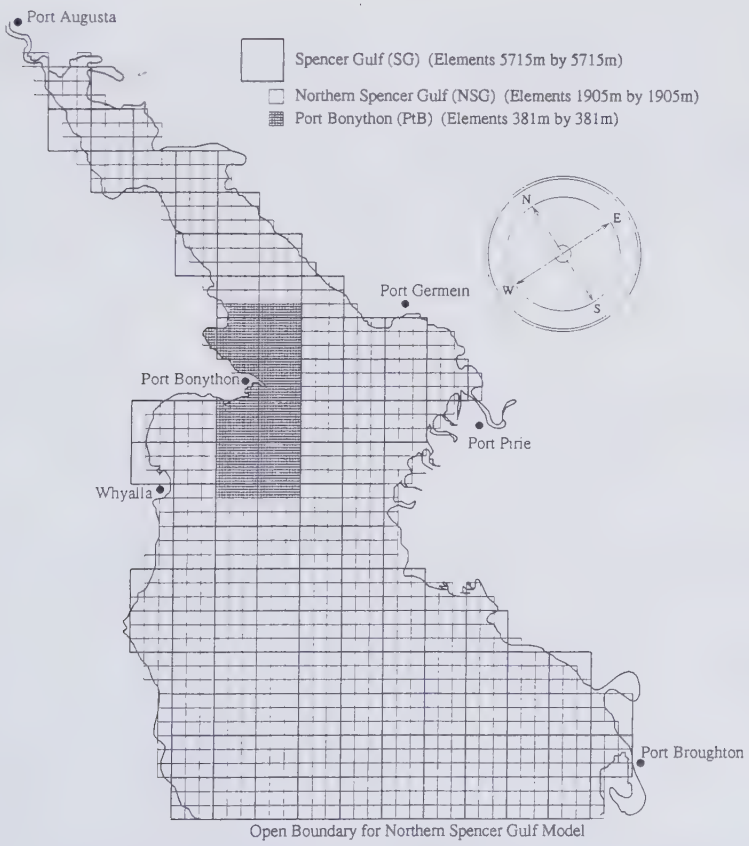

Figure 4. Northern Spencer Gulf, showing the three grids used. 225 fine-grid Port Bonython (PtB) model elements make one coarse-grid Spencer Gulf (SG) element.

Tidal forcing for the medium-grid NSG model is derived from the predictions of a coarse-grid 760 element model of the whole of Spencer Gulf (element dimensions: 5715×5715 m^2) developed by Bills and Noye (1986). This model is shown in full in Figure 1. Measurements of amplitude and phase for the major tidal constituents O_1, K_1, M_2 and S_2 at four positions at the mouth of the Gulf taken by Steinberg (1983) drive the Spencer Gulf (SG) model. Tidal forcing for the PtB model is taken from the NSG model. The PtB model has spatial resolution 225 times that of the SG model.

Radiation open boundary conditions (5) are used for both the fine-grid and medium-grid models since both are wind and tide driven.

NSR Studies

Experimental diesel slick releases tracked by Natural Systems Research Pty. Ltd. (NSR) to calibrate their model were used as a means of testing the fine-grid PtB model. Although trajectories of 21 runs were recorded in the SANTOS (1981a,b) reports (11 in the Summer and 10 in the Winter investigations), only the Summer experiment field conditions are available and these are in the June 1981 report. The scale of the original SANTOS (1981a,b) tracking region is small in comparison to the extent of the Port Bonython grid used here. Not all of the 11 Summer trajectories are suitable for comparison as many make landfall within 1.5 hour close to their release point. This corresponds to the movement of the slick by only a few grid squares on the Port Bonython lattice and does not fully test the model.

Two trajectories were selected for comparison. The input wind data for these cases were taken from the field notes of the original NSR study. The input windspeed (knots) and direction (degrees True) were recorded at given times during the two runs. Linear interpolation was used to provide values between these times.

The results recorded by NSR (SANTOS, 1981a) for the observed and predicted trajectories of these two field releases are illustrated in Figures 5 and 6. Trajectories predicted by the hydrodynamic/advection-diffusion model (TED/ADM) developed here are included for comparison. The TED/ADM program produces output describing the movement and evolution of the entire slick, and is not specifically developed for tracking the centroid of a slick. A routine that finds the position of highest mass concentration based on the locations of the four adjacent gridsquares of highest oil concentration is therefore used to plot the centroid of the slick. In both runs, the trajectory given by the TED/ADM program compares favourably with observations. Best performance is observed when the slick moves quickly (Figure 5). The qualitative behaviour in Run 6 is similar to the event of 30th August 1992, when the slick quickly rounded Point Lowly and headed north. In this case, the NSR model predicts landfall near Point Lowly.

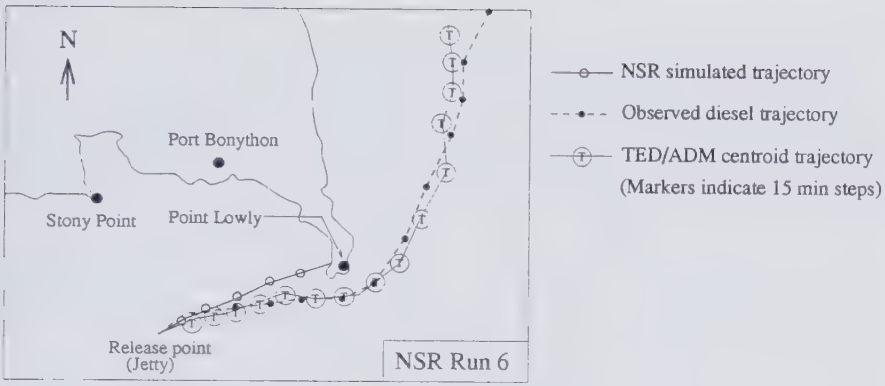

Figure 5. Trajectories produced by NSR and TED/ADM models c.f. observations for Run 6.

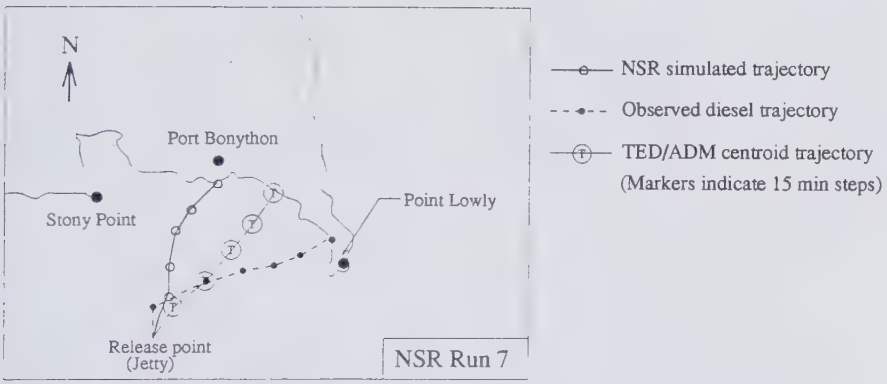

Figure 6. Trajectories produced by NSR and TED/ADM models c.f. observations for Run 7.

From the runs presented in Figures 5 and 6 it can be seen that, given the limitations discussed earlier, the model performs well. The comparison with NSR Run 6 shows the model's ability to produce trajectories in agreement with those observed when movement of the slick is comparable to the grid scale. Run 7 illustrates the scale problem with our method. When landfall is made in a short time, non-zero mass concentration is present in only a few grid elements and the predictions of the centroid algorithm are not reliable; a Lagrangian particle tracking method may be better suited in this instance.

The NSR parametric model was used by SANTOS Ltd. during the August 1992 spill at Port Bonython but proved unable to predict the trajectory of the slick.

The August 1992 slick moved outside the bounds of the PtB fine-grid model. Details of the contingencies used to keep track of the slick with the NSG medium-grid model follow.

August 1992 Spill

At 10:42 a.m. on Sunday 30th August 1992, during rough weather, the tugboat "Turmoil" holed the tanker "ERA". The resultant release of 296 tonnes of heavy engine oil created a slick which was driven across the Gulf by tidal and wind action. Some 20 tonnes eventually made landfall in sensitive mangrove areas south of Port Pirie. At least 600 sea birds died and local fishermen are seeking compensation for anticipated damage to the fishery in that area.

In addition to having first hand observations of the position of the slick from SANTOS staff, the Bureau of Meteorology has provided half hourly wind data for the entire period from Whyalla airport, only 18 km from the site of the spill.

For the immediate vicinity of Port Bonython, the 1500 element fine-grid tide and wind-driven PtB model of Figure 4 is used with a time step of 16sec. The spilled oil is released into this model and tracked until it is about to leave the model through its north-eastern open boundary, when its location is then transferred to the 930 element medium-grid NSG model, used with an 80sec time step. The slick is tracked within this model until it reaches landfall on the eastern coast of Spencer Gulf.

The wind data for the models is obtained at each respective time step by linear interpolation of the given wind data. Since wind data for only one station is available it is assumed that the interpolated wind field applies to the entire model at the given time. This assumption is clearly more valid for the PtB model than for the NSG model.

The value of surface vertical eddy viscosity used is crucial to how well the slick is modelled. If taken too high the slick barely moves, but oscillates back and forth with the wind and tide driven currents. If too low, the slick races across the Gulf under the influence of the wind and quickly makes landfall north of Port Germein. As little practical information for the selection of a value for the surface eddy viscosity was available, ten values in multiples of 0.001 m^2s^{-1} in the range 0.001-0.010 m^2s^{-1} were tried in order to ascertain the importance of this parameter. These surface values of vertical eddy viscosity are low compared to the maximum attained lower down in the water column and so the function used to describe the vertical distribution of eddy viscosity was taken to be a parabola with maximum at mid-depth.

The marine fuel slick is modelled by releasing the 296 tonne spill over a period of 3 hour 25min (the observed duration of the spill) into the grid square on the PtB grid corresponding to the end of the 2.4 km long Port Bonython jetty. The centroid trajectories corresponding to the use of the surface values of vertical eddy viscosity 0.001-0.010 m^2s^{-1} were calculated and Figure 7 shows three of these.

When the slick approaches the open boundary of the PtB model, the position of the slick is transferred to the corresponding position in the Northern Spencer Gulf model. The trajectories followed by the centroid for the three surface vertical eddy viscosity values 0.001 m^2s^{-1} , 0.005 m^2s^{-1} and 0.010 m^2s^{-1} , after transfer to the NSG model until landfall, are illustrated in Figures 8-10. The observed trajectory, provided by SANTOS Pty. Ltd., is shown for comparison in Figure 11.

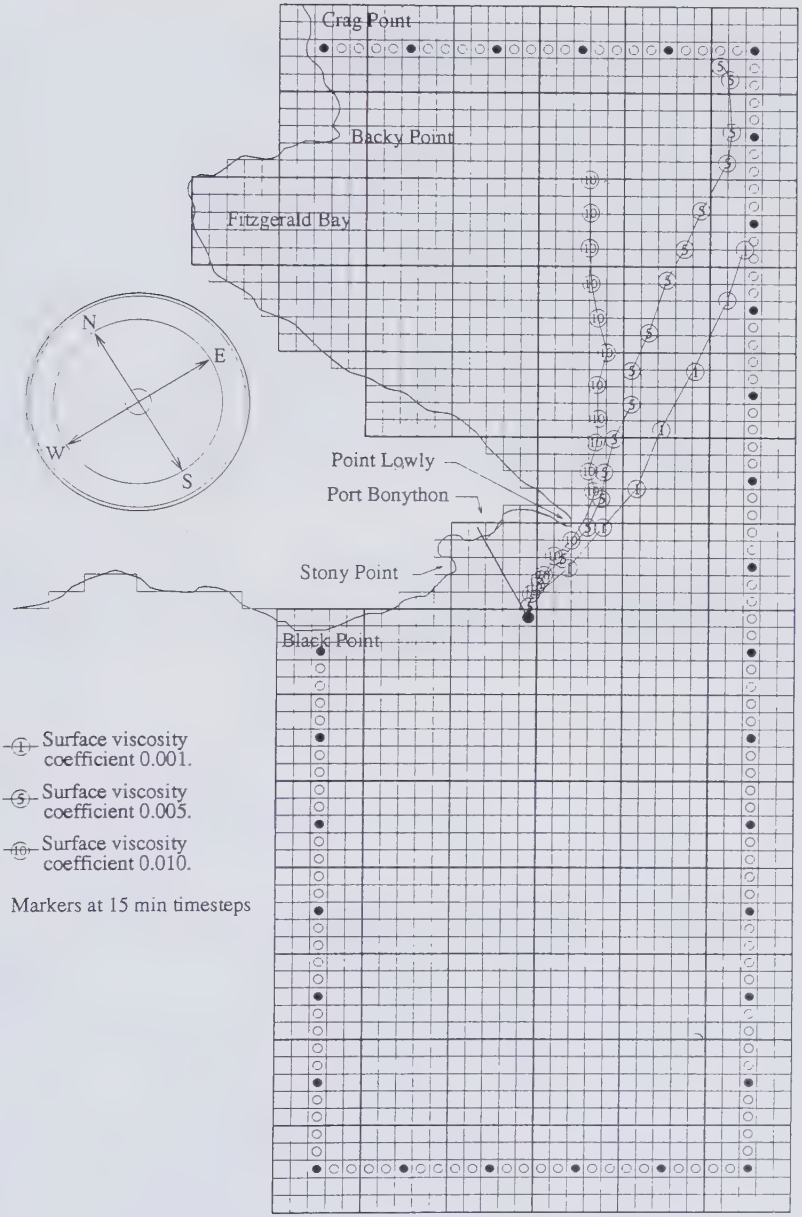

Figure 7. Simulated trajectories for the August 30th 1992 spill from the end of the jetty at Port Bonython. The surface vertical eddy viscosity parameter is varied from 0.001 m^2s^{-1} to 0.010 m^2s^{-1}. Increasing the value slows the eastward movement of the slick.

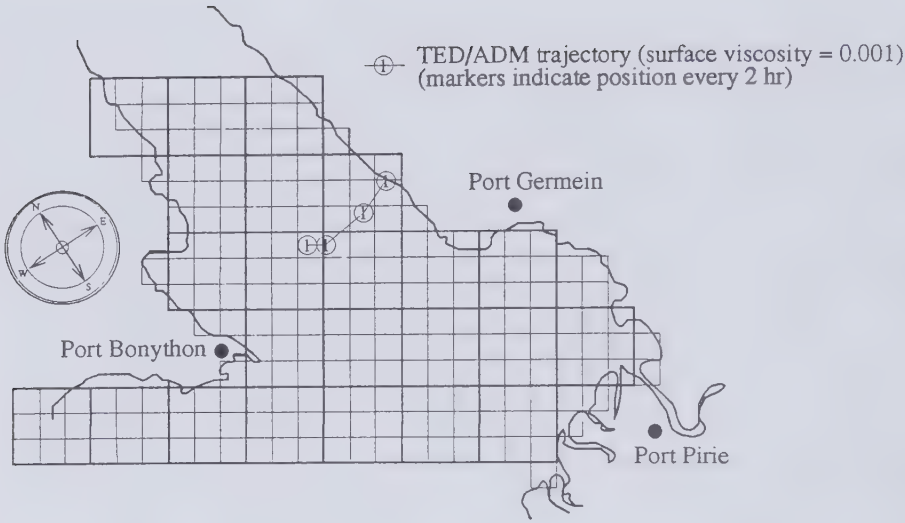

Figure 8. Simulated trajectory for the spill on August 30th 1992 using surface eddy viscosity value 0.001 m^2s^{-1} in the NSG model. Landfall is incorrectly predicted only 6 hour after the transfer is made between models.

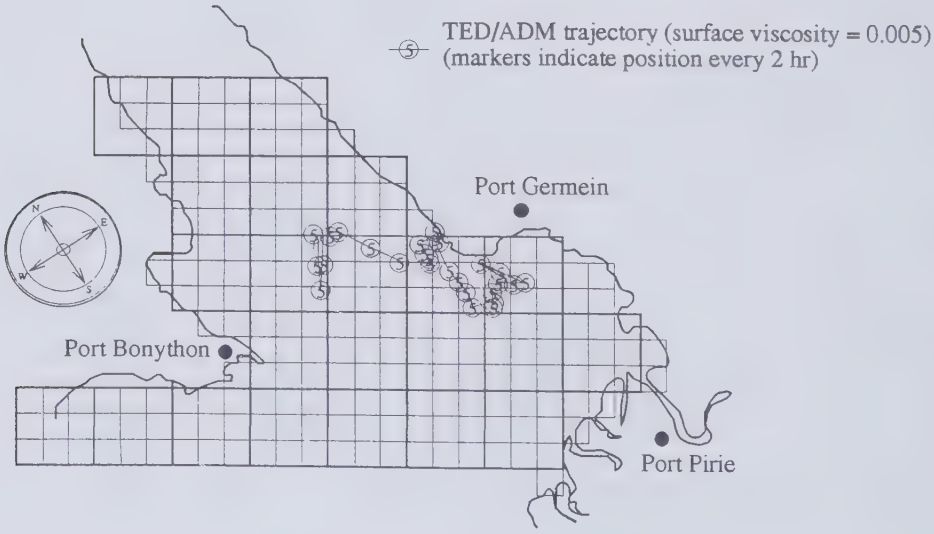

Figure 9. Simulated trajectory for the spill on August 30th 1992 using surface eddy viscosity value 0.005 m^2s^{-1}. Landfall is made near Port Germein.

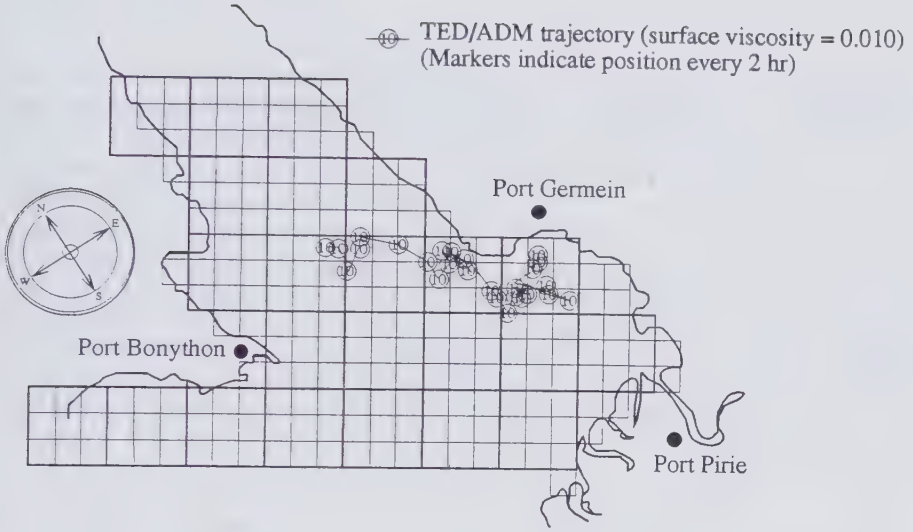

Figure 10. Simulated trajectory for the spill on August 30th 1992 using surface eddy viscosity value 0.010 $m^2 s^{-1}$. The slick remains in Port Germein Bay instead of proceeding south.

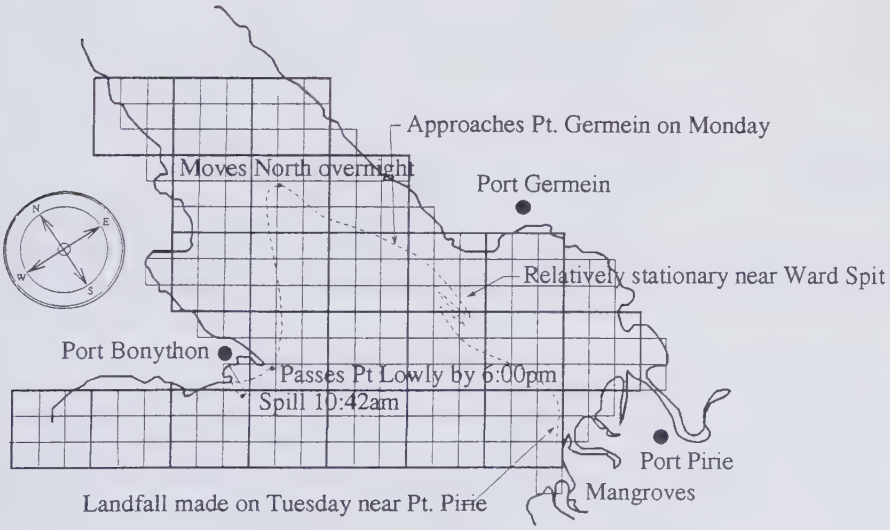

Figure 11. Observed trajectory for the marine fuel spill of 30th August 1992. Landfall is made south-west of Port Pirie in dense coastal mangroves.

Discussion

The application of the TED/ADM model to the marine fuel spill of August 1992 has provided a useful indication of its strengths and weaknesses. Within the fine-grid PtB model the observed trajectory is reproduced well. When the slick is transferred to the NSG model, the trajectory simulation is reasonably accurate until the slick moves close to the coastline. In the NSG model, the grid squares are nearly 2×2 km^2 and this is too coarse a scale at which to resolve the slick which was at one point observed to be only 500m long and 100m wide when it was about 10 km north of Port Pirie. The wind data from Whyalla airport is probably not appropriate for use near the eastern coast of the Gulf, where a local land-sea breeze and the influence of nearby mountain ranges could reduce the effect of the North-Westerly winds measured at Whyalla. Possibly for these reasons, landfall in the mangroves south of Port Pirie was not attained. Greater spatial resolution near coastal boundaries seems necessary to produce accurate tracking near the landfall region.

Conclusions

The events surrounding the oil spill of August 1992 have focused attention on the need to develop an accurate oil slick trajectory model for the Port Bonython region. The spill occurred 2.4 km offshore on the west coast of Spencer Gulf and travelled for two days before making landfall just 20 km away. It's trajectory was complicated, and much effort was expended keeping track of it and deploying personnel to be ready for clean-up on landfall. Using a computer model which accurately predicts the trajectory of the slick could free resources for the clean-up effort.

A trajectory model designed to run in parallel with the tidal program so that on-line meteorological data can be used, has been presented.

The model was tested against field data collected in a previous study by NSR Pty. Ltd. It performed well, but showed a loss of accuracy when movement modelled is small in comparison to the grid scale. Finer spatial resolution seems necessary when slick velocity is small and/or when the slick is near the coast.

The oil spill of 30th August 1992 provided a useful set of data for validating and improving the model. The simulated trajectory of this slick closely paralleled the observed one while within the fine-grid PtB model. When transferred to the coarser NSG grid, accuracy diminished. Among the reasons for this is the fact that the NSG model elements are nearly 2 km square and therefore too coarse to resolve the slick which was much smaller than this as it approached landfall near Port Pirie. Another source of error was the application of wind data from Whyalla airport to the entire NSG model, since it is likely that near the eastern coast local land-sea breezes and the influence of low mountain ranges would modify its speed and direction.

Recommendations for Future Development

The model has been developed to a point where it can form the basis for developing a predictive tool for the tracking of oil slicks in the region of Port Bonython in Spencer Gulf and, provided sufficient driving and calibration information is available, at other sites in the Gulf. There are, however, a number of improvements that can be made:

- Model the three-dimensional structure of the slick.
- Extend the fine-grid model across the Gulf to take in the full path of the slick.
- Improve the modelling of the physics of the slick to include evaporation, emulsification and solidification. The formation of "wind-rows" was observed prior to landfall of the August 1992 spill and this, too, should be investigated. Satellite images taken at the time may improve the observational database.
- Include wind data from Port Pirie to supplement the data from Whyalla airport, and include the influence of atmospheric pressure in the tidal model when it has been extended across the Gulf. This data is already available from the Bureau of Meteorology. Use the recorded tide at Port Bonython to check that the tidal model is correctly forced. It is possible there were significant surge effects present before and after the spill occurred.
- Modify the three-dimensional tidal program to include the wetting and drying of the shallow regions of Spencer Gulf so that the actual bathymetry of the shallow coastal zone can be used.
- Investigate the empirical formula used for surface wind stress (Wu, 1982) to account for the differing shear stress responses of oil and water, and for the characteristics of individual oil types.
- Implement a stochastic model of the movement of the oil slick.

Acknowledgments. The authors wish to thank the Adelaide Bureau of Meteorology for providing the wind data for the period spanning the spill event, and the National Tidal Facility for providing the tide-height constants used to drive and calibrate the tidal models. The provision of the observed trajectory by SANTOS Pty. Ltd. is also gratefully acknowledged. Comments by referees were used to improve the final version of the article.

References

Al-Rabeh, A.H., Models for the simulation of the transport and fate of oil spills in the Arabian Gulf, *Arabian J. for Sci. Engng*, in press, 1993.

Al-Rabeh, A.H., H.M. Cekirge and N. Gunay, A stochastic simulation model of oil spill fate and transport, *Appl. Math. Modelling*, 13, 322-329, 1989.

Al-Rabeh, A.H. and N. Gunay, On the application of a three-dimensional hydrodynamic model for a limited sea area, *Coastal Engng*, 17, 173-194, 1992a.

Al-Rabeh, A.H. and N. Gunay, On the application of a particle dispersion model, Coastal Engng, 17, 195-210, 1992b.

Bills, P.J., Barotropic depth-averaged and three-dimensional tidal programs for shallow seas, Ph.D. thesis, The University of Adelaide, 1991.

Bills, P.J. and B.J. Noye, Tides of Spencer Gulf, South Australia, in *Computational Techniques and Applications: CTAC-85*, edited by J. Noye and R. May, Elsevier Science Publishers B. V. (North-Holland), 519-531, 1986.

Bills, P.J. and B.J. Noye, Numerical model of a coastal sea with tidal flats, in *Computational Techniques and Applications: CTAC-91*, edited by J. Noye, B. Benjamin and L. Colgan, 117-126, 1992.

Fay, J.A., The spread of oil slicks on a calm sea, in *Oil on the Sea*, edited by D.P. Hoult, Plenum Press, 53-63, 1969.

Holloway, P., Determination of eddy diffusion coefficients for Northern Spencer Gulf, Cruise Report 4, Flinders Institute for Atmospheric and Marine Sciences, Flinders University of South Australia, 19 pp., 1974.

Hoult, D.P., Oil spreading on the sea, Annual Review of Fluid Mechanics, 4, 341-368, 1972.

I'Anson, K., A numerical model of the movement of prawn larvae in Spencer Gulf, Honours thesis, The University of Adelaide, 164 pp, 1989.

Lardner, R.W., W.J. Lehr, R.J. Fraga and M.A. Sarhan, A model of residual currents and pollutant transport in the Arabian Gulf, Appl. Math. Modelling, 12, 379-390, 1988.

Noye, J., Physical processes and pollution in the waters of Spencer Gulf, Mar. Geol., 61, 197-220, 1984.

Noye, B.J. and P.J. Bills, A three-dimensional tidal model for coastal seas, *Proc. of the Third Australian Supercomputer Conference*, The University of Melbourne, Australia, December 3-6, 1990.

Noye, B.J. and P.J. Bills, A three-dimensional tidal model for coastal seas, in *Computational Techniques and Applications: CTAC-91*, edited by J. Noye, B. Benjamin and L. Colgan, 373-384, 1992.

Noye, B.J., P.J. Bills, K. I'Anson, and C.C. Wong, C.C. Prediction of prawn larvae movement in a coastal sea, in *Computational Techniques and Applications: CTAC-91*, edited by J. Noye, B. Benjamin and L. Colgan, 385-392, 1992.

Orlanski, I., A simple boundary condition for unbounded hyperbolic flows, *J. Computational Physics*, 21, 251-269, 1976.

SANTOS Limited, Liquids Project: Oil Spill Trajectory Study, Final Report on the Stony Point Summer Investigations, June 1981, 30 pp. + Appendices, 1981a.

SANTOS Limited, Cooper Basin Liquids Project: Oil Spill Trajectory Study, Final Report, September 1981, 29 pp. + Appendices, 1981b.

Standingford, D. W. F., A wind and tide driven oil spill trajectory model of the Port Bonython region of Spencer Gulf, South Australia, Honours thesis, The University of Adelaide, 162 pp, 1992.

Steinberg, C.R., Tidal exchanges at the mouth of Spencer Gulf, South Australia, Honours thesis, Flinders University of South Australia, 79 pp, 1983.

Stolzenbach, K.D., O.S. Madsen, E.E. Adams, A.M. Pollack, and C.K. Cooper, A review and evaluation of basic techniques for predicting the behaviour of surface oil slicks, Ralph M. Parsons Laboratory for Water Resources and Hydrodynamics, Report No. 222, Dept. Civil Engineering, M.I.T., 1977.

World Almanac and Book of Facts, New York World Telegram Corporation, 1991.

Wu, J., Wind stress coefficients over sea surface from breeze to hurricane, *J. Geophys. Res.*, 87, 9704-9706, 1982.

6

Tide-Induced Residual Currents Generated by the Stokes Layer in the Rotating Tidal Basin

H. Yasuda

Abstract

Tide-induced residual currents due to the nonlinear effect of the bottom Stokes layer have been analysed in the idealized basin with the Earth's rotation effect. The nonlinear effect generating the residual current can be produced by the horizontal variations of tidal currents besides existence of the Stokes layer. This study shows that the Earth's rotation effect can induce the depth-averaged residual current in the tidal basin with horizontal variations of a tidal current though such averaged currents are not generated by any means in the non-rotating basin. This depth-averaged residual currents are generated in the longitudinal and lateral directions of the tidal current if the tidal current has lateral and longitudinal gradients, respectively, and they get larger with the increase of the Coriolis parameter. In the case where the tidal current has longitudinal variation, the residual current forms a vertical circulation even in the basin with no Earth's rotation effect, which has been presented so far both theoretically and experimentally, while the vertical circulation becomes quieter by the rotation effect. The tide-induced residual currents obtained in this study can be applied to the residual currents observed in Hiuchinada Sea of the Seto Inland Sea, Japan, in the south area of the North Sea, Europe, and in the hydraulic experimental basin.

Mixing in Estuaries and Coastal Seas
Coastal and Estuarine Studies Volume 50, Pages 95-109
Copyright 1996 by the American Geophysical Union

Introduction

The tide-induced residual currents, due to the nonlinear effect of the tidal currents, have been studied by many researchers and several generation mechanisms of the current have been presented so far (Zimmerman, 1981, Robinson, 1981, Wright and Loder, 1986 etc.). In Hiuchinada Sea of the Seto Inland Sea, Japan, there flows the residual current well-known to the local fishermen and oceanographers, but such residual current cannot be observed in the hydraulic scale model by any means, the scale ratio of which are respectively 1/2000 and 1/160 in the horizontal and vertical directions (Yasuda, 1989). The generation mechanism of this residual current has been obscure for a long time though many kinds of field observations have been carried out in this sea. Judging from the fact that this residual current can be observed all the year round, it is considered to be caused mainly by the nonlinear effect of tide or tidal current. The basic tide, i.e., M_2-component of tides is reproduced acculately in the whole area of this model and the current in the model also well corresponds to the reality in general regarding the M_2-component. As this scale model has no Earth's rotation effect, the observed residual current in the real sea is expected to be generated by the effective action of the Earth rotation.

Further, it has been shown that the vertically averaged along-isobath residual currents generated over the ridge depended on the Coriolis parameter in strength and the along-isobath residual current was not recognized in the non-rotating basin if the tidal current crossed over the ridge perpendicularly (Yasuda and Zimmerman, 1986). It is suggested eventually that these residual currents could be obtained in the tidal basin with the Earth's rotation effect by taking account of the bottom Stokes layer and the horizontal variation of tidal currents. Combination of the horizontal and vertical variations of tidal current can generally produce the nonlinear effect inducing residual currents even in the non-rotating basin.

In this study, the tide-induced residual current due to the Stokes layer will be analysed in a rotating tidal basin with the amplitude of tidal currents varying horizontally, and this analytical result will be applied to the generation of the residual current in Hiuchinada Sea and the other basins.

An Analysis of the Tide-Induced Residual Currents

If the nonlinear effect of currents is very weak, motion equations governing the tidal currents can be decomposed into those of the basic oscillatory, residual and the other tidal components (Yasuda, 1981). The motion equations of the basic oscillatory and residual currents can be written as

$$\frac{\partial u_T}{\partial t} - v_T f = -g\frac{\partial \eta_T}{\partial x} + \nu_z \frac{\partial^2 u_T}{\partial z^2} \qquad (1)$$

$$\frac{\partial v_T}{\partial t} + u_T f = -g\frac{\partial \eta_T}{\partial y} + \nu_z \frac{\partial^2 v_T}{\partial z^2} \tag{2}$$

$$-v_s f = -g\frac{\partial \eta_s}{\partial x} + \nu_z \frac{\partial^2 u_s}{\partial z^2} - \left\langle u_T \frac{\partial u_T}{\partial x} \right\rangle_s - \left\langle v_T \frac{\partial u_T}{\partial y} \right\rangle_s \tag{3}$$

$$u_s f = -g\frac{\partial \eta_s}{\partial y} + \nu_z \frac{\partial^2 v_s}{\partial z^2} - \left\langle u_T \frac{\partial v_T}{\partial x} \right\rangle_s - \left\langle v_T \frac{\partial v_T}{\partial y} \right\rangle_s \tag{4}$$

where u and v are respectively components of current velocity in x and y directions of the horizontal plane, and η, f and ν_z are the displacement of the sea surface, the Coriolis parameter and the vertical viscosity, respectively. The axis z indicates the vertically upward direction from the sea floor. Suffixes T and S denote respectively the basic oscillatory and the residual components. The horizontal friction terms are neglected here assuming that the horizontal variation of the tidal current given as a condition of this model is much gentler than the shear of the Stokes layer formed by the horizontal viscosity.

The third terms of Eqs. (1) and (2) express the pressure gradient due to the tide. If the amplitude of this third term can be regarded as constant horizontally, we can get the analytical solution of the vertical structure of the oscillatory current as follows (Yasuda, 1987);

$$u_T = \frac{F}{\sigma} \mathrm{Re}\left[i\left\{ \frac{1+f^*}{2}(1-\alpha f^*)e^{-(1-i)bz} + \frac{1-f^*}{2}(1+\alpha f^*)e^{-(1-i)az} - (1-\alpha f^*) \right\} e^{-i\sigma t} \right] \tag{5}$$

$$v_T = \frac{F}{\sigma} \mathrm{Re}\left[\{ \frac{1+f^*}{2}(1-\alpha f^*)e^{-(1-i)bz} - \frac{1-f^*}{2}(1+\alpha f^*)e^{-(1-i)\alpha z} - f^*(1-\alpha) \} e^{-i\sigma t} \right] \tag{6}$$

where σ is the frequency of the basic tide and F is the amplitude of the pressure gradient force due to the tide. Symbol i expresses the imaginary unit concerning time. The coefficient F/σ is the conventional amplitude of the tidal current in the outside of the boundary layer and f^* the Coriolis ratio to the tidal frequency, f/σ. a and b are respectively $(1 + f^*)^{1/2}\beta_s$ and $(1 - f^*)^{1/2}\beta_s$, and β_s is $(\sigma/2\nu_z)^{1/2}$ the reciprocal of which indicates the characteristic thickness of the Stokes layer. α determining the tidal current ellipse depends on the width of the basin. When α takes unity, the ellipticity of the tidal current gets zero in the outside of the boundary layer. Although the vertical component of the current might be induced by the continuity of water, its effect will be neglected here since it depends on the

horizontal topography and it makes this problem complicated vainly. The solution process of the equations governing the oscillatory component and the details of (5) and (6) have been described in Yasuda (1987).

If the tidal currents have similarity in both of the lateral and longitudinal directions, the fourth and fifth terms of Eqs. (3) and (4) become known and we can get the analytical solution of the residual current somehow. Although there are another terms generating the residual component except for these terms in fact, they consist of higher frequency tidal currents and can be neglected as small quantities in the very weak nonlinear model. Equations (3) and (4) yield the following vorticity equation in the vector expression.

$$\nu_z \frac{\partial^3 X_s}{\partial z^3} - jf \frac{\partial X_s}{\partial z} = Q \tag{7}$$

where $X = u + jv$ and j is the imaginary unit concerning space, which is different from the above i concerning time. Q is the vorticity of the generating force of the residual current due to the basic oscillatory current, equal to $\partial T_x/\partial z + j\partial T_y/\partial z$ if $T_x = \langle u_T \partial u_T/\partial x \rangle_s + \langle v_T \partial u_T/\partial y \rangle_s$ and $T_y = \langle u_T \partial v_T/\partial x \rangle_s + \langle v_T \partial v_T/\partial y \rangle_s$. Although Q is rather complicated in the concrete, (7) is a nonhomogeneous ordinary differential equation and we can analytically solve it. A general solution of (7) can be given as

$$X_s = C_1 + C_2 e^{\gamma z} + C_3 e^{-\gamma z} + \frac{j}{f}\left[\int_0^z Q d\xi - \frac{e^{\gamma z}}{2}\int_0^z Q e^{-\gamma\xi} d\xi + \frac{e^{-\gamma z}}{2}\int_0^z Q e^{\gamma\xi} d\xi\right] \tag{8}$$

where C_1, C_2 and C_3 are complex integral constants regarding j and γ is $(1 + j)(f/2\nu_z)^{1/2}$. $(f/2\nu_z)^{1/2}$ will be rewitten as β_f, the reciprocal of which means the characteristic thickness of the Ekman layer. Boundary conditions for the special solution are described as follows; (1) current velocity is zero at the sea floor, (2) no stress is given at the sea surface, (3) vertically integrated velocity the component of which is perpendicular to the coast is zero and (4) the pressure gradient along the coast is zero.

The generation term Q can be introduced as follows. If u and v can be respectively expressed as $\mathrm{Re}[f_1 e^{-i\sigma t}]$ and $\mathrm{Re}[f_2 e^{-i\sigma t}]$, the periodical average of the product of the both can be written as $\mathrm{Re}[f_1 \cdot f_2^*]/2$, where * means the conjugation of the complex number. Since the amplitude F/σ consists of the real part only, the real and imaginary parts of Q can be respectively expressed as

$$\frac{\partial T_x}{\partial z} = \frac{\partial}{\partial z}\left[\frac{U}{2}\frac{\partial U}{\partial x}\{f_u \cdot f_u^*\} + \frac{U}{2}\frac{\partial U}{\partial y}\{f_u \cdot f_v^*\}\right]. \tag{9}$$

$$\frac{\partial T_y}{\partial z} = \frac{\partial}{\partial z}\left[\frac{U}{2}\frac{\partial U}{\partial x}\{f_u \cdot f_v^*\} + \frac{U}{2}\frac{\partial U}{\partial y}\{f_v \cdot f_v^*\}\right] \tag{10}$$

where U is representative of F/σ, the horizontal variation of which is assumed to be as calm as the horizontal viscous term can be neglected. f_u and f_v correspond to the z-dependence terms in (5) and (6), respectively, such that $u_T = \mathrm{Re}[Uf_u e^{-i\sigma t}]$ and $v_T = \mathrm{Re}[Uf_v e^{-i\sigma t}]$. The right generation terms will be used well in the right case of two typical models in the following section.

Tidal Currents in Two Typical Model Basins

If the variations are rather gentle compared to that in the lateral Stokes layer due to the horizontal viscosity, the amplitude of the vertical profile of the tidal current is considered to keep similarity horizontally. Therefore the horizontal variation can be expressed by the variation of the tidal current in the outside of the bottom Stokes layer and the vertical variation can be given by that of the solutions (5) and (6). The hodograph of vectors of the basic tidal current generally forms ellipse, called tidal current ellipse, and the ellipticity depends on the Coriolis ratio and the nonlinearity of the tidal current (Yasuda, 1987). For simplicity of consideration, the ellipticity is assumed zero in the outside of the bottom Stokes layer in this study although the ellipticity might be recognized in the inside of the Stokes layer. The vertical profiles of the element of the tidal current ellipse are drawn in Figure 1. (a), (b), (c) and (d) in the figure show the amplitude of the tidal current, the ellipticity, i.e. the ratio of the minor axis to the major one, the phase lag of the major axis and the orientation of the major axis, respectively. Each ordinate is normalized by the characteristic thickness of the Stokes layer and numerals in the figure indicate the ratio of the Coriolis parameter to the frequency of the basic tide. The ellipticity and the deflection of the major axis orientation get larger with the increase of the Coriolis parameter ratio.

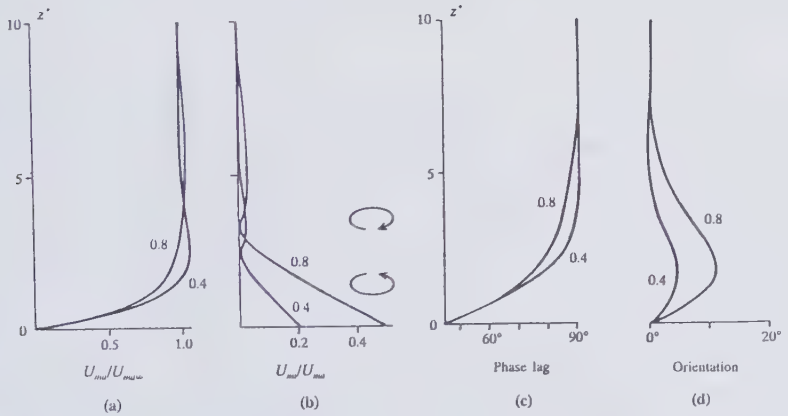

Figure 1. The vertical profiles of the element of the tidal current ellipse: (a) the amplitude, the major axis of the tidal current ellipse; (b) the ellipticity, the ratio of the minor axis to the major one; (c) phase lag of the major axis; (d) the orientation of the major axis.

Solution Curves of the Residual Current in Two Typical Cases

The tidal currents drawn in Figure 1 give generating terms of the residual current concretely and the residual current can be obtained by taking account of the boundary conditions (1), (2), (3) and (4). Figure 2 shows situations of two typical cases representing the horizontal variation of tidal currents. The upper of this figure is the first case where the major axis of the tidal current ellipse has a grandient only in the lateral direction. We could assume that the coastline runs along the x-axis in the first case. The lower is the second case where the major axis of the tidal current ellipse has a gradient only in the longitudinal direction. It may be reasonable that the coastline runs in the y-direction in the second case.

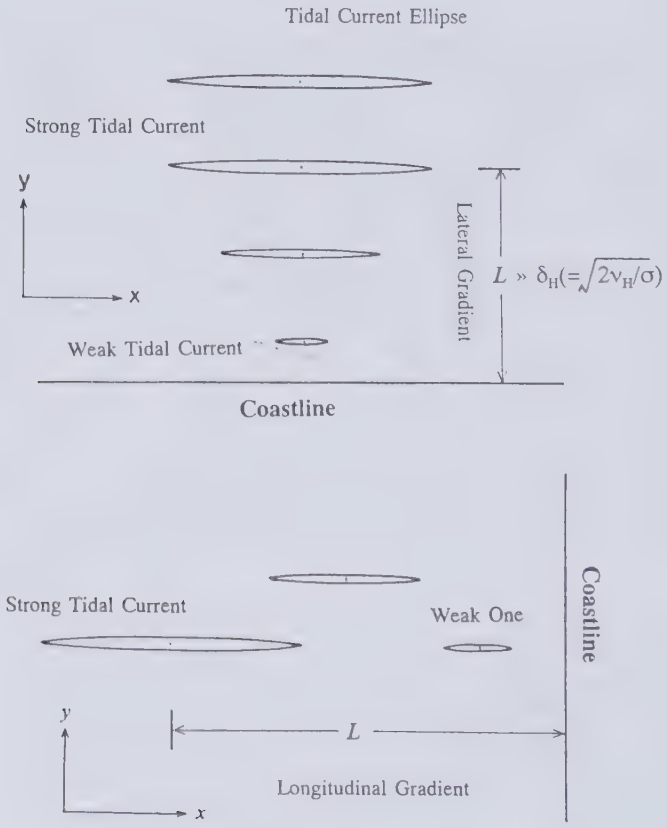

Figure 2. Two typical examples representing the horizontal variation of the tidal current ellipse. The upper figure shows the first case where the ellipticity of the tidal current has gradient only in the lateral direction and the lower the second case where the ellipticity has gradient in the longitudinal direction only.

The generation term Q_1 in (7) is written in the first case as

$$Q_1 = \frac{\partial T_x}{\partial z} + j\frac{\partial T_y}{\partial z} = \frac{U}{2}\frac{dU}{dy}\frac{d}{dz}\{(f_u \cdot f_v^*) + j(f_v \cdot f_v^*)\} \tag{11}$$

The fifth term of (8), $j/f[\int Q_1 d\xi - e^{\gamma z}/2 \int Q_1 e^{-\gamma\xi} d\xi + e^{-\gamma z}/2 \int Q_1 e^{\gamma\xi} d\xi]$, can be concretely solved as

$$\frac{j}{f}[\cdots\cdots] = \frac{U}{\sigma}\frac{dU}{dy}[\frac{A^2}{2}\frac{-f^* + j2(1-f^*)}{5f^{*2} - 8f^* + 4}e^{-2bz} + \frac{B^2}{2}\frac{-f^* + j2(1+f^*)}{5f^{*2} + 8f^* + 4}e^{-2az}$$

$$-\frac{1}{2}\frac{AB}{ab}e^{-p_1 z}(\sin p_2 + j\cos p_2) + \frac{A}{2}e^{-bz}\{(D_2 - \frac{D_2\beta_f{}^2 + D_1 b^2}{1-2f^*})\cos bz$$

$$-j(D_2 - \frac{D_2 b^2 + D_1\beta_f{}^2}{1-2f^*})\sin bz\}$$

$$+\frac{B}{2}e^{-az}\{(D_2 + \frac{D_2\beta_f{}^2 + D_1 a^2}{1+2f^*})\cos az - j(D_2 + \frac{D_2 a^2 + D_1\beta_f{}^2}{1+2f^*})\sin az\} - \frac{D_2{}^2}{2f^*}] \tag{12}$$

where $a = \beta_S(1 + f^*)^{1/2}$, $b = \beta_S(1 - f^*)^{1/2}$, $A = (1 + f^*)(1 - \alpha f^*)/2$, $B = (1 - f^*)(1 + \alpha f^*)/2$, $p_1 = a + b$, $p_2 = a - b$, $D_1 = 1 - \alpha f^{*2}$ and $D_2 = f^*(1 - \alpha)$. Although it is rather complicated, we can impliedly understand the vertical dependence of the residual current. The second and third terms of (8) simply give the vertical profiles of the steady current with the Ekman layer.

Figure 3 shows the vertical profiles of the residual current in this case. (a) of this figure is the x-directional component, the direction of which corresponds to the longitudinal one of the tidal current, and (b) the y-directional component. The positive directions of x and y-axes are indicated in the first figure of Figure 2. The ordinate and the abscissa of Figure 3 are normalized by the characteristic thickness of the Stokes layer $(2\nu_z/\sigma)^{1/2}$ and $U/\sigma \cdot dU/dy$, respectively, and numerals in the figure indicate the Coriolis ratio. U represents the the characteristic value of the major axis of the tidal current ellipse in the outside of the boundary layer. These vertical profiles are drawn in the case where the normalized depth of the tidal basin is 20. The current velocity is uniform in the region which is at a distance more than ten from the floor in the basin the depth of which is more than ten. The x-directional (along-coast) residual current flows in the same direction in the whole depth, while the y-directional one is recognized around the Stokes layer, i.e., just above the sea floor only. These residual currents become larger as the Coriolis parameter ratio increases, which are not generated in the basin with no Coriolis effect.

Figure 3. Vertical profiles of residual current in the first case: (a) x-directional (longitudinal) component and (b) y-directional (lateral) component.

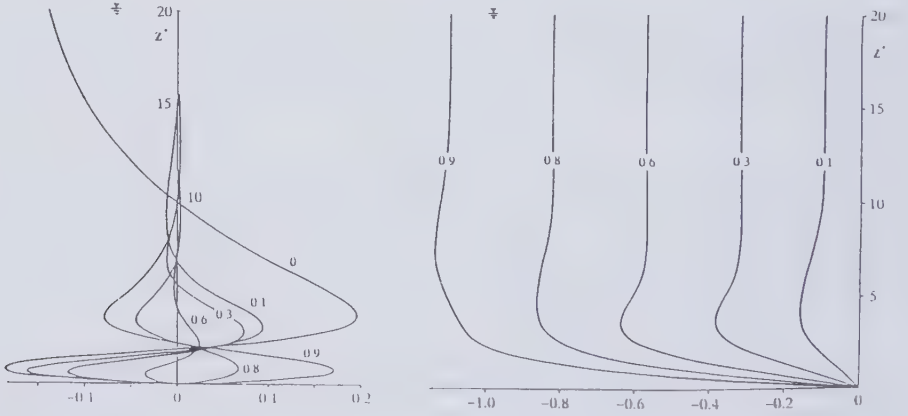

Figure 4. Vertical profiles of residual current in the second case: (a) x-directional component and (b) y-directional component.

The generation term, Q_2, is written in the second case of Figure 2 as

$$Q_2 = \frac{U}{2}\frac{dU}{dx}\frac{d}{dz}\{(f_u \cdot f_u^*) + j(f_u \cdot f_v^*)\} \tag{13}$$

The analytical integral of (13) corresponding to (12) is omitted here for page saving since it is also as complex as (12) and yet the z-dependence is similar to it. Figure 4 shows the residual currents in the second case of Figure 2. The y-directinal

residual current, flowing in the whole depth across the major axis of the tidal current seeing the weak tidal current area on the left side, is not generated when the Coriolis ratio is free and it gets larger with the increase of the Coriolis ratio just like the first case. In this case, the x-directional current inside of the Stokes layer flows toward the strong tidal current area when the Coriolis ratio is less than 0.5, on the other hand it flows reversely when the ratio is more than 0.5. Although no residual current is generated in the above first case with no Earth's rotation effect, the longitudinal residual current is generated in this case even when no Coriolis effect, which has been presented as tide-induced vertical circulations by Ianniello theoretically (1977) and Yasuda experimentally (1981).

Application to the Real Residual Currents and Concluding Remarkes

In Hiuchinada Sea of the Seto Inland Sea in Japan the mean depth of which is around 20m (Figure 5), there flows a residual current in the whole depth along the east coast as drawn in Figure 6 (Yasuda, 1989). Arrows in Figure 7 show 15 days-averaged residual currents measured by my institute (Higo, Takasugi and Tanabe, 1980). Since the density of the sea water is fairly uniform and the residual current can be observed all the year round, this resiudal current is considered to be generated by tides or tidal currents.

Judging from the horizontal topography, it is expected that the residual current might be generated by the headland at the north side (Pingree and Maddock, 1979). However, such residual current cannot be measured by any means even in the hydraulic scale (Froudian) model where current separation can be induced more easily than the real sea (Yasuda, Higuchi and Hayakawa, 1979), and yet the tidal

Figure 5. Location of Hiuchinada Sea in the Seto Inland Sea.

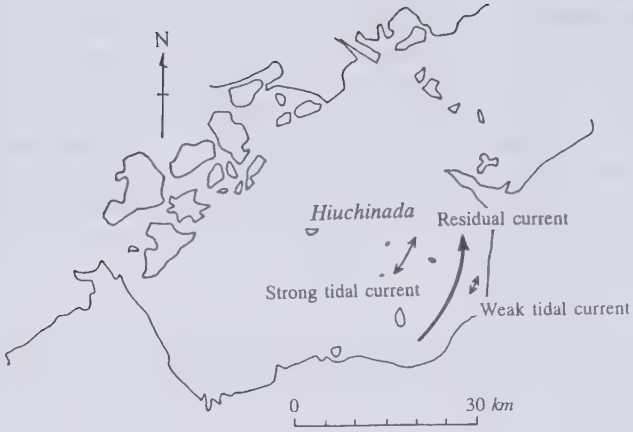

Figure 6. The outline feature of the residual current and the M_2-tidal current observed in Hiuchinada Sea.

bank presented by Pingree and Maddock (1979) cannot be recognized near the head land. This is because the tidal current is not so strong as the current separation is induced. This residual current has not yet been expounded as the density current, the wind-induced current nor the headland flow, in other words, no generation mechanism of the current has been presented thus far.

Contour lines in Figure 7 show the amplitude of M_2-current measured in the above scale model, where the oscillatory component is reproduced well, and numerals beside arrows indicate the amplitude of M_2-current measured in the field observation which fit the contour of the scale model. Numerals in the brackets are the values of the residual current vectors. The lateral shear of the tidal current is considered to be formed as something like a dead zone by the effect of the peculiar horizontal topography. The off-shore residual current in the inside of the Stokes layer given by the analytical solution (Figure 3) can be verified by the grain-size distribution on the floor in this sea, in which the grain-size is rather rough in spite of the weak tidal current as drawn in Figure 8 (Tanimoto, Kawana and Yamaoka, 1984). These facts suggest that the residual current in this sea corresponds to the first case of the generation mechanisms of the residual current.

In the south area of the North Sea between England and the Continent, the residual current has been recognized which flows southward along the coast of England and eastward along the coast of the Continent (Figure 9 illustrated after Haren and Joordens (1990)). It is expected considering the topography that the tidal current is strong near the straight and decreases with the distance from the straight to the north. These mean that this residual current flows seeing the weak tidal current area on the left side. The tidal current pattern around this sea has a possibility to generate the

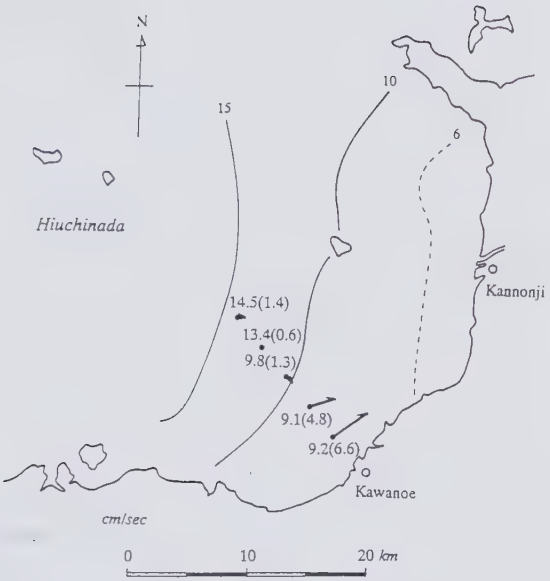

Figure 7. Residual current vectors over 15 days and the distribution of the amplitude of M_2-current (cm/sec). Numerals beside vectors indicate the amplitude of M_2-current.

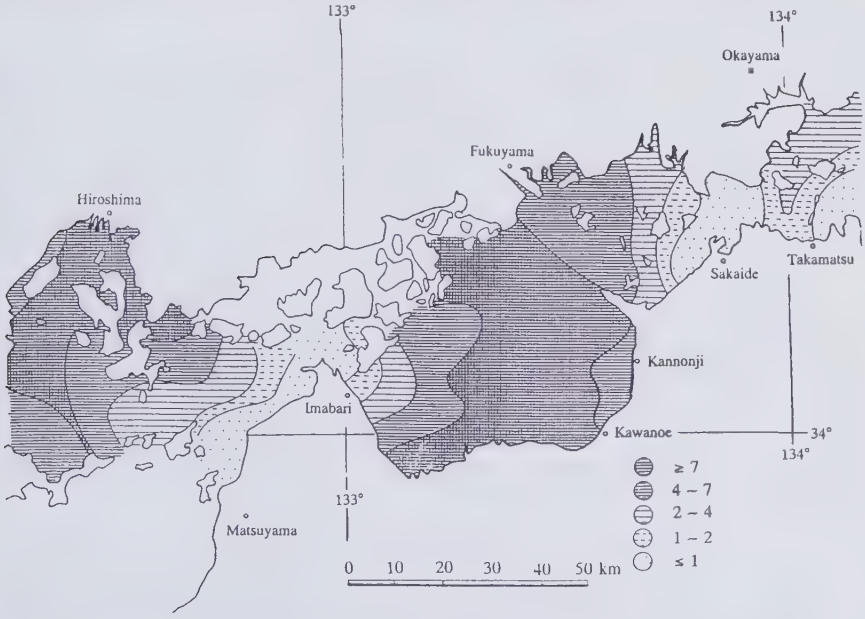

Figure 8. Distribution of the grain-size of the sea floor (Mdø) around the middle area of the Seto Inland Sea.

Figure 9. The residual current observed in the south area of the North Sea (after Haren and Joordens, 1990).

residual current there considering the second case of the present generation model. Although some generation models have been so far presented as to this residual current, the author would like to pose this new model as one of the generation mechanism of the residual current in this sea.

Yanagi and Yoshikawa (1983) have shown through Eulerean measurement of the floats' movement in a hydraulic basin that the cyclonic residual circulation was induced in a rectangular tidal bay with constant depth on a rotating table (Figure 10) though the residual current was not obviously observed in the case of no rotation. In their experiment, the major axis of the tidal current, the ellipticity of which was nearly zero, was uniform in the lateral direction and decreased linearly from the mouth to the head of the bay. If we apply the second case of the generation mechanism to their experiment, the lateral residual current expected in the whole depth ought to decrease linearly similar to the tidal current because the magnitude of the residual current is proportional to $U/\sigma\ dU/dx$ (indicated by R. in Figure 10). In the rectangular basin, the integrated value of the lateral component of the residual current ought to be zero as a matter of course. If we take account of this new condition, the lateral residual current is considered to counterbalance the slope current in the longitudinal section from the mouth to the head of the bay. Therefore the cyclonic circulation results from this slope current being uniform longitudinally (indicated by S.).

Figure 11 shows the vertical profiles of the resultant residual current near the bay mouth (distance normalized by the bay length is 0.2 from the bay mouth) and near the bay head (normalized distance, x^*, is 0.8) in the case where the Coriolis ratio is 0.8. (a) and (b) in this figure are respectively x (longitudinal) and y (lateral) components. This difference of the lateral components of the residual current might

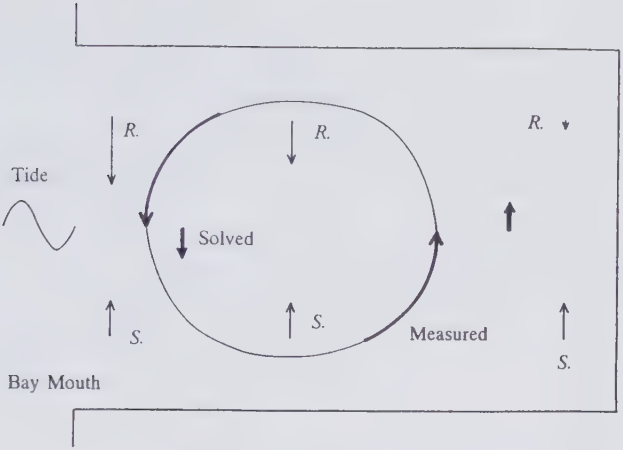

Figure 10. The outline feature of the residual current measured in the rectangular tidal basin with the rotation effect by Yanagi and Yoshikawa (1983). Signs R. and S. show respectively the expected residual current in an unbounded sea and the slope current due to the side-wall.

realize the formation of the cyclonic residual circulation in this bay as shown in Figure 10.

Although Ianniello (1977) and Yasuda (1981) showed that the tide-induced residual current at the water surface flows outward from the bay head in a rectangular non-rotating tidal basin, Yanagi and Yoshikawa (1983) reported that no residual current was observed in the case with no rotation effect in their hydraulic experiment. This is considered to come from the fact that their experimental basin was not long enough to recognize the residual current at the water surface and that the lateral residual current at the middle latitude is estimated as several times larger than this outward residual current. The residual current would be recognized by the close observation even in their experiment if the basin length were longer.

This study can elucidate the experimental results carried out in a fairly small basin where the current is almost laminar since the residual current in this model has been analyzed on the assumption of the constant viscosity. The viscosity is, however, variable both spatially and temporally in the real sea. Thus I am afraid that the generating behavior of the residual current might be more complicated or different from this result. This is because Yasuda (1981) has shown that the tide-induced vertical circulation could flow reversely in the case of the different vertical profile of the oscillatory current. Although this study has elucidated a possibility of generation of the tide-induced residual current in the rotating basin, more realistic analysis is being expected for further understanding. A turntable with a tidal basin for hydraulic experiments (7 m x 4 m horizontally) is now under construction in my institute, and then experimental studies on the residual current in the rotating system will be carried out in the near future.

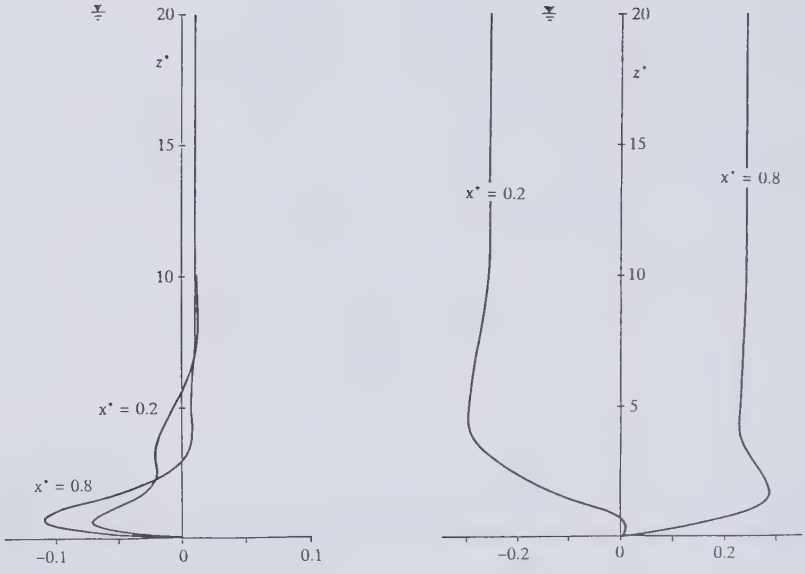

Figure 11. The vertical profiles of the residual current expected near the bay mouth (x = 0.2) and near the bay head (x = 0.8) in the y-directionally bounded basin in the second case where the Coriolis ratio is 0.8 as one example.

References

Haren, J.J.M. and Joordens, J.C.A. Observations of physical and biological parameters at the transition between the southern and central North Sea. *Observations on the Structure of Currents at Tidal and Sub-Tidal Frequencies in the Central North Sea*, 89-102, 1990.

Higo, T., Takasugi, Y. and Tanabe, H. Tidal currents in the Seto Inland Sea. *Rep. of Govern. Ind. Res. Inst. Chugoku*, 12, 81-120, 1990 (in Japanese).

Ianniello, J.P. Tidally induced residual currents in eatuaries with constant breadth and depth. *J. Mar. Res.*, 35, 755-786, 1977.

Pingree, R.D. and Maddock, L. The tidal physics of headland flows and offshore tidal bank formation. *Mar. Geol*. 32, 269-289, 1979.

Robinson, I.S. Tidally induced residual flows. *Phys. Oceanogr. of Coastal and Shelf Seas, Elsevier Oceanogr. Series*, 35, 321-356, 1981.

Tanimoto, T., Kawana, K. and Yamaoka, Y. Grain size parameters and organic matter of bottom sediment in the Seto Inland Sea. *Rep. of Govern. Ind. Res. Inst. Chugoku*, 21, 1-12, 1984 (in Japanese).

Wright, D.G. and Loder, J.W. A depth-dependent study of the topographic rectification of tidal currents. *Geophys. Astrophys. Fluid Dyn.*, 31, 169-220, 1985.

Yanagi, T. and Yoshikawa, K. Generation mechanisms of tidal residual circulation. *J. Oceanogr. Soc. Japan*, 39. 156-166, 1983.

Yasuda, H., Higuchi, H. and Hayakawa, N. On the scale effect of the hydraulic tidal model. *Coastal Eng. in Japan*, 21, 201-211. 1979.

Yasuda, H. Tide-induced vertical circulation in a bay with homogeneous water -theory and experiment-. *J. Oceanogr. Soc. Japan*, 37, 74-86, 1981.

Yasuda, H. and Zimmerman, J.T.F. Tide-induced residual currents with Stokes and Ekman layers over an undulatory sea floor. *J. Oceanogr. Soc. Japan*, 42, 276-293, 1986.

Yasuda, H. Vertical structure of the tidal current ellipse in a rotating basin. *J. Oceanogr. Soc. Japan*, 43, 309-318, 1987.

Yasuda, H. Tide-induced residual current caused by the Coriolis effect. *Hydraulic and Environmental Modelling of Coastal, Estuarine and River Waters*, 95-104, 1989.

Zimmerman, J.T.F. Dynamics, diffusion and geomorphological significance of tidal residual eddies. *Nature*, 290, 549-555, 1981.

7

Wave and Dispersion Studies in Shallow Water Using Side-Scan Sonar

S. A. Thorpe, A. Graham and A. Hall

Abstract

Two studies of coastal processes using high frequency sonar are reported. An exploratory study has been made to establish the viability, or otherwise, of making useful sonar measurements of waves approaching a beach. A rig carrying four sonar transducers was deployed on a smooth sandy beach with sonar beams pointing along and up the beach. Ranges of about 150 m were achieved with 80 and 90 kHz sonars. The along-beach beam can detect longshore currents, visualised in the sonograph images as acoustic targets (bubble clouds) which change their range with time. Both beams respond to surface waves. The period of the waves, and their wavelengths and speeds in the two beam directions, has been measured from the sonars, and the dispersion relation used as a test to establish that progressive surface gravity waves are indeed being detected. The ratio of speeds (or wavelengths) in the two beams provides an estimate of the propagation direction of the waves. The maximum achieved up-beach sonar range was however limited to that of the edge of the surf zone. Patterns which appear to be caused by wave groups are clearly visible, especially in low wind conditions. In the second study, the acoustic transducers were deployed on a rig lowered onto the sea bed from a vessel moored in a depth of about 40 m in the southern North Sea. The vessel remained on site providing power to the sonars and collecting data via a cable in much the same way as in the nearshore studies (but with more risk to the instruments). Bands of bubbles associated with the surface convergent regions of Langmuir circulation can be detected, advected by the tidal stream through the sonar beams. The sonar data has been digitised and reduced to a form which displays only the pattern of convergence regions in range versus time. This is used as the basis of a computer simulation to

Mixing in Estuaries and Coastal Seas
Coastal and Estuarine Studies Volume 50, Pages 110-134
Copyright 1996 by the American Geophysical Union

model the dispersion of 'floating particles' which are released into the pattern and tracked as they move towards, enter, and are carried in, the convergence regions, subsequently being released and recaptured.

Introduction

Sonar offers a powerful, robust, non-intrusive, remote sensing technique to study near-surface processes and to quantify their effects. Ranges of 100-200 m can be achieved in sea water at sound frequencies of 80-250 kHz. Short pulse lengths can be used, typically 0.1 milli-sec, providing a range resolution of about 15 cm. This sampling window from 15 cm to 100 m is sufficient to resolve many of the surface wave and turbulence-related features which lead to the vertical transfer of heat and momentum in the upper part of the water column. At the high sonar frequencies of these studies, sound is efficiently scattered by small, 50 μm-scale, bubbles produced at the sea surface by breaking wind waves, and the clouds of small bubbles produce acoustic targets which provide telling indicators of near-surface processes. These bubbles rise very slowly (50 μm radius bubbles rise at about 5 mm s^{-1}), and persist for several minutes before dissolving (providing a route for air-sea gas transfer) or returning to the surface, during which time their horizontal displacement in the sonar beam can be detected and measured, even when the sonar itself is uncalibrated (i.e. the target strength is not known). The information collected by a sonar directed up towards the surface at a small angle to the horizontal can provide indirect measurements of surface currents, including variation in both range and time. The measurements of position and displacement, rather than speed (e.g. by Doppler sonar; see Herbers, Lowe and Guza, 1991), provide graphic images of wave-related processes.

High frequency pulsed side-scan sonar has now been used for a number of years to make measurements in coastal waters. The processes studied and described so far in coastal environments include vertical diffusion (Thorpe, 1982; 1984; 1986), tidal estuarine fronts caused by brackish water discharged from a sea loch (Thorpe *et al.*, 1983), internal waves and whitecaps (Thorpe *et al.*, 1987), a tidal race (Thorpe *et al.*, 1985), air-sea gas flux (Thorpe, 1982; Farmer *et al.*, 1993), the effects of oil slicks (Belloul and Thorpe, 1992), breaking surface wave groups and Langmuir circulation (Thorpe and Hall, 1983; Thorpe, 1992). The sonar has been used fixed to a frame mounted on the sea bed in a water depth of 35 m, with power provided to the sonars and data carried back to shore via an underwater cable. The sonar system is not subject to the extremes of hazard of severe motion and wave action, or of the risk of damage by passing craft and fishing, to which conventional near-surface 'in situ' sampling instruments are often exposed. It has also been used, in the oil slick and tidal race studies, towed from a small vessel and, in open waters, it has been operated mounted on a submarine in a study of near-surface turbulence (Osborn *et al.*, 1993), and as a free floating internally recording package (Vagle and Farmer, 1992). A measure of the robust nature of the instrument is provided by the fact that

we are using one of the same transducers as was used in our initial exploratory studies with sonar in Loch Ness (Thorpe and Stubbs, 1979).

We report here two experiments which provide further evidence of the value and potential of sonar in the coastal region. The sonar data were sampled at 44.1 kHz by a PCM digital audio processor and recorded on a VCR. The 80 and 90 kHz sonars were always recorded, together with one or other of the 250 kHz sonars. The 80 and 90 kHz sonars have a 20 ms 'deafened zone' following the trigger pulse and cannot therefore record signals from ranges less than approximately 15 m (0.5×20 ms $\times$ sound speed). Recording of two sonar channels was also made on a Waverley thermal linescan recorder to provide immediate visual images.

Waves Approaching Shore

The Site and Instrumentation

An exploratory investigation was made on a smooth sandy beach, Auburn Sands, some 4 km south of Bridlington on the North Sea coast of the UK. The equipment used is fully mobile and was set up at the site and operational within 5 hr of our arrival. Auburn Sands face due east. The beach stretches unobstructed 4 km to Bridlington Harbour to the north and 55 km to Spurn Head to the south. It is slightly concave, with a seaward local radius of curvature of about 20 km. The beach is remarkably featureless and level, with a mean slope in the area of observations of 1.02°. The surface is composed of fine sand and mud. The tidal range during the period of the observations was about 4 m.

A weighted rig carrying 4 sonar transducers was placed on the beach at low tide and connected to recording instruments contained in a van via 200m of cable (Figure 1). The rig is a rectangular framework 1.5 m $\times$ 1.5 m $\times$ 1 m high, with a graduated vertical pole to aid water depth and position estimates. The linear sonar transducers were set to point horizontally, producing narrow vertical fan beams. Orientation and transducer angles were maintained to better than 4°, in most cases better than 2°, during the 5 day experiment. A 250 kHz and a 90 kHz sonar were directed to point in direction 282° from North, up the beach, and a 250 kHz and a 80 kHz sonar pointed to 192°, roughly parallel to the shore line. Once covered by the rising tide, the sonars were switched on and operated in pulsed mode. The pulse lengths were 0.136 ± 0.002 ms for the 80 and 90 kHz sonars and 0.096 ms for the 250 kHz sonars, giving range resolutions of about 0.2 m and 0.14 m respectively. The pulse repetition rates were set at 5, 6 or 8 Hz. The sonars produce broad vertical and narrow horizontal beams (typically 35° and 3° wide in these two directions respectively) which then isonofy narrow sections of water, typically some 1-5 m wide up or parallel to the beach. The tidal range at the rig was about 3.2 m. The cable connecting the rig to the van was buried in the sand for protection. The sonars were operated over 7 tidal cycles, two being overnight demonstrating the viability of a 24 hour per day operation.

Given the exploratory nature of the study, supporting observations were only made of:

(a) Wind speed and direction;
Wind speeds ranged from 2 ms^{-1} to 15 ms^{-1} (gusting to 19 ms^{-1}) in directions between 180° and 240°, thus generally with an off-shore component. These conditions were perhaps less than favourable for the observations since the wind may have contributed to near-surface off-shore currents carrying bubbles and suspended sediment from the surf-zone towards the sonar, thus attenuating the transmitted sound before it reached the surf-zone itself.

(b) Wave periods, heights and direction well off-shore;
The sonar data provide information about wave periods (see later). Rough estimates of wave heights were made by observing the sea surface motion at the pole on the rig. The heights varied between 0.2 and 0.75 m. Wave directions were estimated using a sighting compass.

(c) Mean water depth, water line position and width of the surf-zone;
Positions of the rig and water line were measured relative to a large concrete block high up the beach (Figure 1). The width of the surf-zone was regularly estimated using the known rig position on the beach as a reference. The width of the surf-zone varied from 20 to 90 m.

(d) Beach slope and profile;
The beach was measured using a surveyors' theodolite. Slopes varied from about 0.7 to 1.2° over the observation area.

(e) Precipitation and temperatures;
The weather was generally dry with no heavy rain (which is known to contribute acoustic targets; Thorpe and Hall, 1983). Air temperatures were 4-9°C and the water temperature was 6.2°C.

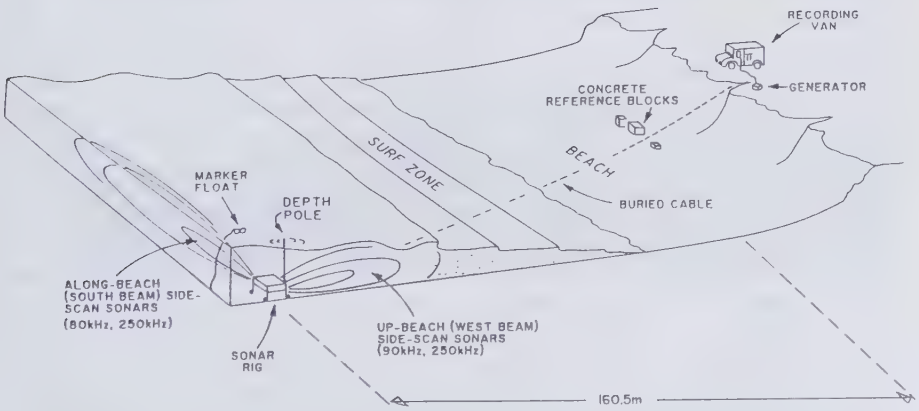

Figure 1. Sketch showing the site and the sonar beam orientations. North is along the beach towards the reader.

The Observations

Figure 2 is an example of a sonograph record (range versus time) obtained using the two lower frequency transducers in winds of 11 ms^{-1} (gusting to 14 ms^{-1}) blowing from 180°, parallel to shore. The water depth at the sonar was 1.9 m and the waves, observed to be breaking well inshore of the rig position, were estimated to have a period of 3.7 s and a height of 0.4-0.7 m at the edge of the surf zone. The upper record is the 80 kHz transducer record parallel to shore and shows streaks (e.g. at A) with low slopes representing targets moving towards the sonar (range decreases with time) at speeds of about 13 cm s^{-1}. Occasionally the origin of these streaks was visible as a dark, well-defined target which earlier studies (e.g. Thorpe, 1992; Osborn *et al.*, 1993) have identified as breaking waves. These streaks are due to bubble clouds, persisting in the water for 2-5 mins, advected down the beam by the mean longshore current. Their movement therefore provides an estimate of the alongshore component of current near the sonar, and in the water depth of the sonar, in the same way as sonar images of bubble clouds in deep water have been used to infer surface currents (Thorpe and Hall, 1983). Smaller scale, regularly spaced lines (e.g. along the direction B), appearing to approach the sonar more rapidly at speeds of about 6.4 ms^{-1}, are also present. These lines have lengths of up to 60 m and period of 3.5 s.

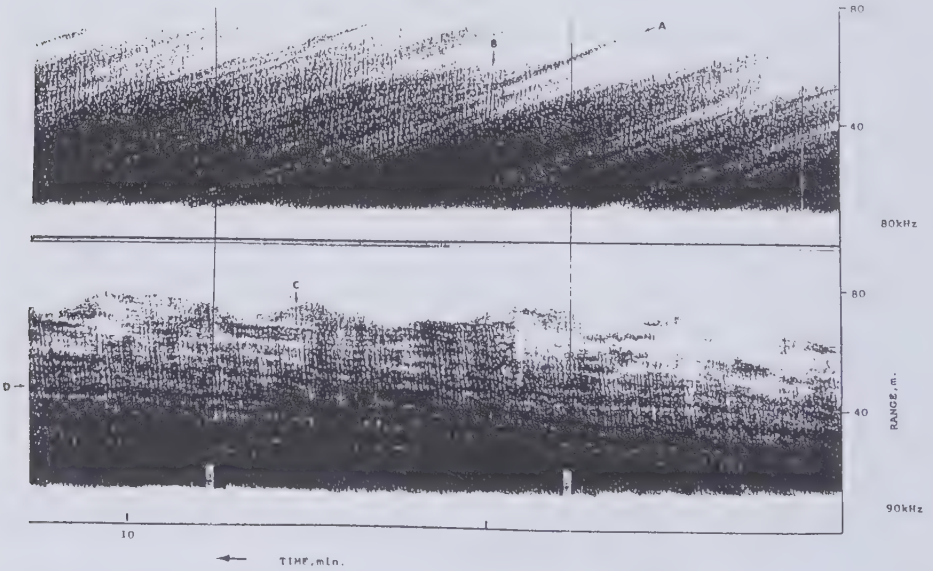

Figure 2. Sonograph record, range versus time with, above, 80 kHz parallel-to-shore sonar and, below, 90 kHz shorewards pointing sonar. Time increases to the left. The separation between the vertical lines is 5 mins. Wind 11 ms^{-1} from 180°. Water depth at sonar = 1.9m. The letters are explained in the text. The features can best be seen by viewing the figure at a low angle in the direction of the arrows marking them.

Their wavelength in the sonar beam direction parallel to shore is about 23 m. Similar lines, moving away from the sonar, are visible in the 90 kHz, shoreward pointing, beam (e.g. along direction C). These have the same period but imply less rapid motion, approaching shore at 5.1 ms^{-1}. These lines generally curve (an effect more evident in Figure 8) with a consequent reduction in the speed as targets move into shallower water. The 90 kHz record also shows banded structures (e.g. at D) moving slowly, at speeds of about 1.3 cms^{-1}, away from the sonar, typically with separations of 5-7 m and persisting for 5-10 mins. The target strength as judged by the intensity of the record falls off with range, an indistinct edge being visible in the 90 kHz beam. Its position varies by some 10 m about a range of 75 m.

The high frequency lines with period of about 3.5 s are identified as being progressive surface waves moving towards shore from a direction, determined from the relative apparent speeds of the lines in the two beams, of 141°. The equality of period of the higher frequency lines in the two beam directions implies that the two sonars are selecting the same frequency waves from the wave spectrum in the two directions. Given the estimates of phase movement in the beams, c_p (6.4 ms^{-1}) in direction 192°. and c_n (5.1 ms^{-1}) in direction 282°, the phase speed of the wave,

$$c = \frac{c_p\, c_n}{\left(c_p^{\,2} + c_n^{\,2}\right)^{1/2}} \qquad (1)$$

can be estimated as 4.0 ms^{-1}, as can the wavelength, $\lambda = c\,T$, =14 m, where T is the observed period of the lines.

We can then test whether the features identified as surface gravity waves satisfy the linear dispersion relation

$$\sigma^2 = gk \tanh kh \qquad (2)$$

for surface gravity waves (where $\sigma = 2\pi/T$ is the wave frequency, k is the wavenumber = $2\pi/\lambda$, and h the water depth at the rig), by plotting $\sigma^2/gk = 2\pi c^2/g\lambda$ against tanh (kh). Figure 3 is based on averages, each over some 20 waves, of wave period and speed at different times during the 5 days of observation, and shows there is substantial agreement, implying that the high-frequency lines are indeed due to propagating surface waves.

Close inspection of the 90 kHz sonograph shows that at places where the surface wave lines intersect the edges of the lower frequency bands, the latter are displaced towards the sonar; between the wave lines there is a displacement towards the shore. This can be seen in Figure 4, a record obtained shortly after that of Figure 2. The displacement is (1.0 - 1.4) m. The phase of the motion implies that the wave lines are themselves associated with times of little or no onshore motion. The motion preceding a wave line is offshore, and that following is onshore. This identifies the source of the wave lines as being on the leading face of waves as they approach shore, between the wave trough where the induced flow is backwards and the wave

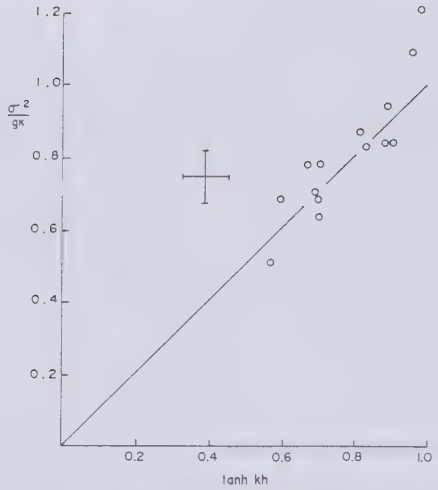

Figure 3. A test that the high frequency bands seen in the sonographs satisfy the linear dispersion relationship for surface gravity waves. Plotted are σ^2/gk and tanh kh. A linear relationship with unit slope indicated by the line should be satisfied if the bands are linear surface waves.

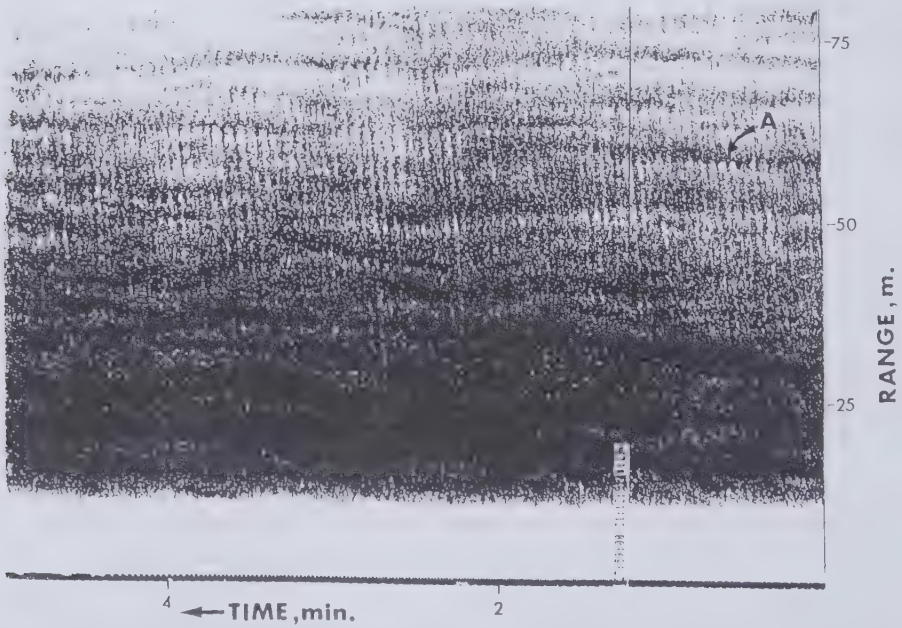

Figure 4. Sonograph record of the 90 kHz shoreward pointing beam showing, for example at A, the horizontal displacements of bubble bands as waves propagate past them. This record was obtained about 30 min after Figure 2.

crest when motion is forwards, in the direction of wave propagation. This implies that waves are detected in the shoreward pointing beam by sound being reflected by specular reflection at the rippled faces of onshore propagating waves. The amplitude of the observed displacement is consistent with the mean depth-integrated horizontal onshore displacements, $x = (2a/kh)\cos\alpha$, produced by progressive waves. Here c is the phase speed of the waves, 2a = 0.4-0.7 m is the wave height, and α is the angle of the wave crests to the shore line, all estimated at a distance of 60 m up the beach (the range of the features arrowed in Figure 4) from the sonar where the water depth, h, is 0.9 m. The estimated value of c of waves of 3.5 s period in a depth of 0.9 m is 2.8 ms^{-1}, and the wavelength is 9.8 m. Since the alongshore wavelength, 23 m, remains unchanged as the waves approach shore, the angle α is $\sin^{-1}$ (9.8/23), and x = (0.63 - 1.1) m.

The separation and time-scale of the low frequency bands in the 90 kHz record is consistent with their being caused by Langmuir circulation, creating bands of bubbles roughly parallel to the wind direction (see Thorpe, 1984; Zedel and Farmer, 1991; and later section). Their persistence time of 5-10 mins in a longshore current of 13 cms^{-1} implies a length of about 40-80 m, or 7 to 12 times the band separation.

Estimates of the distance of the sonar from the edge of the visible record in the 90 kHz beam have been compared with the distance of the edge of the surf-zone estimated by observers on shore. The distances are compared in Figure 5. There is considerable uncertainty in the observers' estimates, and, as shown in Figure 6, the sonograph records show considerable variability in range. The correspondence in the two estimates however indicates that, to a first approximation, the sonar range in the shoreward direction is limited to that of the distance of the outer edge of the surf-zone from the rig. Rarely is there significant sound penetration into the surf-zone itself. Within the surf zone the bubbles produced by breaking waves and the sediment brought into suspension strongly attenuate the acoustic signal. Similar results have been observed by Smith (1993) using 195 kHz Doppler sonar (see also Thorpe and Hall, 1993).

Evidence of this attenuation can be found in Figure 6. The record is similar to that of Figure 2 (obtained some 11 hours later on the previous tide) except that the 90 kHz sonar range is twice abruptly reduced by about 35 m. Attenuation is preceded by the appearance of filamentary bands (marked by arrows) emanating from the high frequency surface wave lines. The filaments appear sequentially, those first to appear being furthest from the sonar, subsequent filaments appearing from later surface wave lines some 4-5 m further off-shore. The filaments are themselves advected by subsequent waves. They generally persist for some 35 s, or 6-8 wave periods, before their signal is lost. These filaments appear to be due to groups of waves breaking and leaving bubble clouds (the scatterers which compose the filaments) in the water. The bubble clouds themselves scatter and attenuate the signal, and contribute to the loss in signal range. Subsequent loss of signal from the filaments (i.e. the bubble clouds) seems likely to be due to sound attenuation caused by sediment lifted from the bed. The signal level is gradually reestablished some 30-40 s later, with a dark scattering region remaining at the approximate range

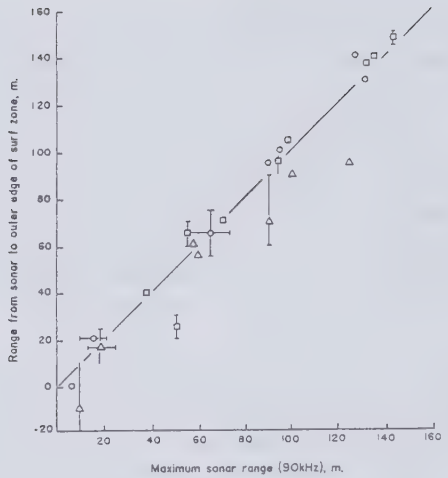

Figure 5. The variation of the range of the edge of the surf-zone from the sonar as judged by visual observations versus the maximum range obtained by the 90 kHz sonar. Different symbols are used for tides on different days. Vertical bars indicate the predicted uncertainty of estimates.

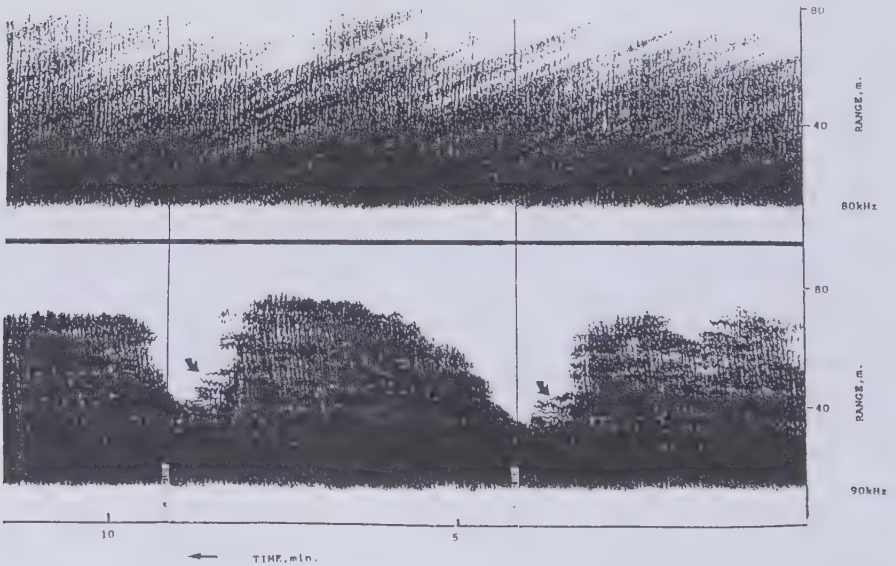

Figure 6. Sonograph record displayed as in Figure 2 showing wave breaking preceding sound attenuation at the edge of the sonar range in the 90 kHz record. Wind 8 ms^{-1} from 180°. Water depth at sonar = 2.0 m.

location of the strongest of the original filaments, presumably due to the continuing presence of small sound-scattering bubbles after the return of a significant proportion of the sediment to the sea bed. The mean fall speed of the sand grains composing the sediment was about 3 cms^{-1} which, in the mean water depth of the filaments, 1.3m, would lead to their removal in about 45 s. Bubble clouds observed in coastal waters contain bubbles of 50μm radius, or less, (Johnson and Cooke, 1979) which rise at 5 mms^{-1}, or less, and persist for several minutes.

Changes in sonar range like those shown in Figure 6 were common in windy conditions, but were not generally as large. Figure 7 contains evidence of a structure or pattern of lower frequency than the waves in the period preceding the reduction in range (marked at A), a structure containing 4-6 waves, propagating with approximately the same speed as the waves but at a speed which is clearly reduced as it approaches shore. The position of the Langmuir bands and the maximum range are moved by these patterns as they pass. Such patterns are generally transient, appearing together 3-10 times before loosing coherence, but occasionally and particularly when observations were made in lower wind speeds, the patterns are more persistent in their recurrence. Figures 8 and 9 show further examples. The structure modulates the limit of sonar range over distances of 2-3 m and at speeds of 37 ± 5 and 45 ± 9 cms^{-1} in Figures 8 and 9 respectively. The shortest ranges appear at times when the strength of the targets approaching shore are most intense.

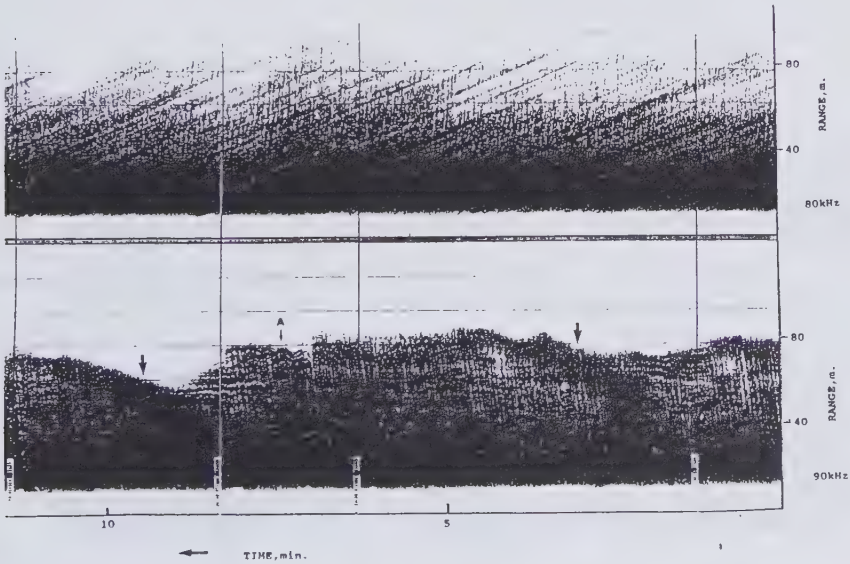

Figure 7. Sonograph record displayed as in Figure 2. Wind 7.5 ms^{-1} from 180°. Water depth at sonar = 1.7m. Note the appearance in the 90 kHz record (below) of diffuse scattering regions marked by arrows at about 2 and 9 mins into the record which move towards shore, migrating through the bands associated with Langmuir circulation at approximately constant range to form the edge of the sonar range.

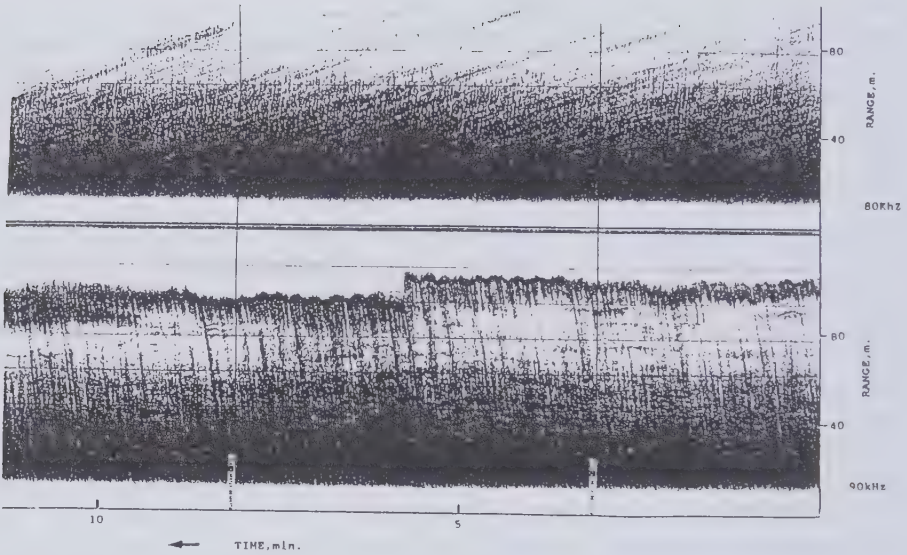

Figure 8. Sonograph record displayed as in Figure 2. Wind 4 ms^{-1} from 230° after winds of 8 m s^{-1} 30 mins earlier. Water depth at sonar = 2.5m. The 90 kHz sonograph (below) shows the appearance of a pattern with a periodicity of some 16s containing about 5 waves and causing movement of the edge of the sonar range.

Figure 9. Sonograph record displayed as in Figure 2. Wind 3 ms^{-1} from 236°. Water depth at sonar = 3.2m. The 90 kHz record (below) shows a pattern of bands in low wind conditions. A few scatterers were present which are visible in the 80 kHz beam and indicate tidally- induced longshore currents.

These patterns appear to be caused by wave groups approaching shore. For example, in Figure 9, c_p = 4.43 ms^{-1} and c_n = 15.15 ms^{-1}, so that (1) gives c = 4.25 ms^{-1} and, since T is measured as 2.27 s, λ = 9.65 m. We can then estimate the component of group velocity towards shore,

$$c_{gn} = \frac{c_n}{2}\left(1 + \frac{2kh}{\sinh 2kh}\right) \qquad (3)$$

as 8.6 ms^{-1} which compares with the speed of banded targets associated with the low-frequency pattern near the sonar, 8.0 ms^{-1}, measured from its slope in Figure 9. (Because of the 'deafening' of the 90 kHz sonar and the loss of short-range signal, this may be an underestimate). Use of (2) allows the estimation of k near the edge of the sonar range (near 140 m in Figure 9) where h = 0.7 m. Since the component of wavelength parallel to the beach is conserved, we can then estimate the wavelength normal to the beach at the edge of sonar range and hence find c_n, since the period is known. Use of (3) then allows an estimate of c_{gn} to be made at this second location, 2.36 ms^{-1}, which compares well with that measured from the sonograph, 2.38 ms^{-1}, supporting the hypothesis that the patterns are indeed associated with the onshore propagation of groups of waves.

The small amplitude theory which accounts for the effect of radiation stress under wave groups (Longuet-Higgins and Stewart, 1962) predicts, however, that a maximum current in a direction opposite to the direction of propagation of the wave group occurs at the position of maximum set-down at the location of maximum wave amplitude in the group. If the strongest targets forming the pattern are indeed associated with the highest waves in the group, an offshore component of current would be expected at this location. Instead the offshore *displacement* is a maximum, and the maximum offshore current appears to precede the strongest targets (i.e. the highest waves). Whilst an interpretation of the patterns as being caused by wave groups seems presently the most plausible, a more thorough study needs to be undertaken to examine, for example, whether the bands could be produced by interference of different waves, perhaps by the progressive modification of the wave spectrum as the outer edge of the surf-zone is approached, or by the evolution of long swell waves approaching shore (see, for example, Madsen, Mei and Savage, 1970). Figure 8 (some 6 min into the record) illustrates abrupt changes in range which contrast in structure from those noted in Figures 6 and 7; the original range is not reestablished. In these conditions the tidal movement of the maximum sonar range generally follows the rising or falling tide but with abrupt backward steps superimposed at 5-10 min intervals.

Discussion

We have here focused attention on the variety of signals which are visible in the region beyond the surf-zone. In windy conditions (winds exceeding 8 ms^{-1}) patterns possibly associated with Langmuir circulation persisting for 5-10 mins are detected,

and sonar offers a means to study the effect of variable depth on the pattern of circulation. Higher frequency targets consistent with surface gravity waves and wave groups can also be seen. The tests applied, namely whether the features satisfy the dispersion relation, serve to illustrate the wealth of information, both temporal and spatial, contained in the sonar records. These tests, however, assume the waves are linear and monochromatic, are able to adjust and conform to the dispersion relation even though the water depth is decreasing, and ignore the presence of longshore currents (generally valid since these are much less than the estimated longshore components of apparent phase speed, c_p). Methods to provide more comprehensive objective analysis and tests of the digital data set are being developed. The maximum range of the sonar beam pointing towards shore is modulated by wave breaking (Figure 6) and by wave groups, and limited to a range prescribed by the presence of sound-attenuating sediment. (The technique may be more effective in studying wave breaking within the surf zone on a gravel beach where less sediment is carried into suspension). The presence or absence of wave groups incident on the surf zone and the location of their breaking are central to the dynamics of the surf zone and to the radiation of waves from it, particularly to surf beats (Symonds *et al.*, 1982; Guza and Thornton, 1985). The observations point to the intermittency of incident wave groups and demonstrate a novel and powerful tool with which to study the offshore region.

Outside the surf zone persistent slow-moving features were sometimes detected in the up-beach beam. These were aligned approximately in the wind direction and are the subject of the second study reported here.

Langmuir Circulation and Dispersion

The Experiment

In regions and at times where bubbles are generated at the sea surface, either uniformly as in heavy rain or randomly by breaking wind-waves in deep water, accumulation of bubbles occurs in regions of surface convergence and subsurface downwelling. These regions are detected by side-scan sonar, and the resulting sonographs therefore provide 'maps', in range and time, of the patterns of surface convergence.

The central aim of the experiment was to concurrently investigate these patterns, and to study the dispersion of dye and diesel oil plumes, in the southern North Sea (52° N, 2° E). The water column is unstratified over its 45 m depth and is subject to tidal currents reaching 1 m s^{-1}. The sea bed is flat and sandy. The same weighted rig frame as detailed in the earlier section on waves approaching shore (minus vertical pole) was used to carry the sonars, and was deployed on the sea bed by a vessel (Figure 10). Once the rig was in position, the load line was detatched from the vessel, and the latter then anchored on a two-point mooring some 50 m

(horizontally) from the rig by its bow anchors. The rig remained connected to the vessel by a 200 m cable, powering the sonars, two inclinometers and a compass, and relaying their signals for real time display and digital recording. The two-point mooring, and the cable connection to the vessel, limited the safe duration of the deployment to a tidal half-cycle. The rig was then recovered and, once the tide had turned, was redeployed as daylight permitted. Four sea trials were conducted in all over May to September 1991, yielding fifteen sonar deployments, amounting to some sixty hours of data.

Further practical work was also undertaken from July to September 1992, on board a different vessel capable of a four-point mooring. This permitted the rig to be deployed over many tidal half-cycles, increasing the amount of data — the total stands at over 150 hours — and yielding data for the low currents close to slack tide. In principle, the contribution which processes identified in this extensive sonar data set make to the observed dispersion of the neutrally buoyant rhodamine B dye, or of the (buoyant) diesel, may be ascertained by appropriate modelling. (The plume dispersion experiment and its results will be reported elsewhere).

The 80 and 90 kHz sonars were used in side-scan mode, inclined up at 20° to the base of the rig and pointing at right angles to one another. For all the deployments, rig inclinations off the horizontal of less than 10° were achieved. The beams were some 35° wide in the vertical and 3° in the horizontal, isonifying narrow sections of water which are some 3 m across at the surface, and which pointed away from the vessel. The pulse repetition rate was 4 Hz, yielding a maximum horizontal beam range of 180 m; the signal was rarely distinguishable from noise at this range. For most deployments, the shear between the vessel and the rig as the latter was lowered was successfully exploited, so as to leave the 90 kHz beam pointing nearly normal, and the 80 kHz beam nearly parallel, to the mean flow.

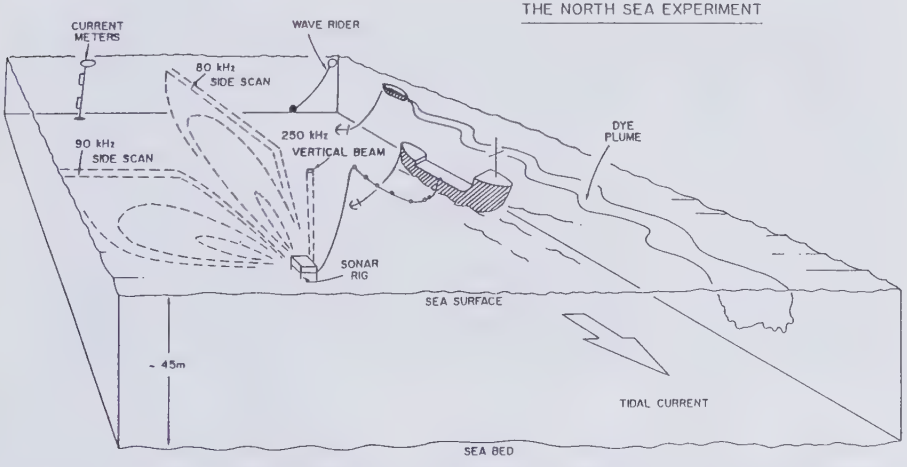

Figure 10. Sketch showing the site and sonar beam orientations in the North Sea experiment. Note that a narrow beam upward-looking sonar was employed on the rig in addition to the two side-scan sonars.

Environmental data included current and wave measurements from current meters and a waverider buoy respectively, deployed about 1 km from the rig. Weather data recorded on the vessel included wind, sea surface and wet/dry bulb temperatures, and the solar heat flux.

(a) Current speed and direction;
Sonar data were collected over current speeds ranging from 10 to 110 cm s^{-1}. For speeds of 30 cm s^{-1} or more, which holds for all but some 20 minutes either side of slack tide, the current is uni-directional along a line 20° to the right of the meridian. The current shear was measured by employing instruments at the surface, 1/3 and 2/3 depth, and by using an ADCP to sample the top half of the water column.

(b) Wind speed and direction;
An anemometer and wind vane mounted at a high point on the vessel recorded wind speeds, W_{10}, ranging from 0 to 12 m s^{-1}, when averaged over 30 second intervals and adjusted to 10 m reference height, with the direction predominantly close to meridional.

(c) Wave height and period;
Hourly averages of the height and period of the dominant wave group ranged from 30 to 130 cm, and 2.9 to 6.2 s respectively.

(d) Air-sea temperature;
The mercury-in-glass air temperature measured over the trials ranged from 9.9 - 18.7 °C, while that of the sea surface ranged from 9.5 to 17.3 °C. The temperature of the air relative to the sea ranged from -2.8 to +2.9 °C.

(e) Precipitation and sea state;
Rain was observed during two deployments, heavily for one and as drizzle for the other. Sea states varied from near mirror calm to agitation sufficiently great to prevent deployment of the sonar rig and the plume discharges. Windrows of foam were seen clearly by eye in trials in May and June, 1991.

Observations

For most deployments, the 80 kHz sonar was directed up-current, hence yielding information on the advection of bubble clouds by near-surface currents, and so supplementing the current meter data (Figure 11). The sonographs of the cross-current sonar, usually the 90 kHz, of the side-scan pair, reveal strongly backscattering bands (Figures. 12, 13) where surface convergence occurs, and so provide space-time plots of surface convergence. Many of the features are linear and continuous, with a velocity component along the beam close in value to v_y, the speed with which a bubble band aligned perfectly straight with wind, and advected passively by the current, would move:

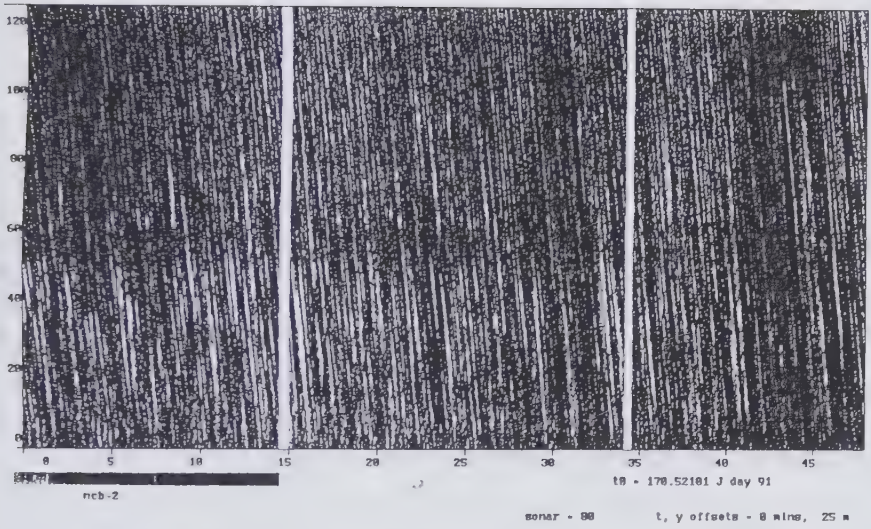

Figure 11. Sonograph record of surface range against time for the 80 kHz up-current sonar. Wind 7 m s^{-1} from 160 ± 15°. left of the sonar beam. The surface current systematically increased from 59 to 86 cm s^{-1} over the duration of the sonograph, while its heading swung from 160 to 172°, as measured toward the right of the beam (beam direction 25° true). The zones of missing data were due to a deficiency in the VCR's supply voltage.

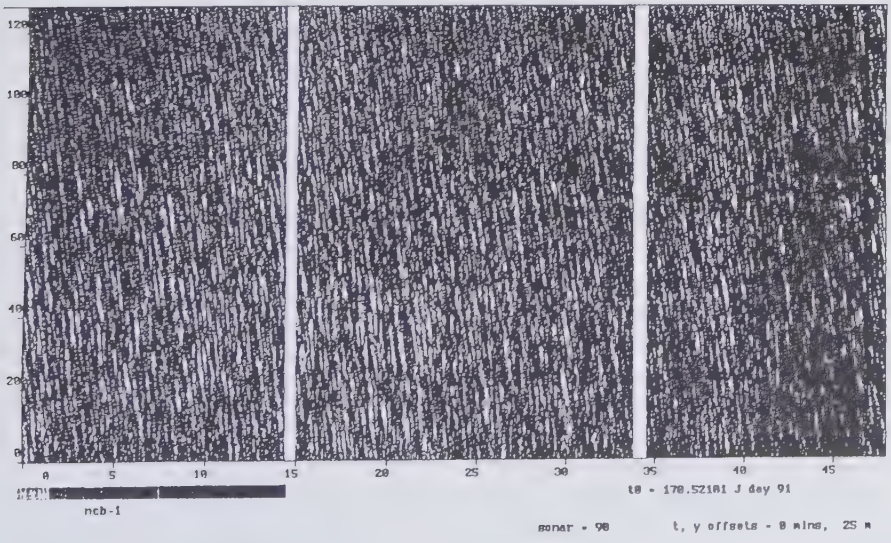

Figure 12. Cross-current sonograph for the same period as Figure 11. Wind and current directions relative to the beam, adjusted for the 90° difference between sonars (see Figure 10), are now, respectively, from 70°, and toward 110 to 98°, as measured left of the beam.

$$v_y = V\frac{\sin(\alpha-\beta)}{\sin\alpha}, \qquad (4)$$

where α, ß are the angles of the windrow (that is, the wind direction) and current relative to the sonar beam, respectively. These features are identified as bubble clouds accumulating in the surface convergence regions of Langmuir circulation. Convergence regions, which could be detected in the beam for several minutes, are evident and, given the current speeds, these persistence times correspond to lengths of up to 200 m. Other features that are not linear or are discontinuous are also sometimes prevalent. These are absent in the deep water, sometimes stratified, low current environment of Loch Ness, and therefore appear to be related to turbulence generated by the tidal flow over the sea bed. Further support for this hypothesis has been obtained from aircraft photographs showing evidence of sediment clouds with a scale, comparable to the water depth, similar to that of the irregular patterns seen in the sonographs.

Data Processing and Preliminary Analysis

Techniques have been developed to reduce the digitised sonographs to their essential features. Firstly, the image is low-pass filtered and edge-enhanced, to reduce its fine-resolution pixel distributions to the "shapes" immediately obvious to the eye. By supplying threshold values of intensity (as a percentage of the image by area) and shape perimeter (as a pixel number), these sonograph shapes are further filtered, and the remainder are then collapsed or "skeletised" to lines, using a technique developed by Mr. Curé (Thorpe and Curé, 1994). An example constructed from the sonograph, Figure 13, is shown in Figure 14. Necessarily inherent in this shape identification approach is a trade-off between clearly delimiting the features on one hand, and resolving features of the smallest length and time scales on the other.

Since the tidal current is non-steady, at times changing steadily by as much as 1 cm s^{-1} per minute, the skeleton image is transformed onto a two-dimensional spatial field, using the current meter data. The length and time scales of the class of features of interest, and their direction relative to the sonar (a) and wind may then be computed. To calculate inter-feature statistics such as the mean feature spacing, D, — as well as to permit modelling of the dispersion of buoyant tracers due to the observed surface convergence pattern — the features are approximated as "frozen" in the field over all time t, $t_0 \le t \le t_0 + \Delta t$ (Figure 15). We now postulate that the features possess a spectrum of lifetimes centred at, and narrow with respect to, a "characteristic" lifetime, τ. For $\Delta t > \tau$, the frozen field approximation will beinvalid when taken over the whole field, but remains applicable for the computation of length and time scales smaller than $\int^{t+t} V(\xi)d\xi$, τ respectively. In this way, we circumvent having to postulate the existence of, and to model, sources and sinks of Langmuir circulation outside the sonar beam.

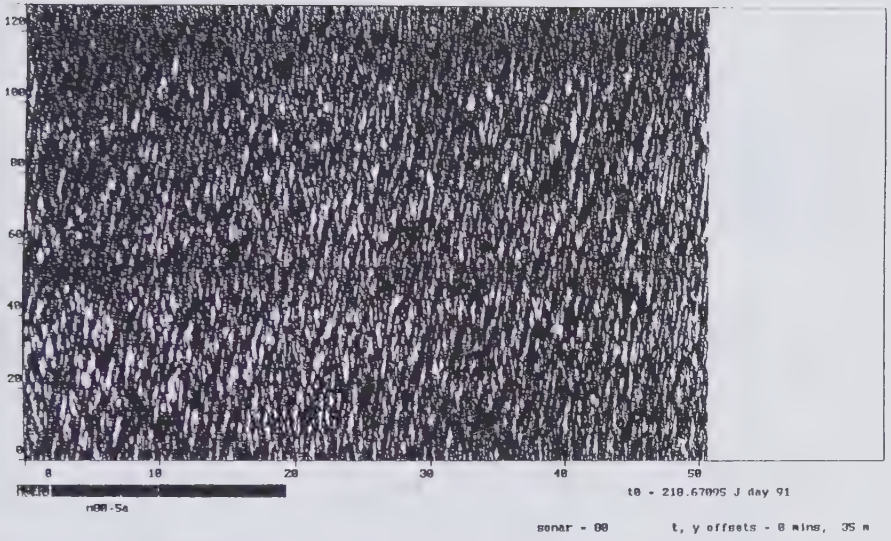

Figure 13. Another cross-current sonograph, illustrating the variety of patterns seen, including some of the nonlinear and discontinuous features that have been observed. Wind 10 m s^{-1} swinging from 85 to 95 ± 15° over the duration of the sonograph, as measured from right of the beam. The surface current systematically increased from 64 to 81 cm s^{-1} over the sonograph time, while its heading swung from 97 to 104°, as measured toward the right of the beam (beam direction 98° true).

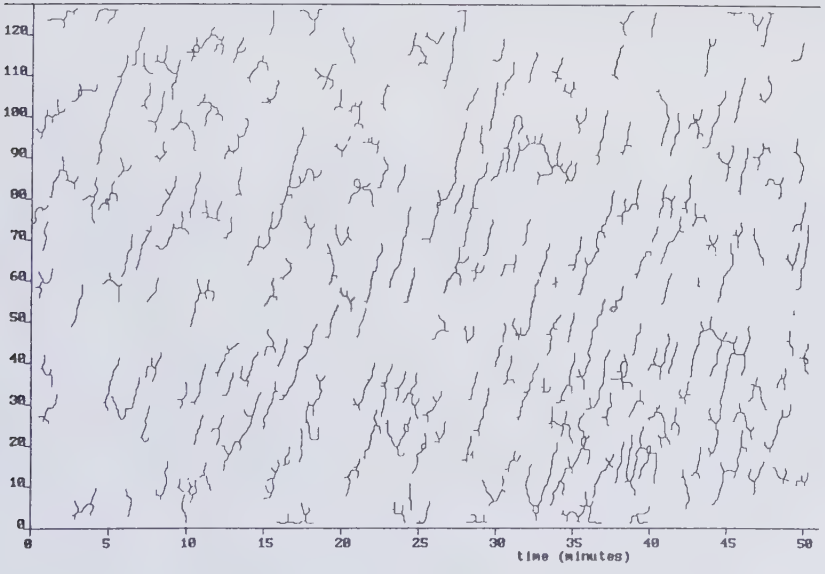

Figure 14. Skeletisation of Figure 13.

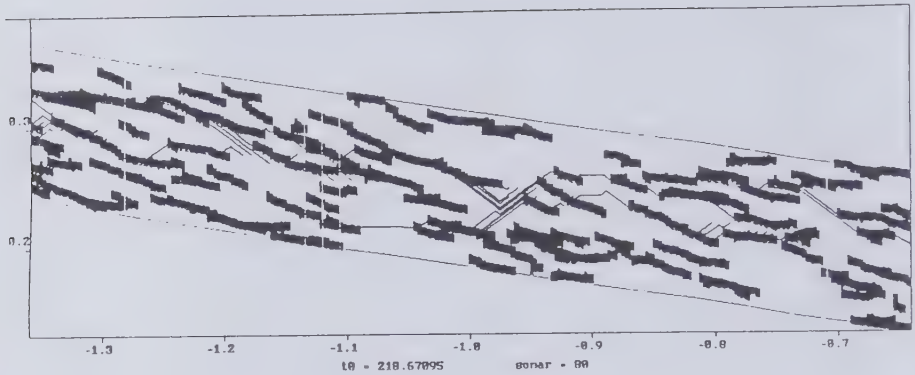

Figure 15. Tracer movement with respect to the frozen field windrows, illustrating the degree of convergence induced by Langmuir circulation. The thickness of the frozen field skeleton features has been exaggerated to distinguish them from the tracers.

The frozen field is of kilometre scaling and is generated from Figure 14 between t = 16:26 mins. and t = 33:29 mins. The cross current sonar is situated out-of-picture at the origin, and is directed along the y-axis. The sonograph skeletons are thus generated as the frozen field is advected by the mean current through the beam.

For this figure, the windrow lifetime prescribed for the tracers was made infinite. Note that if a tracer is only aligned with a windrow in one direction, and lies further than half the windrow spacing from it, it is not assigned a Langmuir circulation convergence velocity. This is to prevent net tracer inflow at the frozen field boundaries.

A number of length and time scales may be evaluated directly from this spatial field (Thorpe *et al.*, 1994). The mean orientation of each feature allows highly nonlinear or "off-wind" features to be excluded, and the mean over the ensemble of many features to be computed. A value of 24° to the right of the wind, with standard deviation 20°, has been obtained averaging over a number of sonographs. This value does not necessarily imply a significant deviation from the measured wind direction, as from (4), it could alternatively be due to a mean feature advection velocity that differs from the measured mean near-surface flow. Indeed, we should anticipate that this be so, as the mean surface flow is inflated in the presence of Langmuir circulation, due to the additional downwind current in the vicinity of a windrow (Pollard, 1977).

The scales of features over two representative wind speed regimes are shown in Table 1. The "longest" features are those which exceed the mean by more than one standard deviation.

TABLE 1. Showing the scales of the observed bands

wind $m\ s^{-1}$	length m		separation m	
	all	largest	all	largest
6.3 ± 0.5	49 ± 23	87 ±45	22 ± 5	26 ± 7
9.5 ± 0.5	63 ± 15	128 ± 37	25 ± 3	39 ± 4

By postulating that the features possess a spectrum of lengths centred at, and narrow with respect to a characteristic length, L, a simple analytical model of pattern advection through the sonar beam has been developed in (Thorpe *et al.*, 1994). (The length, L, is longer than that following from a frozen field hypothesis since the model seeks to detect the decay that occurs before the bands pass completely through the sonar beam). For the high wind speed data (W_{10} = 9.5 m s^{-1}), this model yields estimates of L and τ, the lifetime of the bubble bands, of 516 ± 351 m and 274 ± 69 s respectively for the longest features; 149 ± 26 m and 206 ± 31 s respectively when features of all lengths are included. The lower wind speed data is too scattered to permit a usefully accurate estimate of L, but is consistent with shorter lifetimes of 139 ± 108 s for the longest features, and 113 ± 56 s for the full set of feature lengths. The high wind speed L/D cellular aspect ratio is thus estimated to be 13 ± 9 for the longest, and 6 ± 1.5, for all the features respectively. We note that the estimates of lifetime probably understate the persistence of the Langmuir circulation and are much less than similar estimates made in the low current environment of Loch Ness.

Dispersion Modelling

A deterministic model has been developed to simulate horizontal dispersion due to the Langmuir circulation inferred from the sonographs. Full details are reported in Thorpe *et al.* (1994). The technique follows the concepts of Langmuir circulation diffusion proposed by Csanady (1983) and Faller and Auer (1987), and the dispersion model of Thorpe and Curé (1993). The dispersion of buoyant tracer particles over time scales of between two minutes to an hour, and hence over (longitudinal) distances of 50 m - 2 km, is computed in an absolute sense - that is, the dependence of the dispersion statistics on their locality in time and space is smoothed out to accumulate the statistics of the whole horizontal area concerned. This area is the "skeletised frozen field". The skeletonised sonographs that have been used as input have been taken from times when the bubble band features were both highly regular, and consistent with the presence of Langmuir circulation alone, and from times when bottom-generated turbulence appeared to be present as well. As the model described here is for floating particles, and the bubble clouds that mark the convergence zones have a scattering intensity which decays rapidly with depth (Thorpe, 1984), we have ignored details of the vertical structure of the surface convergence currents in

running the model. Similarly, measures of the contribution of wind-induced current, or of tidal shear, to the mean surface flow are implicitly included by using the measured (1 m) surface current in the model. The tracers are released from a subset of grid points over the field, chosen so as to both optimise the time each tracer spends in the field, and to keep the tracer density broadly constant. The tracers then disperse in the field, while the latter is advected (with negligible horizontal shear) by the mean current through the sonar beam.

Each tracer's motion is thus the vector sum of its motion relative to the field, and the motion of the field relative to the sonar. The tracer motion relative to the field (Figure 15) is determined by prescribing it a velocity component parallel to the wind, to allow for drift at the surface relative to the features, and a component perpendicular to the wind, directed toward the nearest feature, to reflect Langmuir circulation convergence. The latter component is set using estimates for Loch Ness (Thorpe and Curé, 1993).

With respect to the frozen field, the tracer thus moves downwind and toward the nearest feature. Once captured, it remains in the feature until it reaches the feature's end, or until the feature develops an appreciable off-wind orientation, or until the time for which the tracer has "preferred" the feature over any other exceeds τ. The calculation of the horizontal diffusivity follows from the first and second moments of the excursions of the tracers from their respective starting points: selected results are presented in the following section. We lastly note that when the model is extended to 3-D, non-floating tracers will escape from the surface convergence zones primarily by being carried below the surface in the downwelling current associated with Langmuir circulation. The tracers may then move across the cells, perhaps exchanging with neighbouring cells in the process. The lateral dispersion will therefore be increased.

Dispersion Estimates

An example of a model simulation is now detailed, with the current, wind and sonar data corresponding to Figures. 13 to 15 as input. The downwind tracer drift was set to 0.5% W_{10}, rising to 0.8% W_{10} on capture by a windrow; the lifetime was set to 10 mins. A total of 205 tracers were released at separations not less than 7.5 m. Figures 16 and 17 illustrate the resulting dispersion.

The mean time for first capture in a windrow was 266 s, while the mean time between all capture events (that is, including the first capture and any subsequent recaptures, following release from a windrow) was 172 s. The latter number is smaller due to those features that meander in space at a rate sufficiently high so as to "eject" their captured tracers for a short time. The mean duration of a capture was 85 s, while the mean proportion of time spent captured per tracer was 0.30. The mean windrow preference time was 209 s, but on an average of 0.49 occasions per tracer, the preference time reached the lifetime (10 mins, as specified above), causing the tracer to exit the windrow.

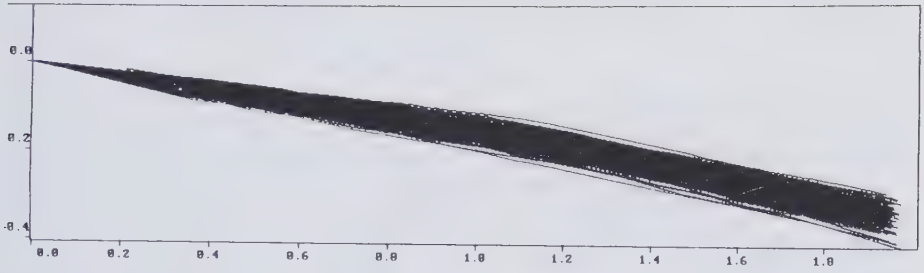

Figure 16. The excursions of tracers from their release points, as shown in the (inertial) sonar frame (wind and current as given for Figure 13) with kilometre scaling. This illustrates the degree of dispersion induced by the Langmuir circulation, superimposed on strong tidal advection. The tracers in Figure 15 are reintroduced into the frozen field where necessary, to ensure each excursion takes place over the full diffusion time.

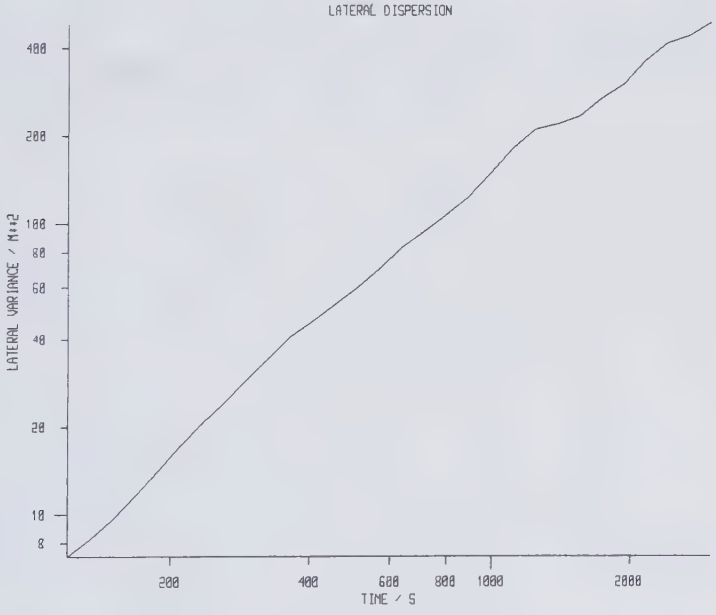

Figure 17. A graph of the lateral variance, computed from the excursions of Figure 16, against diffusion time (wind and current as given for Figure 13).

The lateral power law and diffusivity may be computed from Figure 17. Approximating the time dependence of the lateral variance σ^2 over the whole diffusion time by a monomial, $\sigma^2 \propto t^n$, the best fit power law index n is 1.3. The lateral diffusivity K, defined as

$$K = \frac{1}{2}\frac{d\sigma^2}{dt}, \qquad (5)$$

is 0.11 $cm^2 s^{-1}$ after 45 minutes. The graph does, however, indicate that the power index is prone to decrease with time, with pronounced change close to the mean time for first capture by a windrow, and again after the tracers have, on average, interacted with several windrows. Simulations run under the same model parameter settings, but conducted using data from other deployments of the sonar, have produced diffusivities an order of magnitude smaller, in particular at lower wind speeds (near 5 ms^{-1}). The observed standard deviation of the associated power law index, n, over the different data sets was 0.1. These estimates of diffusivity are relatively high compared to those values reported at similar wind speeds for caged dispersion (Thorpe and Curé, 1993) (as is the power law index), and for the dispersion induced by a numerical model of windrow meandering and splitting (Faller and Auer, 1987). This is perhaps unsurprising, given that either the tracers (in the former model) or the convergence regions themselves (in the latter model) are relatively constrained compared to the model outlined here. In its range of output diffusivities, our model demonstrates a variability more in keeping with observations than the models of Csanady (1973) and Faller and Auer (1987).

The longitudinal dispersion may be similarly parameterised, although it cannot be measured practically in a continuous dye release experiment such as that of the North Sea trials. In the model simulations conducted so far, for downwind drift speeds between 0% and 1.5% W_{10} (rising to between 0.1% and 2.5% W_{10} respectively on capture by a windrow), and lifetimes of 5 to 20 mins, the longitudinal variance has not been observed to rise significantly greater than its lateral analogue, and can be some 50% less.

The dependence of the two horizontal dispersion variances, power laws and diffusivities on the wind speed will be evaluated, and the sensitivity of these quantities to the prescribed lifetime, downwind drift and Langmuir circulation convergence current assessed. The model will also be extended to compute relative diffusion (Csanady, 1973), for direct comparison with the diesel plume studies conducted concurrently. The results will be reported elsewhere. The lateral dispersion example given here is for parameter values close to our current best estimates.

Conclusions

The objective of this paper is to demonstrate the potential of side-scan sonar in making observations of waves near shore and of dispersion in shelf seas. We have provided examples of measurements which can be made, for example of wavelength, wave speeds and periods, of particle motions in waves moving towards shore, of wave group structure, of patterns of surface convergence associated with Langmuir

circulation, of the time and space scales of this circulation, and of the diffusion of floating particles as a consequence of its presence. Some of these measurements and the information they carry, especially about Langmuir circulation, are novel. The sonars are uncalibrated and the signal processing is unsophisticated. Much could be improved with consequent increase in information. There is much information yet to be gleaned about the dynamics of the near-surface processes using high-frequency sonar. Above all, it is the information obtained simultaneously about space and time scales of motion in the spectral window of the instrumentation, and the visual images (the sonographs) which it produces, which establish side-scan sonar as a such powerful tool to advance the scientific knowledge and insight into the workings of the seas.

Acknowledgments: We are grateful to Professor H Peregrine and Dr G Watson for helpful comment on the beach studies. Able assistance in the collection of data was provided by M Cure, A Crawford and J Jackson. The work was carried out with support from the US Office of Naval Research under grant number N00014-92-3-1288. The work in the southern North Sea work forms part of an EEC MAST funded collaboration with the DTI Warren Spring Laboratory, for which we are most grateful. A preliminary account of the surf-zone studies is given by Thorpe and Hall (1993).

References

Belloul, M.B.E. and S.A. Thorpe Acoustic observation of oil slicks at sea. *J. Geophys. Res*. In press, 1992.

Csanady, G.T. *Turbulent diffusion in the environment*. Reidel, 1973.

Faller, A.J. and S.J. Auer. The role of Langmuir circulation in the dispersion of surface tracers. *J. Geophys. Res*., 83, 3617-3633, 1987.

Farmer, D.M., C.L. McNeil and B.D. Johnson. Evidence of the importance of bubbles in increasing air-sea gas flux. *Nature*, 361, 620-623, 1993.

Guza, R.T. and E.B. Thornton. Observations of surf beat. *J. Geophys. Res*., 90, 3161-3172, 1985.

Herbers, T.H.C., R.L. Lowe and R.T. Guza. Field verification of acoustic Doppler surface gravity wave measurements. *J. Geophys. Res*., 96, 17,023-17,035, 1991.

Johnson, B.D. and R.C. Cooke Bubble populations and spectra in coastal waters: a photographic approach. *J. Geophys. Res*. 84, 3761-3766, 1979.

Longuet-Higgins, M.S. and R.W. Stewart. Radiation stress and mass transport in gravity waves with application to 'surf-beats'. *J. Fluid Mech*. 13, 481-504, 1962.

Madsen, O.S., C.C. Mei and R.P. Savage The evolution of time-periodic long waves of finite amplitude. *J. Fluid Mech*. 44, 195-208, 1970.

Osborn, T., D.M. Farmer, S. Vagle, S.A. Thorpe and M. Curé. Measurements of bubble plumes and turbulence from a submarine. *Atmosphere-Ocean* 30, 419-440, 1993.

Pollard, R.T. Observations and theories of Langmuir circulations and their role in near surface mixing, in *A Voyage of Discovery*; G.R.Deacon 70th Anniversary Volume 9ed. M.Angel, 235-251. Pergamon, 1977.

Smith, J. Performance of a surface-scanning Doppler sonar near shore. *J. Atmos. Oceanic Technol.*, 10, 760-777, 1993.

Symonds, G., D.A. Huntley and A.J. Bowen. Two-dimensional surf beat: long wave generation by time-varying breakpoint. *J. Geophys. Res*. 87, 492-498, 1982.

Thorpe, S.A. On the clouds of bubbles formed by breaking wind-waves in deep water and their role in air-sea gas transfer. *Phil. Trans. Roy. Soc*. A 304, 155-210, 1982.

Thorpe, S.A. The effect of Langmuir circulation on the distribution of bubbles caused by breaking waves. *J. Fluid Mech*. 142, 151-170, 1984.

Thorpe, S.A. Measurements with a Automatically Recording Inverted Echo Sounder; ARIES and the bubble clouds. *J. Phys. Oceanogr.* 16, 1462-1478, 1986.

Thorpe, S.A. Bubble clouds and the dynamics of the upper ocean. *Q.J.R.Met.Soc*., 118 ,1-22, 1992.

Thorpe, S.A., M.B. Belloul and Hall, A.J. Internal waves and whitecaps. *Nature,* 330, 740-742, 1987.

Thorpe, S.A. and M.S. Curé. One-dimensional dispersion in a lake inferred from sonar observations, in *Mixing and Transport in the Environment* edited by K. Bevan, P. Chatwin and J. Millbank, 17-28, J. Wiley & Sons Ltd, 1994.

Thorpe, S.A., M.S. Curé, A. Graham and A.J. Hall. Langmuir circulation and dispersion; sonar observations of space and time variability. Accepted for publication in *J. Atmos. Oceanic Technol.*, 1994.

Thorpe, S.A. and A.J. Hall. The characteristics of breaking waves, bubble clouds, and near-surface currents observed using side-scan sonar. *Continental Shelf Res*. 1, 353-384, 1983.

Thorpe, S.A. and A.J. Hall. Near-shore side-scan sonar studies. *J. Atmos. Oceanic Technol.*, 10, 778-783, 1993.

Thorpe, S.A., A.J. Hall, A.R. Packwood and A.R. Stubbs. The use of towed side-scan sonar to investigate processes near the sea surface. *Continental Shelf Research*, 4, 597-608, 1985.

Thorpe, S.A., A.J. Hall and S. Hunt. Bouncing internal bores of Ardmucknish Bay. Nature, 306,167-169, 1983.

Thorpe, S.A. and A.R. Stubbs. Bubbles in a freshwater lake. *Nature*, 279, 403-405, 1979.

Vagle, S. and D.M. Farmer. The measurement of bubble size distribution by acoustic backscatter. *J. Atmos. Ocean. Tech.,* 9, 630-644, 1992.

Zedel, L. and D.M. Farmer. Organised structures in subsurface bubble clouds: Langmuir circulation in the open sea. *J. Geophys. Res*. 96, (C5), 8889-8900, 1991.

8

Detailed Cross-Frontal Structure of a Tidal Front in the Kii Channel, Japan

T. Yanagi, T. Yamamoto, T. Ishimaru and T. Saino

Abstract

Intensive field observations of the vertical distribution of water temperature, salinity, chlorophyll *a*, turbidity and current across a tidal front in the Kii Channel, Japan was carried out with the use of a towed CTD and ADCP on 2 July 1991. A distinct tidal front was observed between the well-mixed region in the northern part and the stratified region in the southern part of the Kii Channel. The local maximum of chlorophyll *a* was found in the subsurface layer of the stratified region and the local maximum of turbidity in the middle layer of the well-mixed region. The surface convergence was found to be situated between the well-mixed region and the stratified region. The well-mixed water intrudes into the subsurface layer of the stratified region and the strong westward current core is found in the subsurface layer of the well-mixed region

Introduction

A tidal front is generated in a transition region between vertically well-mixed water where the tidal stirring is strong and the stratified water where the tidal mixing is relatively weak and the effect of surface heating is important. A tidal front is considered to play an important role in material transport in a coastal sea. However, its quantitative role in the material transport has not been revealed because the detailed flow structure around a tidal front has only been recently by Lwiza *et al.* (1991). The measurement of flow structure around a tidal front is very difficult as the front migrates depending on the tidal stage.

Mixing in Estuaries and Coastal Seas
Coastal and Estuarine Studies Volume 50, Pages 135-144
Copyright 1996 by the American Geophysical Union

Yanagi and Okada (1993) revealed that a tidal front is developed in the northern part of the Kii Channel, the Seto Inland Sea, Japan with use of NOAA 9 infrared image and this tidal front is located where the value of log (H/U^3) is about 2.5 (where H is the water depth in meters and U the amplitude of M_2 tidal current in ms^{-1}).

In this paper, the detailed cross-frontal structure across a tidal front at the Kii Channel, Japan is revealed with use of towed CTD and ADCP (Acoustic Doppler Current Profiler) data.

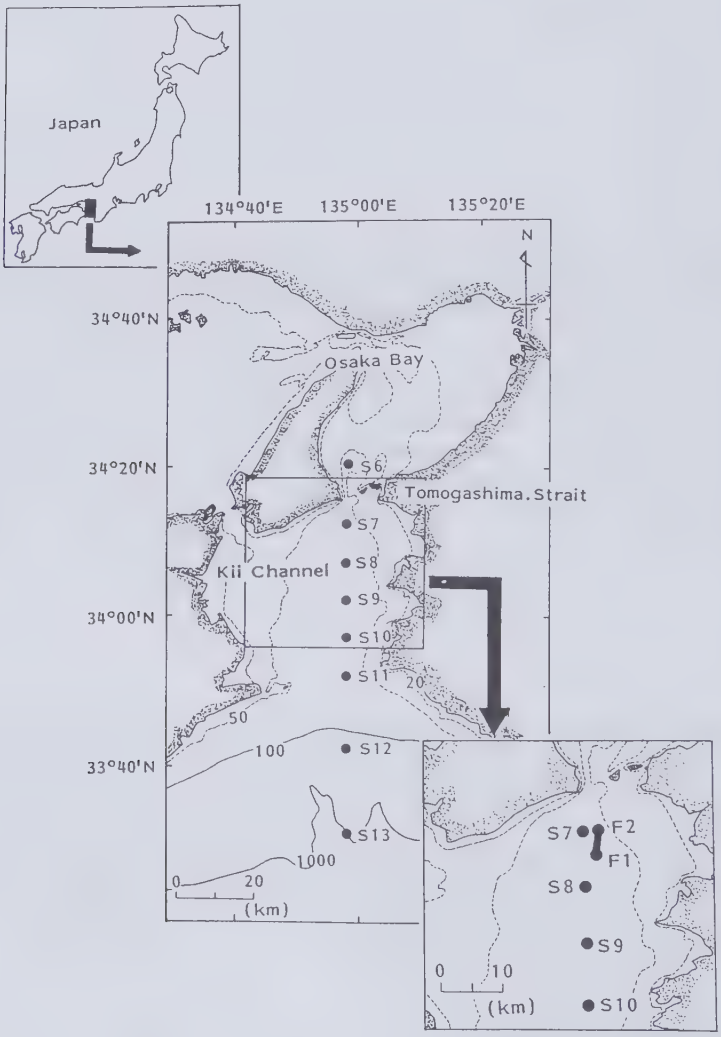

Figure 1. Observation Stations in the Kii Channel. Broken line and full line denote the bottom contour with the number of depth in meter.

Observation

The field study was undertaken in the Kii Channel (Figure 1) by RV "*Tansei-Maru*" of the Ocean Research Institute, University of Tokyo, from 27 June to 2 July 1991. The synoptic distribution of water temperature, salinity and density from Station S6 to Station S13 (Figure 1) were recorded on 27 and 28 June to define the position of the tidal front.

Detailed distribution of water temperature, salinity, density, fluorescence, beam-transmittance and current across the front was recorded from Stations Fl to F2 normal to the front between 12:00 and 13:45 on 2 July 1991 (intermediate state from spring to neap). The time of slack water from flood to ebb (i.e. HW) at Tomogashima Strait predicted by Maritime Safety Agency was 13:01 on 2 July 1991. The horizontal distribution of surface (5 m) water temperature and salinity were continuously measured with the use of a thermistor and a salinometer. The vertical distributions of water temperature, salinity, beam transmittance and fluorescence were observed using the OCTOPUS system (Ishimaru *et al.*, 1984) descending and ascending continuously in a yo-yo fashion from the RV "*Tansei-Maru*" with a speed of 2 knots. Simultaneously, the ADCP (R.D. Instruments, 300 kHz) was towed and current profile records were obtained every 3 minutes (i.e. approximately 190 m in the horizontal direction and 2 m in the vertical direction). The instrument was used in bottom tracking mode, in which the ADCP measures the apparent velocity of the sea floor and vectorially subtracts this from the measured water velocity. The water velocity is therefore measured relative to the sea floor. The raw current data were averaged using a box filter with the horizontal length of 380 m and the depth of 4 m.

Results

The synoptic vertical distribution of water temperature, salinity and density from Station S6 to Station S13 are shown in Figure 2. The vertically well-mixed region exists near Tomogashima Strait, around Stations S6 and S7, and the stratified region in the Kii Channel. A tidal front is developed between Stations S7 and S8 shown by an arrow in Figure 2 which was confirmed by the existence of surface convergence of drifting material on the sea surface.

The horizontal distribution of surface water temperature and salinity from Stations F1 to F2 are shown in Figure 3. Water temperature decreases from 23 to 21.5 °C and salinity increases from 31.5 to 32.0 pss across the front shown by an arrow in Figure 3 where we can observe the gathering of drifting material and foam on the sea surface by eye from the vessel as shown in Figure 4. The detailed vertical distribution of water temperature, salinity, density, beam-transmittance and chlorophyll *a* from Station F1 to Station F2 are shown in Figure 5 (a) to (e). The vertically well-mixed region exists near Station F2 and stratified region near Station F1. The most turbid water exists in the middle layer of the well-mixed region and the local maximum of

chlorophyll *a* is found in the subsurface layer of the stratified region. This is the first time that the detailed cross-frontal distributions of chlorophyll *a* and turbidity across a tidal front have presented although water temperature, salinity and density distribution has been observed using an undulating CTD system (Simpson *et al.*, 1978, Allen *et al.*, 1980).

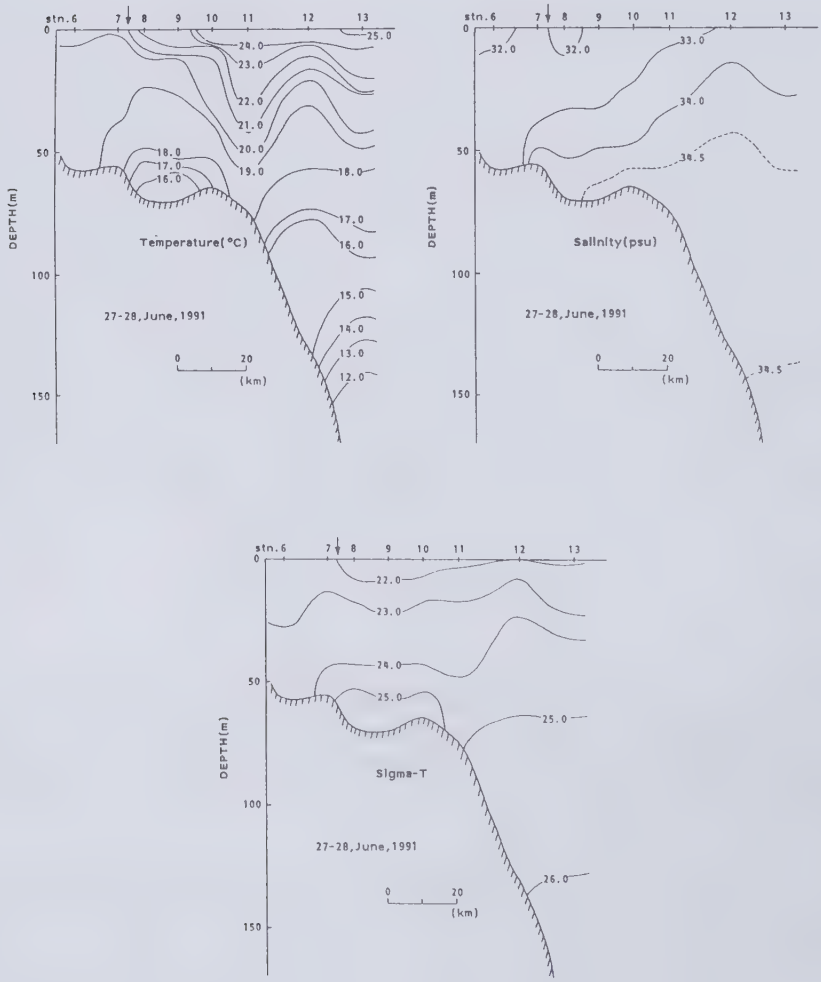

Figure 2. Vertical distributions of water temperature, salinity and density from Station S6 to Station S13. An arrow denotes the position of a tidal front.

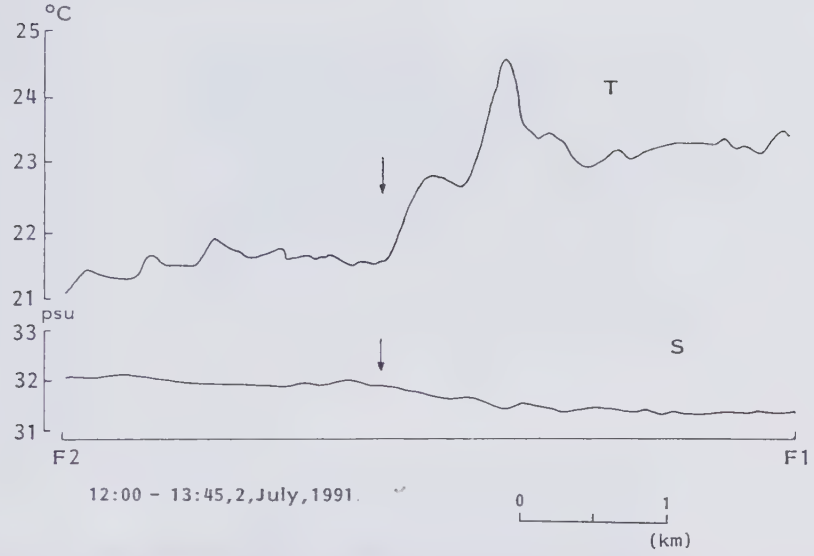

Figure 3. Horizontal distributions of water temperature and salinity 5 below the sea surface from Station F1 to Station F2. An arrow denotes the position of surface convergence shown in Figure 4.

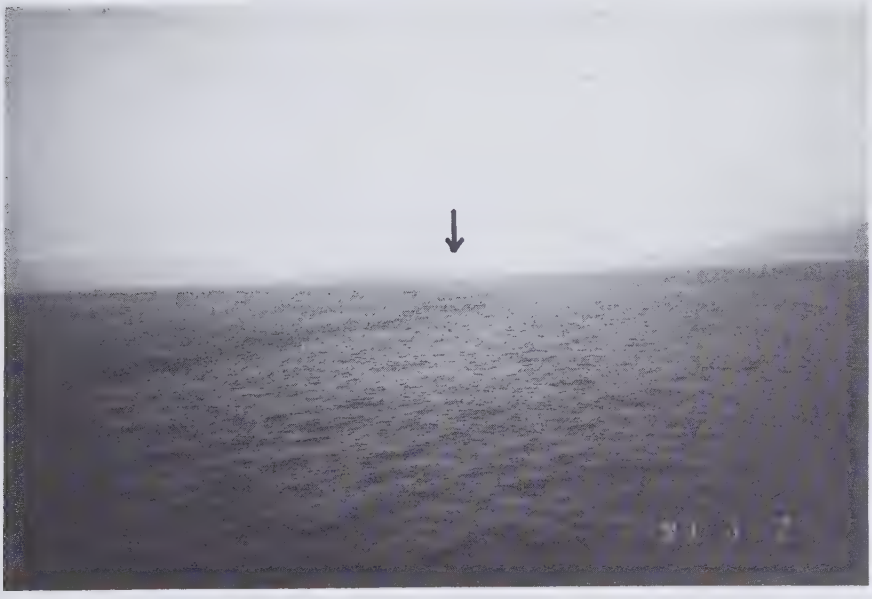

Figure 4. A surface convergence accompanying with a tidal front in the northern part of the Kii Channel. An arrow shows the position of surface convergence. The left side is and the right side the vertically well-mixed region.

(a)

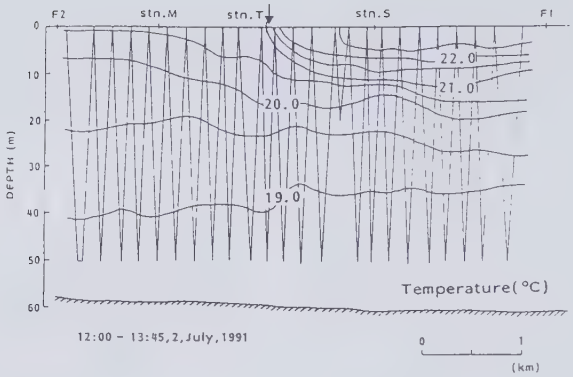

(b)

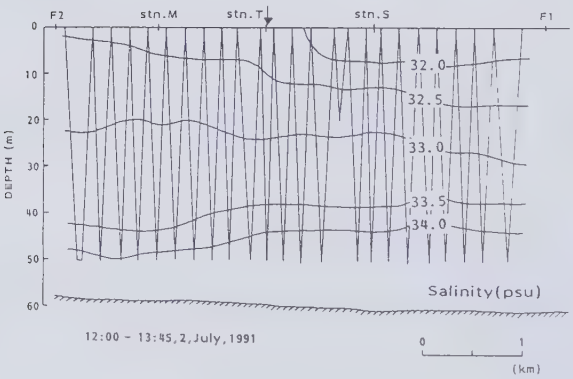

(c)

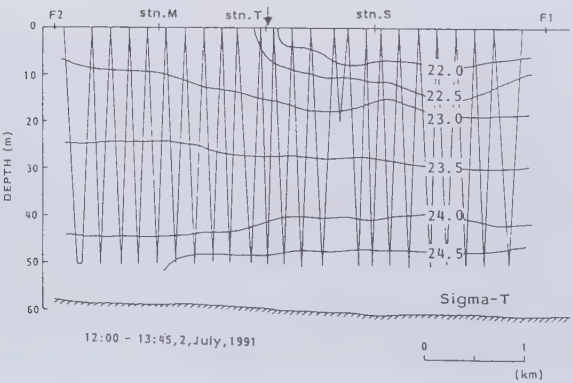

Figure 5. The vertical distributions of water temperature (a), salinity (b), density (c), beam-transmittance (d) and chlorophyll *a* (e) across a tidal front in the northern part of the Kii Channel. An arrow denotes the position of surface convergence shown in Figure 4.

(d)

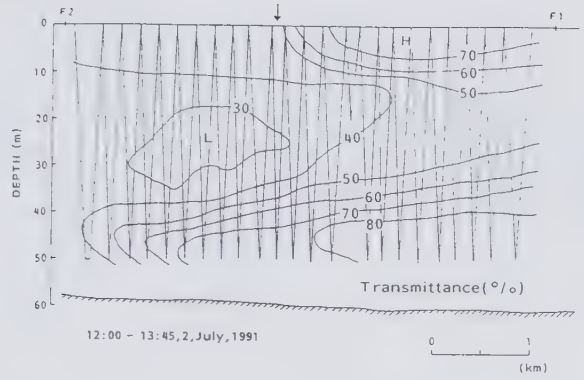

(e)

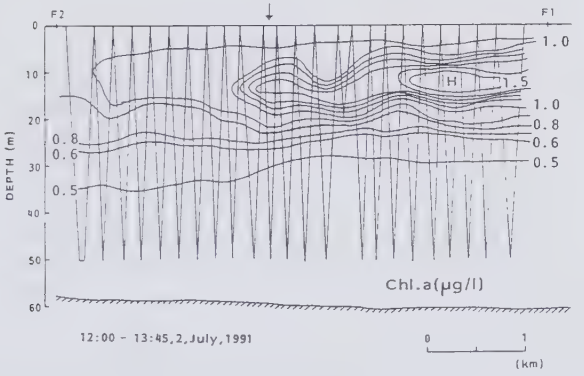

Figure 5 (continued). The vertical distributions of water temperature (a), salinity (b), density (c), beam-transmittance (d) and chlorophyll *a* (e) across a tidal front in the northern part of the Kii Channel. An arrow denotes the position of surface convergence shown in Figure 4.

The current data were averaged vertically at each observed point and the vertically averaged (barotropic) eastward and northward velocities are shown in the upper part of Figure 6 (a) and (b), respectively. The northward current in the southern part near Station F1 changes to southward in the northern part near Station F2 as shown in Figure 6(b). Such spatial change may be considered to correspond to the temporal change from flood (northward current) to ebb (southward current) around the time of 13:01. We may treat such barotropic velocities as the tidal current component at this time and subtract them from the observed current data. The detailed distribution of the residual baroclinic eastward current (parallel to the front) and baroclinic northward current (perpendicular to the front) across the front are shown in Figure 6 (a) and (b), respectively. The ADCP data are limited to a maximum depth of 28 m. The strong westward current core up to 10 cm s^{-1} (a frontal jet) is found in the subsurface layer of the well-mixed region and the surface layer of the stratified region flows eastward (Figure 6a). This is in qualitative agreement with the

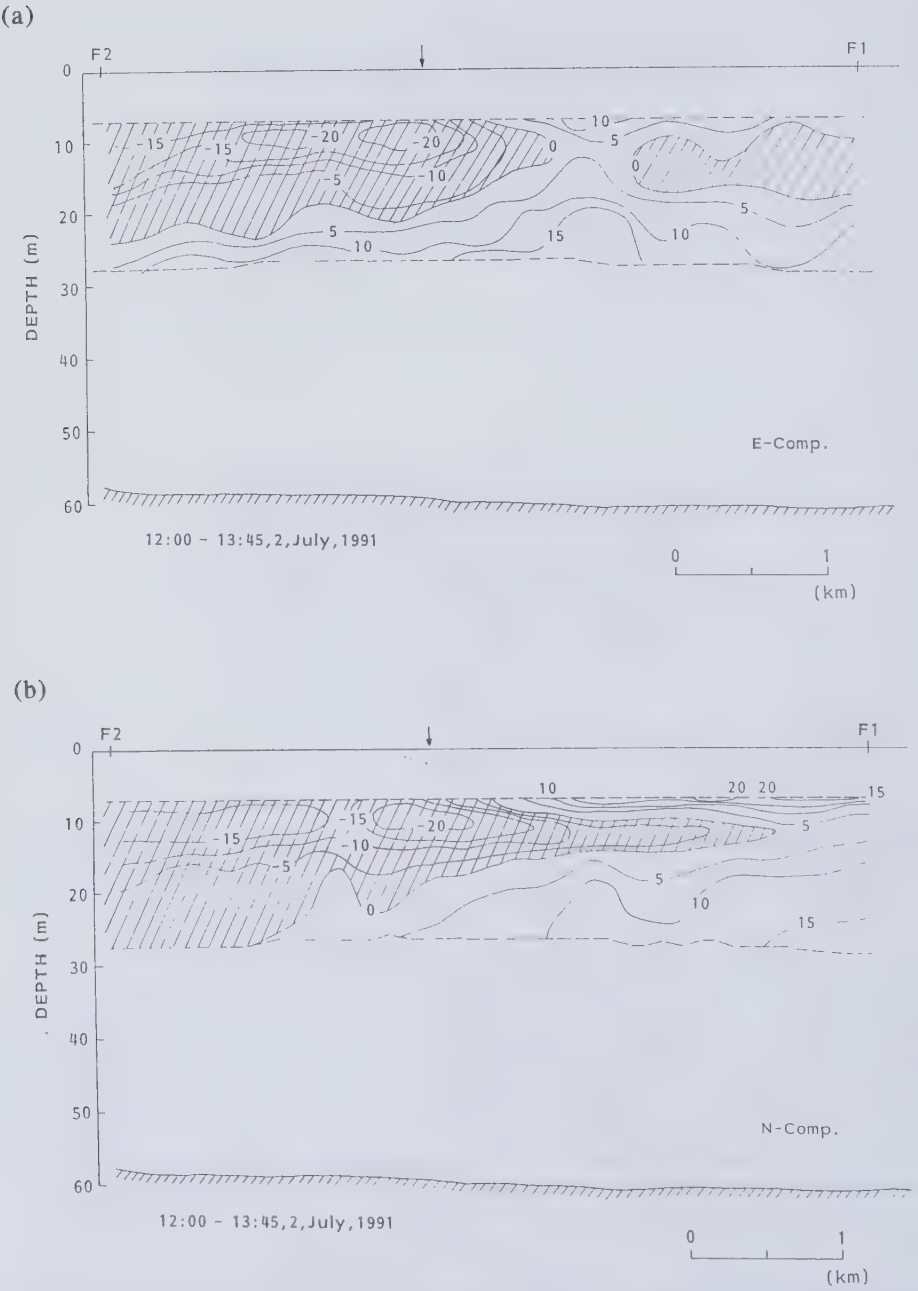

Figure 6. The vertical distributions of eastward current (a) and northward current (b) across a tidal front in the northern part of the Kii Channel. The shadow regions denote the westward or southward current. An arrow denotes the position of surface convergence shown in Figure 4.

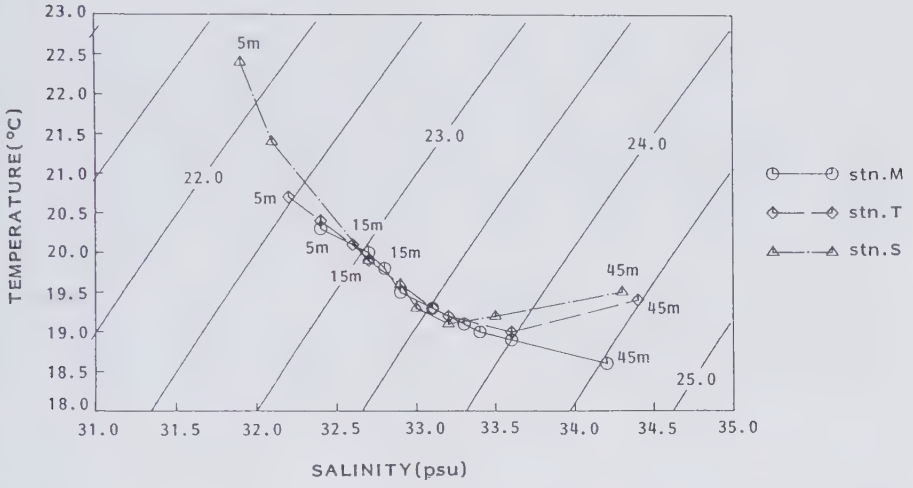

Figure 7. T-S diagrass at Stations M, T and S.

geostrophic flow based on the density field. The surface layer of the well-mixed region flows southward and that of stratified region northward and the surface convergence exists at the point shown by an arrow (which denote the position of surface convergence shown in Figure 4) between the well-mixed region and the stratified region. The southward flow of the well-mixed region intrudes into the subsurface layer of the stratified region. Such an intrusion is confirmed by T-S diagram shown in Figure 7. The subsurface water at Station S within the stratified region does not result from mixing of the surface and bottom water at Station S but has the same TS characteristics as the sub surface water at Station M. Such cross-frontal intrusion may relate to the local maximum of chlorophyll *a* in the subsurface layer of the stratified region as shown in Figure 5 (e) when the northward intrusion transport nutrients from the well-mixed region into the subsurface layer of stratified region. This process was also suggested (Takeoka *et al.*, 1993) from the observations of a tidal front at the Sea of Iyo in the Seto Inland Sea, Japan.

Discussion and Conclusion

We reveal the detailed cross-frontal structure of a tidal front at the northern part of the Kii Channel. As for the frontal jet, Lwiza *et al.* (1991) showed that the frontal jet with currents up to 15 cm s^{-1} is stronger during spring tides and weaker during neap tides. Our observations were undertaken in the intermediate state from spring to neap with currents in the frontal jet with currents reaching 10 cm s^{-1}. Higher currents would be expected during spring tides. The local maximum of turbidity in the middle

layer of the well-mixed region may result from the inorganic matter which are suspended by the strong tidal mixing because such turbidity has low chlorophyll *a* value. On the other hand, the local maximum of chlorophyll *a* may result from the light conditions, stability of the stratified region and the horizontal supply of nutrients from the well-mixed region by the cross-frontal intrusion in the subsurface layer. The cross-frontal intrusion is theoretically demonstrated by Garrett and Loder (1981) but has not been observed in the field. The cross-frontal intrusion shown in Figure 6(b) is the first evidence in the field because Lwiza *et al.* (1991) did not observe such cross-frontal circulation across a tidal front in the North Sea.

Acknowledgments. The authors express their sincere thanks to Dr. H. Takeoks of Ehime University for his helpful discussions and the crew of RV *Tansei-Maru* for their help in the field observations. This study was partially supported through funding from the Ministry of Education, Science and Culture, Japan.

References

Allen, C.M., J.H. Simpson and R.M. Carson, The structure and variability of shelf sea fronts as observed by an undulating CTD system. *Oceanol. Acta*, 3, 59-68, 1980.

Garrett, C.J.R. and J.W. Loder, Dynamical aspects of shallow-sea fronts. *Phil. Trans. Roy. Soc. London*, A302, 563-581, 1981.

Ishimaru, T., H. Otobe, T. Saino, H. Hasumoto and T. Nakai, OCTOPUS, an octo parameter underwater sensor, for use in biological oceanography studies. *J. Oceanogr. Soc. Japan*, 40, 207-212, 1984.

Lwiza, K.M.M., D.G. Bowers and J.H.Simpson, Residual and tidal flow at a tidal mixing front in the North Sea. *Continental Shelf Res.*, 11, 1379-1395, 1991.

Simpson J.H., C.M. Allen and N.C.G. Morris, Fronts on the continental Shelf. *J. Geophysical Res.*, 83, 4607-4614, 1978.

Takeoka, H., O. Natsuda and T. Yamamoto, Processes causing the chlorophyll *a* maximum in the tidal front in Iyo-Nada, Japan. *J. Oceanogr. Soc. Japan*, 49, 57-70, 1993.

Yanagi, T. and S. Okada, Tidal Fronts in the Seto Inland Sea. *Memoirs of the Faculty of Engineering*, Ehime University, 12, 337-343, 1993.

9

A Field Investigation of Water Exchange Between a Small Coastal Embayment and an Adjacent Shelf

P. E. Holloway

Abstract

A discussion is presented of the flow structure and water exchange through the entrance of Jervis Bay, a small coastal embayment situated on the east coast of Australia. In an area of weak tidal flushing, low frequency circulation is shown to dominate the exchange process. At a period of around 6 days, coastally trapped waves are thought to generate internal Kelvin waves which are shown to be capable of causing significant exchange between the bay and shelf. The rate of exchange is enhanced with increasing stratification. A background, or mean, flow also very effectively flushes the bay with inflow concentrated near the surface on the southern side of the entrance and compensating outflow strongest near the seabed on the northern side of the bay entrance.

Introduction

An important property of many coastal embayments is the rate at which water, and dissolved and particulate matter, is exchanged between the embayment and the adjacent continental shelf. In this paper, the circulation through the entrance of Jervis Bay, a small coastal embayment situated on the east coast of Australia, and the resulting water exchange is investigated through the analysis of observational data. The bay is being subjected to increasing environmental pressures from local

Mixing in Estuaries and Coastal Seas
Coastal and Estuarine Studies Volume 50, Pages 145-158
Copyright 1996 by the American Geophysical Union

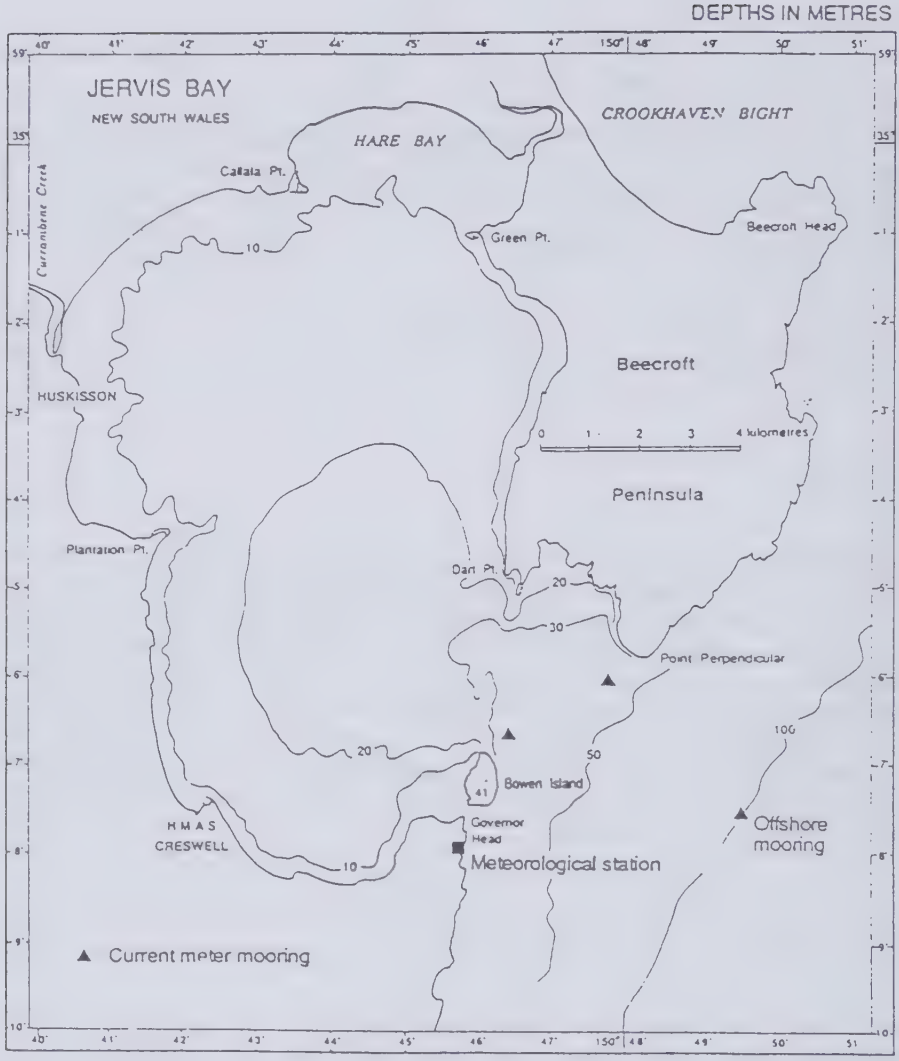

Figure 1. Map of Jervis Bay showing the locations of moorings and the meteorological station.

development raising concerns about the fate of potentially increasing levels of sewage, suspended solids, and chemicals such as tributyltin. Jervis Bay receives very little freshwater input for most of the year, is not subjected to high evaporation, and has a weak tidal regime. This is in contrast to many estuaries which are fed by freshwater river input or high evaporation, with a resulting strong gravitationally driven circulation, and are often subjected to strong tidal mixing.

There are numerous studies reported in the literature of the circulation and exchange processes in estuaries. As classified by Hansen and Rattray (1966), estuaries are generally influenced, to varying degrees, by tidal mixing and by gravitationally induced circulation resulting from longitudinal density variations caused by river input or high evaporation and being open to the ocean. Strong tidally driven estuaries tend to be vertically homogeneous so that exchange along the estuary is dependant on longitudinal dispersion as found, for example, in the Mersey Estuary in the United Kingdom (Bowden, 1965) and in the Bay of Fundy on Canada's east coast (Holloway, 1981). In contrast, weak tidal estuaries form strong vertical salt gradients, often forming a salt wedge, so that circulation is primarily controlled by density driven flows, e.g. the Mississipi River in the United States, as discussed by Officer (1976). The effects of tidal mixing inhibiting the more efficient gravitationally driven exchange is clearly demonstrated in Spencer Gulf, South Australia where a pronounced Spring-Neap tidal cycle creates periods of strong then weak turbulence (Nunes and Lennon, 1987). The effect of vertical mixing reducing the gravitational circulation has also been demonstrated in laboratory experiments by Linden and Simpson (1986).

Jervis Bay has a surface area of approximately 124 km^2, an average depth of 15 m and an entrance 3.75 km wide and 40 m deep connecting to the open shelf (Figure 1). The bay is thermally stratified for much of the year and tends to remain slightly cooler (1°C) than the shelf waters. Currents in the bay are weak at both tidal and sub-inertial periods with typical flows of 0.05 ms^{-1}. In contrast, the shelf currents are energetic and influenced by both northward propagating shelf waves with periods of around 8 days (Church *et al.*, 1986) and warm core eddies associated with the poleward flow of the East Australia Current (Nilsson and Cresswell, 1981).

The plan of this paper is to briefly discuss current observations from the bay entrance measured over a 12 month period; summarize from an earlier paper several possible mechanisms capable of forcing flow through the bay entrance; and to define the volume exchange, or flushing, rates through the entrance and discuss the processes by which the exchange occurs.

Observations

Four current meters were moored in the bay entrance and maintained, with some data gaps, for a year from April 1989 to March 1990. Two current meters were at 12 and 30 m depths in 35 m water depth approximately 0.7 km off Bowen Island, on the southern side of the entrance, and the other two were at 12 and 34 m depths in 38 m water depth, 0.7 km off Point Perpendicular on the northern side of the entrance. In addition, there was a string of three current meters on the shelf in 100 m water depth between April and November 1989. Locations of the moorings and a meteorological station are shown in Figure 1.

Time series of low-pass filtered (half amplitude response at 10 days) vector current-sticks from the four entrance current meters are plotted in Figure 2 with the shelf

currents plotted in Figure 3. The filtered currents through the bay entrance are generally weak with maxima of 0.15 ms^{-1} and typical values of 0.05 ms^{-1}. On the other hand, the shelf currents are strong, up to 1.0 ms^{-1} with typical values of 0.4 ms^{-1}. The shelf currents are predominantly poleward, particularly at 30 m depth, although they show oscillations with periods of around 10 days producing equatorward flows. The current sticks from the bay entrance plotted in Figure 2 are orientated to show inflow (outflow) by sticks pointing up (down) the page. It can be clearly seen that at periods longer than 10 days there is a near continual outflow of water at 34 m depth on the northern side of the entrance (Point Perpendicular) and a near continual inflow of water at 12 m depth on the southern side of the entrance (off Bowen Island). The other two current meters, 12 m depth off Point Perpendicular and 30 m depth off Bowen Island, show weaker and more variable flows.

Holloway *et al.* (1992) have calculated coherences between the various combinations of current pairs from the bay entrance. Considering the inflow/outflow component of the currents (with inflow defined as currents 60° west of north), strong coherence was found between the deep currents off Point Perpendicular and surface currents off Bowen Island over the period range 7 to 16 days with a 180° phase difference.

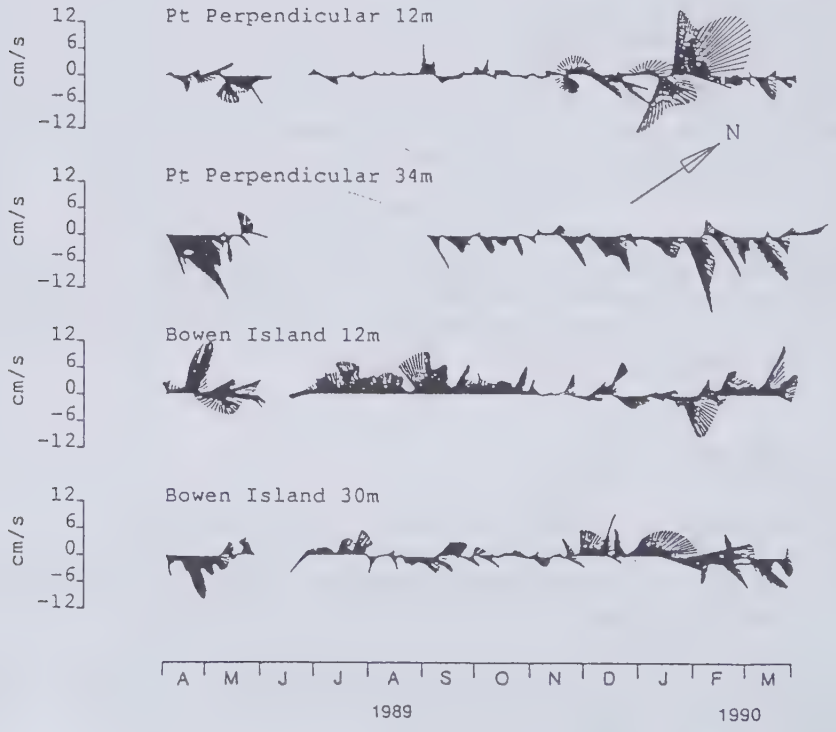

Figure 2. Vector sticks of low-pass filtered (half amplitude response at 10 days) currents through the bay entrance. Orientation is such that sticks pointing upwards show flow into the bay.

The other pairs of currents showed no significant coherence at low frequencies except for the 12 and 34 m deep currents off Point Perpendicular that are coherent between 16 and 26 days with little phase lag.

A mean flow pattern through the bay entrance is defined by computing the mean value, over the 12 month period April 1989 to March 1990, of the inflow/outflow current component for each current meter. Note that there is a larger gap in the 34 m Point Perpendicular current measurements than at the other locations, and this could produce a small bias in the averages. The averages from the four locations are linearly interpolated and extrapolated across the bay entrance to produce the contoured distribution of currents shown in Figure 4. This shows maximum inflow at the surface off Bowen Island of 0.04 ms^{-1}, the zero velocity isotach running diagonally from near the surface at Point Perpendicular to the sea bed off Bowen Island, and maximum outflow near the seabed off Point Perpendicular at 0.04 ms^{-1}. There is a close balance between the inflow and outflow volume fluxes, as expected for the low evaporation and river input.

The picture of circulation in the bay that emerges is one of a near continual clockwise circulation within the bay with water entering at the surface near Bowen Island and exiting at greater depth off Point Perpendicular. In addition, this near continual circulation pattern is modulated by flows with periods of between 7 and 16 days, corresponding to coastally trapped wave periods.

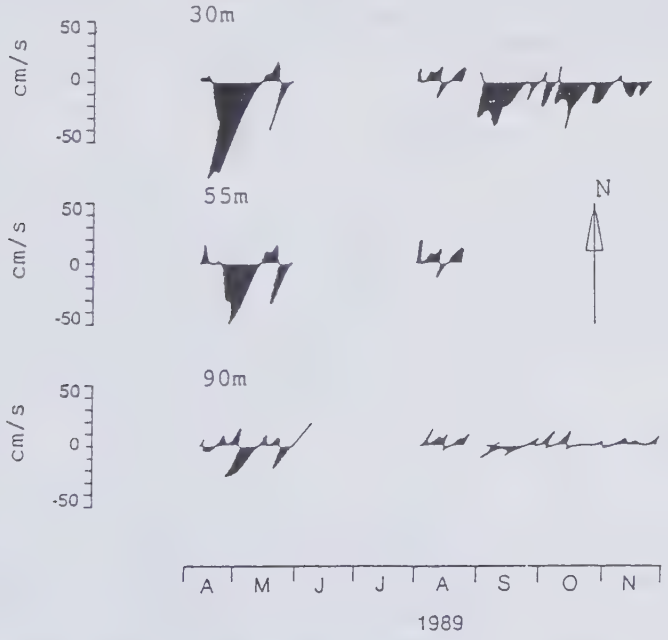

Figure 3. Vector sticks of low-pass filtered (half amplitude response at 10 days) currents on the shelf adjacent to the entrance of Jervis Bay in 100 m water depth. Sticks pointing up the page show northward flow.

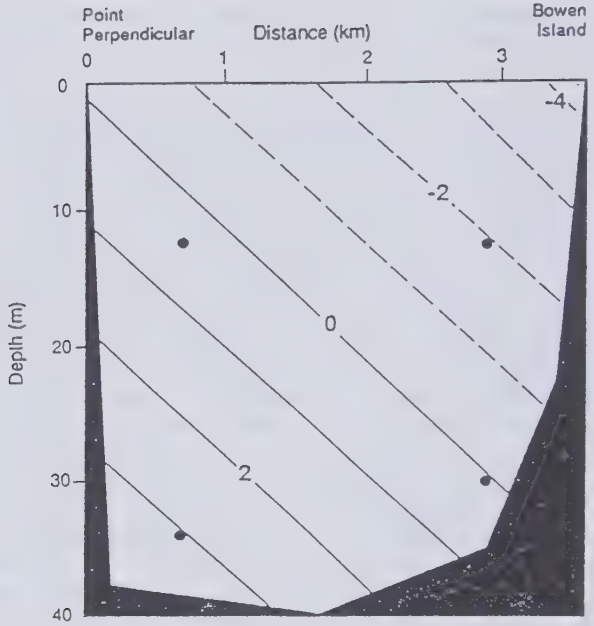

Figure 4. Contoured distribution of average of currents through the bay entrance, based on time series from the four observation points as marked by dots over the period April 1989 to March 1990. Negative values show inflow, positive values show outflow.

Forcing of the Observed Flows

Holloway *et al.*, (1992) discuss a number of forcing mechanisms that could be responsible for driving the observed flows through the entrance of Jervis Bay, although, there is still considerable uncertainty involved in fully understanding the relevant mechanisms. In this section, a brief summary of their discussions is presented. The effectiveness of wind in forcing currents through the bay entrance was assessed by computing the coherences between the wind and current components in the inflow/outflow direction from the bay entrance moorings. Results from the analysis of a 5 month data segment from September 1989 to January 1990 showed that the 12 m deep currents off Bowen Island and the 34 m deep currents off Point Perpendicular were both significantly coherent with the wind over a narrow period range of 7 to 10 days. The surface inflow off Bowen Island lagged the wind by 45° and the deep inflow off Point Perpendicular lead the wind by 138° i.e. there was a 180° phase difference between the two locations. Currents from the other locations in the bay entrance showed no significant coherence with the wind. The analysis did not support wind as a driving mechanism for flows at longer periods.

Craig and Holloway (1991) used a simple quasi-geostrophic numerical model representing Jervis Bay to investigate the influence of coastally trapped waves on

driving a circulation in the bay. A first baroclinic mode of a coastally trapped wave propagating along the shelf could cause vertical oscillations of the temperature or density field on the shelf. Such waves have been well documented for the East coast of Australia (Church *et al.*, 1986). The model imposes a temperature oscillation at the southern side of the bay entrance with the bay represented as a rectangular bay of constant depth and buoyancy frequency. An oscillation of 8 day period generates a clockwise propagating internal Kelvin wave with a width of 1 - 2 km and currents of a few cms^{-1}. Evidence for currents driven through the bay entrance by this mechanism was sought from the observations by Holloway *et al.* (1992) by computing the coherence between the water temperatures on the shelf (at 30 m depth) and the inflow/outflow currents through the bay entrance. Results from an analysis over a 7 week period from April to May 1989 showed strong coherence between the shelf temperatures and the Bowen Island inflow/outflow currents, at both 12 and 30 m, at periods of 6 to 8 days. Weaker but significant coherence (at 95% confidence level) was also found with the 34 m deep Point Perpendicular currents at the same periods. There was a 180° phase difference between the two levels off Bowen Island and also between the upper Bowen Island and deep Point Perpendicular values. These coherences are consistent with the idea of shelf wave forcing of flow through the bay entrance and with a baroclinic Kelvin wave structure.

The persistent or mean flow through the entrance, shown by the current time series in Figure 2 and annual averages in Figure 4, requires an equally persistent forcing mechanism. For much of the year a horizontal density gradient persists between the shelf and bay waters with the shelf slightly warmer (1°C) and less dense than the bay. It is suggested that the temperature contrast is maintained by the advection of warm water on the shelf from the north by the East Australia Current. Holloway *et al.* (1992) suggested that the resulting pressure gradient could be of sufficient magnitude to drive the observed persistent currents of a few cm s^{-1}. The hypothesis was a flow with the horizontal pressure gradient (from the bay-shelf temperature contrast) balanced by vertical and bottom friction, as is often found in horizontally stratified estuaries. Numerical modelling work by Craig and Andrewartha (1992) also supports this idea of flow forced by density contrasts between the bay and shelf. Their model results produce a clockwise (anti-clockwise) circulation through the bay entrance and throughout the bay for density contrasts between the bay and shelf with the bay waters denser (less dense) than the shelf waters.

Flushing of the Embayment

In this section an attempt is made at describing the volume exchange between the bay and shelf and the flushing rate of the bay. With the weak tidal flow in the bay, tidal flushing is expected to be slow. Holloway *et al.* (1991) present tidal current constituents from the entrance current meters, showing the largest constituent to be M_2 with semi-major axes between 0.066 and 0.034 ms^{-1}, aligned in/out of the bay. Within the bay tidal currents are much weaker, only 0.02 ms^{-1} for M_2 near the centre of the bay (Holloway *et al.*, 1989). The tidal excursion, defined as u_oT/π where u_o is

the tidal current amplitude and T the period, is then only a few hundred meters and with an M_2 tidal amplitude of 0.5 m (Holloway *et al.*, 1991) the intertidal volume of water moved into and out of the bay is only small. Tidal prism calculations (e.g. Officer, 1976) then predict a flushing time of over 12 months, indicating the weak effects of tidal flushing. Alternatively, flushing from advection by the lower (than tidal) frequency flows discussed in section 2 is considered. Any exchange by turbulent mixing processes is neglected.

The inflow/outflow current velocities are low-pass filtered to remove tidal and higher frequency currents using a filter with a half amplitude response at 32 h. These currents are then linearly interpolated across the cross-section at the entrance of the bay in order to compute time series of the sub-tidal frequency inflow and outflow volume fluxes. At these frequencies, the fluxes must be approximately equal as the bay is a closed system with sufficiently small river input and evaporative losses to cause negligible currents through the entrance. A time series of exchange flux is then defined as the average of the absolute values of the inflow and outflow volume fluxes and this represents the rate at which water is being exchanged between the bay and shelf through the bay entrance. A net flux (inflow plus outflow volumes) is also calculated to give a measure of how accurately the zero volume flux condition is met. The calculations were repeated for a number of definitions of the direction taken as defining inflow/outflow and a value of inflow as 57° west of north minimized the net flow summed over the measurement duration (12 months). However, the values of exchange flux were only weakly dependent on this orientation for variations of ± 20°. The resulting time series of volume exchange flux is plotted in Figure 5 where it should be noted that the interpolation of currents across the entrance involved only three current meters during July and August.

The spectrum of the exchange flux time series, over the period June 1989 to March 1990, is plotted in Figure 6. The spectrum has a distinct peak at around 6 days with increasing energy at lower frequencies. The root-mean-squared value of the exchange flux (E_{rms}) is computed from the spectral value (S), at a period of 6 days,

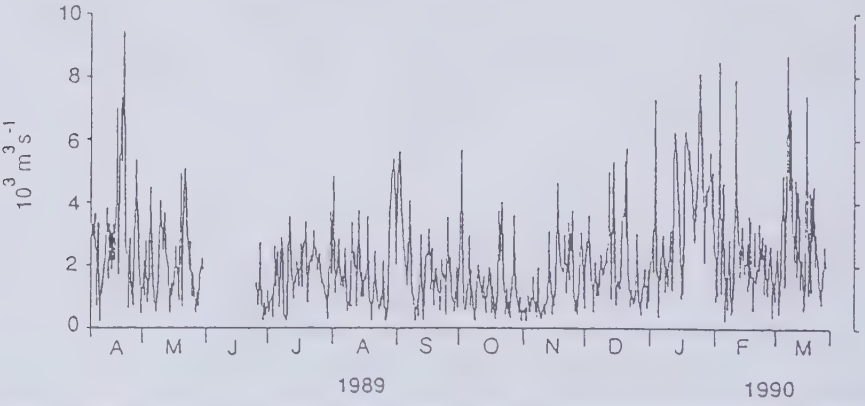

Figure 5. Time series of exchange flux through the bay entrance computed from low-pass filtered currents where the filter has a half amplitude response at 32 h.

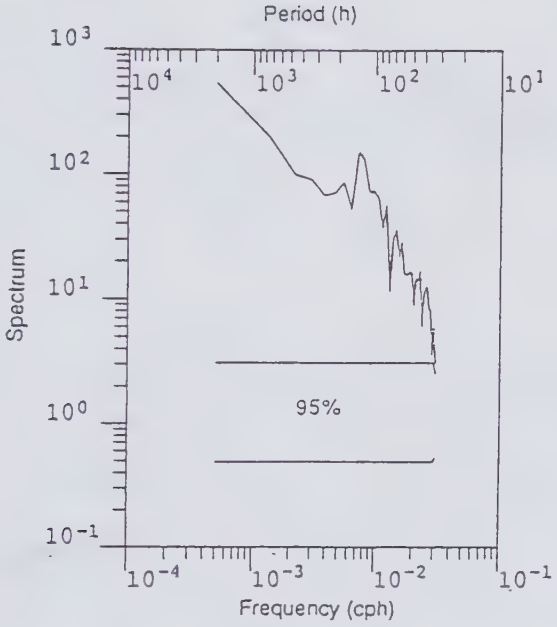

Figure 6. Spectrum of the exchange flux through the bay entrance (computed from currents low-pass filtered with filter half amplitude response at 32 h) over the period July 1989 to March 1990.

as $E_{rms} = [\Delta\omega S(\omega)]^{1/2}$ where $\Delta\omega$ is the frequency band width of the spectrum at frequency ω. Further, for sinusoidal motion, the average value of the exchange flux is given by $\sqrt{2}\, E_{rms}$. This gives the average exchange flux between June 1989 and March 1990 as 510 m^3s^{-1} at a period of 6 days. If the flushing time of the bay is defined as the bay volume ($1.89 \times 10^9\ m^3$) divided by the exchange flux, then the average flushing time by oscillating motion at 6 day period is 43 days.

The spectral peak in exchange flux at 6 days is consistent with the periods of coastally trapped waves discussed earlier. It was suggested by Craig and Holloway (1992) that such motion propagated clockwise around Jervis Bay as an internal Kelvin wave. Here, the effectiveness of such a Kelvin wave in flushing the bay is considered.

Consider an interval Kelvin wave with alongshore velocity amplitude v_o at the coast propagating along a straight coastline in an ocean of constant depth (h). The alongshore-velocity structure is given as,

$$v(x,y,z,t) = v_o\, \phi(z) \sin(ly - \omega t)\, e^{-x/R} \qquad (1)$$

where $\phi(z)$ is the vertical modal function, x is the distance offshore, zero at the coast, l is the alongshore (y-direction) wavenumber, ω the wave frequency, t is time and R is the internal Rossby Radius of deformation defined as,

$$R = \frac{c}{|f|} \tag{2}$$

where f is the Coriolis parameter (-8.38 x 10^{-5} s^{-1} for Jervis Bay) and c is the phase speed for long internal gravity waves (LeBlond and Mysak, 1978). For an ocean of constant buoyancy frequency (N_o) and for first mode waves,

$$\phi(z) = \cos\left(\frac{\pi z}{h}\right) \tag{3}$$

and

$$c = \frac{N_o h}{\pi} \quad . \tag{4}$$

At any particular cross-section through the Kelvin wave (1) represents a volume flux in one direction in the upper part of the water body and an equal flux in the opposing direction in the lower half of the water body. The magnitude of this flux, in say the upper half of the water body, can be found from (1) and (3) as,

$$V(y,t) = \int_0^{h/2} \int_0^{\infty} v_o \cos\left(\frac{\pi z}{h}\right) \sin(ly - \omega t)\, e^{-x/R}\, dx\, dz \quad ,$$

which gives,

$$V = \frac{v_o R h}{\pi} \sin(ly - \omega t) \quad . \tag{5}$$

The volume of water transported past a particular point (say, y = 0) is then the volume flux, given by (5), integrated over half a wave period. Over the other half period, there is an equal transport in the same direction in the other half of the water body. Therefore, the total volume flux in one direction, where T is the wave period, is, from (2), (4) and (5),

$$\bar{V} = \frac{2}{T} \int_0^{T/2} \frac{v_o R h}{\pi} \sin(ly - \omega t)\, dt \quad ,$$

which gives,

$$\bar{V} = \frac{2 v_o N_o h^2}{\pi^3 |f|} \quad . \tag{6}$$

This shows that the volume exchange that could be induced by a Kelvin wave propagating through the entrance of a bay, providing the entrance is wide compared to the Rossby radius, is linearly dependent on both the wave amplitude and the buoyancy frequency.

A time series of buoyancy frequency is calculated from the temperature difference between 12 and 30 m depths recorded by current meters off Bowen Island. The low-pass filtered time series (half amplitude response of the filter is at 10 days) is plotted

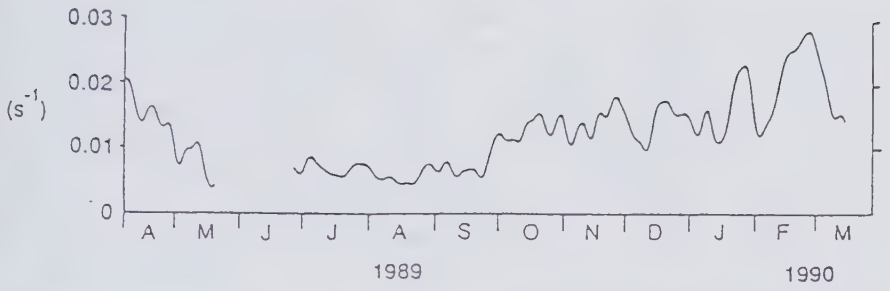

Figure 7. Time series of low-pass filtered buoyancy frequency (filter with half amplitude response at 10 days) computed from the temperature difference between the 12 m and 30 m depth Bowen Island current meters.

in Figure 7 and shows maximum values in summer of 0.03 s^{-1} and winter minima of approximately 0.005 s^{-1}. Using (2) and (4) with h = 15 m, the Rossby radii varies from 0.3 to 1.7 km from winter to summer for Jervis Bay. These narrow radii mean that the Kelvin wave will propagate (clockwise) around the bay edge (where the radius of curvature of the bay is about 5 km at the northern end) and the assumption of a wave propagating along a straight coastline, used in deriving (6), is a reasonable approximation.

The variations in stratification as shown in Figure 7 mainly from winter to summer, imply a corresponding variation in the volume flux as given by (6). This is supported from a comparison of spectra of the exchange flux from winter (July to September) and summer (December to February) as plotted in Figure 8. The summer spectral peak at a period of 6 days gives an exchange flux of approximately 960 $m^3\ s^{-1}$ whereas in winter the spectral peak is shifted to a period of 4.5 days and is significantly smaller in magnitude.

Ideally, an estimate of v_o, the coastal amplitude of the Kelvin wave, from the current meters moored in the bay entrance is required. These moorings are 0.7 km from the coast, which in winter, is over 2 Rossby Radii from the coast, making an estimate highly unreliable. In summer the moorings are approximately half a Rossby Radius from the coast and, combined with the vertical modal function as given by (3), from (1) the currents meters at 12 m depth would be measuring approximately 25% of the amplitude of v_o and the deeper current meters approximately 50% of v_o during summer. Spectra of the inflow/outflow currents in the bay entrance over the summer period December to February give amplitudes of currents at a 6 day period of between 0.020 and 0.036 ms^{-1} from the different moorings. With the above estimate of the change in velocity with depth and distance from the coast, the spectral values lead to estimates in v_o, during summer, of approximately 0.1 ms^{-1}. However, there is a good deal of uncertainty in these estimates.

Application of (6) to estimate the volume flux induced by a Kelvin wave for Jervis Bay in summer, with h = 15 m, N_o = 0.03 s^{-1} and v_o = 0.1 ms^{-1}, gives V = 520 $m^3\ s^{-1}$.

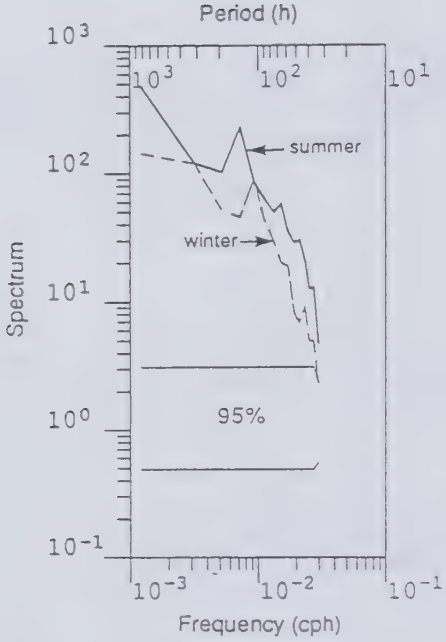

Figure 8. Spectrum of exchange flux through the bay entrance (computed from low-pass filtered currents with filter half amplitude response at 32 h) over winter (July to September) and summer (December to February) periods.

Figure 9. Time series of exchange flux through the bay entrance computed from low-pass filtered currents where the filter has a half amplitude response at 10 days.

This compares favourably, considering the uncertainties involved, to the spectral values of exchange flux at a 6 day period obtained from the observations (960 m^3 s^{-1}), supporting internal Kelvin waves as a possible mechanism of flushing Jervis Bay. The corresponding residence or flushing time for the bay, from the summer spectral value of volume exchange, is 23 days.

Next, the exchange between the bay and shelf by the very low frequency (periods longer than 10 days) or mean flows is considered. The exchange flux is recomputed using the method described earlier, but using current velocities low-pass filtered with a filter having a half amplitude response of 10 days. It should be noted that this is not the same as filtering the exchange fluxes previously calculated and plotted in Figure 5. The new time series of exchange flux is plotted in Figure 9. The average value is 1530 m^3s^{-1}, about three times larger than that due to 6 day period motion, and gives an annual average flushing time of 14 days. The standard deviation in this exchange flux time series is 900 m^3s^{-1}, and $\pm$ 1 standard deviation about the mean value gives flushing times ranging from 9 to 35 days. There are also a number of peaks in the time series of exchange flux with values of around 4000 m^3s^{-1} and with a maximum of 4500 m^3s^{-1} giving a flushing time of only 5 days.

Discussion

In this paper a discussion has been presented of the observed flow structure through the entrance of a small coastal embayment. The observations have been used to estimate the flushing time of the bay, defined as the time required for one bay volume to be advected through the bay entrance by low-frequency (sub-tidal) currents.

The mechanism of tidal flushing, where water is oscillated back and forth through the entrance with near uniform flow across the entrance, is found to be weak due to the low tidal regime and relatively deep bay. Effective tidal exchange relies on the mixing of the inter-tidal volume, or tidal prism, with the bay waters so that a significant volume of the original bay water is removed on each tidal cycle. It has been shown in this paper that a more effective exchange for Jervis Bay is brought about by advection of water through the bay entrance by low-frequency currents, with typical periods of 6 days, and also by persistent or mean flows. These flows are found to have a structure through the entrance with inflow strongest near the surface on the southern side of the bay entrance, compensated by outflow on the northern side of the bay entrance with a maximum near the sea bed. This is found in both the mean and oscillating currents and is consistent with a clockwise circulation around the bay. The advective exchange then results from simultaneous inflow and outflow by currents that are either of long enough period and/or sufficient strength to significantly penetrate into the bay.

Spectra of the calculated exchange flux showed a significant peak at a period of around 6 days, thought to be a result of forcing by coastally trapped waves that propagate northward along the shelf. The exchange is interpreted as resulting from an internal Kelvin wave propagating clockwise around the bay and is shown to depend on the wave amplitude and the buoyancy frequency. This rather narrow (small internal Rossby radius) wave produces a maximum exchange in summer, when stratification is strongest, leading to a summer average flushing time of 23

days. However, it is expected that shorter term variability would produce periods of more rapid exchange. It is further shown that the background or mean flows result in very effective advective flushing of the bay, with an annual average of 14 days and maximum rates of around 5 days.

In conclusion, it is seen that in this coastal embayment, the lowest frequency flows are the most effective in exchanging water between the bay and shelf, even though currents are only a few cms^{-1}. Tidal currents, although of similar magnitude to the low frequency flows, are less effective in flushing the bay due to the small inter-tidal volume that is exchanged. Effective exchange is induced by coastally trapped wave motion, and this exchange is enhanced with increasing stratification which causes an increase in the internal Rossby radius of Kelvin waves that can propagate around the embayment.

References

Bowden, K.F. Horizontal mixing in a sea due to a shearing current. *J. Fluid Mech.* 21, 83-95, 1965 .

Church, J.A., H.J. Freeland and R.L. Smith, Coastal-trapped waves on the East Australian Coast, Part 1: Propagation of modes. *J. Phys. Oceanogr.* 16, 1929-1943, 1986.

Craig, P.D. and J. Andrewartha, Modelling the water circulation in Jervis Bay. CSIRO Division of Oceanography Report OMR 52/8. Prepared for Department of Defence Jervis Bay Baseline Study, 50 pp, 1992.

Craig, P.D. and P.E. Holloway, The influence of coastally trapped waves on the circulation in Jervis Bay, New South Wales, pp 9-33. In *Dynamics and Exchanges in Estuaries and the Coastal Zone*. ed. D. Prandle, Springer Verlag 747 pp, 1991.

Hansen, D.V. and M. Rattray, New dimensions in estuary classification. *Limnology and oceanography* 11, 319-326, 1966.

Holloway, P.E. Longitudinal mixing in the upper reaches of the Bay of Fundy. *Estuar., Coastal and Shelf Sci.,* 13, 495-515, 1981.

Holloway, P.E., G. Symonds, R. Nunes Vaz, M. Jeffrey, and J. Mathias, Oceanographic measurements in Jervis Bay, December 1988 to January 1989. Working Paper 1989/2, Dept. of Geography and Oceanography, University College, Australian Defence Force Academy, Canberra, 44 pp, 1989.

Holloway, P.E., G. Symonds, R. Nunes Vaz and M. Jeffrey, Oceanographic measurements in Jervis Bay, April 1989 to April 1990. *Working Paper 1991/1* Dept. of Geography and Oceanography, University College, Aust. Defence Force Academy, Canberra, 48 pp, 1991.

Holloway, P.E., G. Symonds, R. Nunes Vaz, Observations of Circulation and exchange processes in Jervis Bay, New South Wales. *Aust. J. Mar. Freshwater Res.* 43, 1487-1515, 1992.

LeBlond, P.H. and L.A. Mysak Waves in the Ocean, Elsevier, New York, 602 pp, 1978.

Linden, P.F. and J.E. Simpson Gravity driven flows in a turbulent fluid. *J. Fluid Mech.,* 172, 481-497, 1986.

Nilsson, C.S., and G.R. Cresswell. The formation and evolution of East Australian Current warm-core eddies. Prog. Oceanogr. 9, 131-183.

Nunes, R.A. and G.W. Lennon Episodic stratification and gravity currents in a marine environment of modulated turbulence. *J. Geophys. Res.,* 92, C5, 5465-5480, 1987.

Officer, C.B. Physical Oceanography of Estuaries and Associated Coastal Waters. John Wiley, New York, 465 pp, 1976.

10

A Note on the Influence of a Deep Ship Channel on Estuarine-Shelf Exchange in a Broad, Shallow Estuary

W. W. Schroeder, J. R. Pennock and W. J. Wiseman Jr.

Abstract

Satellite imagery indicates the occasional presence of warm, clear surface waters directly over the main ship channel of Mobile Bay, Alabama, while the adjacent lateral shoal regions generally remain cold and turbid. This feature is observed only under conditions of strong wind stress from the north and low-to-moderate river discharge. Hydrographic data suggests that upwelling occurs at the landward end of the main ship channel under such conditions. These observations are discussed in terms of simple wind-driven estuarine exchange processes.

Introduction

Broad, shallow estuaries have long been thought to be relatively uninteresting systems driven in a simple manner by the winds and the tides. Recent work by Zimmerman (1980), Ridderinkhof (1988) and their colleagues has demonstrated the fallacy of this notion in strongly tidally-driven regions where non-linearities in the equations of motion become important. Even in much simpler systems, the presence of bathymetric changes and a variable wind field account for a spectrum of transport patterns. Of particular interest are the effects of multiple inlets and dredged ship channels. The interaction of these features with the pressure gradients generated by the wind, within the frictionally-dominated estuary and over the rotationally-

Mixing in Estuaries and Coastal Seas
Coastal and Estuarine Studies Volume 50, Pages 159-170
Copyright 1996 by the American Geophysical Union

dominated shelf, result in important and non-trivial temporal and spatial transport variability. When present, stratification in the deeper portions of these estuaries, as well as in the deep ship channels, will modify the typical wind-driven system.

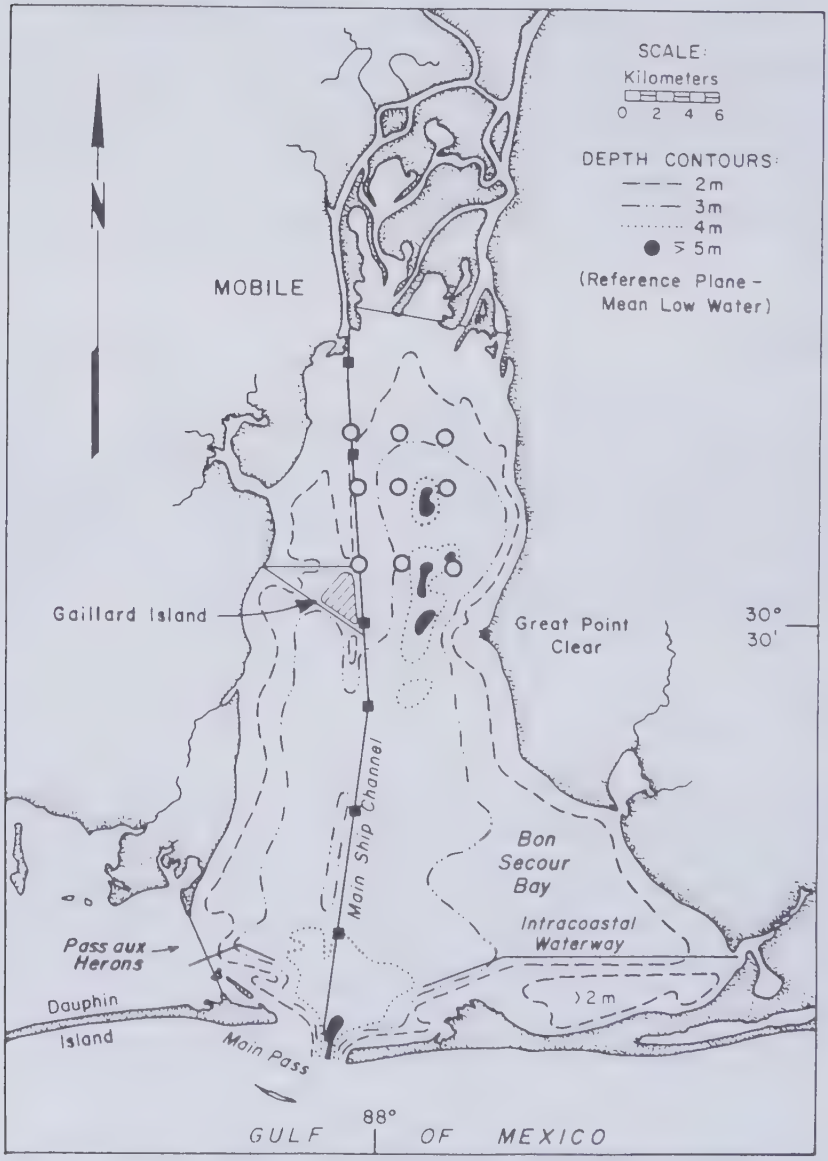

Figure 1. Bathymetric chart of Mobile Bay, Alabama, indicating the position of the main ship channel. Field survey station locations along the main ship channel and lateral transects of upper Mobile Bay are represented by boxes and circles, respectively.

Twenty-three field surveys and over two-hundred cloud-free Landsat images have been examined and used to document the role the main ship channel of the Mobile Bay, Alabama (USA) estuary plays in the development of various hydrographic regimes observed in that system. Mobile Bay is a broad, shallow estuary on the Alabama coast of the northern Gulf of Mexico (Figure 1). It has a maximum width of 38 km and extends 50 km in the north-south direction. The estuary connects to the Gulf of Mexico through Main Pass which, on average, carries approximately 85% of the mass flux. The remaining flux occurs to the east, to Mississippi Sound through Pass aux Herons. A narrow (215-230 m) ship channel extends from Main Pass to the Port of Mobile at the northern end of the bay. This channel is 13-15 m deep while the remainder of the bay averages 3 m deep at mean high water. The bay is the estuary of the Mobile River system which annually discharges approximately 1850 m^3s^{-1} of fresh water. The rivers flood in spring and low flow conditions dominate throughout the fall and early winter. Winds are predominantly gentle breezes from the south (mean speeds range from 2 to 3.5 ms^{-1}) during the summer with a significant diurnal sea-breeze component. Wintertime is characterized by strong winds from the north (mean speeds range from 4.5 to 6 ms^{-1}) associated with cold-air outbreaks (CAO). Astronomical tides in this region of the Gulf of Mexico are principally diurnal and small in amplitude with a mean range of 0.4 m. Meteorological tides can generate water level changes as much as twice this value. Thus, they are extremely important in affecting estuarine-shelf exchanges.

Strong stratification is nearly always present in the ship channel (e.g. Austin, 1954; McPhearson, 1970). The shoaler regions of the bay, which can also be strongly stratified (Schroeder, 1978; Schroeder *et al.*, 1990b), are often well-mixed, particularly during the windy winter months (Schroeder *et al.*, 1990b). The strength of the stratification is modulated by river runoff and the redistribution of this fresh water by wind-driven currents and mixing (Schroeder *et al.*, 1990a).

While the seasonal cycles of stratification are reasonably clear and well-documented, these are intimately linked to and punctuated by short-lived predominantly wind-driven events. Herein, we will demonstrate that the ship channel functions as a conduit for warm, saline Gulf of Mexico water to be transported into the upper reaches of the bay during periods of strong, down-estuary winds associated with winter cold air outbreaks or other storms. These bottom waters are aperiodically transported to adjacent bay bottom areas by a variety of processes.

Results

Remote Sensing

Over two-hundred cloud-free Landsat Multispectral Scanner visible band 5 (0.5-0.6 μm) scenes of the Mobile Bay region have been examined. In at least 13 cases, the main ship channel leading from the Port of Mobile to the Gulf of Mexico has been

Figure 2. Landsat MSS band 5 image from 20 November 1981. Note the dark outline of the main ship channel from Main Pass to Mobile. (See Figure 1 for location map.)

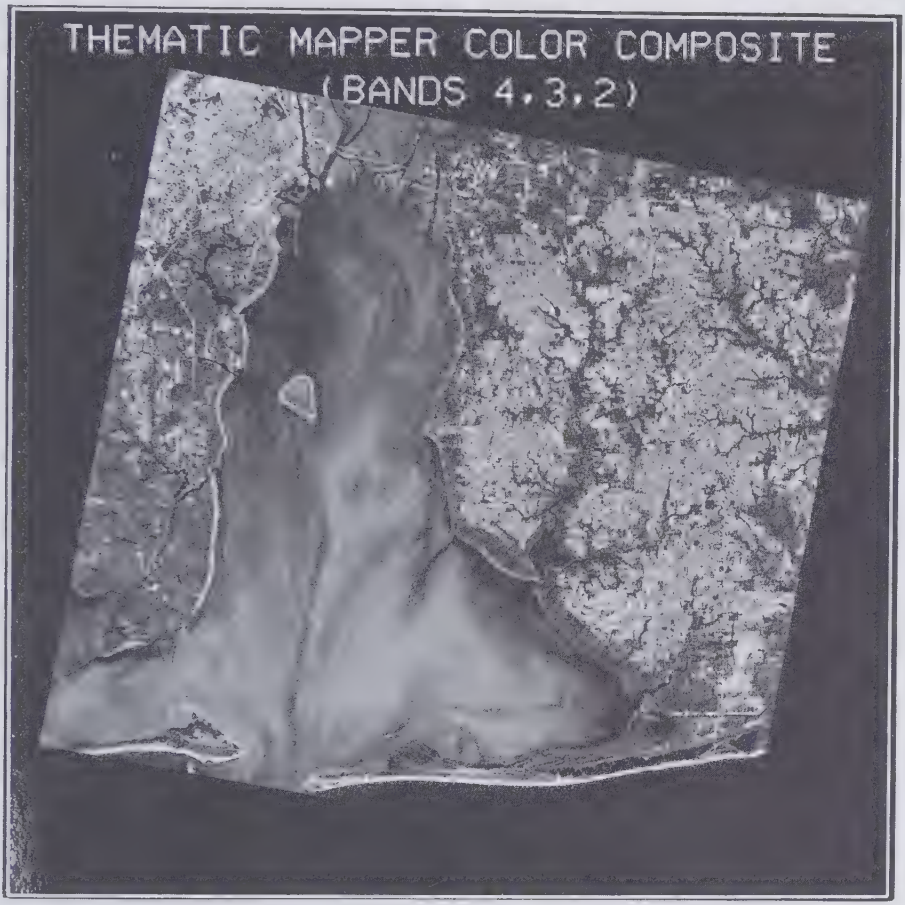

Figure 3. Composite of visible bands (2, 3 and 4) from Landsat Thematic Mapper scene, 10 February 1989. Note the dark outline of the main ship channel from Main Pass to Mobile. (See Figure 1 for location map.)

distinctly outlined by clear water (e.g. Figure 2). A single occurrence has been observed in both the visible bands [2(0.52-0.6 μm), 3(0.63-0.69 μm), and 4(0.76-0.90 μm)] and thermal IR band [6(10.4-11.7 μm)] from a Thematic Mapper (TM) scene. Surface water temperature mapping utilizing TM band 6 followed the methodology set forth by Lathrop and Lillesand (1986). In this case, the channel is delineated by warm, clear water (Figures 3 and 4). Principal component analyses (Kendall and Stuart, 1966) were performed on the pixel values of all seven bands of Thematic Mapper data. The first two principal components distinguish between land and water within the image. The third (Figure 5) and fourth principal components of the image account for more than 10% of the variance in the image and describe an association

Figure 4. Thermal band (6) from Landsat Thematic Mapper scene, 10 February 1989. Note warmer water (8.4°C) outlining the ship channel in the lower bay and the pool of warmer water (10.6°C) centered over the ship channel in the northwestern corner of the bay. (See Figure 1 for location map).

of warm and clear water. A pool of warm, clear surface water is observed in the northwestern corner of the bay (Figures 3 and 4). This pool is centered over the ship channel and appears to have an origin from upwelled water transported to this site by the ship channel from the Gulf of Mexico.

Associated environmental data records have also been examined. The periods during which the outline of the ship channel is visible on satellite imagery all correspond to periods of low-to-moderate river flow. Five to seven day average discharges during these times ranged between 300 and 1500 m^3s^{-1} with most falling below 800 m^3s^{-1}. Furthermore, the wind-forcing over the bay was always from the north and relatively strong, greater than 5-6 ms^{-1}.

Figure 5. Third principal component from Landsat Thematic Mapper scene, 10 February 1989. Note the light outline of the main ship channel from Main Pass to Mobile. (See Figure 1 for location map).

Field Surveys

Over the past 20 years, numerous quasi-synoptic surveys of hydrographic properties within Mobile Bay have been made from small, fast boats. Vertical profiling of the water column has been undertaken utilizing either a Hydrolab Surveyor II (pre-1990) or a SeaBird Electronics SBE-25 CTD (post-1990). While these data sets tend to be fair weather biased, a few have been made immediately following strong wind

events from the north. When these latter surveys are associated with low river discharge, the isohalines and isotherms are observed to upwell in the ship channel at the northern end of the bay (Figure 6). Under higher runoff conditions, the hydrographic structure along the ship channel more often resembles a salt-wedge estuary (Figure 7).

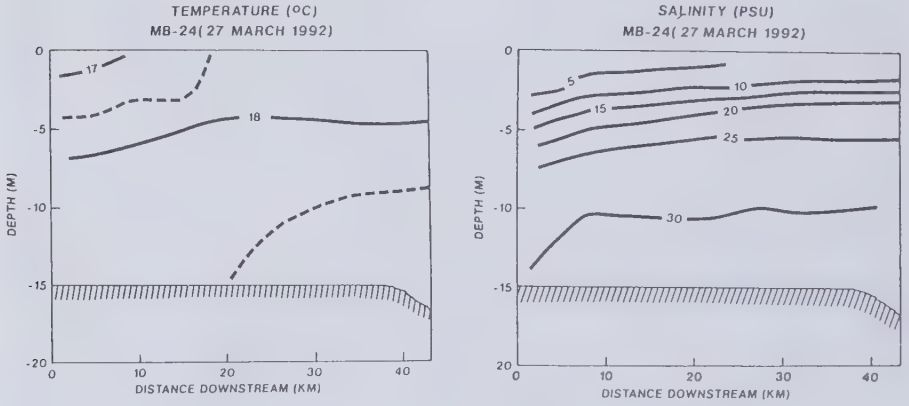

Figure 6. Longitudinal sections of temperature and salinity along the Main Ship Channel of Mobile Bay under low river flow conditions following a northerly wind stress event. (See Figure 1 for station locations.)

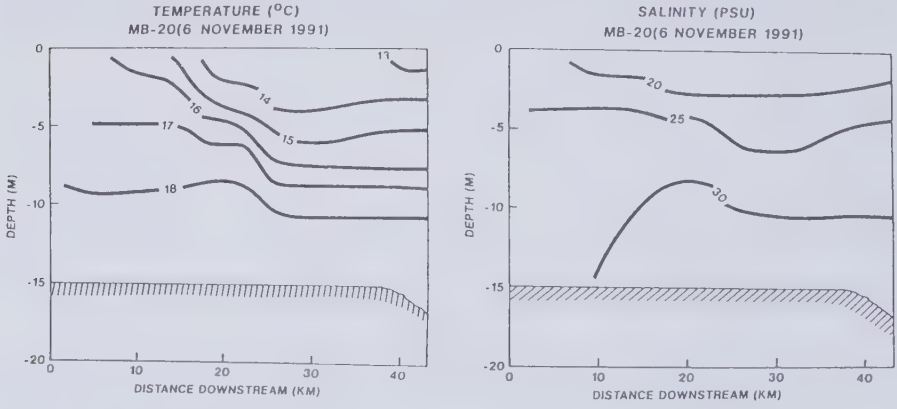

Figure 7. Longitudinal sections of temperature and salinity along the Main Ship Channel of Mobile Bay under high river flow conditions. (See Figure 1 for station locations.)

Discussion

While the necessary field data is not available for corroboration, we believe the sequence of events leading to the observed thin strip of warm, clear water directly above the ship channel to be the following. CAO along the northern Gulf of Mexico are generally preceded by a period of moderate winds from the southeast and south. Such winds will cause both an Ekman convergence at the coast and a frictionally-driven set-up of waters at the northern end of Mobile Bay. Both will, initially, cause water to flow from the ocean into the bay. After the wind stress is balanced by the barotropic pressure gradient within the bay, a two layered circulation will develop with upstream flow in the near-surface layers and downstream flow below. As the leading edge of the cold air outbreak passes over the coast, the winds shift rapidly to a strong flow from the north. The coastal waters set down under the reversed wind stress and the bay waters reverse their slope. The reversed barotropic pressure gradient within the bay now drives deep flow northward within the ship channel while the wind stress drives near surface water seaward, enhancing the compensatory upstream flow in the deeper water layers. Under low river discharge conditions, the lower salinity upper water layers will be greatly thinned. Wind-induced mixing will homogenize the shallow waters in the lateral regions of the bay, but reduce the turbidity and increase the temperature of the waters directly over the ship channel through entrainment of warm, clear coastal waters which have intruded up the ship channel. At the landward end of the ship channel, under a sufficiently strong wind event, upwelling of these warm, saline waters will occur (Figure 6).

Dense water, normally found in the deeper portions of the ship channel, is regularly found in the deeper regions of the adjacent lateral shoals of the bay. One mechanism allowing import of this water into the shoal regions and establishment of stratification is associated with the observed upwelling along the channel, particularly at the northern end. The deep waters are lifted above the level of the natural bay bottom or dredged spoil banks on the sides of the channel and spill over onto the lateral shoals where they spread as a gravity current until wind-driven mixing (Schroeder *et al.*, 1990a) breaks down the stratification. As the wind event which initiated the upwelling relaxes, the mass of upwelled water may propagate seaward along the channel as an internal gravity wave. Water will flow laterally from the crest as the wave moves southward. This process appears to have been captured in a pair of surveys taken some 14 hours apart on 2 November 1976. During the early morning (AM) survey, saline water was upwelled at the northern end of the ship channel (Figure 8) as a result of winds from the north, with a strength of 5 to 7 ms^{-1}, prevailing over the previous 24 hours. The winds decreased to less than 2.5 ms^{-1} within 3 hours following the AM survey. This would result in an unbalanced longitudinal baroclinic pressure gradient. The linear internal wave speed within the channel was estimated to be roughly 0.55 ms^{-1}. It was estimated as

$$c = \sqrt{\frac{\Delta\rho}{\rho} \cdot g \cdot \frac{hh'}{h + h'}}$$

where h and h' are the depth of the upper and lower layers, g is gravity and ρ and $\Delta\rho$ are a mean density and the density difference between the two layers, respectively. This speed is probably an overestimate as it does not account for friction. It certainly allows the wave crest to propagate well past the second cross-bay section monitored during the time between surveys as seen in the early evening (PM) survey (Figure 8). Lateral flow of dense water clearly occurred at this section and a wave crest is indicated to lie between the second and third cross-bay sections.

Schroeder and Wiseman (1986) investigated low-frequency shelf-estuarine exchange processes in Mobile Bay by examining the relationships among wind stress, river discharge, water level, and water flow through Main Pass and within Mobile Bay.

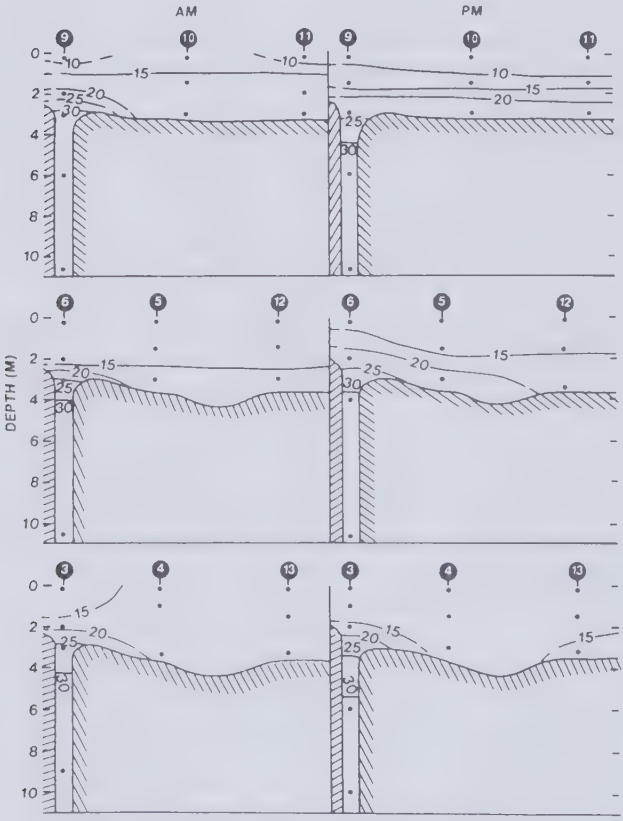

Figure 8. Lateral cross-sections of upper Mobile Bay salinity on 2 November 1976. Upper panel: Northern Transect; Middle panel: Central transect; Bottom panel: Southern transect. (See Figure 1 for station locations.) The AM survey was conducted between 0525 and 0820 CST and the PM survey between 1925 and 2235 CST.

They inferred that at least three forcing functions cause significant flow variations over three different time scales. Exchanges at periods of 2 to 4 d are driven by the cross-shelf along-estuary wind stress, while coastal Ekman convergence/divergence, driven by the alongshore wind stress, produces exchanges at periods of 3 to 20 d. At seasonal scales, river runoff was shown to contribute to both the barotropic and baroclinic exchanges. In addition, Wiseman *et al.* (1988) suggest, from the analysis of one month of current meter data from lower Mobile Bay, that the contributions of subtidal advection, mean advection, and tidal dispersion (as estimated from Austin 1954) to exchange through Main Pass are of the same order of magnitude. The processes we have described contribute to the subtidal exchange.

With the present data set we are unable to predict, with any degree of certainty, how often this phenomena may occur. However, it is possible to estimate the frequency of occurrence of times when strong wind stress from the north coincide with periods of low-to-moderate river runoff. On average, the combination of these conditions occurs during the fall and early winter months, i.e. in the last half of the dry season, when CAO first start to move across the northern Gulf of Mexico. This is supported by the fact that dates of 9 of the 14 satellite scenes with the outline of the ship channel fell into this time frame: 4 during the month of November, 3 during the month of December, 2 each for the months of October and February, and once for each of the months of January, March, and April. The average number of CAO during the period between September through December is 24 (DiMego *et al.*, 1976). The mean duration of the northerly winds following a front is of the order of a day. Thus, one might expect these patterns described above to be important between 5 to 10% of the year, but concentrated in the late fall/early winter.

Acknowledgements. This work is the result of research sponsored by the U. S. Geological Survey/Geological Survey of Alabama [14-08-0001-A0075], The University of Alabama Marine Science Program and the Marine Environmental Sciences Consortium of Alabama. Partial support was also received from U. S. Geological Survey contract 14-08-0001-23411 with Louisiana State University. Contribution No. 208 of the Aquatic Biology Program, The University of Alabama; Contribution No. 229 of the Marine Environmental Sciences Consortium, Dauphin Island, Alabama. We wish to thank Michael C. Baker for providing the Landsat Thematic Mapper data and Principal Component Analyses, Ms. Celia Harrod for preparing the figures, and Ms. Carolyn Wood for keyboarding the manuscript.

References

Austin, G. B., Jr. On the circulation and tidal flushing of Mobile Bay, Alabama, Part 1. Technical Report No. 12, Oceanographic Survey of the Gulf of Mexico, Texas A&M Research Foundation, College Station, Texas, pp. 28, 1954.

DiMego, G. J., L. F. Bosart and G. W. Endersen. An examination of the frequency and mean conditions surrounding frontal incursions into the Gulf of Mexico and Caribbean Sea. *Monthly Weather Rev.*, 104, 709-718, 1976.

Kendall, M. G. and A. Stuart. *The advanced theory of statistics*; Volume 3: Design and analysis, and time-series. Charles Griffin and Co., Ltd., London, 1966.

Lathrop, R. G., Jr. and T. M. Lillesand. The utility of Thematic Mapper data for temperature mapping in the Great Lakes. Technical Papers, 1986 ACSM-ASPRS Annual Convention, March 16-21, Washington, D.C., Volume 5 (Remote Sensing): 151-157, 1986.

McPhearson, R. M., Jr. The hydrography of Mobile Bay and Mississippi Sound, Alabama. *J. Mar. Sci. Alabama* 1, 1-83, 1970.

Ridderinkhof, H. Tidal and residual flows in the Western Dutch Wadden Sea,I: Numerical Model Results. *Neth. J. Sea Res.*, 22, 1-22, 1988.

Schroeder, W. W. Riverine influence on estuaries: A case study, in *Estuarine Interactions*, edited by M. L. Wiley, 347-364, Academic Press, Inc., New York, New York, 1978.

Schroeder, W. W. and Wm. J. Wiseman, Jr. Low-frequency shelf estuarine exchange processes in Mobile Bay and other estuarine systems on the northern Gulf of Mexico, in *Estuarine Variability*, 355-367 edited by D. A. Wolfe, Academic Press, New York, New York, 1986.

Schroeder, W. W., Wm. J. Wiseman, Jr. and S. P. Dinnel. Salinity stratification in a river-dominated estuary. *Estuaries*, 13, 145-154, 1990a.

Schroeder, W. W., Wm. J. Wiseman, Jr., A. Williams, Jr., D. C. Raney and G. C. April. Climate and Oceanography, In: Mobile Bay: Issues, Resources, Status and Management. NOAA Estuary-of-the-Month Seminar Series Number 15, U. S. Department of Commerce, Wash., D. C., 27-52, 1990b.

Wiseman, Wm. J., Jr., W. W. Schroeder and S. P. Dinnel. Shelf-estuarine water exchanges between the Gulf of Mexico and Mobile Bay, Alabama. *American Fish Society Symposium*. 3, 1-8, 1988.

Zimmerman, J. T. F. Vorticity transfer by tidal currents over an irregular topography. *J. Mar. Res.*, 38, 601-630, 1980.

11

Tidal and Low Frequency Flushing of a Coastal Lagoon Using a Flexible Grid Model

N. P. Smith

Abstract

Tidal and low frequency nontidal exchanges of water between a coastal lagoon and adjacent continental shelf are investigated within the context of flushing, using a computer model based on the continuity equation. Flushing is quantified by the 50% renewal time. The arrival of new ocean water occurs as a result of longitudinal diffusion and a degree of advective transport governed by the flexibility of segment boundaries to move with the ebb and flood of the tide. The model is applied to the Indian River lagoon system, lying along the Atlantic coast of Florida, USA. Flushing rates are quantified for three sub-basins of Indian River lagoon, and for Banana River lagoon, connected to the northern sub-basin of Indian River lagoon. The lagoons are microtidal and depend upon low frequency exchanges to maintain water quality.

One-year simulations for the Indian River lagoon system as a whole show that the 50% renewal time is approximately 140 days when transport by advection. When the renewal of lagoon water is by longitudinal diffusion alone, the 50% renewal level is not reached after 365 days. A second series of simulations compares flushing rates for the three sub-basins of Indian River lagoon and for Banana River lagoon, assuming a completely flexible grid. The southern and central sub-basins of Indian River lagoon receive a 50% renewal of new ocean water in about 5 and 12 days, respectively; the northern sub-basin of Indian River lagoon and Banana River lagoon reach approximately 30% renewal by the end of the one-year simulation.

Mixing in Estuaries and Coastal Seas
Coastal and Estuarine Studies Volume 50, Pages 171-183
Copyright 1996 by the American Geophysical Union

Introduction

Mixing processes in estuaries dictate the rates at which salt water and fresh water enter and leave, respectively, and thus are of crucial importance in determining temporal and spatial variations of salinity, and the flushing characteristics of the estuary in general. Energetic mixing within an estuary, in combination with active estuarine-shelf exchanges, reduces the residence time of fresh water, and at the same time encourages the incursion of salt water. Thus, whether flushing is quantified by the flushing time (Officer, 1976) or, for example, the 50% renewal time of new ocean water (Pritchard, 1960), mixing within an estuary determines the estuary's natural ability to maintain or reestablish water quality.

Early flushing models (Ketchum, 1951; Stommel and Arons, 1951) used time steps of one semidiurnal tidal cycle and assumed complete mixing within segments partitioned according to the local intertidal volume. While simple flushing models continue to be used (Dyer and Taylor, 1973; Robinson, 1983; Merino et al., 1990; Miller and McPherson, 1991) and serve a useful purpose as quicklook tools (Wood, 1979), three basic features compromise their ability to provide realistic results. First is the assumption of complete mixing, which was challenged at an early date (Austin, 1954), although Wood (1979) has suggested a modification to deal with this issue. Second is the need to work with a single tidal constituent, which eliminates the opportunity to investigate variations in flushing rates over a synodic month, for example. Third, although freshwater outflow can be incorporated into tidal prism models, low frequency nontidal exchanges between estuarine and continental shelf waters cannot. Nontidal exchanges often provide an important supplement to tidal flushing.

This paper constitutes one of a series of studies that has been designed to quantify flushing rates for Indian River lagoon, lying along the Atlantic coast of Florida (Figure 1). The lagoon is, 196 km long and generally 2-4 km wide. Water depths are characteristically between 1 and 3 m, though the Atlantic Intracoastal Waterway, forming the longitudinal axis of the lagoon, has a depth of 3.5 m. The lagoon is divided into three sub-basins, defined by three inlets, all of which are in the southern half of the lagoon. Banana River lagoon is connected to the northern sub-basin. The northern end of Indian River is connected to the southern end of Mosquito Lagoon by Haulover Canal (Smith, 1993a). Indian River lagoon is microtidal, with the semidiurnal M_2 tide serving as the principal constituent (Smith, 1987). M_2 amplitudes in the northern sub-basin are generally 0-5 cm. Amplitudes in the central and southern sub-basins are 5-10 cm and 10-15 cm, respectively. Banana River lagoon is virtually tideless, with amplitudes of all tidal constituents less than 0.5 cm.

The first paper in the series (Smith, 1993b) quantified the intertidal volume by using harmonic constants of the principal semidiurnal and diurnal tidal constituents recorded at 28 study sites. Amplitudes were multiplied by the surface areas they represent, and phase angles were incorporated to account for the movement of tidal waves through the lagoon. A precise measure of the intertidal volume was obtained

for spring and neap conditions, including effects of diurnal inequalities. The second paper (Smith, 1993c) applied these results to a flushing model that incorporated both advective and diffusive transport of fresh and salt water, and that compared flushing rates with and without ancillary nontidal exchanges. An important distinction between this approach and hydrodynamic models is that the rise and fall of the tide is specified within the model, using the predicted tide (Schureman, 1958), rather than simulated by adjusting friction within the model. As a result, tidal exchanges are modeled more precisely. Mixing within the lagoon must be specified, however, just as with a hydrodynamic model, and model verification will involve matching hydrographic measurements.

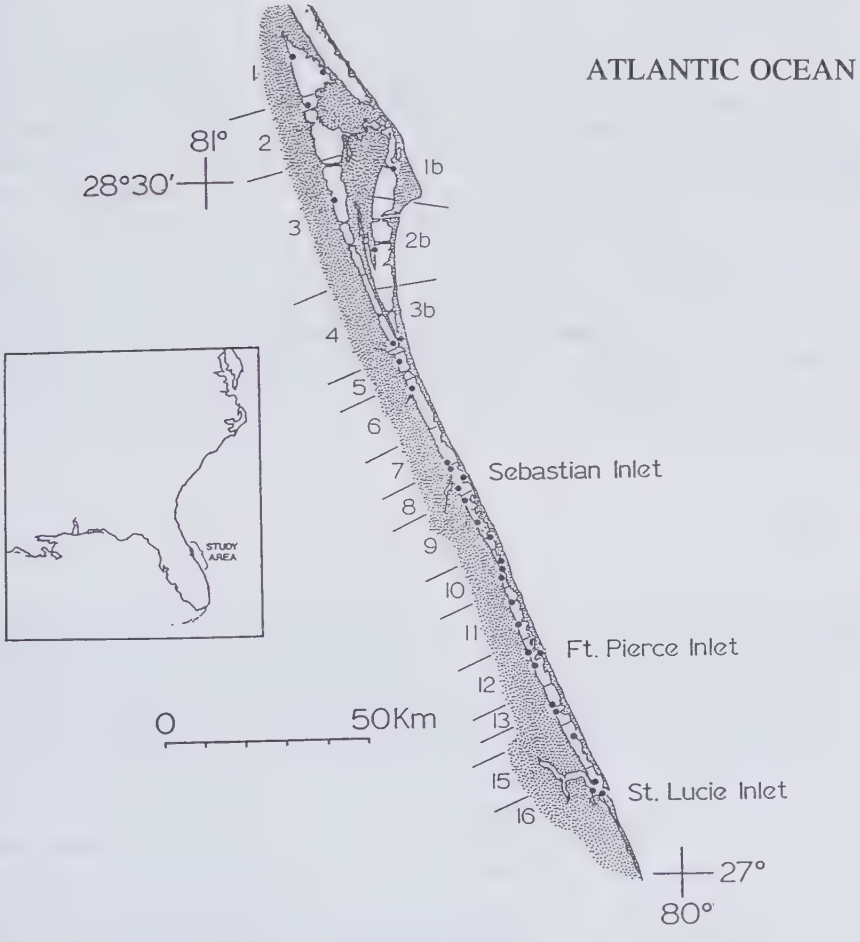

Figure 1. The Indian River lagoon system on Florida's Atlantic coast, including Indian River lagoon and Banana River lagoon. Dots show locations of water level recorders; lateral lines define segments 1-16 in Indian River lagoon and segments 1b-3b in Banana River lagoon.

Neither of the above studies incorporated Banana River due to a lack of information on tidal conditions. Also, the flushing model assumed a complete mixing of water moving from one segment to the next, as have most of the earlier tidal prism models. This third study expands the geographic scope of earlier work on Indian River lagoon by incorporating the exchange of water between the northern sub-basin and Banana River lagoon. Also, the model used here has a flexible grid that controls the extent to which segment boundaries move along the longitudinal axis of the lagoon with the ebb and flood of the tide. When the grid flexes freely with the longitudinal flow, no advective transport from one segment to the next results, and transport is by diffusion only. When the grid is fixed and inflexible, advective transport between adjacent segments is similar to that specified in the tidal prism models. In that case, diffusion is not considered.

Indian River lagoon is well understood in terms of tidal dynamics (Smith, 1987, 1990), but a dearth of hydrographic data has prevented the verification of results of flushing studies (Sheng and others, 1990, Smith, 1993c). Models can be useful in the diagnostic mode for gaining insight, however, even while the data base necessary for verification is being assembled. The model used in this study is intended to quantify flushing rates, not elucidate the dynamics of the lagoon. For that, one must turn to hydrodynamic models.

The scope of this study is intentionally restricted to flushing in response to two-way lagoon-shelf exchanges. Fresh water effects are considered in other studies (see Smith, 1993c). The specific aims of the study are to obtain flushing estimates of flushing rates for the three sub-basins of Indian River lagoon and Banana River lagoon, and to compare the assumption of complete mixing with the assumption that mixing occurs by diffusion only.

Observations

Water level records from the 31 locations shown in Figure 1 were obtained between, 1969 and 1992 using Stevens Model A and Model F analog recorders, and a Stevens Model 7031 digital recorder. Water levels were read to the nearest 0.1 cm or 0.01 foot (0.3 cm). Time series varied in length, but most were between two and three months long. All records provided information on the nontidal rise and fall in lagoon water level (Smith, 1986); longer time series, in excess of one year, were used to characterize seasonal cycles.

The surface areas of Indian River and Banana River lagoons represented by each of the 31 study sites were determined using a compensating polar planimeter and navigational charts. Study sites were not distributed uniformly, and individual water level time series represented surface areas of from 1.4 to 98.0 km^2. Some of the smaller segments were combined, especially near the inlets, where small volumes could be completely flushed within the one-hour time steps used in the simulations. In its final form, the model included three segments in Banana River lagoon and 16

segments in Indian River lagoon, as shown in Figure 1. The model does not require data from a dense network of tide gauges. The necessary number is that required to reproduce the spatial variability of amplitudes and phase angles for the principal tidal constituents.

Historical water level records were also used to quantify low frequency nontidal variations in lagoon water level. Eight years of data from a water level recorder located in segment 11 indicated that in the interior of the lagoon 95% of the high and low tide levels are within 20 cm of median values. Histograms constructed from tidal predictions (not shown) indicate that diurnal inequalities, combined with spring-neap tide conditions, explain about half of this variability. The rest can be attributed to nontidal processes. Shorter time series from throughout Indian River were used to characterize both the time scales of the low frequency rise and fall in lagoon water level and the magnitude of the local nontidal fluctuations.

Current measurements from the southern end of Banana River lagoon, made with a General Oceanics Model 2010 film recording inclinometer, were used to confirm that tidal and nontidal exchanges between Indian River segment 4 and Banana River segment 3b were being simulated properly. Figure 2 is a composite of total (top), tidal (middle) and low-pass filtered nontidal currents (bottom) based on measurements made over a 52-day period in early, 1983. Amplitudes of the principal tidal constituents were compared to the flood and ebb current speeds generated by the model in the absence of nontidal exchanges. Nontidal currents, shown at the bottom of Figure 2, are generally within ± 20 cm s^{-1}. The restricted cross-sectional area at the southern end of Banana River forced a ± 17 cm s^{-1} current speed when a ± 20 cm variation in sea level and an extinction coefficient of 0.003 h m^{-1} (see equation 3) were used in the model.

Methods

Harmonic analysis (Dennis and Long, 1971) provided the amplitudes and local phase angles needed to identify six principal tidal constituents (M_2, S_2, N_2, K_1, O_1 and P_1). These harmonic constants were used in turn to predict water levels needed to quantify the hour-by-hour tide-induced changes in volume for each segment (Schureman, 1958). When time series from individual study sites were longer than about 35 days, analyses of overlapping 29-day time periods provided a sample of amplitudes and phase angles which could be vector-averaged, as suggested by Haurwitz and Cowley (1975), to obtain a more representative measure of the constituent.

Low frequency variations in coastal sea level over time scales on the order of one week are frequent enough and of sufficient magnitude to augment tidal flushing in a meaningful way, especially in the northern sub-basin, where tidal motions are significantly damped. Low frequency water level variations penetrate further into the

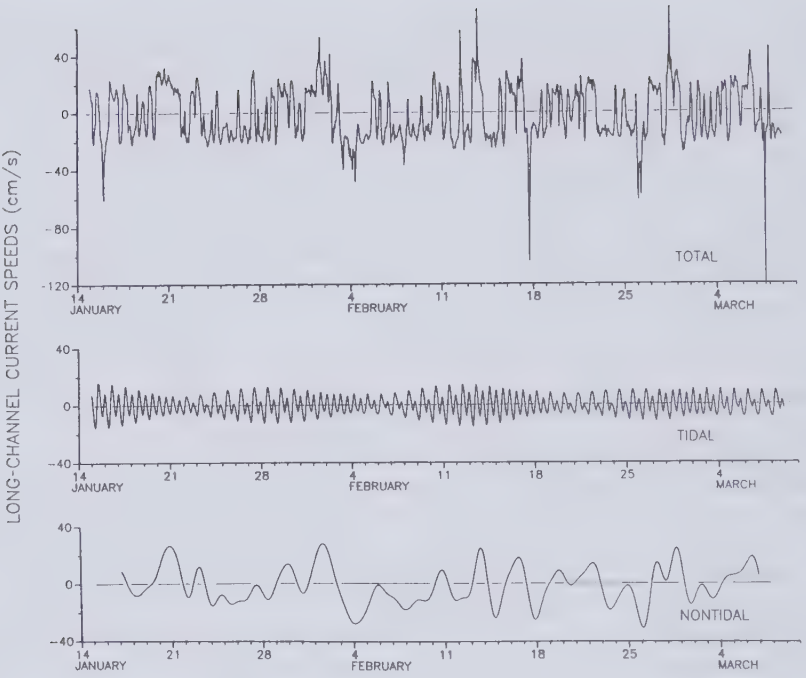

Figure 2. Composite of current meter data recorded at the southern end of segment 3b in Banana River lagoon, January 15 to March 8, 1983. Total along-channel component flow is shown at the top of the composite, the predicted tide is given by the middle plot and the low-pass filtered nontidal flow appears at the bottom. Positive along-channel speeds indicate flow into Banana River lagoon.

lagoon and thus can impact areas beyond the reach of tidal exchanges. Time scales of nontidal water level variations were specified using plots (not shown) of low-pass filtered time series of water level recorded throughout the lagoon. In some cases, low frequency variations in lagoon water level are of lower amplitude in summer months than in fall and winter months, but a distinct seasonality does not appear consistently in time series from different locations and different years. In general, the nontidal rise and fall in lagoon water level relative to the local seasonal mean is 5-10 cm, with higher values occurring close to inlets (Smith, 1986). In some cases, the range in low frequency water level in the interior of the lagoon can reach 15-20 cm, but low frequency variations greater than ±20 cm are rare.

Low frequency water level variations were modeled using

$$\eta''_m = A''_m \sin\left[\frac{2\pi(t-\tau_m)}{T''}\right] \qquad (1)$$

where A_m is the amplitude of the nontidal water level in the m^{th} segment, t is time, τ is the time lag of high water in the m^{th} segment relative to that at the nearest inlet, and T is the period of the nontidal water level variation. The double prime notation is used to denote nontidal processes. The time lag in the m^{th} segment was modeled by assuming that low frequency water level fluctuations move through the lagoon as shallow-water waves:

$$\tau_m = \sum_{j=1}^{m} \frac{X_j}{(gH_j)^{1/2}}, \qquad (2)$$

where g is gravity, H is the mean depth of the segment and x is the length of the segment along the longitudinal axis of the lagoon. An unpublished 157-day study of nontidal water level variations in the northern sub-basin of Indian River showed an average time delay of just under 5 hours for water levels recorded in segment 4 relative to segment 8. This is equivalent to a propagation speed of about 8 km h^{-1}. While this implies a mean depth of only 0.2 m, this speed is within the 5-10 km h^{-1} range of M_2 tidal wave speeds found throughout the lagoon (Smith, 1987). The spatial decrease in amplitude of low frequency water level fluctuations was modeled as an exponential extinction:

$$A''_m = A''_o \exp\left(-k \frac{\sum_{j=1}^{m} X_j}{T'} \right), \qquad (3)$$

where A_o is the amplitude of the low frequency water level variation at the inlet. A value of 0.003 h m^{-1} was used for the extinction coefficient, k. By combining the extinction coefficient with the ratio of the distance to the period of the low frequency fluctuation, the decrease in amplitude is relatively small at locations near inlets, and for sufficiently long periodicities.

The intertidal volume of the m^{th} segment, V_m, is obtained from the product of the surface area, S, and the sum of the tidal and nontidal water levels, assuming that the surface area of the segment does not vary with water level:

$$V_m = S_m\left(\eta''_m + \eta'_m\right) \qquad (4)$$

where the prime notation refers to tidal fluctuations.

To quantify the flushing of Indian River lagoon, the simulations begin with the assumption that the lagoon is filled with "lagoon water"– an undefined mixture of fresh and salt water. The time required for tidal and low frequency nontidal exchanges to replace half of the lagoon water with new ocean water is referred to as the "50% renewal time," R_{50}. This time interval can be determined for the lagoon as a whole, for specific sub-basins, or for any individual segment. With both tidal and

nontidal exchanges, the fraction of new ocean water at a given location can fluctuate significantly over time scales on the order of several hours to several days, as new ocean water slowly replaces lagoon water. Thus, R_{50} is defined to be the midpoint between the first time the new ocean water fraction reaches 50% and the last time a fraction below 50% is recorded.

The Model

The one-dimensional numerical model used to quantify flushing incorporates both advective and diffusive transport terms. In differential form, the time rate of change in an ocean water tracer, T, is given by

$$\frac{\partial T}{\partial t} = U' \frac{\partial T}{\partial x} + K_x \frac{\partial^2 T}{\partial x^2}, \tag{5}$$

where U' is the cross-sectionally averaged current speed in the x-direction relative to the movement of a flexible boundary separating two segments, and K_x is a longitudinal diffusion coefficient, given by

$$K_x = 63\ c_r\ U_m\ R^{5/6} \tag{6}$$

(McDowell and O'Connor, 1977), where c_r is Manning's roughness coefficient and R is the hydraulic radius. The ocean water tracer can be expressed in parts per thousand and treated exactly like salinity. The diffusion coefficient varies significantly in both space and time. The mean for the lagoon was about 40 $m^2\ s^{-1}$, but mean values near inlets were nearly double this value. In the northern part of the northern sub-basin, the mean was 10-15 $m^2\ s^{-1}$.

The cross-sectionally-averaged current speed at segment boundaries is calculated using a finite difference form of the continuity equation:

$$U_m = \frac{1}{A_m \Delta t} \sum_{j=1}^{m} V_j, \tag{7}$$

where the summation gives the hourly change of the volume of the lagoon landward of the lateral cross-section, and A_m is the cross-sectional area of the seaward side of the m^{th} segment. The cross-sectionally-averaged current speed is related to the relative speed given in Equation (5) by

$$U' = nU_m, \tag{8}$$

where n can vary from 0.0 to 1.0. A value of 0.0 produces a segment boundary that expands and contracts freely with the ebb and flood of the total current (tidal plus

nontidal). This will restrict the accumulation of new ocean water to that resulting from longitudinal diffusion. A value of 1.0 produces inflexible (stationary) segment boundaries, and the accumulation of new ocean water will occur as a result of advection only.

Both the central and southern sub-basins of Indian River lagoon are served by two inlets. In these cases, phase angles of the M_2 tidal constituent (Smith, 1987) were used to determine the segments with maximum phase lags relative to the rise and fall of the tide at the nearest inlet, and U_m was calculated with the boundary condition that no long-term net transport occurred through the interior segment with the greatest phase lag.

Results

Results are sub-divided into two parts. In the first part, simulations trace the accumulation of new ocean water in the Indian River lagoon system, including Banana River lagoon, which is treated as a fourth sub-basin. Two simulations compare the assumptions of no intersegment advective transport ($n = 0$ in equation (8)), then complete advective mixing ($n = 1$). These assumptions correspond to completely flexible and completely inflexible segment boundaries, respectively. In the second part of this section, a series of simulations, based on the assumption of no advective transport, compares the rates of accumulation of ocean water individually for the three sub-basins of Indian River lagoon and for Banana River lagoon.

Figure 3 shows the accumulation of new ocean water in the Indian River lagoon system under the assumption of completely inflexible segment boundaries (curve a) and completely flexible boundaries (curve b). Simulations were based on observed tidal conditions, and coastal sea level varied between +20 and -20 cm with a period of 168 hours. Results indicate that at the end of a one-year simulation the renewal of new ocean water resulting from unrestricted advective transport (curve a) is 167% of the renewal occurring in response to transport associated with longitudinal diffusion only. The 50% renewal time indicated by curve (a) is approximately 140 days, while R_{50} for curve (b) has not been determined at the end of the simulation.

Combining Banana River lagoon with the three sub-basins of Indian River lagoon to quantify flushing by lagoon-shelf exchanges for the Indian River lagoon system as a whole masks significant differences in flushing rates of individual sub-basins. A final series of simulations considers flushing individually for Banana River lagoon and for the three sub-basins of Indian River lagoon, as defined by the three inlets that connect the lagoon with shelf waters of the Atlantic Ocean. In these simulations, the three segments in direct contact with the three inlets were not included. They flush almost completely on each tidal cycle, and with the exception of segment 16 it was not clear how a given segment should be sub-divided and assigned to the two adjacent sub-basins.

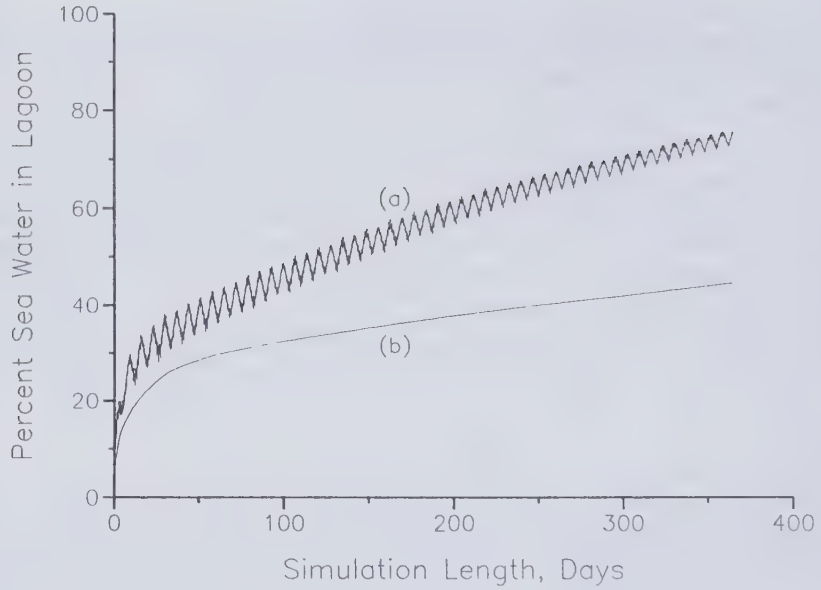

Figure 3. Composite showing the accumulation of new ocean water in the Indian River lagoon system (three sub-basins of Indian River lagoon plus Banana River lagoon), assuming complete mixing of water advected into a new segment (curve a) and no advection due to flexible segment boundaries (curve b). Simulations include tidal exchanges and assume coastal sea level variations of ±20 cm with a period of seven days.

Figure 4 summarizes results for the four sub-basins individually and reveals distinct differences in flushing rates. The southern and central sub-basins of Indian River lagoon accumulate new sea water at relatively rapid rates. Curves (a) and (b) indicate R_{50} values of approximately 5 and 12 days, respectively. In the lower part of the plot, curves (c) and (d), representing the northern sub-basin of Indian River lagoon and Banana River lagoon, respectively, indicate decidedly slower flushing rates. By the end of the one-year simulation, both sub-basins contain less than 30% new ocean water. It is of interest to note that initially the accumulation of new ocean water in Banana River lagoon is much slower than the accumulation of new ocean water in the northern sub-basin of Indian River lagoon. This is because Banana River lagoon gets its ocean water through segment 4 of Indian River lagoon (see Figure 1), which in turn is well removed from Sebastian Inlet. Once new ocean water has begun to accumulate in segment 4, however, Banana River lagoon accumulates ocean water faster than does the northern sub-basin of Indian River lagoon. This is because the total volume of segments 1-3 in Indian River lagoon is one-third greater than the total volume of Banana River lagoon. The crossing of the curves after about 340 days is probably not physically meaningful, however, given the very slow rates at which both sub-basins accumulate new ocean water through Sebastian Inlet.

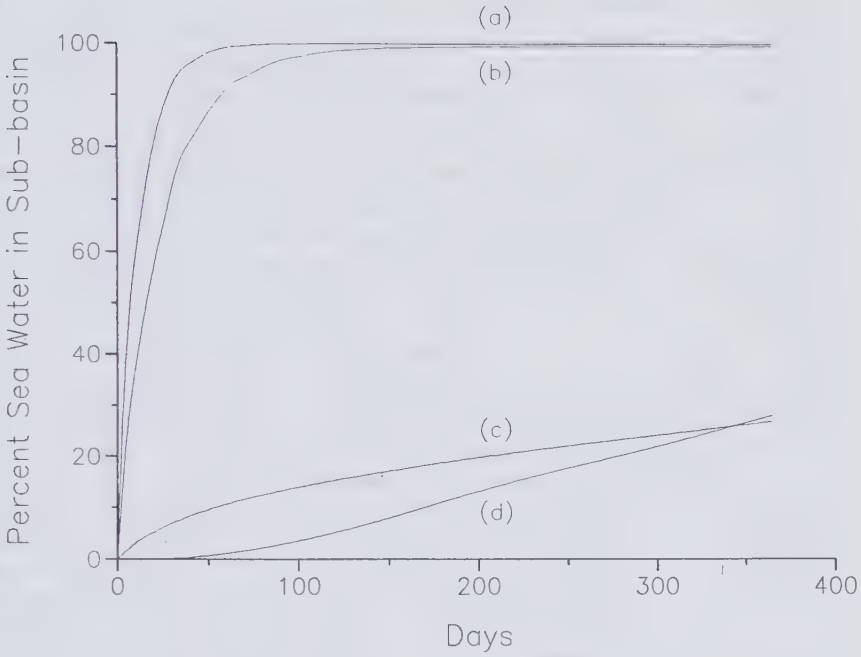

Figure 4. Same as Figure 3, but for the southern (curve a), central (curve b) and northern (curve c) sub-basins of Indian River lagoon; and for Banana River lagoon (curve d). Simulations assumed a completely flexible grid and no net advective transport of sea water.

Discussion

Results from this study quantify the expected differences between flushing rates calculated with unrestricted advective transport, and flushing rates calculated with no advective transport of water between segments. While the flushing rates themselves, whether for the lagoon system as a whole or for individual sub-basins, are undoubtedly subject to revision in view of the roles played by freshwater outflow (Smith, 1993c), wind stress (Sheng et al., 1990) and density currents (Smith, 1990), the divergence of the curves in Figure 3 suggests that the specification of transport is an important feature of any flushing model.

While it is tempting to follow Wood (1979) and use partial advective transport (i.e., intermediate values of n) to represent intersegment transfers associated with freshwater outflow or with wind-driven or density-driven transport, such processes are more appropriately investigated explicitly with a hydrodynamic model than implicitly with a model based on the continuity equation. Similarly, it is better to

use a model that sub-divides lateral cross-sections to account explicitly for flood-dominant and ebb-dominant layers and channels than to use values for n (equation 8) lying between zero and unity. Thus, as hydrographic data become available to verify simulations, it will be preferable to pursue the investigation of lagoonal flushing with a hydrodynamic model than to search for a best-fit value of n.

Three limitations should be kept in mind when using a model based on the continuity equation. First, while one can reproduce tidal flushing with considerable accuracy, one learns more about effects of tidal flushing than about its causes. The dynamics of flushing are not addressed. A second limitation stems from the model's inability to incorporate freshwater effects, whether associated with rainfall, surface runoff or groundwater seepage. The boundary condition specifying the speed of the longitudinal flow relative to the speed of the segment boundary (equation 7) determines what percent of the longitudinal transport will be retained in a given segment. Thus, when a segment contains a quasi-steady freshwater source, even a partial retention results in the quasi-steady growth of the segment. Segments in the interior of the lagoon will eventually expand to the point where they force other segments out of the lagoon through the inlets. Only with tidal and/or low frequency co-oscillating flow patterns will segments alternately expand and contract, and thereby retain manageable sizes. Finally, this approach does not quantify the long-term net transport through the interior of a lagoon between inlets of unequal size (van de Kreeke and Cotter, 1974). In the case of Indian River lagoon, however, this will occur only in the central and southern segments of the lagoon, where flushing rates are already relatively high.

Even with a model that is restricted to flushing by lagoon-shelf exchanges, however, distinctly different rates at which the four sub-basins receive new ocean water (Figure 4) suggest that the regular renewal of ocean water in the central and southern sub-basins occurs substantially faster than in the northern sub-basins, including Banana River lagoon. Indeed, incorporating freshwater sources and sinks has the effect of establishing a net outflow that opposes the importation of new ocean water and reduces the 50% renewal time still further. Smith (1993c) found 50% renewal times of less than one week for the southern sub-basin of Indian River lagoon, but still well in excess of one year for the northern sub-basin under high rainfall conditions.

Acknowledgement. Water level records from 17 of the 31 study sites were collected and provided by the National Ocean Service (NOS); additional water level records were provided by the Florida Medical Entomology Laboratory in Vero Beach, Florida. Ms. Elizabeth Smith assembled and edited the NOS portion of the data base. Partial support for this work was provided by the Florida Department of Environmental Regulation through Contract No. CM-118, and by the Florida Department of Natural Resources through Grant Agreement No. 6598. Harbour Branch Oceanographic Institution, Contribution Number 1012.

References

Austin, G. B. On the circulation and tidal flushing of Mobile Bay, Alabama, Part 1. Reference 54-20T, Department of Oceanography, Texas A & M University, College Station, Texas, 1954.

Dennis, R.E. and E.E. Long, A user's guide to a computer program for harmonic analysis of data at tidal frequencies. NOAA Tech. Rept. 41, U.S. Dept. of Commerce, Rockville, MD, 1971.

Dyer, K.R. and P.A. Taylor, A simple, segmented prism model of tidal mixing in well-mixed estuaries. *Est Coastal Mar Sci*, 1, 411-418, 1973.

Haurwitz, B. and A. Cowley, The barometric tides at Zurich and on the summit of Santis. *Pure Appl Geophys* 113, 355-365, 1975.

Ketchum, B. The exchanges of fresh and salt waters in tidal estuaries. *J Mar Res*, 10, 18-38, 1951.

McDowell, D.M. and B.A. O'Connor, Hydraulic behaviour of estuaries. John Wiley & Sons, New York, 1977.

Officer, C.B. Physical Oceanography of Estuaries (and Associated Coastal Waters). John Wiley & Sons, New York, 1976.

Pritchard, D.W. Salt balance and exchange rate for Chincoteague Bay. *Chesapeake Sci*, 1, 48-57, 1960.

Sheng, Y.P., S. Peene and Y.M. Liu, Numerical modeling of tidal hydrodynamics and salinity transport in the Indian River lagoon. *Florida Sci*, 53, 147-168, 1990.

Smith, N.P. The rise and fall of the estuarine intertidal zone. *Estuaries* 9, 95-101, 1986.

Smith, N.P. An introduction to the tides of Florida's Indian River lagoon. I. Water levels. *Florida Sci*, 50, 49-61, 1987.

Smith, N.P. Tidal and wind-driven transport between Indian River and Mosquito Lagoon, Florida. *Florida Sci,* 56,235-246, 1993a.

Smith, N.P. The intertidal volume of Florida's Indian River lagoon. *Florida Sci*, 55, 209-218, 1993b.

Smith, N.P. Tidal and nontidal flushing of a Florida's Indian River Lagoon. *Estuaries* 16, 739-746, 1993c.

Stommel, H. and A.B. Arons, A mixing length theory of tidal flushing. *Trans AGU*, 32, 419-421, 1951.

van de Kreeke, J. and D.C. Cotter, Tide-induced mass transport in lagoon-inlet systems. *Proc. Conf. Coastal Engr.*, 2290-2301, 1974.

Wood, T. A modification of existing simple segmented tidal prism models of mixing in estuaries. *Est Coastal Mar* Sci 8, 339-347, 1979.

12

Circulation and Transport in Sarasota Bay, Florida: The Effect of Tidal Inlets on Estuarine Circulation and Flushing Quality

Y. P. Sheng, S. Peene and E. Yassuda

Abstract

Using field data obtained in 1991, a three-dimensional numerical model of circulation and transport is developed and utilized to investigate the effects of tidal inlets on the circulation and flushing in the Sarasota Bay system of the study. In particular, the model is used to assess the potential impact of the opening of a small tidal inlet, Midnight Pass. Results indicate that the degree of flushing in various segments of the estuary depends on their locations with respect to the tidal inlets. Areas with poor flushing also have low visibility in water. If Midnight Pass were to be opened, flushing in the area behind the Pass will significantly improve, while flushing in Roberts Bay area will actually deteriorate, because of the northward movement of the null zone from the Midnight Pass area.

Introduction

Tidal inlets link numerous shallow estuaries in Florida and the coastal ocean. The opening or closure of a tidal inlet can significantly affect the circulation and water quality within an estuary. On the other hand, the stability of a tidal inlet is affected by the tidal prism in various parts of an estuarine system. This paper presents a study on the effect of tidal inlets on the circulation and water quality in the Sarasota Bay system (including Sarasota Bay and Little Sarasota Bay), which is a multiple-inlet shallow (average depth is 2 m) coastal lagoon located in Southwest Florida (Figure 1).

Mixing in Estuaries and Coastal Seas
Coastal and Estuarine Studies Volume 50, Pages 184-210
Copyright 1996 by the American Geophysical Union

Since the closure of Midnight Pass (Figure 2) in 1984, there has been degradation of water quality in Little Sarasota Bay. Recent measurement of DO (Dissolved Oxygen) over a 7-day period behind the closed Midnight Pass showed diurnal fluctuation between 1 and 8 ppm (Figure 3). The concentration was below 4 ppm much of the time, although the early morning data were generally between 6 and 8 ppm. To improve the water quality of the Little Sarasota Bay, it has been suggested that the Midnight Pass be reopened. One objective of this study is to investigate the potential impact of the opening of Midnight Pass on the circulation and water quality in the estuarine system. Another objective is to determine if dredging of the IntraCoastal Waterway (ICW) contributed to the closure of the Midnight Pass.

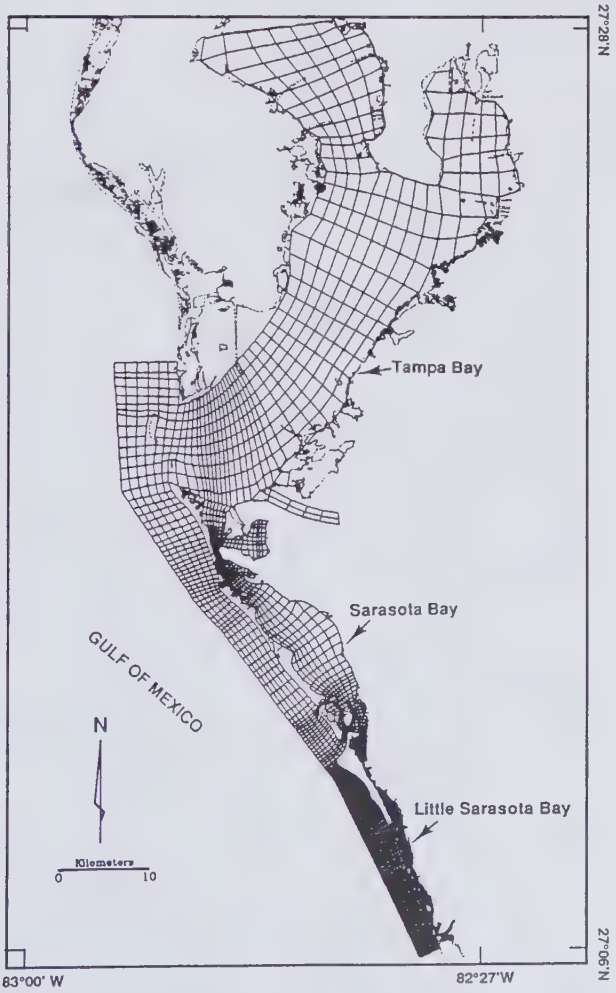

Figure 1. Map and curvilinear grid of the Sarasota/Tampa Bay system in Florida.

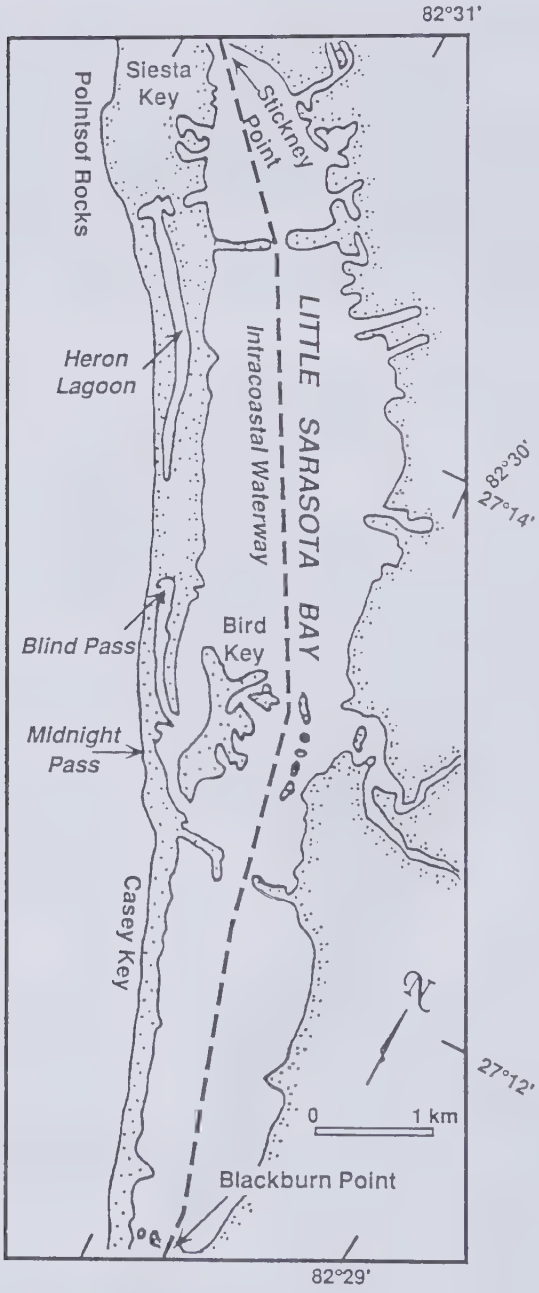

Figure 2. Map of Midnight Pass and Little Sarasota Bay in Sarasota County, Florida.

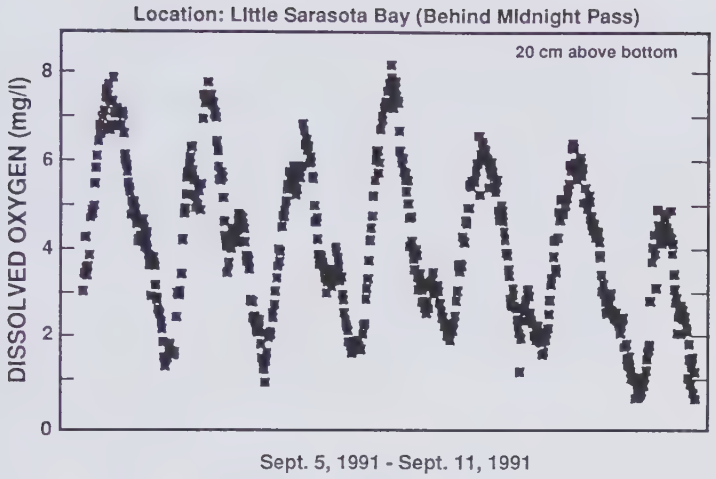

Figure 3. Dissolved oxygen levels in Little Sarasota Bay during September 5 to September 11, 1991.

Estuarine Circulation and Tidal Inlets

Estuaries are semi-enclosed water bodies where salt water from the ocean is measurably diluted by fresh water from the tributaries (Cameron and Pritchard, 1963). Estuarine circulation is driven by tide, wind, and density variation in the water, while influenced by geometry and bathymetry of the basin and rotation of the earth. Tides in estuaries are primarily forced by ocean tides at the entrance of the estuaries, i.e., tidal inlets. In large coastal water bodies (e.g., Gulf of Mexico), tides result from direct gravitational forcing by the sun and the moon as well as forcing at the open boundaries (e.g., Yucatan Channel and Florida Straits).

Tides propagate as long waves in the ocean and estuaries and are reflected and dissipated by the boundaries. In an estuary where the basin length is less than the 1/4-wavelength of tidal propagation (e.g., Tampa Bay and Sarasota Bay), water level in the entire estuary fluctuates up and down simultaneously (i.e., in phase) during the "flood" cycle and "ebb" cycle. When the basin length is near 1/4 of the tidal wavelength (e.g., Long Island Sound), near resonance occurs such that tidal amplitude increases while tidal current decreases from the ocean entrance toward the river (Ippen and Harlemen, 1966). If the basin length exceeds the 1/4-wavelength of tidal propagation (e.g., James River estuary in Virginia), part of the basin may be in "flood" cycle while other part of the basin is in "ebb" cycle. When the natural frequency of a basin (e.g., Gulf of Mexico) is comparable to a tidal period (e.g., the diurnal period), the tidal constituent is amplified. This is why tides on the Gulf coast of Florida consist of a mixture of semi-diurnal tides (M2 and S2) and diurnal tides

(O1, K1 and P1), while tides on the Atlantic coast of Florida are semi-diurnal (M2 and S2).

Tidal circulations are modified due to the effects of wind and density structure in the water. The wind enhances vertical mixing, creates vertical flow structure (e.g., surface flow in the downwind direction and bottom flow in the upwind direction), causes set-up or set-down in water level, and alters the residual circulation patterns. While wind- and tide-driven currents can affect the distribution of temperature and salinity in estuaries, the resulting density structure can in turn induce baroclinic circulation to significantly modify the flow field.

Classical tidally-averaged estuarine circulation consists of seaward flow of fresh water near the surface and landward flow of ocean water near the bottom (Hansen and Rattray, 1965). Depending on the relative importance of tidal mixing with respect to the river flow, vertical salinity structure in estuaries may be highly stratified (low tidal mixing), well mixed (strong tidal mixing), or partially stratified (intermediate). However, circulation in estuaries is highly dynamic. Significant vertical stratification may occur even in well mixed estuaries. Thus, the effect of density gradient on estuarine circulation must be considered when studying long-term residual circulation (Zimmerman, 1978) in estuaries.

Most U.S. estuaries are coastal plain (drowned valley) estuaries and are quite shallow, typically consisting of a deep navigation channel where significant stratification exists and shallow adjacent flats where salinity and temperature are generally well mixed. Salt intrusion takes place primarily within the bottom water of the deep navigation channel. Recent studies in Chesapeake Bay (Sheng *et al.*, 1989a; Johnson *et al.*, 1989) and Tampa Bay (Sheng *et al.*, 1992) showed that currents in the navigation channel are generally parallel to the channel and gradients in salinity and velocity exist across the channel. Transports of momentum and salinity along the channel are generally more important than the cross-channel transports.

In a multiple inlet estuarine system such as the Sarasota Bay system, tides enter from various inlets and can interact with each other. The geometry and bathymetry of tidal inlets have significant effect on various aspects of estuarine circulation including tidal currents, tidal prism, tidal flushing, and residual flow, which in turn affect the water quality dynamics in an estuarine system. For example, tidal pumping (Fischer *et al.*, 1979) often causes interesting residual circulation patterns and gyres near tidal inlets. Null zones with little flow and mixing may be formed in areas far from tidal inlets, thus causing poor flushing and water quality there. To effectively manage an estuarine system, it is essential to identify null zones with poor water quality. One objective of this study is to identify areas with poor flushing within the Sarasota Bay system.

Estuarine circulation can in turn affect the stability of tidal inlets. Davis *et al.*, (1987) hypothesized that the closing of the Midnight Pass in 1984 was caused by the dredging of the IntraCoastal Waterway (ICW), which contributed to reduced tidal prism through the Pass. In this study, we will examine whether dredging led to the closure of the Pass and quantify the potential impact of reopening of the Midnight Pass.

Studies on estuarine circulations generally involve field experiment, laboratory physical modeling, and numerical modeling. Field experiment involves the measurements of various meteorological parameters (e.g., wind, air temperature, atmospheric pressure, and solar radiation, etc.) and hydrodynamic parameters (e.g., water level, water currents, temperature, and salinity, etc.) over long time. However, due to the inherent scaling problem and the high maintenance cost, physical models have been gradually replaced by numerical models as the primary tool for estuarine studies. Numerical models of estuarine circulation of various (one, two, three) dimensions have been developed. Some of the recent estuarine circulation models, e.g., the Chesapeake Bay model (Sheng *et al.*, 1989a, Johnson *et al.*, 1989), utilize curvilinear grid that conforms to the complex shorelines and bathymetry of estuaries, thus giving more accurate results than the rectangular-grid models. We will use a similar three-dimensional curvilinear grid circulation model (Sheng and Peene, 1991) for this study.

Effect of Circulation on Water Quality Dynamics

In many U.S. estuaries and lakes, increased external loading of nutrients through tributaries and rivers has led to accelerated eutrophication, seagrass loss, and reduced fishery production. For example, three decades of increased loading of nutrients has resulted in extensive area of anoxia (zero oxygen concentration) and hypoxia (low oxygen concentration) in Chesapeake Bay during the summer months. Hillsborough Bay in Florida also has an extensive area of hypoxia in summer. Tomasko (1992: personal communication) attributed the cause for seagrass loss in Sarasota Bay to increase in epiphytic algae population, which resulted from increased nutrient loading.

Nutrients entering an estuary may undergo a series of advection-deposition-resuspension-transformation processes before residing at a low-energy location or entering the ocean. Thus, nutrients entering an estuary may actually affect the water quality at a location sufficiently far away from the river entrance, instead of that immediately near the river. To develop a rational management plan for estuarine resources, it is essential to be able to first quantify the transport of nutrients and other water quality parameters in an estuary under its present condition. This requires an extensive amount of field and laboratory data and numerical modeling.

Due to the site-specific nature of the nutrient transport processes, water quality models for one estuary may not be readily applicable to another estuary. Models developed for the deeper and temperate estuaries in the north are not expected to be applicable to the shallow Florida estuaries. In shallow Florida estuaries, physical processes have much stronger effects on the water quality processes and many of the water quality problems are not driven by phytoplankton algae, but by epiphytic algae and macroalgae. Although water quality modeling is not attempted in this study, we will use results of the circulation model to conduct flushing calculations that could help to locate areas of poor light intensity and water quality.

Field Study

To investigate the potential impact of opening of the Midnight Pass, we conducted a field and modeling study of the Sarasota Bay system to first quantify existing hydrodynamic conditions. Continuous data of wind, current, temperature, salinity and Optical Back Scatter were collected at four platforms (UF-01, UF-02, UF-03 and UF-04) during one 2-month period in 1991. In 1992, data were measued at the same four staions plus a new station UF-05.

Figure 4 shows the locations of the data stations maintained by the University of Florida and USGS and NOAA/NOS. USGS obtained tidal level data at several locations (Anna Maria Sound, Sarasota Bay East, Sarasota Bay West, Roberts Bay and Big Pass, etc.) in 1990 and 1991. The 1991 field experiment coincided with an intensive field program by NOAA/NOS in the adjacent Tampa Bay, which include measurements of vertical profiles of current and salinity at many stations using RADS acoustic doppler system.

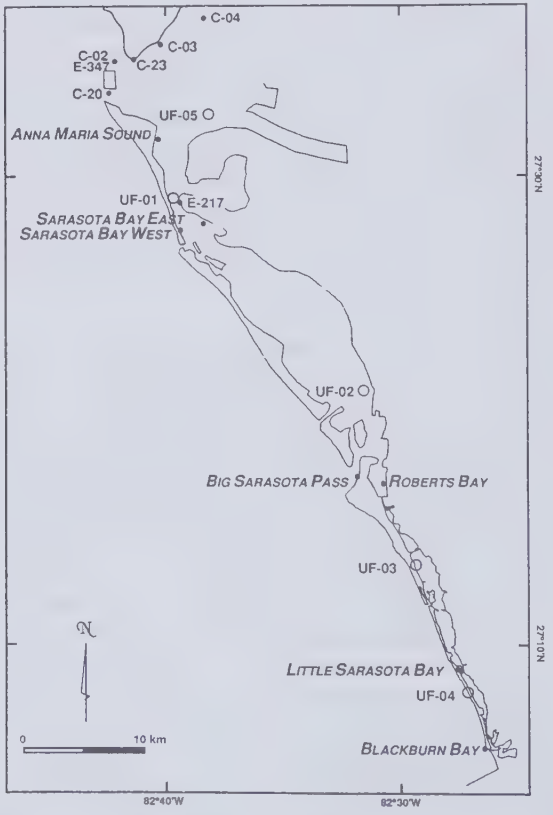

Figure 4. Locations of data stations of the University of Florida, USGS and NOAA/NOS.

Field data showed that tidal circulation in Sarasota Bay is forced by tides at the Anna Maria Sound, Long Boat Pass, New Pass, Big Pass, and Venice Inlet. Tides at the open boundaries are composed of semi-diurnal (M2 and S2) and diurnal (O1, K1, and P1) components with relatively low tidal amplitudes (40-80 cm) and slight (less than 1 hour) shift in tidal phases.

Field data indicated that strong currents exist within the tidal inlets, and tide propagation into the estuary is strongly influenced by the inlet configuration. Spectral analysis of long-term current data showed that 80% of the energy is associated with the tides, while 20% of the energy is associated with the wind and baroclinicity. Circulation within the shallow estuarine system is strongly influenced by the navigation channel. Strong currents up to 1 m s^{-1} could be found within the navigation channel (about 36-10 m deep), whereas currents in the adjacent shallows (0.3 to 1 m) are much weaker.

Interesting residual flow patterns have also been observed. For example, the low pass current-filtered data at Station 1 in Anna Maria Sound (Figure 5) showed a persistent north to south flow during July and August 1991. Although the filtered wind velocity was primarily from south to north, both the near-surface and the near-bottom residual currents were from north to south. An examination of the current and salinity data obtained from the area (Figure 6) suggests that the residual transport from north to south may contain low-salinity water from Manatee River, which is the largest source of freshwater in the vicinity. Thus, the north to south residual current is primarily driven by tidal action (nonlinearity and tidal pumping) and freshwater flow from Manatee River, and is countered by the south to north wind-driven flow.

Near-bottom currents at Station 2 near Whittaker Bayou, and Station 4 in Blackburn Bay are shown in Figure 7. At both stations, the north-south currents (10-30 cm s^{-1}) dominate over the east-west currents (5-10 cm s^{-1}). At Station 2 and Station 4, salinity were well-mixed vertically and fluctuated between 32 and 34 ppt during this time period. At Station 3, salinity varied more significantly between 24-29 ppt due to the influence of freshwater from river and rain. Nevertheless, spectral analysis of current data showed that 80% of the energy is associated with tides with less than 20% energy associated with wind and baroclinicity.

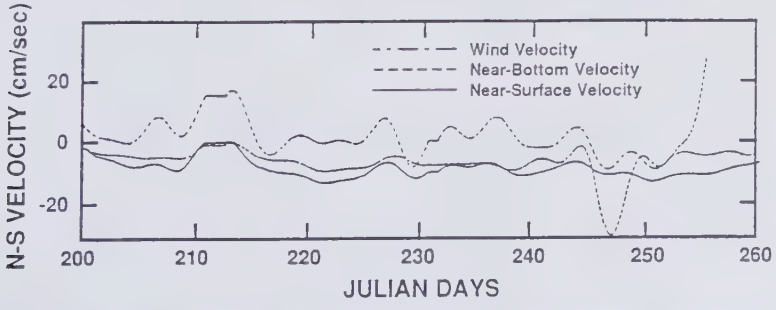

Figure 5. Filtered (by a fourth order Butterworth filter, which removed all tidal constituents with 24-hour period or less) near-surface current, near-bottom current and 3% of wind velocity in the north-south direction at UF Station 1 during Julian days 200 through 260, 1991

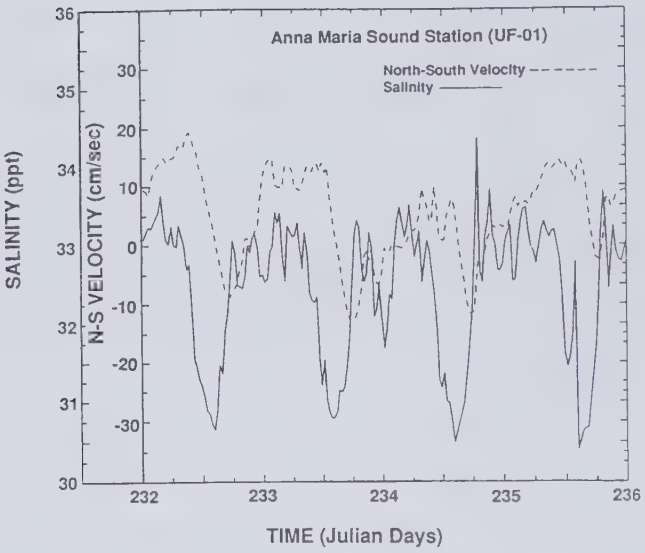

Figure 6. Measured near-surface north-south current and salinity at UF Station 1 (Anna Maria Sound) during a 4-day period in July 1991. Notice the significant southerly residual flow.

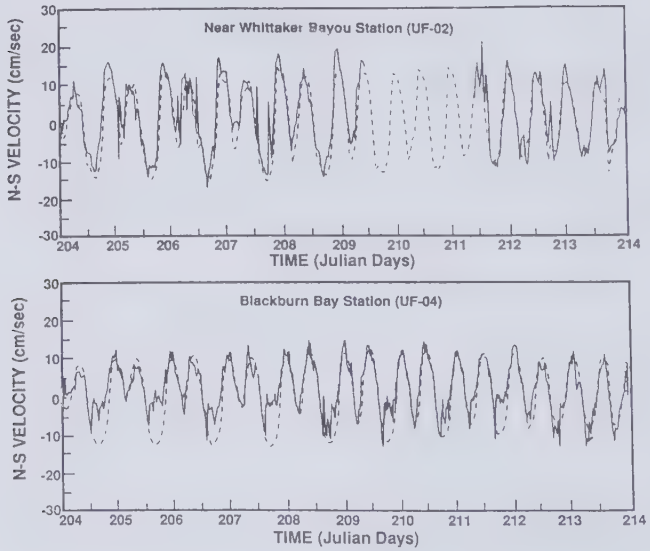

Figure 7. Simulated (dashed line) and measured (solid line) north-south currents at the bottom layer at UF stations (a) near Whittaker Bayou and (b) in Blackburn Bay during July 1991. Solid line: data. Dashed line: model results.

Modeling Study

Based on the field data obtained in 1990 and 1991 and the curvilinear-grid model (CH3D) developed by Sheng (1987 and 1989), we developed a three-dimensional numerical model of circulation and salinity transport in the Sarasota-Tampa Bay system. A brief description of the model is given in Appendix A. The boundary-fitted grid allows accurate representation of circulation and transport in the entire estuarine system (Figure 1), including the navigation channels. The minimum grid spacing is 30 m. A time step of 60 sec was used for numerical simulations. Boundary conditions included offshore tidal forcing and river flows.

Simulated near-bottom currents at Stations 2 and 4 during Julian days 204 to 214 were shown in Figure 7. Tidal elevation at the offshore open boundary during this period is shown in Figure 8. During flood tide, ocean water enters the Sarasota Bay through all the passes and the Anna Maria Sound, creating strong flood currents, particularly in the Big Pass. During ebb tide, estuarine water recedes into the ocean and creates strong ebb currents. Currents in Sarasota Bay between the Longboat Pass and the New Pass are generally much weaker than currents in other regions. As an example, Figure 9 shows the vertically-integrated ebb currents in Sarasota Bay at 4 p.m. on Julian day 207, 1991.

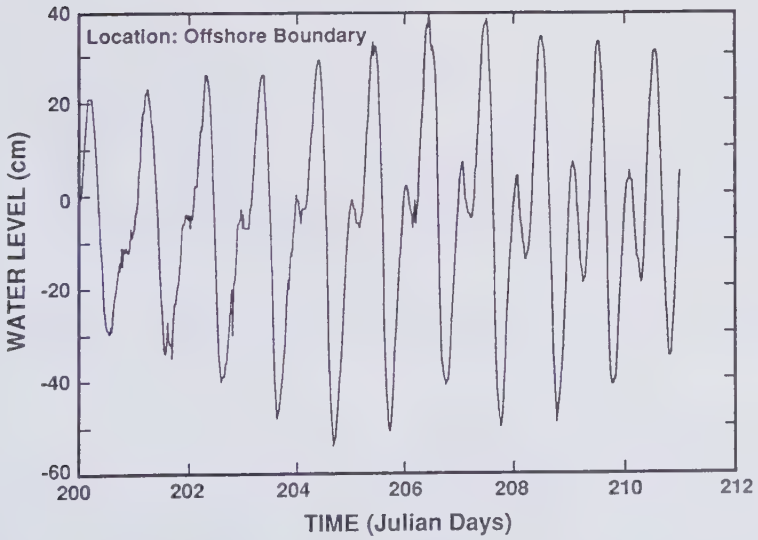

Figure 8. Tidal elevation at the offshore open boundary near Sarasota during Julian days 200 to 211, 1991.

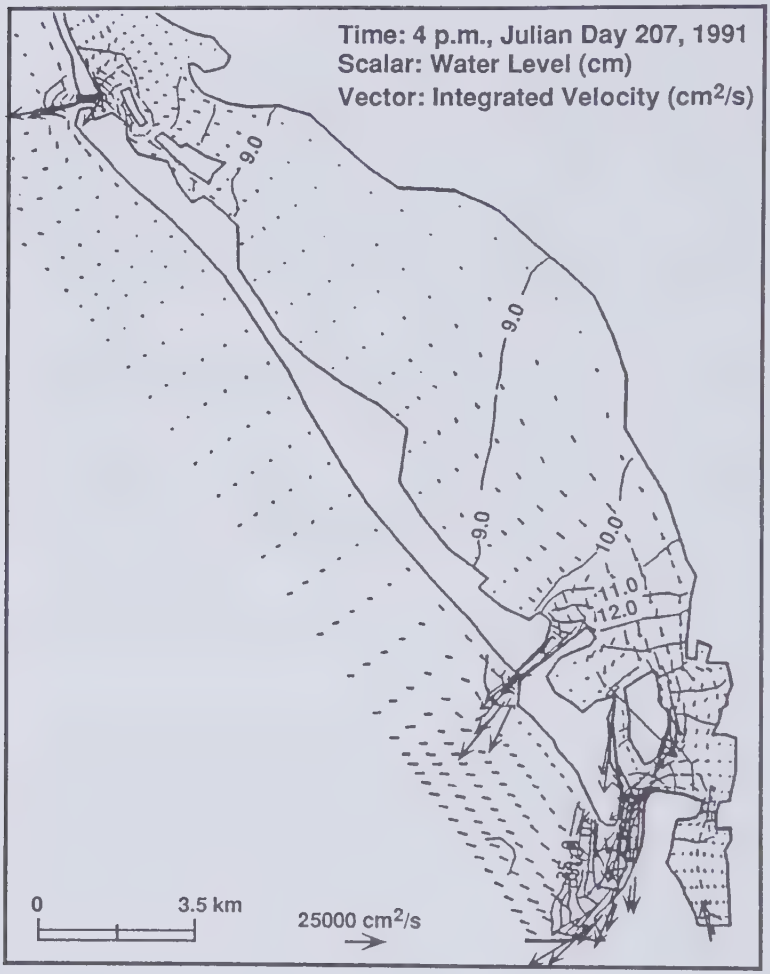

Figure 9. Simulated water level and horizontal currents in Sarasota Bay at 4:00 p.m. on Julian day 207 in 1991.

Since the primary focus of this study is the potential effect of opening of Midnight Pass on circulation and mixing in Little Sarasota Bay, it is of interest to examine the simulated and measured currents at Stations 3 and 4. As shown in Figures 10 and 11, the basic trends in measured currents were well simulated by the model, although the "noises" in data are absent in model results.

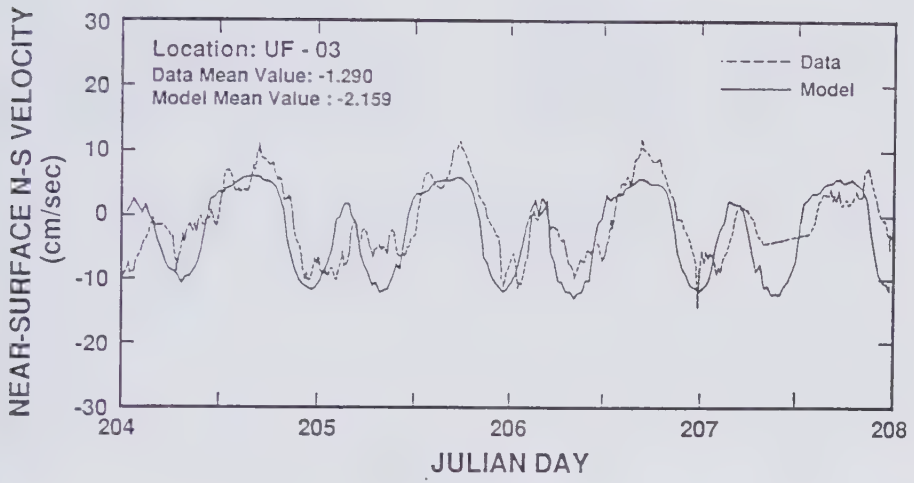

Figure 10. (a) Simulated and measured near-surface north-south current at Station 3 during Julian days 204 to 208, 1991.

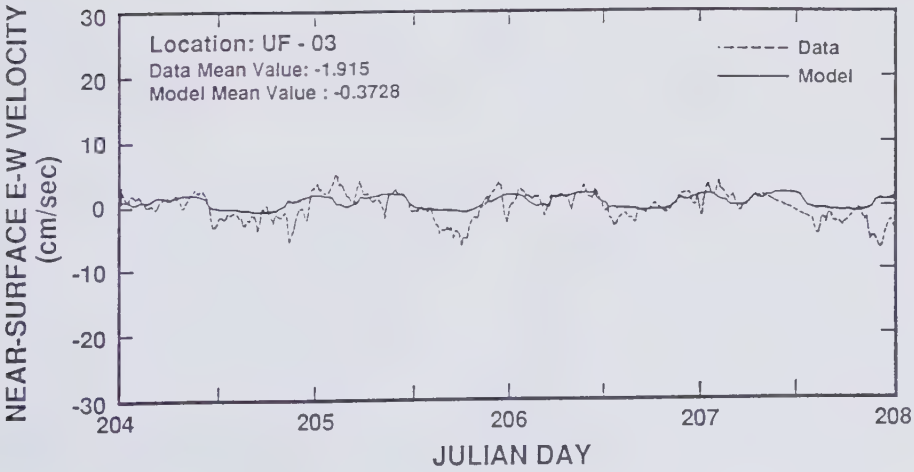

Figure 10. (b) Simulated and measured near-surface east-west current at Station 3 during Julian days 204 to 208, 1991.

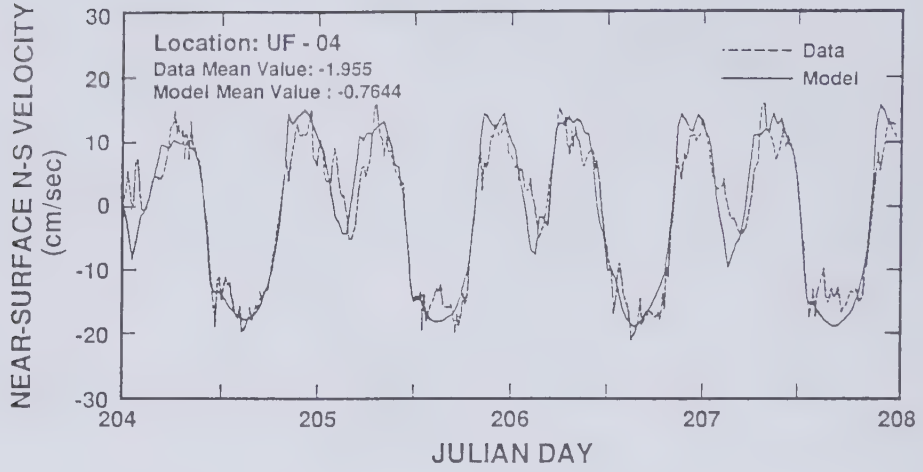

Figure 11. (a) Simulated and measured near-surface north-south current at Station 4 during Julian days 204 to 208, 1991.

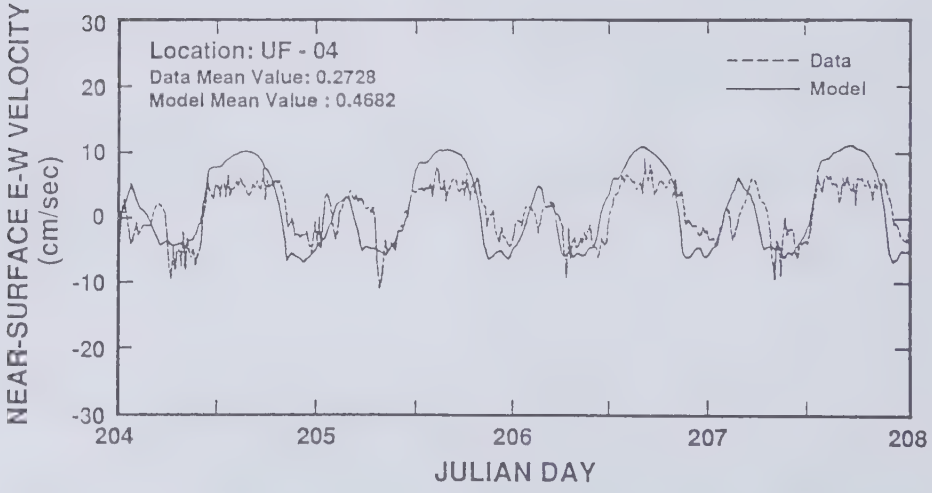

Figure 11. (b) Simulated and measured near-surface east-west current at Station 4 during Julian days 204 to 208, 1991.

Earlier, Sheng and Peene (1991) developed a three-dimensional model of tidal circulation in Sarasota Bay, based on the CH3D model developed by Sheng *et al.* (1989a) for Chesapeake Bay. Using a numerical grid for the Sarasota Bay only (not including Tampa Bay and Little Sarasota Bay), they successfully simulated the tidal water level fluctuation at various stations, as shown in Table 1.

TABLE 1. Flushing rates of conservative constituent in 8 sections of the Sarasota Bay System.

(Percent of Mass Flushed After 10 Days)

SECTION	SEGMENTS	LOCATION DESCRIPTION	PERCENT FLUSHED AFTER 10 DAYS		
			Before ICW	Present Condition	Pass Open
1	1, 2	Anna Maria Sound Cortez Bridge	81	81	81
2	3	Palma Sola Bay	31	31	31
3	4, 5, 6	Longboat Pass Tidy Island	64	64	64
4	7, 8	Middle Sarasota Bay	32	32	32
5	9. 10, 11, 12	New Pass, Big Pass Southern Portion of Sarasota Bay	81	81	81
6	13	Roberts Bay North Little Sarasota Bay	52	76	48
7	14, 15	Little Sarasota Bay Midnight Pass	71	27	74
8	16	Blackburn Bay	70	72	83

Peene, Sheng and Houston (1992) simulated the tide- and wind-driven currents in the Sarasota Bay system during the passage of Tropical Storm Marco in October 1990 using the numerical grid shown in Figure 1. The numerical model simulated the measured water level fluctuations at the USGS stations quite accurately (within 5-14%). Simulated currents at the NOS stations were within 10-23% of the measured data, due to the fact that the NOAA current meters were deployed in the deep navigation channel, which was not well represented by the numerical grid. In addition to the simulation of water and currents, we also computed the concentration of a conservative constituent during Julian days 204 to 214 for the estimation of flushing time in various parts of the estuarine system, with the Midnight Pass closed (present condition) and opened (proposed condition). The following conclusions were derived from these flushing calculations.

Effect of Navigation Channel on Little Sarasota Bay Circulation

Before 1956, there was no navigation channel (ICW) in the Sarasota Bay system. To investigate the impact of navigation channel on circulation in the Sarasota Bay system, we performed model simulation of tidal flushing of a conservative species in various segments of the Bay, first with the pre-1956 bathymetry (with Midnight Pass but no ICW) and then with the post-1956 but pre-1983 bathymetry (with ICW and Midnight Pass). The model domain is divided into eight sections (Table 1) based on the 16 segments shown in Figure 12. At the beginning of a numerical simulation (e.g., a 12-day period in July 1991 in this case), a conservative substance of 30 ppt is released into all the numerical grid points within a section, while concentration in all other sections are given zero values. As the simulation proceeds, the relative amount of conservative substance (as a percentage of the initial mass) remaining in the section can be calculated.

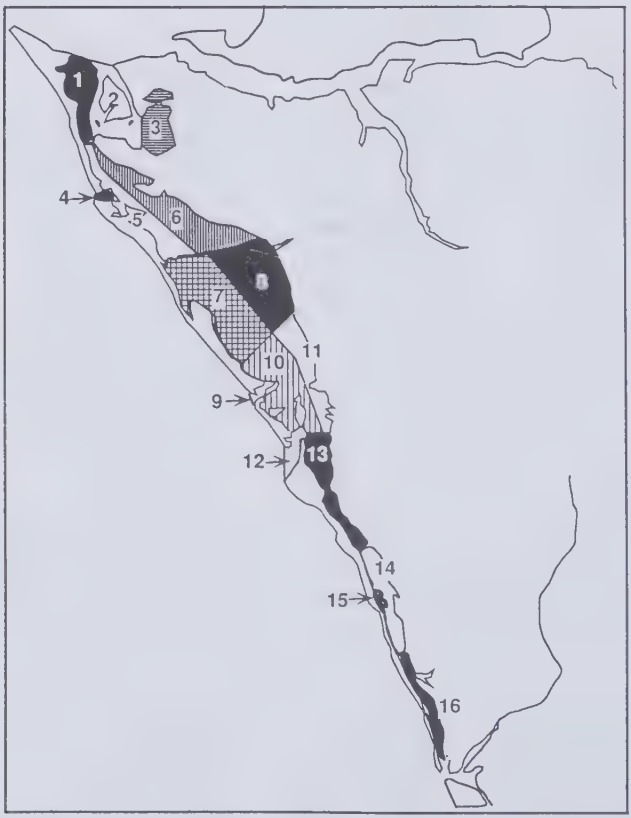

Figure 12. Sarasota Bay NEP study area segments.

Relative tidal flushing rates in three sections of Little Sarasota Bay were computed with the pre-1956 bathymetry first. As shown in Figure 13, relative flushing through the middle section (Segments 14 and 15) was the fastest, while flushing through the northern section (Segment 13) was the slowest, due to the presence of a null zone (stagnation point) there.

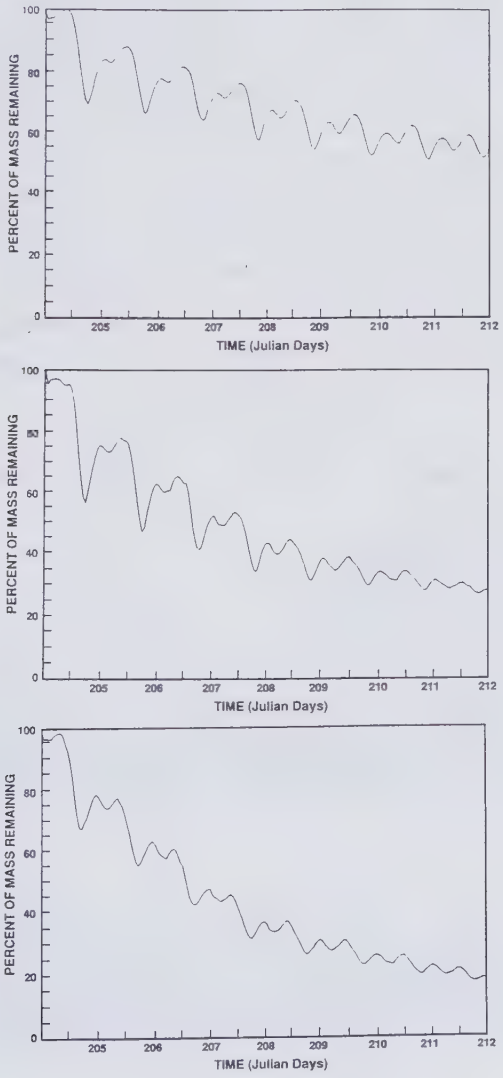

Figure 13. (a) Relative tidal flushing at Segment 13, (b) Segments 14 and 15, and (c) Segment 16 during a 12-day period with pre-1956 bathymetry and geometry.

Relative flushing rates for the three sections computed with the post-1956 but pre-1983 bathymetry (with navigation channel and Midnight Pass) are shown in Figure 14. Flushing rates increased in the middle and southern sections, while remained about the same in the northern section. Although it was reported that the relative tidal exchange through Midnight Pass was reduced, this effect is not apparent from Figure 14 since Segments 14 and 15 are combined in our calculation. Although it is reasonable to expect that the reduced tidal prism through Midnight Pass may have contributed to accelerate the instability and closure of the inlet, this effect was probably very gradual as Midnight Pass was in fact closed by human action instead of natural action.

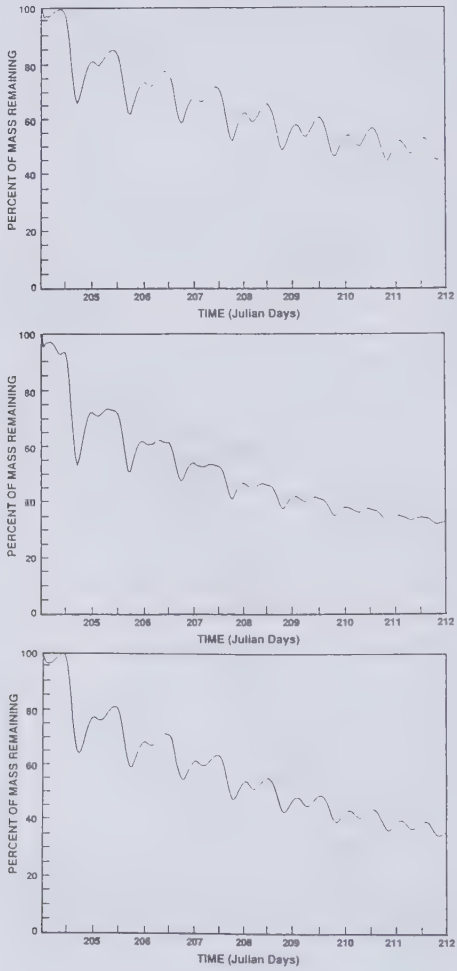

Figure 14. (a) Relative tidal flushing at Segment 13, (b) Segments 14 and 15, and (c) Segment 16 during a 12-day period with pre-1983 bathymetry and geometry (with Midnight Pass open).

The relative flushing rates in various segments of the Sarasota Bay system as shown in Table 1 compare very well with the relative water quality map (Figure 15) established for Sarasota Bay based on four bay-wide monitoring events, which sampled numerous parameters (depth, secchi depth, extinction coefficient, color, turbidity, total phosphorus, ortho phosphate, nitrate plus nitrite, total kjeldahl nitrogen, total inorganic carbon, total organic carbon, and salinity).

Effect of Closure of Midnight Pass on Little Sarasota Bay Circulation and Water Quality

Tidal flushing rates in the same three sections computed with the present bathymetry are shown in Figure 16. Since Midnight Pass is presently closed, tidal flushing in the middle section is very poor. Flushing through the northern section was enhanced from the pre-1983 condition, due to the elimination of the null zone (stagnation point). Flushing through the southern section was somewhat reduced. Measured dissolved oxygen concentration in the area behind Midnight Pass in 1991 (Figure 3) showed unacceptable values of 1 to 4 ppm during much of the time.

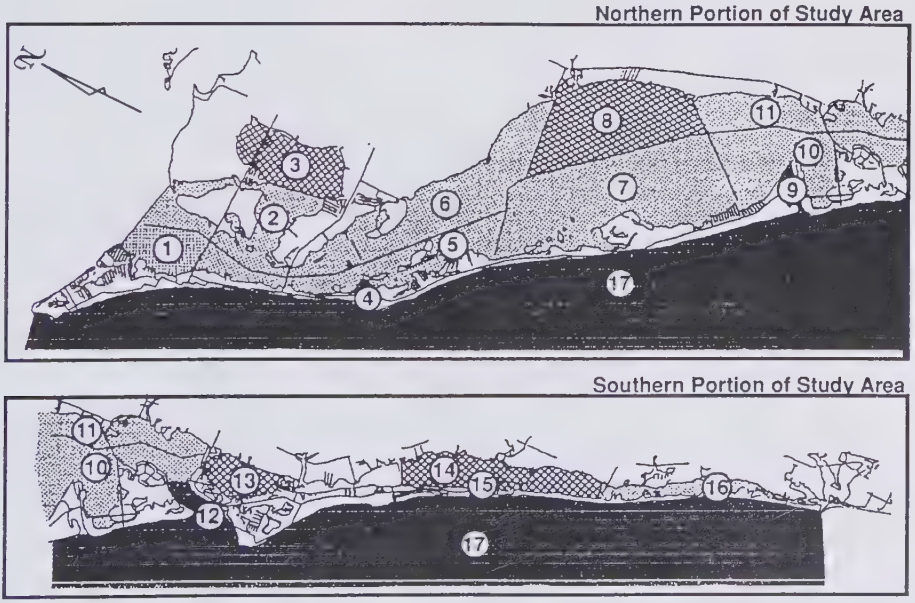

Figure 15. Relative water quality for Sarasota Bay segments. Shaded areas have the best; stippled areas have intermediate; cross-hatched areas have the poorest. (a) Northern and (b) southern portions of study area.

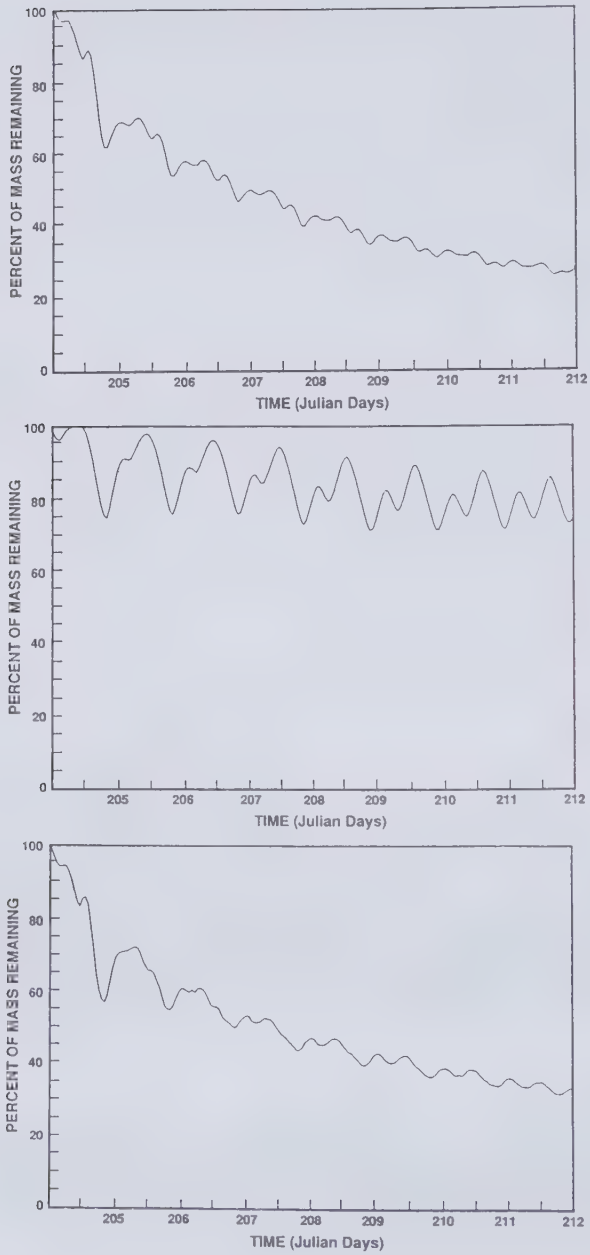

Figure 16. (a) Relative tidal flushing at Segment 13, (b) Segments 14 and 15, and (c) Segment 16 during a 12-day period with present bathymetry and geometry.

Potential Influence of Opening of Midnight Pass on Circulation and Water Quality in Little Sarasota Bay

The opening of Midnight Pass will significantly alter the circulation patterns in the Little Sarasota Bay. Tidal fluxes (vertically-integrated currents) in the area are shown for the present condition (Figure 17) and the opened condition (Figure 18).

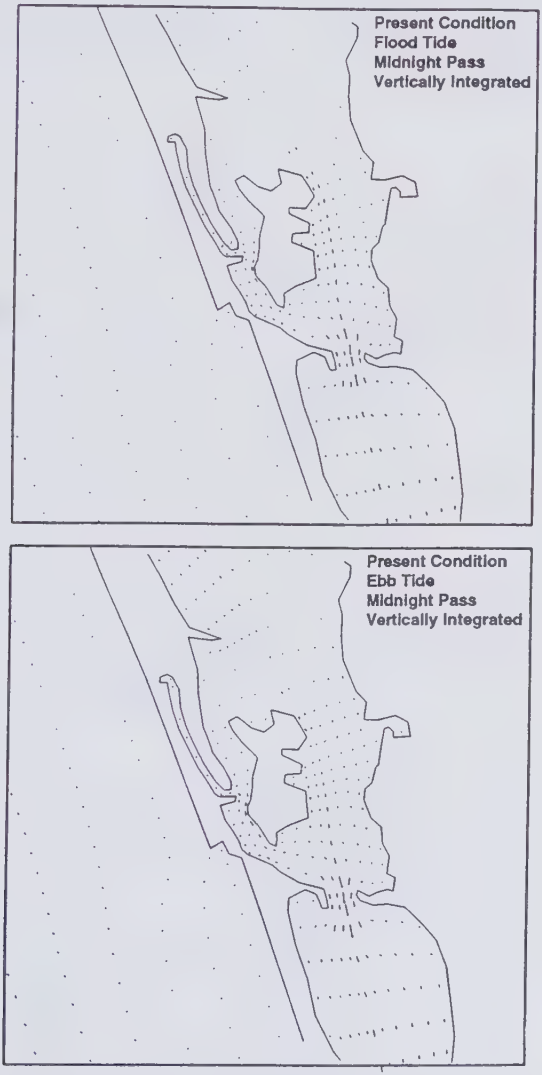

Figure 17. Vertically-integrated currents at (a) flood tide and (b) ebb tide with present conditions.

As suggested by the tidal flushing calculations shown above, the opening of Midnight Pass may lead to enhanced flushing in the middle section of the Little Sarasota Bay. The enhanced flushing means the water quality behind the Middle Pass will be significantly improved. However, water quality in the northern section of Little Sarasota Bay may in fact deteriorate due to the reduced flushing rate there. However, these suggestions are based on flushing calculations for a conservative species that did not consider the transformation processes of water quality parameters (e.g., nutrients and metals). For more quantitative estimation on the impact of Midnight Pass opening, a comprehensive water quality monitoring and modeling effort should be undertaken.

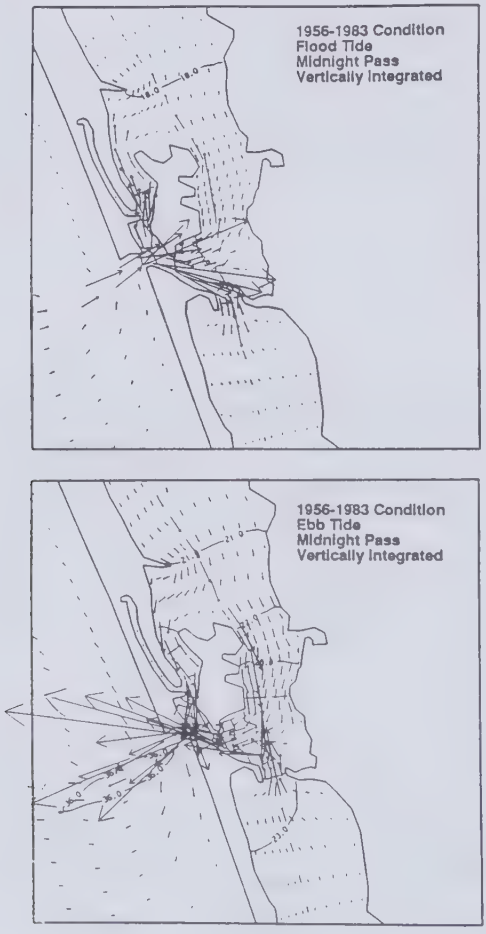

Figure 18. Vertically-integrated currents at (a) flood tide and (b) ebb tide with the Midnight Pass opened.

Inlet Stability

Based on data that date back to 1888, Midnight Pass was a natural opening, free to migrate and to vary in cross-sectional areas. Davis *et al.* (1987) documented the locations and various names assigned to present Midnight Pass and other inlets in the adjacent area (Figure 19). They stated that tidal exchange between Little Sarasota Bay and the Gulf of Mexico had not been dominated by Midnight Pass at any time. On the other hand, they also suggested that the dredging of the ICW is the primary reason for the deterioration of Midnight Pass. However, they did not provide any rigorous analysis to validate their suggestion. Our modeling study did not confirm their suggestion either.

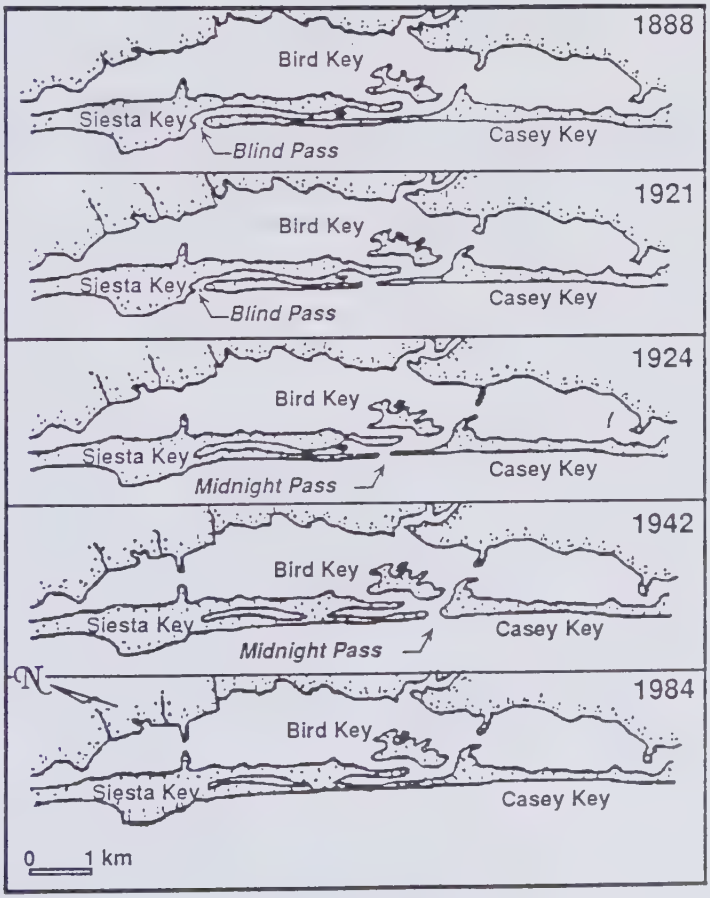

Figure 19. Historical inlet positions in the vicinity of Midnight Pass (Davis *et al.*, 1987).

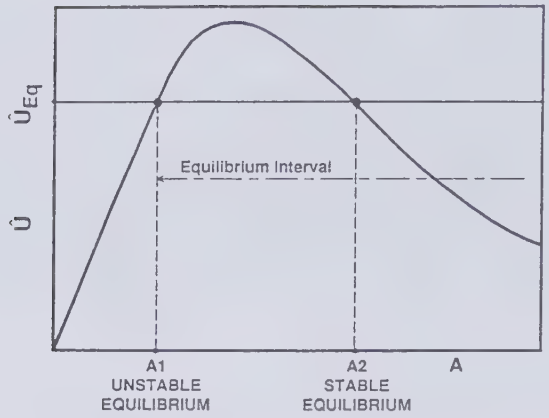

Figure 20. Escoffier diagram adapted from Escoffier (1940 and van de Kreeke (1992).

To study the stability of a tidal inlet, one can use the simple analysis of Escoffier (1940). For a multiple inlet system, the analysis is more complicated as shown by van de Kreeke (1985). Basically, for a single inlet system, one needs to calculate a "closure curve" that relates the cross-sectional area of an inlet with the maximum current in the inlet for given tidal conditions, inlet length and inlet shape (Figure 20). The next step is to compute an equilibrium velocity (U_{eq}) at which the "sediment transport capacity" of the inlet currents is just sufficient to remove the sediment deposited in the inlet. Thus, as shown in Figure 20, an inlet with cross-sectional area between A_1 and infinity is a stable inlet, while the inlet becomes unstable if the cross-sectional area is less than A_1.

The closure curve and the equilibrium current have generally both been determined by using simple empirical relationships, as was discussed by van de Kreeke (1992). van de Kreeke (1990) pointed out that to determine the exact closure for a real tidal inlet, it requires a full-fledged multi-dimensional model for the hydrodynamics of the inlet and the bay. Existing inlet closure curves were determined by using simpler models that contain the unrealistic assumption of a uniformly fluctuating bay level, and are hence not accurate. With the 3-D hydrodynamic model developed in this study, it is possible to compute the closure curve for Midnight Pass. The 3-D model results showed that the maximum current in Midnight Pass could reach more than 1 ms^{-1}, which is larger than the typical equilibrium current of 0.8 ms^{-1} (van de Kreeke, personal communication).

Conclusions

A field and modeling study on the circulation and transport in Sarasota Bay has been conducted. This study focused on the effects of tidal inlets on circulation and

flushing in Sarasota Bay. Based on the field data collected in 1991, a three-dimensional circulation model of the Sarasota Bay system has been developed.

Results of the study showed that the inlets affect the Sarasota Bay system in several ways. Due to the interaction of tides that enter from different inlets, null zones with little flow are formed in Palma Sola Bay, the middle of Sarasota Bay, and behind the closed Midnight Pass in Little Sarasota Bay. Flushing calculation showed low flushing rates in these areas. Near the inlets, interesting residual flow patterns are observed. Persistent north-to-south residual flow has been observed at the Anna Maria Station. Recent studies (Sheng and Peene, 1993 and Sheng *et al.*, 1994) showed that the southerly residual flow was caused by the combined actions of nonlinear tidal circulation, wind and fresh water flow from Manatee River. The southerly residual flow was successfully simulated.

Using the 3-D circulation model, we examined the potential impact of opening Midnight Pass. Model results showed that if Midnight Pass was to be reopened, flushing behind Midnight Pass will improve. However, since the null zone is pushed north, flushing in Roberts Bay will decrease.

Acknowledgement This study is supported by the Sarasota Bay National Estuary Program, U.S. Geological Survey and Supercomputing Center of Florida State University.

References

Cameron, W.M. and D.W. Pritchard, Estuaries, in *The Sea*, edited by M.N. Hill, **2**, pp. 306-324, Wiley, New York, 1963.

Davis, R.A., Jr., A.C. Hine, and M.J. Bland, Midnight Pass, Florida: Inlet Instability Due to Man-Related Activities in Little Sarasota Bay, *Coastal Sediments* 2062-2077, 1987.

Escoffier, F.F., The Stability of Tidal Inlets, *Shore and Beach*, 8(4), 114-115, 1940.

Fischer, H.B., E.J. List, R.C.Y. Koh, J. Imberger, and N.H. Brooks, 1979: *Mixing in Inland and Coastal Waters*, Academic Press.

Hansen, D.V. and M. Rattray, Gravitational Circulation in Straits and Estuaries, *J. Mar. Res.*, 23, 104-122, 1965.

Ippen, A.T. and D.R.F. Harlemen, Tidal Dynamics in Estuaries, in *Estuary and Coastline Hydrodynamics*, pp. 493-545, McGraw Hill, 1966.

Johnson, B., Y.P. Sheng, K. Kim, and R. Heath, Development of a Three-Dimensional Hydrodynamic Model of Chesapeake Bay, *Estuarine and Coastal Modeling* edited by M.L. Spaulding, pp. 162-171, ASCE, 1989.

Peene, S.J., Y.P. Sheng, and S. Houston, A Field and Modeling Study of Tidal and Storm Wind-Driven Circulation in Sarasota Bay, In *Estuarine and Coastal Modeling*, pp. 357-368, ASCE, 1992.

Sheng, Y.P. Numerical Modeling of Coastal and Estuarine Processes Using Boundary-Fitted Grids, *Technical Memo No. 86-02*, Aeronautical Research Associates of Princeton, N.J., 1986a.

Sheng, Y.P. On Modeling Three-Dimensional Estuarine and Marine Hydrodynamics, in *Three-Dimensional Models of Marine and Estuarine Dynamics* edited by J.C.J. Nihoul and B.M. Jamart, pp. 35-54, Elsevier Oceanographic Series, Elsevier, 1987.

Sheng, Y.P. Evolution of a Three-Dimensional Curvilinear-Grid Hydrodynamic Model for Estuaries, Lakes, and Coastal Waters: CH3D, In *Estuarine and Coastal Modeling* edited by M.S. Spaulding, pp. 40-49, American Society of Civil Engineers, 1989.

Sheng, Y.P. and S.J. Peene, A Modeling and Field Study of Circulation and Transport in Sarasota Bay, a National Estuary, In *Proceedings of 1991 NEP Science Symposium*., 1991.

Sheng, Y.P. and C. Villaret, Modeling the Effect of Suspended Sediment Stratification on Bottom Exchange Processes," *J. Geophys. Res.*, 94(C10), 14429-14444, 1989.

Sheng, Y.P., J.-K. Choi and A.Y. Kuo, Three Dimensional Numerical Modeling of Tidal Circulation and Salinity Transport in James River Estuary, in *Estuarine and Coastal Modeling* edited by M.L. Spaulding, pp. 209-218, ASCE, 1989b.

Sheng, Y.P., H.-K. Lee and K.H. Wang, On Numerical Strategies of Estuarine and Coastal Modeling, *Estuarine and Coastal Modeling* edited by M.L. Spaulding, pp. 291-301, ASCE, 1989a.

Sheng, Y.P., X.-J. Chen, M. Fisher, and K.R. Reddy, Resuspension of Fine Sediments and Nutrients during an Episodic Event in a Shallow Estuary. *Technical Report,* Coastal & Oceanographic Engineering Department, University of Florida, Gainesville, Florida 32611, 1992.

Sheng, Y.P. and S.J. Peene, A Field and Modeling Study of Residual Circulation in Sarasota Bay and Tampa Bay, Florida, in *Estuarine and Coastal Modelling III* edited by M.L. Spaulding, *et al.,* pp. d641-655, ASCE, 1993.

Sheng, Y.P., E. Yassuda, S. Schofield and S.J. Peene, A Study on the Effect of Manatee River Discharge on Circulation and Transport in Sarasota Bay, Technical Report, Coastal & Oceanographic Engineering Department, University of Florida, Gainesville, Florida, 32611, 1994.

Tomasko. Personal communication, 1992.

van de Kreeke, J. Stability of Tidal Inlets - Pass Cavallo, Texas," *Estuarine, Coastal and Shelf Science*, 21, 33-43, 1985.

van de Kreeke, J. Personal communication, 1993.

van de Kreeke, J. Stability Analysis of a Two-Inlet Bay System,' *Coastal Engng*, 14, 482-497, 1990.

van de Kreeke, J. Stability of Tidal Inlets; Escoffier's Analysis, *Shore and Beach*, 9-12, 1992.

Zimmerman, J.T.F. Topographic Generation of Residual Circulation by Oscillatory (Tidal) Currents, *Geophys. Astrophys. Fluid Dynam.*, 11, 35-47, 1978.

Appendix A

A Brief Description of CH3D

CH3D is a three-dimensional curvilinear-grid hydrodynamics model developed by Sheng (1987, 1989). Basic assumptions of the model include: (1) the pressure distribution is hydrostatic, (2) the Boussinesq approximation is valid, and (3) the eddy viscosity concept is valid. With these assumptions, equations of motion for an incompressible fluid can be written in terms of the contravariant velocity components u and v, and the vertical velocity, ω in a horizontally curvilinear (ξ and η) and vertically stretched (σ) grid system $\sigma = (z - \zeta)/(h + \zeta)$ where:

$$\zeta_t + \frac{1}{J}\left[\frac{\partial}{\partial\xi}(JHu) + \frac{\partial}{\partial\eta}(JHv)\right] = 0 \qquad \text{(A-1)}$$

$$\frac{1}{H}\frac{\partial Hu}{\partial t} = -g\left[g^{11}\frac{\partial\zeta}{\partial\xi} + g^{12}\frac{\partial\zeta}{\partial\eta}\right] + \frac{g^{12}}{J}fu + \frac{g^{22}}{J}fv$$

$$+\frac{1}{HJ^2}\left\{x_\eta\left[\frac{\partial}{\partial\xi}(y_\xi JHuu + y_\eta JHuv) + \frac{\partial}{\partial_\eta}(y_\xi JHuv + y_\eta JHvv)\right]\right.$$

$$\left. - y_\eta\left[\frac{\partial}{\partial\xi}(x_\xi JHuu + x_\eta JHuv) + \frac{\partial}{\partial_\eta}(x_\xi JHuv + x_\eta JHvv)\right] - J^2\frac{\partial Hu\omega}{\partial\sigma}\right.$$

$$-\frac{g}{\rho_0}\left[H\int_\sigma^0\left(g^{11}\frac{\partial\rho}{\partial\xi} + g^{12}\frac{\partial\rho}{\partial\eta}\right)d\sigma\right.$$

$$\left.+\left[g^{11}\frac{\partial H}{\partial\xi} + g^{12}\frac{\partial H}{\partial\eta}\right]\left(\int_\sigma^0\rho d\sigma + \sigma\rho\right)\right] + \frac{1}{H^2}\frac{\partial}{\partial\sigma}\left(A_v\frac{\partial u}{\partial\sigma}\right)$$

+ Horizontal Diffusion (A-2)

$$\frac{1}{H}\frac{\partial Hv}{\partial t} = -g\left(g^{21}\frac{\partial\zeta}{\partial\xi} + g^{22}\frac{\partial\zeta}{\partial\eta}\right) - \left(\frac{g^{11}}{J}fu + \frac{g^{21}}{J}fv\right)$$

$$+\frac{1}{HJ^2}\left\{y_\xi\left[\frac{\partial}{\partial\xi}(x_\xi JHuu + x_\eta JHuv) + \frac{\partial}{\partial_\eta}(x_\xi JHuv + x_\eta JHvv)\right]\right.$$

$$\left. - x_\xi\left[\frac{\partial}{\partial\xi}(y_\xi JHuu + y_\eta JHuv) + \frac{\partial}{\partial_\eta}(y_\xi JHuv + y_\eta JHvv)\right] - J^2\frac{\partial Hv\omega}{\partial\sigma}\right.$$

$$-\frac{g}{\rho_0}\left[H\int_\sigma^0\left(g^{21}\frac{\partial\rho}{\partial\xi} + g^{22}\frac{\partial\rho}{\partial\eta}\right)d\sigma\right.$$

$$\left.+\left[g^{21}\frac{\partial H}{\partial\xi} + g^{22}\frac{\partial H}{\partial\eta}\right]\left(\int_\sigma^0\rho d\sigma + \sigma\rho\right)\right] + \frac{1}{H^2}\frac{\partial}{\partial\sigma}\left(A_v\frac{\partial v}{\partial\sigma}\right)$$

+ Horizontal Diffusion (A-3)

where the horizontal diffusion terms are listed in Sheng (1986a). The temperature (T) and salinity (S) equations are similar as described in the following equation for ϕ which stands for either T or S:

$$\frac{1}{H}\frac{\partial H\phi}{\partial t} = \frac{\partial}{H^2\partial\sigma}\left(D_v\frac{\partial\phi}{\partial\sigma}\right) - \frac{1}{HJ}\left[\frac{\partial}{\partial\xi}(JHu\phi) + \frac{\partial}{\partial\eta}(JHv\phi)\right] - \frac{1}{H}\frac{\partial H\omega\phi}{\partial\sigma} + D_H\left[g^{11}\frac{\partial^2\phi}{\partial\xi^2} + 2g^{12}\frac{\partial^2\phi}{\partial\xi\partial\eta} + g^{22}\frac{\partial^2\phi}{\partial\eta^2}\right] \quad \text{(A-4)}$$

where J is the Jacobian of transformation, g^{ij} is the metric coefficient, (A_v, D_v) and (A_H, D_H) are the vertical and horizontal turbulent eddy coefficients, $H = h + \zeta$ and h is the mean depth measured from mean sea level. For the flushing calculation, Equation A-4 is also used to describe the dynamics of concentration of a conservative species.

The vertical turbulent eddy coefficients A_v and D_v in the above equations are computed from a simplified second-order closure model (Sheng, 1987; Sheng *et al.*, 1989b; Sheng and Villaret, 1989). The horizontal turbulent eddy coefficients are assumed to be constant and computed by multiplying the smallest grid size and a fraction of the maximum horizontal current.

Water level obtained at the offshore stations (one near Tampa Bay and two near Sarasota Bay) were interpolated along the open boundaries for forcing of the model. Freshwater flows from several tributaries were also included.

13

Internal Tidal Asymmetry in Channel Flows: Origins and Consequences

D. A. Jay and J. D. Musiak

Abstract

Non-linear, shallow-water processes transfer energy from the surface tide to higher and lower frequencies to create a barotropic tidal spectrum. Production of higher harmonics or overtides at multiples of the dominant tidal frequency is termed "barotropic tidal asymmetry" because it distorts the free surface and causes flood- or ebb-dominant currents, depending on the relative phases of the tide and its overtides. Tidal distortion of the density field drives an analogous transfer of energy to residual and overtide internal modes; i.e., an "internal tidal asymmetry." The actual mechanism responsible for the internal non-linearity is an asymmetry in bed stress that has two primary aspects: (1) differential tidal advection (tidal straining) of a strong horizontal density gradient brings about tidal variations in stratification and thus in vertical turbulent mass and momentum exchange; and (2) baroclinic and barotropic pressure gradients act in concert on flood but in opposition on ebb. Observations from the Columbia River estuary show that internal tidal asymmetry can cause an entire spectrum of overtide currents. The most prominent of the internal overtides is M_4 (the first overtide of M_2), with maximum current amplitudes of 0.25-0.4 ms^{-1} in an environment where the amplitude of the dominant (M_2) current constituent is O(1-1.4 ms^{-1}). These internal M_4 currents are three to 10 times larger than the currents associated with the barotropic M_4 tide (amplitude 0.01 to 0.03m), and they exhibit 180° phase changes in the vertical, another factor that distinguishes them from barotropic tidal currents. Furthermore, the residual surface-to-bed velocity difference of ~1 ms^{-1} is too large to be accounted for by linear processes (gravitational circulation and mean outflow), and model calculations show that internal tidal asymmetry is also the predominant mechanism causing vertical shear

Mixing in Estuaries and Coastal Seas
Coastal and Estuarine Studies Volume 50, Pages 211-249
Copyright 1996 by the American Geophysical Union

in the residual flow. A literature survey has identified 20 estuaries in addition to the Columbia that exhibit signs of internal tidal asymmetry, and it is likely a common feature of narrow systems with strong tides and riverflow. Finally, observations suggest that overtide and residual currents generated by internal tidal asymmetry play a dominant role in maintaining the salt and sediment balances in narrow, stratified estuaries.

Introduction

Quadratic tidal non-linearities will in general drive both higher harmonics or overtides at multiples of the basic tidal frequency, and low-frequency residual flows. Ianniello (1977) and others have explored the implications of this fact for non-linear residual circulation modes generated by convective acceleration and a Stokes drift. Recent investigations of tidal barotropic overtide generation have argued, however, that bed stress non-linearities are the dominant cause of barotropic overtides (Parker, 1991; Godin, 1991; Friedrichs and Madsen, 1992). The resulting barotropic overtides follow one of two patterns. In narrow systems where tidal changes in depth are the primary generating factor, wave steepening occurs, leading to short sharp floods and long slow ebbs. This is an example of the classical finite-amplitude non-linearity examined by Stokes (1847). It may progress to such a degree that the transition from low water to high water is effectively instantaneous, and a bore is formed. In estuaries with broad flats on the other hand, tidal variability in width can cause short sharp ebbs and long slow floods. The term "barotropic tidal asymmetry" has arisen to describe both of these forms of barotropic non-linearity because of their distorting effects on the free surface. Such barotropic effects are important, because they alter the times of high and low water and may cause substantial sediment transport. The latter may be either flood or ebb-dominant, depending on the sense of the non-linearity (Speer *et al.*, 1990).

Most previous studies of baroclinic forcing in estuarine tidal channels from Hansen and Rattray (1965) to McCarthy (1993) have, in contrast to those of barotropic processes, focused on steady two-layer motions driven by a horizontal density gradient. A dynamical picture of estuarine circulation in which barotropic non-linearities are predominantly frictional, leading to both residual and overtide generation, while internal circulation exists only in the residual frequency band and is driven by a steady density gradient and/or convective accelerations is incomplete and even contradictory. If there is an asymmetry in bed stress, it must interact with the density and turbulence fields. This will excite barotropic and baroclinic motions at a variety of frequencies. The role of time-varying stratification in generating residual flows was recognized by Jay (1987, 1990), Jay and Smith (1990a), Uncles and Stephens (1990) and West *et al.* (1990). Quadratic non-linearities must produce, however, both overtide and residual flows as has long been recognized in barotropic analyses. Despite the work of Trowbridge and Madsen (1984) on generation of higher harmonic motion driven by time-varying, vertical turbulent stress divergence in neutrally stratified, wave boundary layers, the analogy between baroclinic and

barotropic non-linearities was not exploited until Jay (1991a) suggested that "internal tidal asymmetry" ought to generate overtides as well as residual flow.

The primary purpose of this paper is to present observations and model results for the Columbia River estuary that show internal asymmetry to be the largest source of both overtide and baroclinic residual currents in a strongly forced tidal channel. Just as in the case of barotropic non-linearities, the dominant forcing mechanisms are associated with the vertical stress divergence rather than non-linear convection. The logic of the argument that follows is straightforward. Aside from topographic scattering (Baines, 1982) of incoming barotropic overtide waves, there are no known linear mechanisms to drive internal overtide circulations. While other internal processes such as secondary, cross-channel circulation caused by channel curvature may also bring about internal overtide and residual flows, only internal tidal asymmetry can produce the observed pattern of elevated currents. Linear topographic scattering is not relevant to the present case for two reasons. First, there is not enough energy (by a factor of about three to 10) in barotropic overtide modes near the estuary mouth to produce the observed internal overtide circulation; energy must be transferred by non-linear processes from the primary tidal circulation. Second, topographic scattering preferentially produces short gravity-wave internal tides with characteristics aligned with the bottom slope in the generation region. Only long internal tides can exist (other than as local perturbations) in typical estuarine geometries, where the ratio of depth to length is typically $O(10^{-4})$. This ratio is one to two orders of magnitude less than is typical for continental shelf environments, where short internal tides often play an important role. Interpretation of observations of internal residual circulation is complicated by the existence of a variety of linear processes that may contribute to residual shear, including riverflow, atmospheric forcing and gravitational circulation. Simple models of the pertinent residual flow processes are therefore used to demonstrate that internal tidal asymmetry is the dominant residual flow process as well. Finally, a few observations are presented to show the importance of internal asymmetry in suspended sediment transport in shallow, stratified estuaries. Thus, the presence of large internal overtides demonstrates the existence of potent internal non-linearities.

Dynamics of Internal Tidal Asymmetry

Causes and Consequences of Tidally Varying Stratification

Internal tidal asymmetry is caused by the presence of a strong horizontal density gradient that does not change sign tidally, though its strength is tidally modulated by compression and dilation of the density field. This density gradient comes into play in two distinct ways (Jay, 1990). First, the baroclinic and barotropic pressure gradients act together near the bed on flood, while they are in opposition on ebb. Second, tidal straining of the horizontal density gradient causes tidal variations in stratification. On flood, any near-surface velocity maximum causes advection of

denser water over lighter water, minimizing stratification. On ebb, shear in the water column advects lighter water over denser water, increasing stratification.

These two aspects of internal tidal circulation interact through vertical turbulent momentum exchange. This can be understood by considering the flow associated with a single barotropic tidal constituent in a hypothetical, weakly stratified channel of constant width and depth, assuming also the existence of a horizontal density gradient caused by a riverflow imposed from the landward end. Because of differential advection (tidal straining) of the density field and the baroclinic pressure gradient, flood flows in such a system would be nearly uniform in the vertical or concentrated near the bed. In the lower part of the flow at least, vertical turbulent momentum exchange would approach a value typical for a neutrally stratified tidal flow and cause a maximum in bed stress during flood in a positive estuary. Increased stratification on ebb would inhibit vertical momentum exchange. Shears would become large with ebb outflow concentrated near the free surface, resulting in a considerable reduction of bed stress.

One must then ask how internal tidal asymmetry would manifest itself in a harmonic analysis in the above hypothetical estuary. As a consequence of the flood-to-ebb change in vertical distribution of the horizontal tidal flow, the Eulerian current does not reverse exactly at each depth (Figure 1). A simple Fourier decomposition shows that internal asymmetry causes quadratic non-linearities in vertical momentum exchange to appear as internal overtide and residual modes (Jay, 1991a). Z_0 (mean), M_4 and M_8 currents will emerge in the current record in the proportion of about 0.63δ, 0.42δ and 0.08δ, respectively, with δ as defined in Figure 1. These modes are internal in that they do not generate a surface tide or any net overtide transport; thus they must show a 180° phase reversal in the vertical. The overtide and residual flow near the bed in Figure 1 act to strengthen the flood near the seabed and the ebb near the free surface. By analogy to the barotropic case, we may refer to this type of the internal asymmetry as "flood-oriented".

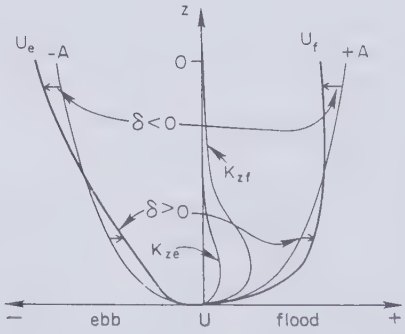

Figure 1. Definition sketch for internal tidal asymmetry. U_f and U_e represent, respectively, flood and ebb observed tidal velocity profiles exclusive of mean flow effects. A represents the reversing part of the tidal flow; i.e., that portion associated with the dominant M_2 tidal constituent in a harmonic analysis. δ represents the non-reversing part of the tidal flow associated with internal tidal asymmetry; it integrates to zero by definition.

The above, idealized distribution of flow energy amongst the various constituents pertains only if: 1) there is only one major tidal species; 2) the flow is two-dimensional in the along-channel (x) and vertical (z) directions; 3) both flood and ebb velocity profiles increase monotonically from the bed; 4) maximum and minimum stratification are exactly 180° degrees out of phase; and 5) the dependence of vertical eddy diffusivity K_m on gradient Richardson number (and thus on stratification) is linear everywhere. In fact, multiple tidal constituents, three-dimensional effects, subsurface velocity maxima on flood, complex time variations in stratification, and other non-linearities are present. These features generate an entire spectrum of internal overtides with complex cross-sectional distributions in the data presented below.

Distinctive Symptoms of Internal Tidal Asymmetry

Linear density forcing and barotropic and internal tidal asymmetry should leave distinctive signatures in the residual flow band of current records. It is difficult however, to collect sufficiently long current records in enough locations to actually distinguish these contributions to the residual flow. Thus analysis of the overtide band, to which steady, linear density forcing does not contribute, has proven to be the simplest way to identify internal asymmetry. Still, internal tidal asymmetry is not the only source of overtide currents or even the only internal overtide mode. Two other processes need also to be considered in shallow tidal channels: barotropic overtides and cross-channel, secondary circulation due to channel curvature. Barotropic overtides should, like internal tidal asymmetry, be predominantly along-channel oriented, but do not have the 180° phase shift in the vertical that is characteristic of an internal mode. Secondary circulation due to channel curvature is an internal mode that also appears at mean and overtide frequencies—near-surface flow moves to the outside of a channel bend on both flood and ebb. This process differs from internal asymmetry because it is primarily directed cross-channel, not along-channel. Observed overtide currents at most locations show a combination of these three effects.

Harmonic analyses of current and surface elevation data can be used together to differentiate these three overtide modes. Specific factors that distinguish internally generated overtides from those produced by other mechanisms are: 1) along-channel currents that are stronger than can be justified by the barotropic surface tide; 2) a 180° phase reversal in the vertical; and 3) a decrease in current amplitude at the upstream limits of salinity intrusion. Moored current meter records are useful for the statistical accuracy that is available from a relatively long record and for the number of overtide constituents that may be distinguished. Comparison of overtide amplitudes in current meter data to those found in tidal height records distinguishes internal and barotropic modes. The method is based on mass conservation and the assumption that the flow is essentially two-dimensional in the along-channel (x) and vertical (z) directions, so that tidal transport and tidal elevation are related by the ratio of frequency to complex wavenumber. The simplest procedure is to calculate a

normalized overtide current amplitude at individual current meters; that is to divide the ratio of M_4 current to M_4 height amplitude by the ratio of M_2 current to M_2 height amplitude. This normalized overtide current amplitude should be O(1-2) in the absence of non-linearities driven by internal processes and channel curvature, because impedance (the ratio of wave transport to elevation) varies only weakly with frequency in the presence of even small along-channel changes in cross-sectional area (Jay, 1991b). It is unusual, however, for more than three current meter records to be available for a single mooring, and the greater spatial resolution of ADCP data is required to define the cross-sectional distribution of internal overtide currents. This has been determined from 25 to 50 hr ship-mounted ADCP time series.

Observations of Internal Tidal Asymmetry

All three requisite types of data listed in the previous section – moored current meter records at multiple depths, time-series of ADCP observations, and surface elevation records – appear at the moment to be available only in the Columbia River estuary (Figure 2). Let us, therefore briefly sketch the oceanographic context of this system based on previous studies (Jay and Smith, 1990 a,b,c). Like other west-coast United States estuaries, the Columbia has a mixed tide with M_2 being the largest constituent; its amplitude is about 0.9 to 1 m in the estuary. Strong tidal currents and a riverflow of about 3,000 to 15,000 $m^3\ s^{-1}$ cause the estuary to be primarily sand bedded. There are two narrow channels through broad sand flats in the lower estuary. Internal overtides require the presence of a strong horizontal salinity gradient, and tidal-maximum salinity intrusion in the Columbia varies with riverflow and the neap-spring cycle from about km-20 to km-40 (Jay and Smith, 1990c). The resulting salinity gradient of 33 psu over 20 to 40 km is perhaps typical for a river-estuary, but is considerably stronger than that found in many drowned coastal plane systems.

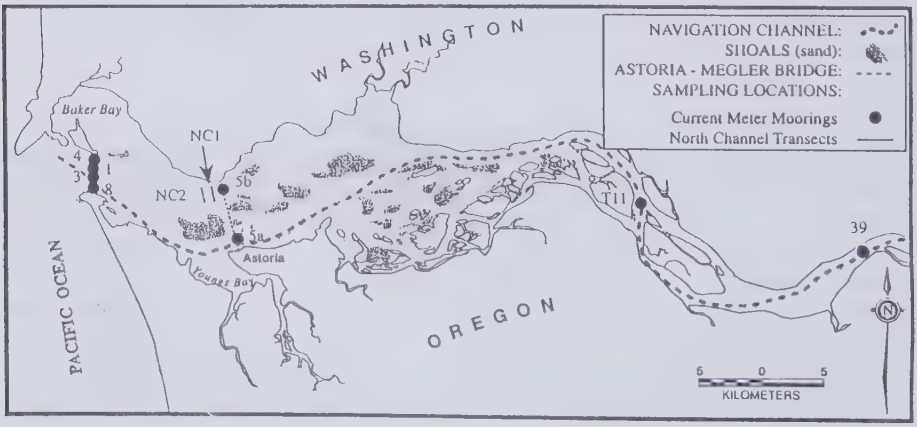

Figure 2. Location sketch for the Columbia River estuary showing the locations of current meter and ADCP stations used in subsequent analyses.

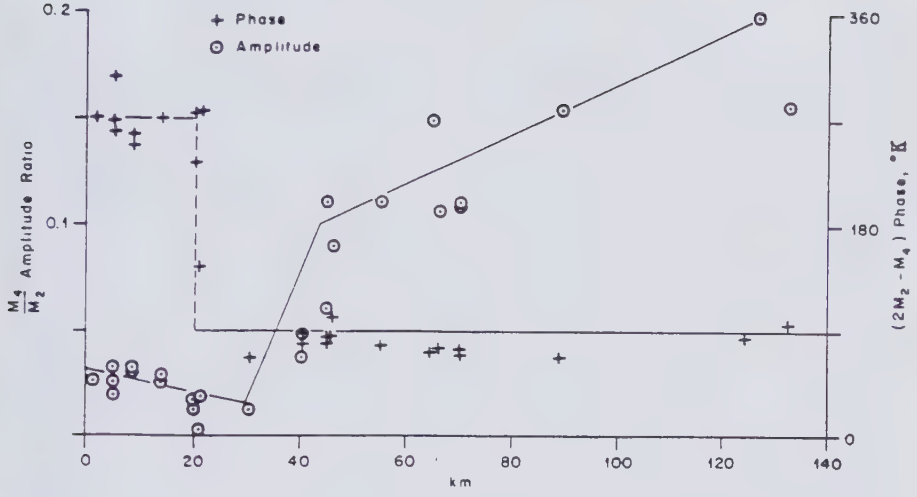

Figure 3. Characteristics of the barotropic M_4 surface tide in the Columbia River and estuary, based on surface elevation records ranging from 3 to 12 months in length (adapted from Jay, 1991a). Normalized surface elevation amplitude (M_4/M_2) and phase difference ($2M_2$ - M_4) are plotted against river km.

Prominent neap-spring transitions from highly stratified to weakly stratified or even partially mixed are another feature that the Columbia shares with other estuaries showing evidence of internal tidal asymmetry. Internal asymmetry never entirely disappears even under weakly stratified conditions, but the flows excited thereby appear to be much larger under highly stratified conditions. The variability over the tidal month of the density field and in the flows driven by its advection further complicates the spectrum of currents driven by internal asymmetry.

The Columbia is also a good system in which to examine internal asymmetry, because barotropic overtides are quite small except landward of salinity intrusion, and internal processes are the dominant cause (we can say in retrospect) of both residual and overtide currents. The M_4/M_2 ratio in surface elevation records is between 0.01 and 0.05 seaward of km-40 (Figure 3). Just landward of this reach, the M_4/M_2 ratio grows rapidly. Narrow tidal channels usually exhibit finite amplitude wave steepening, but the $2M_2$–M_4 phase difference in the Columbia is about 270° below km-35, indicating neither flood nor ebb dominance. Upstream of this point, the phase difference is 70-90° or weakly ebb dominant, and almost 180° out of phase with the overtide flow further seaward. The reasons for this pattern have not been clarified, but strong riverflow and a weakly convergent geometry evidently modify the wave-steepening process usually seen in such channels.

Evidence of Internal Asymmetry from Moored Instrument Data

Normalized M_4 current amplitudes (the ratio of M_4 current to M_4 height divided by the ratio of M_2 current to M_2 height; Figure 4) present a very different pattern from that of the barotropic heights (Figure 3). In the tidal river above salinity intrusion normalized amplitude is between 0.75 and 2.5. Deviations from unity in this reach may reflect the influence of channel curvature or may be associated with frequency dependence of the impedance. In contrast, the normalized current amplitudes within the estuary proper are, with one exception, between 3 and 12. Further evidence for the existence of overtides driven by internal tidal asymmetry can be seen in 11 current meter records each of 15 to 30 days duration collected by the National Ocean Survey in August-September 1981 on a section at about km-8 (stations 1, 3, 4 and 8 in Figure 2). While M_2 amplitude shows only a single maximum focussed in the north channel, M_4 amplitude shows maxima in both north and south channels. Anomalously large normalized current amplitudes at some locations in the cross-section and 180° phase changes characteristic of internal tidal asymmetry are evident in harmonic analyses of along-channel velocity (Table 1). But it is unclear, because of the gap between 7.3 and 18.9 m in the deepest part of the channel at CM-3, how to contour these phase data and whether a 180° phase reversal occurs in the vertical at any location. As with the ADCP data discussed below, cross-channel overtide velocities (not listed) are substantial and indicate the influence of channel curvature.

TABLE 1. Moored Current Meter Harmonic Constants for Clatsop Spit Section, August-September 1981, Along-Channel Velocity[1]

Station and water depth, m	Meter depth m	Distance from north side m	M_2 amplitude ms^{-1}	M_2 phase °g	M_4 amplitude ms^{-1}	M_4 phase °g	Normalized amplitude[2]	Relative phase $2M_2$-M_4 °g
CM-4/14.9	3.5	210	1.29	192	0.110	77	4.84	307
	8.5		0.97	185	0.075	97	4.49	274
	13.7		0.57	169	0.091	103	9.27	237
CM-1/14.0	5.0	630	1.86	186	0.038	210	1.19	163
	8.0		1.39	192	0.050	264	2.10	120
	13.1		0.78	178	0.016	188	1.22	169
CM-3/22.0	4.3	1650	1.40	194	0.082	129	3.32	260
	7.3		1.36	190	0.039	134	1.67	246
	18.9		0.67	177	0.012	87	1.03	266
CM-8/11.0	5.8	2360	0.75	179	0.086	255	6.56	104
	9.8		0.35	168	0.050	232	8.17	104

[1] The normal to the section was taken to be 100°T. Raw current meter data provided courtesy of the National Ocean Survey.

[2] Normalized current amplitude is, as discussed in the text, the ratio of M_4 current to height over the ratio of M_2 current to height.

Comparison of normalized amplitudes for a variety of overtide frequencies at two stations within the estuary showing substantial internal overtide effects (CM-4 and CM-8 at river km-8, Figure 2 and Table 2a) with typical data from upriver of salinity intrusion (CM-T11 at river km-62 and CM-39 at river km-87, Figure 2 and Table 2b) is useful in understanding differences between estuarine, internally generated overtides and riverine, barotropic overtides. First, constituents at CM-4 and CM-8 in the terdiurnal (e.g., M_3), quarterdiurnal (e.g., M_4), seventh-diurnal and possibly eighth-diurnal bands show enlarged normalized amplitudes, while amplitudes for these constituents are all, except for S_4 and M_8 at two locations, O(1) at CM-T11 and CM-39. Fifth- and sixth-diurnal constituents show more amplification upriver than in the estuary for reasons that are obscure. Their enlargement does not appear to be associated with an increase in impedance with frequency, because $3MK_7$ and M_8 do not show a similar increase. Moreover, all peaks that show enlargement at CM-T11 are quite small (0.001-0.01 m) in the tidal height analysis, and all change amplitudes substantially if a different nearby tide gauge is used in the normalization. $2SM_6$, for example, does not show the same enlargement of normalized current amplitude at CM-39, where its height amplitude is larger, as at CM-T11. This suggests that statistical significance may have been lost for some small constituents in the currents or heights analyses. Another striking difference is that normalized amplitudes from CM-39 and CM-T11 show very little vertical variation in the terdiurnal and quarterdiurnal bands, while such variations are substantial at CM-4 and CM-8. Finally, there is an important difference between the current meter harmonic analysis results in Tables 1 and 2 and those that follow for ADCP data. Internally generated currents are sensitive functions of the density field, which changes substantially over the tidal month (Jay and Smith, 1990c). Thus 15 to 30 day harmonic analyses of current data will inevitably average out much of the detail that is present in the ADCP results.

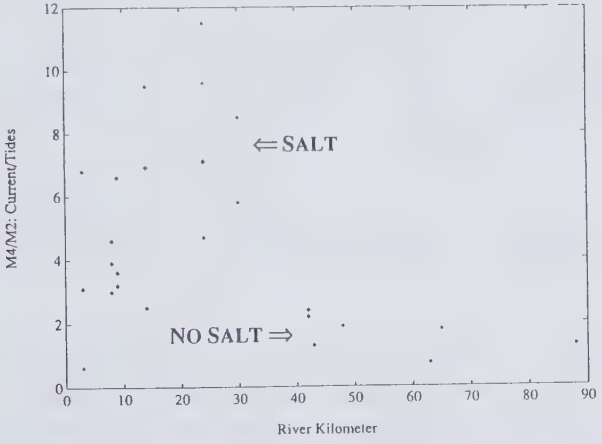

Figure 4. Ratio of normalized M_4 to M_2 current amplitude vs. river kilometer. Tidal height amplitudes are used to normalize both M_4 and M_2 currents. Normalized ratios substantially greater than one are confined to that portion of the system where salinity intrusion is found, which strongly suggests that internal tidal asymmetry is responsible for the phenomenon.

TABLE 2a. The overtide spectrum at selected stations — Normalized along-channel current amplitudes[1] in the estuary

Station[2]/river km meter depth, m/depth, m	CM-4/ 8 3.5/14.9	CM-4/ 8 8.5/ 4.9	CM-4/ 8 13.7/14.9	CM-8/ 8 5.8/11.0	CM-8/ 8 9.8/11.0
Constituent:					
MO_3	-	3.57	-	-	0.63
M_3	1.95	7.46	3.61[3]	1.05[3]	7.41
MK_3	-	2.31	-	-	3.51
SK_3	1.83	2.28	5.18	-	2.05
MN_4	-	0.91	-	-	4.27
M_4	4.84	4.49	9.27	6.56	8.17
SN_4	-	8.93	-	-	-
MS_4	3.58	2.08	7.18	-	4.13
S_4	0.11	6.06	13.0	-	1.42
$2MK_5$	0.59	1.14	1.69	0.71	1.21
$2SK_5$	0.50	2.69	5.61	3.86	2.67
$2MN_6$	-	2.31	-	-	2.49
M_6	1.87	1.43	1.56	2.56	2.61
$2MS_6$	2.41	2.00	0.33	-	1.69
$2SM_6$	1.96	1.21	12.5	-	2.88
$3MK_7$	5.86	2.06	1.75	6.06	6.39
M_8	2.35	3.48	5.87	3.97	2.41

1 Normalized along-channel current amplitude is the ratio of M_4 current amplitude to M_4 height amplitude over the ratio of M_2 current amplitude to M_2 height amplitude.

2 Raw current data courtesy of National Ocean Survey.

3 The M_3 current has been compared to the MK_3 height, the largest terdiurnal height constituent. If M_3 heights are used then values between 5 and 18 result.

In summary, analyses of moored instrument data show 180° overtide phase reversals with depth, and amplification of M_4 and possibly M_8 normalized current amplitudes, as predicted by the simple theory summarized in Figure 1. This confirms the importance of internally generated overtides. The fact that a variety of other overtide constituents are also amplified indicates a need for a more detailed theoretical analysis. In contrast, normalized current amplitudes are O(1) for most overtide constituents upriver of salinity intrusion, because internal overtides are absent in this part of the system.

TABLE 2b. The overtide spectrum at selected stations — Normalized along-channel current amplitudes[1] upstream of salinity intrusion

Station[2]/river km meter depth, m/depth, m	CM-T11/ 62 1.5/15	CM-T11/ 62 8.2/15	CM-39/ 87 4.6/18	CM-39/ 87 7.6/18	CM-39/ 87 15.8/18
Constituent:					
MO_3	1.13	1.19	--	--	--
M_3	0.80	1.77	1.08[3]	1.17[3]	2.04[3]
MK_3	0.62	0.73	--	--	--
SK_3	0.84	1.80	0.64	1.14	1.80
MN_4	0.67	0.53	--	--	--
M_4	0.91	0.91	1.73	1.78	1.86
SN_4	0.88	1.35	--	--	--
MS_4	1.23	1.07	1.56	1.60	1.53
S_4	3.81	3.33	0.60	1.62	1.05
$2MK_5$	1.04	1.18	2.03	1.96	2.06
$2SK_5$	6.25	5.00	2.57	4.57	6.00
$2MN_6$	1.75	2.06	–	–	–
M_6	3.46	2.23	1.04	1.26	1.77
$2MS_6$	5.33	3.55	1.86	2.67	3.33
$2SM_6$	8.33	10.8	1.84	2.89	1.84
$3MK_7$	0.68	0.54	3.64	1.89	0.95
M_8	2.91	1.45	2.60	2.22	4.07

1 Normalized along-channel current amplitude is the ratio of M_4 current amplitude to M_4 height amplitude over the ratio of M_2 current amplitude to M_2 height amplitude.

2 Raw current data courtesy of National Ocean Survey (CM-39) and the U.S. Army Corps of Engineers, Portland District (CM-T11).

3 The M_3 current has been compared to the MK_3 height, the largest height constituent. If M_3 heights are used then values between 7 and 15 result.

Evidence of Internal Asymmetry from ADCP Data

Details of the cross-sectional distribution of internally generated currents can best be understood using vertical and cross-sectional distributions derived from ADCP and CTDO [conductivity-temperature-depth-optical backscatter (OBS) profiler] observations. These data were collected during three ADCP/CTDO surveys of five to

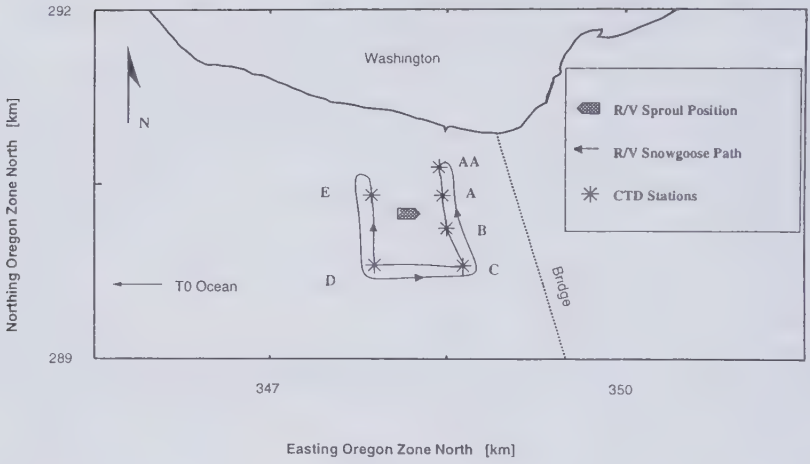

Figure 5. Schematic of vessel track of the R/V Snow Goose and CTDO station locations for data collection on sections NC1 and NC2. Section NC1 consists of stations AA, A, B and C, NC2 of stations D and E. Biological, sedimentological and geochemical studies were carried out on an anchored vessel, the R/V Sproul.

seven weeks duration that were conducted in fall 1990, summer 1991 and spring 1992. The normal pattern of shipboard operations was to obtain 25-50hr time-series of ADCP data along a U-shaped course encompassing two sections (e.g. Figure 5). The two sections would include four to seven CTDO stations. Successive time series were separated by six to12 hr anchor stations at one of the CTDO stations. Thus while only 25-30 hrs of continuous data are available for an entire cross-section, individual stations may have time series of ADCP and CTDO data up to 100 hrs long. At other times, multiple passes back and forth along longitudinal sections were made over 25-30 periods. Most sections were occupied on both spring and neap tides.

ADCP data were collected with a RD Instruments 1.2 mHz narrow-band profiler using 1 m bins; the instrument was set to optimize accuracy in a high-shear environment. Ship velocity was removed by bottom tracking. Vessel orientation was provided by a digital output from the vessel's gyrocompass. Ship position was determined from the vessel's Loran C receiver 1990 (and occasionally as a backup in 1991 and 1992) or GPS (most 1991 and 1992 data). Two North Channel sections at about km-17.5 (Figure 2) were frequently occupied, because they were near the middle of the estuarine turbidity maximum (ETM) that was the primary object of our studies. Each of the two sections was divided into 5 boxes of width ~250 m for analysis of ADCP data. ADCP data were collected on both traverses across the two sections during every circuit around the course, yielding at least two but more typically four to 10 ping ensembles every 45-75 minutes for every box. Each ping ensemble consisted of groups of 10 acoustic "pings" averaged in the ADCP's internal firmware. (A "ping" is an acoustic signal sent out by the ADCP, reflected by particles moving with the flow

and then analyzed by the ADCP for Doppler shift and thus water velocity relative to the instrument.) Ping groups were averaged over 20 seconds in the ADCP processing software to form ping ensembles representing 60-70 individual acoustic pings. Ping ensembles were used without further averaging for harmonic analysis and plots; ADCP errors are discussed below. There were four CTDO stations on section NC1 and two on section NC2 (Figure 5). CTDO data were collected (using an Ocean Sensors model 100 CTD) every 45-75 min on one traverse across each section, so that the other traverse was made without any change of course or speed.

Time series of along-channel velocity U, salinity and gradient Richardson number Ri_g generated from ADCP and CTDO data on 30-31 July 1991 at NC-B, the deepest station on section NC1, are shown in Figure 6. Following the ideas of Geyer (1988), it is desirable to include the effect of both tidal/mean flow shear (measured by the ADCP) and internal wave shear (not resolved by the ADCP) in a total Richardson number denoted by Ri_{gt}. This is accomplished by assuming equipartition of kinetic and potential energy in a saturated internal wave field. Thus, $Ri_{gt} \approx N^2/(S^2+N^2)$, where $N^2 = -g/\rho_0 \, \partial\rho/\partial z$, and S^2 is the square of the shear determined from both along and across-channel ADCP velocity. The vertical differencing involved in calculating Ri_{gt} is a severe test of data quality, and some smoothing is required of both data sets. The CTDO data (originally spaced at about 0.1 m) were filtered and decimated to 1 m to match the ADCP sampling; density inversions were filled. The 20s ADCP ping ensembles were further averaged to 1 min, and a few anomalous pings were eliminated. Because of the central differences used to calculate derivatives and the partial overlap of data between ADCP bins, the inherent resolution of the calculated Ri_{gt} is about 3 m.

Tides during this period were nearly equatorial (i.e., having a small diurnal inequality) but relatively weak; the lesser and greater diurnal ranges were 1.9 and 2.2 m, respectively. Riverflow was about 5,200 m^3s^{-1} or about 60% above seasonal minimum and 80-85% of the annual average. The vertical average of the riverflow velocity in this part of the estuary was about 0.14 ms^{-1}, with Stokes drift compensation flow adding an estimated 0.05-0.06 ms^{-1}. A salt-wedge like salinity intrusion with a prominent, mid-depth velocity maximum occurred on each flood (Figure 6). The strongest ebb velocities occurred near the free surface. Because of the relatively weak tides, substantial net upstream bottom flows were observed, as in Jay and Smith (1990c). Near-bed salinities decreased on ebb as much by vertical mixing as by advection, because very little outflow occurred at the bed. Thus on the weaker ebb, some salinity remained in the bottom few meters even at the onset of the following flood. Both near the free surface and at 10-15 m, flood-ebb differences in velocity suggest a δ of O(1 ms^{-1}). Maximum values of Ri_{gt} were found near the bed at the end of ebb and at the top of the pycnocline at the end of flood. Strong tidal variation in Ri_{gt} occurred at most levels of the flow except at the bed and near the free surface where $Ri_{gt} \approx 0$ throughout the tidal cycle.

Flood and ebb "snapshots" of NC1 cross-sectional distributions of U, σ_t and acoustic echo intensity indicate important features associated with internal asymmetry (Figures 7 and 8). The strongest salinity intrusion is in the deepest part of the

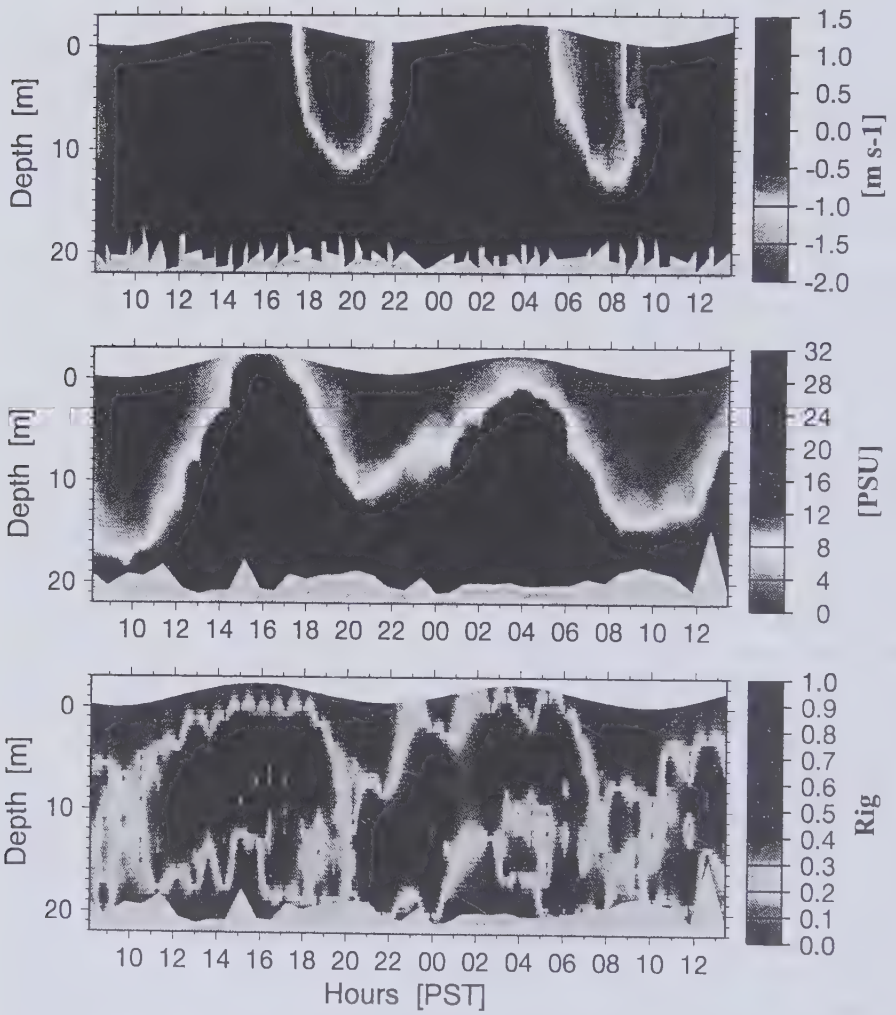

Figure 6. Times series of along-channel velocity (top), salinity (middle) and Ri_g (bottom) at station B in the deepest part of section NC1. Geyer (1988) found that the critical value of the total Ri_g as defined here was O(°) in the Fraser River estuary and that pycnocline thickness adjusted to give near-critical values of Ri_g. The outer part of the flow was often nearly inviscid on flood. Results here are roughly similar, except that the critical value appears to be O(0.4- 0.6) or so. This is not surprising, because the ADCP does not fully resolve the shear.

channel. The maximum value of U on flood is near the base of the interface atop the intruding salt water mass. Figure 6 and bedstress calculations not presented here show that vigorous mixing occurs near the bed on flood. This is not evident in Figure 8, probably because there is little stratification at this depth. Maximum outward flow is at the surface on the north side of the channel on ebb. Mixing is occurring in the

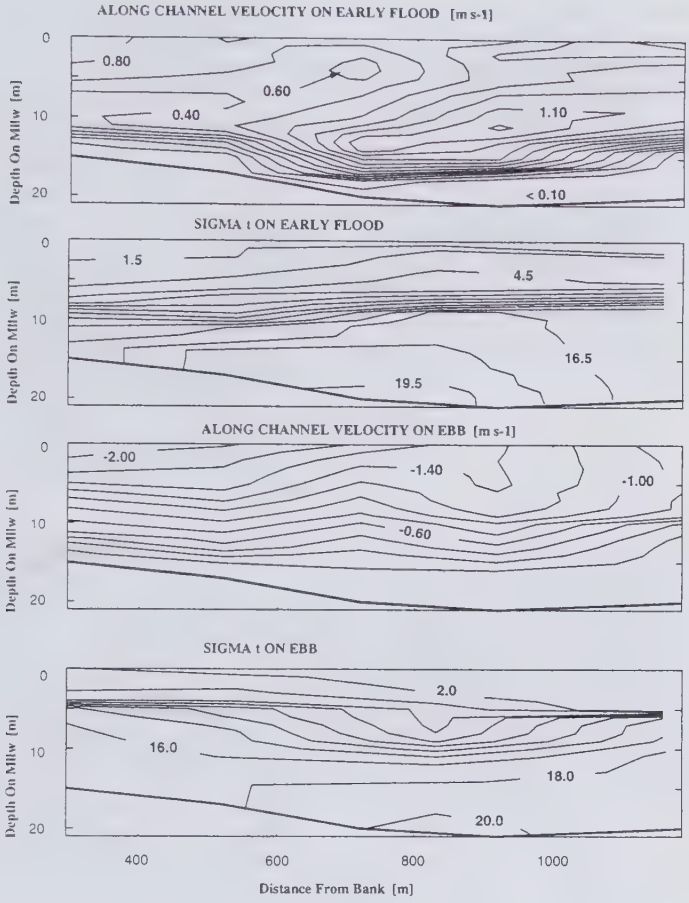

Figure 7. Sections looking upriver from the section NC1 section of U and σ_t for peak flood (above) and peak ebb (below). There is a prominent subsurface, flood velocity maximum in the deepest part of the channel that corresponds well with the intruding salt wedge. Peak ebb velocities appear at the surface on the north side of the channel. The magnitude of the velocity increases monotonically from the bed on ebb and is nearly linear with depth over much of the water column in the left two-thirds of the channel. There is a close correspondence between the velocity and density fields in the deeper part of the channel on both flood and ebb.

upper half of the water column on ebb, as suggested by internal waves and braided structures in Figure 8, and by the disturbed density interface at station B in Figure 7. Figure 6 suggests that bedstress should be weak on ebb at NCB, because salt is never totally washed out of the deepest part of the cross-section. The sediment transport seen in Figure 8 shows, however, that areas of strong bedstress occur on ebb in shallower parts of the channel, where the salinity goes nearly to zero.

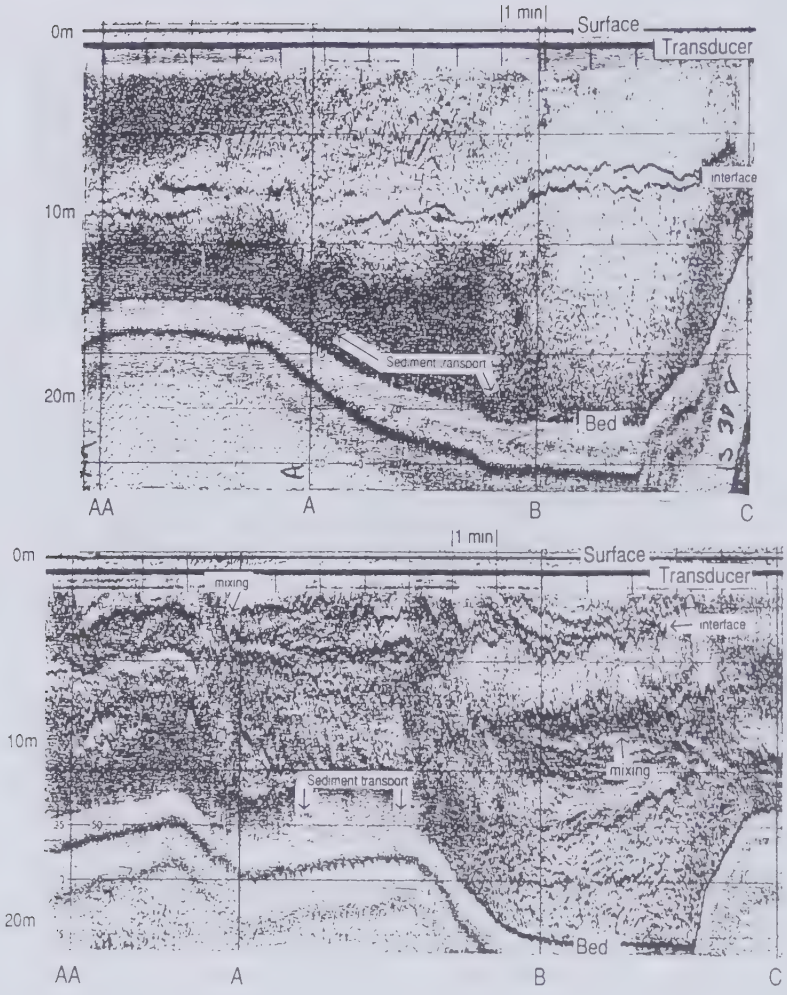

Figure 8. Flood (above) and ebb (below) acoustic echo sounder (200 khz) sections looking upriver at section NC1 that correspond to the density sections in Figure 7. The four vertical lines (time marks) correspond to CTDO casts. The line below the bottom is a secondary reflection. Time and position are not linearly related because of the CTDO casts. In the early flood section taken at 1330 PST on 31 July 1992, the strongest density interface is at mid-depth and rises to right (south). Only weak internal wave action and little mixing are seen on this interface, but larger amplitude waves and some mixing are seen between about 4 and 8 m depth in the middle-left part of the channel. Suspended sediment in transport is seen below 12 m across the left two-thirds of the channel and along the right bank. Active mixing and internal waves of several meters amplitude are seen throughout the upper part of the flow on ebb. Suspended sediment transport and/or erosion obscures the bed in the left half of the channel. On both flood and ebb, there is a close correspondence between the distribution of reflectors and the density distributions in Figure 7.

Harmonic analyses have been carried out on along-channel (Figure 9 and 10) and across-channel velocity components (not shown) using the scalar decomposition routines for unevenly spaced (in time) data described in Foreman and Henry (1979). The mean Z_0 amplitude (Figures 9a,b) shows strong outflow (>0.6 ms^{-1} on both NC1 and NC2) at the surface with a maximum along the north bank, similar to ebb-velocity field in Figure 7. The mean shear is distributed throughout the water column, not concentrated in a well-defined layer. There is a maximum inflow of >0.3 ms^{-1} in the deeper parts of both sections at about 15-16 m depth, yielding a top-to-bottom mean velocity difference of 0.9 to 1 ms^{-1}. M_2 amplitude increases almost monotonically toward the free surface on section NC1 but shows a weak subsurface maximum on section NC2 (Figure 9a,b). Maximum M_2 amplitudes are about >1.2 ms^{-1} on NC1 and >1.4 ms^{-1} on NC2. A bottom-to-surface M_2 phase progression of about 0.7-1 hr occurs on both sections.

(a)

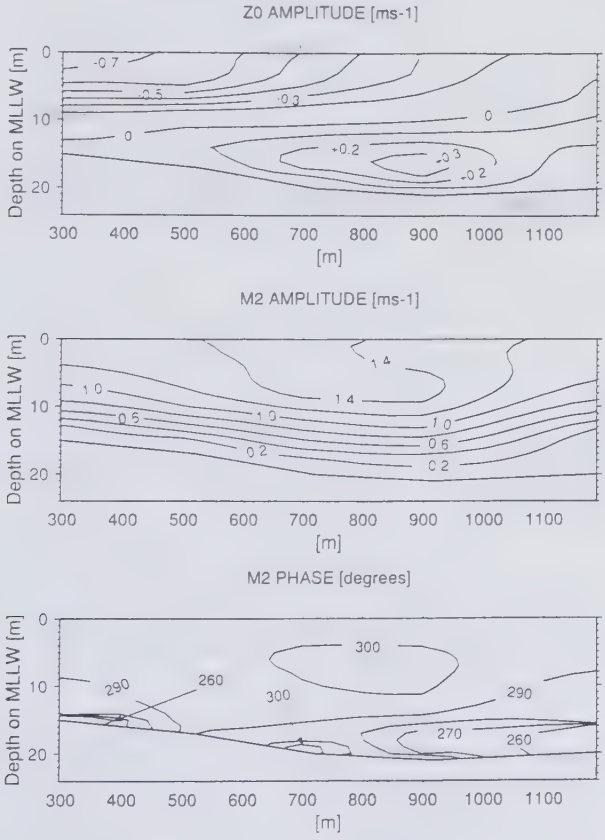

Figure 9. Along-channel velocity harmonic constants for Z_0 (top), M_2 amplitude (middle) and phase (bottom) on section NC1 in (a) and on section NC2 in (b). These were calculated from ADCP observations (see text); the sections are plotted looking landward.

(b)

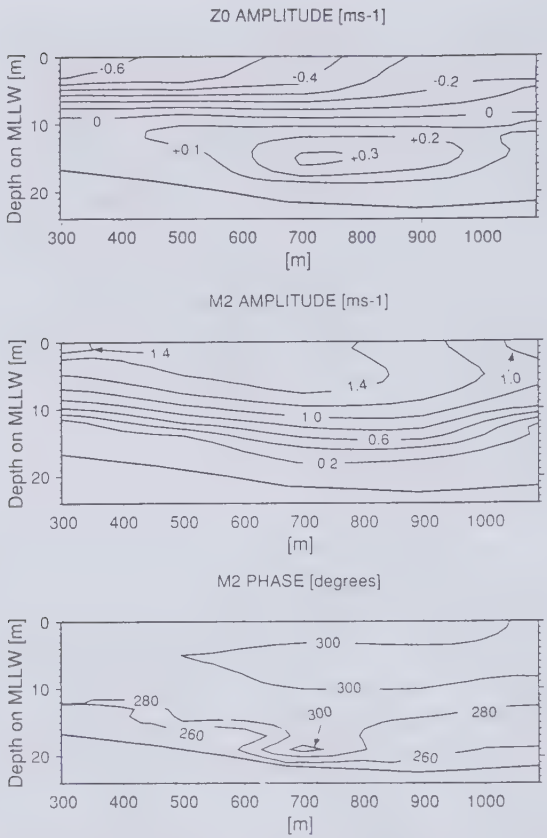

Figure 9 (Continued). Along-channel velocity harmonic constants for Z_0 (top), M_2 amplitude (middle) and phase (bottom) on section NC1 in (a) and on section NC2 in (b). These were calculated from ADCP observations (see text); the sections are plotted looking landward.

This feature is typical of tidal channel flows and is caused by the length of time required for an adverse barotropic pressure gradient to decelerate the strong near-surface flow at the change of tide. A similar vertical M_2 phase lag is seen in current meter harmonic analysis results from the Clatsop Spit section (stations 1, 3, 4 and 8 in Figure 2; Jay and Smith, 1990c).

Cross-sectional distributions of along-channel M_4 amplitude and phase (Figure 10a,b) are significantly more complex than those for Z_0 and M_2. The largest M_4 amplitude on section NC1 is 0.25 ms^{-1}. It occurs at the surface, and a secondary maximum of >0.1 ms^{-1} is found 6 m above the bed in midchannel. M_4 amplitudes are somewhat stronger on NC2, reaching 0.4 ms^{-1} near the surface and 0.2 ms^{-1} in mid-channel near the bed. Minimum M_4 amplitudes of <0.05 ms^{-1} are found at 5-11 m in both sections. The northern third and southern half of section NC1 show rather different M_4 phase distributions with a sharp transition between. The southern half of

the channel shows a very sharp 180° phase change in the vertical at about 8-9 m that separates the two maxima. There is a further 100° phase change between 12 m and the seabed at 17-20 m. The northern third of the channel at NC1 shows a single, more diffuse ~180° phase change in the vertical at about 12 m; thus there are also strong lateral phase changes.

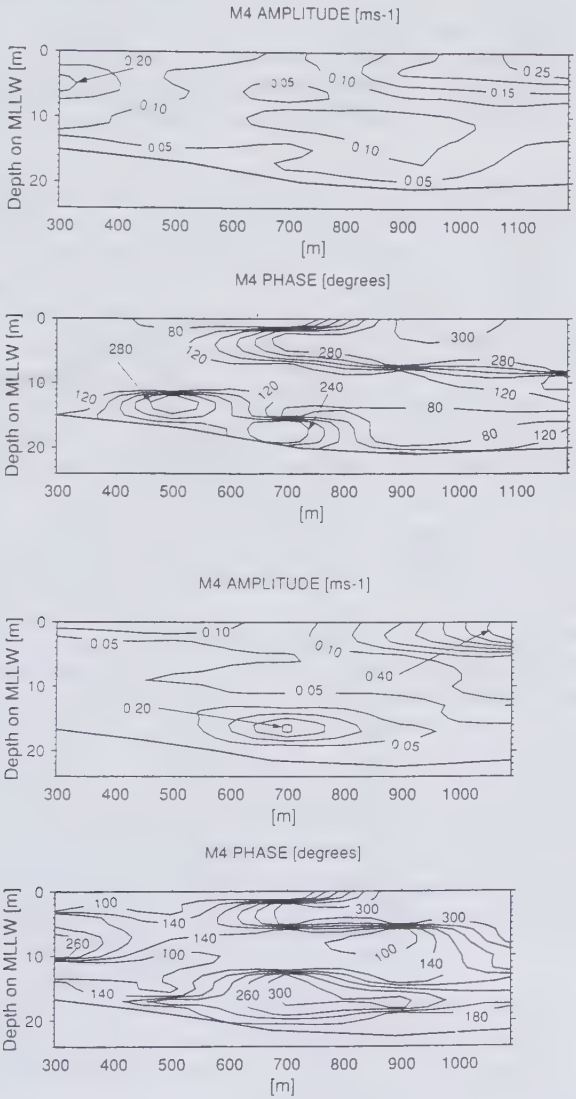

Figure 10. Along-channel velocity harmonic constants for M_4: amplitude (top), phase (bottom) for sections NC1 [in (a)] and for section NC2 [in (b)], as calculated from ADCP observations. The sense of the 2 M_2 - M_4 relative phase difference (not shown) is indicative of flood dominant flow near the bed.

The prominent north-south gradient in M_4 properties across section NC1 may be related to channel curvature around a point just upstream of this section, or to the fact that the north channel splits into two branch channels about 1 km landward of this section. The M_4 phase distribution at NC2 shows about a 180° vertical phase difference between the two maxima, with the sharpest changes just above and below the mid-depth amplitude minimum. There is a further ~100° phase progression toward the bed. Lateral differences are smaller than at NC1, possibly because NC2 is farther from disturbing topographic influences than NC1. The $2\,M_2 - M_4$ relative phase difference (not shown) is close to 0°, indicative of flood-dominant flow near the bed. This is consistent with the direction of suspended sediment transport inferred below.

Cross-channel harmonic analysis results (not-shown) indicate a substantial (up to 0.6 ms^{-1}) M_2 tidal flow to the north on section NC1 which evidently feeds the more northerly branch channel. Cross-channel Z_0 and M_4 currents on NC1 are weaker; there is a near-surface mean flow of 0.2-0.3 ms^{-1} flow to the south and a compensating northward flow of 0.1 ms^{-1} at depth. Maximum M_4 cross-channel current amplitude is <0.15 ms^{-1} with most amplitudes less than 0.1 ms^{-1}. Cross-channel M_4 amplitudes are larger than the corresponding along-channel amplitudes throughout the mid-depth, along-channel velocity minimum seen in Figure 10a,b. There is also a 180° phase reversal between the bed and 10 m depth in the northern half of the channel. These results suggest that secondary circulation due to channel curvature is also important, but is smaller than that caused by internal tidal asymmetry.

Further evidence of the existence of a spectrum of internal overtides can be seen in data collected from station BB1D in the south channel ETM (Figure 2) during a 50-hr time series on 9-10 July 1991 just after a spring tide, during a period of tropic tides with a large diurnal inequality (Figure 11). The greater and lesser diurnal tidal ranges were, respectively, 3.3 and 1.1 m. The river discharge was about average 7,200 m^3s^{-1}, yielding a riverflow of about 0.14 ms^{-1} through this section. As is typical for spring tides in this system (Jay and Smith, 1990a), shear in the mean flow is considerably less than found on a neap tide at sections NC1 and NC2 (Figure 9), because stratification is weaker. The calculated maximum M_2 amplitude of 1.05 ms^{-1} is similar to that seen in the North Channel. M_4, $2MK_5$ and M_6 all show vertical phase changes of nearly 180° and have amplitudes too large to be barotropically generated. The normalized amplitudes (calculated as in Figure 4 and based on the maximum amplitude in the vertical) are: 12.3, 8.16 and 7.37, respectively. M_3 current amplitudes calculated from ADCP data also have an anomalously large normalized ratio of 8.13, but there is only about a 70° phase variation in the vertical (except very close to the bed). This suggests that several processes contribute to the observed M_3 currents. One that might be important is the interaction of M_2 vertical shear with variations in vertical mixing arising from the presence of diurnal tide, which was quite large at this time.

The ADCP/CTDO data presented here represent only a small fraction of that collected in the 1990-92 period at some 15 cross-sections seaward of the upstream limits of salinity intrusion. An additional 17 time series stations were occupied in

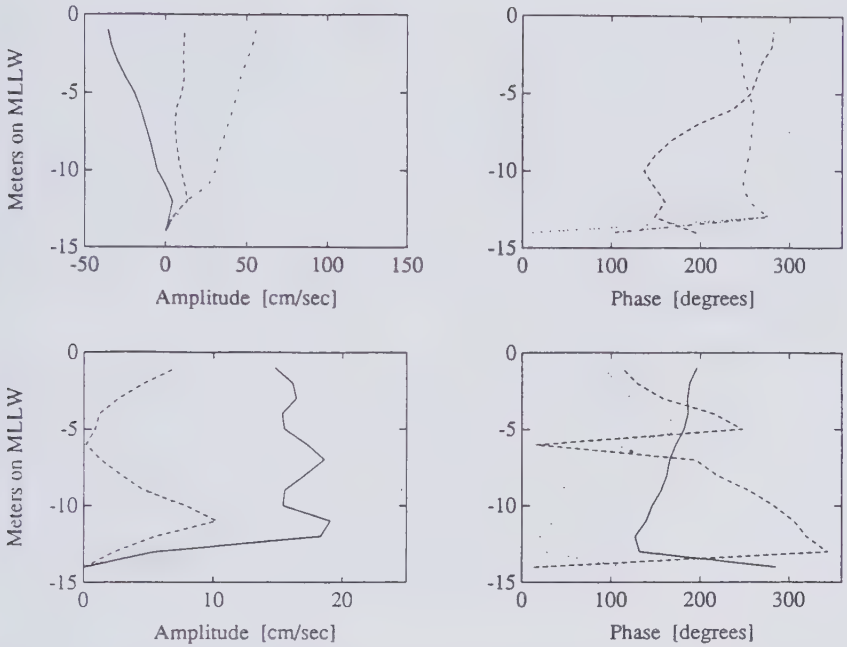

Figure 11. Profiles of BB1D along-channel velocity amplitude and phase determined from harmonic analysis of 50 hrs of ADCP observations. The constituents shown are: Z_0 (—), K_1 (-·-·-), M_2 (···) and M_4 (--) above; and M_3 (—), $2MK_5$ (···) and M_6 (--) below.

October 1980 with a CTD fitted with a Marsh-McBierney electromagnetic current meter. Plots from these time series stations uniformly show evidence of internal tidal asymmetry, as do the bulk of the >200 moored current records collected in 1980-81 by ourselves and the National Ocean Survey. The data here are typical rather than exceptional.

In summary, analyses of CTDO/ADCP, like those of moored current meter data, strongly support the existence and importance of internal overtide currents, because observed overtide currents are too strong to be barotropically generated and exhibit a 180° phase change in the vertical. While such reversals occur in both the across- and along-channel data, the influence of internal tidal asymmetry in creating residual and overtide flows is larger than that of channel curvature.

Errors in ADCP Data

Comment on the accuracy of the ADCP data is merited. The principal concerns for ADCP data collected in open ocean environments are accuracy of the navigation data, calibration of the coefficient between Doppler shift and velocity, and instrument orientation. Errors associated with these factors may cause a part of the

ship speed over ground to appear in the calculated current velocity. The ratio between ship speed and water speed is, however, a factor of 3 to 10 smaller in the estuarine environment, bottom tracking is always used to remove vessel speed, and instrument orientation can be determined in our instrument configuration within about $^1/_2°$. Shallow water depths, moreover, allows us to average 60 to 70 pings over 20s (minimizing random errors), and the "percent good" returned by the ADCP is almost always close to 100%, except within 15% of the flow-depth of the bottom. Thus, the principal concerns for our data set are quite different. They are: accuracy of ADCP shear tracking; the errors induced in near-bed data by direct reflection from the bed (i.e., side-lobe contamination); the effect on the gyrocompass of vessel turns; and the effects of spatial averaging over a rough bed.

RD Instruments has stated that data quality in the bottom 15% of the water column (2-3 m in our case) is suspect, because it may be contaminated by side-lobe reflections from the bed (RD Instruments, 1989). Moreover, shear near the bed is too large to be fully resolved by the instrument (RDI, 1989). Nonetheless, the ADCP data acquisition system (DAS) software contains a switch that enables collection of near-bed data, and this facility was used during the 1991 and 1992 cruises. We strongly suspect that the only reason that the velocity usually appears to go smoothly to zero at the bed for individual ping ensembles is that these two errors tend to offset one another in data from this part of the flow. On the one hand, failure to track shear properly causes an overestimation of near-bed velocities, because velocities are determined from the top of the profile down. On the other, the effect of direct reflection from the bed is to underestimate the calculated velocity magnitude in the bottom 15% of the flow. There are two signs of the latter problem that may be seen through careful inspection of individual ping data (personal communication, J. Gast, RD Instruments, 1993). First, vessel motion causes a systematic turning in the direction of that motion in the near bed data. This is the natural result of averaging ship motion over the bed into the calculated velocity. Second, signal return strength (the "AGC" parameter) usually but not invariably shows an anomalous increase near the bed despite sound attenuation with depth. This phenomenon could result from reflection off sediment in transport above the bed, but it occurs even when the OBS and echo sounder indicate that suspended sediment is absent. The net result of these two offsetting errors appears to be an aliasing of current direction more than of current magnitude. In particular, current phases near the bed are likely to be affected only to the extent that along- and across-channel currents are out of phase. Limited experience suggests, in fact, that near-bed along- and across-channels velocities are almost in phase, possibly because the latter arises from the former primarily through centrifugal acceleration.

The effect of vessel turns on the gyrocompass is hard to evaluate. Although our gyrocompass was compensated according to the manufacturers instructions, 90° course changes every few minutes (Figure 5) may still have caused some errors. Fortunately however, the Schuler oscillation that may be induced in an improperly compensated gyrocompass by sharp vessel turns does not have a period that corresponds to any of the tidal constituents calculated above. It should not, therefore, contaminate harmonic analysis results. Finally, ping ensemble averaging

over 20s implies, given a typical ship speed over ground of 4 ms^{-1}, spatial averaging over a path of ~80 m. Movement over sand waves and other changes in bottom depth will cause errors that will typically be at a maximum near the bed.

The number and complexity of the various errors discussed above do not allow any quantitative estimates of errors in ADCP velocities to be made. Nonetheless, ADCP data from about a dozen stations in the Columbia River estuary show signs of internal tidal asymmetry, as do moored current meter records. The qualitative consistency of these results suggest that uncertainties in harmonic analyses of ADCP data are on the order of a few cms^{-1} throughout most of the water column. Even if the near-bed data were ultimately to be rejected as invalid, this would not affect any part of the above argument concerning the existence and magnitude of internal tidal asymmetry. It might, however, render indeterminate the sense of the asymmetry (flood or ebb-dominant) near the bed, because overtide phase change rapidly with depth here. Fortunately, conclusions presented below concerning the importance of internal asymmetry to sediment transport do not rest entirely on CTDO and ADCP data, but are buttressed by current meter data as well. Nor can any error estimates be given for the Ri_g calculations presented in Figure 6. Turbulent overturning of the water column causes inversions in the densities calculated from CTDO data; these were eliminated during processing. Thus, the major uncertainties in calculated Ri_g can surely be ascribed to the limited resolution of shear and random errors inherent in ADCP data.

Models of Linear and Non-Linear Residual Flow Modes

The observations presented in the previous section demonstrate the existence of substantial, internally generated overtides and a large, along-channel residual flow with a top-to-bottom velocity difference of ~0.9–1 ms^{-1}. The purpose of this section is to partition this observed mean flow amongst the various residual flow modes that may be expected to contribute to it. We calculate the laterally averaged, linear residual flow in a channel of constant mean depth H under conditions of tidal and buoyancy forcing observed at section NC1. The linear residual is the sum of a mean outflow U_R (riverflow plus Stokes drift compensation flow) and a gravitational circulation U_G. This sum is then compared to the non-linear residual U_{SD} caused by internal tidal asymmetry; i.e., that driven by tidally-varying vertical eddy diffusivity and tidally varying shear. The non-linear residual arising from the convective accelerations has not been estimated, primarily because earlier calculations found it to be small for a channel of constant width and depth (Jay and Smith, 1990b). The analysis is based on a perturbation expansion and proceeds under the assumptions that all residual flow modes are: 1) small relative to the tidal flow; and 2) linearly separable; i.e., they interact with each other only at higher order. A detailed account of the perturbation analysis is not included herein.

The two-dimensional (in x and z) model used in these calculations is a balance of mean vertical momentum flux divergence, including its non-linear component for the

internal asymmetry mode, against a mean pressure gradient. U_G is forced by a tidal mean baroclinic pressure gradient $\partial\rho_0/\partial x$ that is independent of x. The total, integral discharge Q_R is also spatially uniform. These along-channel similarity assumptions were first employed by Hansen and Rattray (1965) and lead a linear residual flow that is independent of x. In contrast to prior analytical solutions for the linear residual flow, the present model uses a realistic vertical eddy diffusivity profile controlled by the gradient Richardson number Ri_g. The eddy diffusivity model used is essentially that of Long (1981), wherein K_m is the product of a neutral eddy diffusivity K_m and a stratification correction S_r (Ri_g), the form of which is due to Bloss (1985):

$$K_m(z) = K_n(z)\, S_r(Ri_g)$$

$$K_n(z) = k\, u_*\, z\, e^{-\ell z}$$

$$S_r(Ri_g) = (1 + \gamma\, Ri_g)^{-1} \qquad (1)$$

where: $k = 0.41$ is von Karmann's constant, $\gamma = 3$, the length scale l was taken as one quarter of the mean depth H, the friction velocity u_* (≈ 0.03 ms^{-1}) was determined interactively in the tidal calculation, and z is taken as upward from the bed. A no-slip condition was applied at $z = z_0$ and a zero-stress condition at the free surface. A value of $z_0 = 0.002$ m was used to account for the presence of fully-developed bedforms. The depth H was taken as 20 m. Calculation of the residual due to internal tidal asymmetry requires determination of the tidal-mean K_{m0} and time-varying K_{m1} parts of K_m in terms of the tidal-mean Ri_{g0} and time-varying Ri_{g1} parts of Ri_g:

$$K_{m0} = K_n(z)\, (1 + \gamma\, Ri_{g0})^{-1}$$

$$K_{m1} = K_m - K_{m0} \cong -\gamma\, Ri_{g1}\, K_m\, (z)\, (1 + \gamma\, Ri_{g0})^{-1} \qquad (2)$$

K_n is taken as time invariant. Each residual flow mode contains two unknowns, the along-channel velocity (a function of z and for U_{SD}, of x also) and a surface slope. The latter is determined for each mode from a mass conservation requirement that is an integral form of the continuity equation. The gravitational circulation and the residual due to internal asymmetry integrate to zero over depth, while the mean outflow integrates to a known river discharge plus Stokes drift compensation flow Q_R. Closed-form solutions for all residual flow modes are readily derived, but these contain integrals that cannot in general be evaluated analytically. Numerical integrations were, therefore, performed in *Mathematica*™.

Forcing functions for all residual modes were taken from observations. The density gradient $\partial\rho_0/\partial x$ that drives the gravitational circulation was determined through harmonic analysis of the along-channel salinity difference between stations NCD and NCB; $\partial\rho_0/\partial x$ increases linearly in magnitude by about 50% from surface to bed. The Ri_{g0} and Ri_{g1} profiles needed to specify K_{m0} and K_{m1} in (2) were determined from harmonic analysis of the time series of calculated Ri_{gt} at station NCB (Figure 6),

taking the M_2 component of the time-variability to represent Ri_{g1}. The forms of Ri_{g0} and Ri_{g1} shown in Figure 12 are analytical approximations to these harmonic analysis results, using the fact that Ri_g is twice Ri_{gt} for $Ri_{gt} = 0.5$. Ri_{g0} had a broad maximum at mid-depth, while Ri_{g1} had maxima just above the bed and below the free surface, and a 180° phase change near mid-depth. These features are inherited by K_{m1}, and the total vertical eddy diffusivity $K_m(z) = K_{m0}(z) + K_{m1}(z)$ is positive definite. This simple formulation reproduces the most essential feature of the fairly complex Ri_{GT} distribution shown in Figure 6; it causes $K_m(z)$ to be relatively large near the bed during late flood and near the free surface during late ebb (Figure 12).

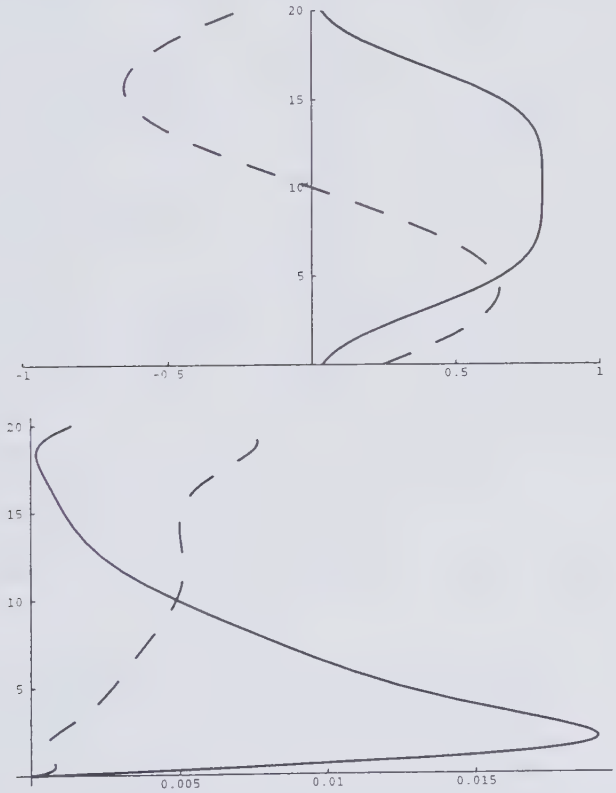

Figure 12. Profiles (above) of mean Ri_{g0} (—) and tidally varying Ri_{g1} (--) parts of the gradient Richardson number Ri_g (the latter shown for late ebb), and below of the vertical eddy diffusivity $K_m = K_{m0} + K_{m1}$ (in m^2s^{-1}) for late flood (—) and for late ebb (--). Depths are in meters. These parameters are used to drive models of gravitational circulation U_G, mean outflow U_R and the non-linear residual due to internal tidal asymmetry U_{SD}. Note that $K_{m0} + K_{m1}$ is positive definite in the model, whereas the model $Ri_{g0} + Ri_{g1}$ is <0 at some times during the tidal cycle. Harmonic analysis of Ri_{gt} in Figure 6 shows that, while the sum of Ri_g at all frequencies must be positive definite, this is not true for the sum of its mean and M_2 parts; thus the model is not unrealistic in this regard. Model properties are discussed in the text.

The mean gravitational velocity solution contains a single non-dimensional number (Jay and Smith, 1990b):

$$\Gamma_1 = (gH^3\Delta\rho_o)/(\rho_o K_0 L_S \hat{U}_i) \qquad (3)$$

where: $g = 9.8\ ms^{-2}$, $K_0 = ku_* H$ is the scale for K_m, L_s is the salinity intrusion length, $\Delta\rho_o/\rho_o \approx 0.02$ is the stratification scale, and $\hat{U}_i$ is a velocity scale for gravitational circulation. Γ_1 and the assumed Ri_g profile control the character of the solution (Figure 13). Γ_1 is determined primarily by its cubic dependence on H because K_0 is, for a given tidal flow, relatively independent of H — changes in H and u_* largely offset one another. The choice of $\hat{U}_i$ is unimportant for present purposes, because the dependence on $\hat{U}_i$ disappears in the dimensional form of the solution shown in Figure 13. The profile of the mean outflow is determined entirely by the Ri_g profile and the outflow Q_R. The surface slope associated with each mode is set by a second non-dimensional number that scales the bedstress; it does not appear in the velocity profile solutions. Q_R, L_S, H, and $\Delta\rho_o/\rho_o$ used in these calculations were all chosen to provide a generous upper limit on the shear that can be produced by steady density-driven circulation and mean outflow.

Experimentation with the model showed that, while details of the riverflow and gravitational circulation profiles were quite sensitive to the Ri_g profile, realistic parameter choices yielded only about 40% of the observed mean velocity difference of $\sim 1\ ms^{-1}$ between top and bottom (Figure 13). In particular, the top-to-bottom velocity difference in the mean outflow profile cannot be more than about 150% of the vertical average of the mean outflow velocity, $0.2\ ms^{-1}$ in this case. Greater mean shears can only be produced by reducing the mixing level in the pycnocline to that of molecular viscosity. This is inconsistent with the mixing seen in echo sounder traces (e.g., Figure 8) and also concentrates too much shear at mid-depth. Moreover, given this large river discharge, it is impossible to develop significant, mean upstream bottom flow in the linear residual flow modes.

The residual along-channel velocity associated with internal asymmetry $U_{SD}(x,z)$ depends upon the vertical shear in a non-dimensional, laterally averaged, tidal velocity solution $U_1(x,z,t) = Re[dM(x)/dx\ P(z)\ e^{it}]$, where $Re[M(x)\ e^{it}]$ is the non-dimensional tidal surface elevation. P(z) is found from a tidal momentum conservation equation including a tidal baroclinic pressure gradient $\partial\rho_1/\partial x$. The boundary conditions are no slip at z_0 and zero stress at the free surface. The wave number in M(x) is set from a vertically integrated wave equation. The assumption of constant depth H requires that the reflected wave vanish; thus, dissipation causes M(x) to decay slowly in the upriver direction. Like $\partial\rho_0/\partial x$, $\partial\rho_1/\partial x$ was found by harmonic analysis. It is in phase with U_1, and its vertical distribution is approximated by a parabola with a maximum at mid-depth. The solution for P(z) was found by a shooting method based on the linear differential equation solution algorithm in *Mathematica*™. $U_1(x,z,t)$ has a weak subsurface maximum due to the joint effects of baroclinic forcing and stratification (Figure 14).

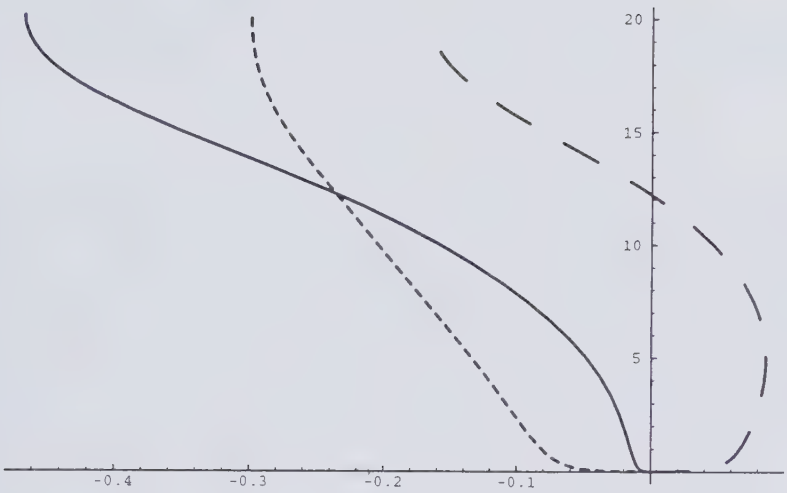

Figure 13. Model predictions of dimensional U_G (--), U_R (...) and their sum U_{NET} (—) in ms^{-1}. Depths are in meters. Note that the sum of the two linear modes does not produce any upstream bottom flow, because of the large mean outflow U_R. The total top-to-bottom velocity difference is also much smaller than that observed (Figure 9).

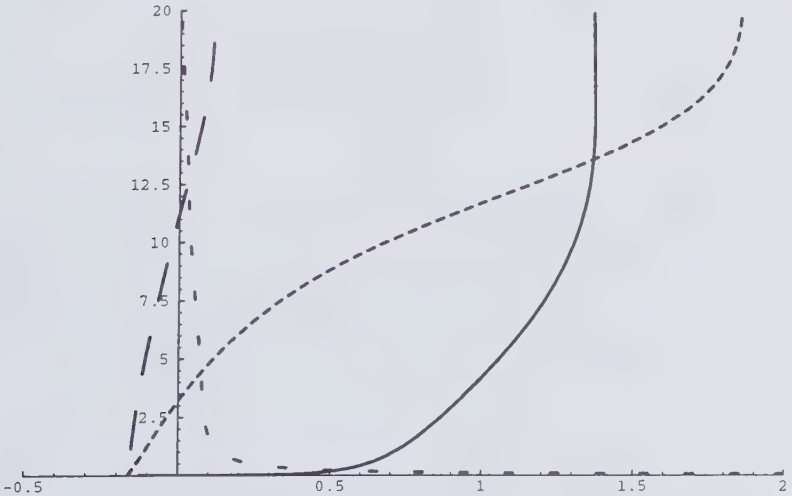

Figure 14. Tidal model predictions of dimensional tidal velocity U_1 amplitude (—) in ms^{-1} and phase (— —) in radians, and shear $\partial U_1/\partial z$ amplitude (- -) in ms^{-1} and phase (···) in radians. Depths are in meters. The correlation of $\partial U_1/\partial z$ and the time-varying vertical eddy diffusivity K_{m1} drive the model for U_{SD}. Note the sub-surface tidal velocity maximum, as in Figure 9.

Both the time-average and tidal parts of K_m are assumed to be independent of x. U_{SD} inherits its along-channel structure directly from $\partial U_1(x,z,t)/\partial z$; thus, $U_{SD}(x,z) = Re[dM(x)/dx\ P_{SD}(z)]$. The along-channel momentum equation for P_{SD} is:

$$(K_{m0}\, P_{SD}')' + \hat{U}/\hat{U}_I \langle (K_{m1}\, P')' \rangle = \Gamma_2\, \partial\zeta_{SD}/\partial x \qquad (4)$$

where: $\partial\zeta_{SD}/\partial x$ is a surface slope, $\hat{U}$ is the tidal velocity scale, $E\hat{U}_1$ is the internal asymmetry velocity scale, a prime indicates a z derivative, brackets $\langle\ \rangle$ indicate a time average of a non-linear term that has both residual and overtide parts, and Γ_2 scales the surface slope relative to the bedstress. This second-order inhomogeneous differential equation may be integrated in closed form. The solution contains integrals of the non-linear forcing term, however, and these were evaluated numerically. The dimensional solution for U_{SD} shown in Figure 15 is independent of $E\hat{U}_1$; its magnitude is set by $\hat{U}$, which is determined by the tidal amplitude and depth. $\partial\zeta_{SD}/\partial x$ is found from the continuity requirement that $\hat{U}_1(x,z)$ integrate to zero; Γ_2 does not appear in the solution for U_{SD}. The structure of U_{SD} is determined principally by: 1) the vertical structures of K_{m0} and K_{m1}; and 2) the phase difference between U_1 and K_{m1} which was specified from harmonic analysis of data presented in Figure 6.

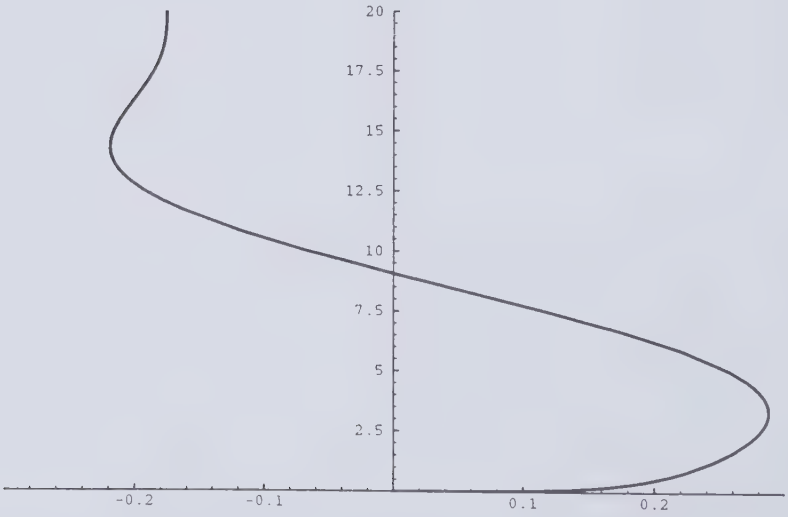

Figure 15. Model prediction of the dimensional residual due to internal tidal asymmetry, U_{SD} in ms^{-1}. U_{SD} is the largest residual flow mode and appears to be responsible for most of the net upstream bottom flow.

The solution (Figure 15) determined for U_{SD} shows a top-to-bottom velocity difference of about 0.5 ms^{-1}, with outflow near the free surface and a maximum of almost 0.3 ms^{-1} of landward flow at about 15 m. The sum of the three modes shown in Figures 13 and 15, that is of the mean outflow, gravitational circulation and internal tidal asymmetry, produces a total top-to-bottom velocity difference of ~0.9 ms^{-1}, very close to that found in nature. Discrepancies between these models and reality may be due to the three--dimensionality of the actual flow, or perhaps to the presence in nature of a non-linearresidual driven by the convective acceleration, which we did not calculate. The latter mode typically causes, however, landward currents near the free surface and seaward flow near the bed (Ianniello, 1977). Nonetheless, these model results indicate that: 1) internal asymmetry is the largest residual flow mode; and 2) most of the residual shear is produced by non-linear, rather than linear processes. While gravitational circulation and internal tidal asymmetry both produce landward flow near the bed, these models suggests that a substantial upstream bottom flow in a tidal river with a large freshwater flow is diagnostic of internal tidal asymmetry.

In summary, there is compelling evidence that overtide currents and mean shears are too large in the Columbia River estuary to be accounted for in terms of barotropic tidal forcing and by steady, density driven circulation, respectively. Observations and model results suggest that the pattern of bottom-intensified floods and surface-intensified ebbs observed in the Columbia River and numerous estuaries is most readily explained in terms of internal tidal asymmetry, which appears in these systems to be the dominant cause of both residual and overtide circulation.

Discussion: The Meaning and Importance of Internal Tidal Asymmetry

An analogy between the tidal distortion of the free surface (commonly known as barotropic tidal asymmetry) and that of the density field (here referred to as internal tidal asymmetry) has played an important role in the analyses presented above. The same analogy leads to several further questions. First, only "flood-oriented" internal tidal asymmetry has been observed. While the mechanisms discussed herein would lead to an "ebb-oriented" internal asymmetry in a negative estuary, it is unclear from available observations whether such an asymmetry is possible in a positive estuary. Furthermore, tidal bores epitomize the development of flood-oriented barotropic asymmetry - does an internal analog exist? We may disregard here internal hydraulic jumps and other processes associated with the interaction of tides with sills - a proper analog to a tidal bore would require at most only a weakly convergent channel. Further observations and analyses are required to answer such questions. Finally, we may ask whether or not internally generated overtides are truly waves. The answer to this question is fairly simple: internal overtides do not have a wave number, decay uniformly with increasing x, and do not propagate. They are, therefore, oscillations but not waves.

Internal Asymmetry and Scalar Transport

It is also important to consider the consequences of internal overtide generation for scalar transport. Jay (1991c) has shown that correlations of velocity shear and scalar stratification at mean, tidal and overtide frequencies bring about the landward transport that maintains estuarine scalar distributions against export by riverflow. Harmonic analysis results show that salinity variability in the Columbia River estuary is primarily at mean and tidal frequencies. Physically, we expect landward transport of salt near the bed by the mean flow, because salinity and velocity both exceed their vertical averages near the bed. To the extent then that the mean flow controls salinity intrusion, internal tidal asymmetry is likely to play a dominant role therein, as previously suggested by West *et al.* (1990). In the Columbia River estuary, however, more than half of the landward salt transport occurs at and above mid-depth by tidal mechanisms (Jay and Smith, 1990c). This occurs because salinity is somewhat higher at mid-depth on flood than on ebb. Internal tidal asymmetry apparently does not play a major role in this tidal salt transport.

Internal tidal asymmetry is more important for suspended sediment transport, because bed stress and suspended sediment concentration have maxima on both flood and ebb. Suspended sediment concentration harmonic components computed from OBS data have, like non-linearly generated baroclinic currents, strong residual and M_4 components near the bed (Figures 16-18). Landward near-bottom flow therefore

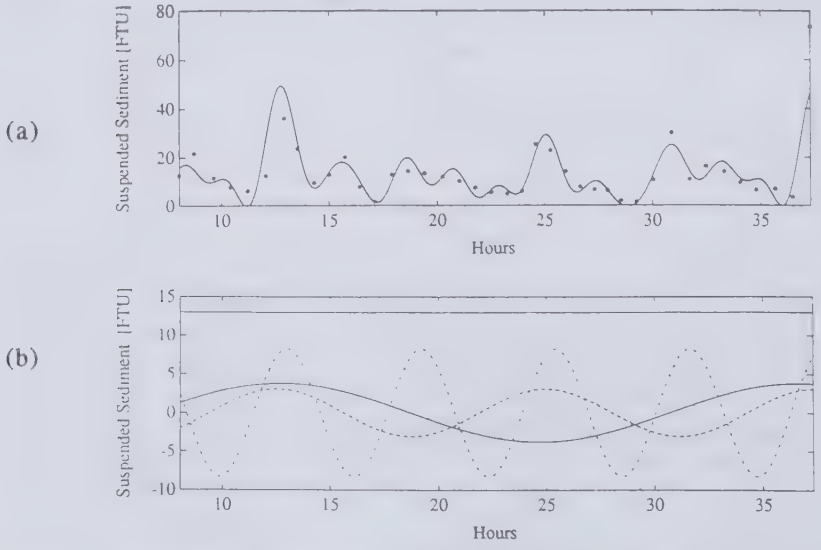

Figure 16. Time series of suspended sediment concentration as OBS output (in formazine turbidity units or FTUs) 4 m above the bed at NC-B (*) and a harmonic fit thereto (—) in (a); and the major constituents of this harmonic decomposition in (b). The constituents shown are: Z_0 (—), K_1 (—), M_2 (--), M_4 (-·-·-) and M_8 (···). Sedimentological analyses show that the OBS-suspended sediment relationship in this system in quite linear; 1 FTU was about 1.5 mg l^{-1} for the 1992 cruise.

(a)

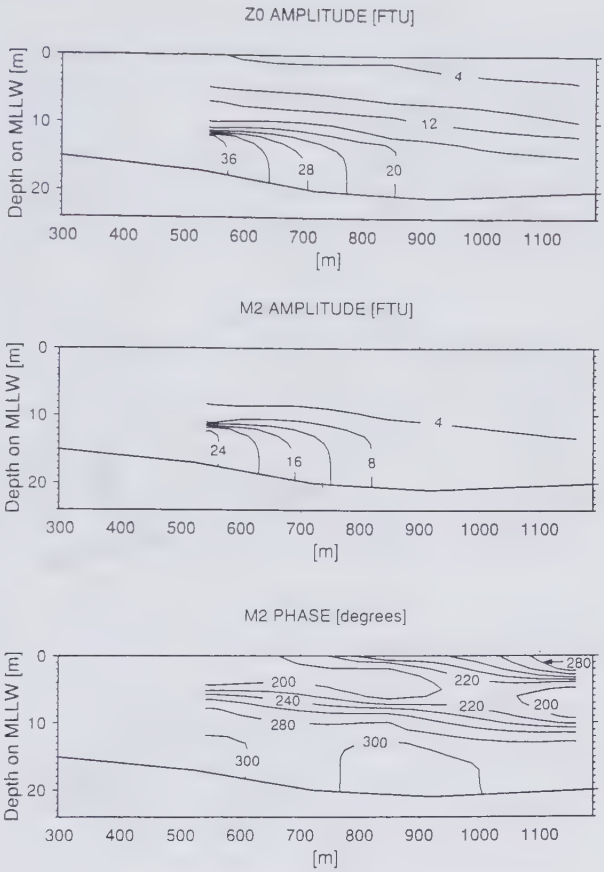

Figure 17. Suspended sediment harmonic constants (in FTUs) for Z_0 (top), M_2 amplitude (middle) and phase (bottom) on sections NC1 (in a) and NC2 (in b) calculated from OBS observations. Landward, near-bed residual flow and substantial residual sediment concentrations cause landward sediment transport on both NC1 and NC2. The small M_2 velocity-sediment phase differences indicate that M_2 also contributes toward landward suspended sediment transport on both sections. M_2 sediment concentrations are, however, quite small on NC2. The sediment concentration time-series at station AA was incomplete, and no harmonic analysis was possible.

implies landward residual sediment transport on both sections NC1 and NC2 (compare Figures 9 and 17). The M_4 components of the sediment and current fields are also nearly in phase (Figures 10 and 18), particularly over the portion of the channel where most sediment transport occurs on section NC1 in Figure 8. One interesting difference between sections NC1 and NC2 is that M sediment concentrations are negligible on the latter but not the former, where semidiurnal

(b)

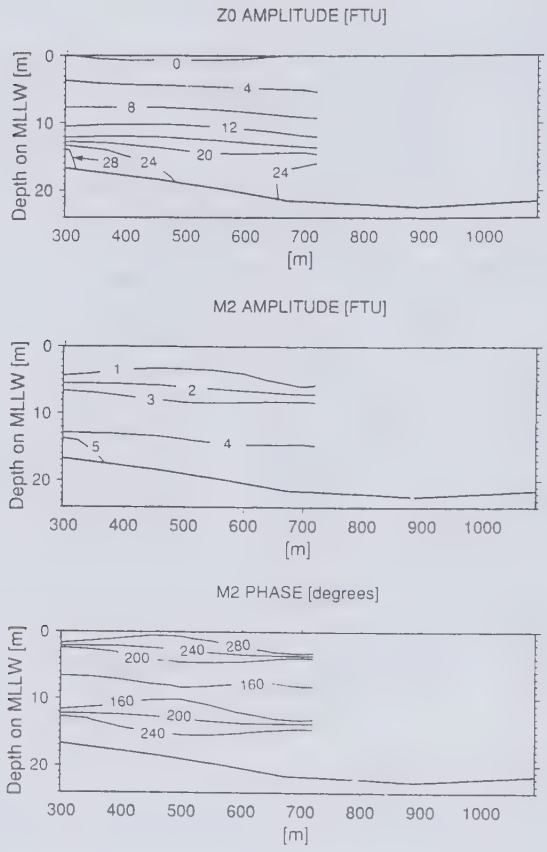

Figure 17 (continued). Suspended sediment harmonic constants (in FTUs) for Z_0 (top), M_2 amplitude (middle) and phase (bottom) on sections NC1 (in a) and NC2 (in b) calculated from OBS observations. Landward, near-bed residual flow and substantial residual sediment concentrations cause landward sediment transport on both NC1 and NC2. The small M_2 velocity-sediment phase differences indicate that M_2 also contributes toward landward suspended sediment transport on both sections. M_2 sediment concentrations are, however, quite small on NC2. The sediment concentration time-series at station AA was incomplete, and no harmonic analysis was possible.

currents also contribute to landward transport (Figures 9 and 17). Harmonic analysis of one month of data from an Aanderaa current meter equipped with transmissometer and placed at 15 m depth on the Astoria-Megler bridge (current meter station 5b in Figure 2) just landward of section NC1 further show the importance of residual and overtide flow for suspended sediment transport. M_4 is (after Z_0) the largest constituent in the transmissivity record, and the along-channel M_4 velocity is in

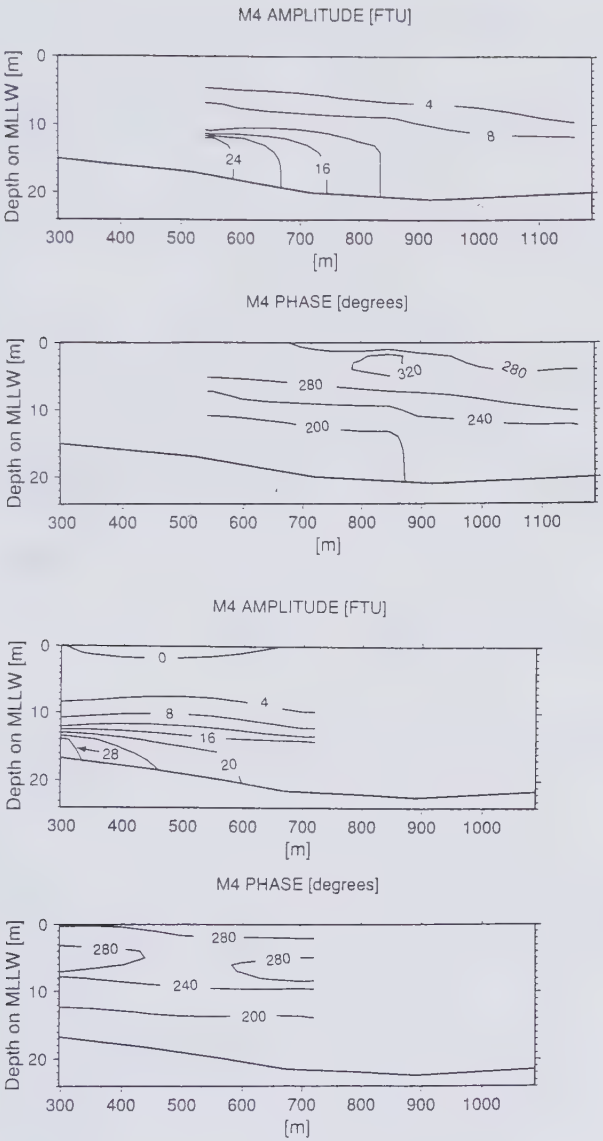

Figure 18. Suspended sediment harmonic constants (in FTUs) for M_4 amplitude (top) and phase (bottom) on sections NC1 (in a) and NC2 (in b) calculated from OBS observations. M_4 contributes to landward suspended sediment transport on both sections.

phase with the transmissivity within 45 min. Data from another near-bed current meter at station 5a (Figure 2) gave very similar results. Thus, internal overtide and residual flows driven by tidal asymmetry are apparently the primary transport

mechanism causing trapping of particulates in estuarine turbidity maxima, at least in the Colombia River estuary (Jay and Musiak, 1993).

Finally, tidal variations in vertical mixing should also influence sediment and salt conservation, not just because of their effects on the velocity field, but also directly; i.e., through the vertical turbulent scalar flux divergence term that appears in scalar conservation equations. Consider salt as an example. Suppose, consistent with observations, that the greatest part of the salinity variance is in the mean and tidal bands. The salinity distributions at these two frequencies should interact with each other through a term in the sediment conservation equation involving time-varying vertical mixing. Time-varying vertical mixing should also provide (in addition to tidal advection of the tidally varying salinity field) a second mechanism for generating overtide variations in salinity concentration. The influence of tidal advection and internal asymmetry should be distinguishable, however, by vertical variations in overtide salinity phase. Tidal advection should cause overtide salinities variations with weak variations in phase over the water column, whereas the overtide salinity variation induced by internal asymmetry should exhibit a characteristic 180° degree change of phase in the vertical.

Observations in Other Estuaries

A definitive evaluation of the importance of internal tidal asymmetry requires the comparison of overtides in current and surface elevation records carried out above for the Columbia River estuary. The basic requirement for the existence of internal tidal asymmetry is, however, the presence of strong forcing by both river and tides, and a preliminary diagnosis can be made on the basis of substantial flood-ebb differences in stratification and the velocity profile. Systems where such variations have been previously observed include: the Great Ouse (West *et al.*, 1984), the Duwamish (Partch and Smith, 1978), the Columbia River estuary (Jay, 1987, 1990); Grays Harbor (Beveredge and Swecker, 1969), North San Francisco Bay (Meade, 1972; Walters *et al.*, 1985), the Hudson River (Zhou, 1992), the Tay (Buller *et al.*, 1975), the Tamar (West *et al.*, 1990; Darbyshire and West, 1991), the Tees (Lewis and Lewis, 1983), the Fraser River (Geyer, 1988), the Weser (Lang *et al.*, 1989), the Scheldt (Nihoul *et al.*, 1978) and the East River tidal strait (Long, 1978; Brown and Dingle, 1983; R. Wilson, personal communication). Three macrotidal estuaries in France (the Seine, Aulne and Gironde; Allen *et al.*, 1977, 1980; Avoine *et al.*, 1981) and four systems in Malaysia (the Klang, Bernam, Langat and Selangor River-estuaries; Ibrahim, *et al.*, 1992) all show strong tidal changes in stratification, but no velocity measurements are available. Even the microtidal Mississippi River exhibits a weak tidal variation in stratification (Wright, 1971; Meade, 1972). Internal asymmetry also routinely appears in numerical simulations. The earliest example is probably the Rotterdam Waterway model of Bowden and Hamilton (1975). Walters (1994) has concluded that time-varying vertical mixing is essential to proper reproduction in a three-dimensional numerical model of even the major barotropic

tidal constituents in Delaware Bay. This again suggests that internal asymmetry is likely very common.

Summary and Conclusions

Moored instrument observations show that overtide currents are often a factor of five to 10 too large to be generated from the barotropic overtide in the Columbia River estuary.

ADCP data indicate that overtide currents typically exhibit a 180° change in phase in the vertical, a characteristic of internal modes that integrate to zero over depth. The fact that these currents disappear upstream of salinity intrusion indicates that their source is related to salinity intrusion. The causative mechanism is an internal tidal asymmetry associated with tidal straining of the horizontal density gradient and consequent tidal variations in stratification. Cross-sectional distributions of M_4 current amplitudes and phases are, however, complex and appear to be influenced by topography and channel curvature as well. The cross-sectional distribution of the mean flow is simpler, resembling in this regard that of M_2. Observations and model results together show that the residual, top-to-bottom velocity difference of ~1 ms^{-1} is too large to be attributed to any combination of river outflow and steady density forcing; internal tidal asymmetry is also the dominant cause of the residual circulation.

Baroclinic residual and overtide flows in shallow, strongly forced estuaries are best thought of in the context of wave non-linearity-generated modes, exactly as is the case for barotropic mean and overtide flows. While steady gravitational circulation is important in the weakly forced asymptote of an essentially steady density field, its influence is overwhelmed by more potent, tidal non-linearities in strongly forced systems. This can also be understood in terms of the Jay and Smith (1988) estuarine classification diagram (Figure 19) for shallow estuaries. This diagram suggests that systems with strong advection of the density field and thus strong internal non-linearities are transitional. They are on or near the boundaries between the highly stratified, partially mixed and/or weakly stratified states. They may exhibit tidal monthly or seasonal changes from one circulation type to another, without however, loosing the characteristic of having strong internal tidal asymmetry. Shallow systems that have a residual circulation dominated by steady, gravitational circulation are those with weak barotropic (F_T small in Figure 19) and weak baroclinic non-linearities (F_B large or small). Such systems occupy the lower left and lower right corners of Figure 19 and may be either partially mixed or highly stratified. Deep estuaries are also likely (at least away from sills and constrictions) to be dominated by gravitational circulation, because its influence increases roughly with the cube of the depth, while tidal non-linearities scale with the ratio of tidal amplitude to mean depth. If an estuary is sufficiently deep relative to its tidal forcing, then steady density-driven circulation will be more important than internal asymmetry. Large, deep estuaries are also often, of course, affected by atmospheric effects not discussed herein.

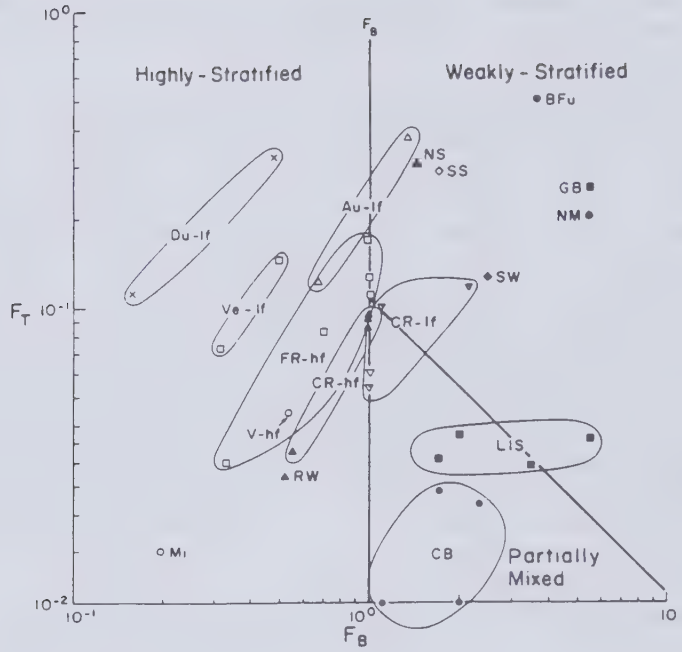

Figure 19. Classification of tidal channel estuaries on the basis of an external Froude number F_T, the ratio of tidal amplitude to mean depth, and an internal Froude number F_B calculated from the density field as described in Jay (1988). Although the dependence of F_B on tidal flow U riverflow U_R varies somewhat with the type of estuary, decreasing U and increasing U_R decreases F_B in all cases. Estuaries with strong internal tidal asymmetry are those where fluvial and tidal forces are balanced such that F_B is O(1). Symbols include lf = low riverflow, hf = high riverflow. Estuaries referred to in the text as showing signs of internal tidal asymmetry include: Au = Aulne, CR = Columbia River estuary, FR = Fraser River estuary, Du = Duwamish Estuary and Mi = Mississippi River. Others are defined in Jay and Smith (1988), from which this figure is adapted.

Internal tidal asymmetry plays an important role in maintenance of estuarine salt balances through its contribution to the residual shear. It is particularly important for suspended sediment transport, because suspended sediment variability is strong at residual and overtide frequencies, and because internal tidal asymmetry causes landward, near-bed transport at these same frequencies.

Acknowledgements. This work has been supported by the National Science Foundation's Land Margin Ecosystem Research program under grant OCE-8918193. We dedicate this paper to the late Dan Stiebritz, a good friend and a terrific skipper of the R/V *Snow Goose*. We also thank Jim Stiebritz of the R/V *Snow Goose*, and

Phil Crawford and Ray McQuin of the R/V *Barnes* for their enthusiastic help in data collection. Robert Wilson of State University of New York at Stony Brook provided helpful plots of unpublished NOS data from the East River tidal strait. Erik Butterworth assisted in the reduction of the ADCP data, and Cynthia Cudaback in the analysis of the current meter data.

References

Allen, G. P., G. Sauzay and P. Castaing. Transport and deposition of suspended sediment in the Gironde Estuary, France. In M. Wiley, ed., *Estuarine Processes,* vol II, Academic Press, New York, pp. 63-81, 1977.

Allen, G. P., J. C. Solomon, P. Bassoullet, Y. Du Penhoat and C. De Grandpré. Effects of tides on mixing and suspended sediment transport in macrotidal estuaries. *Sedimentary Geology* 26: 69-80, 1980.

Avoine, J., G. P. Allen, M. Nichols, J. C. Solomon, and C. Larsonneur. Suspended-sediment transport in the Seine estuary, France: effects of man-made modifications on estuary-shelf sedimentology. *Marine Geology* 40: 119-137, 1981.

Beveredge, J. P. and M. N. Swecker. Estuarine studies in Upper Grays Harbor. Geological Survey Water-Supply Paper 1873-B, 90 pp., 1969.

Baines, P. G. On internal tide generation models, *Deep-Sea Research* 29: 307-338, 1982.

Bloss, S. Parameterization of vertical eddy diffusivities in stratified tidal flow. IUTAM Symposium on Mixing in Stratified Fluids, Margaret River, Western Australia. Centre for Water Research, Report 85-120, 1985.

Bowden, K. F. and P. Hamilton. A numerical model of the vertical circulation of tidal estuaries and its application to the Rotterdam Waterway. *Estuarine and Coastal Marine Science* 3: 281-301, 1975.

Brown, D. R. and G. Dingle. *New York Harbor Circulation Survey 1980-81.* NOS Oceanographic Circulatory Survey Report No. 5, Rockville, MD, 92 pp., 1983.

Buller, A. T., C. D. Green and J. McManus. Dynamics of sedimentation: the Tay in comparison with other estuaries. In: J. Hails and A. Carr, eds., *Nearshore sediment dynamics and sedimentation.* J. Wiley and Sons, London, pp. 201-249, 1975.

Darbyshire, E. J., and J. R. West. Spatial and temporal turbulence characteristics in the Tamar Estuary. In: M. Elliot and J.-P. Ducrotoy, eds., *Estuaries and Coasts: Spatial and Temporal Intercomparisons.* Olsen and Olsen, pp 37-42., 1991.

Foreman, M. G. G. *Manual for tidal currents analysis and prediction*. Institute of Ocean Sciences report 78-6, Sidney, B.C., 101 pp., 1978.

Foreman, M. G. G, and R. F. Henry. *Tidal analysis based on high and low water observations*. Institute of Ocean Sciences report 79-15, Sidney, B.C., 39 pp., 1979.

Friedrichs, C. T. and O. S. Madsen. Nonlinear diffusion of the tidal signal in frictionally dominated embayments. *Journal of Geophysical Research* 97: 5637-5650, 1992.

Geyer, W. R. The advance of a salt wedge front: observations and dynamical model. In: Dronkers, J. and W. van Leussen, eds. *Physical Processes in Estuaries.* Springer-Verlag, Heidelberg, pp 181-195, 1988.

Godin, G. Frictional effects in river tides. In: B. B. Parker, ed. *Progress in Tidal Hydrodynamics*, J. Wiley, New York. pp. 379-402, 1991.

Hansen, D. V. and M. Rattray, Jr. Gravitational circulation in straits and estuaries, *Journal of Marine Research* 23: 104-122, 1965.

Ianniello, J. P. Non-linearly induced currents in tidally dominated estuaries. Ph.D. thesis, University of Connecticut., 1977.

Ibrahim, Z. Z., K.-F. Kam, Z. Norazma, M. S. Surina. Structural changes in equatorial estuaries (abs). In: *Changes in fluxes in estuaries*, joint ECSA/ERF Conference, Plymouth, England, 1992.

Jay, D.A. Residual circulation in shallow stratified estuaries, Ph.D dissertation, University of Washington, 173 pp., 1987.

Jay, D.A. Residual circulation in shallow estuaries: shear, stratification and transport processes, in: R. T. Cheng, ed., *Residual Currents and Long-Term Transport*, Springer-Verlag, pp. 49-63, 1990.

Jay, D.A. Internal asymmetry and anharmonicity in estuarine flows. In: *Progress in Tidal Hydrodynamics*, ed. by B. B. Parker, John Wiley, pp. 521-543, 1991a

Jay, D. A. Green's Law revisited: tidal long-wave propagation in channels with strong topography, *J. Geophys. Res.* 96: 20,585-20,598, 1991b

Jay, D. A. Estuarine salt conservation: a Lagrangian approach. *Estuarine, Coastal and Shelf Science* 32: 547-565, 1991c.

Jay, D. A. and J. D. Musiak. Particle trapping in estuarine turbidity maxima, submitted to *Journal of Geophysical Research*, 1993.

Jay, D.A. and J.D. Smith. Circulation in and classification of shallow, stratified estuaries. In: J. Dronkers and W. van Leussen (eds.), *Physical Processes in Estuaries*, Springer-Verlag, Heidelberg, pp19-41, 1988.

Jay, D.A. and J.D. Smith. Residual circulation in shallow, stratified estuaries. I. Highly-stratified systems. *Journal of Geophysical Research* 95(C1): 711-732, 1990a.

Jay, D.A. and J.D. Smith. Residual circulation in shallow, stratified estuaries. II. Weakly-stratified and partially-mixed systems. *Journal of Geophysical Research* 95(C1): 733-748, 1990b.

Jay, D.A. and J.D. Smith. Circulation, density distribution and neap-spring transitions in the Columbia River Estuary. *Progress in Oceanography*, 25: 81-112, 1990c.

Lang, G., R. Schubert, M. Markovsky, H.-U. Fanger, I. Grabemann, H. L. Kraseman, L.J.R. Neumann, and R. Riethmüller. Data interpretation and numerical modeling of the mud and suspended sediment experiment 1985 *Journal of Geophysical Research* 94(C10): 14,381-14,394, 1989.

Lewis, R. E., and J. O. Lewis. The principal factors contributing to the flux of salt in a narrow, partially stratified estuary. *Estuarine Coastal and Shelf Science* 16: 599-626, 1983.

Long, C. E. *A simple model for time-dependent stably stratified turbulent boundary layers.* University of Washington Ph.D. dissertation, 170 pp., 1981.

Long, E. E. *Tide and tidal current observations from 1965 through 1967 in Long Island Sound, Block Island Sound and tributaries*. NOS Oceanographic Circulatory Survey Report No. 1, Rockville, MD, 91 pp., 1978.

McCarthy, R. Residual currents in tidally dominated, well-mixed estuaries. *Tellus*, in press, 1992.

Meade, R. H. Transport and deposition of sediments in estuaries. *Geological Society of America Memoir* 133: 91-120, 1972.

Nihoul, J. C. J., F. C. Ronday, J. J. Peters and A. Sterling. *Hydrodynamics of the Scheldt Estuary*. In: J. C. J. Nihoul, ed., *Hydrodynamics of Estuaries and Fjords*, Elsevier, Amsterdam, pp. 27-54., 1978.

Parker, B. B. The relative importance of the various nonlinear mechanisms in a wide range of tidal interactions. In: B. B. Parker, ed. *Progress in Tidal Hydrodynamics*, J. J. Wiley, New York, pp. 237-268, 1991.

Partch, E. and J. D. Smith. Time Dependent mixing in a salt wedge estuary. *Estuarine and Coastal Marine Science* 6: 3-19, 1978.

RD Instruments. *Acoustic Doppler current profilers principles of operation: a practical primer*. RD Instruments, San Diego, 36 pp., 1989.

RD Instruments. Velocity measurement bias errors in the ADCP. Technical Bulletin ADCP-89-06, 24 pp., 1989.

Speer, P. E., D. G. Aubrey and C. T. Friedrichs. Nonlinear hydrodynamics of shallow tidal inlet/bay systems. In: B. B. Parker, ed. *Progress in Tidal Hydrodynamics*, pp. 321-340, 1990.

Stokes, G. G. On the theory of oscillatory waves, *Transactions of the Cambridge Philosophical Society* 8: 441-455, 1847.

Trowbridge, J., and O. S. Madsen. Turbulent wave boundary layers 2. Second-order theory and mass transport, *Journal of Geophysical Research* 89: 7999-8007, 1984.

Uncles, R. J., and J. A. Stephens. The structure of vertical current profiles in a macrotidal, partly-mixed estuary, *Estuaries* 13: 349-361, 1990.

Walters, R. H. A model study of the effects of sea level rise in Delaware Bay. Part 1:hydrodynamics. submitted t1993.

Walters, R. H., R. T. Cheng and J. T. Conomos. Time scales of circulation and mixing processes of San Francisco Bay. *Hydrobiologia* 129: 13-36, 1985.

West, J. R., D. W. Knight, and K. Shiono. A not on flow structure in the Great Ouse estuary. *Estuarine Coastal and Shelf Science* 19: 271-290, 1984.

West, J. R., R. J. Uncles, J. A. Stephens, and K. Shiono. Longitudinal dispersion processes in the upper Tamar estuary. *Estuaries* 13: 118-124, 1990.

Wright, L. D. Hydrography of South Pass, Mississippi River. *J. Waterways Port, Coastal and Ocean Division, ASCE* 97(WW3): 491-504, 1971.

Zhou, M. Internal circulation and salt intrusion in the Hudson Estuary, Ph.D dissertation, State University of New York at Stony Brook, N. Y., 1992.

14

Relative Contributions of Interfacial and Bed Generated Mixing to the Estuarine Energy Balance

R. E. Lewis

Abstract

The results of fixed station sampling in a partially stratified estuary have been used to determine the variation in the potential energy anomaly during a tidal cycle. The results indicated that the anomaly at a given station had a similar magnitude at successive high waters. Also, it was found that the rate of change of potential energy anomaly was of similar magnitude to the rate of change of the rotational kinetic energy of the flow throughout the tide. The rate of potential energy change due to mixing during the tide was computed and, by comparing the findings with theoretical values for bed generated energy, the proportion of turbulent energy contributing to mixing was calculated. These mixing efficiencies were found to increase with the layer Richardson number, apparently due to an increasing contribution from interfacially generated energy. At two stations in the central reach of the estuary, the ratio of eddy diffusivity to viscosity coefficients responded to Richardson number in the manner described by Munk and Anderson (1948). The corresponding rate of generation of turbulent energy at the bed of the estuary was estimated to be approximately 5 times the generation rate at the pycnocline. However, locally generated energy was much more efficient in weakening the degree of stratification and, at higher Richardson numbers, less than 10% of the mixing energy originated at the bed. At a station further to landward, the response of mixing efficiency to Richardson number was less rapid, apparently due to the influence of the longitudinal gradient in density.

Mixing in Estuaries and Coastal Seas
Coastal and Estuarine Studies Volume 50, Pages 250-266
Copyright 1996 by the American Geophysical Union

Introduction

Studies of mixing in coastal waters have made use of a parameter ϕ which describes the potential energy anomaly of the water column. In situations where solar heating is considered to be the main source of stability, determinations of ϕ have been used to define regions where thermal fronts occur (Pingree and Griffiths, 1978). By comparing the rate at which turbulent energy is generated by tidal mixing with the rate of supply of stability by heating, observed ϕ values have been used to estimate the fraction of the tidally generated energy utilised in mixing (Simpson and Bowers, 1981). This ratio is termed the mixing efficiency ε.

In an estuary, the input of buoyancy is primarily due to freshwater but this does not have the spatial uniformity of surface heating (Nunes Vaz *et al.*, 1989). For this reason, estimates of the stability increase at a particular location have made use of direct observations of the longitudinal density gradient, as demonstrated in the Irish Sea (Simpson *et al.*, 1990). However, ε is likely to vary with the degree of stratification and allowance for stability effects on efficiency has been included in some models (Simpson, 1981; Simpson and Bowers, 1981).

This paper describes how the rate of potential energy change due to mixing was computed at three stations in the Tees estuary. These results were used to relate the efficiency of mixing to the interfacial stability, as defined by a layer Richardson number. Comparisons of the response of mixing to Richardson number were made with previous studies and estimates were made of the proportion of total mixing energy attributable to dissipation of tidal energy by bottom friction.

Theory

The potential energy anomaly ϕ can be computed from the instantaneous distribution of density over depth using the formula

$$\phi = \frac{g}{h} \int_0^h (\rho - \rho_m)\, z dz \qquad (1)$$

where, ρ, ρ_m represent the density at a depth z down from the surface and the depth mean density over the total depth h respectively.

In an estuary, the centre of mass of the water column rises and falls with corresponding changes in the surface elevation. Taking the mean tide level as the zero of potential energy, elevation or depression of the surface relative to this equilibrium level represents stored potential energy. In the absence of vertical mixing, the ebb tide shear in velocity relative to the mean flow brings less saline water down in the surface layer whilst an equal volume of more saline water is carried landwards in the lower layer. This has the effect of redistributing the density so that the centre of mass is displaced downwards relative to the centre of mass of

the overall (fully mixed) column. This corresponds to an increase in the magnitude of ϕ. Depending on the form of the velocity profile, an analogous process can increase or decrease the potential energy anomaly on the flood tide.

In contrast to the effect of shear, mixing can only decrease the displacement of the centre of mass from that of the fully mixed water column. Thus mixing always tend to reduce the size of the potential energy anomaly. If the rate of lowering of the centre of mass by current shear relative to the depth mean flow matches the rate of raising of the centre of mass by mixing, then the potential energy anomaly remains constant. The dependence of the potential energy anomaly on shear and mixing can be expressed as

$$\frac{\partial \phi}{\partial t} = \frac{\partial \phi_s}{\partial t} - \frac{\partial \theta}{\partial t} \qquad (2)$$

where ϕ_s is that part of the potential energy anomaly associated with current shear and θ is the mixing energy required to render the water column homogeneous. Following Simpson *et al.* (1990), the rate of change in potential energy due to shear can be expressed as

$$\frac{\partial \phi_s}{\partial t} = \frac{g}{h} \int_0^h \frac{\partial \rho}{\partial x} ((u - u_m) \; z dz \qquad (3)$$

where u, u_m are the current and the depth mean current respectively. This implicitly assumes that changes in potential energy due to cross-estuary flows and mixing can be neglected. Although this may be a significant factor towards the edge of an estuary, transverse variations in density tend to be small in the main channel of a narrow estuary and the neglect of such processes may be reasonable (Lewis, 1979). Even in the absence of vertical mixing, oscillatory motion can cause the estuary to stratify on an ebb tide and to destratify on a flood. This was shown by Simpson *et al.* (1990) in estimating the instantaneous contribution of shear to stratification by considering the combined effects of estuarine circulation and tidal straining, the latter process being dependent on the velocity profile due to tidal motion. As $\partial\phi/\partial\tau$ and $\partial\phi_s/\partial t$ can be estimated from observations of the density and velocity structure, $\partial\theta/\partial t$ can be calculated using equation (2).

The mixing efficiency ε represents the fraction of the turbulent kinetic energy, arising from bottom friction, that is used to increase the potential energy of the water column (Bowden, 1983: p 232). It follows that is ε given by

$$\varepsilon = \frac{\partial \theta}{\partial t} / P_b \qquad (4)$$

where P_b is the time rate of generation of turbulence at the bed. P_b can be estimated from the formula

$$P_b = C_d \rho \frac{U_m^3}{h} \qquad (5)$$

where C_d is a drag coefficient and u_m is the depth mean current.

$\partial\theta/\partial t$ is the rate change of potential energy of the whole water column and can be split into terms arising from interfacial and bed generated mixing, so that the mixing efficiency can be expressed as

$$\varepsilon = \left(\frac{\partial\theta_i}{\partial t} + \frac{\partial\theta_b}{\partial t}\right) / P_b \qquad (6)$$

where the subscripts denote turbulence of interfacial and bed origin.

If it is assumed that the contribution of bed generated turbulence to the mixing increases in direct proportion to the rate at which this turbulence is generated at the bed then

$$\frac{\partial\theta_b}{\partial t} / P_b = \varepsilon_k (\text{constant}) \qquad (7)$$

By definition, the flux Richardson number is the ratio of the rate of increase of potential energy to the rate of production of turbulent energy by interfacial shear. Thus Rf is given by

$$Rf = \frac{\partial\theta_i}{\partial t} / Pi \qquad (8)$$

It follows from equations (6), (7) and (8) that

$$\varepsilon = Rf \left(\frac{P_i}{P_b}\right) + \varepsilon_k \qquad (9)$$

There is evidence that the ratio P_i/P_b may be approximately constant since a strong shear at the bed is likely to result in a strong shear across a density interface, as for example, has been observed in the Fraser River estuary (Geyer and Farmer, 1989).

Field investigations

Description of the estuary

The River Tees is situated on the north-east coast of England and flows out into the North Sea (Figure 1). The estuary of the River Tees has been made relatively canal-like at its seaward end by reclamation of the intertidal mud flats and dredging of the shipping channel. The tidal limit is at Middleton St. George, which lies some 44 km from the estuary mouth, but the salt wedge only penetrates about 26 km inland. The landward half of the estuary is made up of a series of meander loops and there is a small tributary, the River Leven, in this section.

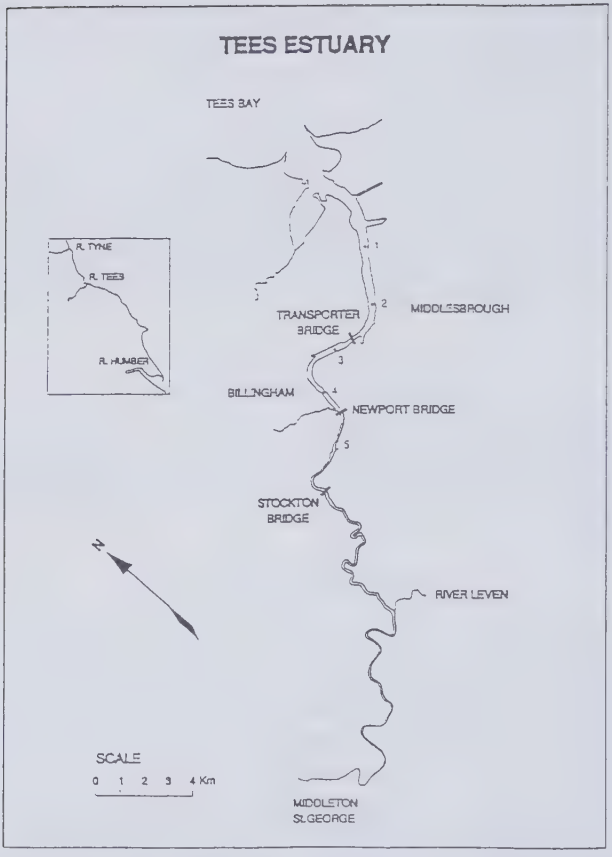

Figure 1. Location and plan view of Tees Estuary showing 1990 survey sampling stations.

The annual average freshwater flow of the River Tees is 20 $m^3 s^{-1}$, with a typical range from 2 to 70 $m^3 s^{-1}$. The mean neap and spring tidal ranges are 2.3 and 4.6 m respectively and, even on the highest range of tide, the estuary remains partially stratified.

Observations

In June, 1990, a survey of the current and density structure of the Tees estuary was determined at 5 anchored stations along a central section. The measurements were undertaken over a full tidal period on three days of neap range and three days of springs. Currents, salinities and temperatures were determined at one metre intervals over depth every half-hour. The current speed and direction were measured with

Braystoke meters (estimated accuracy: velocity ± 0.05 m s^{-1}) and the salinities and temperatures were measured with MC5 conductivity bridges (estimated accuracies: temperature ± 0.1 °C; salinity ± 0.05).

Sets of data obtained on 11 June, 1990, were selected for more detailed analysis because complete records had been obtained on that occasion. These measurements were made at station 3, which was just upstream of the Transporter Bridge, station 4 in the middle of Billingham Reach and station 5, which was located between the Stockton and Newport Bridges (Figure 1). The tidal range on that day was 4.1 m and the freshwater flow was approximately 2.5 m^3 s^{-1}.

Results

The temperature and salinity data from the three stations were used to compute the density at each sampling depth. The potential energy anomaly was then computed from these density values using equation (1) and plotted against time (Figure 2). A feature of these plots is that the ϕ values undergo considerable variation during a tidal period but have approximately the same values at times of high water. Thus at high water, both the water level and the degree of stratification return to similar values to those held at the previous high water. This suggests that, despite considerable changes in the anomaly at all three stations during the tidal period, an internal energy balance occurs. Furthermore, the magnitude of ϕ at high water decreases from station 3 to station 5, implying that there is a decrease in stratification with distance up the estuary.

The time rate of decrease of potential energy due to shear, $\partial\phi/\partial t$, was computed using equation (3) and the variation in this parameter during a tidal cycle was plotted for all three stations (Figure 3). It can be seen that this parameter is generally positive, implying that the effect of shear is to increase the stratification over most of the tidal period. Reduction in the rate of potential energy decrease at the end of the flood tide is apparently due to the surface current increasing the surface layer density faster than that at depth, as would be expected when the tidal shear exceeds that due to the steady state circulation.

Using equation (2), the time rate of increase in the potential energy of the water column, $\partial\phi/\partial t$, due to mixing alone was computed. The variation in these rates during a tide are presented in Figure 4. It can be seen that, generally, the fastest rates occurred at half ebb and half flood, with very little mixing at high and low water slack. It is estimated that the error in the determination of $\partial\theta/\partial t$ was $\pm 3 \times 10^{-3}$ J m^{-3} s^{-1} which is sufficient to account for the occasional negative value. In practice, a negative value for $\partial\theta/\partial t$ cannot occur since mixing can only increase the potential energy of the water column. Allowing for this degree of error, it can be seen from Figure 4 that the $\partial\theta/\partial t$ values reached relatively similar levels on the ebb tide at all three stations, corresponding to about 0.02 J m^{-3} s^{-1}, although there was an appreciable time difference between these occurrences.

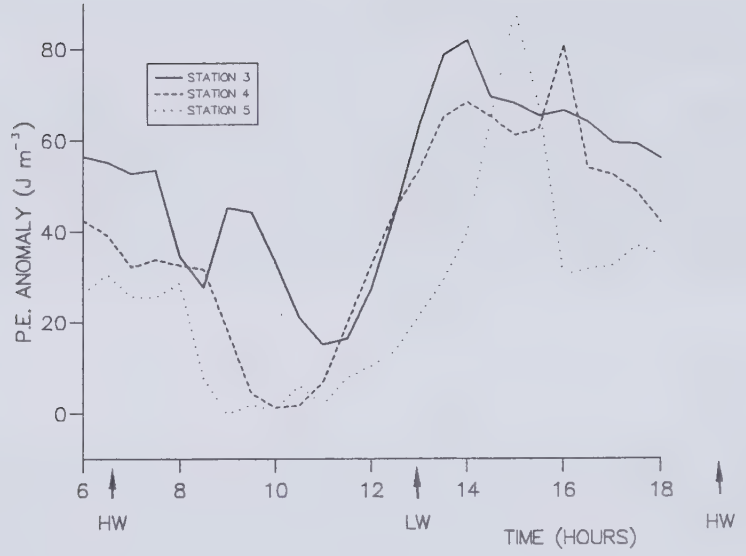

Figure 2. Variation in potential energy anomaly during tide.

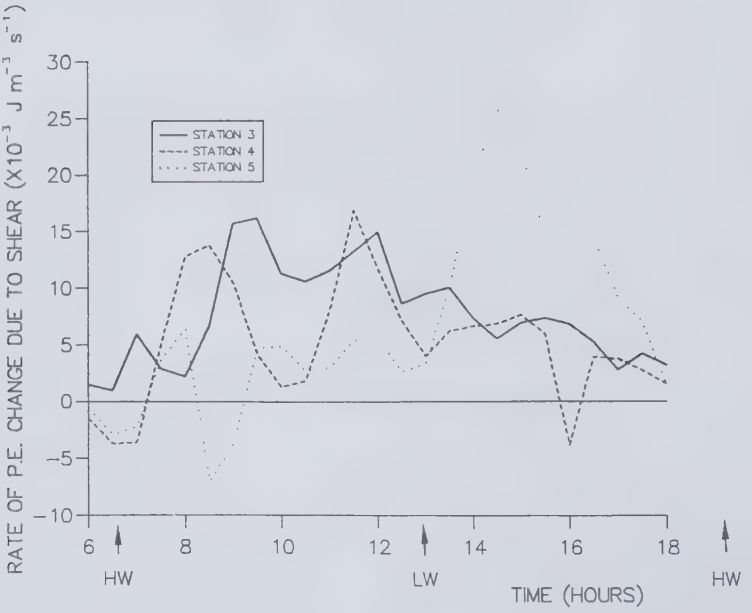

Figure 3. Tidal variation in rate of potential energy change due to shear.

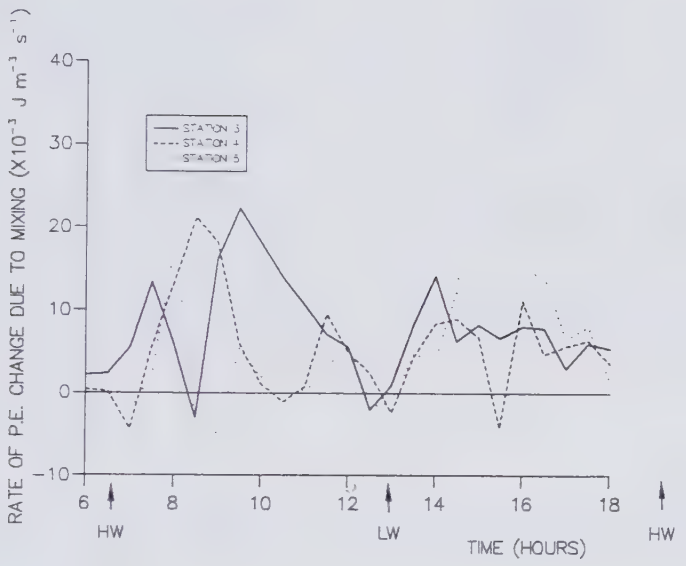

Figure 4. Variation during a tidal period of the rate of increase in potential energy due to mixing.

Discussion

Internal Energy Balance

From differences in ϕ at successive time intervals, the rate of change of potential energy anomaly, $\partial\phi/\partial t$, was computed. The rotational kinetic energy due to shear in the velocity profile at each sampling time was also calculated from the relation

$$\mu = \frac{1}{2h} \int_0^h \rho \, (u - u_m)^2 dz \qquad (10)$$

Differences between successive values for μ were used to compute the time rate of change of the kinetic energy, $\partial\mu/\partial t$, associated with current shear. Figure 5 shows a plot of $\partial\mu/\partial t$ and $\partial\phi/\partial t$ during the tidal cycle at station 4 in Billingham Reach. Although a correlation between these parameters is not as evident in this plot as in data from previous years (Lewis *et al.*, 1994), it does appear that the rates of change were of similar magnitude, implying that these potential and kinetic energy changes maintain the energy balance of the internal structure. The parameter μ includes the

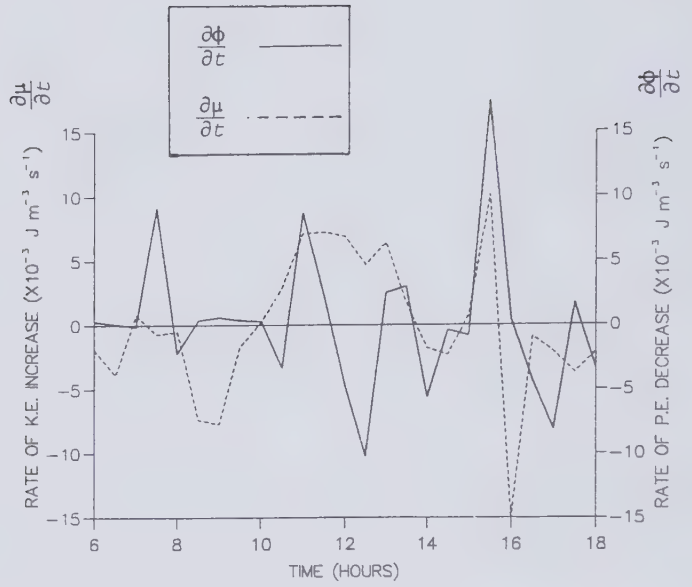

Figure 5. Comparison of the rate of increase in rotational kinetic energy with the rate of decrease in potential energy as determined at station 4.

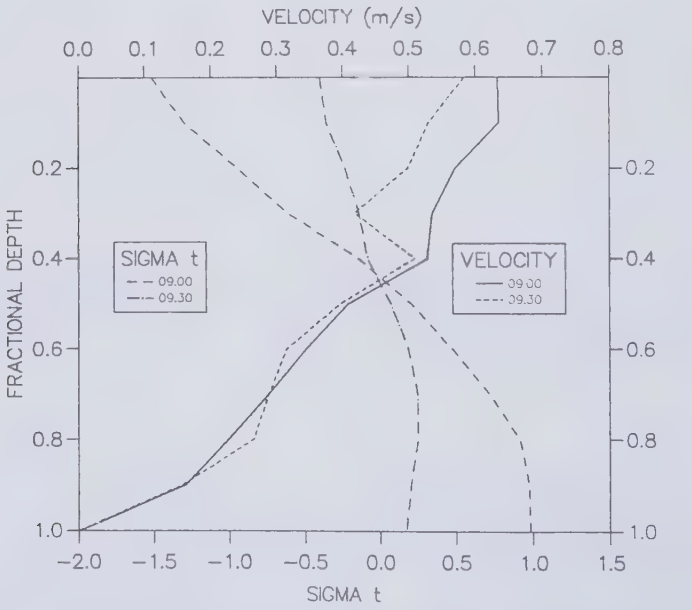

Figure 6. Comparison of velocity profiles with profiles of the deviation from depth mean density; station 4, 12/6/90.

effect of velocity profile changes which are not attributable to changes in the vertical distribution of density and, therefore, a good correlation between $\partial\mu/\partial t$ and $\partial\phi/\partial t$ would not be expected. For example, a change in the surface slope over the half hour interval would alter the velocity profile as the system adjusted the friction loss to balance the change in the driving force.

Figure 6 presents an example of the density and velocity profile changes over a half-hour interval; these profiles were determined at about half ebb at station 4. To demonstrate how the density profile alters, the sigma-t values are given relative to the depth mean density, sigma-t being defined as (ρ-1000) in MKS units. Although the corresponding velocity data were not precise enough to give a smooth profile, it can be seen that the change in the profile was most marked near the surface.

Mixing Efficiency

Generally, potential energy change in a water column is associated with mixing at the pycnocline. This mixing may be induced by turbulence generated at the bed or by instabilities forming on the interface. Although it has been estimated that 90% of the turbulent energy is generated in the lower 10% of the water column, the effect on stratification depends on this energy being diffused or advected up into the vicinity of the pycnocline (Bowden, 1983: p 239).

The rate of turbulent energy generation from the bed, P_b, during a tidal period was computed using equation (5). Figure 7a presents the observed variation in the depth mean density, expressed as sigma-t, and the depth mean current for all three stations. It should be noted that flood currents were lower than those on the ebb at stations 3 and 4. This factor was the principal reason for the inequality in the P_b values shown in Figure 7b. In addition there is an inequality in the magnitude of drag coefficients in the Tees estuary, with greater values occurring on the ebb than the flood (Lewis and Lewis, 1987), and this would was also taken into account in deriving values for P_b. For the flow conditions of the 1990 survey, typical drag coefficients were generally 0.0045 with values up to 0.016 on the ebb tide.

Mixing efficiencies, ε, were computed from the rates of increase in potential energy due to mixing and the corresponding P_b values using equation (4). Most of the estimates of ε were less than 0.1 but a few particularly high values were derived. These corresponded to small values of P_b, as occurred near times of slack water or at station 3 on the flood, and it was assumed that the error associated with P_b was too large for the estimates of to be reliable. Therefore, in determining mixing efficiency, values greater than 0.15 and those corresponding to negative mixing rates were discounted.

Interfacial mixing in a shear flow is characterised by the flux Richardson number Rf. Linden (1979) showed that Rf varies with an overall Richardson number in such a way that Rf increases up to a maximum value and then decreases as the Richardson

number exceeds a critical value. To define the degree of stability across the density interfaces in the Tees, a layer Richardson number, Ri , was defined as

$$Ri_L = \frac{\Delta\rho g d}{\rho(\Delta u)^2} \tag{11}$$

where $\Delta\rho$, Δu are the density and velocity differences across a pycnocline of depth d. Ri_L has a similar definition to the overall Richardson number employed by Linden (1979).

(a)

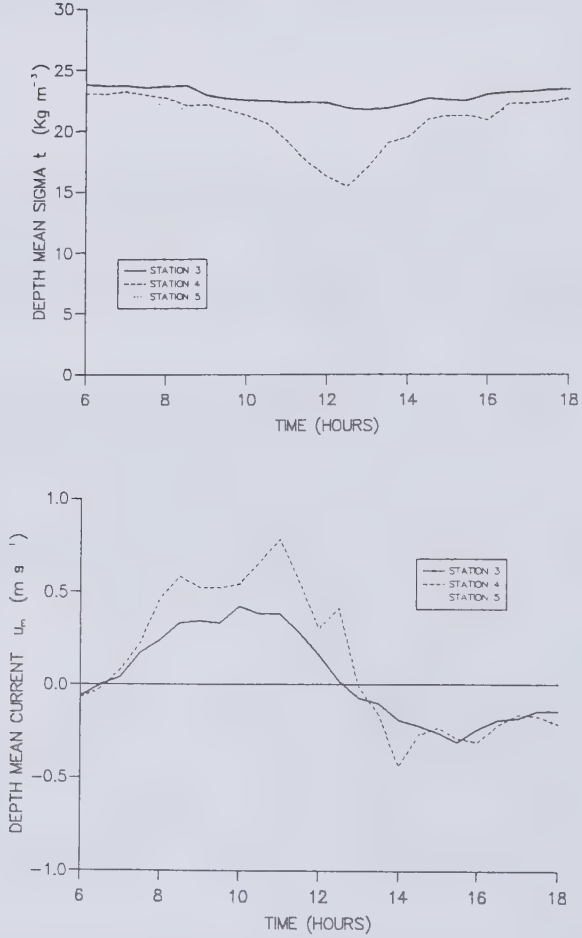

Figure 7. (a) Tidal variation in the depth mean density, expressed as sigma-t, and the depth mean current. (b) Corresponding plot of the tidal variation in the estimated rate of generation of turbulent energy from the bed at the three stations.

(b)

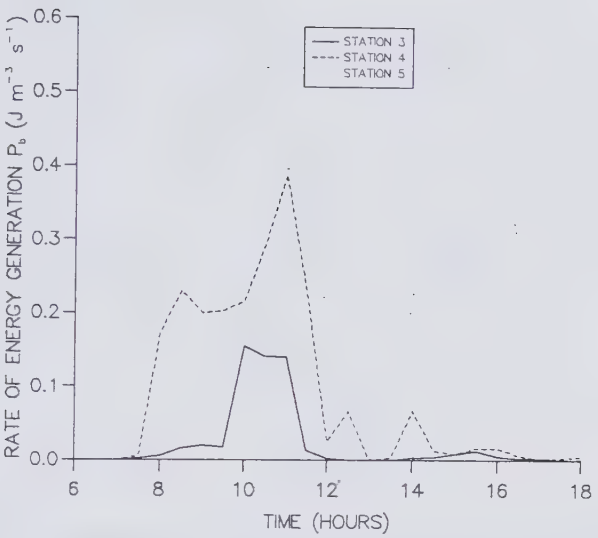

Figure 7 (continued). (a) Tidal variation in the depth mean density, expressed as sigma-t, and the depth mean current. (b) Corresponding plot of the tidal variation in the estimated rate of generation of turbulent energy from the bed at the three stations.

Figure 8 shows values for the mixing efficiency plotted against layer Richardson number. It can be seen from this Figure that the efficiencies rise with increase in Richardson number. The increase in ε was relatively similar at stations 3 and 4, but a much shallower rate of rise was computed for station 5. The initial rise in ε with Ri_L may be due to the increasing occurrence of instabilities on the density interface so that the mixing energy becomes less dependent on bed generated turbulence. For example, once the layer Richardson number exceeds 0.25, mixing may be aided by Kelvin-Helmholtz shear instability (Geyer and Farmer, 1989). It was suggested by Linden (1979) that the drop in R_f, and hence mixing efficiency, above a critical Ri_L could be due to the stability becoming high enough for internal waves to form and take kinetic energy away without contributing to the mixing. This proposal is supported by spectral analysis of salinity fluctuations in Southampton Water (Dyer, 1988).

For any given layer Richardson number, the mixing efficiencies in Figure 8 appear to reach a maximum value. The scatter of values below this limit is apparently due to times at which the bed generated energy is much greater than that utilised in mixing. It has been seen above that raising the potential energy by mixing reduces the degree of shear; this reduction occurs at the bed and across the density interface. Thus mixing results in a negative feedback which limits the creation of turbulence for promoting further breakdown of the pycnocline. This may explain the occurrence of maximum efficiencies. It should be noted that this argument, originally outlined by Rossby and Montgomery (1935), takes no account of the combined effect of shear and the longitudinal density gradient in altering stability. When the longitudinal

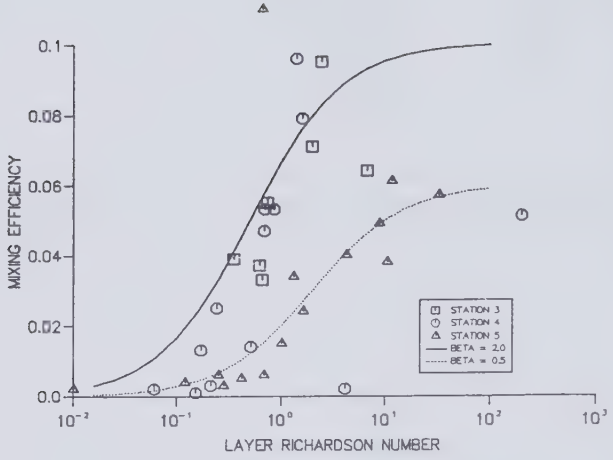

Figure 8. Mixing efficiency plotted against layer Richardson number. The curves correspond to equation (15) with the parameter values given in Table 1.

density gradient is appreciable, shear may enhance the degree of stratification. In such an instance, reduction in shear due to mixing has the dual effect of lowering the rate of turbulent energy generation at the interface and of reducing the rate of stratification. This would result in the mixing efficiency reaching its limit value more rapidly than at locations where the longitudinal density gradient is weak.

When the shear acts with the longitudinal density gradient to increase the potential energy anomaly, mixing has to exceed this deficit before feedback can reduce the generation of turbulent energy by shear. Thus, the limit to mixing efficiency would be reached at a higher energy usage by mixing than would be the case when the longitudinal density gradient is small.

When the Ri_L value was about 0.1 the contribution of interfacial effects to mixing would be expected to be small; the mixing efficiencies were then typically about 0.004, a magnitude which is supported by estimates of ε in the Celtic and Irish Seas (Simpson and Bowers, 1981). If the highest observed efficiencies represent the maxima, although the evidence is only tentative, then the corresponding Ri_L values represent critical limits in the flow. The highest ε values corresponded to layer Richardson numbers of about 1.0 and 10 at stations 3, 4 and 5 respectively, and are equivalent to interfacial Froude numbers of 1.0 and 0.3. A critical Froude number of 1.0 would be expected in two layer flow and a theoretical value of 0.3 is predicted for a continuously stratified flow. Thus the highest efficiencies observed may reflect the generally greater degree of stratification at stations 3 and 4 compared with station 5 (Figure 2).

Variation in eddy coefficients

It can be seen from equation (9) that at higher mixing efficiencies

$$\varepsilon \approx R_f \left(\frac{P_i}{P_b} \right) \tag{12}$$

so that, assuming P_i/P_b is constant, the mixing efficiency becomes a measure of the flux Richardson number.

By definition

$$Rf = \frac{K_z}{N_z} Ri_L \tag{13}$$

where K_z, N_z are coefficients of eddy diffusivity and viscosity.

The form of the curve when Rf increases with Ri_L depends on the ratio of the eddy diffusivity and viscosity coefficients; with increased stability the transfer of matter is inhibited to a greater extent than momentum. Various expressions have been developed to quantify this ratio in estuaries (Dyer, 1988).

Typically, these have the form

$$\frac{K_z}{N_z} = \frac{1}{(1+\beta Ri_L)^n} \tag{14}$$

It follows from equations (12), (13) and (14), that

$$\varepsilon = \frac{\alpha Ri_L}{(1+\beta Ri_L)^n} \tag{15}$$

where $\alpha = P_i/P_b$.

The two curves shown in Figure 8 were derived from equation (15) using the parameter values given in Table 1. The curves approximately define the upper limit to the mixing efficiencies for the combined data from stations 3 and 4, and for the single set of data from station 5. In selecting the parameter values, emphasis was put on the efficiencies corresponding to the higher Ri_L values since these were less likely to be influenced by energy derived from the bed.

Figure 9 presents plots of the K_z/N_z curves as given by equation (14) using the parameter values from Table 1. For comparison, curves suggested by Munk and Anderson (1948) and Bowden and Gilligan (1971) are also shown in the Figure. It can be seen that the curve for stations 3 and 4 lies relatively close to the curve suggested by Munk and Anderson. The curve for station 5 implies that K_z/N_z would

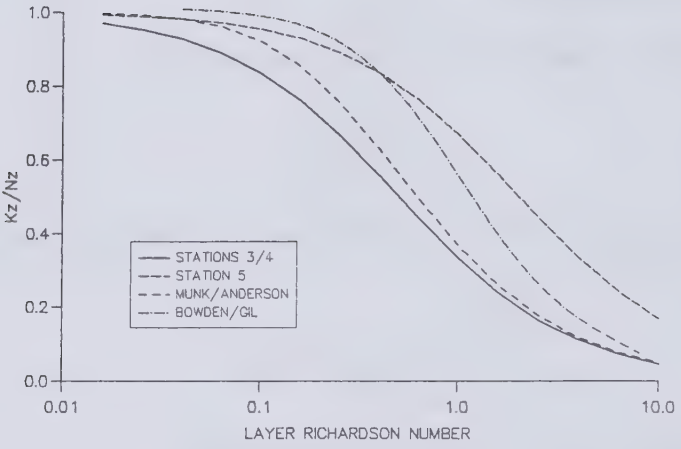

Figure 9. Variation of K_z/N_z with Ri_L for the three stations. Curves derived by Munk and Anderson (1948) and Bowden and Gilligan (1971) are plotted for comparison.

be higher than given by Munk and Anderson's formula at a given layer Richardson number and has some similarity with a curve derived by Bowden and Gilligan for the Narrows of the Mersey estuary (Dyer, 1988). As explained above, relatively high mixing at the limit for a given Ri may arise when there is a strong gradient in density along an estuary. At station 5, the mean spring tide gradient is about 2.5 km as compared with a gradient of about 0.6 km at stations 3 and 4. Although the density gradient in the Mersey Narrows is relatively similar to that at stations 3 and 4, being typically about 0.5 km , the marked current shear in the Mersey would have favoured a higher level of mixing.

TABLE 1. Parameter values selected for equation (15)

Station	α	β	n
3 and 4	0.2	2.0	1
5	0.03	0.5	1

Relative contribution to mixing

The value for α given in Table 1 suggests that the rate of generation of turbulent energy at the bed is about 5 times that at the interface at stations 3 and 4, assuming that energy generated elsewhere in the water column is negligible. Between stations

4 and 5, the Tees estuary converges and the tidal current is appreciably strengthened, typical spring tide amplitudes being 0.5 m s^{-1} and 0.8 m s^{-1} at the two positions. The α value at station 5 implies that the bed energy is generated at a rate which is some 30 times that at the interface, a finding which is consistent with the strong current at that location.

Figure 8 suggests that the maximum efficiencies for stations 3/4 and station 5 were about 0.1 and 0.05 respectively. It follows from the α values and equation (12) that the corresponding Rf values were 0.5 and 1.6. The former Rf value lies at the upper limit of the quoted range of 0.15 to 0.5 (Dyer, 1988). The latter value exceeds the maximum allowable limit for R_f of 1.0 but this may be due to the dominance of bed generated mixing.

It can be seen from equations (6) and (7) that the fraction of the total mixing energy which is derived from bed turbulence is given by $\varepsilon_k/\varepsilon$. Although ε_k could not be determined with confidence from the data, the estimated value of 0.004 when Ri_l was about 0.1 was assumed on the grounds that it is comparable with determinations in coastal waters of similar stability. Figure 8 shows that, when the layer Richardson number is about 0.1, $\varepsilon \approx \varepsilon_k$ and nearly all the mixing energy is of bed origin at the three stations. With increase in Ri_L the proportion of energy derived from interfacial mixing increases rapidly at stations 3 and 4 so that, when Ri_L is about 0.5, only approximately 10% of the mixing is due to bed generated turbulence. However, at station 5 the contribution from the bed does not decrease to 10% of the mixing energy until Ri_L approaches 5.0.

Conclusions

The analysis of density and velocity structure data from the 1990 survey of the Tees estuary suggested that:

(a) The potential energy anomaly varied appreciably during the tidal period but returned to a similar value at successive highwaters at each of the three stations. Throughout the tidal period, the rate of potential energy increase due to mixing was of similar magnitude to the rate of decrease in the rotational kinetic energy of the flow.

(b) The variation of the ratio K_z/N_z with Richardson number approximates to the formula proposed by Munk and Anderson (1948), provided that the tidal current shear and the longitudinal density gradient are not large.

(c) The rate of generation of turbulent energy at the bed was about 5 times that at the density interface in the central reach of the estuary; convergence of the estuary cross-section appeared to be responsible for this factor increasing to about 30 times at a position further upstream.

(d) The contribution of bed generated energy to the overall mixing decreased with increasing Richardson number. Assuming a mixing efficiency of 0.004 under relatively well mixed conditions, it was found that when Ri_L approached 0.5, only about 10% of the energy was of bed origin. At the upstream station the current was stronger and Ri_L reached about 5.0 before the bed generated energy made up only 10% of the total mixing energy.

References

Bowden, K.F. and Gilligan, R.M. Characteristic features of estuarine circulation as represented in the Mersey estuary. *Limnol. Oceanog.*, 16(3), 490-502., 1971

Bowden, K.F. Physical Oceanography of Coastal Waters. Ellis Horwood, Chichester., 1983.

Dyer, K.R. Tidally generated estuarine mixing processes. In "Hydrodynamics of Estuaries" (Ed. Kjerfve) Chap. 4, 41-57., 1988.

Geyer, W.R. and Farmer, D.M. Tide-induced variation of the dynamics of a salt wedge estuary. *J. Physical Oceanography*, 19, 1060-1072, 1989.

Lewis, R.E. Transverse velocity and salinity variations in the Tees estuary. *Estuarine, Coastal and Shelf Science* 8, 317-326, 1979.

Lewis, R.E. and Lewis, J.O. Shear stress variations in an estuary. *Estuarine, Coastal and Shelf Science* 25, 621-635, 1987.

Lewis, R.E., Riddle, A.M. and Lewis, J.O., Energy adjustment in a partially stratified estuary. *Estuarine, Coastal and Shelf Science* (In press), 1994

Linden, P.F., Mixing in stratified fluids. *Geophys. Astrophys. Fluid Dynamics*,13(3), 3-23, 1979.

Munk, W.H. and Anderson, E.R., Notes on a theory of the thermocline. *J. Marine Research* 7, 276-295, 1948.

Nunes Vaz, R.A., Lennon, G.W. and de Silva Samarasinghe, J.R., The negative role of turbulence in estuarine mass transport. *Estuarine, Coastal and Shelf Science* 28, 361-377, 1989.

Pingree, R.D. and Griffiths, D.K., Tidal fronts on the shelf seas around the British Isles. *J. Geophysical Research*, 83(C9), 4615-4622, 1978.

Rossby, C.G. and M.ontgomery, R.B. The layer of frictional influence in wind and ocean currents. *Papers Physical Oceanography Meteorology* 3(3), 1-101, 1935.

Simpson, J.H. and Bowers, D, Models of stratification and frontal movement in shelf seas. *Deep Sea Research* 28A (7), 727-738, 1981.

Simpson, J.H., The shelf sea fronts: implications of their existence and behaviour. *Phil. Trans. Roy. Soc.*, A302, 531-546, 1981.

Simpson, J.H., Brown, J., Matthews, J. and Allen, G., Tidal straining, density currents and stirring in the control of estuarine stratification. *Estuaries*, 13(2), 125-132., 1990

15

Short Salt Wedges and the Limit of No Salt Wedge

J. B. Hinwood

Abstract

The conditions for the exclusion of a salt wedge from an estuarine channel are deduced by extrapolating the depth at the sea to zero. Since the flow in the upper layer is critical at the sea, salt water will be excluded if the upstream flow is critical. Simple approximations for these flows have been found to overestimate the required upstream Froude number (Fo = 1). Additional factors are included in the present analysis, giving improved predictions (Fo $\simeq$ 0.85) when compared with data. Extrapolation of the length of the salt wedge to zero should also give another estimate of the conditions for exclusion. Keulegan's early experiments on the dimensions and dynamics of the salt wedge had a profound influence on all workers in this area, and his empirical expression for the length of a wedge is still used. His studies on the conditions for exclusion of a salt wedge from an estuary are still the most comprehensive, despite the small dimensions of his apparatus, and hence low Reynolds numbers in his experiments. The present paper reanalyses his data for the length of both short and long salt wedges and shows that they fit a version of the Schijf and Schonfeld equation which includes the additional factors referred to above. Extrapolation of this expression resulted in Fo = 1.

Mixing in Estuaries and Coastal Seas
Coastal and Estuarine Studies Volume 50, Pages 267-277
Copyright 1996 by the American Geophysical Union

Introduction

Background

Under conditions of low tidal energy, sea water may enter an estuary and form a wedge-shaped layer beneath the fresh water of the river, with little mixing between the two layers. Under high river flows the length of the salt wedge in an estuary is reduced. Under sufficiently high flows the salt wedge will be flushed from an estuary. Prediction of this limiting condition is of value in assessing river flow management practices, including the use of river water for agriculture, and in predicting estuarine sedimentation patterns since the upstream transport of sediment in the salt wedge is an important factor. The form and dynamics of the salt wedge have been reviewed by a number of authors (including Ippen and Harleman, 1966; Officer, 1976; Parthenaides, 1992), hence there is no need to review its characteristics here.

The two main approaches to determination of the limiting condition are firstly the use of a critical Froude or bulk Richardson number, and secondly the extrapolation of salt wedges of finite length to the case of zero length. Both approaches were used by Keulegan (1957). Neither approach gave results which exactly matched Keulegan's experimental data, despite this, his work remains the most comprehensive and useful in the study of this limit. Keulegan's data were obtained from experiments in three laboratory channels, of widths 52, 113 and 229 mm. Hence, the conclusions using his data apply quantitatively only to laboratory scale flows but it is believed that the concepts developed are applicable to prototype estuaries.

Following a brief outline of the relevant one-dimensional relationships for salt wedges, this paper attempts to predict the conditions for exclusion of the salt wedge from an estuary, first extrapolating to zero depth at the sea in section 2, then extrapolating to zero salt wedge length in section 3. In the course of the latter attempt, Keulegan's data are reexamined and it is shown that his short and long salt edges fit the same law.

Critical Froude Number and Depth at the Sea

With reference to Figure 1 and assuming that $U_2 << U_1$, the densimetric Froude number for the upper layer may be written as

$$F_1 = \frac{U_1}{\sqrt{g\frac{\Delta\rho}{\rho}(D-d)}} \qquad (1)$$

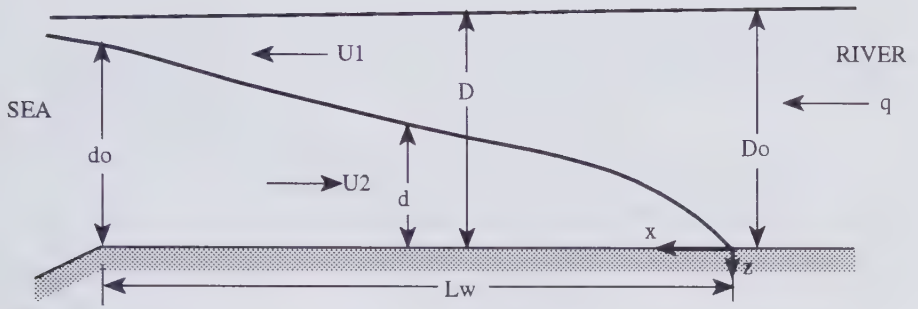

Figure 1. Definition of symbols

For an estuary of constant rectangular section, or by an appropriate definition of an equivalent section, F_1 may be written in terms of the upstream densimetric Froude number, F_o, where

$$F_o = \frac{q}{D_o}\sqrt{g\frac{\Delta\rho}{\rho}D_o} \qquad (2)$$

and q is the river discharge per unit breadth, $\Delta\rho$ is the difference between the densities of river water and sea water, ρ is the density of river water, and the variation of D with x has been neglected.

From (1) and (2),

$$F_1 = \frac{q/(D_o - d)}{\sqrt{g\frac{\Delta\rho}{\rho}(D_o - d)}} = F_o\left(\frac{D_o}{D_o - d}\right)^{3/2} \qquad (3)$$

Farmer (1951) found by experiment that the value of F_1 at the sea was very close to unity. Schijf and Schonfeld (1953) obtained this result theoretically. This result may be used to predict the depth of the salt wedge at the sea:

$$\frac{d_o}{D_o} = \left(1 - F_o^{2/3}\right) \qquad (4)$$

As shown in his figure, reproduced as Figure 2, Keulegan's (1957) experiments gave a value close to, but systematically different to one; Hinwood (1964) obtained similar results for a salt wedge in a stepped channel. The experiments of Stommel and Farmer (1952), also on Figure 2, were for stratified flow through a constricted entrance to a completely mixed basin, and again differed from one. The discrepancy between experiment and theory makes the extrapolation to zero depth at the sea unreliable.

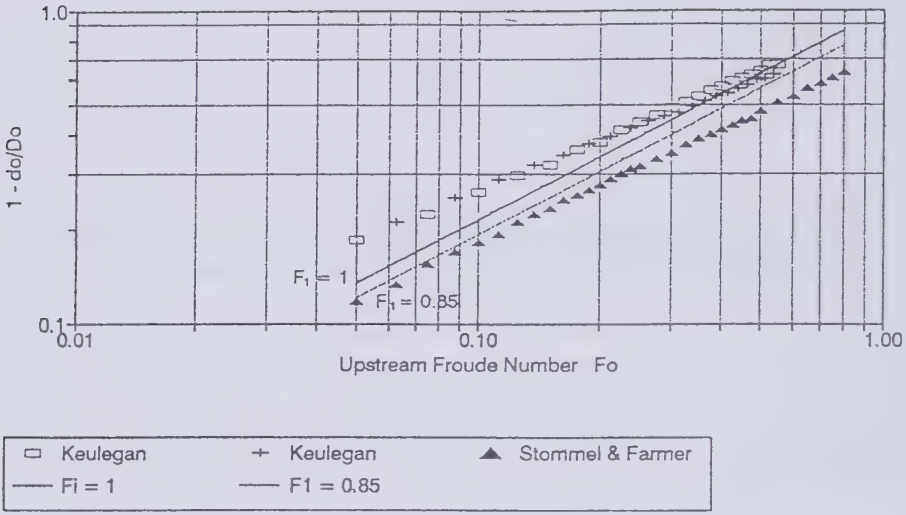

Figure 2. Depth of fresh water at the sea - Experiments of Keulegan (1957) and Stommel and Farmer (1952).

For the case of a moving lower layer the critical condition has been shown to be:

$$F_1^2 + F_2^2 = 1 \qquad (5)$$

Arita and Jirka (1987b) also considered a moving lower layer using a schematic velocity profile in a two layer numerical model. They used a previous study to estimate the flow in the lower layer, which was a function of the Reynolds number. They predicted that the critical value of F_1 was about 0.95 for high Reynolds number flows, falling to 0.7 for the low values in small scale model studies.

Length of the Salt Wedge

The conditions for exclusion of salt water may be obtained by extrapolating the length of the salt wedge to zero. Keulegan (1952) obtained the following expression for the length of salt wedges in his laboratory flume:

$$L_w = A_o R_d F_o^{-5/2} \qquad (6)$$

where

$$R_d = D_o \sqrt{g \frac{\Delta\rho}{\rho} D_o} \Big/ \nu$$

and A_o is a constant. Since Keulegan (1957) did not deliberately vary D_o or ν, R_d could be replaced by $\Delta\rho/\rho$. This result was obtained empirically from a log-log plot of his data. It was not extrapolated to zero length, as it would clearly give the absurd result that F_o is infinite.

Improved expressions for the length of the salt wedge may be obtained from the interface profile equations of Farmer and Morgan (1952) and Schijf and Schonfeld (1953); these were extended and tested against data by Parthenaides et al. (1975). Officer (1976) derived an expression similar to that of Schijf and Schonfeld, and stated that there was little difference in the predictions of his and the first two equations.

Officer assumed uniform velocity in the upper layer, no entrainment across the interface, that the lower layer has velocities which are very much smaller than the upper layer velocities and has a constant eddy viscosity, and that the interfacial friction is proportional to the square of the local velocity in the upper layer. Officer's equation may be written as

$$\frac{L_w}{D_o} = \frac{1}{3\,kF_0^{\,2}}\left(\frac{d_0}{D_o}\right)^2\left\{1-\frac{16}{9}\frac{d_o}{D_o}+\frac{19}{18}\left(\frac{d_o}{D_o}\right)^2-\frac{8}{405}\left(\frac{d_o}{D_o}\right)^3+\ldots\right\} \qquad (7)$$

where k is a constant interfacial friction factor. Officer did not test his equation against data, and none of the above authors considered the case of zero length. If L_w is set equal to zero, equation (7) shows, unhelpfully, that d_o is zero or F_o is infinite. Each of these authors used equation (4) in the derivation of their equations.

While the other authors cited above assumed in their analytical equations that the interfacial shear was constant for each wedge, Officer permitted it to vary. The literature on interfacial shear is large and the reader is referred to the reviews by Arita and Jirka (1987a) and Parthenaides (1992). No one expression for the form of the dependence of interfacial shear on the parameters of the flow has become universally accepted, although each of the reviews just mentioned provide similar semi-theoretical expressions confirmed by data, showing a dependence on ReF_o^2 and either F_o or $\Delta\rho/\rho$, where Re is a Reynolds number.

Reanalysis of Salt Wedge Depth at the Sea

Two factors which have been omitted from the above analyses of the critical Froude number will now be considered. They are the non-uniformity of the velocity profiles and the entrainment from the lower layer into the upper layer. The effects of entrainment on short salt wedges will be to reduce the density difference between the layers, and to cause a small net upstream velocity in the lower layer. When added to the small shear- and pressure-driven recirculating flow in the lower layer, the lower layer velocity may cease to be negligible.

If the flow in the upper layer is non-uniform, the kinetic energy per unit mass in the upper layer becomes $U_1^2 \alpha_1/2$, where U_1 is now the depth-averaged velocity in the upper layer, and 1 is the kinetic energy correction factor having a value a little less than unity. If F_1 is regarded as the square root of the ratio of the kinetic energy to the gravitational potential energy of the upper layer, F_1 may be rewritten for the case of non-uniform velocity in the upper layer as

$$F_1 = \frac{U_1\sqrt{\alpha_1}}{\sqrt{g\frac{\Delta\rho}{\rho}(D-d)}} \tag{8}$$

A similar expression may be written for F_2, but the non-uniformity is generally more marked in the lower layer and α_2 may be appreciably more than unity.

To consider the effect of entrainment across the interface, let the flow entrained into the upper layer over the whole length of the salt wedge be eq. Then the total flow in the upper layer at the sea is (1+e)q. The density in the upper layer will be increased by entrainment, resulting in a reduction of the density difference between the layers at the sea to the new value $\Delta\rho/(1+e)$. Hence, again neglecting the variation of D with x, the densimetric Froude number in the upper layer at the sea becomes

$$F_1 = \frac{q(1+e)/(D_o-d_o)}{\sqrt{g\frac{\Delta\rho}{\rho(1+e)}(D_o-d_o)}} \tag{9}$$

In the lower layer, the flow at the sea to provide the entrained fluid is eq, hence, at the sea,

$$F_2 = \frac{eq/d_o}{\sqrt{g\frac{\Delta\rho}{\rho(1+e)}d_o}} \tag{10}$$

where the symbols are as above, with ρ taken as the density of river water to the accuracy of the Boussinesq approximation.

By including the kinetic energy correction, the net flow in the lower layer and the reduction of the density difference, equation (5) becomes:

$$\left(\frac{D_o}{D-d_o}\right)^3 \alpha_1(1+e)^3F_o^2 + \alpha_2 e^2F_o^2(1+e)\left(\frac{d_o}{D_o}\right)^{-3} = 1 \tag{11}$$

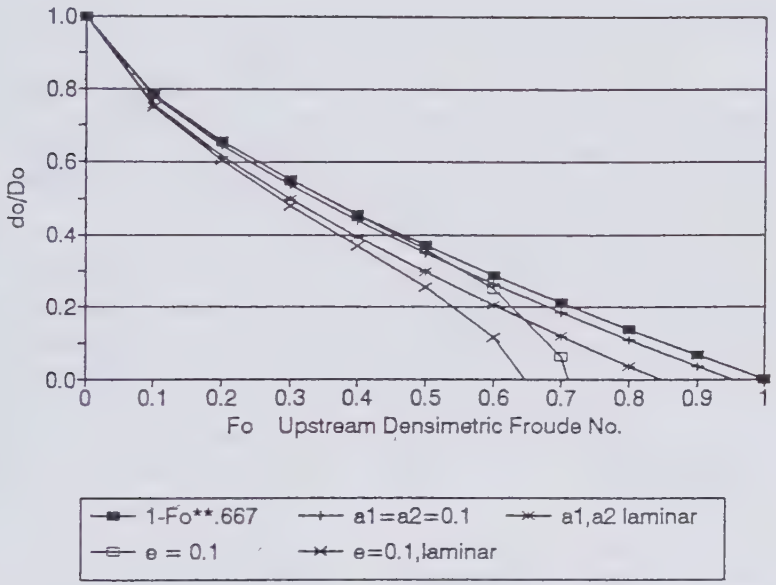

Figure 3. Computed depth of salt water at the sea

By rearranging and solving iteratively for do/Do the following expression is obtained:

$$\frac{d_o}{D_o} = 1-F_o^{2/3}\left\{1+\frac{1}{3}(\alpha_1-1)(1+e)^3\frac{1}{3}\alpha_2 e^2(1+e)\left(\frac{F_o^{2/3}}{1-F_o^{2/3}}\right)^3+\ldots\right\} \qquad (12)$$

Sample solutions of this equation are shown in Figure 3. In the figure the filled symbols give the result for uniform flow in the upper layer with no entrainment. The two lines closest to this are also for no entrainment, the upper with coefficients α_1, α_2 appropriate to turbulent flow, the lower for laminar flow. The figure shows that the effect of including the kinetic energy correction factor is to reduce the depth at the sea for large values of F_o.

The remaining two curves have entrainment of 10% - quite a realistic value for a long salt wedge but too high for a very short wedge. The effect on the critical Froude number is marked and arises mainly from the change in momentum and kinetic energy fluxes rather than from the reduction in the density difference.

These calculations show that the use of $F_o = 1$ as the limiting condition is likely to overestimate the flow required to prevent salt intrusion.

Reanalysis of Salt Wedge Length

Considering now the method of extrapolating the salt wedge length to zero, it was shown above that neither Keulegan's equation (6), nor Officer's equation (7) for the length of the salt wedge could be used to predict the limiting case. Expressions based the equation of Schijf and Schonfeld generally assume that equation (4) applies, and hence cannot provide a more accurate result.

Keulegan attempted to obtain such an expression by performing a series of experiments in which he measured the dimensions of 7 sequences of salt wedges. He held D_o and $\Delta\rho/\rho$ constant in each sequence, while varying the river flow and hence varying the length of the wedge. He then plotted the wedge length against F_o on a linear plot, redrawn here as Figure 4. He extrapolated graphically on this figure to obtain the criterion $F_o = 0.75$. For the data of Figure 4, this procedure is obviously prone to error, but the data may be used by extrapolating with the aid of a dynamically based equation for the salt wedge length which fits Keulegan's data for both short and long salt wedges.

By substituting from equation (12) into equation (7), the length of a salt wedge may be found with the effects of entrainment and non-uniform velocities included. In Figures 5 and 6 the length of the salt wedge has been found by this calculation and has been fitted to the salt wedge length data obtained by Keulegan, for the long and short wedges respectively. For both sets of data the fit is very good.

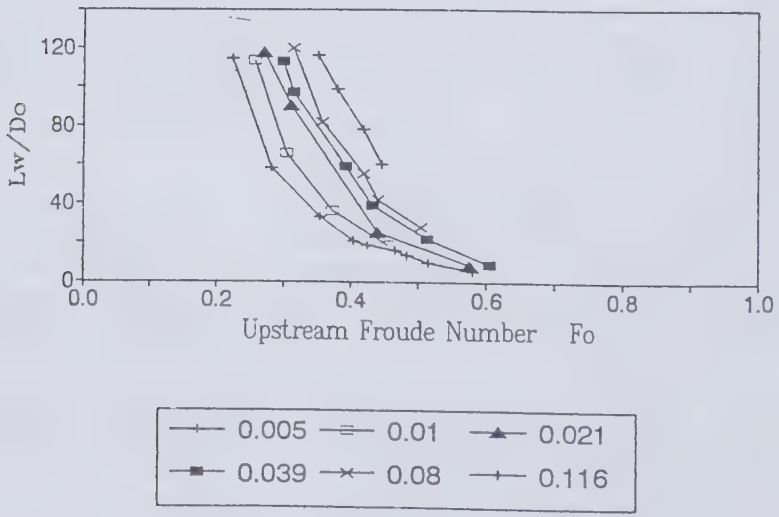

Figure 4. Length of short salt wedges (Keulegan 1957)

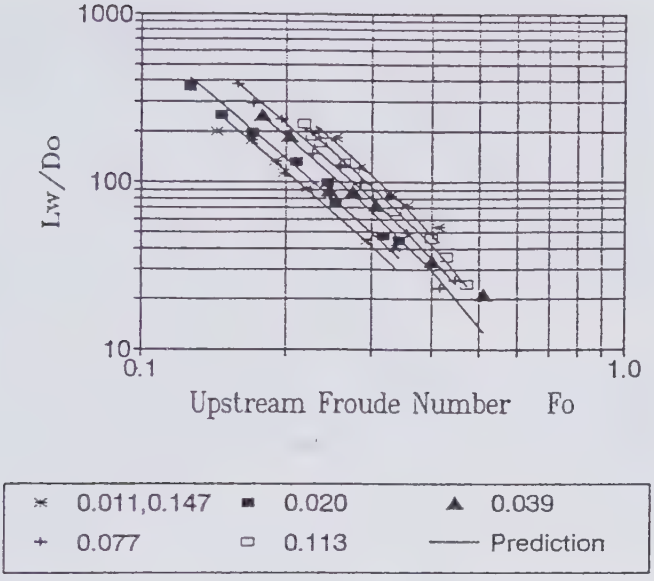

Figure 5. Length of salt wedges; long wedges of Keulegan (1957)

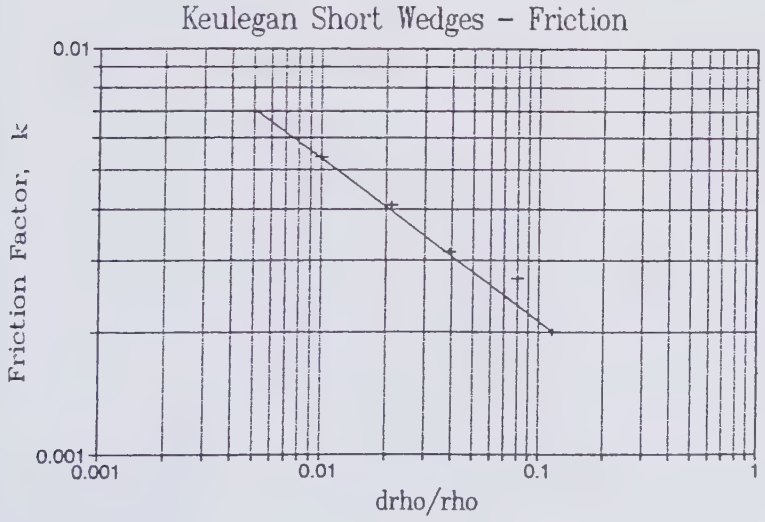

Figure 6. Length of salt wedges fitted to prediction of equation (7) and (12) Experimental data for short salt wedges from Keulegan (1957)

In order to fit the prediction to the data, the interfacial friction factor, k, has been chosen by eye to best fit the data. The k values used to obtain Figure 6 are plotted in Figure 7. It may be seen that k varies consistently with $\Delta\rho/\rho$, providing some measure of confidence in the fitting of k. It is not within the scope of this paper to attempt to derive a generally applicable expression for k; refer to Arita and Jirka (1987a) or Dermissis and Parthenaides (1983). It is merely noted that for the small flume tests of Keulegan, fitted to equations in the fashion described above, the slope of the regression line for k is $(\Delta\rho/\rho)^{-0.4}$ but k does not vary directly with F_o; both D_o and viscosity were constant for each value of density difference. Keulegan in fact presented his results showing a dependence on the Reynolds number, Re, a relationship confirmed and greatly extended by Arita and Jirka (1987b).

Inspection of equations (7) and (12) shows immediately that to first order in the small quantities e, α_1^{-1}, α_2^{-1}, the of result of setting the length of the salt wedge to zero will be equation (4), and hence $F_o = 1$ in the limiting case. To second order in these small quantities a host of terms is obtained making numerical evaluation the only realistic procedure in the general case. However, for a wedge of nearly zero length it is difficult to see how either entrainment or non-uniform flow in the lower layer can have an effect. After eliminating those terms, again equation (4) is obtained.

Thus the second approach suggested in the Introduction has confirmed the improved depth relationship obtained in the previous section, producing an excellent fit to the data, but has not provided a second estimate of the conditions for exclusion of the salt wedge.

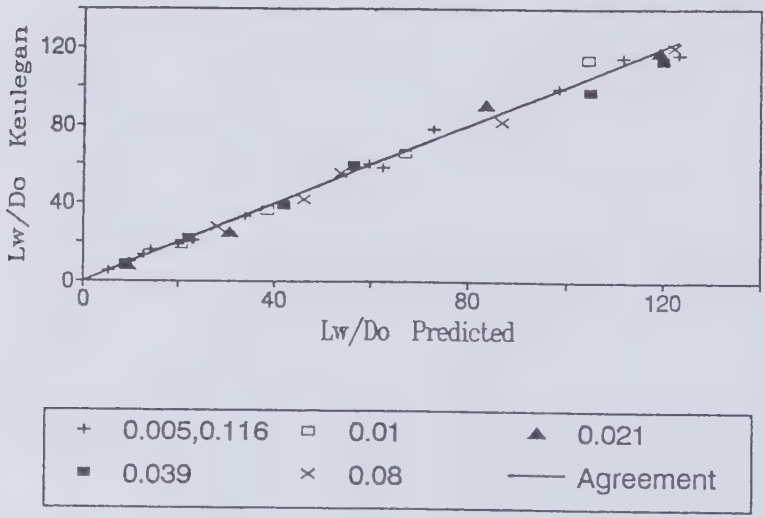

Figure 7. Interfacial friction factor k for data in Figure 6

Conclusions

It has been shown that in a salt wedge the flow at the sea in the upper layer is critical. Salt water will be excluded when the calculated upstream Froude number is critical.

The effect of non-uniform velocity profiles and entrainment into the upper layer reduce the critical value of the upstream Froude number, F_o, as previously shown by Arita and Jirka. For exclusion of salt water F_o is reduced from 1.0 for uniform flow to about 0.85 for small laboratory experiments and about 0.9 for high Reynolds number flows. The depths of salt water at the sea, calculated with these corrections, adequately match the laboratory data of Keulegan.

Both the short and long salt wedge data of Keulegan are well fitted by a relationship due to Officer. The fit is improved by the inclusion of allowance for the non-uniform velocity profiles, confirming the calculation of the limiting upstream Froude number.

References

Arita, M. and G.H. Jirka, Two-layer model of saline wedge I: Entrainment and interfacial friction, J. Hydr. Eng., 113, 1229-47, 1987a.

Arita, M. and G.H. Jirka, Two-layer model of saline wedge II: Prediction of mean properties, *J. Hydr. Eng.*, 113, 1249-63, 1987b.

Dermissis, V. and E. Parthenaides, Interfacial resistance in stratified flows, *J. Waterway, Port Coastal Eng.*, 110, 231-250, 1983.

Farmer, H.G. An experimental study of salt wedges, *Reference 51-99*, Woods Hole Oceanog. Inst., 1951.

Farmer, H.G. & G.W. Morgan, The salt wedge, *Proc. 3rd. Conf. Coastal Eng.*, Cambridge Mass., 54-64, 1952.

Hinwood, J.B. Estuarine salt wedges: Determining their shape and size, *Dock & Harbour Authority (London)*, 65: 79-83, 1964.

Ippen, A.T. and D.R.F. Harleman, *Estuary and Coastline Hydrodynamics*, McGraw-Hill, ch. 11-13,1966.

Keulegan, G.H. Form characteristics of arrested saline wedges, *11th Progress Rept. on Model Laws for Density Currents*, U.S. National Bureau of Standards, Washington, 1957.

Officer, C.B. *Physical Oceanography of Estuaries*, John Wiley & Sons, ch.4, 1976.

Parthenaides, E., V. Dermissis and A.J. Mehta, On the shape and interfacial resistance of arrested saline wedges, *Proc. 16th Congr. Intl Assoc. Hydr. Res.*, 1, 157-164, 1975.

Parthenaides, E. Stratified flow, salinity intrusion, and transport processes, in *Handbook of Coastal and Ocean Engineering*, edited by J.B. Herbich, 1992, ch.11 of vol.3, Gulf Publishing Co., 1992.

Schijf, J.B. & J.C. Schonfeld, Theoretical considerations on the motion of salt and fresh water, *Proc. 5th. Cong. Intl Assoc. for Hydr. Res.*, Minnesota, 321-333, 1953.

Stommel, H. & H.G. Farmer, Abrupt change in width in two-layer open channel flow, *J. Mar. Res.*, XI.2:205-214, 1952.

16

A Spring-Neap Flushing Box Model

Z. Z. Ibrahim

Abstract

Simple box models are useful in presenting and developing concepts of flushing and mixing in an estuary. Most box models consider only complete mixing and a mean tide condition for simplicity. However, time variable factors such as the spring-neap tide transition, can be important in determining the flushing characteristics. A simple box model is presented here which takes into account the variation in the tidal prism over the spring-neap tide transition. The model considers the flushing of a pollutant through the box if the pollutant input is a single pulse (one-shot) or if the input is continuous. In addition incomplete mixing is allowed for by linking tidal range to mixing extent.

Introduction

Simple estuarine box models are useful for developing and explaining concepts of mixing as well as for quickly assessing the flushing capability of an estuary. In a review of box models, Officer (1979a) concluded that although these models were gross simplifications of estuarine hydrodynamics they could be applied to estuaries where horizontal net circulation exchanges dominated horizontal non-advective exchanges. The simplest of the box models is the tidal prism model. In this model the amount of water available for flushing is the tidal prism, defined as the volume of water in the estuary between low and high tide. The flushing rate, in tidal cycles, is then given by the ratio of the total estuary volume at high tide to the tidal prism volume. In 1950, Ketchum (1951a, b) proposed that the tidal prism model should be modified to account for incomplete longitudinal mixing and for oscillatory flow in

Mixing in Estuaries and Coastal Seas
Coastal and Estuarine Studies Volume 50, Pages 278-290
Copyright 1996 by the American Geophysical Union

the estuary. This modification took the form of segmentation of the tidal prism model. Further modifications were made by Dyer and Taylor (1973) and Wood (1979) to make the model internally consistent and to allow for dispersion between the segments. These modifications to the tidal prism model, however, do not address the effects of stratification and bottom density currents on mixing (Rawn, 1951) nor do they incorporate the effects of time variable factors. The importance of the latter was also noted by Officer (1979a) who recognized that the major insights into understanding estuarine behaviour would be through the correct analytical and numerical78-ors, such as the spring to neap tide transition, which appear as determing factors in estuarine behaviour.

The variation in tidal range over the spring to neap tide transition can have considerable effect on estuary behaviour (Allen *et al.*, 1980; Milliman *et al.*, 1984; Uncles *et al.*, 1985). The mixing of waters, salinity structure, sediment transport and flushing of chemical constituents vary with the volume of sea water entering the estuary at different tidal ranges. However, the changes in the estuary over the spring to neap tide transition is seldom considered except in complex numerical models. In these complex models, the primary focus is also on the mean conditions or net transport over the spring to neap tide transition. We should, however, be able to consider in a simple manner, if there is a difference in flushing if a chemical constituent is introduced at a spring or a neap tide or at sometime inbetween. We should also be able to consider the effect of incomplete mixing. This would be of interest if we need to consider the timing of the discharge of a pollutant into the estuary. It would be useful to be able to consider these temporal changes using only a simple model.

It is the purpose of this paper to investigate the time varying effect of the spring to neap tide transition on the flushing of an estuary using only a simple box model. The variations due to a one-shot input and to a continuous input of pollutant, as well as complete and incomplete mixing, over the spring to neap tide transition are considered. The model illustrates the difference in flushing rates and, when extent of mixing is included, also points to differences in pollutant concentration depending on increasing (neap-spring tide transition) or decreasing (spring-neap tide transition) tidal range in the estuary.

The Box Model

A simple box model is used (Figure 1) following that of Ibrahim (1989). It is assumed that the estuary may be modeled by a closed box with a net river discharge volume per tidal cycle of Q m^3. The volume of water within the estuary is given by P m^3. Superscripts denote high (H) and low (L) tide conditions while subscripts denote the tide cycle (n) occuring. There is no egress of mass from within the box through the upstream boundary. Complete mixing at high water is assumed and the river discharge volume enters the box only at low water. The river discharge volume per tidal cycle is small compared to the estuary volume, P. In this model we also assume steady river discharge into and out of the box.

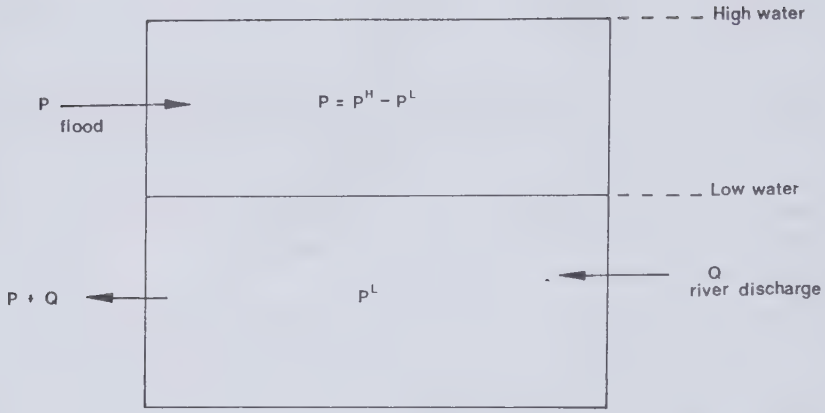

Figure 1. The filling box model for the Klang River inner estuary. (P^L, P^H - Prism volume at low (L) and high (H) tide respectively; P - Prism volume; Q - River discharge over a tidal cycle of 12.5 hours.)

The input of a pollutant into the upstream end of the box may be considered to be one of two cases: a one-shot input or a continuous input. Within the box the following changes would occur over a tidal cycle. At tidal cycle n, a discrete mass $M^{L}{}_{n}$ of pollutant enters the system at low water from the upstream end. If mixing is complete, at high water the pollutant concentration, $C^{H}{}_{n}$, is given by

$$C^{H}{}_{n} = M^{H}{}_{n}/P^{H}{}_{n} \quad (1)$$

and

$$M^{H}{}_{n} = M^{L}{}_{n} \quad (2)$$

as there is no loss of pollutant mass through the upstream boundary. At ebb the estuary box suffers a loss of pollutant mass due to discharge of the tidal prism volume ($P^{H}{}_{n} - P^{L}{}_{n}$). Thus the remaining pollutant mass in the box at the new low water volume, $P^{L}{}_{n+1}$, is given by

$$M^{L}{}_{n+1} = P^{L}{}_{n+1}\, C^{H}{}_{n} \quad (3)$$

However, there is also a loss of volume equivalent to the river discharge volume over a tidal cycle, Q. Thus, the resultant mass in the estuary box is

$$M^{L}{}_{n+1} = (P^{L}{}_{n+1} - Q)C^{H}{}_{n} \quad (4)$$

For a one-shot input of pollutant in tidal cycle n, at the next high water the new concentration ($C^{H}{}_{n+1}$) is given by

$$C^{H}_{n+1} = \frac{(P^{L}_{n+1} - Q)C^{H}_{n}}{P^{H}_{n+1}} \quad (5)$$

For a continuous pollutant input of M^{L}_{n} for each tidal cycle, at the next high water the new concentration (C^{H}_{n+1}) is given by

$$C^{H}_{n+1} = \frac{(P^{L}_{n+1} - Q)C^{H}_{n} + M^{L}_{N}}{P^{H}_{n+1}} \quad (6)$$

The percentage reduction or decay in mass of a pollutant at any tidal cycle, j, compared to that mass initially introduced at the first tidal cycle, n, may therefore be calculated.

$$\text{reduction } \% = \frac{M^{L}_{j} \times 100}{M^{L}_{n}} \quad (7)$$

The original model was based on the physical conditions of the high mesotidal Klang River estuary, Malaysia. The tides in this estuary result in considerable variation in salinity stratification between neap and spring tides. This lead to the consideration of tidal range influence on mixing extent which is presented below. The typical tides and volume ratios for that estuary are used for the model application here. The tides used are semi-diurnal with spring tidal ranges of approximately 4.3 m and neap tidal ranges of approximately 1.2 m. This model is applied to an estuary **X** of rectangular cross-section with dimensions of 7 m depth (at 0 m water level), 450 m width and 10 km length. The river discharge volume used is 1.35 x 10^6 m^3 for a 12.5 hour tide cycle. Thus the residence time of the river discharge is long, greater than 23 tidal cycles or approximately 12 days.

The model results presented are for the change in pollutant mass and concentration over two conditions of tide transition: the change from large to small tidal range (spring-neap tide transition) and the change from small to large tidal range (neap-spring tide transition). These two conditions give, respectively, changes of strong to weak tidal stirring and weak to strong tidal stirring. Complete and incomplete mixing are considered for these two cases.

Complete Mixing

One-Shot Input

The results of a series of calculations for pollutant mass and concentration are shown in Figure 2 for a one-shot input of mass at spring tide and at neap tide. The rate of reduction from the original mass (Table 1, Column a) was much faster during the spring tides than during the neap tides. About 36% of pollutant mass was lost in the

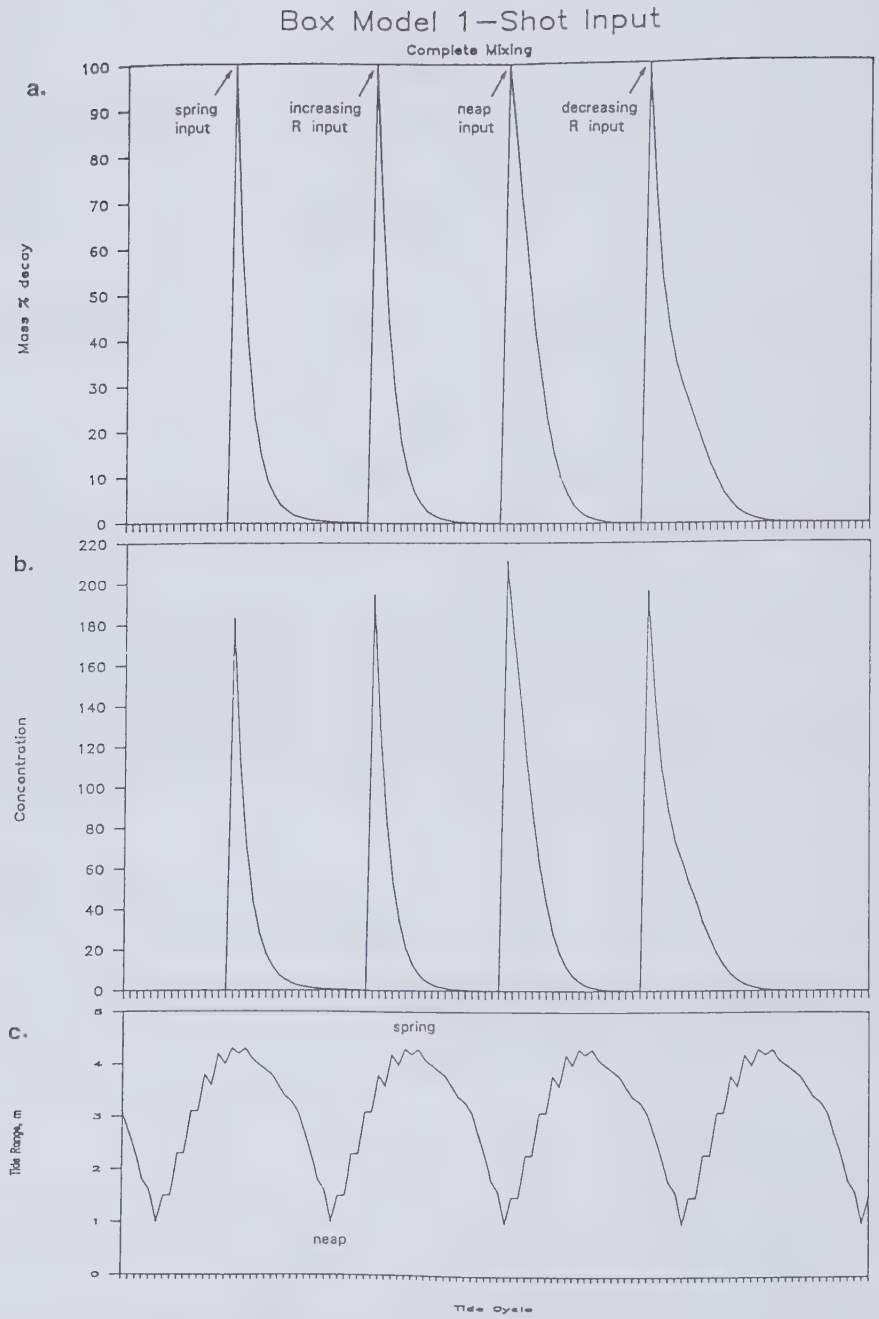

Figure 2. The predicted variation in pollutant (a) mass and (b) concentration for a one-shot input of mass over the (c) spring-neap tide transition. Mixing is complete.

first spring tide as opposed to only 14% pollutant mass lost during the first neap tide. The reduction to less than 25% of the original mass occurs at the sixth tidal cycle for neap tides and at the third tidal cycle for spring tides. The data demonstrates a reduced flushing and dilution ability of the estuary in the neap-spring tide transition compared to the spring-neap tide transition due to the reduced amount of tidal prism volume available for mixing at neaps. This difference becomes less apparent with time.

Continuous Input

For the case of continuous input of pollutant, the mass of pollutant within the box increases (Figure 3) until a stable state is reached. The final mass within the box oscillates from 500% to 250% of the mass of the first pollutant input. The maximum amount of mass within the box occurs just after neap tides while the minimum amount of mass in the box occurs just after spring tides. This also supports the result of the one-shot input model that flushing ability reduces during small tidal ranges and increases during large tidal ranges.

Incomplete Mixing

Parameterizing Mixing with Tidal range

The major weakness of this model is in the assumption of complete mixing. We may, however, compensate for this assumption by parameterizing a mixing factor, m, as a function of the tidal range. For example, we may chose an arbritrary linear relationship such that

$$m = aR + b \tag{8}$$

where m - mixing factor,
R - tidal range,
a, b - constants,

giving increased mixing with increasing tidal range. A baseline mixing due to the river flow is allowed for by the constant b. When m=1, mixing is complete (100%) and when m=0, no mixing occurs. For the tide conditions used here, the constants a and b may be selected to give a range of mixing factors. The extent of the salinity stratification within the estuary at various tidal ranges, for example, may be used to set limits to this expression. We select a mixing factor due to the river flow only, with no tide, of 0.05 or 5% mixing. Therefore, if we select a mixing extent of 90% for a maximum expected tidal range of 5 m we may calculate the constant a to be 0.17. In this exercise a linear function is selected, but any non-linear function of tidal range may serve the purpose as well.

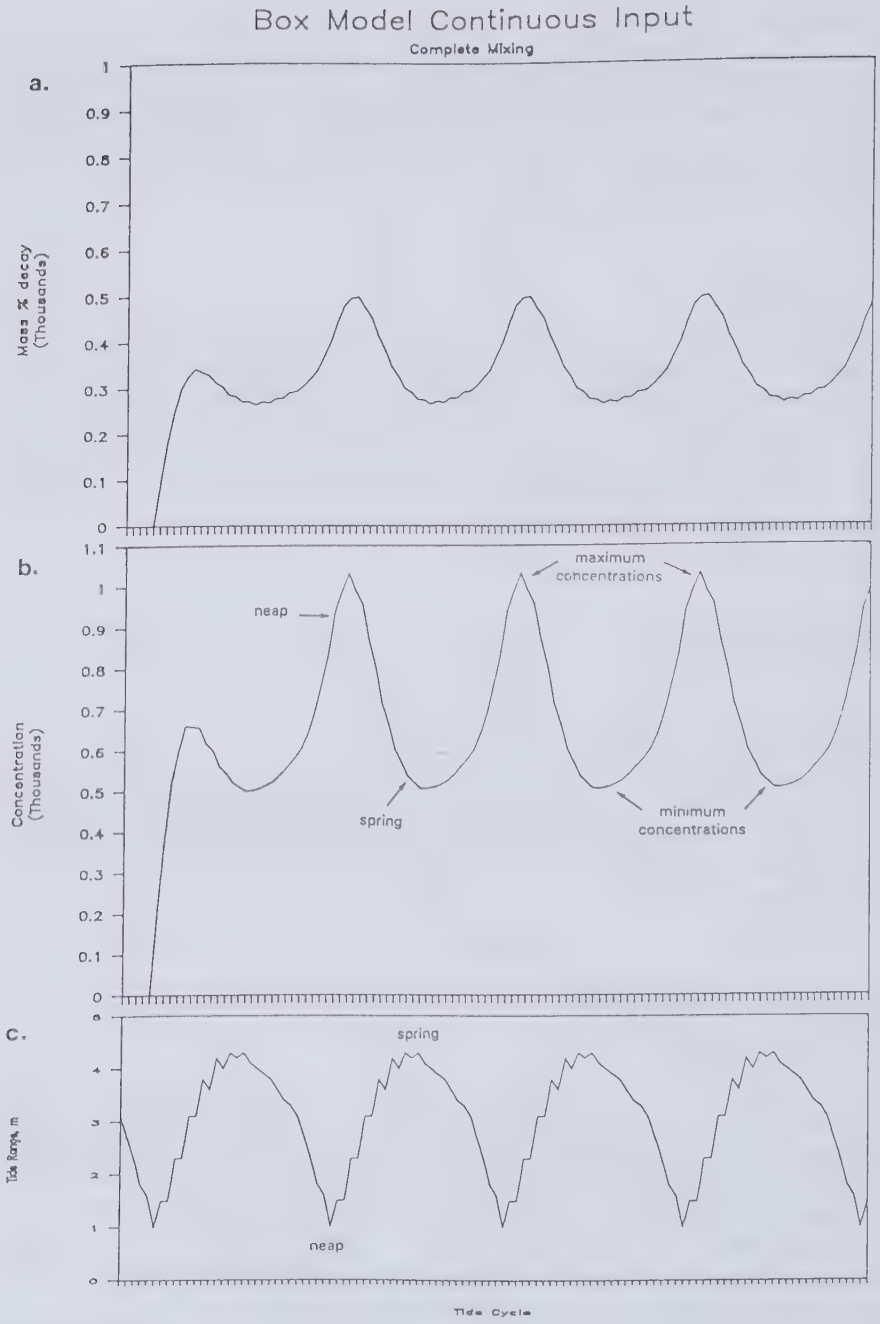

Figure 3. The predicted variation in pollutant (a) mass and (b) concentration for a continuous input of mass over the (c) spring-neap tide transition. Mixing is complete.

We assume that the pollutant mass, introduced at low water as M^L, only mixes into the water column at a rate dictated by m. The portion (1-m) of pollutant mass which does not mix into the water column resides within the box and is available for future mixing. This situation can be compared to pollutants which are associated with and partitioned into suspended sediments. As mixing reduces, the longer residence time of water within the estuary may allow the pollutants to be taken up or partitioned onto sediments. As mixing increases, with tidal range and velocity, these sediments can be suspended and the pollutants released into the water column. Thus, we may calculate the concentration at high water for a tidal range, R, with a mixing factor, m, as

$$C^H_{n-1} = \frac{(M^L_{n-1})\ m_{n-1}}{P^H_n} \tag{9}$$

At low water, after discharge of the volume of river input, the concentration is

$$C^L_n = \frac{(P^L_n - Q)\ C^H_{n-1}}{P^L_n} \tag{10}$$

One-Shot Input

The results for the box model with the mixing factor are illustrated in Figure 4 for the same tidal conditions as before. The spring-neap tide transition shows only a slight variation from the complete mixing model. The neap-spring tide transition, however, is different. Note that the first tidal cycle reduces the initial mass by only 3.2% as opposed to 14.3% (Table 1, Column b) when complete mixing occurs and that the drop to less than 50% of original mass occurs after 7 tides instead of 4.

Continuous Input

What is interesting, though, is the pattern of the variation in mass and concentration (Figure 5) when the input of pollutant is continuous. The mass and concentration of pollutant at any one tidal cycle is greater than for the case of complete mixing. As for the complete mixing case the minimum concentration occurred just after neap, when the mixing factor was low. At spring tidal ranges, although the mixing factor was larger and more of the pollutant is present in the water column, the larger volume of water act as a diluent. At intermediate tides, however, the condition depends on whether tidal range is increasing or decreasing.

Concentrations increase to a maximum during increasing tidal range. It should be noted also that maximum concentrations occur at intermediate tidal ranges rather

TABLE 1. Decay in pollutant mass and concentration of a one-shot input over the spring-neap and neap-spring tide transition for (a) complete mixing and (b) when a mixing factor (m) is applied.

		(a) Complete Mixing			(b) Imcomplete Mixing m = 0.17R+0.05			
Tidal cycle	Tidal range R	Mass	Mass % original	Concen-tration	Mass	Mass % original	Concen-tration	Input condition
1	4.3	10000.0	100.0	183.7	10000.0	100.0	143.4	Spring-neap tide input
2	4.2	6033.1	60.3	113.6	6901.8	69.0	99.3	
3	4.3	3834.6	38.3	4980.3	49.8	71.4		
4	4.1	2313.4	23.1	43.9	3437.3	34.4	48.8	
5	4.0	1502.7	15.0	28.0	2537.5	25.4	34.6	
6	3.9	934.5	9.3	17.,9	1837.0	18.4	25.1	
7	3.8	620.3	6.2	11.7	1396.7	14.0	18.3	
8	3.6	399.5	4.0	7.7	1050.7	10.5	13.4	
9	3.4	274.4	2.7	5.3	832.9	8.3	10.0	
10	3.3	182.2	1.8	3.6	657.1	6.6	7.9	
11	3.1	127.4	1.3	2.5	536.3	5.4	6.1	
12	2.7	92.4	0.9	1.8	451.4	4.5	4.6	
13	2.3	68.5	0.7	1.4	391.9	3.9	3.5	
14	1.8	54.7	0.5	1.1	357.0	3.6	2.6	
15	1.6	44.5	0.4	0.9	333.5	3.3	2.2	
16	1.0	38.3	0.4	0.8	318.4	3.2	1.5	
17	1.5	32.8	0.3	0.7	308.4	3.1	1.9	
18	1.5	27.1	0.3	0.6	291.9	2.9	1.8	
19	2.3	21.7	0.2	0.4	274.4	2.7	2.4	
20	2.3	16.3	0.2	0.3	244.1	2.4	2.2	
21	3.1	12.2	0.1	0.2	216.7	2.2	2.4	
1	1.0	10000.0	100.0	211.6	10000.0	100.0	46.6	Neap-spring tide input
2	1.5	8571.4	85.7	176.4	9685.7	96.9	60.8	
3	1.5	7063.5	70.6	146.7	9166.0	91.7	58.1	
4	2.3	5677.2	56.8	112.6	8617.3	86.2	75.4	
5	2.3	4257.9	42.6	86.0	7667.3	76.7	68.3	
6	3.1	3174.1	31.7	60.8	6806.6	68.1	75.2	
7	3.1	2189.0	21.9	42.7	5587.7	55.9	62.8	
8	3.8	1497.7	15.0	28.0	4569.6	45.7	59.4	
9	3.6	969.1	9.7	18.6	3447.1	34.5	43.7	
10	4.2	634.9	6.3	11.7	2660.2	26.6	37.3	
11	4.0	388.3	3.9	7.4	1870.8	18.7	25.9	
12	4.3	248.9	2.5	4.6	1380.5	13.8	19.8	
13	4.2	150.2	1.5	2.8	952.8	9.5	13.7	
14	4.3	95.4	1.0	1.8	687.5	6.9	9.9	
15	4.1	57.6	0.6	1.1	474.5	4.7	6.7	
16	4.0	37.4	0.4	0.7	350.3	3.5	4.8	
17	3.9	23.3	0.2	0.4	253.6	2.5	3.5	
18	3.8	15.4	0.2	0.3	192.8	1.9	2.5	
19	3.6	9.9	0.1	0.2	145.0	1.4	1.9	
20	3.4	6.8	0.1	115.0	1.1	1.4		
21	3.3	4.5	0.0	0.9	90.7	0.9	1.1	

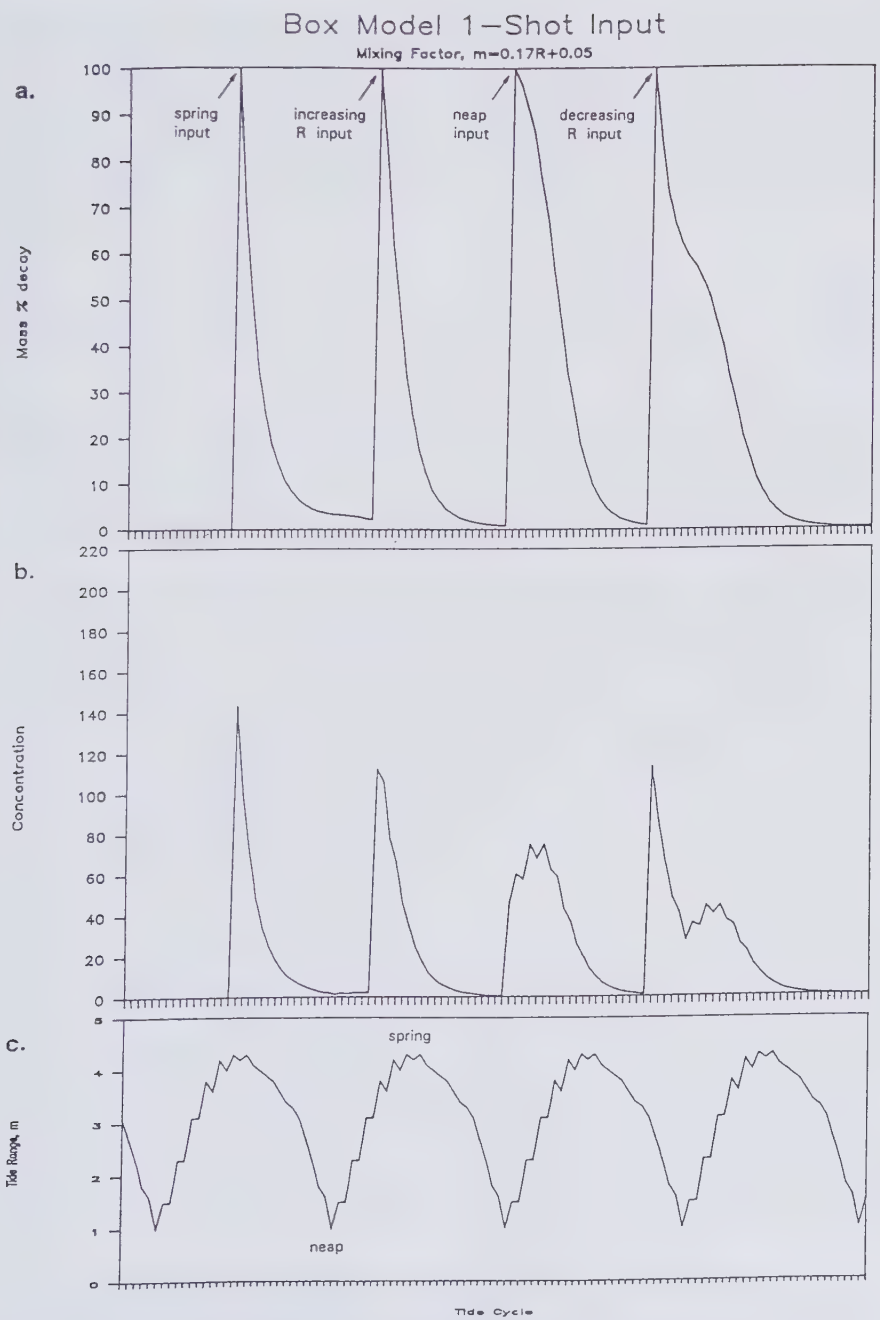

Figure 4. The predicted variation in pollutant (a) mass and (b) concentration for a one-shot input of mass over the spring-neap tide transition when a mixing factor (m) is applied. The mixing factor is given by m = 0.017R+0.05, where R = tidal range.

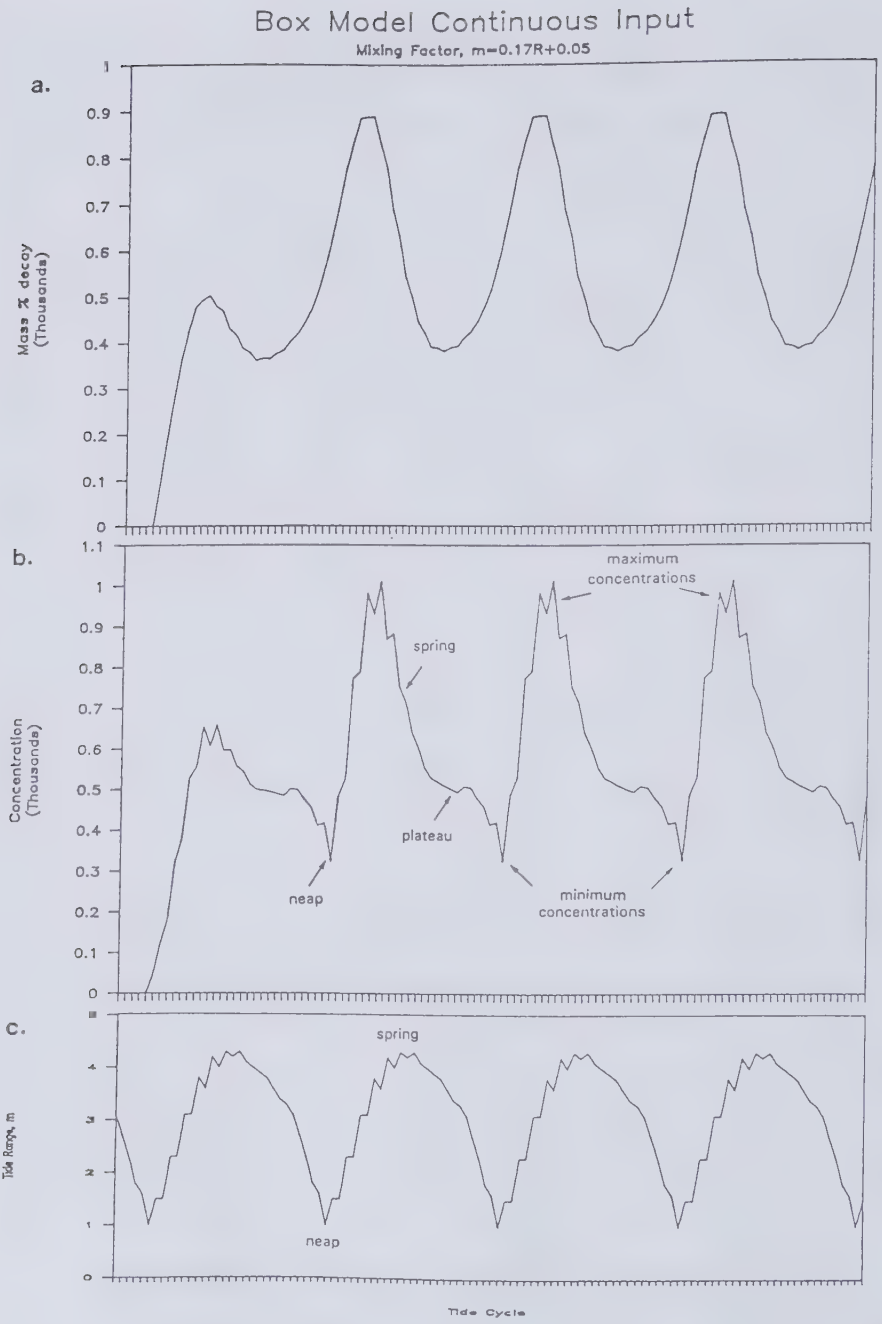

Figure 5. The predicted variation in pollutant (a) mass and (b) concentration for a continuous input of mass over the (c) spring-neap tide transition when a mixing factor (m) is applied. The mixing factor is given by m = 0.017R+0.05, where R = tidal range.

than at small tidal ranges. During decreasing tidal range the concentration is fairly stable. This difference in behaviour may be explained by the disparity between mixing rate change and dilution due to tidal prism volume rate change. Mixing increases at a rate greater than dilution by increasing volume of water, thus, the concentration of the pollutant increases. For the spring-neap tide transition, the disparity between mixing and dilution acts to arrest the decrease in concentration and a 'plateau' stage is achieved.

Discussion and Conclusion

This simple box model illustrates clearly the role of tidal range in partially controlling the flushing of pollutants through an estuary. In estuaries where the changes in tidal mixing and tidal volume at different tidal ranges are great, the variation of tidal range and the direction of variation, from spring to neap and from neap to spring results in different patterns of pollutant concentrations and mass loss.

The model presented here is only of a single box representing the whole estuary. It may be argued, as Ketchum (1951a, b) had, that complete longitudinal or horizontal mixing is difficult to achieve, especially in many ria-type estuaries of great width, and that segmentation should be carried out. This certainly is a valid arguement and should be the next step in the development of this model. The importance of this model is in the incorporation of temporal variations in the tide and of incompleteness of mixing. The results of this indicates that the spring-neap tide transition is different from the neap-spring tide transition. It demonstrates that the prevalent assumption of many estuarine investigators that it is sufficient to measure at neap and at spring or at an 'average' tide may not be valid.

In addition, Officer (1979b) noted that in many studies of estuarine chemistry or biology, measurements are made at different locations within the estuary at different states of the tide and often only of surface samples. Invariably the tide state during sampling is not revealed as it is regarded to be an unimportant factor. The reason behind this approach has been the belief that salinity could be used as a direct indicator of mixing of the chemical components within the estuary and that mixing is complete vertically. This belief may be sufficient for conservative chemical components which do not react with any material in the estuary, but not for the many non-conservative components. The simple approach taken here, and the results, show clearly the type of variation which may occur when there is imcomplete mixing.

In light of this, therefore, it must be recognized that to avoid erroneous conclusions being drawn, the measurement of pollutants and other chemical or biological components, and the analysis of such data, need to be related to a known tide time-frame.

Acknowledgements to Professor David A. Huntley for comments on model assumptions and two referees for their comments. Financial support and facilities was provided by the Department of Environmental Sciences and Universiti Pertanian Malaysia though project code no. 4-07-05-041.

References

Allen, G.P., J.C. Salomon, P. Bassoullet, Y. Du Penhoat and C. De Grandpre. Effects of tides on mixing and suspended sediment transport on macrotidal estuaries. *Sedimentary Geology* 26: 69-90, 1980.

Dyer, K.K. and P.A. Taylor. A simple segmented prism model of tidal mixing in well mixed estuaries. *Estuarine and Coastal Marine Science* 1:411-418, 1973.

Ibrahim, Z.Z. An integrated approach to the investigation of an equatorial estuary: The Klang River estuary, Malaysia. PhD thesis. University of Southampton, U.K, 1989.

Ketchum, B.H. The exchanges of fresh and salt waters in tidal estuaries. *Journal of Marine Research* 10:18-38, 1951a.

Ketchum, B.H. The flushing of tidal estuaries. *Sewage and Industrial Wastes* 23:198-208, 1951b.

Milliman, J.D., Y. Hsueh, D.-X. Hu, D.J. Pashinski, H.-t. Shen, Z.-s. Yang and P. Hacker. Tidal phase control of sediment discharge from the Yangtze River. *Estuarine, Coastal and Shelf Science* 19: 119-128, 1984.

Officer, C.B. Box models revisited. Workshop on Wetlands and Estuarine Processes and Water Quality Modelling. June 18-20, 1979,1979a.

Officer, C.B. Discussion of the Behaviour of nonconservative dissolved constituents in estuaries. *Estuarine and Coastal Marine Science* 9:91-94, 1979b.

Rawn, A.M. Discussion. *Sewage and Industrial Wastes* 23:208-209, 1951.

Uncles, R.J., R.C.A. Elliot, and S.A. Weston. Observed fluxes of water salt and suspended sediment in a partly mixed estuary. *Estuarine, Coastal and Shelf Science* 20: 147-167, 1985.

Wood, T. A modification of existing simple segmented tidal prism models of mixing in estuaries. *Estuarine and Coastal Marine Science* 8:339-347, 1979.

17

Studies on Transport Times and Water Quality in the Weser Estuary (Germany)

I. Grabemann, H. Kühle, B. Kunze and A. Müller

Abstract

Times for the transport of conservative substances by advection and diffusion through the Weser Estuary derived from both model calculations and field observations are presented. They depend strongly on the river discharge. The retention time of a water parcel for the inner part of the estuary (about 65 km in length) varies from about 27 days (long-term minimum discharge) to 3 days (long-term maximum discharge). The transport times affect locations and strengths of oxygen and nutrient extremes within the longitudinal section. In warmer months when biological activity is high, wastewater will be decomposed, resulting in a decrease of the oxygen content. The occurrence of oxygen minima and nutrient peaks in the longitudinal section is closely associated with the retention time of a water parcel. While there are narrow and well pronounced extremes in the upstream part of the estuary during low river discharges, diffused extremes are observed more downstream during mean river discharges.

Introduction

The prediction of the transport behaviour of a pollutant cloud in a river or estuary is of great importance. In order to alleviate potential negative impact, it is necessary to predict its time of arrival at sensitive locations.

Like many other estuaries the Weser Estuary, one of the North German estuaries (Figure 1), is used as navigational channel to important harbours and as receiving

Mixing in Estuaries and Coastal Seas
Coastal and Estuarine Studies Volume 50, Pages 291-301
Copyright 1996 by the American Geophysical Union

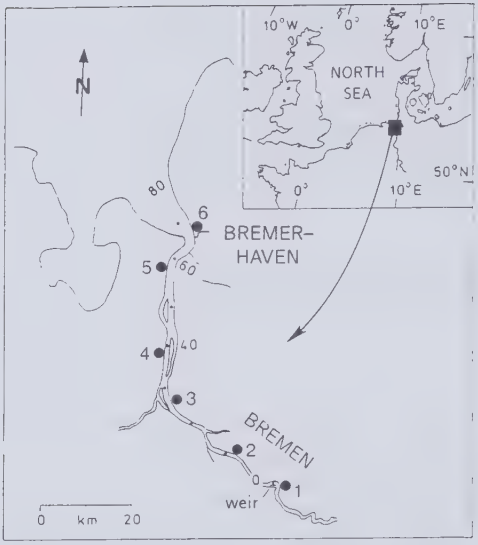

Figure 1. Map of the Weser Estuary (Lower Weser River: weir to km 65). The black dots denote bankside monitoring stations 1-6. The numbers along the river give the kilometres downstream of Bremen.

body for both urban and industrial sewage. Additionally, large amounts of various substances such as nutrients and trace elements enter the estuary from the river. Whereas conservative substances are affected by advective and diffusive transport, nutrients are also subject to biological processes. The time scales of self-purification processes are in the same order of magnitude as tidally averaged transport times. For example, in the Weser Estuary the specific rates for both biodegradation of organic carbon and biodegradation of ammonium to nitrite and nitrate (nitrification) are in the order of 1×10^{-6} s^{-1} (Muller *et al.*, 1992). Thus, the time for decomposition of these substances is about ten days. The transport of trace elements attached to suspended matter is also influenced by sedimentation, resuspension and the occurrence of a turbidity maximum and has higher retention times.

Transport times have been estimated for several German rivers, e.g. Elbe (Schoer, 1988), Rhine (Brüggemann and Trapp, 1989), and Main (Krause *et al.*, 1987). The calculation of such times for estuaries is complicated by the periodical current reversal due to tides. The spreading of warm water plumes in the Weser Estuary has been calculated by Hanisch (1975) and Hauser *et al.* (1981).

In this paper, transport times of conservative substances through the Weser Estuary have been derived from both measurements and model simulations using salt as a tracer. Due to salt mining in the catchment area, salinity, even in the "freshwater" region of the estuary, can reach up to 2 ppt. Reduced salt input at weekends provides for salt minima in the salinity time series at the head of the estuary. These

minima are clear signals which can be followed over a distance of about 30 km along the estuary. First, long time series of salinity measured at three monitoring stations in the freshwater region of the Weser Estuary have been analysed and tidally averaged transport times have been derived from the time-lag between the minima at these three stations. Second, a time dependend cross-section averaged numerical model has been used to simulate movements of water parcels or conservative substances and to calculate tidally averaged transport times. Transport times derived from the measured salinity variations are then compared to those derived by using the numerical model. Until now only transport times of conservative substances are available from measurements for model verification. Finally, longitudinal profiles of oxygen and nutrient contents are discussed with respect to these carculated transport times.

Weser Estuary

The Weser Estuary is a coastal plain estuary. The tides are semi-diurnal and asymmetrical. The estuary is seperated from the non-tidal part of the River Weser by a weir to the south of Bremen (Figure 1). The mean tidal amplitude is about 3.6 m at Bremerhaven and about 3.9 m at Bremen. The maximum current velocities during ebb or flood tide are greater than 1 $m\,s^{-1}$. The long-term mean river discharge is about 326 $m^3\,s^{-1}$, the long-term minimum and maximum discharge is 120 and 1200 $m^3\,s^{-1}$, respectively (mean values 1941/1987, Deutsches Gewasserkundliches Jahrbuch, Weser-/Emsgebiet, 1987). As previously mentioned, the salinity in the freshwater region varies up to 2 ppt. During times of low river discharge, noticeable influence of the seawater salinity can be observed as far upstream as 40-45 km. The inner part of the Weser Estuary has a channel-like character. It is the result of engineering works carried out over the last 100 years to fulfil the requirements of navigation. The mean water depth in the fairway is about 10 m. The outer estuary downstream of Bremerhaven is funnel-shaped within the Wadden Sea area. Here, the mean water depth in the fairway is about 15-20 m.

The water quality of the Lower Weser River (upstream part of the Weser Estuary) is monitored in a comprehensive. The monitoring of the discharge of effluents is performed by the appropriate water authorities as well as by sewage treatment plants, industrial plants and power stations discharging wastewater into or taking water from the Weser river. The water authorities are also responsible for monitoring the river water by taking regular longitudinal profile measurements from a ship almost once a month. Furthermore, continuous measurements are undertaken at six onshore stations: one near the weir, three in the freshwater region and two in the brackish water zone of the Lower Weser (Figure 1). Additionally, special field investigations have been jointly carried out by different institutions (ARGE Weser, 1982; Muller *et al.*, 1990; Grabemann *et al.*, 1993). With regard to water quality modelling, information for boundary conditions and wastewater inputs as well as values for model verifications have been derived from these data sets.

Transport Times for Conservative Substances

Transport times derived from salinity measurements

The salt input by potash industry into the inland river is reduced for short times causing minima in the time series of salinity or conductivity at the monitoring stations. Time series of conductivity are presented in Figure 2. At station 1 at the head of the estuary these minima are generally obvious and can be followed to stations 2 (about 15 km downstream) and 3 (about 30 km downstream; Figure 2). Their times of arrival at these stations depend on the river discharge.

Due to the longitudinal dispersion these minima broaden and the salinity (represented by the conductivity) therein increases. Depending on the salinity gradient and the tidal amplitude, the signal is more or less weakened at the stations 2 and 3, where it is superimposed by the tidal oscillations. However, no influence of the seawater salinity is observed there.

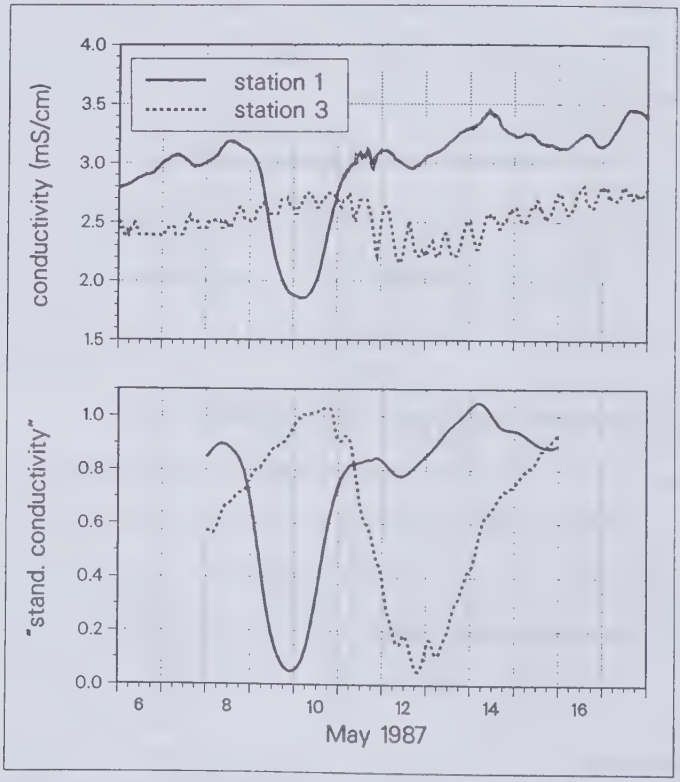

Figure 2. Time series of conductivity for the monitoring stations 1 and 3 in the "freshwater" region of the estuary (top). Filtered and standardised series for the duration of the salt minimum (bottom).

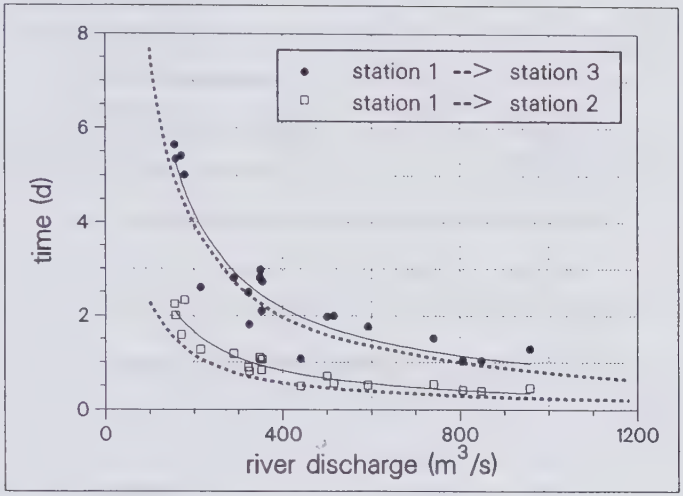

Figure 3. Tidally averaged transport times for the distances station 1 → station 2 and station 1 → station 3 as functions of the river discharge R. The dots and open rectangles (fitted by the thin lines) denote those derived from salinity measurements. The thick dashed lines present those derived from model calculations.

The time series for the three stations have been "filtered" (running average) to eliminate the tidal oscillations and standardised to the same minimum and maximum, respectively. The time-lag between the minima of the different series gives the tidally averaged transport times. For the example shown in Figure 2, the time-lag between the salt minima at station 1 and station 3 is 71.5 h.

Twenty salinity minima during different river discharge conditions have been analysed. The tidally averaged transport times between monitoring stations 1 and 2 and 1 and 3, respectively, are shown in Figure 3 as functions of the river discharge. The corresponding residual currents (defined by the quotient 'distance between the stations / respective transport time') vary between

	discharge: 160-170 $m^3 s^{-1}$	*discharge: 700-800 $m^3 s^{-1}$*
Stations 1 to 2	(0.08 ± 0.02) $m^3 s^{-1}$	(0.37 ± 0.05) $m^3 s^{-1}$
Stations 1 to 3	(0.07 ± 0.01) $m^3 s^{-1}$	(0.33 ± 0.04) $m^3 s^{-1}$

On its way through a river or estuary, a pollutant cloud will be mixed with non-polluted water and also influenced by bottom shear stress, wind stress, turbulence caused for example by breakwaters, harbour areas or shipping, and discharges from tributaries. Therefore, the longitudinal dispersion has also been considered.

At a fixed location, the longitudinal spreading of a signal due to longitudinal dispersion results in a prolongation of the time needed for the signal to pass the station. Therefore, in the salinity time series of station I (station 2 or 3) the

longitudinal dispersion provides for a "widening" of the salinity signal. Δt_i presents this widening relative to the width of the signal in the time series of station 1.

The Δt_1 have been determined for the 20 salinity signals. At station 2, Δt_2 varies between 0 and 21.8 h and at station 3, Δt_3 varies between 0 and 41 h. For the example shown in Figure 2 we have Δt_3 = 18.5 h. No significant correlation between the longitudinal dispersion and the respective river discharge or wind velocity and direction has been found.

Transport times derived by model calculations

A one-dimensional time-dependent cross-section averaged numerical water quality and transport model (Muller *et al.*, 1992) has been verified for the Lower Weser River. For calculating water level and currents the St. Venant equations are used. For boundary conditions daily averages of the river discharge upstream of the weir and water levels measured at ten gauges are available. Previous studies have shown that it is possible to determine the water level in the Lower Weser River with sufficient accuracy by linear interpolation between the ten gauges. Thus, in this case only the continuity equation was used for calculation of the currents. For simulation of all other variables an advection-diffusion equation is used. For conservative substances (e.g. salinity) this equation has the form

$$\frac{\partial}{\partial t}(A \cdot f \cdot S) + \frac{\partial}{\partial s} A \cdot \left(u \cdot S - \frac{\lambda}{f} \cdot \frac{\partial S}{\partial s} \right) - q = 0 \qquad (1)$$

$$\lambda = 50 \cdot |u| \left(\frac{f \cdot A}{p} \right)^{5/6} . \qquad (2)$$

t is the time [s], s the space coordinate [m], p(s,t) the wetted perimeter [m], A(s,t) the flow cross section [m^2], u(s,t) the cross section averaged current velocity [$m^2\ s^{-1}$], f(s,t) a dimensionless factor resulting from the curvilinear coordinate system, q(s,t) the external input [kg $m^2\ s^{-1}$]. λ(s,t) is the longitudinal dispersion coefficient [$m^2\ s^{-1}$] and S(s,t) the concentration of the substance (salt) [g/L]. The values from the monitoring stations 1 and 6 are used as boundary values.

For different river discharges, movements of a water parcel or conservative tracer which starts at time zero at the weir at Bremen have been simulated as follows. The salinity at the downstream boundary (station 6) was assumed to be zero, that at the upstream boundary (station 1) was assumed to be high (10 ppt). The propagation of this "step" has been followed through the estuary. The effects of such a step are more pronounced than a salinity minimum and therefore, easier to identify. In Figure 4 the movements of the step which will be equated with a conservative substance are displayed for a river discharge of R = 324 $m^3\ s^{-1}$ (long-term mean discharge). The movements show the periodic reversal with ebb and flood currents. Tidal averages of these movements result in curves for the net mass transport.

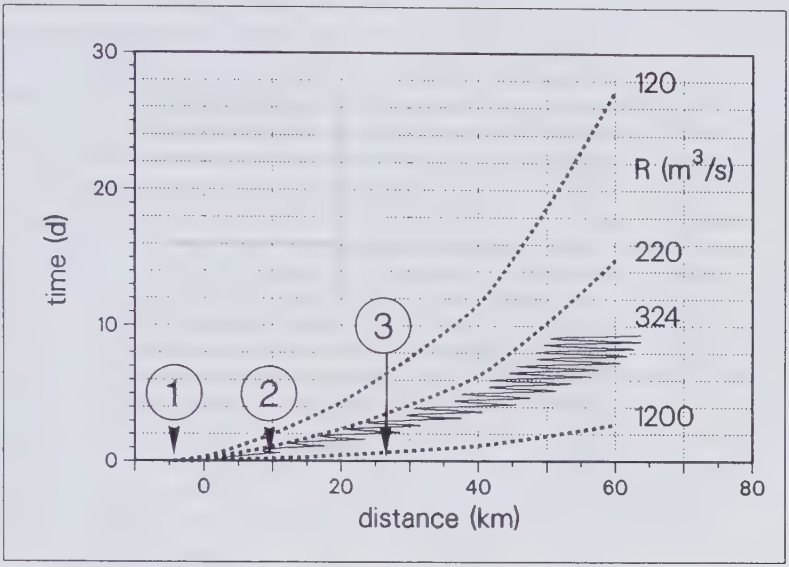

Figure 4. Calculated movements of a water parcel for R = 324 $m^3 s^{-1}$. Tidal averages result in curves for the net transport and are given for different river discharges R (dashed lines).

These curves are characterised by the river discharge. In periods of low discharge, a water parcel require approximately 27 days to pass the 65 km long inner part (weir to UW-km 60) of the estuary. This time is reduced to 11 days during periods of mean discharge and to 3 days during periods of high discharge.

Figure 3 shows that transport times calculated by model runs compare reasonably well with those derived from salinity measurements.

In order to check the longitudinal dispersion coefficient used in the model (eq. (2)) the measured salinity signal shown in Figure 2 is applied as boundary condition for the upstream boundary. River discharge was chosen to be the same as during the time of measurements (360 $m^3 s^{-1}$). Modelled and measured Δt_1 are then compared. The model simulation gives $\Delta t_{3\ (model)}$ = 20.7 h for the widening of the salinity signal at station 3. This differs slightly from the measured widening of Δt_3 = 18.5 h. This difference may result from numerical diffusion in the model (explicit numerical scheme, forward in time, centred or upstream differences in space, respectively, difference length 125 m, time step 20 s).

Nutrient Extremes and Transport Times

In the previous section, movements of water parcels as well as tidally averaged transport times have been determined. These movements and transport times affect location and strength of oxygen and nutrient extremes within the longitudinal section.

Biological decomposition processes depend on water temperature and season (e.g. Benoit, 1971; Rinaldi *et al.*, 1979). Measured longitudinal profiles of ammonium and oxygen contents are presented in Figure 5. In winter, the high ammonium load from upstream of the weir (about 0.75 mg/L) further enlarged by wastewater discharges into the estuary is transported into the North Sea without biodegradation. Thus, dissolved oxygen is also high (about 12.5 mg/L). In contrast, during the summer when the biological activity is high, wastewater will be decomposed resulting in an oxygen minimum (Figure 5) in the Lower Weser River caused by biodegradation and nitrification. Due to self-purification processes in the inland river, the ammonium load from upstream the weir is low during the summer. During May to October, wastewater inputs into the Lower Weser River cause an ammonium peak between km 10 and 40 which is followed by a nitrite peak due to nitrification. Measured longitudinal sections of nitrate and phosphate content show no significant peaks. As the nitrate load at the weir is high (about 5 mg/L), the nitrate increase due to nitrification in the Lower Weser river is negligible. Within the brackish water zone the nutrient contents decrease due to mixing with sea water (Grabemann *et al.*, 1993). Despite this dilution, a second ammonium peak followed by a nitrite peak can occur in the Bremerhaven area due to respective inputs (Figure 5 and 6).

TABLE 1: Number of passages of a water parcel at two locations for four river discharges. The water parcel starts at time zero at the weir. NP gives the number of its passages at the location. The values have been derived from model simulations as shown in Figure 4 for a river discharge of 324 $m^3 s^{-1}$.

River discharge	NP	
($m^3 s^{-1}$)	Station 2	Station 3
120	5	15
324	3	5
600	1	3
1200	1	3

Table 1 gives the calculated number of passages of a water parcel (derived from model calculations) at two locations which are near wastewater inputs. The number of passages of a water parcel at a fixed location and, therefore, the frequency of wastewater inputs into this parcel increase with decreasing river discharge. Thus, ammonium and nitrite peaks are much more pronounced in the upstream part of the estuary during low river discharges (Figure 5: R = 140 $m^3 s^{-1}$) whereas diffused extremes are observed more downstream during mean river discharges (Figure 5: R = 430 $m^3 s^{-1}$). Especially, the nitrite peak is much more pronounced during low river discharge (Figure 6) when the residence time of a water parcel in the upstream part is longer and the ammonium decrease due to nitrification takes place within a smaller area. The change of ammonium content in a water parcel can be written in the simplified form

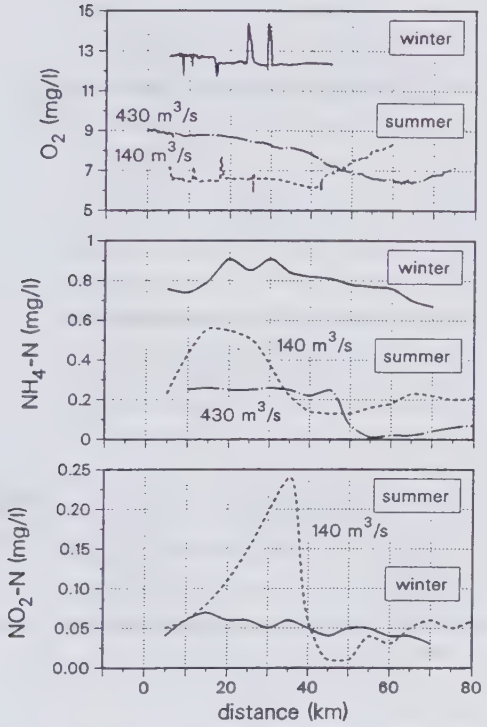

Figure 5. Longitudinal profiles of oxygen (O_2, top), ammonium-nitrogen (NH_4-N, middle), and nitrite-nitrogen content (NO_2-N, bottom) for winter and summer situations (two river discharges: R = 140, 430 $m^3 s^{-1}$).

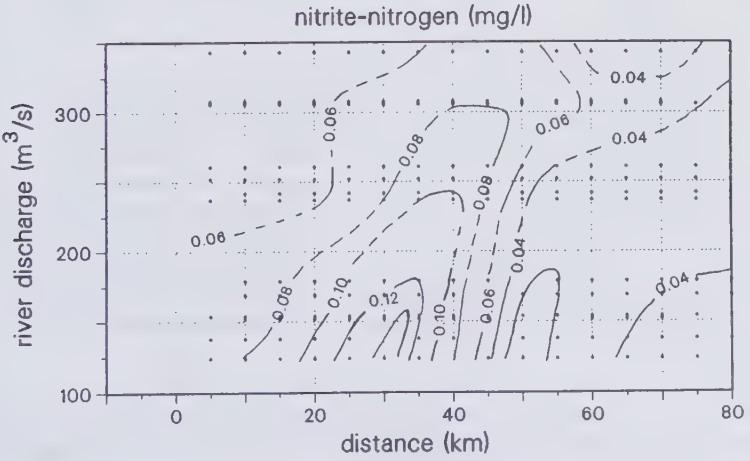

Figure 6. Lines of equal nitrite-nitrogen-content (mg/L) in a distance/river discharge diagram. The values are obtained from longitudinal profile measurements during the warmer season.

$$\frac{dN}{dt} = -f_N \cdot N . \qquad (3)$$

N is the ammonium content and $f_N = 1 \times 10^{-6}\ s^{-1}$ (Muller *et al.*, 1992) the specific degradation rate. It takes 8 days to reduce an initial ammonium concentration to half its value.

If we assume an initial ammonium concentration resulting mainly from discharges of a large sewage treatment plant located at km 10, the position $X_{1/2}$ where the initial concentration has been reduced to half its value is a function of transport time and thus river discharge. $X_{1/2}$ was obtained from measured longitudinal summer profiles of the ammonium-nitrogen content. The results are listed in Table 2. In order to avoid ammonium decrease due to dilution by sea water, only such profiles have been included for which the river discharge was relatively low and no influence of the seawater salinity was noticeable as far upstream as $X_{1/2}$. A water parcel needs the time τ_{Diff} for its first passage at km 10 to its last passage at position $X_{1/2}$. This time can be derived from the simulated movements of a water parcel as shown in Figure 4 for a discharge of 324 $m^3\ s^{-1}$. Such times are also given in table 2 for the various discharge intervals and distances km 10 $\rightarrow X_{1/2}$. These times are in the range of the calculated time using equation 3. In 8 days a water parcel is transported about 14 km downstream during 90-120 $m^3\ s^{-1}$ whereas it travels about 28 km during 180-210 $m^3\ s^{-1}$. The ammonium reduction in one case takes place within a reach of 14 km in the other case within 28 km.

TABLE 2. $X_{1/2}$ denotes the position at which an ammonium reduction to half the value of that at km 10 has occurred (in the vicinity of km 10 large ammonium loads are discharged). This position is listed for four river discharge intervals. n is the number of the analysed longitudinal profile measurements. τ_{Diff} is the time difference between the first passage of the water parcel at km 10 and the last passage at $X_{1/2}$.

River discharge (m s)	n	x (km)	τ
90 - 120	6	24 ± 5	7.2
120 - 150	5	33 ± 4	9.3
150 - 180	7	34 ± 4	8.0
180 - 210	2	38 ± 7	7.5

Concluding Remarks

Averaged transport times of conservative substances in the Weser Estuary as a function of river discharge have been derived from both model calculations and field observations. The results of both methods agree well. Such a comparison was only possible because the changing salt input by the potash industry results in defined

signals. They can be followed over a distance of about 30 km along the estuary to determine transport times. The calculation of transport times of e.g. nutrients, suspended matter and trace elements bound to suspended matter is complicated either by biological processes or by sedimentation, resuspension and occurrence of a turbidity maximum. Until now, no measurements of such transport times are available for the Weser Estuary.

Acknowledgements. The authors thank the Wasserwirtschaftsamt Bremen for supporting the studies.

References

ARGE Weser (Arbeitsgemeinschaft zur Reinhaltung der Weser), Weserlastplan, Bremen, 1982.

Benoit, R.J. Self-purification in natural waters. In *Water and Water-Pollution Handbook 1*, Ciacco, G.C. (ed.), Marcel Decker, New York, 223-259, 1971.

Bruggemann, R. and S. Trapp, Schadstoffausbreitung im Rhein. *Dt. Gewasserkl. Mitt.* 33, 24-26, 1989.

Grabemann, I., B. Kunze and A. Muller, Lower Weser water quality monitoring and water quality situation. In *Urban Waterside Regeneration - Problem and Prospects*, White, K.N., Bellinger, E.G., Saul, A.J., Symes, M., Hendry, K. (eds.), Ellis Horwood Limited, Ellis Horwood Series in Environmental Management, Science and Technology, 302-311, 1993.

Hanisch, H.-H. Warmwassereinleitungen in Tideflusse. *Dt. Gewasserkl. Mitt.* 19, 109-113, 1975.

Hauser, J., D. Eppel, A. Muller, A. Nelsen and F. Tanzer, A thermal impact assessment model with measured field data applied to the tidal river Weser. In *Proceedings of the third Waste Head Management and Utilization Conference,* Sengupta, S., Lee, S. (eds.), Hemisphere Publishing corporation, Washington, D.C., USA, 1981.

Krause, W.J., H. Mundschenk, H. and W. Rost, Zur Bestimmung von FlieBzeit und longitudinaler Dispersion im Main mit 3HHO als Leitstoff. *Dt. Gewasserkl. Mitt.* 31, 107-119, 1987.

Muller, A., M. Grodd and P. Weigel, Lower Weser Monitoring and Modelling. In *Estuarine Water Quality Management,* Michaelis, W., Springer Verlag, Berlin, Heidelberg, New York, Coastal and Estuarine Studies 36, 285-294, 1990.

Muller, A., I. Grabemann and B. Kunze, Water quality modeling: prediction of the transport of water constituents in the Weser Estuary (Germany). In *Estuarine and Coastal Modeling*, Spauling, M.L., Bedford, K., Blumberg, A., Cheng, R., Swanson, C. (eds.), Americal Society of Civil Engineers, New York, 405-417, 1992.

Rinaldi, S., R. Soncini-Sessa, H. Stehfest and H. Tamura, *Modeling and Control of River Quality*. McGraw Hill, New York, 1979.

Schoer, J. Zur Abschatzung von Transportzeiten in der Elbe unter Verwendung von Tschernobyl-Fallout als kunstlicher Tracer. *Dt. Gewasserkl. Mitt.* 32, 154-159, 1988.

18

Modelling Suspended Sediment Dynamics in Tidally Stirred and Periodically Stratified Waters: Progress and Pitfalls

S. E. Jones, C. F. Jago and J. H. Simpson

Abstract

A model capable of simulating the dynamics of suspended particulate matter (SPM) has been incorporated into a 1-D hydrodynamic/turbulent energy model. It has been used to hindcast 5-20 day observational data sets from the southern North Sea, using measured initial SPM concentration profiles and settling velocities. Entrainment from the sea bed is parameterised by best-fitting model output to the data. Two SPM components were used: one relatively rapidly settling and subject to periodic entrainment from the sea bed, the other in quasi-permanent suspension and subject to horizontal advection along concentration gradients. The model has been tested using data from three dynamically distinct sites in the southern North Sea: (A) well-mixed, (B) seasonally thermally stratified, (C) periodically stratified by freshwater runoff. At Site A, tidal entrainment, vertical mixing, and deposition of rapidly settling SPM was combined with horizontal advection of slowly settling SPM from a distant source. At Site B, the onset of seasonal stratification trapped SPM below the thermocline, this being subsequently deposited and resuspended under tidal currents. At Site C, strong tidal stirring and haline stratification alternately controlled SPM dynamics, with horizontal advection of slow-settling SPM trapped above the pycnocline during neap tides and entrainment and vertical mixing throughout the water column during spring tides. Successful simulations of the time evolution of currents, water column structure and SPM concentrations were obtained at all three sites. The model confirmed that, at Sites A and B, entrainment was restricted to a finite superficial 'fluff' layer, with no erosion of the sea bed itself. Some limitations of this essentially simple approach to modelling SPM dynamics have also been

Mixing in Estuaries and Coastal Seas
Coastal and Estuarine Studies Volume 50, Pages 302-324
Copyright 1996 by the American Geophysical Union

highlighted. Discrepancies between model and observations occurred during phytoplankton blooms because of the additional influence on SPM of biogeochemical processes. A further complication arose for those shallow water sites where significant wave activity was observed, producing enhanced bed shear stresses due to wave/current interaction which was not incorporated in the model. Finally, the model can currently handle horizontal advection along depth-uniform (and slowly varying) concentration gradients only.

Introduction

Suspended particulate matter (SPM) plays a major role in primary productivity, biogeochemical cycling and pollutant transfer in shallow shelf seas, and hence is one of the key determinants of water quality (Eisma, 1990, Tett *et al.*, 1993). As a result, considerable attention has been focussed in recent years on development of models of SPM dynamics, which can then be integrated with biogeochemical process models and ultimately incorporated into shelf-wide water quality models (Huthnance *et al.*, 1993).

Both horizontal transport paths and vertical distribution of SPM depend on a number of factors, of which perhaps the most important are those influencing deposition to, and subsequent resuspension or entrainment from, the sea bed. It is settling, deposition, and entrainment which distinguish SPM from more conservative constituents of the water column such as salinity. Vertical flux of SPM is controlled by the bed shear stress, vertical mixing by turbulent diffusion, and settling under gravity. These controls are readily incorporated into numerical models of SPM dynamics, but their quantitative parameterisation remains poorly understood. While there have been many laboratory-based studies of deposition and resuspension rates under different hydrodynamic conditions, there is doubt as to their validity in the field, especially those pertaining to cohesive sediments. To compound these uncertainties, field data at appropriate time and space resolution have been sparse; hence there have been problems in validating models of SPM dynamics.

However, recent technological advances have allowed collection of SPM concentration data at high spatial and vertical resolution over increasingly long periods of time (Lavelle *et al.*, 1984, Jago *et al.*, 1993, Jones *et al.*, 1994). This has enabled an alternative approach to the 'parameterisation problem'. Appropriate models can be applied to simulate a high quality observational data set, using the model simulation to estimate certain parameters. This works best for 1-D vertical process models, using data from moored instrument strings and fixed station CTD-based profiling.

This paper describes one approach to the development of 1-D models of SPM dynamics. An appropriate hydrodynamic model has been first adapted to include SPM entrainment, vertical diffusion and deposition, then primed and tested using observational data from a range of shelf environments, including those characterised by density stratification.

Model

In order to successfully predict temporal/spatial evolution of SPM concentration profiles, a sound hydrodynamic model is required. Any model which computes vertical profiles of current velocity (and hence bed shear stress), density and eddy diffusivity in response to tidal and/or storm forcing can be adapted to simulate suspended particulate dynamics. If it is to be generally applicable in the North Sea (and in most shelf seas), it must also be capable of handling periodic or episodic density stratification. That is, it must incorporate the influence of seasonal thermocline formation in deeper parts of shelf seas (e.g. Simpson and Bowers, 1984) and of halocline formation due to freshwater run-off in coastal waters adjacent to major river mouths (Simpson *et al.*, 1990, 1993).

A suspended particulate dynamics 'module' has been produced which, in theory, is suitable for incorporation into the full 3-D water quality models currently under development. However, module development to date has concentrated on 'point' (1-D) models which have been applied to simulate relatively short time scales (5-25 days). This approach was considered most appropriate to the available observational data base, and also to preliminary sensitivity analyses. Use of such models is justified in regions where advective terms are weak, and serves as a necessary first step in building confidence for 3-D applications.

To this end an existing 1-D hydrodynamic model, capable of simulating observed profiles of density and current velocity, has been adapted to incorporate suspended particulate dynamics. The hydrodynamic model closely follows that described by Simpson and Sharples (1991). Two hydrodynamic equations are required:

$$\frac{\partial u}{\partial t} = fv - g\frac{\partial \eta}{\partial x} - g(h-z)\frac{1}{\rho}\frac{\partial \rho}{\partial x} + \frac{\partial}{\partial z}\left(N_z\frac{\partial u}{\partial z}\right)$$

$$\frac{\partial v}{\partial t} = -fu - g\frac{\partial \eta}{\partial y} - g(h-z)\frac{1}{\rho}\frac{\partial \rho}{\partial y} + \frac{\partial}{\partial z}\left(N_z\frac{\partial v}{\partial z}\right) \qquad (1)$$

using conventional notation where $z = 0$ at the sea bed and $z = h$ at the sea surface. η is the surface elevation, $\rho(z)$ is the density, $N_z(z)$ is the turbulent eddy viscosity and f is the Coriolis parameter. The forcing includes two components of tidal pressure gradient, calculated from surface slopes, and, where necessary, two components of horizontal density gradient. This gradient is held constant over tidal cycles, although it can be varied between successive tidal cycles. The sea-surface boundary condition equates shear stress to the wind-induced stress via an aerodynamic drag coefficient (e.g. Apel, 1987). The bottom boundary condition similarly relates the two components of bed shear stress τ_0 to the near bed flow velocity via a quadratic friction law:

$$\tau_{0x} = -N_z \rho \left.\frac{\partial u}{\partial z}\right|_{z=z_0} = -c_{D100} \rho U u_{100}$$

$$\tau_{0y} = -N_z \rho \left.\frac{\partial v}{\partial z}\right|_{z=z_0} = -c_{D100} \rho U v_{100} \qquad (2)$$

$$U = \left(u_{100}^2 + v_{100}^2\right)^{1/2}$$

where the velocity components at 1m above the bed (u_{100}, v_{100}) are interpolated from the bottom two model depth bins, and c_{D100} is a drag coefficient.

The model also features a generalised advection/diffusion equation, which can be used to compute temperature, salinity (and hence density) and SPM profiles:

$$\frac{\partial A}{\partial t} = -u\frac{\partial A}{\partial x} - v\frac{\partial A}{\partial y} + \frac{\partial}{\partial z}\left(K_z \frac{\partial A}{\partial z}\right) + W_z \frac{\partial A}{\partial z} \qquad (3)$$

where A is 'concentration' of a parameter whose settling velocity is w_S (which can be set to zero when A is salinity or temperature), and K_Z (z) is the turbulent eddy diffusivity. Note that horizontal advection of background concentration gradients is included in equation 3, but these must be specified externally in this 1-D formulation.

The equation requires separate boundary conditions depending on whether A represents temperature, salinity or SPM concentration. For salinity, zero fluxes are assumed at sea bed and sea surface. For temperature, zero flux is assumed at the sea bed, but sea-surface heating/cooling is allowed as a function of incident solar irradiation, sea-surface and air temperatures, relative humidity, wind speed (e.g. Simpson and Bowers, 1984) and suspended sediment concentration (which influences the degree of penetration of incident light energy). The latter is incorporated by computing a light attenuation coefficient for the upper layers and distributing irradiated energy appropriately (Tett, 1990).

For suspended particulates, a zero net flux sea-surface boundary condition is imposed, while at the sea bed (u = v = 0) fluxes due to entrainment/ deposition must be taken into account:

$$-w_s A - K_z \frac{\partial A}{\partial z} = E - w_d A \qquad (4)$$

where E is the entrainment rate (units g/m^2 /s) and w_d is a 'deposition velocity'. For this application w_d is assumed to be the same as the settling rate w_S, i.e deposition via diffusion is ignored (Lavelle *et al.*, 1984).

Equations (1) and (4) are solved via a level 2 (Mellor and Yamada, 1974) turbulence closure scheme which computes N_Z, K_Z profiles from U, V, and density profiles, assuming local ('instantaneous') equilibrium between production and dissipation of turbulent kinetic energy. A depth-varying (parabolic) mixing length specification is used, which behaves like κz (where κ is von Karman's constant) near the bottom boundary and falls off to zero at the sea-surface.

Tidal forcing is simulated by computing N-S and E-N surface slopes for a particular site from elevations computed by a shelf-wide 2-D model at the four grid cells adjacent to the site (Proctor and Smith, 1991). The model uses an explicit finite-difference scheme with depth interval normalised by the water depth, which varies tidally (again according to the 2-D model output). The time step and depth interval are selected as a trade-off between total computational time and appropriate stability criteria.

The influence of wind stress on tidal currents is incorporated via the surface boundary condition: however, the effect of wave/current interaction on bed shear stress (e.g. Davies, 1992) has not yet been included. This simplification can be justified at this stage because significant wave activity was not generally present during the observational periods dealt with here.

Simulation of hydrodynamics at a particular site proceeds as follows. The model is applied to hindcast current, salinity and temperature profiles at that site, using measured (where available, otherwise typical) meteorological data (wind speed, solar irradiation, air temperature, relative humidity). After a preliminary 'settling down' period, it is initialised using a measured salinity/temperature profile. Evolution of that profile, along with velocity, is then monitored over a 5-20 day period. Adjustment of the bottom drag coefficient and a 'background' eddy diffusivity (both within reasonable limits) allow fine-tuning of the model until predicted and observed current/density profiles compare favourably.

Once a satisfactory simulation of the water column physics has been obtained, suspended particulate dynamics can be incorporated. The model is simply re-run with additional calls to the advection/diffusion routine at each time step, with each call corresponding to a separate settling velocity class of suspended particle. The run is initialised using a concentration profile for each settling velocity class. Two populations of particles, with different settling velocities, have been included so far.

Parameter Specification

A model which contains too many adjustable parameters becomes unwieldy: for this reason the number of parameters allowed to vary was kept to a minimum. Settling velocity distributions were measured directly using settling tubes during observation periods at each site (Jago *et al.*, 1993). These tubes, which were specially designed for use in low-concentration environments, collect an undisturbed horizontal water sample at a fixed height above the bed, then are set vertical on recovery and the contents allowed to settle. Settling velocity distributions are then obtained by withdrawal and filtering of subsamples at specified time intervals (Owen, 1970). Using this method, model settling rates were estimated as the modes of distinct sub-populations observed at 1m above the bed during periods of maximum flow: at these times it was assumed that the distributions fully represented the available entrainable material. Two distinct components were generally observed: a slowly

settling 'background' component ($w_s = 10^{-7}$ - 10^{-6} ms^{-1}) which was present at all times and a more rapidly settling 'local resuspension' component ($w_s = 10^{-4}$ - 10^{-2} ms^{-1}).

Horizontal concentration gradients were assumed to comprise only the slowly settling 'background' material (since it could be assumed that the sea bed, and hence local resuspension, were homogeneous over scales corresponding to tidal advection). They were also assumed to be depth-invariant, which is most likely to hold for slowly-settling particles. Such gradients appear to be prevalent in many regions of shelf seas (Weeks and Simpson, 1991, Jago *et al.*, 1993, Jones *et al.*, 1994). Since they must be prescribed for this 1-D model, gradients were first estimated by inference from moored instrument time series, then 'fine-tuned' after comparison of model output with observations.

Estimation of the entrainment rate (E) involved a more speculative approach. It was assumed to be a simple function of the bed shear stress:

$$E = f_i \alpha |\tau_0|^n \qquad (5)$$

with α, n as adjustable parameters (and τ_0 computed via (2)) and f_i representing the available fraction of entrainable material of the ith settling velocity class. Note that an entrainment (or deposition) threshold has not been incorporated. This allows both deposition and resuspension to occur simultaneously, and simplifies the model bottom boundary specification. This approach is currently controversial (Lavelle and Mojfeld, 1987): however, it is possible to obtain similar strongly non-linear entrainment rate functions whether or not a threshold stress is used. Other experimental/modelling studies have used a range of values for n between 1.0 and 5.0. In practice n was chosen (at integral increments from 1) to best simulate the observed form of the resuspension signal, with a then being adjusted to obtain correct tide-mean concentration values.

Different values of α and n for different w_s populations were not introduced: different proportions of each were allowed to entrain at each time step according to the value of f_i. For the simplest case where it was assumed that there was an infinite supply of both populations, this was set constant. However, as will be shown it was necessary to introduce a constraint on the entrainment rate by limiting the amount of entrainable particulate matter available on the sea bed. This involves keeping track of net fluxes of material to and from the bed, and comparing against an original (finite) start level. It has the effect of introducing an additional benthic 'layer' of resuspendable material (for each population involved), with the entrainment rate (at each time step) constrained according to the amount of material available within that layer. For this case, $f_i = 1$ (for both populations) where there is sufficient material, and $f_i = 0$ when all material has been entrained. This requires an additional parameter (essentially an initial condition): namely the total mass of the entrainable layer of particles at the start of the model run.

Possible additional processes which could (and perhaps should) be incorporated are: aggregation (i.e particle settling rate changing with time), consolidation of deposited

material, mixing of the resuspendable layer into the sea bed via bioturbation, and biogeochemical processes within the water column or on the sea bed, all of which clearly influence either particle characteristics or supply. However, inclusion of these processes would involve an additional hierarchy of parameters, which are difficult if not impossible to quantify independently and therefore introduce unacceptable complexity, at least at this stage. Fortunately, for the low SPM concentrations encountered in the examples considered here (1-10mg/L), aggregation processes (which depend on collision frequency and hence concentration) can be justifiably neglected. The time scales are also relatively short, which limits any effects of benthic bioturbation or consolidation processes to second order. However, as the examples discussed here will show, these simplifications may not apply in all cases, especially where biogeochemical processes in the water column are significant.

Experimental Observations

In order to initialise, parameterise and ultimately test the model, intensive observational data sets are required, preferably from a range of contrasting physical and sedimentological environments. Fortunately, important technological developments are now enabling longer term, high temporal/spatial resolution measurements of appropriate parameters. Recent studies in the Southern North Sea have yielded such data sets, including time series of SPM concentration profiles using moored and CTD-mounted optical beam transmissometers, directly measured settling velocity spectra and particle composition (e.g. chlorophyll concentrations from CTD-mounted fluorometers, organic carbon content). Three contrasting study sites are discussed here (Figure 1): a shallow water sandy site (A) characterised by strong tidal mixing, a deeper muddy sand site (B) characterised by periodic stratification due to seasonal thermocline formation and breakdown, and a shallow muddy sand site (C) characterised by periodic stratification due to the variable interaction of local freshwater runoff and wind/tide stirring. Table 1 summarises available particle composition data.

At the well-mixed, sandy site A, time series of SPM concentrations indicate several scales of variability (Jago *et al.*, 1993, Jago and Jones, 1993). The tidal response comprises two components: a quarter-diurnal vertical flux component, from locally-derived resuspension (rapidly diffusing up and settling down through the water column) and a semi-diurnal horizontal flux component, from advection of a horizontal 'background' concentration gradient past the mooring (Figure 2). Measurements of composition, settling velocity and size of the 'resuspension' component indicate that it comprises a different population of particles from the rippled sand of the sea bed: in fact it forms a layer of light, easily entrainable organo-mineral aggregates ('fluff') at the sediment/water interface. Strong spring-neap variability in both these components is observed. Biological processes within the water column also produce significant seasonal variation in both concentration and composition of SPM.

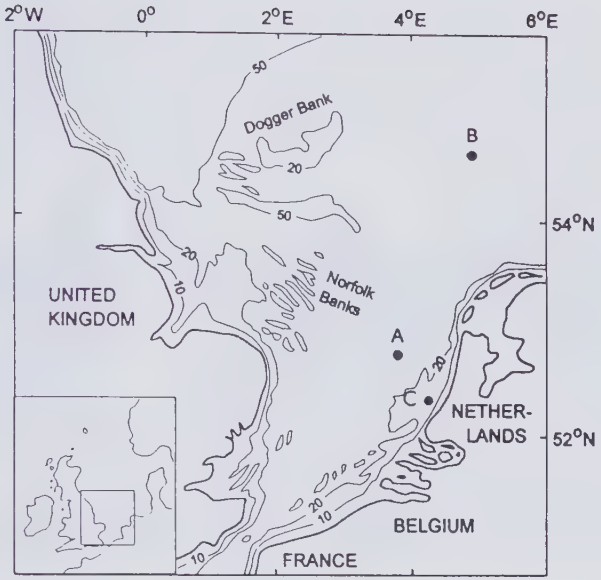

Figure 1. Bathymetric map showing location of study sites.

TABLE 1. Mean particle composition data from water bottle samples during each observational period. Sites A & B: values averaged from surface, mid-depth and near bed (+5m) samples at two-hourly intervals over tidal cycles. Site A values are depth averaged. Site C: time/depth averaged values from Day 10-20.

	SITE A		SITE B			SITE C
			Day 1	Day 5	Day 9	
% Particulate Organic Carbon	7.5	Near bed	6	7	-	30
		Surface	11	8	-	
Chlorophyll µg/L	0.5	Near bed	1.6	4.6	3.3	
		Surface	2.2	0.7	1.0	
C/N ratio	9.5	Near bed	8	6	-	-
		Surface	5	6	-	

At the deeper water, seasonally stratified Site B, SPM dynamics are extensively controlled by seasonal factors (Jago *et al.*, 1993, Jones *et al.*, 1993). During winter storms, combined wave/tidal currents result in sea bed erosion: vertical mixing then produces a significant increase in SPM throughout the water column, which settles out within a few days. More generally, however, tidal currents at the site are insufficient to disrupt the sea bed and resuspension is confined to biologically produced 'fluff', which settles out after plankton blooms. This process is seasonally modulated, in response to variation in temperature and nutrient/light availability.

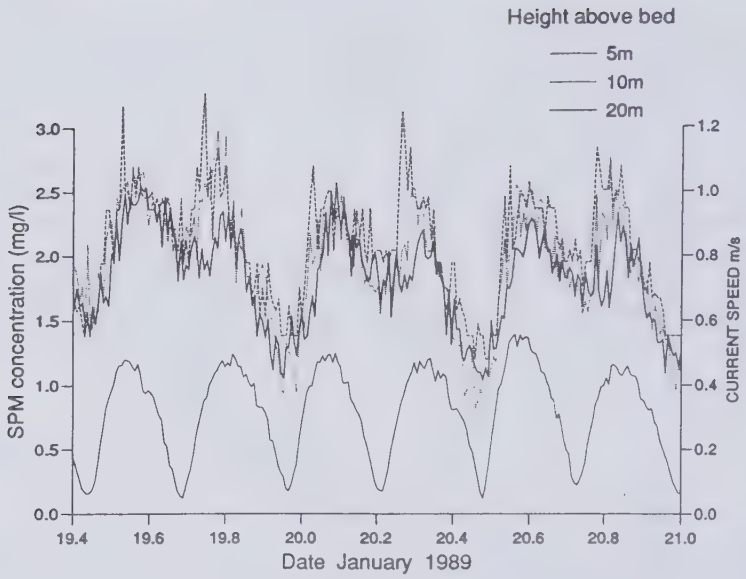

Figure 2. Sample of moored transmissometer/current meter data from Site A, showing quarter-diurnal resuspension/vertical diffusion/settling superimposed on semi-diurnal horizontal advection.

Vertical fluxes of such SPM at Site B are also strongly influenced by controls of vertical mixing in the water column. Thermocline development coupled to the Spring phytoplankton bloom resulted in entrapment of settling phytoplankton in the lower part of the water column and clearing of the upper part (Figure 3). This allowed further growth and produced a photosynthetically active component which was subject to tidal resuspension, diffusion up to the thermocline, and redeposition over a period of several days.

Thus far the sites described are characterised either by strong tidal stirring or by seasonal density (temperature) stratification, with each having a significant effect on SPM dynamics. Site C (in the Rhine outflow region) exhibits both strong tidal currents and periodic density stratification, modulated by the spring/neap cycle (Simpson *et al.*, 1993). During spring tides, the water column was well-mixed and tidal resuspension of bed material was observed (Figure 4). Strong onshore gradients in SPM concentration resulted, with higher concentrations in shallower areas. This resuspension was further enhanced during periods of wave activity, producing substantial increases in SPM throughout the water column. During neap tides, gravitational relaxation of horizontal density gradients, combined with reduced tidal stirring, caused the water column to stratify, and tidal resuspension was suppressed. The more rapidly settling components of resuspended SPM sedimented out within hours, but residual fine-grained, slowly settling material remained. Since spring-tide resuspension of slowly settling SPM was enhanced in shallower water, tidal straining

of fresher (inshore) water over saline (offshore) water produced high concentrations of slowly settling SPM in the upper part of the water column, while the lower part cleared rapidly. Tidal advection past a point mooring therefore produced high SPM concentrations and a characteristic strong semi-diurnal signal near the sea surface, and low SPM concentrations (with very small semi-diurnal signal) below the pycnocline.

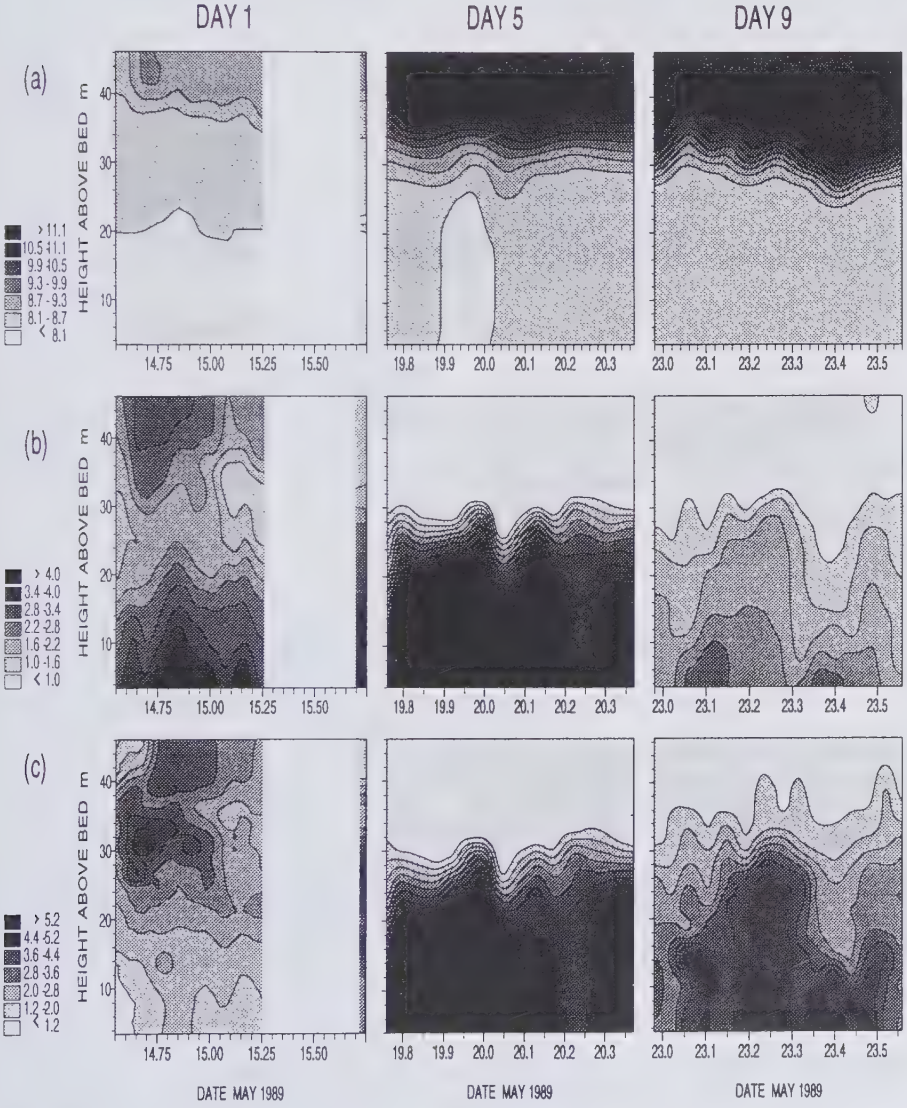

Figure 3. Contour plots of (a) temperature, (b) total SPM concentration and (c) chlorophyll concentration, obtained from hourly CTD casts at site B during 3 12.5 hour tidal cycles. An additional isolated CTD cast is also shown c. 12 hours after Tide 1.

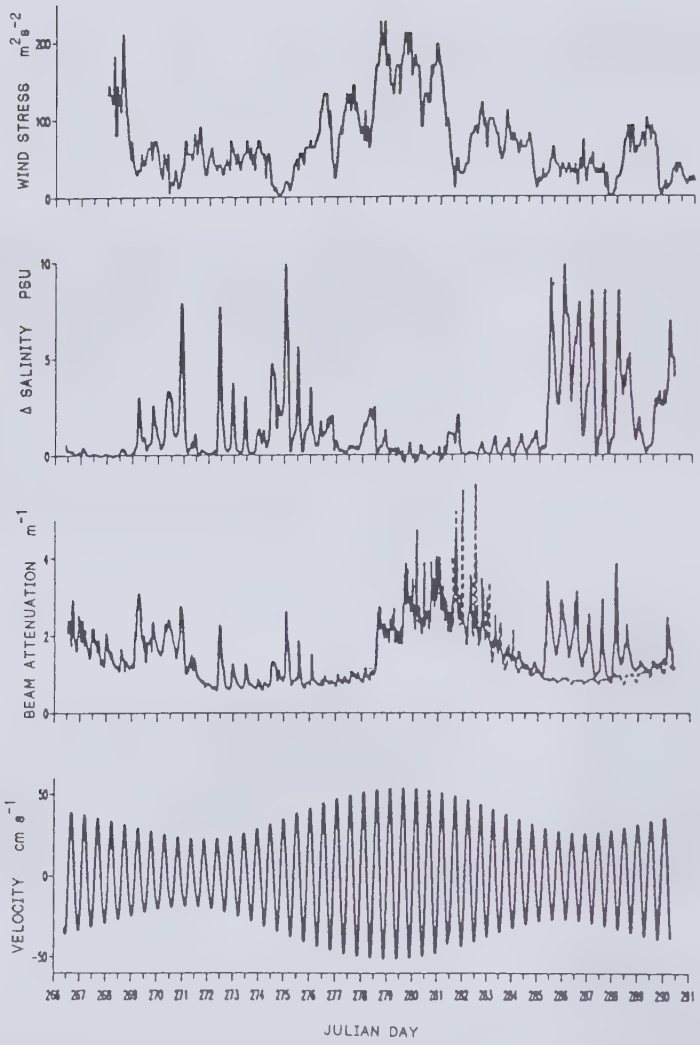

Figure 4. Time series of wind speed squared, bottom-surface salinity difference, beam attenuation from moored transmissometers at 5m above bed (dashed line) and 1m below the sea surface (solid line), and flow velocity at Site C. Beam attenuation can be converted to SPM concentration after empirical on-site calibration.

Model Simulations

The model has been applied to observational data from all three sites with encouraging preliminary results. The parameters adopted for each case have been listed in Table 2.

TABLE 2. Model parameters

	Site A		Site B	Site C
	Mixed		*Seasonally Stratified*	*R.O.F.I.*
DENSITY GRADIENT	-		-	f(t)
SPM CLASS 1:				
W_S mm/s	5		2	1
CONCENTRATION GRADIENT mg/L/km	0		0	0
SPM CLASS 2:				
W_S mm/s	1×10^{-4}		0.1	0.1
CONCENTRATION GRADIENT mg/L/km	0.06		0	f(t)
EROSION RATE				
SUPPLY LIMIT	NO	YES	YES	NO
n	1	3	3	4
alpha $\times 10^{-7}$ kg/m^2/s	0.8	0.06	2.5	0.001
f_1	0.99	1	1	0.95
DEPTH BINS	15 × 2m		15 × 3m	10 × 2m
TIME STEP hrs	0.001		0.0005	0.0005

Site A

At the well-mixed, sandy site A, good agreement was obtained between model and observed current velocity profiles (Figure 5). Two different SPM simulations were performed. Both used the same (constant) background horizontal concentration gradient, inferred from the semi-diurnal component of observed time series.

The first case (Figure 6) considered an unlimited supply of resuspendable material, while the second (Figure 7) assumed that all available material was already in suspension at the start of the model run (which was at maximum tidal flow). Reasonable agreement was obtained with data at three heights above the bed for both cases: however, for the first (unlimited) case, there was a distinct phase lag between model and observed data, with peak observed values occurring before the predicted ones. Agreement in both phase and form was much improved for the second case (Figure 8), because by limiting the supply it was possible to simulate a 'sharper' resuspension signal (by specifying a higher n-value in (5)), which was suppressed once all available material was exhausted.

The rather poorer agreement obtained during 21st-22nd January can be explained by significant wave activity observed at that time, which is not incorporated into the model. This had the effect of suppressing deposition of SPM during slack water (as can be seen in Figure 7 and 8) although it did not enhance resuspension during maximum flow, because the supply was already source-limited.

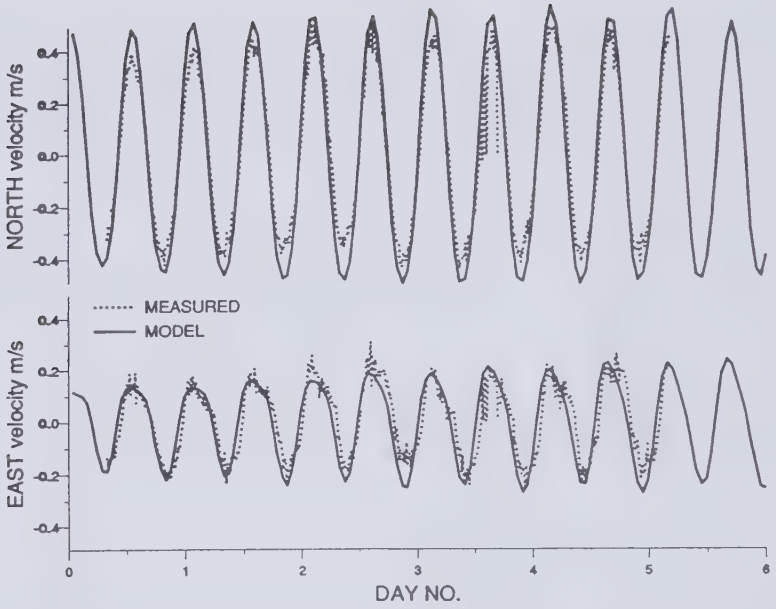

Figure 5. Comparison of model and measured depth-average flow velocity at Site A.

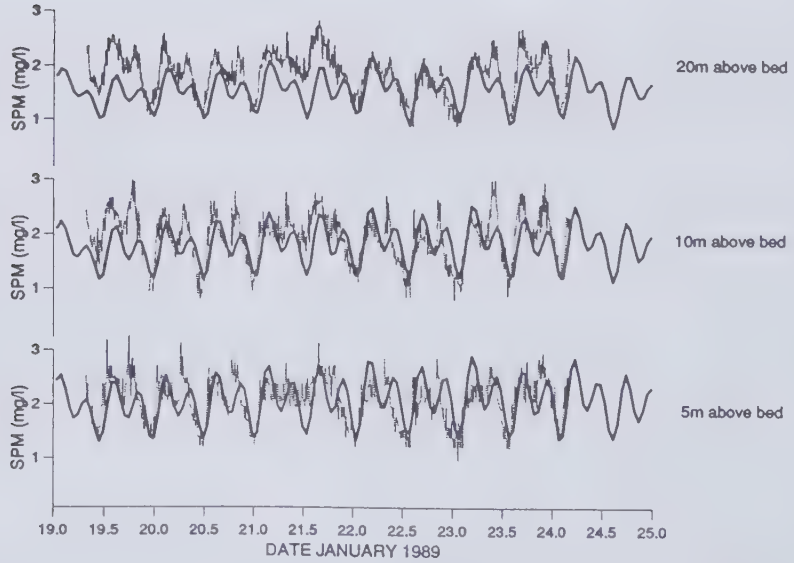

Figure 6. Comparison of model and measured total SPM concentration at Site A for the case where supply of entrainable material is unlimited.

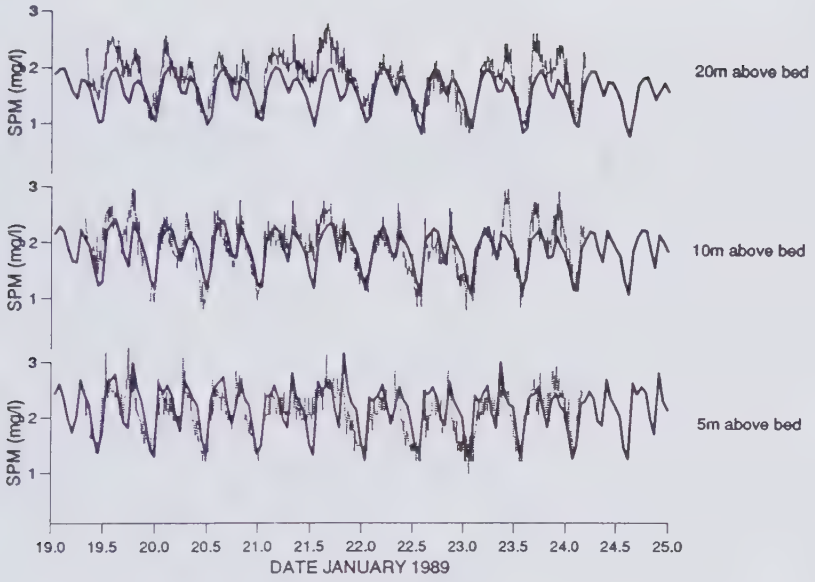

Figure 7. Comparison of model and measured total SPM concentration at Site A for the case where supply of entrainable material is limited to the total amount observed in the water column at maximum flow at the start of the model run.

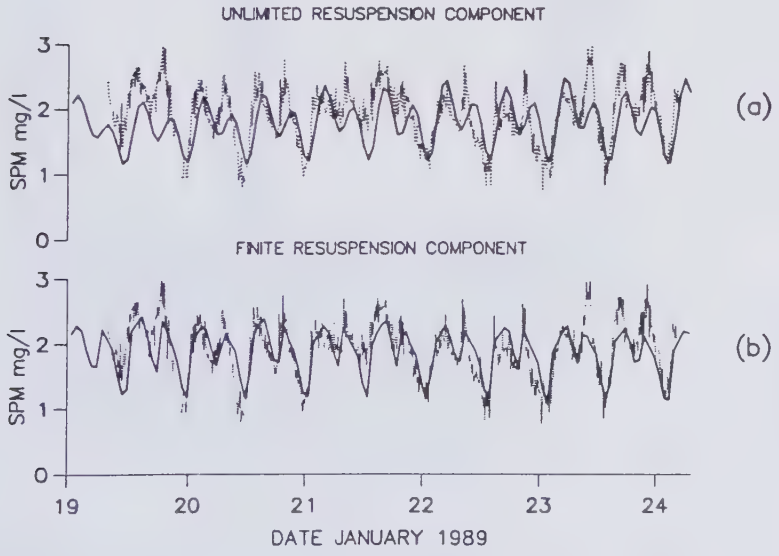

Figure 8. Comparison of two model runs described in Figure 6 and 7, at 10m above bed.

Site B

At the seasonally stratified site B, the model has been applied to the Spring data set, when thermocline development was observed. Reasonable agreement with both temperature and current profiles was obtained, with correct prediction of formation, depth and magnitude of the thermocline (Figure 9). However, a rather sharper thermocline formed than was predicted, indicating that correct simulation of water column physics at this site has not quite been achieved. This may be because the fixed parabolic mixing length specification is not strictly appropriate in cases where strong stratification occurs: overestimation of mixing length may enhance diffusion near the thermocline, causing divergence from observations. There was also some disagreement between observed and predicted current velocity (Figure 10), especially in phase of the N-S velocity component.

The suspended particulate component also proved to be more complicated in behaviour than at Site A. An initial surface phytoplankton bloom was trapped beneath the thermocline as it developed, settled out and then was subject to periodic resuspension/deposition as currents increased towards spring tides. Another component, this time not photosynthetically active, was also present both at and near the bed. This component was assumed to be detrital material from a previous phytoplankton bloom.

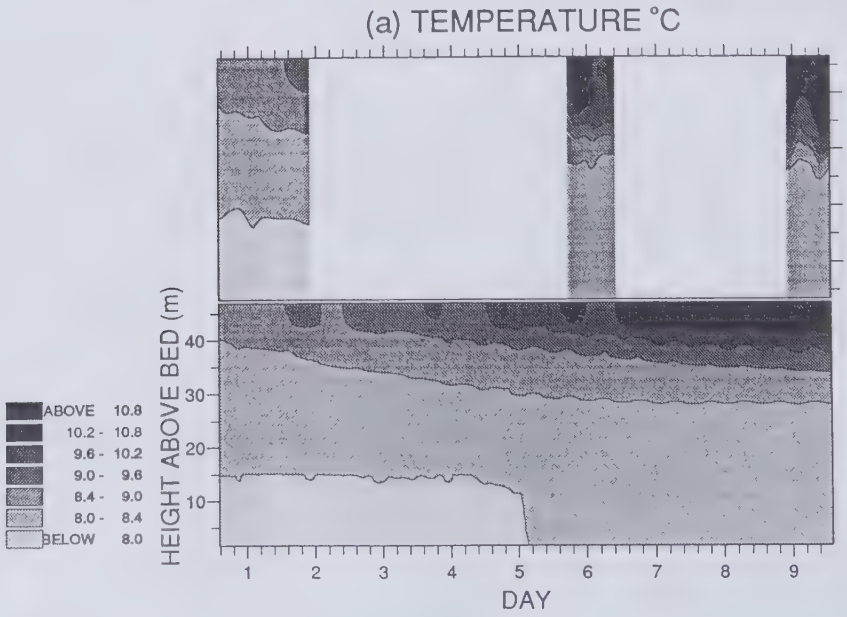

Figure 9. Comparison of model and measured time-evolution of temperature at Site B, using CTD cast data from Figure 3.

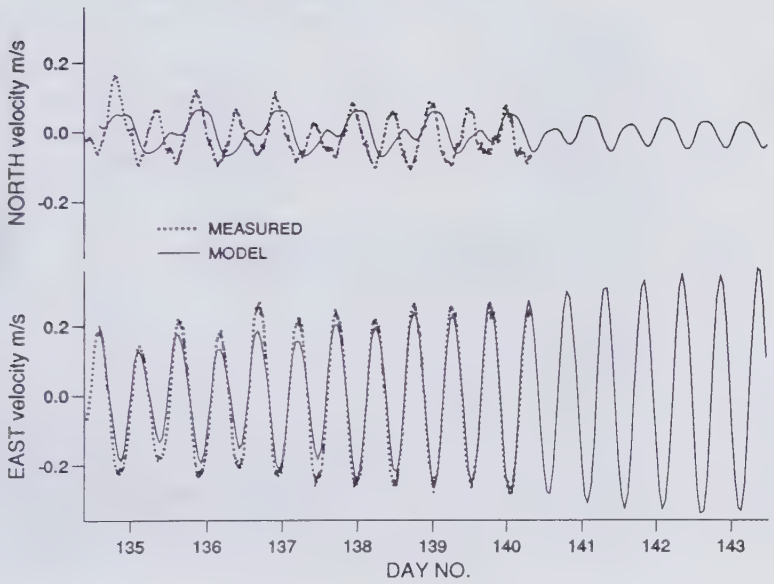

Figure 10. Comparison of model and measured flow velocity at Site B.

Using two 'resuspension' populations corresponding to the photosynthetically active component and the detrital component, reasonable agreement between observed and predicted total SPM concentration profiles was obtained (Figure 11). The initial concentration profile of the photosynthetically-active component was estimated using observed chlorophyll concentration data, with the detrital component forming the remainder of the observed total SPM concentration. In this case, advection along horizontal 'background' concentration gradients was not significant and could be ignored. However, as at Site A, best results were achieved by restricting the supply of both populations to the amount present in the water column at maximum flow at the start of the model run (i.e it was assumed that the sea-bed supply was exhausted at that time).

The pattern of surface plankton settling, becoming trapped beneath the thermocline and then being subject to resuspension was reproduced successfully. However, observed concentrations of both components (and especially the detrital one) reduced markedly towards the end of the study period, to an extent which could not be reproduced by the model. Clearly biogeochemical processes (growth, mortality and biodegradation), were altering both supply and composition (and hence settling/entrainment rates) of SPM during this time. Such processes cannot be simulated by a purely physical resuspension model. There is also evidence that phytoplankton aggregation processes were important in 'scavenging' particles from the water column during the observation period (Jones *et al.*, 1993b), which may explain the observed reduction in SPM concentration.

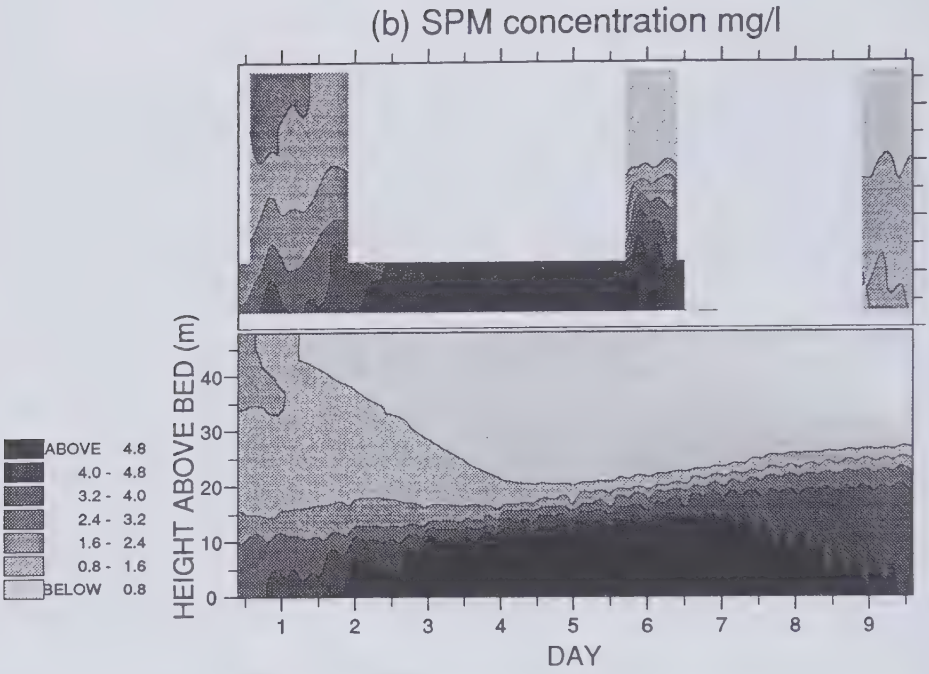

Figure 11. Comparison of model and measured time-evolution of total SPM concentration at Site B, using CTD cast data from Figure 3 combined with moored transmissometer data at 5m and 10m above the sea bed for the first 6 days.

Site C

Site C was influenced by strong horizontal density gradients due to regional freshwater runoff: during periods of stratification tidal straining produced characteristic frontal structures which advected past the study site. The hydrodynamic model therefore required prescription of horizontal density gradients (which was unnecessary at Sites A and B). These were obtained from appropriate filtering of moored conductivity cell time series. They were found to vary significantly during the deployment period, in response to varying regional environmental conditions and time-evolution and advection of water-column structure. Strictly, a full 3-D model is required to simulate this complex problem: however, it can be reduced to a 1-D case by provision within the model for updating the 'ambient' horizontal density gradient at the start of each ebb tide. The onset and breakdown of stratification was predicted correctly by this method (Figure 12), although work is still in progress to improve the simulation of pycnocline depth.

Similar prescription of time-varying 'background' SPM concentration gradients was also required, and was performed after inspection of observed time series. Although

this gradient-prescription procedure allows inference of regional heterogeneity, and hence has some intrinsic value, it clearly has no predictive capacity.

By setting horizontal SPM concentration gradients to zero, simulation of entrainment/diffusion/settling processes by the 1-D model can be properly tested. Good agreement was obtained between model and measured SPM concentration time series during spring tide resuspension and subsequent settling near surface (Figure 13 (b)) and at 5m above the bed (Figure 14(b)). Spring-tidal resuspension of both settling velocity classes produces the observed quarter-diurnal (primarily the faster settling population) and spring-neap (primarily the slower settling population) signals. However, the model was found to either slightly underestimate tidal resuspension at maximum spring tide, or overestimate resuspension as currents increased towards springs (as shown in Figure 13(b)), depending on the entrainment rate chosen. This is probably because resuspension was further enhanced by wave activity during maximum springs, due to enhanced bed shear stress. Since the model does not include the effects of wave/current interaction, this effect could not be incorporated. Therefore the values of α and n chosen to simulate observed wave/current resuspension (Days 11-16) produced overestimates of current-only resuspension (Days 8-11).

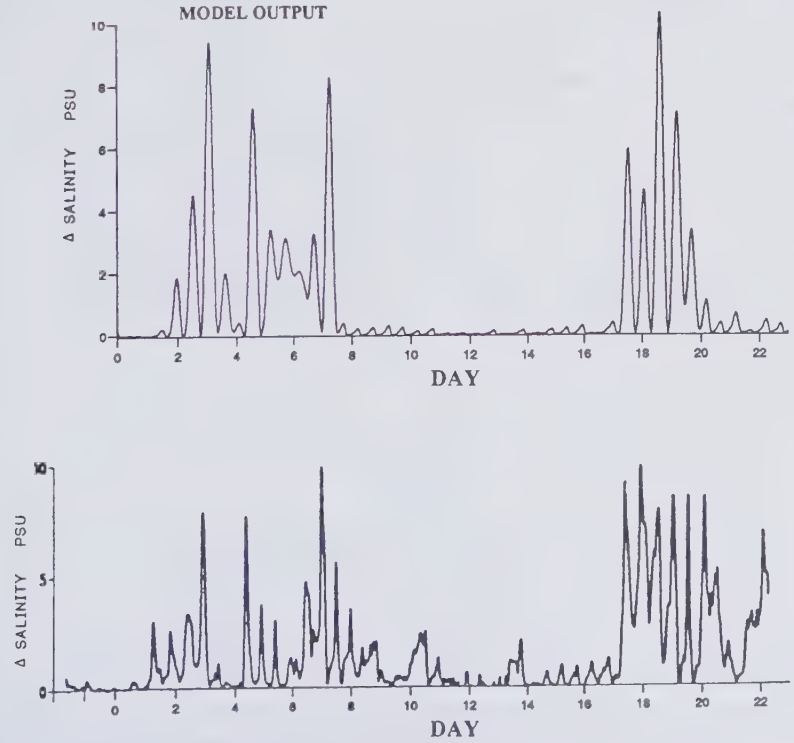

Figure 12. Comparison of model and measured bottom-surface salinity difference at Site C, using moored conductivity cell time series.

After prescription of horizontal concentration gradients, good correspondence was obtained between observed and predicted time series for the near-surface layer (Figure 13(c)). However, in the near bed region the advective signal was overestimated by the model (Figure 14(c)). This arises from the fact that the model assumes depth-uniform SPM concentration gradients. However, a 12.5 hour time series of fixed-station SPM concentration profile observations (Figure 15) shows a strong tidal advection signal only in the region above the pycnocline, suggesting that horizontal concentration gradients are restricted to upper part of the water column.

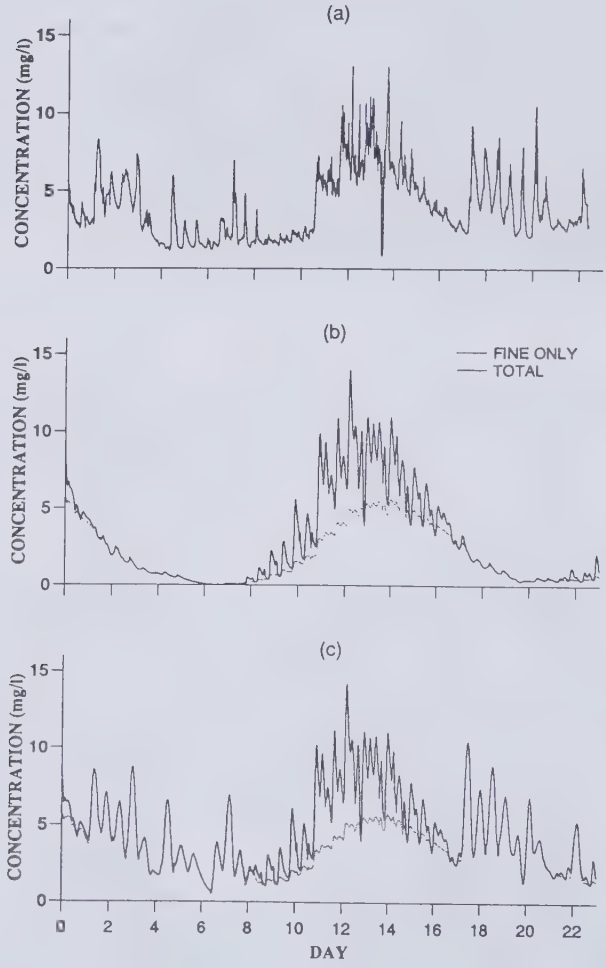

Figure 13. Site C: Comparison of model and measured SPM concentration at 1m below the sea surface, with model output split into slow-settling (fine) and fast-settling contributions. (a) Measured data, (b) model output without specifying horizontal SPM concentration gradients, (c) model output with time-varying horizontal concentration gradients.

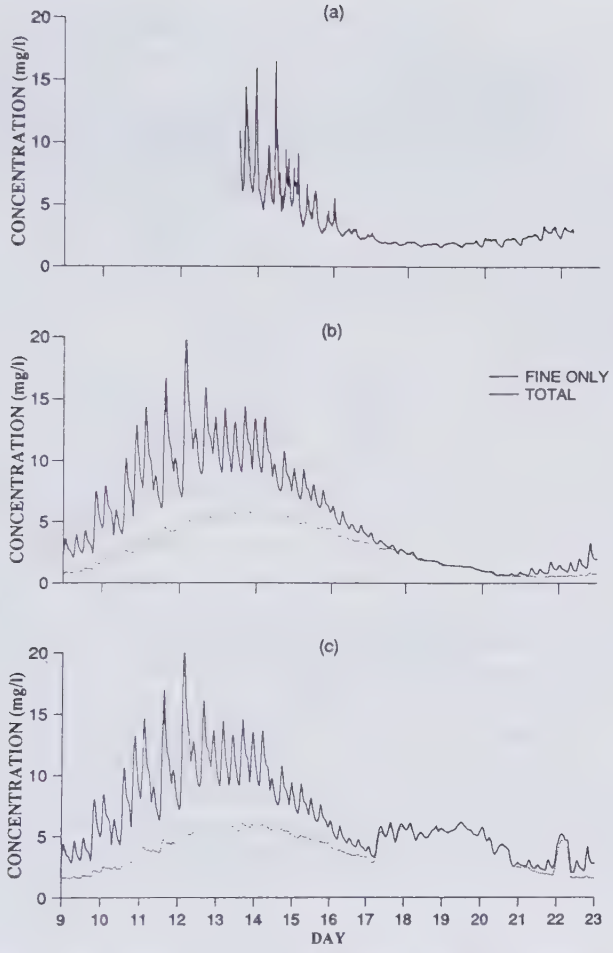

Figure 14. Site C: Comparison of model and measured SPM concentration at 5m above the sea bed, with model output split into slow-settling (fine) and fast-settling contributions. (a) Measured data, (b) model output without specifying horizontal SPM concentration gradients, (c) model output with time-varying horizontal concentration gradients.

Variation in Entrainment Rate Constants

It is interesting to compare the entrainment rate constants used at the different sites (Table 2). Best fit values of n = 3 were obtained for both Site A (assuming supply-limited entrainment) and Site B, but values of α were much higher at Site B than at A, indicating that the material was almost ten times more easily entrained. This is explained by the lower value of settling velocity of the local resuspension fraction (Class 1) at Site B, indicating smaller diameter/lower density particles. At

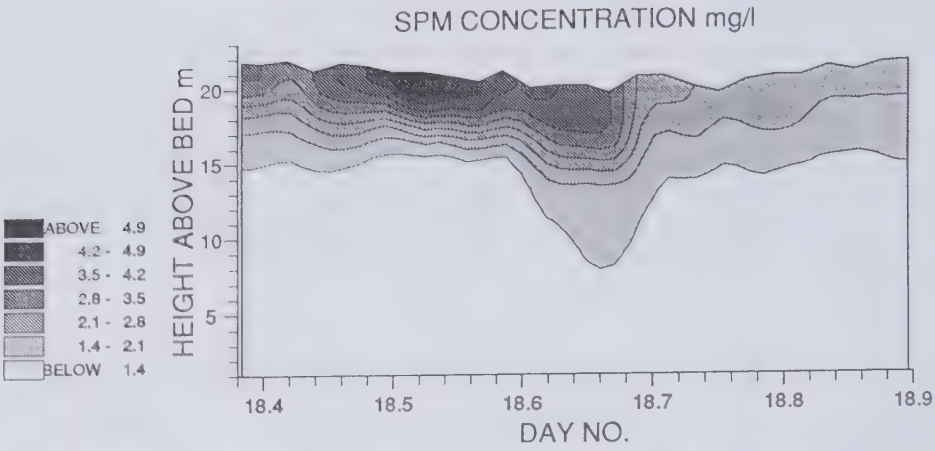

Figure 15. Contour plot showing tidal variation of SPM concentration profiles at Site C on Day 18, obtained from hourly CTD casts.

Site C, comparison is harder because a higher exponent (n=4) was obtained. Also, the entrainment rate parameters may not be strictly comparable with those obtained for Sites A and B because they may include effects of wave/current interaction. However, the stronger non-linearity in entrainment rate function indicated could reflect the fact that material was being entrained from a cohesive bed (rather than from within a superficial 'fluff layer' as at Sites A and B). Moreover, this bed remains undisturbed during neap tides, perhaps allowing some consolidation to occur. At low shear stresses, cohesive interparticle bonds prevent significant entrainment, but once those bonds have been broken subsequent entrainment is much easier, and large quantities of relatively slowly settling particles can be released.

Discussion and Conclusions

It has been shown that appropriate 1-D models can be applied to hindcast SPM concentration profiles, and hence fluxes, over relatively short time scales, provided that they are primed with a suitable observational data set. This clearly stops a long way short of achieving full predictive capability, which is the ultimate aim of environmental modellers.

However, the preliminary successes obtained by integrating 'point' hydrodynamic models with modules simulating suspended particulate behaviour are significant. Reducing the 3-D problem to 1-D with prescribed horizontal gradients provides a powerful tool for investigation of physical processes, and is particularly suitable for applying to point observations such as fixed-station CTD-profiles or mooring data. This has allowed investigation of appropriate parameters to describe entrainment

from the sea bed, and has also highlighted shortcomings in the model formulations adopted. There is still much to be gained from investigation of SPM dynamics in different environments by this approach.

Because of the computational advantage involved, it is tempting to adapt 2-D depth-averaged shelf-sea models to simulate SPM fluxes. Provided that settling rates are small compared to diffusion, vertical structure can be safely ignored. However, this work has shown that even in areas where entrainment of bed material should only occur during storms, plankton and other detritus can form significant concentrations of rapidly settling and resuspending material, leading to vertical variation in concentration (and hence flux). Further, SPM fluxes are strongly influenced by pycnocline formation and breakdown in regions subject to stratification. These both indicate that full 3-D models will be required for accurate simulation of shelf-wide SPM dynamics. Fortunately the techniques developed here can be readily adapted to 3-D schemes, although the problems of parameterisation of horizontal/ seasonal heterogeneity in entrainment rate, settling rate and supply must not be underestimated.

This work has also provided insight into appropriate processes which must be incorporated into full 3-D models. In particular, it has highlighted the importance of supply-restricted, resuspendable (and biogeochemically active) 'fluff' at both shallow water and seasonally stratified sites. It indicates that future models must incorporate biogeochemical process 'modules' in addition to SPM dynamics before longer term simulations can be achieved. It will also be necessary to incorporate wave/current interaction, since SPM dynamics have been shown to be highly sensitive to wave-stirring in shallow areas.

Acknowledgements. This work was completed within the NERC North Sea Community Project, with additional finance for the Rhine Outflow work provided by the EC under the MAST-0050C contract. The authors would like to thank J. Sharples for valuable discussions on turbulence modelling and A. Souza for providing hydrodynamic/physical parameters for running the model at Site C.

References

Apel, J.R. *Principles of Ocean Physics.* International Geophysics Series Volume 38. Academic Press, London 1987.

Davies, A.G. Modelling the vertical distribution of suspended sediment concentration in combined wave-current flow. In: *Dynamics and Exchanges in Estuaries and the Coastal Zone* edited by D. Prandle, A.G.U Coastal and Estuarine Studies Vol. 40, Chapter 22, 441-466, 1992.

Eisma, D. Transport and deposition of suspended matter in the North Sea and the relation to coastal siltation, pollution and bottom fauna distribution. *Reviews in Aquatic Sciences* 3(2-3): 181-216, 1990.

Huthnance, J.M., J.I. Allen, A.M. Davies, D.J. Hydes, I.D. James, J.E. Jones, G.E. Millward, D. Prandle, R. Proctor, D.A. Purdie, P.J. Statham, P.B. Tett, S. Thomson and R.G. Wood. Towards water quality models. *Phil. Trans. Roy. Soc. Series A* 343(1669): 569-584, 1993.

Jago, C.F., A.J. Bale, M.O. Green, M.J. Howarth, S.E. Jones, I.N. McCave, G. Millward, A.W. Morris, A.A. Rowden and J.J. Williams. Resuspension Processes and seston dynamics. *Phil. Trans. Roy. Soc. Series A* 343(1669): 475-491, 1993.

Jago, C.F. and S.E. Jones. Dynamics of suspended particulate matter in the Southern North Sea. I. Tidally mixed waters. Submitted to *Cont. Shelf. Res.* 1993.

Jones, S.E., C.F. Jago, D. Prandle and D. Flatt. Suspended sediment dynamics, their measurement and modelling in the Dover Strait. In *Physical Mechanisms of Transport and Dispersion in the Environment.* edited by K. Beven, P. Chatwin and J. Millbank, Chapter 10, 183-201, John Wiley, 1994.

Jones, S.E., C.F. Jago, A.J. Bale, D. Chapman, R. Howland and J. Jackson. Dynamics of suspended particulate matter in the Southern North Sea. II. Seasonally stratified waters. Submitted to *Cont. Shelf. Res.* 1993.

Lavelle, J.W., H.O. Mojfeld and E.T. Baker. An in situ erosion rate for a fine-grained marine sediment. *J. Geophys. Res.* 89(C4): 6543-6552, 1984.

Lavelle, J.W. and H.O. Mojfeld. Do critical erosion stresses for incipient motion and erosion really exist? *J. Hydraul. Eng.* 113(3): 370-393, 1987.

Mellor, G.L. and T. Yamada. A hierarchy of turbulence closure models for planetary boundary layers. *J. Atmospheric Sciences* 31: 1791-1806, 1974.

Owen, M.W. A detailed study of the settling velocities of an estuary mud. Hydraulic Research Station, Wallingford, U.K. Report INT 78: 28pp, 1970.

Proctor, R. and J.A. Smith. *Depth-averaged residual circulation on the North-West European Shelf, Aug-1988-October 1989.* Proudman Oceanographic Laboratory report No. 20, U.K, 1991.

Simpson, J.H and D.G. Bowers. The role of tidal stirring in controlling the seasonal heat cycle in shelf seas. *Annales Geophysicae* 2(4): 411-416, 1984.

Simpson, J.H., J. Brown, J. Matthews, G. Allen. Tidal straining, density currents and stirring in the control of estuarine stratification. *Estuaries* 13: 125-132, 1990.

Simpson, J.H. and J. Sharples. Dynamically active models in the prediction of estuarine stratification. In: *Dynamics and exchanges in estuaries and the coastal zone,* edited by. D Prandle, 101-113. Springer-Verlag, 1991.

Simpson, J.H, W.G. Bos, F. Schirmer, A.J. Souza, T.P. Rippeth, S.E. Jones and D. Hydes. Periodic stratification in the Rhine ROFI. *Oceanologica Acta* 16(1): 23-32, 1993.

Tett, P. The Photic Zone. In: *Light and Life in the Sea* edited by P.J. Herring, A.K. Campbell, M. Whitfield and L. Maddock, Cambridge University Press, 1990.

Tett, P.B., I.R. Joint, D.A. Purdie, M. Baars, S. Oosterhuis, G. Daberi, F. Hannah, D.K. Mills, D. Plummer, A.J. Pomroy, A.W. Walne and H.J. Witte. Biological consequences of tidal stirring gradients in the North Sea. *Phil. Trans. Roy. Soc. Series A* 343(1669): 493-508, 1993.

Weeks, A. and J.H. Simpson. The measurement of suspended particulate concentrations from remotely sensed data. *Int. J. Remote Sensing* 12(4): 725-737, 1991.

19

Bottom Friction Reduction in Turbid Estuaries

B. King and E. Wolanski

Abstract

The Fly River estuary, in Papua New Guinea, is a broad, shallow estuary with 3 distinct channels forming a delta. The South Alligator River, in Australia, is a 100 km long fan-shaped shallow estuary. Both estuaries are macro-tidal and have rugged bottom features. The freshwater discharge of the South Alligator River estuary is negligible; that of the Fly River estuary is about 6,000 $m^3 s^{-1}$. Nevertheless the flow is largely barotropic. Both estuaries are very turbid with suspended sediment concentrations often exceeding 5 gL^{-1}. The propagation of the tidal wave was modeled in both systems and verified against field data. The Manning's friction parameter in both estuaries was found to be unusually small (n = 0.015 - 0.020). The low values of the frictional coefficient may be due to drag reduction in a suspension of clay and/or to fluid mud at the bottom relaxing the no-slip condition for the bulk of the water column.

Case Study 1: The Fly River Estuary

The Fly River estuary in Papua New Guinea (Figure 1) is fan-shaped and shallow (depth < 10m). An accurate bathymetry survey of the region is available (Wolanski *et al.*, 1992a) and is shown in Figure 2. Rugged bottom fluctuations (wavelengths < 1000 m) consist of extensive mud banks, pools, channels and sand dunes.

Mixing in Estuaries and Coastal Seas
Coastal and Estuarine Studies Volume 50, Pages 325-337
Copyright 1996 by the American Geophysical Union

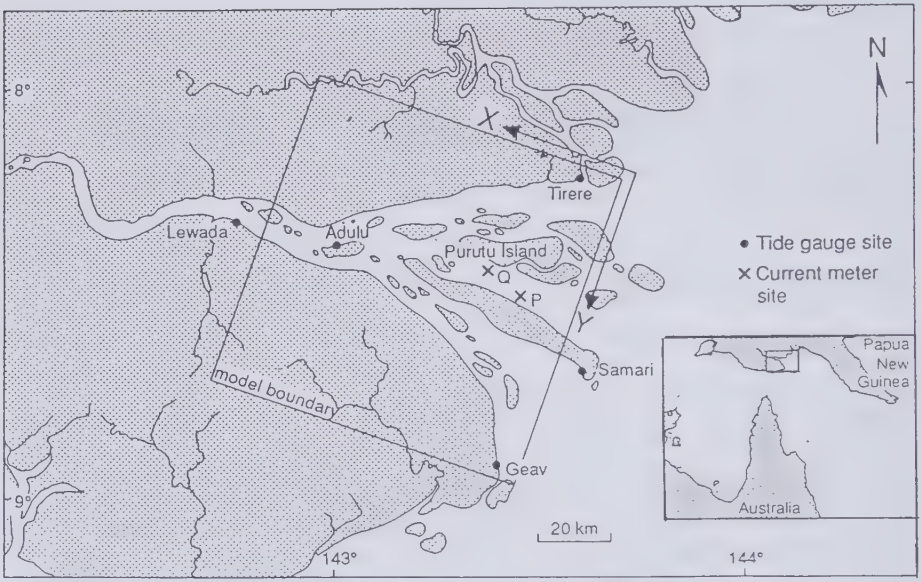

Figure 1. Location maps showing the Fly River delta, the Gulf of Papua, the position of the model boundaries and the location of the major measurement sites.

The river carries a freshwater discharge of about 6,000 $m^3 s^{-1}$ with little seasonal variations, and a mean suspended sediment concentration of 0.5-1.0 gL^{-1} (Salomons and Eagle, 1990; OTML, 1988). From extensive field studies reported in Wolanski *et al.*,(1990, 1992a, 1992b) and Wolanski and Eagle (1991), we know that the estuary is macro-tidal with a 5 m spring tide, a 1 m neap tide, and a strong diurnal inequality (see Figure 3). The tidal limit rarely extends more than 150 km upstream of Lewada (Figure 1).

The tidal currents are very strong, peaking at 2.5 m s^{-1} at some locations. The saltwater intrudes up to Sumogi Island. The Southern Channel receives about 60% of the freshwater discharge and is partially stratified in salinity. The Northern Channel is also partially stratified in salinity and the vertical stratification in salinity seems to become stronger during neap tides than at spring tides. The Far Northern Channel is vertically well-mixed in salinity at all tides.

Tide gauges were deployed between 1990 and 1992 at Lewada, Adulu, Tirere, Samari and Geav and maintained for periods greater than one year (see table 1). Concurrently, vector-averaging current meters were deployed in frames, at 1.3 m above the bottom, at sites Q and P only for about 10 days, as well as other selected stations. The frames also contained back-scatter nephelometers to measure suspended sediment concentration profiles (see Wolanski *et al.*, 1992b). These data sets were subsequently used to verify the hydrodynamic model.

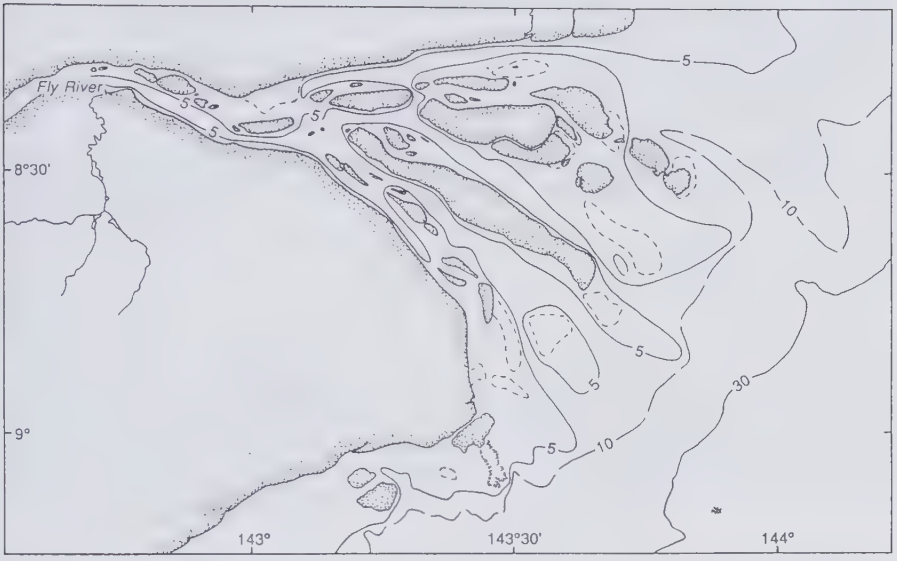

Figure 2. The bathymetric chart of the Fly River estuary derived from: SMEC bathymetric data, the navigation chart for the Far Northern Channel and our bathymetric survey data.

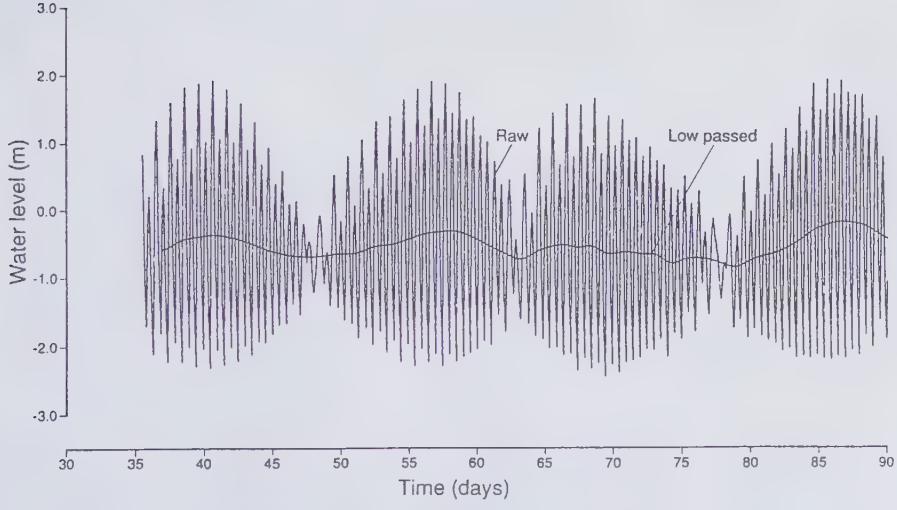

Figure 3. Time-series plots of water level fluctuations at Adula before and after low-pass filtering.

TABLE 1. The amplitudes and phases for the major constituents from all tidal measurements within the estuary.

	TIRERE		SAMARI		GEAV		ADULU		LEWADA	
	A(m)	Θ	A(m)	Θ	A(m)	Θ	A(m)	Θ	A(m)	Θ
M_2	1.049	341.7	0.733	327.9	0.899	321.4	1.115	36.3	1.080	64.4
S_2	0.587	321.3	0.380	308.7	0.617	302.2	0.597	20.5	0.598	42.7
N_2	0.327	323.8	0.239	312.5	0.297	314.5	0.311	17.1	0.266	43.8
K_1	0.312	211.2	0.307	210.7	0.311	204.1	0.333	237.5	0.313	262.6
O_1	0.161	159.7	0.166	156.3	0.171	161.4	0.174	185.8	0.187	197.7
Ms_f	0.052	8.0	0.061	16.8	0.064	137.1	0.125	29.0	0.182	356.6
M_4	0.075	296.3	0.068	263.7	0.055	178.1	0.159	0.7	0.063	72.8

Based on the field observations to date, it is possible to justify the modelling of the tidal dynamics of this estuarine system using a two-dimensional depth-averaged model because of the strong barotropic tidal currents which are predominantly two-dimensional and much stronger than the baroclinic currents.

The depth-averaged hydrodynamic model ('HYDRO') described by Wolanski and King (1990) was employed to model the currents and tides within the Fly River estuary. HYDRO uses a semi-implicit, centered, second-order finite-difference scheme to solve the two-dimensional, depth-averaged, momentum equations and continuity equation, to obtain barotropic currents and sea elevation at defined points at discrete times. These equations can be written as:

$$\frac{\partial UH}{\partial t}+\frac{\partial U^2 H}{\partial x}+\frac{\partial UVH}{\partial y}-fVH+gH\frac{\partial \eta}{\partial x}+\frac{gU|U+V|}{C^2}-\mu_H\left[\frac{\partial^2 UH}{\partial x^2}+\frac{\partial^2 UH}{\partial x^2}\right]=0$$

$$\frac{\partial VH}{\partial t}+\frac{\partial VUH}{\partial x}+\frac{\partial V^2 H}{\partial y}+fUH+gH\frac{\partial \eta}{\partial y}+\frac{gV|U+V|}{C^2}-\mu_H\left[\frac{\partial^2 VH}{\partial x^2}+\frac{\partial^2 VH}{\partial x^2}\right]=0$$

$$\frac{\partial \eta}{\partial t}+\frac{\partial UH}{\partial x}+\frac{\partial VH}{\partial y}=0$$

where t is the time; x and y the horizontal axes; H is the total depth; U and V the depth-averaged horizontal velocities; f is the Coriolis parameter; g is gravitational acceleration; η is the free surface elevation; μ_H is the horizontal eddy viscosity coefficient and C is the Chezy coefficient (= $H^{1/6}/n$, where n is the Manning roughness coefficient).

The solution grid applied to the study area was a square 65×65 mesh. Figure 1 shows the details of this mesh with the X axis aligned in the general along-estuary direction (285° clockwise from North) and the Y axis aligned in the general across-river direction (195° clockwise from North). The resolution of each grid cell was 1410 m × 1410 m. The time step was set at 120 seconds. These open boundaries are employed to specify the external influences of the system to the model computations. This is achieved by describing the water elevation condition at each open boundary.

The Upstream Boundary

The upstream boundary occurs near Lewada (see Figure 1) and is forced by water level fluctuations as measured at this site. The water elevation varies according to the river discharge and the tidal forcing. The elevation of the datum of the tidal station relative to that of the mouth was unknown. This value is calculated through the sensitivity analysis process detailed later in the text.

The Downstream Boundary

The downstream boundary of the model crosses each of the major channels near the mouth (Figure 1). The sea level fluctuations along this boundary are predominantly the tides. Thus, the observed tidal fluctuations, as measured at Geav, Samari and Tirere, are used to specify the water elevation at the closest grid point. The remaining points are then determined by interpolation.

Model Verification

For the purposes of verification, several runs were performed. Each run utilised the open boundary data, for periods coinciding with the occasional in-situ current meter data. Also, the model was verified against the Adulu tide data (which proved an excellent match, though this is not a sensitive test since this station is close to Lewada). In particular, since the estuary current meter data were collected at a number of sites, we were able to test the parameters for their applicability and generality to the estuarine system as a whole. Using this methodology, the values for the frictional parameter were determined as well as the mean along-channel slope as a function of the freshwater discharge.

As would be expected for a shallow estuarine system, such as the Fly River delta, frictional effects play an important role in the resulting hydrodynamics of the system. Initial sensitivity analysis of the Manning roughness coefficient (n) confirmed this belief. It was observed that small values of the Manning coefficient ($n < 0.020$) produced a propogating tidal wave up the estuary with strong tidal currents; larger

values could not match the phase propagation required by the system, and generated an unrealistic standing wave due to trapped water level perturbations in the system. A Manning coefficient of n = 0.015 produced the correct phase propagation of the tidal wave. This small value of the Manning's coefficient implies a weakly frictional flow.

Figure 4 illustrates the propagation of the predicted tidal wave at equi-distant points, from Samari, along the Northern Channel up to Lewada, using n = 0.015. This figure also demonstrates the funnelling effect at the junction of the channels, downstream of Adulu, where the tidal amplitude is magnified as the tidal energy from each channel is combined. Also note that this amplitude reaches a maximum at about 3/4 length upstream of the delta; after which, frictional effects gradually erode this amplitude, as noted by the smaller tidal amplitude at Lewada.

For the purposes of verifying the model predictions, the current meter data at sites P and Q were used, as the measurements covered a spring-neap cycle. In this case the model was run with an elevation of the datum of the tide gauge at Lewada, necessary to produce the freshwater discharge that prevailed at that time. The

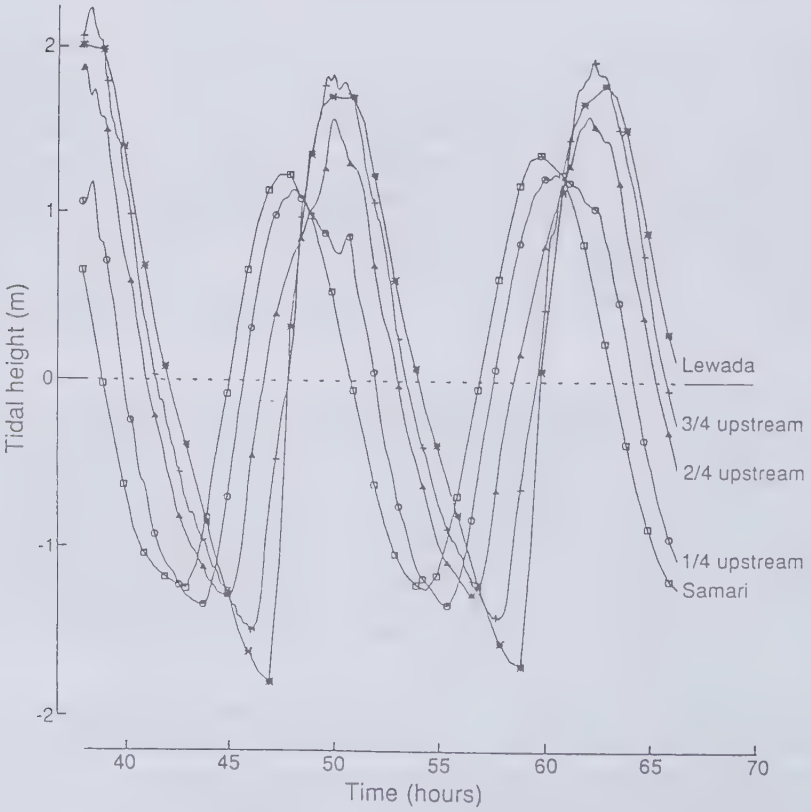

Figure 4. Time-series of predicted water elevations at five points within the estuary.

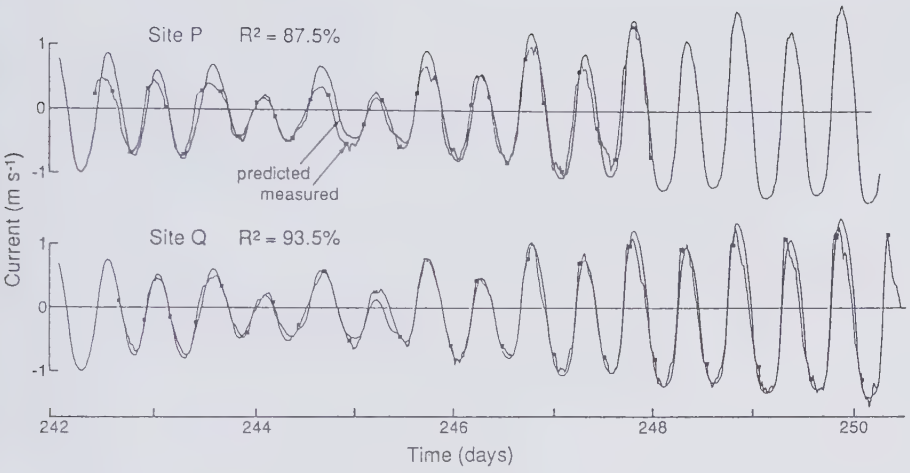

Figure 5. Comparison plots of the predicted and observed along-channel currents at sites P and Q.

discharge at this time was known to be approximately 4000 $m^3 s^{-1}$ (M. Eagle, pers. comm.) and the datum at Lewada was raised by 0.085 m in order to reproduce this discharge in the model. The resulting match between the predicted and observed currents for this value is shown in Figure 5 with a R^2 value of 87.5% for site P and 93.5% for site Q. Both these values for R^2 are significant and demonstrate the accuracy of the model predictions using n = 0.015.

Case Study 2: South Alligator River Estuary

The South Alligator River estuary (Figure 6), in tropical Australia, is tidal for about 93 km. It is funnel-shaped, macro-tidal and suspended solids concentration can exceed 10 gL^{-1}, especially in its upper reaches (Woodroffe *et al.*, 1986; Wolanski *et al.*, 1988). It is shallow (mean depth in the thalweg of only a few meters). The bathymetry has been surveyed and referred to a common datum. The tidal currents are strong, peaking at 2.5 m s^{-1} at spring flood tide, with a strong tidal asymmetry; the flood tidal currents being measurably larger than the ebb tidal currents. The waters are vertically well-mixed in temperature and salinity. The bed sediments are a mixture of sand, silt and mud. Rugged bedforms, including macro-dunes (wavelength of several meters, amplitude up to 0.5 m) exist throughout the estuary (Vertessy, 1990). Freshwater inflow is only significant in the wet season (the austral summer); in the (austral) winter, freshwater runoff becomes negligible (< a few $m^3 s^{-1}$) compared to the tidal discharge, and can even vanish. High evaporation and small freshwater discharge result in the formation of a salinity maximum zone (Wolanski, 1986).

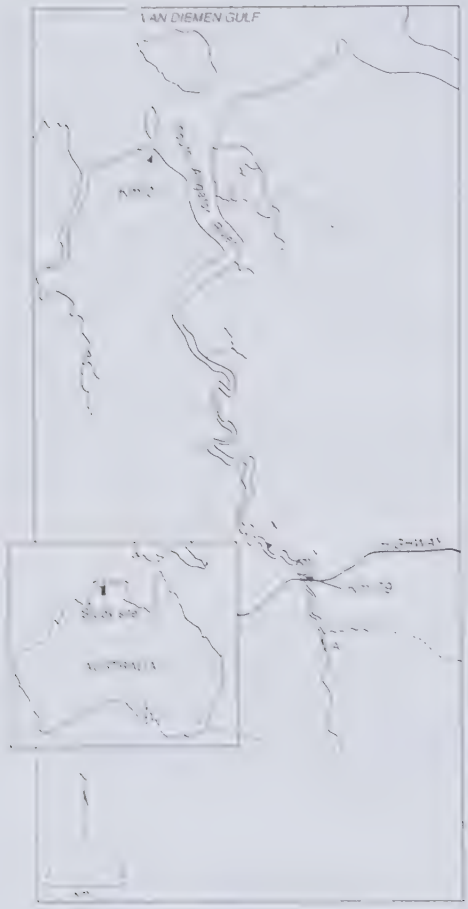

Figure 6. Location map of the South Alligator River Estuary.

Tidal data from four stations (at the river mouth, and at km 37.25, km 61.75 and km 79) were available for several days of spring tides in September 1985, at a time when freshwater runoff was negligible. The data are shown in Figure 7. Note that, while the sea level at the mouth is sinusoidal, the water level fluctuations at km 79 are quite asymmetric, with the ebb tide lasting longer than the flood tide. This explains the asymmetry of the tidal currents.

Because the estuary is fringed by only a minimal area of mangrove swamps, and since the flood plains are not inundated by the tides, the tidal dynamics can be modeled using a one-dimensional model. This model is fully implicit, centered, and solves, by finite-difference, the equations for unsteady flow in open channels (Harleman, 1971).

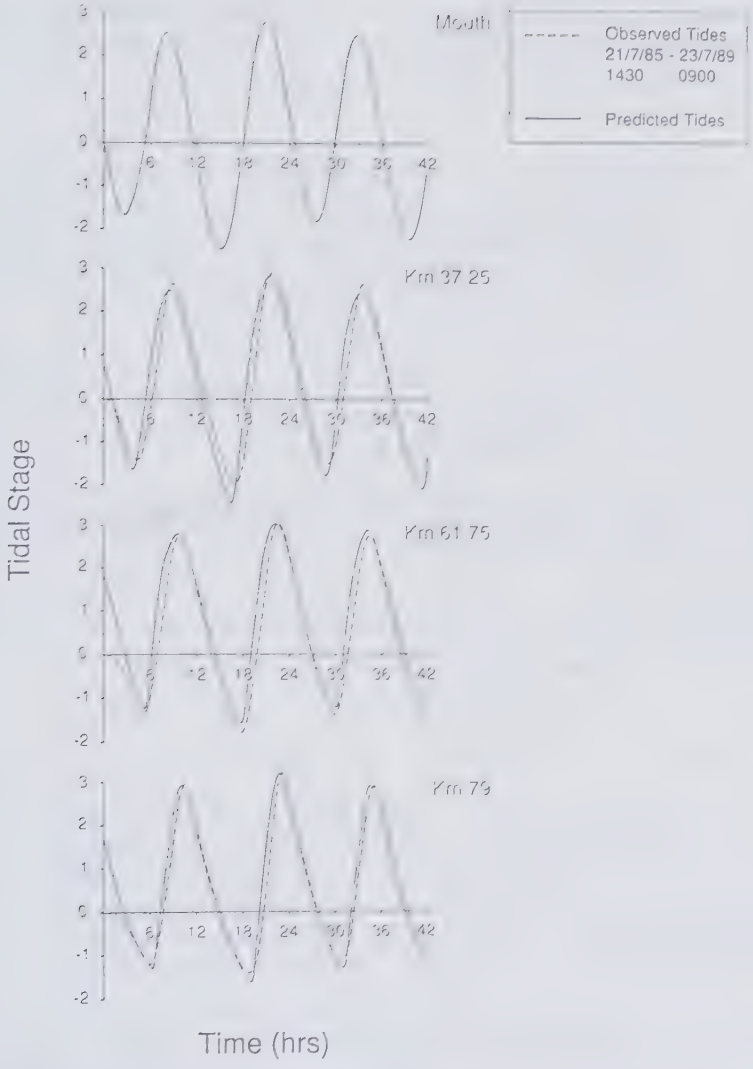

Figure 7. Observed and predicted tidal fluctuations at 4 stations along the South Alligator River estuary.

$$\partial A/\partial t + \partial Q/\partial x = 0$$

$$\partial Q/\partial t + \partial(Q^2/A)/\partial x + g\ A\ \partial(y+z)/\partial x + g\ A\ S_f = 0$$

where x is the distance along the river oriented down-stream, t the time, Q the discharge, y the depth, A the cross-sectional area of the stream, g the acceleration

due to gravity, z the elevation of the bottom of the stream cross-section, y the water depth, and S_f is the frictional slope (Henderson, 1966) where, in metric units

$$S_f = n^2 |Q| Q B^{4/3} / A^{10/3}$$

where n is the Manning roughness coefficient and B the wetted perimeter.

The estuary was discretised in 35 cross-sections. The open boundary conditions are the observed sea level fluctuations at the mouth and the zero discharge at the tidal limit (in the austral winter). The initial conditions are a horizontal fluid at rest; the model was allowed to warm up until the tidal fluctuations can be reproduced at successive tides; this took about 3 tidal cycles.

Figure 8 shows the time series plot of the tides at the mouth and the predicted water level at km 79 for two values of the Manning's coefficient (n). It can be seen that the tides at km 79 are very sensitive to the adopted value of n.

A series of model runs were then undertaken and the predictions were compared with observations. The fit between observations and predictions was very encouraging (Figure 7) for n between 0.018 and 0.020.

It was impossible to obtain a reasonable fit between observations and predictions for 'usual' values of n of between 0.033 and 0.040 (Henderson, 1966). Such values of n result in unrealistic tides at km 79 (Figure 8).

South Alligator River Cusps

One particular feature of the South Alligator River estuary is the presence of river cuspates in the mid-region of the estuary (see Figure 9). Independent field observations by Vertessy and Wolanski (unpubl. results) have revealed the presence of flow separation near these cuspates, with tidal eddies being generated in the lee of the cuspates; the tidal flow approach the cuspates along the inner meander at a velocity peaking at 2.0 m s^{-1} and separate from the inner meander at the cuspate.

The flow near such cuspates was modeled using the 2-D model HYDRO. The mesh size was 40 m. We found that definite eddies could only develop in the model if the Manning's friction parameter was about 0.018. Figure 9 shows such a prediction. For values of Manning's n of order 0.033, return flow was negligible, the waters being nearly stagnant in the lee of the cuspates.

Conclusions

One- and two-dimensional mathematical models were used to predict the tidal circulation in two very turbid estuaries, the Fly River estuary in Papua New Guinea and the South Alligator River estuary in tropical Australia. Both estuaries are very

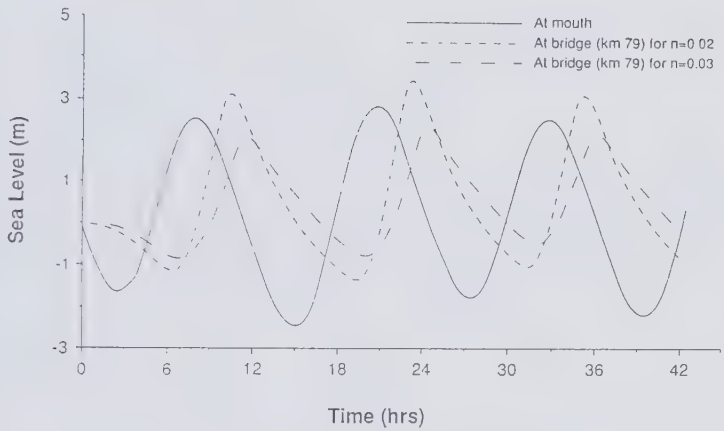

Figure 8. Time series plot of the sea level at the mouth, and predicted water level at km 79 for a value of the Manning's bottom friction coefficient of respectively 0.020 and 0.030.

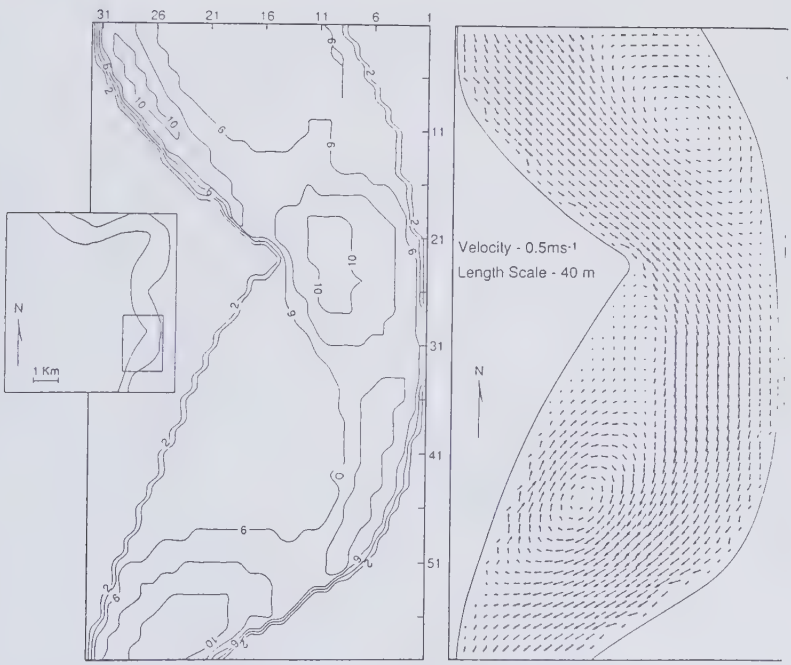

Figure 9. Synoptic distribution of the water currents around a cuspate, South Alligator River estuary. Mean depth of approximately 4 m.

turbid, with suspended solids concentrations often reading 10 gL^{-1} near the bottom. The model was verified against observations of both tides and currents (for the Fly River estuary) and of tides (for the South Alligator River estuary). In both cases the friction was represented using Manning's formula. The Manning's roughness coefficient, n, was found to be of order 0.015 in the Fly River estuary, and 0.018 - 0.020 in the South Alligator River, i.e. measurably smaller than 'usual' values (0.033 - 0.040) quoted for sandy rivers and estuaries (Henderson, 1966). In the case of the South Alligator River estuary, the model was also applied to study the circulation near river cuspates; field observations reveal the existence of strong recirculating eddies of the lee of river cuspates, and these were well reproduced when modeled for small values (n ~ 0.018) of the Manning's roughness coefficient.

These observations suggest that in these two very turbid, muddy estuaries the Manning's roughness coefficient n is of order 0.015 - 0.020, significantly smaller than its value (0.033 - 0.040) for less turbid estuaries of similar bedforms. Because the frictional stress in the momentum equation varies with the second power of n, the bottom stress in these two turbid estuaries is only about 20% of that in less turbid estuaries. Su Jilan and Rocky Geyer (pers. comm.) have also observed similar low values of the Manning friction coefficient in very turbid Chinese estuaries and the inner Amazon shelf and this may be due to the presence, in some areas, of fluid mud near the bottom, enabling the bulk of the flow to slip over the muddy layers, thus decreasing the bottom stress (Wolanski *et al.*, 1992b).

This reduction in the friction cannot be neglected in tidal dynamics; indeed it has a controlling effects on tidal propagation in these very turbid estuaries, as well as a significant local effect in generating circulating flows behind cuspates.

It is suggested that the reduction in the friction is brought upon by the interaction of the fluid with the suspended sediment. In very turbid estuaries the presence of fluid mud or very high suspended sediment concentration near the bed may enable a two-fluid system to exist, the bulk of the water essentially slipping over the near-bottom high-concentration layer; rheological effects may also contribute to a decreased friction, such as an alignment of clay particles, leading to the drag reduction in a suspension of clay; and the inhibition of turbulence in the bottom boundary layer (e.g. Adams *et al.*, 1990; Gust, 1976; Gust and Walger, 1976; McAnnally and Hayter, 1990; McCave and Jones, 1988; Mehta and Srinivas, 1993; Ross and Mehta, 1989; Wolanski *et al.*, 1988 and 1989). The determination of the relative importance of these effects would be a very difficult task in the field but may be possible in controlled laboratory experiments.

Acknowledgements. This study was supported by the Australian Institute of Marine Science, the Australian National University and Ok Tedi Mining Limited. Dr. R. Vertessy kindly provided the tidal data for the South Alligator River.

References

Adams, C.E., J.T. Wells and Y.A. Parke. Internal hydaulics of a sediment-stratified channel flow. *Mar. Geol.*, 95, 131-145, 1990.

Gust, G. Observation of the turbulent-drag reduction in a dilute suspension of clay in sea water. *J. Fluid Mech.*, 75, 29-47, 1976.

Gust, G. and E. Walger. The influence of suspended cohesive sediments on boundary-layer structure and erosive activity of turbulent seawater flow. *Mar. Geol.*, 22, 189-206, 1976.

Harleman, D.R.F. One-dimensional models, in *Estuarine Modeling, An Assessment*, Water Quality Office, U.S.E.P.A., 16070 DZV 02/71, Washington, D.C., 1971.

Henderson, F.M. Open Channel Flow. 96-101, Macmillan, New York, 1966.

McAnnally, W.H., Jr. and E.J. Hayter. Estuarine boundary layers and sediment transport, in *Residual Currents and Long-Term Transport*, edited by R.T. Cheng, Springer-Verlag, New York, 260-275, 1990.

McCave, I.N. and K.P.N. Jones. Deposition of ungraded muds from high-density non-turbulent turbidity currents. *Nature,* 333, 250-252, 1988.

Mehta, A.J. and R. Srinivas. Observations on the entrainment of fluid mud by shear flow, in *Estuarine Cohesive Sediment Transport*, edited by A. J. Mehta, American Geophysical Union, Washington D.C., 224-246, 1993.

OTML "Sixth supplemental agreement environmental study, 1986-1988". Final Draft Report, Vols I, II & III (unpublished), 1988.

Ross, M.A. and A.J. Mehta. On the mechanics of lutoclines and fluid mud. *J. Coastal Research,* 5, 51-61, 1989.

Salomons, W. and A.M. Eagle. Hydrology, sedimentology and the fate and distribution of copper in mine-related discharges in the Fly River system, Papua New Guinea. *The Science of the Total Environment,* 18, 291-314, 1990.

SMEC Ok Tedi project. Hydrodynamic survey of the Fly River. Snowy Mountains Engineering Corporation report, 1982.

Vertessy, R. Morphodynamics of macro-tidal rivers in northern Australia. PhD thesis, Department of Biogeography and geomorphology, Australian National University, 1990.

Wolanski, E. An evaporation-driven salinity maximum zone in Australian tropical estuaries. *Estuarine, Coastal and Shelf Science*, 22, 415-424, 1986.

Wolanski, E., J. Chappell, P. Ridd and R. Vertessy. Fluidization of mud in estuaries. *J Geophys. Res.*, 93, 2351-2361, 1988.

Wolanski, E., T. Asaeda and J. Imberger. Mixing across a lutocline. *Limnol. Oceanogr.,* 34, 931-938, 1989.

Wolanski, E. and B. King. Flushing of Bowden Reef lagoon, Great Barrier Reef. *Estuarine, Coastal and Shelf Science,* 31, 789-804, 1990.

Wolanski, E., M. Trenorden and B. King. Fly River Estuary and Gulf of Papua: oceanography and sediment dynamics. Data Report prepared for Ok Tedi Mining Ltd, November, 1990.

Wolanski, E. and M. Eagle. Oceanography and fine sediment transport, Fly River Estuary and Gulf of Papua. 10th Australasian Conference on Coastal and Ocean Engineering, Auckland, New Zealand, 453-457, 1991.

Wolanski, E., B. King, P. Ridd and M. Trenorden. A field and model study of the hydrodynamics of the Fly River estuary. Report to Ok Tedi Mining Ltd, 1992, 1992a.

Wolanski, E., P. Ridd, B. King and M. Trenorden. Fine sediment transport, Fly River Estuary, Papua New Guinea. Report to Ok Tedi Mining Ltd, January, 1992, 1992b.

Woodroffe, C.D., J. Chappell, B.G. Thom and E. Wallensky. Geomorphological dynamics and evolution of the South Alligator tidal river and plains, Northern territory. Mangrove Monogr. 3, 190 , NARU, Australian National University, Canberra, 1986.

20

Tidal Dynamics and Sediment Transport in a Shallow Macrotidal Estuary

G. Lessa

Abstract

The morphodynamics of shallow estuaries have been studied under two broad types of tidal conditions, named micro-mesotidal and macrotidal. Because micro-mesotidal shallow estuaries occur more often in nature, they have been more intensively studied and their dynamics are better understood. The few process studies performed on shallow estuaries in macrotidal environments have focused on the current patterns over different tidal cycles, establishing the dissimilarities between flow characteristics depending on whether or not the marshes are submerged. These studies have not presented detailed analysis of the tides nor made any attempt to correlate the morphodynamics of shallow macrotidal estuaries with their micro-mesotidal counterparts. The present study investigates the morpho-dynamics of a shallow macrotidal estuary on the Central Queensland Coast (Australia). The tides are extremely asymmetrical (M_4/M_2=0.21), with the rising tide shorter than the falling tide. However, the expected flood dominance in the current regime and sediment transport was attained only at small tides, when the mangrove banks were not submerged. Threshold values for tidal height and amount of water required to be stored in the mangroves to drive stronger ebb fluxes are determined. Calculations of the estuarine long term net sediment transport direction suggest that the estuary is slightly ebb dominant. This is the opposite of what might be predicted if the analysis were solely based upon the characteristics of the vertical tide. The differences observed between micro-mesotidal and this macrotidal shallow estuary appear to depend on the relatively higher levels of the macrotidal marsh banks. Here, marsh banks are overflowed only at times of higher tidal ranges and always at the later stages of the rising tide, thus having a negligible effect on the overall tidal wave shape.

Mixing in Estuaries and Coastal Seas
Coastal and Estuarine Studies Volume 50, Pages 338-360
Copyright 1996 by the American Geophysical Union

Introduction

Shallow estuaries may be defined as coastal indentations with restricted but permanent connection(s) to the ocean (inlet), receiving little fresh water input and presenting a well defined tidal drainage network unfolding over an infilled basin. The system generally lies behind a clastic barrier and displays an intertidal area often occupied by salt marsh communities. Common non-dimensional tidal wave height (tidal amplitude over mean channel depth at mean sea level) of shallow estuaries lies between 0.1 and 0.5. Following the classification proposed by Kjerfve (1989), they can be defined as coastal plain salt marsh estuaries. Examples of such systems in the literature are Price Inlet (Fitzgerald and Nummedal, 1983), North Inlet (Kjerfve and Proehl, 1979), Nauset Inlet (Aubrey and Speer, 1985) and Murrells Inlet (Aubrey and Friedrichs, 1988) amongst others in U.S., and Brencaster Marshes (French and Stoddart, 1992) and Overy Marsh (French *et al.,* 1990) in U.K.

The morphodynamics of these shallow estuaries have been studied in two broad tidal environments, namely micro-mesotidal coasts and macrotidal coasts under the classification proposed by Davies (1980). Shallow estuaries under micro and mesotidal conditions are subjected to a small tide range relative to mean channel depth, while under macrotidal conditions the tidal fluctuation becomes comparable to the average channel depth. Hitherto no comparison between the morphodynamics of estuaries in these two tidal environments have been made. This may be partly credited to the idea that estuaries associated with barriers and inlets do not exist in macrotidal coasts (Davis and Hayes, 1984; Hayes, 1991). Therefore, a large amount of research and a better process understanding exists for micro and mesotidal shallow estuaries.

The aim of this paper is to present preliminary outcomes of a study undertaken in a shallow macrotidal estuary on the Central Queensland coast (Australia), and to compare the results with those reported either on micro-mesotidal and macrotidal shallow estuaries. In the following chapter a brief review of the process studies undertaken in these estuaries will provide the basis for discussion.

Process Studies

The propagation of the ocean tide over frictionless shallow coastal systems, where the wave amplitude is comparable with the total water depth, may be treated as the movement of a long wave with celerity $c = [g (d + 1.5 \eta)]^{0.5}$, where g is gravity, d is the water depth and η wave amplitude (Pugh, 1987 p. 239). This suggests that the wave speed decreases as the water depth decreases, which causes the crest of the wave to move closer to the trough ahead. This results in a distorted wave shape with a steep face and a gentle backslope, i.e., a shorter rising and a longer falling tide. A more realistic description of this transformation, however, accounts for the effects of bottom friction and the non-linearities arising from it. Spectral analysis of the

shoaling tide shows an increasing transfer of energy (height) from lower tidal harmonics (generally above 12 hours) to their sub-harmonics (1/2, 1/4, ... of the original period) and compound tides (Aubrey and Speer, 1985). Thus the tidal distortion will be controlled by the phase and amplitude of the higher harmonics relative to basic wave phase.

For semi-diurnal tides the analysis is commonly based upon the lunar M_2 tidal component and its first sub-harmonic M_4. When the phase difference ($2M_2$-M_4) falls between 0° and 180° the asymmetry is characterized by a shorter rising and a longer falling tide, while phase differences between 180° and 360° cause the tide to fall fast and to rise slowly. A more comprehensive description can be found elsewhere (Boon and Byrne, 1981; Speer and Aubrey, 1985; Pugh, 1987). It has been shown that for micro-mesotidal shallow estuaries the phase difference between M_2 and M_4 varies depending on the geometry of the system through which the tide propagates (Boon and Byrne, 1981; Fitzgerald and Nummedal, 1983; Aubrey, 1986; Aubrey and Speer, 1985; Dronkers, 1986; DiLorenzo, 1988; Aubrey and Friedrichs, 1988; Friedrichs and Aubrey, 1988). Basically, if the amount of water contained in the channel at mean sea level (MSL) is large compared to the amount of water which can be stored on the tidal flats, the phase angle difference ($2M_2$-M_4) will move closer to 270°. On the other hand, a larger storage capacity on the flats shifts the phase angle difference towards 90°. Fitzgerald and Nummedal (1983) employed the principle of continuity to explain how the topography of the estuary affects the tidal wave shape. They formulate the continuity equation assuming a constant velocity (V) and the throat cross-sectional area (A_c) varying linearly with the tides, such that

$$A_b \, (dh_b/dt) = A_c \, V \qquad [1]$$

where A_b is the water surface area in the estuary and dh_b/dt is the rate of the change in water level in the estuary. The rate of change of water volume in the estuary (left hand term) equals the discharge through the inlet (right hand term). Rearranging the equation it follows that the dh_b/dt is directly proportional to A_c/A_b. For estuaries with large marsh areas the ratio A_c/A_b will increase during ebbing tide because of the water drainage from the estuary, augmenting the speed of the falling tides. For estuaries with smaller marsh areas the ratio dh_b/dt will be more affected by the area of A_c only, implying faster flooding tide.

The difference in the rate of the rising and lowering of the water level in an asymmetric tide has severe implications on the magnitude of the flooding and ebbing fluxes. The higher the rate of rising (falling) the faster the flood (ebb) flow. Since the bed-load transport q is a function of the velocity u to the third power ($q \sim u^3$), any small difference between the average flood-ebb flow magnitude will cause a trend in the near bed sediment transport. Thus, systems in which $2M_2$-M_4 is around 90° will be classified as flood dominant, for the net sediment transport is in the flood direction, and systems with $2M_2$-M_4 around 270° will be ebb dominant. Actually, although the greatest tidal asymmetry in flood-dominant estuaries occurs at 90°, Friedrichs and Aubrey (1988) have shown that a more accentuated absolute distortion is observed as $2M_2$-M_4 moves closer to 0°.

A relation between estuarine geometry and tidal asymmetry and sediment transport ratio (flood/ebb) has been proposed by Aubrey (1986), Friedrichs and Aubrey (1988) and Fry and Aubrey (1990). The degree to which near-bottom sediment transport is dominated by flood or ebb fluxes can be accessed using mean channel depth (h), ocean M_2 amplitude (a), storage volume in tidal flats-marshes (Vs) and channel at mean sea level (Vc). An increase in the storage volume over the flats (Vs/Vc > 1) tends to enhance ebb dominance and an increase in the tidal amplitude in relation to channel depth (a/h > 1) tend to enhance flood dominance. Nevertheless, Friedrichs and Aubrey (1988) suggest that when a/h ratio is larger than about 0.35 the effects of friction on the flow always overcome the storage characteristics of the tidal flats, and a flood dominance will evolve.

Process studies on shallow macrotidal estuaries have been limited to the Norfolk coast (U.K.), where a series of salt marsh systems develop on a back-barrier environment (Bayliss-Smith *et al.*, 1978; Pethick, 1980; French *et al.*, 1990; French and Stoddart, 1992). In general these studies have investigated the flow regime of the estuaries over different tidal cycles, pointing out an ebb dominance on sediment transport for over-marsh tides, i.e., tides which overtop the marshland. During small tides, when the water is confined to the channels, a stronger flood flow takes place. Tidal distortion in these estuaries assumes the shape of a flood dominant tidal wave, with ratio of flood/ebb duration varying from 0.65 to 0.9 at neaps and springs respectively (French and Stoddart, 1992). Bayliss-Smith *et al.* (1978) have reported ebb flow duration 4-6 times longer than the flood duration. Unfortunately no detailed analysis of the tides have been provided and the most representative studies were restricted to upstream parts of the main estuarine channel (French and Stoddart, 1992). So far there has been no attempt to correlate the dynamics of these shallow macrotidal estuaries with their micro-mesotidal counterparts.

Study Site and Methods

The present study was carried out at Louisa Creek, a 6.6 km long tidal estuary near Mackay (Queensland, Australia) (Figure 1). The estuary is represented by a single meandering channel inside an infilled basin colonized by mangroves, limited on the mainland side by small rocky hills and on the ocean side by a single sandy barrier 1.8 km long and 250 m wide (Figure 2). The channel displays three distinct zones: a) a very well defined mouth nearly 100 m wide and 3 m deep at mean sea level (MSL), with a coarse shelly-sand bottom; b) a wide section in the mid estuary, where a shallow (about 2 m deep at MSL) and irregular thalweg path is influenced by fine-medium sand shoals, and c) an upstream meandering section, representing half of the estuary length, with a narrower and well defined channel 2.3 m deep at MSL presenting a featureless bed composed of a coarse sand mixture. Although the channel becomes very shallow (0.2 m deep) at spring lows in some points in the second section, it is never completely dry. The only fresh water source for the creek is the sporadic run-off from its 33 km^2 catchment area, with monthly maximum

values of 5 $m^3 s^{-1}$. This represents about 1% of the smallest measured discharge through the mouth.

The tides in the area are semi-diurnal with a slight diurnal inequality, significant only at high waters. M_2 and S_2 (principal lunar and solar) components represent 33.9% and 12.6% of the tidal range, and due to the relatively large range of the S_2 component there is a significant difference between neap and spring tides as well as between new and full moon spring tides. Mean tidal range over the lunar month ranges from 2.3 m at neaps to 5 m at springs (Australian Tide Tables, 1992), and new moon spring tides can be as high as 1.1 m above full moon springs. The height of the mangrove banks varies from 0 to 1.7 m above the Australian Height Datum (AHD), the values increasing in the upstream direction. The mangroves were inundated about 540 times in 1992, or 76% of the total number of tidal cycles (Australian Tide Tables 1992). Highest astronomical tides reach 3.8 m above the (AHD). Off-shore significant wave height and period is 0.6 m and 5 s, reaching heights of 2 m and periods of 10 s during storms (BPA, 1979). Storm surges are common in this cyclone prone area, the highest registered so far reaching 3.65 m in 1918 (Gourlay and Hacker, 1986).

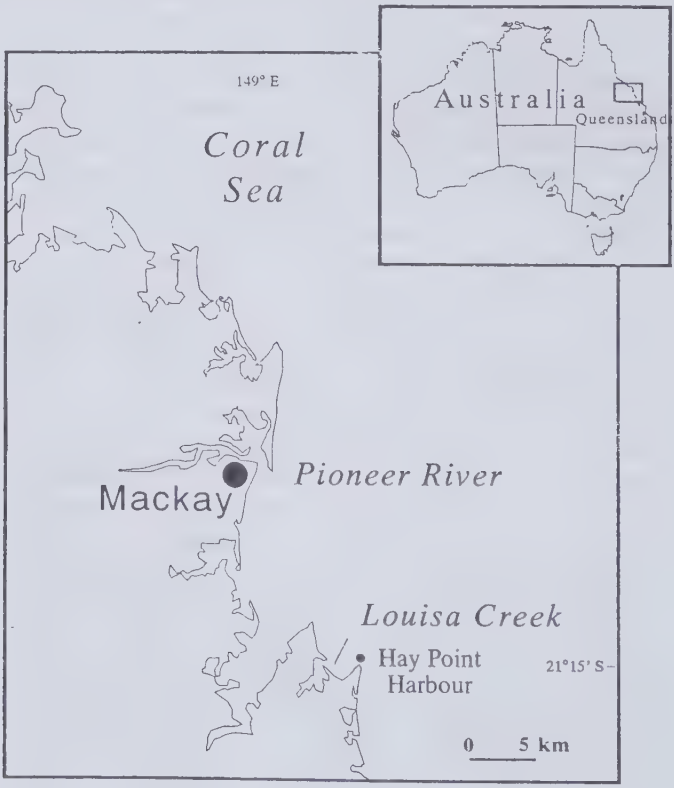

Figure 1. Location map for Mackay region and Louisa Creek. Also indicated is the location of the ocean tide gauge station in the area.

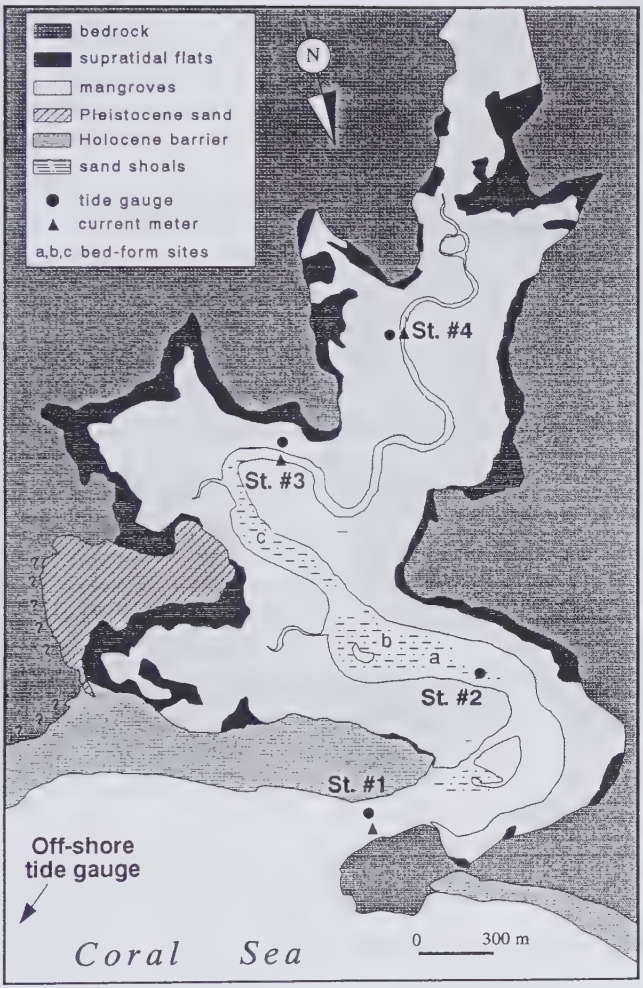

Figure 2. Tidal, current meter and bed-form monitoring sites in Louisa creek.

Field measurements of tides, current and bed form migration were obtained during a 33 day campaign carried out in February and March 1992. Water level at stations #1, #2, #3 and #4 (Figure 2) were continuously recorded with Bristol tide gauges, and values for every 30 minutes were read from the tidal chart after correction was made for any time deviation. Ocean tides were recorded 2 km east of the field site (Hay Point Harbour) by the Queensland Department of Transport. Current speeds at stations #1, #3 and #4 were recorded every 10 minutes with Aanderaa current meters, deployed at 0.5 m above the bed. Current profiles were obtained in different

positions of the estuary, mainly near the shoals during spring and neap tides, using hand held current meters deployed from a boat. Daily bed-form migration rates were surveyed over a length of 15 meters at locations a, b and c (Figure 2) using stake lines as reference points. The surveying of location 'a' started in a later date, and its data set is the shortest.

Depth averaged velocities for #1, #3 and #4 were calculated by applying a modified universal velocity defect law equation proposed by Black and Healy (1986)

$$U = 5.75\ u_* \log(0.87d/z_o) \qquad [2]$$

where U is the mean flow speed of a vertical profile, u_* is the shear velocity, d is the water depth and z_o is the roughness length. The shear velocity was accessed applying the logarithmic Karman-Prandtl equation for rough turbulent flow (Dyer, 1986)

$$u/u_* = 2.5 \log z/D + 8.5 \qquad [3]$$

where u is the current speed at a height z (0.5 m in this study) and D is the mean sediment diameter. At #3 and #4 z_o was considered as the mean grain size, while at #1 it was regarded as bed-form roughness,

$$z_o = 2H\ (H/\Lambda)^{1/4} \qquad [4]$$

(Wooding *et al.*, 1973) where Λ is bed-form length and H is bed form height measured from echo-sounding profiles. Discharge computations were based on the product of the cross sectional area, as a function of tidal height, and mean cross-section flow speed U' . U' was calculated by dividing the depth average velocity U by 1.16, which is a factor estimated by Knight (1981) to account for the decrease of U at positions away from the thalweg.

Near bottom sediment transport at #1, #3 and #4 was determined using the bed-load transport formula of Meyer-Peter and Müller (1948)

$$q = 8\ [D\ U\ (\rho_s - \rho/\rho)\ \rho g D]\ (\Psi - \Psi_c)^{3/2} \qquad [5]$$

where q is the rate of transport per unit width, Ψ is the Shield's parameter, Ψ_c is the critical Shield's parameter for sediment entrainment, ρ is the density of water and ρ_s is the density of sediment. Due to battery problems with two of the current meters (#3 and #4), only the analysis for the first two weeks (covering new moon spring to neap cycle) of currents are presented. The volumetric sediment transport due to bed-form migration was calculated as the half of the product of bed-form celerity, bed-form height and sediment porosity (Zarillo, 1985; van de Berg, 1986) assuming a two-dimensional bed-form of triangular cross-section, and expressed by the formula

$$S_b = \rho_s\ (1\text{-}p)\ C\ H \qquad [6]$$

where S_b is the bed-load transport per unit width ($ML^{-1}\ T^{-1}$), ρs is the sediment density, p is the sediment porosity (0.4 for sand), C is the bed-form celerity and H is the bed-form height.

Results and Analysis

Tides

The tide in Louisa creek exhibits an asymmetry characterized by a faster rise and a slower fall of the water level. This distortion becomes stronger as the tidal wave propagates along the channel. The rising of the tide at #1 lasts an average of 4.9 hours, while the falling tide takes an average of 7.5 hours. At #3 and #4 the tide takes about 3.87 hours to rise and 8.6 hours to fall. The flood/ebb duration ratio is not constant and is smaller at springs, indicating a direct relationship between tidal asymmetry and tidal range (Figure 3).

Tidal attenuation along the estuary is also evident, and more accentuated during spring than during neap tides. Figure 4 shows the average tidal attenuation at each station for three springs and 2 neaps, indicating a clear trend of increasing tidal attenuation with tidal range. Damping is more pronounced at #3, where the average tidal range was 60% of that in the ocean during the two new moon springs. Tidal data from #4 will be excluded from the tidal analysis due to a possible tide gauge malfunction. Tidal ranges measured at #4 are larger than those at #3, which is unusual regarding the progressive reduction in the cross sectional area upstream. The likelihood of such a phenomena be caused by a standing wave is minimal, for it would have to be related to the 100th harmonic of the tide with an amplitude of 0.1m.

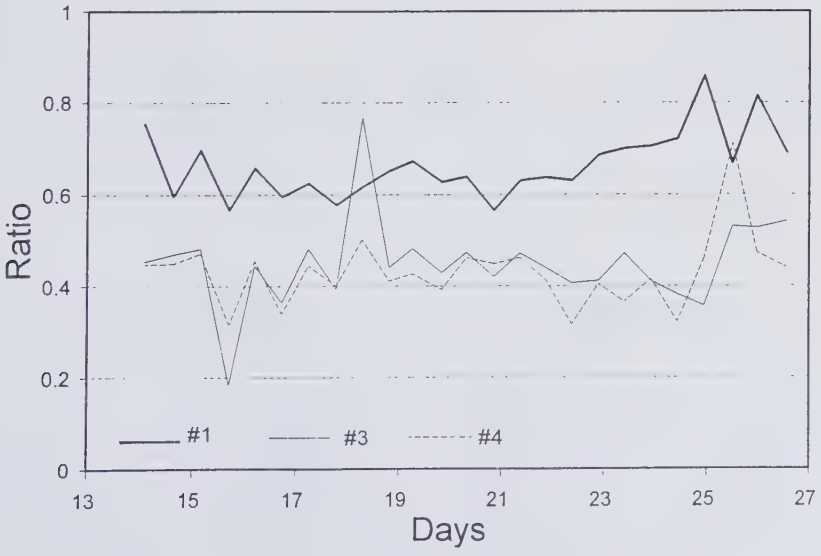

Figure 3. Ratio rising/falling time of the tides for stations #1, #3 and #4.

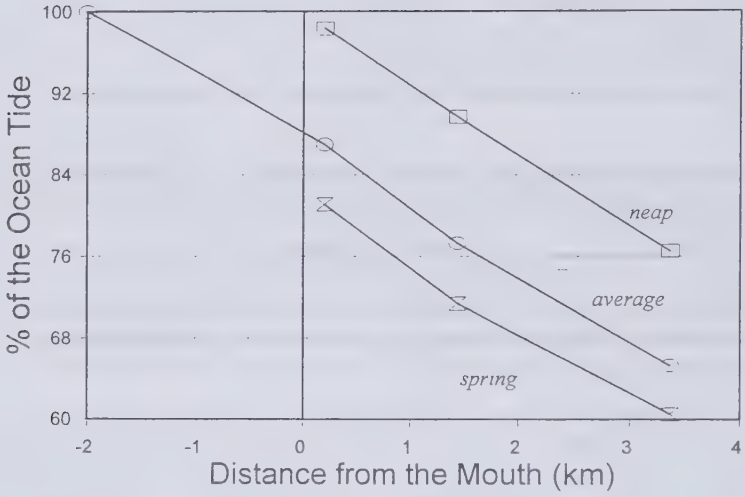

Figure 4. Attenuation of the ocean tide inside the estuary during neaps, springs and a month average. Negative distance is seaward of the mouth.

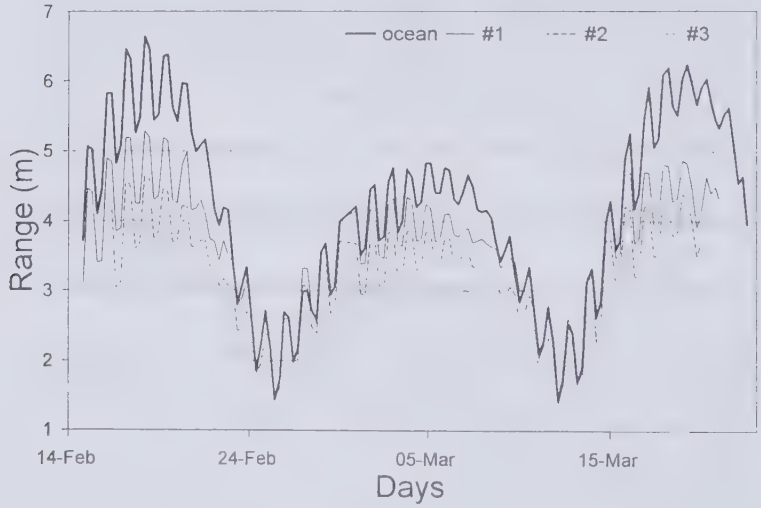

Figure 5. Tidal range variation within a lunar cycle.

Significant tidal range variations between spring and neap tides were recorded, with maximum spring range of 6.7 m and minimum neap range of 1.5 m (Figure 5). Differences in the maximum ranges between full and new moon spring tides, as large as 2 m, and the variation of the tidal attenuation between springs and neaps can also be noticed.

Harmonic analysis of a 3 year data set for the ocean station (performed by The Flinders University) and a month long data set for #1, #2, #3 shows the boost in tidal distortion along the estuary with the amplification of the relative energy of higher and compound harmonics (Figure 6). Aubrey and Speer (1985) found that as the tide moves upstream there is a decay of diurnal and semi-diurnal (O_1, K_1, M_2, S_2, N_2) constituents and a growth of compound (Msf, MK_3, MN_4, MS_4, $2MK_5$) and overtide (M_4, M_6, M_8) components. The ratio M_4/M_2 augments ten fold inside the estuary, from 0.02 in the ocean to 0.2 at #3, while the ratio M_6/M_2 is enhanced from 0.017 to 0.06 (Figure 7). It must be kept in mind that the time span involved in the harmonic analyses for the ocean station and the others inside the estuary does not coincide, and so the relation between the degree of the tidal asymmetry in the ocean and in the estuary may vary. As Boon (1988) pointed out, the intensity of the tidal asymmetry in a particular place varies periodically, and may differ by a factor of 4 over a month.

The phase relationship between M_2 and M_4, described by $2M_2$-M_4, shifts from 100° in the ocean down to 40° in the mouth and reaches 0° just past #3 (Figure 8). This can be explained by the fact that the ease of water exchange near low water between

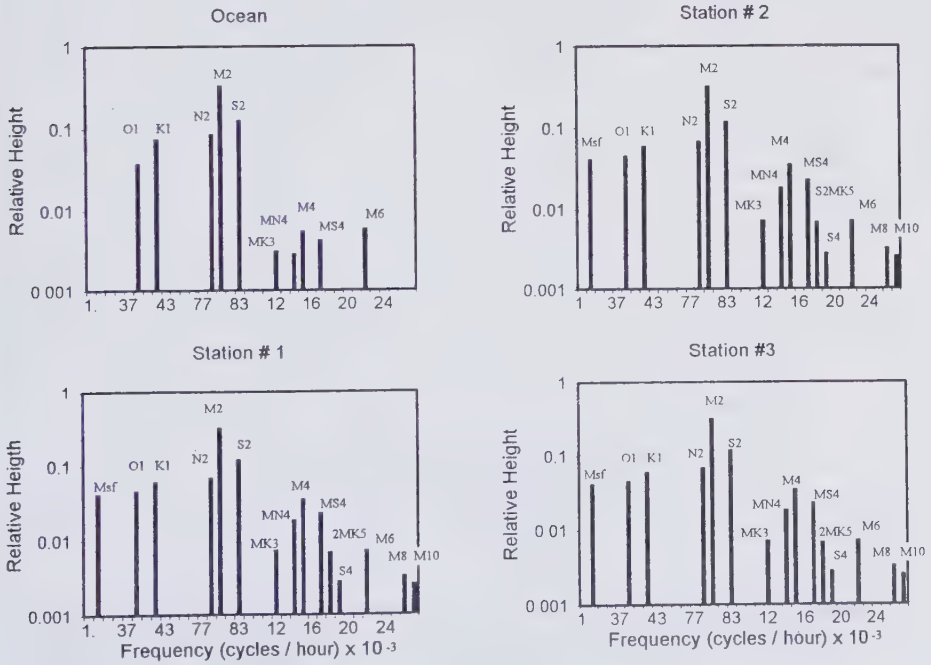

Figure 6. Peridogram for selected tidal components. The height is relative to the total tidal height at that station.

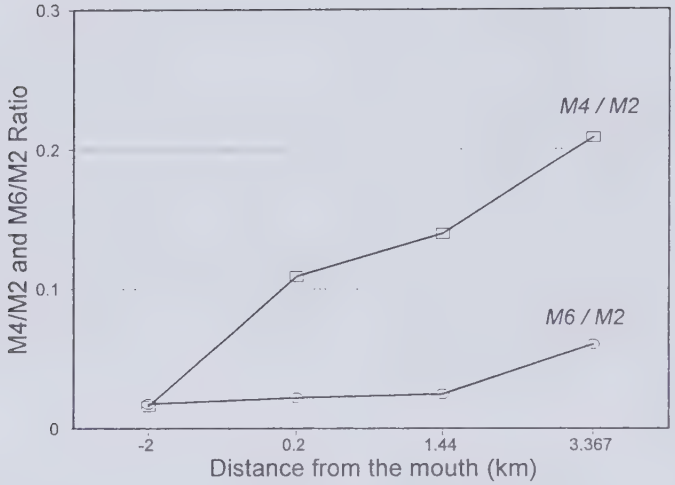

Figure 7. Variation of the degree of the tidal distortion (M_4/M_2 and M_6/M_2) inside the estuary.

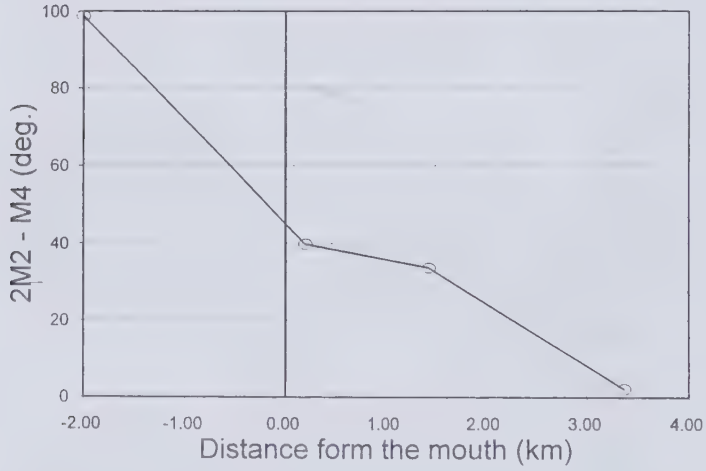

Figure 8. Phase difference between M_2 and M_4 ($2M_2$-M_4) tidal components inside the estuary.

the channel and the ocean, is gradually reduced upstream by the shoals, forcing a quasi stationary sea level at low water. This progressively shifts the M_2 and M_4 phase close to 0°, and produces a situation close to double low water, even though the water level rises faster as the tide propagates upstream. The result is that while high tide at #3 lags the ocean high tide by less than 1 hour, the low tide lags by 3 hours.

Currents

The direct result of the above asymmetry is a shorter flood and a longer ebb tide. Figures 9a and 9b shows the current at #1, #3 and #4 (0.5 m above the bed) during one tidal cycle at spring and neap tides. The currents are strongly reduced along the first and second sections of the estuary, between #1 and #3, but maintain the same magnitude upstream from #3. Current damping seems to be more effective at neaps, when maximum currents decay by a factor of 2 or 3, than at springs, when they decay by a factor 0.5. Faster ebb currents are attained about the same time along the channel at neap and springs. Faster flooding currents at the inward stations have a small but varying lag behind the mouth, never more than 1 hour. Both flood and ebb maximum

(a)

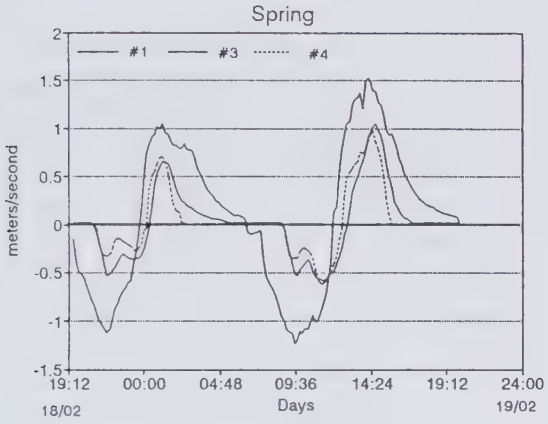

(b)

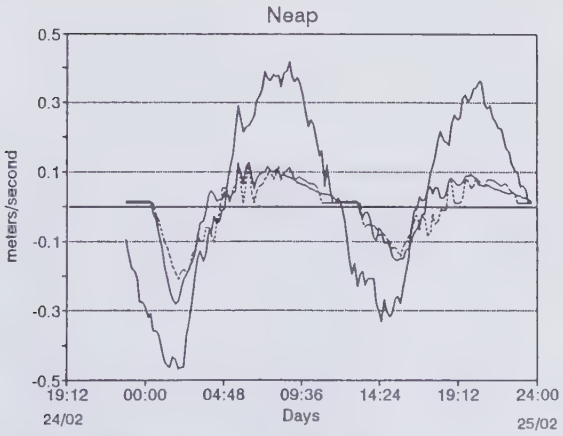

Figure 9. Near-bed current pattern at stations #1, #3 and #4 at spring (a) and neap (b) tides. Note the two maxima attained by the flooding tide at #3 and #4 during spring.

currents move closer to high tide during spring tides. At this stage the flood currents attain two maxima (Figures 9a and 10b), before and after mangrove bank inundation.

The current acceleration observed after mangrove inundation is explained by a sudden expansion of the tidal prism. Cross sectional areas in the upstream reaches are still confined to the channel area by the dense vegetation alongside the banks, and the increase in discharge results in larger flow velocities. This event does not occur near neaps for the tides do not reach enough height to overflow the mangrove flats. This same pattern has been reported by Bayliss-Smith *et al.* (1978) and French and Stoddart (1992) on macrotidal creeks, and is displayed in the velocity plots of Boon (1975), Myrick and Leopold (1963) and Zarillo (1985) on microtidal estuaries, although more subtle and in the earlier stages of the rising tide.

(a)

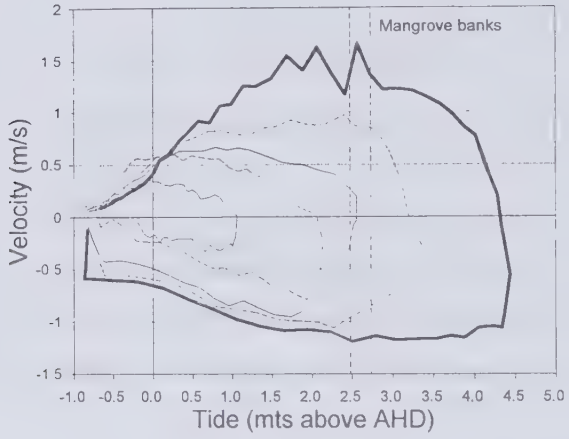

(b)

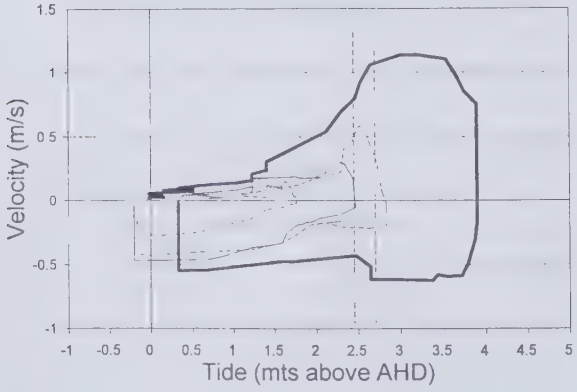

Figure 10. Near-bed velocity-stage curves during a tidal cycle at different tidal ranges at stations #1 (a) and #3 (b).

A plot of the discharge versus tides shows a pattern similar to a partially standing wave, with the discharge curve leading the tide by about 90° (Figure 11a,b). A standing mode appears to be better defined at neap tides, when high current speeds close to high water at springs are absent. Cross-spectral analysis performed on current and tidal data of #1, #3 and #4 supports the above evidence, revealing phase angles for the semi-diurnal frequencies of 100° for #1 and 75° for #3 and #4, varying slightly between neaps and springs. Nevertheless, it shows that the phase angle shifts closer to 90° at springs.

The expected flood dominance in the tidal currents, resulting from the above asymmetry in the vertical tide, occurred only during neaps. Table I shows maximum flood and ebb velocities, measured at 0.5 m above the bottom, for spring and neap tides at #1, #3 and #4. Ebb velocities greatly exceed flood velocities during spring tides, and are associated with the inundation of mangrove flats and high discharge at the beginning of the falling tide (Figure 10a, b), as also reported by French and Stoddart (1992). The ocean tidal height threshold necessary to trigger off a faster ebb appears to vary along the estuary, lying close to 3.0 m AHD for #1 and around 2.5 m AHD for inland stations (Figures 12a, b). The lower upstream threshold may be related to proximity of those stations to the mangrove flats, as opposed to #1 which is approximately 1000 m from a major mangrove area. It is observed at #1 that tidal cycles with low high water level are also subject to stronger ebb fluxes.

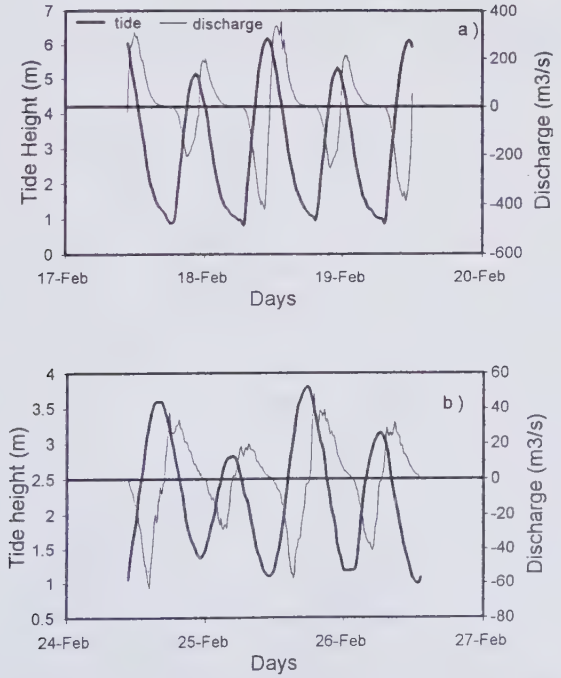

Figure 11. Discharge and tidal fluctuation at station #1 at neap (a) and spring (b) tides.

TABLE 1. Maximum flood and ebb velocities (in m s^{-1}) for spring and neap tides at Stations #1, #3 and #4 (see figure 2 for locations).

		# 1	# 3	# 4
Spring	Flood	- 1.2	- 0.66	- 0.94
	Ebb	1.61	1.13	1.01
Neap	Flood	- 0.47	-0.46	- 0.25
	Ebb	0.42	0.38	0.14

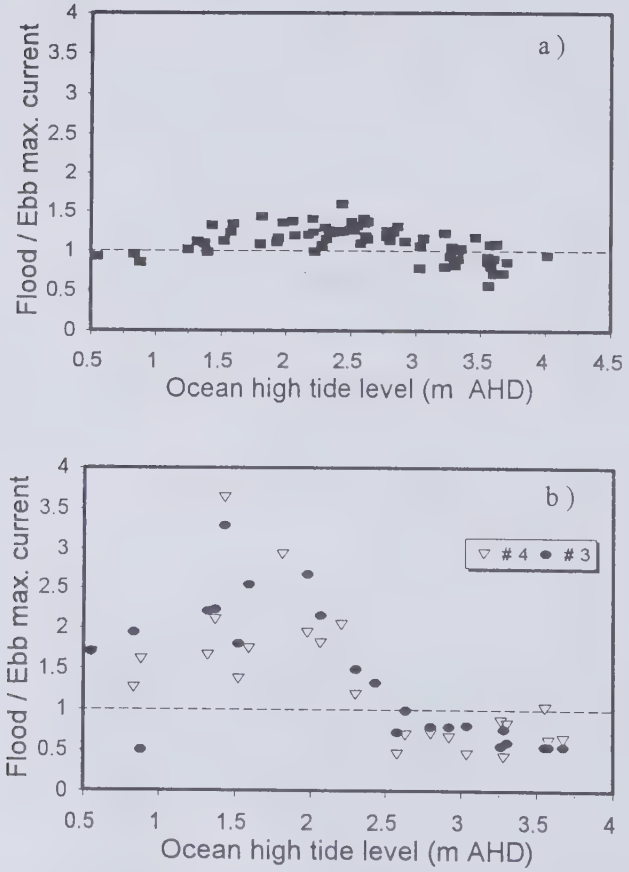

Figure 12. Ratio of maximum flood/ebb currents at stations # 1(a) and #3 and and #4(b) versus ocean high tide level.

This can be explained by the shallow shoals increasing bottom friction, weakening the flow and making the shallows to function as an area for water storage. Although the tidal asymmetry does not invert at these occasions, the ratio flood/ebb duration decreases from as high as 1.85 down to 1.15. The stronger flood dominance at the upstream stations, perceived through higher flood/ebb ratios, agrees with the shift of the M_2-M_4 ($2M_2$-M_4) phase angle close to 0° (Figure 8). As observed by Friedrichs and Aubrey (1988), $2M_2$-M_4 relative phase moves away from 180° in stronger flood dominant estuaries.

The higher ebb velocities for above mangrove tides may be credited to the larger water exchange efficiency at high water. Measurements of water surface slopes on similar macrotidal estuaries have reported that at springs higher water surface slopes occur during ebbing tide and that larger resistance coefficients come about during flooding tides (French and Stoddart, 1992).

Sediment Transport

The sediment transport pattern follows, as expected, the current pattern. Figure 13 shows the total sediment transport for each tidal cycle at stations #1, #3 and #4, where mean grain diameter and sorting values are 0.73 and 0.65 mm, 0.59 and 0.83 mm and 0.98 and 1.2 mm respectively. Due to the marked differences between spring and neap tidal ranges, and corresponding flow velocities, the volume of transported solids is considerably larger during springs, when ebb overcomes the flood. During neaps, when ocean tidal range drops below 4 m, for #3 and #4, or below 3 m, for #1, sediment transport is insignificant. Ratios of flood/ebb transport over a tidal cycle is constantly below 1 for the upstream stations, and conforms with the lag nature of the bottom sediments of that reach of the channel. At #1 the ratio tends to vary around 1 between spring and neap, indicating an alternating fortnightly cycle in sediment transport direction.

Bed form average length and height were 4.2m and 0.22m for location 'a', 5.2m and 0.25m for location 'b' and 4.5m and 0.34m for location 'c' (Figure 2). Bed-form migration rates indicate a net flood transport at neaps and a net ebb transport at springs. Flood currents at neap tides are more energetic than the ebb currents, but impact only the lower levels of the shoals. At the time the higher levels become submerged, the flow is no longer strong enough to entrain sediments. During spring tides both current directions act upon the entire shallows, but ebb currents are more vigorous, and develop when the water level is still very high. Current measurements on the shoals registered maximum average velocities of 1.2 m s^{-1} (ebb) at springs and 0.5 m at neaps (flood). Figure 14 shows clear cycles of net sediment transport direction on three sections on the shoals (Figure 2), where location a) is at -0.4 m and locations b) and c) are about 0.4 m above AHD. Arrows in Figure 14 indicate the occasions when bed-forms moved more than one wave-length, and as these episodes happened during spring conditions it is assumed that the net direction was seaward.

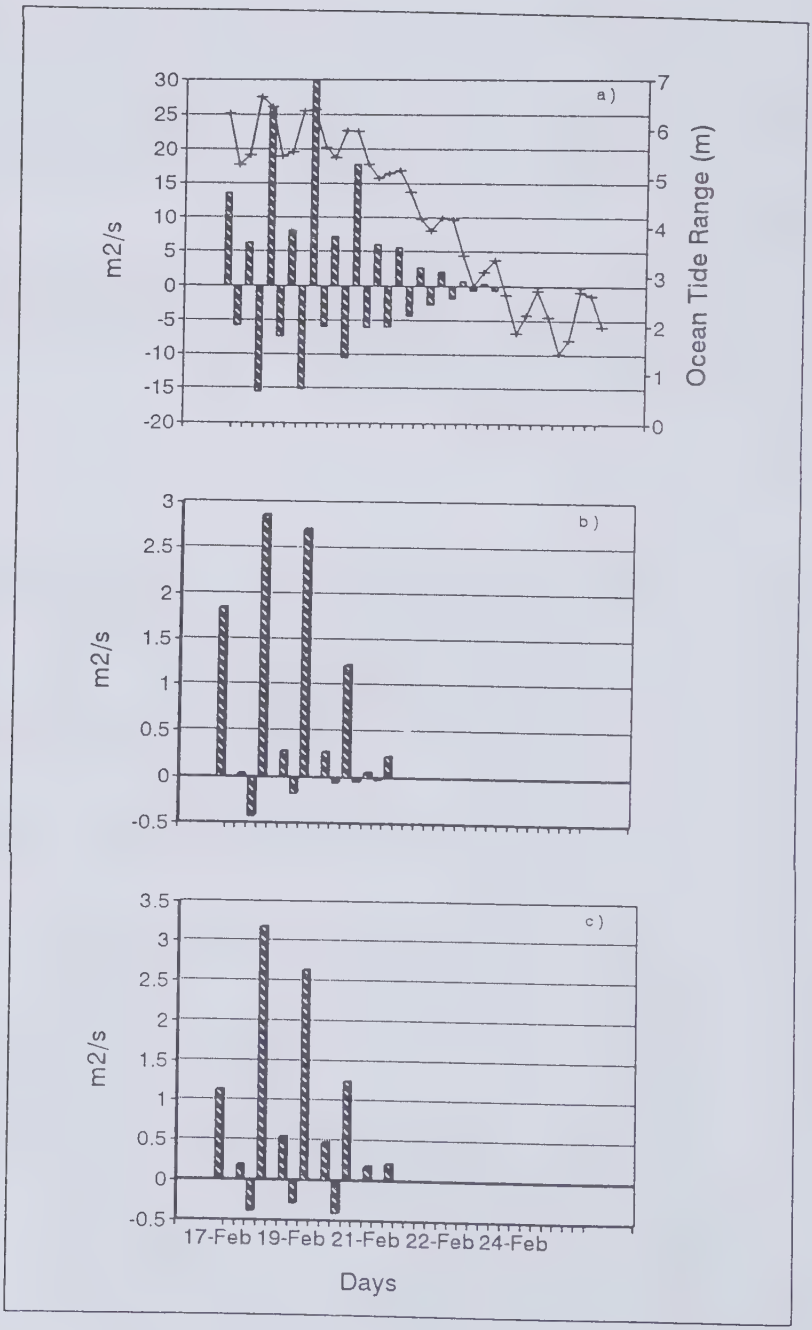

Figure 13. Variation of the total flood and ebb sediment transport for each tidal cycle at stations #1 (a), #3 (b) and #4 (c). Ocean tidal range during this period is shown in 'a'.

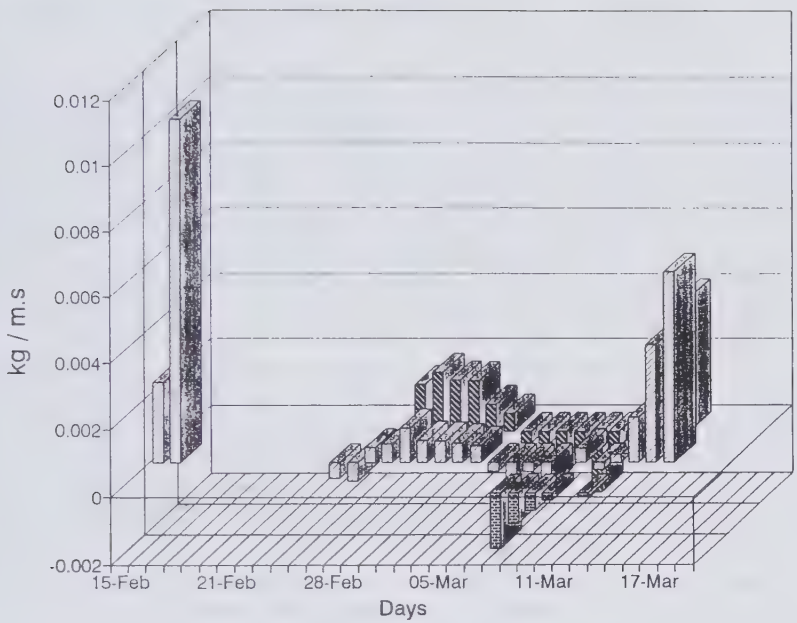

Figure 14. Net sediment transport on the shoals following bed form monitoring.

Estuarine Geometry

As mentioned above the parameters being utilized to predict estuarine morphodynamics are the M_2 amplitude (a), channel depth (h), volume on the mangrove area (Vs) and channel volume at mean sea level (Vc). Table 2 shows the variations of these parameters inside Louisa Creek. Channel and mangrove volumes were assessed through tidal prism calculations at #1. For above mangrove bank tides, it was assumed that the water did not flow within the mangroves, and the flow was confined in the channel. Mangrove storage volume calculation was based on the tidal prism of the highest spring tide, the area of the channel and the water depth above mangrove banks, while the estimation of the channel volume relied upon the average of the tidal prisms related to tidal cycles of 1 m high water level (AHD), the average height of the mangrove banks.

TABLE 2. Louisa Creek Dimensions

M_2 amplitude (a) (m)	Channel depth (h) (m)	Mangrove storage volume (Vs) (m^3)	Channel storage volume (Vc) (m^3)	Ratio Vs/Vc	Ratio a/h
1.56	2.0	1.44×10^6	4.9×10^5	2.75	0.78

The ratio a/h, also called the non-dimensional wave height, is 0.78 and the ratio Vs/Vc is 2.75, both well above average values of 0.31 and 0.7 found in field experiments in the U.S. (Friedrichs and Aubrey, 1988). Speer and Aubrey (1985) have shown that large a/h induces large time varying geometry and increases the friction, leading to an $2M_2$-M_4 phase angles difference of 90° or less, or a longer ebb. This in fact agrees well with measured phase angles ($2M_2$-M_4) and tidal wave shape in Louisa Creek, where phase angle tends towards 0° and the tide becomes strongly distorted (M_4/M_2=0.21). With these characteristics a growth in the flood dominance would be expected. However it does not happen. The tidal wave asymmetry is maintained more or less the same throughout the lunar cycle, but there is a threshold in the volume of water stored in the mangroves which triggers off faster ebb currents.

Assuming that the volume of water in the mangroves varies linearly with tidal height, the volume of the water stored in the mangroves in each tidal cycle was calculated by subtracting the volume of the channel below mangrove banks (4.9×10^5 m^3) from the tidal prism and multiplying the result by 0.46. This value represents the ratio between the volume of water stored in the mangroves and that accumulated in the channel area above the mangrove banks at the highest spring tide. Figure 15 plots the ratio of maximum flood/ebb currents for #1, against Vs/Vc ratio. The zero value in the x axis marks the threshold of mangrove inundation, with negative values meaning dry mangrove banks during the tidal cycle. The points follow a well defined curve with flood currents becoming stronger even after the inundation of the mangroves. The descent in the flood dominance starts when Vs/Vc reaches about 1.5, and is eventually overcome by the ebb when Vs/Vc is near 2.5. Although the ratio remains more or less the same for Vs/Vc > 3, the actual velocities are larger and the ebb dominance in sediment transport does increase.

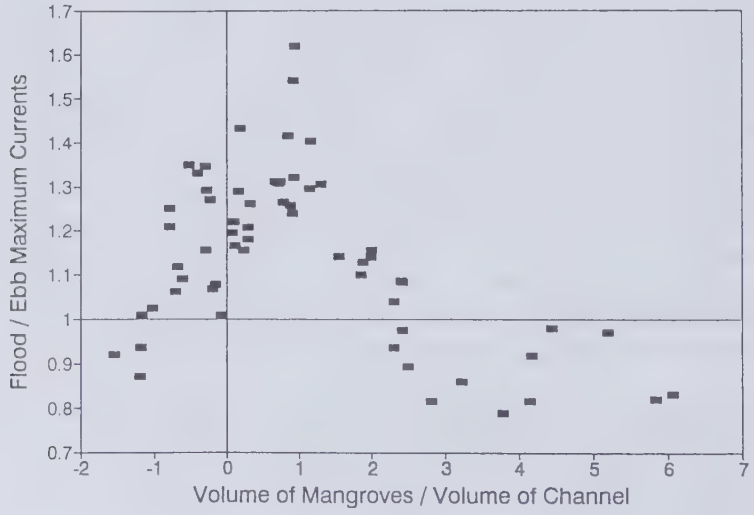

Figure 15. Vs/Vc ratio versus ratio of flood/ebb maximum currents at station #1.

Conclusion

In view of the results obtained so far, the dynamics of Louisa Creek, and probably several similar estuaries on Central Queensland coast, do not agree entirely with the models developed for shallow estuaries on the U.S. coast, where tidal range varies mostly between 0.5 and 2 m. As could be predicted, the large a/h ratio of Louisa Creek increases the intensity of the tidal distortion (M_4/M_2) upstream, and leads to an asymmetry in the vertical tide characterized by a longer falling tide. This type of asymmetry produces flood dominant currents. The flood dominance increases up to a high tide level around 2.7 m (AHD), after which it decreases. Inconsistencies start to occur when high tide levels advance over 3.4 m (AHD), and ebb currents become dominant.

Even though these events did not happen very often, 4-6 times at springs during the field campaign, the total volume of sediments entrained by ebb tidal currents during these episodes were superior to the volume transported by the flood currents. Based on the characteristics of the vertical tide described above and utilizing the model proposed by Fry and Aubrey (1990), total flood sediment transport, allowing for an entrainment threshold, should be 2 to 4 times larger than the ebb. This situation is only observed during neap tides.

The key question is whether the frequency of above 3.4m (AHD) tides during a longer period will cause a net sediment transport seaward. Based on the Australian Tide Tables, tides above 3.4 m occurred 132 times during 1992, or 19% of the total number of tidal cycles. Figure 16 (a and b) shows the net sediment transport for each tidal cycle as a function of high water level at stations #1, #3 and #4. At #1 it is seems that tides with high tide level below 2 m (AHD) do not induce net transport, while between 2 and 3.4 m (AHD) the net transport is landward with an average of 3 m^2 per unit width of the channel. Above 3.4 m (AHD) the net transport is seaward and increases dramatically with increasing tide level. An average value for these conditions is about 10 m^2 per unit width of the channel. As the number of tidal cycles with high tide level between 2.0 and 3.4 m (AHD) in 1992 was 280, the averages above indicate that the mouth is slightly ebb dominant or in a condition close to equilibrium. Stations #3 and #4 are clearly ebb dominant. It must be emphasized that the analysis undertaken is primarily qualitative, for the amount of error included in the calculations of average flow velocity and sediment discharge, though similar for both flow directions, may be large.

Louisa Creek also shows strong similarities with the macrotidal creeks described by French and Stoddart (1992) and Baylish-Smith *et al.* (1978). The so called velocity "transients" identified for over-marsh tides are identified here for over-mangrove tides, and, like the former, plays an important role in estuary sediment dynamics. Additionally, the flood/ebb duration ratio is higher during springs than during neaps, indicating that the tides in both estuaries adapt in a similar fashion to the decrease in the channel time varying geometry.

At this stage it is believed that the main differences between micro-mesotidal and macrotidal estuaries hydraulics lies not only in the larger tidal amplitude to depth

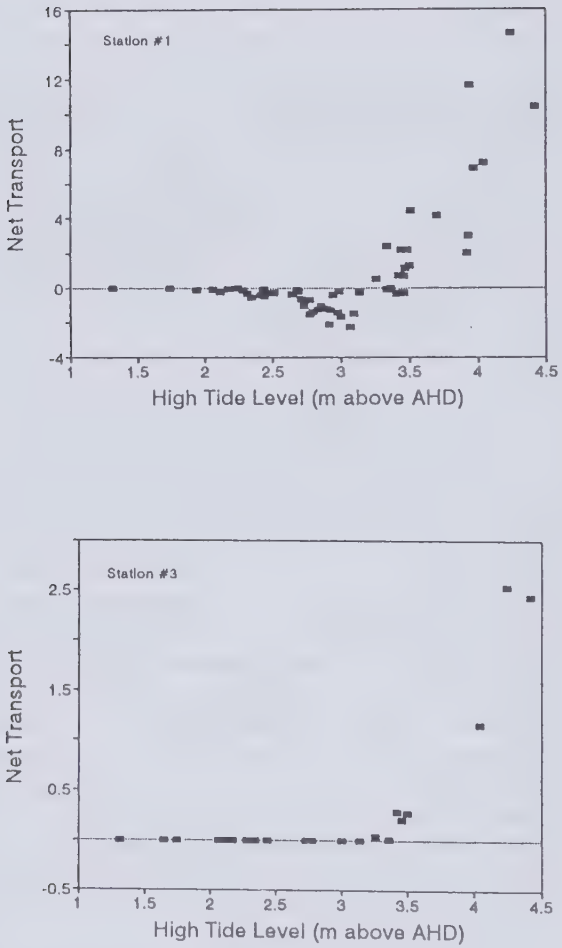

Figure 16. Net sediment transport for individual tidal cycles at station #1 (a) and #3 and #4 (b) versus ocean high tide level.

ratio of the macrotidal estuaries, but also upon the relatively high levels of the marsh banks. Higher marsh banks are only overflowed at times of higher tidal ranges, and always at the later stages of the rising tide, thus having negligible effect on the overall tidal wave shape. It is questioned whether, with the same tidal range a lower marsh level would provide conditions for slower flood tides to occur. Further data analysis is being performed in Louisa Creek and another similar macrotidal estuary to address this question.

Acknowledgements. I wish to thank Dr. Andrew Short and Dr. Peter Cowell for the comments made on this paper. I am also thankful to Gerd Masselink for the many hours of discussion spent on the data. Dr. Richard Davis, Graham Loyd, Peter Kerr and my wife Bere are acknowledged for their assistance in the field. Ocean tide data and harmonic analysis were kindly provided by the Queensland Department of Transport (DOT) and Beach Protection Authority (BPA). David Mitchel helped to set up the current meters and Dr. Peter Harris assisted with the software to convert the Aanderaa data. The author has been sponsored by the Conselho Nacional de Desenvolvimento Cientifíco e Tecnológico (CNPq) - Brazil.

References

Aubrey, D. G. Hydrodynamic controls on sediment transport in well mixed bays and estuaries. In: *Physics of Shallow Estuaries and Bays* (van de Kreek, J., ed.). Berlin, Springer-Verlag, 245- 258, 1986.

Aubrey, D.G. and Speer, P.E. A study of non-linear tidal propagation in shallow inlet/estuarine systems. Part I: Observations. *Estuarine Coastal Shelf Sci,* 21,185-205, 1985.

Bayliss-Smith, T.P.; Healey, R.; Lailey, R.; Spencer, T. and Stoddart, D.R. Tidal flows in salt marsh creeks. *Estuarine Coastal Mar Sci,* 9, 235-255, 1978.

Beach Protection Authority of Queensland. Wave Data Recording Programme: Mackay Region. 47, 1986.

Black, K.P. and Healy, T.R. The sediment threshold over tidally induced megaripples. *Mar Geol,* 69, 219-234, 1986.

Boon, J.D. Tidal discharge asymmetry in a salt marsh drainage system. *Limnol Oceanogr*, 20, 7180, 1975.

Boon, J.D. Temporal variation of shallow-water tides in basin-inlet systems. In: D. Aubrey & L. Weishar (eds) *Hydrodynamics and Sediment Dynamics of Tidal Inlets*, New York, Springer-Verlag, 24-53, 1988.

Boon, J.D. and Byrne, R.J. On basin hypsometry and the morphodynamic response of coastal inlet systems. *Mar Geol*, 40,27-48, 1981.

Davis, R.D. and Hayes, M.O. What is a wave dominated coast? *Mar Geol,* 60,313-329, 1984.

Davies, J.L. *Geographical Variation in Coastal Development* (2nd ed.). Longman, New York, N.Y., 212, 1980.

DiLorenzo, J.L. The overtide and filtering response of small inlet/bay systems. In: D. Aubrey & L. Weishar (eds) *Hydrodynamics and Sediment Dynamics of Tidal Inlets*, New York, Springer-Verlag, 24-53, 1988.

Dronkers, J.J. Tidal asymmetry and estuarine morphology. *Netherlands Journal of Sea Research*, 20, 117-131, 1986.

Dyer, K.R. *Coastal and Estuarine Sediment Dynamics*. John Wiley & Sons, 342, 1986.

Fitzgerald, D.M. & Nummedal, D. Response characteristics of an ebb-dominated tidal inlet channel. J Sediment Petrol, 53(3), 833-845, 1983.

French, J.R.; Spencer, T & Stoddart, D. Backbarrier salt marshes of the Norfolk coast: geomorphic development and response to rising sea-levels. UCL Discussion Papers in Conservation, 54, 35, 1990.

French, J.R. and Stoddart, D.R. Hydrodynamics of salt marsh creek systems: implications for marsh morphological development and material exchange. *Earth Surface Processes and Landforms*, 17, 235-252, 1992.

Friedrichs, C.T. and Aubrey, D.A. Non-linear tidal distortion in shallow well-mixed estuaries: a synthesis. *Estuarine Coastal Shelf Sci* 27, 521-545, 1988.

Fry, V.A. and Aubrey, D.G. Tidal velocity asymmetry and bed-load transport in shallow embayments. *Estuarine Coastal Shelf Sci* 30, 453-473, 1990.

Gourlay, M.R. & Hacker, J.L.F. Pioneer River Estuary Sedimentation Studies. University of Queensland Printery, Brisbane, 207, 1986.

Hayes, M.O. Geomorphology and sedimentation patterns of tidal inlets: a review. Proceedings Coastal Sediments '91. A.S.C.E. Seattle, WA, 1991.

Knight, D.W. Some field measurements concerned with the behaviour of resistance coefficients in a tidal channel. *Estuarine Coastal Shelf Sci*, 12, 303-322, 1981.

Kjerfve, B. Estuarine geomorphology and physical oceanography. In: *Estuarine Ecology* (John Day Jr., Charles Hall, Michael Kemp & Alejandro Arancibia eds). John Wiley & Sons, 47-78, 1989.

Kjerfve, B. & Proehl, J.A. Velocity variability in a cross-section of a well-mixed estuary. *Journal of Marine Research*, 37, 409-418, 1979.

Meyer-Peter, E. and Müller, R. Formulae for bed-load transport. Proc. 2nd Meeting IAHR., Stockholm, 39-44, 1948.

Myrick, R.M. & Leopold, L.B. Hydraulic geometry of a small tidal estuary. USGS Prof. Paper, 422.b, 18, 1963.

Pethick, J.S. Velocity surges and asymmetry in tidal channels. *Estuarine Coastal Mar Sci*. 11, 331-345, 1980.

Pugh, D.T. *Tides, Surges and Mean Sea-Level*. John Wiley &Sons Ltd., Avon (U.K.), 470, 1987.

Speer, P.E. & Aubrey, D.G. A study of non-linear tidal propagation in shallow inlet/estuarine systems. Part II: theory. *Estuarine Coastal Shelf Sci*, 21, 207-224, 1985.

Zarillo, G.A. Tidal dynamics and substrate response in a salt-marsh estuary. *Mar Geol*, 67, 13-35, 1985.

van de Berg, J.H. Bed-form migration and bed-load transport in some rivers and tidal environments. In: *Aspects of sediment and morphodynamics of subtidal deposits of the Oostercheld (the Netherlands)* by J.H. van de Berg. Rijkswaterstaat Communications, no. 43, 91-121, 1986.

Wooding, R.A; Bradley, E.F. & Marshall, J.R. Drag due to irregular arrays of roughness elements of varying geometry. *Boundary Layer Meterol*, 5, 282-308, 1973.

21

Net Transport of Fine Sediment in a Homogeneous Tidal Channel

J. van de Kreeke

Abstract

For a tidal channel with water of homogeneous density, a semi-analytical expression is derived for the tidally-averaged displacement of a sediment particle in terms of the amplitudes and phases of the harmonic constituents of the Lagrangian velocity. Transport of sediment is by erosion—advection—deposition. The amplitudes and phases of the Lagrangian tidal current constituents are related to the amplitudes and phases of the Eulerian tidal current constituents and the gradient of the amplitude of M_2. It is assumed that the Eulerian velocity field consists of a mean current and M_2 and its overtides. From the semi-analytical expression for the net particle displacement it follows that the direction of the sediment transport is determined by the phase between the M_2 and M_4 constituent of the Lagrangian velocity. In terms of the Eulerian velocity field this phase angle depends on the phase between M_2 and M_4, the ratio of the amplitudes of M_2 and M_4 and the gradient of the amplitude of M_2. Application to channels with a length of 100 km and a depth of 10 m shows a divergence of the net sediment transport with a seaward net transport in the seaward one third of the channel. This is in agreement with results of calculations in which the advection diffusion equation for sediment transport was solved numerically.

Mixing in Estuaries and Coastal Seas
Coastal and Estuarine Studies Volume 50, Pages 361-373
Copyright 1996 by the American Geophysical Union

Introduction

In tidal channels suspended sediment is transported in both the ebb and flood direction. In general the ebb and flood transport do not balance and a tidally averaged or net transport results. The magnitude and direction of the net transport depends on the tide and sediment characteristics. For example, Postma [1954, 1967] postulated a landward transport for a landward decrease in tidal current amplitude. Also, tidal asymmetry associated with M_2 and its overtides can be important in generating a net suspended sediment transport [Postma, 1967; Dronkers, 1985]. To identify more generally the mechanisms for the net transport, in this paper a semi-analytical expression is developed that expresses the net displacement of a sediment particle in terms of pertinent characteristics of the Eulerian velocity field. This rectilinear velocity field consists of M_2, its overtides and an Eulerian mean current. The semi-analytical expression is used to explain the numerically calculated reversals in the direction of the net transport of suspended sediment in homogeneous tidal channels, e.g. Dyer and Evans [1989].

In the conceptual sediment transport model used in this paper, particles are lifted of the bed when the current speed $u(x,t)$ is larger than the critical velocity of erosion u_e and start settling when $u(x,t)$ is smaller than the critical velocity of sedimentation u_s [Mehta, 1988; Odd, 1988]. Here, it is assumed that the vertical velocity distribution is uniform and near bed boundary layer residual transport is neglected. x is measured in the along channel direction and is positive going landward. t is time. Values of u_e and u_s depend on size, shape and density of the sediment particles. In addition, the value of u_e depends on consolidation of the bed and shielding of finer particles by larger particles. In general, $u_e > u_s$. The difference between the two is referred to as the scour lag. After the current speed has decreased below the critical current speed u_s, it will take some time for particles to reach the bed. To account for this a deposition velocity u_d is introduced. The value of u_d corresponds to the current speed at the time the particles reach the bed. It follows that $u_s > u_d$. The difference between the two is referred to as the settling lag. In addition to the flow conditions (turbulence), values of the settling lag depend on suspended sediment concentration and flocculation. For typical sediments and tidal currents values of u_e, u_s and u_d are order 0.1 ms^{-1}.

Numerically Calculated Sediment Transport

Dyer and Evans [1989] calculated the tidally averaged sediment transport in a 100 km long tidal channel with sloping bottom having a depth of 20 m at the open end and 5 m at the closed end. Similar calculations are carried out as part of this study for the two channels presented in Figure 1.

The water motion in the channels is governed by the vertically integrated equations of conservation of mass and momentum with unknowns $u(x,t)$ and $\eta(x,t)$ the

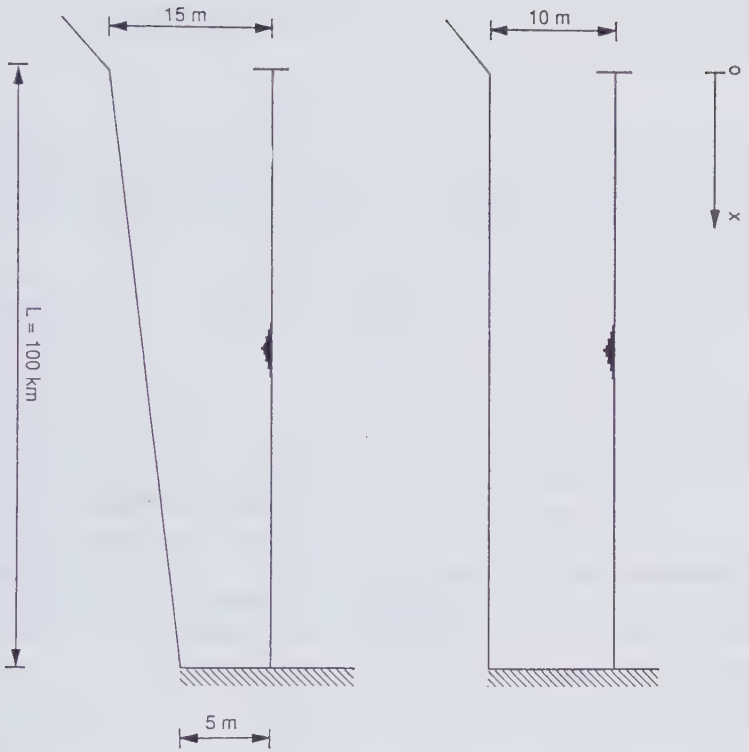

Figure 1. Channel Configurations.

longitudinal velocity and the water level, respectively. x is the longitudinal coordinate; x = 0 at the open end and x = L at the closed end of the channel. t is time. η is measured with respect to the Still Water Level. The equations and appropriate boundary conditions are solved numerically.

The transport of suspended sediment is described by

$$\frac{DA\bar{c}}{Dt} - \frac{\partial}{\partial x}\left(DA\frac{\partial \bar{c}}{\partial x}\right) = \dot{E} - \dot{S} \qquad (1)$$

In Eq. (1), A is the cross-sectional area, t is time and D is a dispersion coefficient, $\bar{c}$ is the vertically averaged suspended sediment concentration. Assumed is a vertically uniform concentration distribution. The operator D/Dt represents the total derivative and therefore the first term on the left hand side of Eq. (1) represents the rate of change of the total mass of suspended sediment in a water column with unit horizontal section and moving with the velocity u(x,t). The second term on the left hand side accounts for the dispersive transport.

On the righthand side of Eq. (1), $\dot{E}$ is the rate of erosion at the bottom and is related to the velocity field by

$$\dot{E} = M_e\left(\frac{u^2}{u_e^2}-1\right) \qquad u \geq u_e$$
$$\dot{E} = 0 \qquad u \leq u_e \tag{2}$$

where M_e is an erosion rate constant. $\dot{S}$ is the rate of sediment deposition and is usually taken as

$$\dot{S} = \bar{c}W\left(1-\frac{u^2}{u_d^2}\right) \qquad u \leq u_d$$
$$\dot{S} = 0 \qquad u \geq u_d \tag{3}$$

In Eq. 3, W is the fall velocity.

To conform to the conceptual sediment transport model described in the Introduction, D in Eq. (1) is given a small value and transport is by advection only. Furthermore it is assumed that all sediment particles are suspended instantaneously when $u = u_e$ and all suspended sediment particles reach the bottom at the same time corresponding to $u = u_d$. In the model this is accomplished by assigning large values to M_e and W. Initially, the bed of the channels are covered with a thin layer of uniform sediment.

Calculations are carried out for two boundary conditions.

$$\eta = 1\cos\omega t \qquad \text{at } x = 0$$

and

$$\eta = 1\cos\omega t + 0.1\cos 2\omega t \qquad \text{at } x = 0$$

The frequency $\omega = 2\pi / 45{,}000$ rad sec^{-1}, corresponding approximately to the M_2 tidal frequency. Individual experiments are listed in Table I.

TABLE I. Experiments

Designation	*Channel*	*Forcing*
AO1	Horizontal Bottom	M_2
AO2	Horizontal Bottom	$M_2 + M_4$
DO1	Sloping Bottom	M_2
DO2	Sloping Bottom	$M_2 + M_4$

First the one-dimensional shallow water wave equations with unknowns $\eta(x,t)$ and $u(x,t)$ are solved using an implicit finite difference scheme with a grid size of 500 m and a time step of 150 sec. [Geurtz, 1990]. The bottom friction factor $F = 2 \times 10^{-3}$ corresponding to a Mannings value n = 0.02. Velocities are Fourier analyzed according to

$$\frac{u}{\hat{u}_1} = \frac{u_o}{\hat{u}_1} + \cos\omega t + \sum_{i=2}^{N} \frac{\hat{u}_i}{\hat{u}_1} \cos(i\omega t - (\beta_i - i\alpha)) \qquad (4)$$

in which $\hat{u}_0$ is the Eulerian mean current. $\hat{u}_1$, α and ω respectively are the amplitudes, phase and angular frequency of the M_2 tidal current constituent. $\hat{u}_i$ and β_i respectively are the amplitude and phase of the i^{th} overtide. $(\beta_i - i\alpha)$ is the phase of the i^{th} overtide relative to M_2. Note that $\hat{u}_1$, $\hat{u}_i$ and β_i are all functions of x.

As an example, for experiment DO1 the amplitudes of the M_2, M_4 and M_6 constituents of the tidal current, respectively $\hat{u}_1$, $\hat{u}_2$, and $\hat{u}_3$ are plotted in Figure 2a. The amplitude $\hat{u}_1$ is an order of magnitude larger than the amplitudes $\hat{u}_2$ and $\hat{u}_3$. In turn $\hat{u}_2$ and $\hat{u}_3$ were found to be an order of magnitude larger than the amplitude $\hat{u}_4$ of the M_8 constituent. This conclusion also holds for the other experiments. The relative phase angles $(\beta_i - i\alpha)$ for the second harmonic (i=2) and third harmonic (i=3) are plotted in Figure 2b.

With the velocity field known, the transport equation, Eq. 1, with $\dot{E}$ and $\dot{S}$ given by respectively Eqs. (2) and (3), is solved using an implicit finite difference scheme [Geurtz, 1990]. To conform to the simplifications discussed in the previous section the following values are selected for the dispersion coefficient, erosion rate constant and fall velocity, $D = 1\ m^2 s^{-1}$, $M_e = 1\ kg\ m^2\ s^{-1}$ and $W = 1\ ms^{-1}$ respectively. It is emphasized that these are not physically realistic values; they are introduced to simulate a transport that is dominated by instantaneous suspension, advection and instantaneous settling. The critical erosion velocity $u_e = 0.3\ ms^{-1}$ and the critical velocity for deposition $u_d = 0.2\ ms^{-1}$. At t=0 the bottom of the channel is covered with a uniform layer of sediment with a density of $0.5\ kg\ m^{-3}$. When all the sediment is in suspension this results in an average concentration of $50\ mg\ L^{-1}$. Sediment that leaves the channels during the ebb does not return on the flood.

Numerical sediment transport calculations are carried out for a period extending over 100 tidal cycles. Although the tidally averaged transports vary in time, the pattern remained stable during the 100 tidal cycles with a tidally averaged transport in the landward direction in the landward part and in the seaward direction in the seaward part of the channel. As an example, for experiment DO1 the net transport for tidal cycle 100 is presented in Figure 3. The location where the transport reverses direction differs for each experiment and varies between x = 30 km and x = 60 km. The sediment transported toward the closed end of the channel is deposited in the region where the maximum velocity is less than the critical velocity of erosion.

The numerical experiments by Dyer and Evans [1989] show similar results. In their experiments forcing is by the M_2 tide at the open boundary having an amplitude of 2.5 m. The friction factor $F = 2.4\ 10^{-3}$. In the transport equation, a dispersive term is included however, the value of the dispersion coefficient could not be ascertained. The value of the erosion rate constant $M_e = 0.001\ kg\ m^{-2}\ s^{-1}$. Hindered settling is included by taking the fall velocity proportional to some power of the concentration.

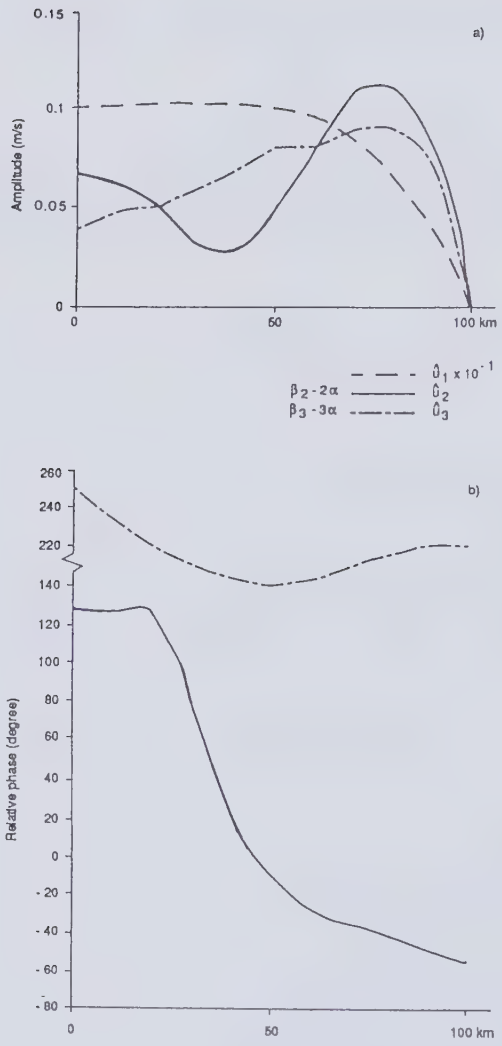

Figure 2. Experiment DO1. a) Amplitudes of First, Second and Third Harmonic. b) Relative Phase of Second and Third Harmonic.

Resulting fall velocities are such that a distinct settling lag occurs. Dyer and Evans [1989] carried out experiments for different values of u_e, ranging from 0.1 ms^{-1} to 0.8 ms^{-1}. In all experiments, $u_d = 0.025$ ms^{-1}. An initial concentration varying from 10 ppm at the open end to 25 ppm at the closed end is imposed. Similar to the results described in this study, the calculations show a change from seaward to landward net sediment transport in the range of 25 km to 50 km, the exact value depending on the value of the critical erosion velocity.

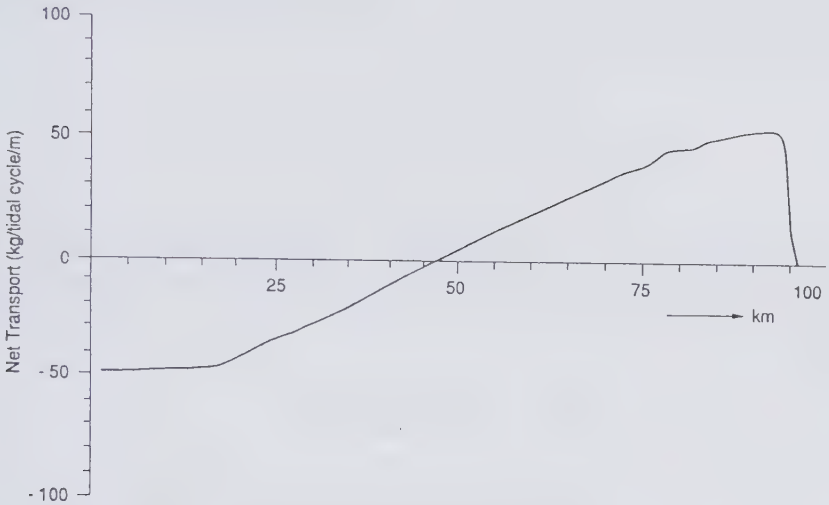

Figure 3. Experiment DO1. The Tidally Averaged Sediment Transport After 100 Tidal Cycles.

The Tidally Averaged Displacement of a Sediment Particle

Based on the sediment transport model described in the introduction and the assumptions of instantaneous suspension when $u=u_e$ and instantaneous settling when $u=u_d$, the behavior of a sediment particle is indicated in Figure 4. A sediment particle located at the bottom at a location x_1 is lifted from the bottom when the local current speed $|u(x,t)|=u_e$. The sediment particle is advected by a water parcel that oscillates about the location x'. The velocity of this water parcel is designated $u_L(x', t)$. The particle is deposited at x_3 where $|u_L(x',t)| = u_d$. The sediment particle is lifted again from the bed when the local velocity $|u(x_2,t)|=u_e$. The sediment particle is then advected by a water parcel that oscillates about x'' and has a velocity $u_L(x'', t)$. The particle is deposited at x , where $|u_L(x'',t)| = u_d$. The positions of the sediment particle in Figures. 4 are not meant to imply that x'' is always larger and x' or x_3 is always larger than x_1; the relative positions will depend on the shape of the velocity-time curve.

The positions x_1, x_2, x_3, x' and x'' are all located within one tidal excursion of each other. Assuming that over that distance the Lagrangian velocity does not change appreciably it follows that to a good approximation

$$u_L(x', t) \approx u_L(x'', t) \approx u_L(x_1, t) \qquad (5)$$

Therefore, provided the maximum ebb and flood velocity are larger than u_e, the net displacement over a tidal cycle of a particle lifted from the bed at a position x by the flood current is

$$s(x) \approx \int_{t^- + \Delta t_e^-}^{t^+ - \Delta t_d^+} u_L(x,t)\, dt + \int_{t^+ + \Delta t_e^+}^{t^- + T - \Delta t_d^-} u_L(x,t)\, dt \qquad (6)$$

In the experimental channels the Lagrangian mean velocity is zero [van de Kreeke, 1981] and therefore a water parcel continues to oscillate about its initial (at rest) position corresponding to t = 0. In that case to a first approximation [Longuet Higgins, 1969]

$$\frac{u_L}{\hat{u}_1} \approx \frac{u}{\hat{u}_1} + \frac{1}{\hat{u}_1} \frac{\partial u}{\partial x} \int_o^t u\, dt \qquad (7)$$

The Eulerian velocity, u, in terms of its harmonics is given by Eq. (4). Substituting for u in Eq. (7) and neglecting terms of 0(0.01) results in the approximate expression for the Lagrangian velocity

$$\frac{u_L}{\hat{u}_1} \approx \cos\omega t + \frac{1}{2\omega} \frac{d\hat{u}_1}{dx} \sin 2\omega t + \sum_{i=2}^{N} \frac{\hat{u}_i}{\hat{u}_1} \cos(i\omega t - (\beta_i - i\alpha)) \qquad (8)$$

For definitions of t^+ and Δt_d^+ etc., see Figure 4.

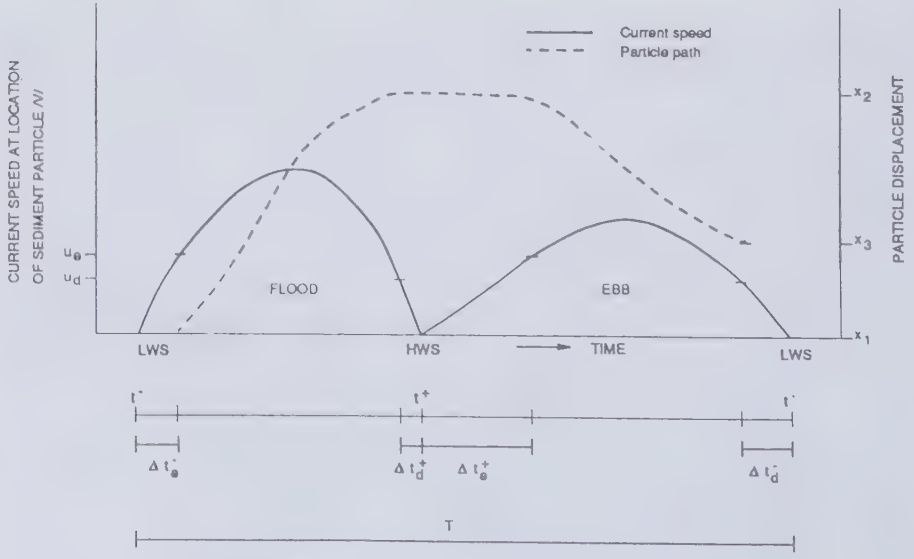

Figure 4. Particle Path; Definition of Time Intervals.

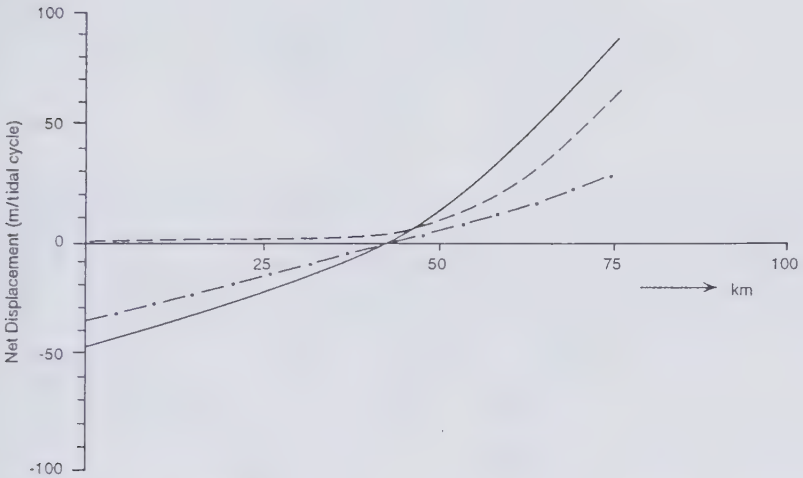

Figure 5. Experiment DO1. Net Particle Displacement as a result of, decrease in tidal amplitude (---) and tidal asymmetry(-·-). Total net displacement (—).

The conditions for Eq. (8) to be valid are listed in Appendix A. Compared to the Eulerian tidal velocity, u(x,t), the Lagrangian tidal velocity, $u_L(x,t)$ contains an additional harmonic with a frequency 2ω and an amplitude that is determined by the gradient of the amplitude of the M_2 tidal current constituent. Note that because the Lagrangian mean velocity is zero, the contribution of the Eulerian mean velocity to the Lagrangian mean velocity is cancelled by the Stokes drift.

Using Eqs (6) and (8) and the known Eulerian velocity field, the tidally averaged displacement of a sediment particle as a function of its longitudinal (x) position is calculated for the experiments listed in Table I. In the calculations $u_e = 0.3$ ms^{-1} and $u_d = 0.2$ ms^{-1}. As an example, for experiment DO1 the tidally averaged displacements are plotted in Figure 5. In a similar fashion to the tidally averaged sediment transport, the tidally averaged particle displacement exhibits a reversal in direction at about x = 45 km.

Discussion

To further illustrate the mechanisms by which the tidally averaged sediment transport is generated, the expression for the tidally averaged displacement of a sediment particle, Eq. (6), is simplified by assuming that in the neighborhood of slack water the Lagrangian velocity-time curve is sufficiently linear [Dronkers, 1985]. This yields

$$s_a = \frac{(u_e^2 - u_d^2)\left(\left|\frac{du_L}{dt}\right|_{LWS} - \left|\frac{du_L}{dt}\right|_{HWS}\right)}{2\left|\frac{du_L}{dt}\right|_{LWS}\left|\frac{du_L}{dt}\right|_{HWS}} \tag{9}$$

in which s_a is the approximate tidally averaged displacement of a sediment particle. LWS refers to time of Low Water Slack and HWS refers to time of High Water Slack. Eq. (9) shows that for a net displacement to exist, $u_e \neq u_d$. This implies that the scour lag and settling lag cannot both be zero. Furthermore, for most applications $u_e > u_d$ and therefore s_a is positive i.e. in the flood direction for

$$\left|\frac{du_L}{dt}\right|_{LWS} > \left|\frac{du_L}{dt}\right|_{HWS} \tag{10}$$

and is negative i.e. in the ebb direction for

$$\left|\frac{du_L}{dt}\right|_{LWS} < \left|\frac{du_L}{dt}\right|_{HWS} \tag{11}$$

Furthermore, with regard to the sum of the M_2 and M_4 harmonics the following property is identified: for a function of the form

$$u_L = a\cos\omega t + b\cos(2\omega t - \gamma) \tag{12}$$

$$\left|\frac{du_L}{dt}\right|_{LWS} > \left|\frac{du_L}{dt}\right|_{HWS} \quad \text{for } \pi < \gamma < 2\pi \tag{13}$$

$$\left|\frac{du_L}{dt}\right|_{LWS} < \left|\frac{du_L}{dt}\right|_{HWS} \quad \text{for } 0 < \gamma < \pi \tag{14}$$

The time derivatives at LWS and HWS are equal for $\gamma = 0$ and $\gamma = \pi$. This implies that for a Lagrangian velocity field consisting of M_2 and M_4 and using Eq. (9), the direction of the tidally averaged particle displacement is solely a function of the phase between M_2 and M_4.

When considering an Eulerian velocity field that consists of only the M_2 tidal current constituent, the Lagrangian velocity is

$$\frac{u_L}{\hat{u}_1} = \cos\omega t + \frac{1}{2\omega}\left|\frac{d\hat{u}_1}{dx}\right| \cos(2\omega t - (-\pi/2)) \tag{15}$$

i.e., a combination of a first and second harmonic with relative phase - $\pi/2$. Therefore, from (13) and Eq. (9) it follows that the tidally averaged particle displacement is in the landward direction everywhere. This is in agreement with the original hypothesis by Postma [1954, 1967].

For an Eulerian velocity field consisting of M_2 and M_4 and neglecting the contribution of the landward decrease in the tidal current amplitude of M_2, it follows from Eq. (8)

$$\frac{u_L}{\hat{u}_1} \approx \cos\omega t + \frac{\hat{u}_2}{\hat{u}_1} \cos(2\omega t - (\beta_2 - 2\alpha)) \tag{16}$$

Taking the numerical experiment DO1 as an example, the value of the phase angle (β_2 - 2α) varies from 130° at the seaward end to - 50° at the landward part of the channel; see Figure 2. As a result the Lagrangian velocity-time curve changes shape when going from the seaward to the landward end of the channel with the times of maximum current being closer to HWS in the seaward part and being closer to LWS in the landward part, or equivalently, in the seaward part the time rate of change of the Lagrangian velocity is larger at times of HWS than LWS whereas the reverse holds for the landward part. In view of (13) and (14), and Eq. (9) it then follows that in the seaward part of the channel the net sediment transport is in the seaward direction and in the landward part is in the landward direction.

When dealing with the sum of a first and third harmonic in the Eulerian velocity and again neglecting the contribution of the landward decrease in the amplitude of M_2, the Lagrangian velocity is

$$\frac{u_L}{\hat{u}_1} \approx \cos\omega t + \frac{\hat{u}_3}{\hat{u}_1} \cos(3\omega t - (\beta_3 - 3\alpha)) \tag{17}$$

Although this function is asymmetric with respect to $t = t_{LWS}$ and $t = t_{HWS}$, it has the property that

$$|u_L(t)| = |u_L(t + T/2)| \tag{18}$$

and consequently the magnitude of the time derivatives at LWS and HWS are the same. Therefore, it follows from Eq. (9) that the resulting net displacement of a sediment particle is zero.

For experiment DO1 the contribution of the decrease in the amplitude of the M_2 tidal current, calculated from Eqs (6) and (15), and the contribution of the interaction of the M_2 and M_4 tidal current, calculated from Eqs (6) and (16), to the tidally averaged particle displacement is indicated in Figure 5. Because the change of $\hat{u}_1$ with x is small in the seaward part, see Figure 2, the magnitude of the particle displacement resulting from the decrease in tidal amplitude in this part of the channel is small. It's value increases when going landward. As explained, the contribution of the combination of M_2 and M_4 to the tidally averaged particle displacement exhibits a reversal in direction. The curves representing the tidally averaged displacements are terminated at x = 75 km. For larger values of x the relatively large change in velocity, see Figure 2a, makes the approximate expression for the Lagrangian velocity, Eq. (8), less accurate. It is apparent from Figure 5 that

the contributions of the net particle displacements associated with a decrease in tidal amplitude and tidal asymmetry do not add up to the total net particle displacement. Because of the nonlinearities involved, the net particle displacements associated with the two processes are not additive. However, separating the two processes and adding the displacements at least qualitatively explains the change in the direction of the tidally averaged particle displacement and therefore the change in direction of the tidally averaged sediment transport.

Finally, it is of interest to compare the net transport of fine and coarse sediment as it is affected by the phase difference between the M_2 and M_4 tidal current constituents. Fine sediment is transported by erosion—advection—deposition; the rate of transport is determined by the Lagrangian velocity. Coarse sediment is transported as bed load; the rate of transport is determined by the local (= Eulerian) velocity . To allow a proper comparison, a uniformly oscillating velocity field for which the Eulerian velocity equals the Lagrangian velocity is selected. This velocity field is given the form of Eq.(12) with a, b and γ taken as constants that are independent of x. For this velocity field, it is shown in this paper that the net transport of fine sediment is in the flood direction for $o < \gamma < \pi$. As shown in van de Kreeke and Robaczewska [1993], the net transport of coarse sediment is in the flood direction for $-\pi/2 < \gamma < \pi/2$. Obviously, in addition to the phase difference between the M_2 and M_4 tidal current constituents, the direction of the net transport of sediment depends on the mode of the sediment transport.

Conclusions

The tidally averaged sediment transport in two closed-end canals is calculated by numerically solving the advection-dispersion equation. The water motion in the channels is forced at the sea boundary by the M_2 or M_2 and M_4 tide constituent. The transport is found to be in the seaward direction in the seaward part and in the landward direction in the landward part of the channels. To explain the transport pattern, the tidally averaged displacement of sediment particles as a function of position is calculated making use of an approximate analytical model. The direction of the calculated tidally averaged sediment transport and tidally averaged particle displacements are in good agreement. The tidally averaged sediment particle displacements are explained in terms of the transport processes suggested by Postma (1967), i.e., a landward decrease in the amplitude of the M_2 component of the Eulerian tidal current and the presence of higher harmonics in the Eulerian tidal current. For this the approximate analytical model is further simplified by assuming that in the neighbourhood of the times of slack water the Lagrangian velocity-time curve is sufficiently linear. It is shown that the decrease in the M_2 tidal current amplitude leads to a landward net particle displacement everywhere in the channels, whereas the tidal asymmetry associated with the combination of M_2 and M_4 results in a seaward net particle displacement in the seaward part and a landward net particle displacement in the landward part of the channels.

Acknowledgement. This study was supported by the Tidal Waters Division of the Rijkswaterstaat under contract DG-439. The study is part of the project DYNASTAR dealing with the dynamics of estuaries. The velocity field and harmonic constants were calculated by Ron P. van Dijk. Sediment transport calculations were the responsibility of Martin J. J. M. Geurtz. Net particle displacements were calculated by Jeljer Hoekstra. I am grateful to Wim van Leussen for his comments on an earlier version of this paper.

References

Dronkers, J. Tide-induced residual transport of fine sediment, in *Physics of Shallow Estuaries and Bays*, edited by J. van de Kreeke, Springer-Verlag pp. 228-245, 1985.

Dyer, K. R. and E. M. Evans Dynamics of turbidity maximum in a homogeneous tidal channel, *J. Coastal Res.*, 5, 23-30, 1989.

Geurtz, M. A Diagnostic model for large scale behavior of fine sediment in estuaries. Rijkswaterstaat DGW, Report GWAD-88.022, pp. 35, 1990 (Dutch Text).

Longuet-Higgins, M. S. On the transport of mass by time-varying ocean currents. *Deep Sea Res.*, 16, 431-447, 1969.

Mehta, A. J. Laboratory studies on cohesive sediment deposition and erosion, in *Physical Processes in Estuaries*, edited by J. Dronkers, J. and W. van Leussen, Springer-Verlag pp. 427-446, 1988.

Odd, N. V. M. Mathematical modelling of mud transport in estuaries, in *Physical Processes in Estuaries*, edited by J. Dronkers, J. and W. van Leussen, Springer-Verlag pp. 503-532, 1988.

Postma, H. Hydrography of the Dutch Wadden Sea. *Archs Neer. Zool* 10, 405-511, 1954.

Postma, H. Sediment transport and sedimentation in the estuarine environment. *Estuaries* edited by G. H. Lauff, Am. Ass. for the Advancement of Science. pp. 158-180, 1967.

van de Kreeke, J. and S. S. Chiu. Tide-induced residual flow in shallow bays. *J. Hydr. Res.*, 19(3), 231-249, 1981.

van de Kreeke, J. and K. Robaczewska, Tide-induced residual transport of coarse sediment; Application to the Ems Estuary. *Netherlands J. Sea Res.*, 31(3), 209-220, 1993.

Appendix A

Conditions for the validity of Eq. (8)

$$\frac{\hat{u}_i}{\hat{u}_1}\frac{d\hat{u}_1}{dx}\frac{1}{i\omega} \le 0.01 \qquad i = 2-N$$

$$\frac{d\hat{u}_i}{dx}\frac{1}{\omega} \le 0.01$$

$$\frac{\hat{u}_i}{\hat{u}_1}\frac{d(\beta_i - i\alpha)}{dx}\frac{1}{\omega} \le 0.01$$

22

Seasonal Variability of Mobile Mud Deposits in the Tamar Estuary

R. J. Uncles, M. L. Barton and J. A. Stephens

Abstract

Measurements describing the spring-neap and seasonal variations of fine, cohesive, suspended particulate matter (SPM) concentrations at two sites and the distribution of bed sediments within the upper reaches of the Tamar Estuary, UK, are presented. The data were obtained using two, near-bed instrument packages and longitudinal grab-sample surveys. Correlations of daily-averaged SPM concentrations with both runoff and tidal range during the separate deployments often showed a significant dependence on these variables. Where statistically significant, increasing tidal range led to enhanced SPM levels because of resuspension of bed sediments. Longitudinal surveys of bed-sediment material were generally consistent with the observed seasonal variations in SPM. During winter, the main channel of the upper several kilometres was largely devoid of unconsolidated, muddy, bed-source sediment. During summer and autumn the unconsolidated bed-source sediment moved into the upper reaches, close to the head and in association with the turbidity maximum, and formed unconsolidated mud layers of up to 1 m thickness.

Introduction

A turbidity maximum (TM) of suspended particulate matter (SPM) occurs in the upper reaches of the Tamar Estuary. The TM is primarily caused by local resuspension and subsequent transport of cohesive bed-source sediment. Physical processes involve transport by tidal and density currents, flocculation and settling

Mixing in Estuaries and Coastal Seas
Coastal and Estuarine Studies Volume 50, Pages 374-387
Copyright 1996 by the American Geophysical Union

during slack water, and fluctuations in water-column stability due to density stratification. Several of these processes have been recognized for some time (e.g. Allen *et al.*, 1977, 1980; Dyer, 1986; Festa and Hansen, 1978; Officer and Nichols, 1980; Officer, 1981; Dronkers, 1986; Hamblin, 1989; Grabemann and Krause, 1989; Uncles *et al.*, 1985 a, b, c; Uncles and Stephens, 1989; Gibbs *et al.*, 1989). However, apart from Grabemann and Krause (1989) and Uncles *et al.* (1988), little attention has been given to seasonal variability of SPM and the movement of mobile (i.e., unconsolidated, fluid-like) bed-source sediment which supplies the TM.

The purpose of this paper is to document and interpret the seasonal variation of fine-sediment, SPM concentrations and movements of mobile bed-source sediment within the main channel of the upper reaches of the Tamar Estuary, UK (Figure 1). Much of the intertidal deposited and suspended sediment within the Tamar consists of mud (that is, primarily cohesive, silt and clay admixtures, Delo (1988)) and large areas of intertidal mudbanks or mudflats exist throughout most of the Tamar's length (Bale, 1987; Bale *et al.*, 1985).

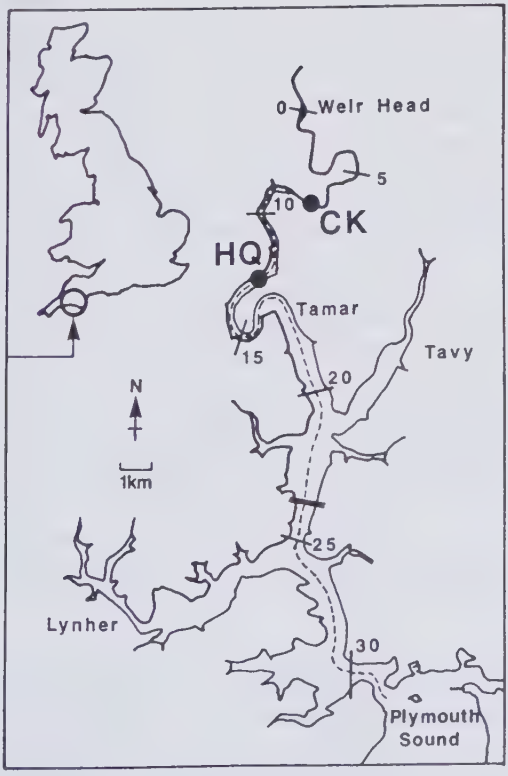

Figure 1. The Tamar Estuary, showing its sub-division into 5 km segments and the locations of Stations CK and HQ in the turbidity maximum region which were used as deployment sites for the near-bed instrument packages.

The SPM data were obtained using two, near-bed instrument packages and illustrate the importance of the fine-sediment supply to SPM concentrations, in accordance with the conclusions of Grabemann and Krause (1989) for the Weser Estuary, Germany. The local bed-sediment supply depends, in turn, on freshwater runoff to the estuary through its effect on tidal current speeds in the upper estuary and the effects of intratidal variations in water-column stability (e.g. Hamblin, 1989; Sheng and Villaret, 1989; Wolanski *et al.*, 1988; Kirby and Parker, 1977) and the presence of the freshwater-saltwater interface (FSI). The seasonal movements of mobile bed-source sediment were monitored using longitudinal, grab-sample surveys of the upper estuary.

Methods

Instrumentation

A near-bed instrument package was used to monitor long-term behaviour of SPM (Uncles *et al.*, 1989). Measurements of SPM concentration were made using Partech Electronics (UK) light-transmittance turbidity meters (0-0.1 kg m^{-3} and 0-10 kg m^{-3}).

The turbidity meters were calibrated against gravimetric determinations of SPM concentrations, using sediment collected from the measurement area (i.e.: by weighing the estuarine particulate matter filtered from a known volume of water and relating these mass-concentration data to the corresponding optical measurements). This calibration procedure does not take into account possible effects of intratidal floc-size variability, such as those described for a nephelometer by Gibbs and Wolanski (1992). We would expect any possible floc-size-induced deviations from the calibrations to be most marked around slack-water periods, when large flocs can form in the Tamar. The TM in the upper estuary consists of fine sediment of around 20-30 microns median diameter at peak currents, as measured by in-situ laser diffraction (West *et al.*, 1990). At around high-water slack, a wide range of SPM particle sizes co-exist but with large, loosely-bound flocs dominating (median diameters 200-300 microns). However, generally, at these times SPM concentrations are very small, and absolute errors in the optically-measured slack-water concentrations are likely to be correspondingly small.

Flume-calibrated, Colnbrook Instrument (UK) electro-magnetic current meters were used to measure horizontal velocity. Valeport Marine (UK) conductivity/temperature sensors were used to determine temperature and salinity.

Measurements were recorded every 5 min. at 0.25 m above the bed. Water depth was determined using a pressure sensor located in the top of the frame at 0.65 m above the bed. Batteries, electronics boards and data logger were also housed at the top of the frame. Horizontal stabilizing legs were fitted to its base.

Deployments

Two of these instrument packages were deployed in the TM region at stations CK and HQ (7 and 12.5 km from the head, Figure 1) for between 8 and 13 days at a time on nine occasions during July 1988 to July 1989 (Table 1). The CK instrument package failed in July 1988 and the HQ package failed in December 1988.

The deployment months were July, November, December of 1988 and March, April, May, June and July (twice) of 1989 (Table 1). The average freshwater runoff into the estuary during each deployment (Q) varied from 1.3 to 50.6 $m^3 s^{-1}$ and the average tidal range at the mouth during each deployment (R) varied from 3.2 to 3.9 m (Table 1).

The mean spring and neap tidal ranges for the Tamar are 4.7 and 2.2 m. The largest (5.9m) and smallest (1.7 m) tidal ranges during July 1988 - July 1989 occurred during spring and autumn. Daily-averaged freshwater runoff maximized during winter (233 $m^3 s^{-1}$) and minimized in summer (1 $m^3 s^{-1}$). There was a long period of low and generally decreasing runoff during May-July 1989 which had an important influence on the fine-sediment concentrations and the location of the easily-erodible, bed-source sediment.

Analysis

Daily averages of SPM (24h 50 min. running means of the 5 min. data, sub-sampled at noon of each day) were derived as an indication of general SPM levels. Runoff and tidal range are presented as daily-averaged data, where the daily-averaged tidal range is the average high-water to low-water range during the day at the mouth of the Tamar.

It is shown later that the daily-averaged SPM levels for a given tidal range depended on whether the spring-neap cycle was rising or falling. Therefore, for consistency, tidal-cycle data are presented for a 3.8 m tidal-range, rising spring tide - or the nearest tide to this within the deployment.

Longitudinal Bed-Sediment Surveys

Five longitudinal surveys were used to observe the distributions of bed-sediment material between April 1989 and March 1990 in the upper 21 km of the Tamar Estuary (Figure 1). Using a small inflatable boat, longitudinal transects were worked along the estuary, during which bed sediments were sampled at approximately 0.5 km intervals. Samples were taken using a van Veen grab (Buller and McManus, 1979; p.89). The sample contents were described in qualitative terms using the classifications of mobile (unconsolidated, fluid-like) mud, hard (compacted) mud, fine to coarse sand and fine to very coarse gravel.

Results

Spring-Neap Behaviour of SPM Concentrations

SPM concentrations at 0.25 m above the bed at HQ, plotted together with the daily-averaged tidal range during the November 1988 deployment (Figure 2(A)), showed the dependence of SPM on tidal range. The near-bed SPM levels fell to very low values during the neap tide on 17 November and then increased on the rising neap tides. Therefore, resuspension of bed sediment by tidal currents provided the main source of SPM for the TM. SPM data at CK were very similar, although concentrations were somewhat higher. Each tidal cycle comprised a main ebb and a main flood SPM peak at both stations.

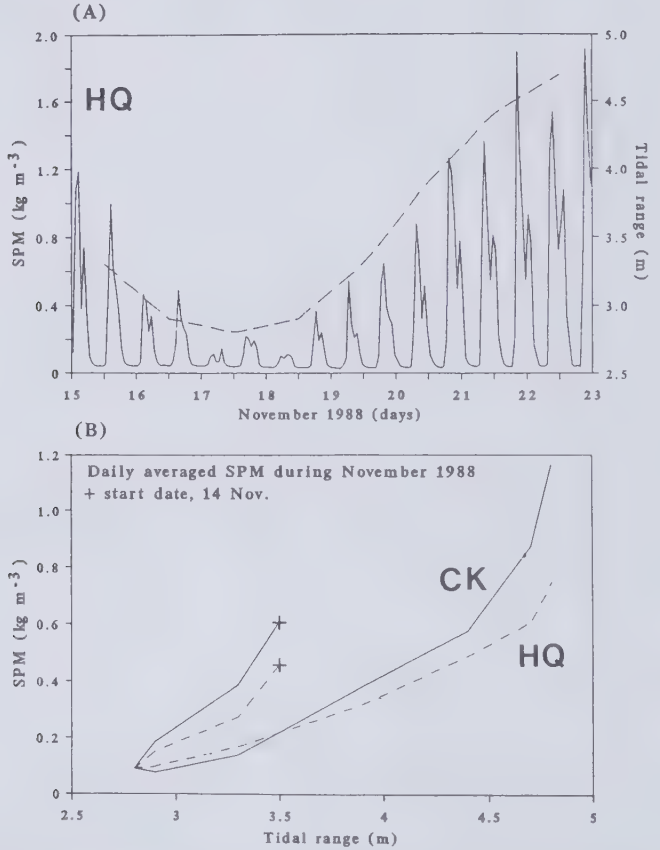

Figure 2. SPM concentration at 0.25 m above the bed and its dependence on tidal range, R, for Nov. 1988. (A): SPM at HQ (-, kg m^{-3}) and daily-averaged tidal range (- -, m) against time in days into Nov. 1988; (B): Daily-averaged SPM concentration (kg m^{-3}) against tidal range (m) for HQ(- -) and CK(-); the starting points are denoted by '+'.

There was a difference between the daily-averaged SPM concentrations on the rising and falling spring-neap cycle. On the rising cycle, the SPM levels were lower than on the falling cycle for the same tidal range. This was a feature of all deployments. During the November 1988 deployment, the daily-averaged SPM concentrations on the falling and rising 3.3 m tidal-range tides were 0.28 and 0.17 kg m^{-3} at HQ and 0.39 and 0.15 kg m^{-3} at CK (Figure 2(B)).

Seasonal Variability of SPM Concentrations

An indication of the relative SPM concentrations between deployments could be derived from the daily-averaged SPM concentrations at a particular spring-neap tidal state. A 3.8 m tidal-range, rising spring tide was chosen because it occurred for most of the deployments and was nearly reached, sufficient to permit extrapolation, for the remainder.

The daily-averaged SPM during 3.8 m tidal-range, rising spring tides at CK and HQ varied from 0.3 kg m^{-3} in July and November 1988 and then fell to 0.01 kg m^{-3} during December 1988 (Table 1). SPM levels were low during March 1989 (0.08 kg m^{-3}, Table 1) at the end of the winter period. Daily-averaged SPM at HQ during April was much higher (0.77 kg m^{-3}, Table 1) than that at CK (0.11 kg m^{-3}) which remained comparable with the March levels.

TABLE 1. Instrument deployment stations CK and HQ. The daily-averaged SPM measured or estimated on a 3.8 m tidal-range, rising spring tide for each deployment is denoted here by P (kg m^{-3}). The deployment-averaged runoff (Q, $m^3 s^{-1}$) and tidal range (R, m) is shown for each deployment. The correlations between daily-averaged SPM and both daily-averaged runoff (C_Q) and daily-averaged tidal range (C_R) within each separate deployment are shown (NS = not significant; +, ++ and +++ denote positive correlations at the 95, 99 and 99.9% confidence levels; -, --, --- similarly denote negative correlations). Correlations are derived from single-variable, linear-regression analyses. ND = no data.

Deployment	Date	P (HQ)	P (CK)	C_Q	C_R	C_Q	C_R	Q	R
Month/year	day/month	kg m^{-3}	kg m^{-3}	(HQ)	(HQ)	(CK)	(CK)	$m^3 s^{-1}$	m
Jul., 88	29/06-11/07	0.29	ND	NS	++	ND	ND	8	3.9
Nov., 88	14/11-25/11	0.30	0.35	NS	+++	NS	+++	7	3.9
Dec., 88	08/12-19/12	ND	0.01	ND	ND	-	NS	18	3.8
Mar., 89	09/03-20/03	0.08	0.07	NS	NS	NS	NS	51	3.7
Apr., 89	17/04-26/04	0.77	0.11	–	NS	—	NS	12	3.9
May, 89	12/05-23/05	0.22	0.98	—	+++	—	+++	6	3.2
Jun., 89	07/06-20/06	0.18	0.41	NS	+++	NS	+	3	3.2
Jul., 89	26/06-07/07	0.08	0.21	–	+++	-	++	2	3.8
Jul., 89	14/07-28/07	0.09	0.23	—	+++	—	++	1	3.7

In May 1989 the daily-averaged SPM concentrations at CK were much higher than those at HQ (0.98 as opposed to 0.22 kg m^{-3}, Table 1). For the June and (both) July 1989 deployments, SPM levels at CK exceeded those at HQ, although at both stations the levels were smaller in July.

Correlations (derived from linear, single-variable regressions) between daily-averaged SPM concentrations and runoff (C_Q), and between SPM and tidal range (C_R), using data for each day during each separate deployment, often showed a significant dependence of SPM on these variables (Table 1). Where significant (better than 95% probability level), increasing tidal range led to enhanced SPM levels. Where significant, increasing runoff reduced SPM levels during a deployment.

Longitudinal Surveys of Bed Sediment

We will not present results from each of the five surveys in detail but rather summarize the results and compare them with earlier experimental studies. The final survey, Survey 5, on 13 March 1990 supplied a winter picture of the bed sediment distribution in the upper 21 km of the Tamar (top panel of Figure 3).

Freshwater runoff had steadily increased over the winter period prior to Survey 5. The peak monthly-averaged flow of 87 m^3 s^{-1} occurred in February 1990. However, during March the runoff had reduced to a monthly-averaged value of 15 m^3 s^{-1}. The strongest flows during March occurred at the beginning of the month and then gradually decreased.

Survey 5 on 13 March 1990 revealed no mobile, muddy sediment on the bed of the main channel of the estuary in the upper 8 km (top panel, Figure 3). Only two regions of unconsolidated mud were observed further down-estuary, one between 9 and 12 km and one between 19 and 21 km.

Some consolidated mud was present in the upper 7 km of estuary (top panel, Figure 3). This was possibly the compacted, shear-hardened remnants of the large summer stock of mobile fine sediment (see later). However, only bedrock and very coarse gravel were present in the upper 3 km. Further down-estuary, the bed comprised mainly sand and gravel deposits.

Measurements of mud accumulations were made in the Tamar Estuary from December 1981 for the following 14 months (Bale *et al.*, 1985; Bale, 1987). Mud poles were positioned on the intertidal mudflats at approximately 1 km intervals and their relative heights measured at monthly intervals. The net erosion or deposition for each 1 km section, per month, was estimated.

The results of the Bale *et al.* (1985) study are compared with a summary of results from our five 1989-1990 grab-sample surveys (middle and bottom panels in Figure 3). From January to April 1982, Bale *et al.* (1985) found that mobile sediment (stippled

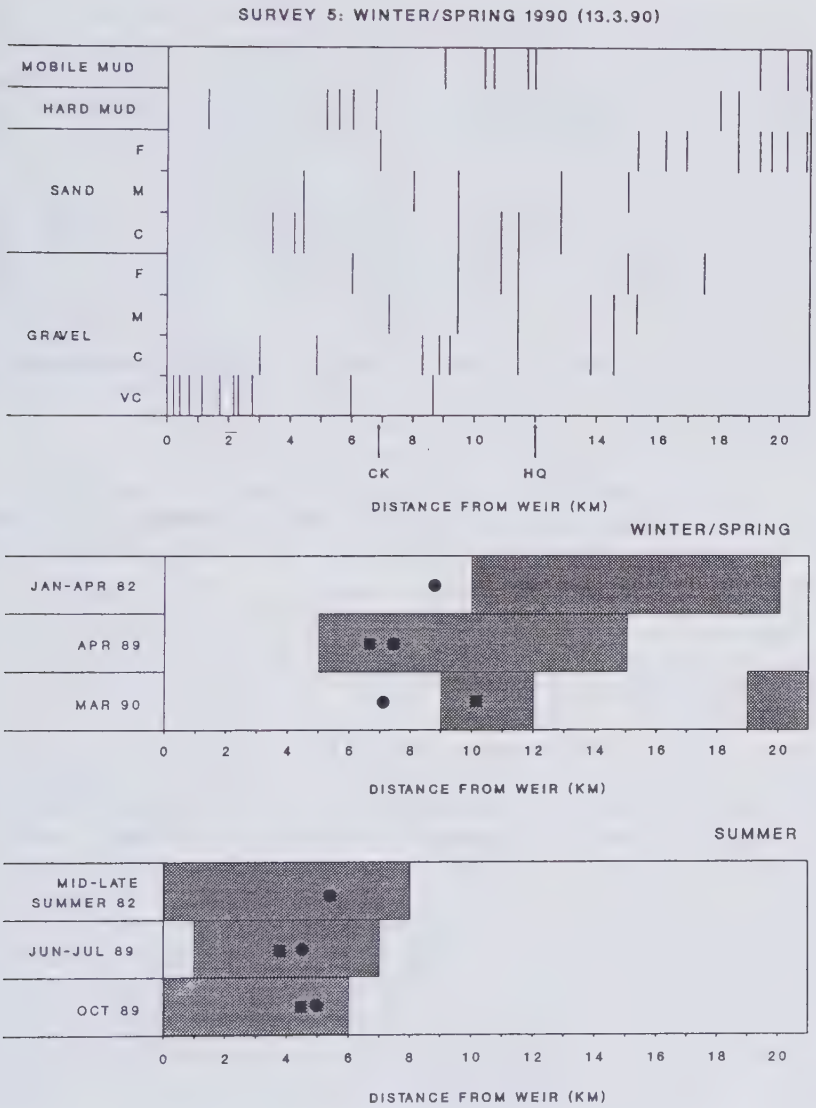

Figure 3. Winter survey of bed-sediment distributions and a summary of the distributions of mobile, unconsolidated, bed-source mud from 1982 mud-pole surveys (Bale *et al.*, 1985) and our longitudinal grab-sample surveys of 1989 and 1990. Top panel: Distributions of mobile mud, hard (consolidated) mud, fine (F) to coarse (C) sand and fine (F) to very coarse (VC) gravel in the upper 21 km of the Tamar during 13 March 1990. Middle panel: Distributions of mobile mud (stippled areas) during January to April 1982, April 1989 and March 1990 in the upper 21 km of estuary. Bottom panel: Distributions of mobile mud (stippled areas) during mid to late summer 1982, June and July 1989 and October 1989 in the upper 21 km of estuary.

areas in middle panel of Figure 3) was absent from the upper 10 km of the estuary, but that it accumulated to depths of 0.1-0.2 m in localized depositional areas between 10 and 20 km from the head (Weir Head). Figure 3 (middle panel) shows how these results compared with the deposits observed by us in April 1989 and March 1990.

The summer observations of mobile sediment accumulations from the 1982 and 1989 surveys were very similar (stippled areas in the bottom panel of Figure 3). The Bale *et al.* (1985) observations represented an average of mid to late summer conditions, and indicated accumulations of up to 0.4 m depth of mobile sediment over the upper 8 km of the estuary. Our observations indicated an up-estuary migration of the mobile bed-source sediment stock between June and October 1989. Mobile sediment occupied a reach extending from 1-7 km from Weir Head during June and July and 0-6 km during October 1989.

Deposited sediments in the mid-estuarine region (10-20 km from Weir Head) were depleted of mobile mud in both Bale's 1982 and our 1989 summer observations. During July 1989, unconsolidated mud depths of up to 1 m were observed in the main channel of the upper 3 km of the estuary.

The Freshwater-Saltwater Interface (FSI)

Longitudinal surveys of salinity were not undertaken at the same time as the grab-sample surveys. However, it is shown by Uncles and Stephens (1993a) that the location of the FSI at local high water can be represented as a power-law function of freshwater runoff. For each of our longitudinal surveys we have estimated the high-water location of the FSI in two ways: first, by using the runoff on the day of the survey (black squares on the middle and bottom panels of Figure 3) and; second, by computing the average, estimated location of the FSI based on daily runoff over the month prior to the survey (black circles on the middle and bottom panels of Figure 3). From an interpretive viewpoint there is little difference between the locations computed by these two methods. For Bale's 1982 surveys we have used the average, estimated FSI location over the period of his measurements (i.e. January through April, 1982 and June through September, 1982).

For the winter/spring surveys (middle panel of Figure 3) the FSI was either located up-estuary of the mobile, bed-source sediment, or towards its upper limits. During summer (bottom panel of Figure 3) the FSI was estimated to be located in the lower reaches of the deposited, mobile, bed-source sediment. Therefore, during the low runoff period, sediments accumulated in the fresh water up-estuary of the FSI. This is evidence for the influence of purely tidal processes in the formation of the TM and its associated stock of bed-source sediment in the Tamar. Other, non-tidal processes are also operative (e.g. Gibbs *et al.*, 1989).

Discussion

Our seasonal monitoring of SPM was restricted to near-bed observations at CK and HQ. However, vertical profiling measurements of SPM during a spring tide (not presented here) showed qualitatively similar intratidal behaviour. Quantitatively, for this tide, the near-bed SPM concentrations were typically between 10-100% greater than depth-averaged values, with the largest differences occurring during times of highest concentrations. Nevertheless, from a qualitative viewpoint, the 'point' SPM data presented here may be considered indicative of SPM concentrations within the water column of the upper reaches of the estuary.

Consolidation of deposited sediment in laboratory experiments, as measured by mean bed density, requires times greater than several hours (Delo, 1988). Therefore, sediment deposited over spring-tide, slack-water periods probably remains unconsolidated. However, consolidation probably occurs throughout much of the estuary during neap tides. The effect of this is to introduce an intertidal, spring-neap asymmetry, or hysteresis, in the resuspension/shear-stress relationship on falling and rising spring-neap tides.

A full discussion of the mechanisms responsible for TM formation in the Tamar is given by Uncles and Stephens (1993b). Measurements of SPM transport in the Tamar demonstrate that tidal pumping of fine sediment occurs in the upper, TM region (Uncles *et al.*, 1985a,b,c). This pumping includes the effects of semidiurnal and overtide perturbations to the SPM and currents (due to buoyancy and other forcing interacting with the tide) as well as that due solely to the barotropic tides. During spring-tide, low-runoff summer conditions, the mechanisms responsible for tidal pumping in the Tamar include flood-dominant currents, an up-estuary maximum in current speeds, and high-water slack periods which are much longer than low-water slack periods.

There is a bed-shear stress below which SPM settles and deposits. This critical bed-shear stress, measured by laboratory experiments, lies between 0.06 and 0.10 N m^{-2} (Delo, 1988). Little time is available for settling and deposition at low water, whereas a considerable time is available at high-water slack. This long, near-bed, slack-water period is due partly to overtide effects and partly to buoyancy effects.

The near-bed, slack currents which occur over the high-water period tend to be directed up-estuary in the stratified region, so that settling flocs move towards the FSI there. Near-bed currents are typically of the order of 0.05 m s^{-1}, so that the up-estuary distance travelled over a 2h period by a particle in suspension is less than 0.4 km. While this distance is short, the mechanism nevertheless provides a tendency towards accumulation of fine sediment in the upper reaches for those particles with very slow settling velocities. This mechanism is illustrated by Gibbs *et al.*, 1989 (their Figure 12).

The settling velocity of Tamar SPM has been measured using an Owen Tube. Values depended on location and season. During July 1988, the median settling

velocity within the Owen Tube had a power-law form with SPM concentration. For SPM concentrations in the range 1-2 kg m^{-3}, flocs settled through 1 m of still water in 5-18 min, indicating significant settling in the upper reaches at low water and pronounced settling at high water. These very fast settling velocities imply the formation of large flocs due to differential settling and appear to be relevant to natural conditions around slack water, because of the order of magnitude increase in floc sizes observed at high water in the Tamar (West *et al.*, 1990). Therefore, at high concentrations, SPM rapidly deposits with the approach of high-water slack, leaving a decaying, low concentration of SPM. This remaining SPM has much slower settling velocities and, close to the bed, moves up-estuary towards the FSI in the slow, near-bed currents. Near the surface, the remaining SPM moves down-estuary. Experimental evidence for these processes, and a discussion of the effects of floc size and buoyancy-driven circulation on the formation of the turbidity maximum in the Gironde Estuary, are given by Gibbs *et al.* (1989).

A summation of these mechanisms is able to qualitatively explain the observed distributions of SPM and mobile, bed-source sediment in the Tamar. However, the isolation of a dominant mechanism for TM formation is not a straightforward exercise. It will require a combination of numerical, sediment-transport modelling and a greatly improved knowledge of SPM characteristics and SPM-water interactions. The interpretive analysis of Gibbs *et al.* (1989) essentially ignores tidal effects, whilst the numerical modelling of Uncles *et al.* (1988) ignores buoyancy effects. Both baroclinic and barotropic effects must eventually be incorporated, together with adequate parametrizations for SPM size and settling velocity characteristics.

Conclusions

Main results from the daily-averaged synthesis of near-bed SPM variability at CK (7 km from the head) and HQ (12.5 km from the head) are:

(1) Correlations between daily-averaged SPM concentrations, runoff and tidal range during the separate deployments often showed a significant dependence of SPM on these variables. Increasing tidal range tended to enhance SPM levels because of resuspension of bed sediments. Increasing runoff tended to lower SPM levels during a deployment.

(2) There was a difference between the daily-averaged SPM concentrations on the rising and falling spring-neap cycle. On the rising cycle, the SPM levels were lower than on the falling cycle for the same tidal range.

Main results from the daily-averaged synthesis of seasonal variability of near-bed SPM at CK and HQ are:

(1) The daily-averaged SPM during 3.8 m tidal-range, rising spring tides at stations CK and HQ were relatively large during July 1988 and November 1988 and then

fell to very low levels during December 1988. This reduction in SPM was a manifestation of the winter period of bed-sediment depletion. Sediment was scoured from the upper estuary by strong ebb currents, which were enhanced by high and increasing runoff.

(2) The daily-averaged SPM concentrations at HQ during April 1989 were very high, being much higher than those at CK; levels at CK remained comparable with March values. This indicates that the bed-sediment supply had moved up-estuary to the vicinity of HQ so that local resuspension was very important there.

(3) Fine sediment continued to move into the upper reaches during the spring to summer period. By May 1989 the daily-averaged SPM concentrations at CK were very high, being much higher than those further down-estuary at HQ. For the June and (both) July 1989 deployments, SPM levels at CK exceeded those at HQ, although at both stations the levels were smaller in July as the limited amount of unconsolidated, fine sediment moved further up-estuary.

These interpretations of the seasonal variations in SPM levels are largely consistent with observations of the bed-sediment distributions and estimates of the FSI locations, although the grab-sample surveys were not undertaken during 3.8 m tidal-range, rising spring tides. Salient features of the seasonal variations in the longitudinal distributions of mobile bed-source sediment are:

(1) The winter survey of 13 March, 1990 revealed no mobile, muddy sediment on the bed of the main channel in the upper 9 km. Only two regions of unconsolidated mud were observed further down-estuary, one between 9 and 12 km and one between 19 and 21 km. These regions probably contained the remnants of the mobile sediment stock which had been accumulated in the upper estuary during the summer months and subsequently redistributed down-estuary during high runoff winter conditions.

(2) It is likely that several freshwater spates were required to completely scour the upper estuary of mobile mud over the winter period. Some of the scoured, fine sediment may have been flushed to sea in the surface waters, but much was redistributed over the intertidal flats in mid-estuary and in localized pockets on the bed.

(3) Results of Bale's 1982 mud-pole study can be compared with those from our 1989-1990 grab-sample surveys. From January to April 1982, Bale *et al.* (1985) found that mobile bed-source sediment was absent in the upper 10 km of estuary, but that it was accumulated to depths of 0.1-0.2 m in localized depositional areas between 10 and 20 km from the head (Weir Head). The distribution of mobile sediment in localized patches, observed in March 1990, was similar to that observed during January to April, 1982. However, in April 1989 the region of mobile sediment lay further up-estuary and was more continuous. This is probably because the freshwater runoff in early 1989 was relatively low, with a

maximum, monthly-averaged runoff of only 40 $m^3 s^{-1}$. In early 1990 the maximum monthly-averaged runoff was 87 $m^3 s^{-1}$, and 53 $m^3 s^{-1}$ in early 1982.

(4) Summer observations of mobile sediment accumulations during 1982 and 1989 were more comparable. Surveys reported by Bale *et al.* (1985) were made during mid to late summer and indicated accumulations of up to 0.4 m depth over the upper 8 km of estuary. Our observations indicated an up-estuary migration of the mobile bed sediment over the mid-summer to autumn period. The mobile mud lay between 1-7 km from Weir Head during June and July and between 0-6 km during October 1989.

(5) Sedimentary deposits in the mid-estuarine region, 10-20 km from Weir Head, were devoid of mobile mud in both sets of summer observations. This reflected the extended period of low freshwater runoff over the two periods, with mobile sediment gradually being moved up-estuary throughout a period of about 6 months.

(6) The increased depth of mud which was observed in the upper estuary during the summer 1982 mudpole surveys was due to accumulation of sediment and its up-estuary movement into regions of decreasing width. This was also the case for our 1989 summer surveys. In July 1989 the thickness of unconsolidated mud within the main channel of the upper 3 km of estuary reached a depth of 1 m.

Acknowledgements. We are grateful to N. Bowley and F. Holt for invaluable assistance during the field work. M.L.B is grateful to the Natural Environment Research Council (UK) for a Ph.D. studentship grant during the course of this study and to Dr J.R. West (Joint supervisor, Department of Civil Engineering, University of Birmingham, UK) for his close interest in the work and encouragement.

References

Allen, G.P., J.C. Salomon, P. Bassoulet, Y. Du Penhoat and C. De Grandpre, Effects of tides on mixing and suspended sediment transport in macrotidal estuaries, *Sedimentary Geology*, 26, 69-90, 1980.

Allen, G.P., G.Sauzay, P. Castaing and J.M. Jouanneau, Transport and deposition of suspended sediment in the Gironde Estuary, France, in *Estuarine processes*, edited by M Wiley, 63-81, Academic Press, N.Y., 1977.

Bale, A. J., The characteristics, behaviour and heterogeneous chemical reactivity of estuarine suspended particles. Ph D Thesis, Plymouth, UK, 216pp, 1987.

Bale, A. J., A. W. Morris and R. J. M. Howland, Seasonal sediment movement in the Tamar Estuary, *Oceanologica Acta*, 8, 1-16, 1985.

Buller, A. T., and J. McManus, Sediment sampling and analysis, in *Estuarine hydrography and sedimentation*, edited by K. R. Dyer, 87-130, Cambridge University Press, 1979.

Delo, E.A., Estuarine muds manual. Report SR 164. Hydraulics Research, Wallingford, U.K., 1988.

Dyer, K.R., *Coastal and estuarine sediment dynamics*, John Wiley, Chichester,pp 342, 1986.

Dronkers, J., Tide-induced residual transport of fine sediment, in *Physics of shallow estuaries and bays*, edited by J. van de Kreeke, 228-224, Lecture notes on coastal and estuarine studies, 16, Springer-Verlag, 1986.

Festa, J.F. and D.V. Hansen, Turbidity maxima in partially mixed estuaries: A two-dimensional numerical model, *Estuarine and Coastal Marine Science*, 7, 347-359, 1978.

Gibbs, R. J., D. M. Tshudy, L. Konwar and J. M. Martin, Coagulation and transport of sediments in the Gironde Estuary, *Marine Geology*, 36, 987-999, 1989.

Gibbs, R. J. and E. Wolanski, The effect of flocs on optical backscattering measurements of suspended material concentration, *Marine Geology*, 107, 289-291, 1992.

Grabemannn, I. and G. Krause, Transport processes of suspended matter derived from time-series in a tidal estuary, *J. Geophysical Research*, 94, 14373-14379, 1989.

Hamblin, P.F., Observations and model of sediment transport near the turbidity maximum of the Upper Saint Lawrence Estuary, *J. Geophysical Research*, 94, 14419-14428, 1989.

Kirby, R.A. and W.R. Parker, The physical characteristics and environmental significance of fine-sediment suspensions in estuaries, in *Estuaries, Geophysics and the environment*, edited by C.B. Officer, 110-120, National Academy Press, Washington, D.C. , 1977

Officer, C.B., Physical dynamics of estuarine suspended sediments, *Marine Geology*, 40, 1-14, 1981.

Officer, C.B. and M.N. Nichols, Box model application to a study of suspended sediment distributions and fluxes in partially mixed estuaries, in*Estuarine Perspectives*, Academic Press, London, 329-340, 1980.

Sheng, Y.P. and C. Villaret, Modeling the effect of suspended sediment stratification on bottom exchange processes, *J. Geophysical Research*, 94, 14429-14444, 1989

Uncles, R.J., R.C.A. Elliott and S.A. Weston, Observed fluxes of water, salt and suspended sediment in a partly mixed estuary, *Estuarine, Coastal and Shelf Science*, 20, 147-167, 1985a.

Uncles, R.J., R.C.A. Elliott and S.A. Weston, Dispersion of salt and suspended sediment in a partly mixed estuary, *Estuaries*, 8, 256-269, 1985b.

Uncles, R.J., R.C.A. Elliott and S.A. Weston, Lateral distributions of water, salt and sediment transport in a partly mixed estuary. *Proc. of the 19th Int. Conf. on Coastal Engineering*, ASCE, 3067-3077, 1985c.

Uncles, R.J., J.A. Stephens and T.Y. Woodrow, Seasonal cycling of estuarine sediment and contaminant transport, *Estuaries*, 11, 108-116, 1988.

Uncles, R.J. and J.A. Stephens, Distributions of suspended sediment at high water in a macrotidal estuary, *J. Geophysical Research*, 94, 14395-14405, 1989.

Uncles, R.J., J.A. Stephens, R.H. Bruce, C.D. Barrett and N.J. Bloomer, Observations of temporal variability in a partly mixed estuary using a new instrument package, in *Developments in estuarine and coastal study techniques*, edited by J. McManus and M. Elliott, 151-158, Olsen and Olsen - International Symposium Series, Fredensborg, Denmark, 1989.

Uncles, R.J. and J.A. Stephens, The freshwater-saltwater interface and its relationship to the turbidity maximum in the Tamar Estuary, U.K., *Estuaries*, 16, 126-141, 1993a.

Uncles, R.J. and J.A. Stephens, Nature of the turbidity maximum in the Tamar Estuary, U.K., *Estuarine, Coastal and Shelf Science*, 36, 413-431, 1993b.

West, J.R., K.O.K. Oduyemi, A.J. Bale and A.W. Morris, The field measurement of sediment transport parameters in estuaries, *Estuarine, Coastal and Shelf Science*, 30, 167-183, 1990.

Wolanski, E., J. Chappell, P. Ridd and R. Vertessy, Fluidization of mud in estuaries, *J. Geophysical Research*, 93, 2351-2361, 1988.

23

Dry Season Hydrodynamics and Sediment Transport in a Mangrove Creek

P. Larcombe and P. V. Ridd

Abstract

Mangroves are tropical ecosystems of great ecological significance, but the relationship between their hydrodynamics and sedimentation patterns has been given little attention in the literature. This study quantified bedload and suspended-load sediment fluxes in Gordon Creek, a 3 km long mesotidal creek and mangrove swamp system in N.E. Australia, which occupies an area of ca. 1.5 km^2. Tidal current, suspended sediment, and bedload transport data were collected in a mangrove creek and adjacent mangrove forest flat during the dry season which operate for 9-10 months of the year. Analysis of this data indicate that sediment transport is influenced by the relative elevation of the mangrove forest flat. 'Overbank' tides, which inundate the mangrove forest flat, create strong ebb currents in the creek, which flush bedload seaward at instantaneous transport rates of up to 0.3 kgs^{-1} per metre of creek width. Suspended sediment fluxes peak on the flood tide, also at 0.3 kgs^{-1} per metre of creek width. 'Within-creek' tides of smaller range have weaker currents, and, because they do not inundate the mangrove forest flat, the flood and ebb currents are of similar strength. Under these conditions, sediment transport rates are greatly reduced.

Dry season conditions produce a tidally-driven annual seaward discharge of bedload sediment in the creek of up to ca. 400 tonnes. Time-series data in the mangrove creek reveal no clear tendency for net transport of suspended sediment, but data from the mangrove forest flat suggest net landward movement of suspended sediment. The upper bound on the calculated accumulation rate of mud is in the order of 1.6 mm/yr.

Mixing in Estuaries and Coastal Seas
Coastal and Estuarine Studies Volume 50, Pages 388-404
Copyright 1996 by the American Geophysical Union

Introduction

Mangrove swamps play a vital role in the nutrient cycle and ecology of coastal waters (Alongi, 1990; Boto and Robertson, 1990; Flores-Verdugo et. al., 1990; Vance *et al.*, 1990). These ecosystems are under increasing pressure from coastal development, but very little is known of how creek-swamp systems respond to man-made alterations. Mangroves are also important in a geological context. Cores through preserved ancient mangrove deposits form a major part of the database on sea-level rise over the last 8-9 ky (Woodroffe, 1990; Carter *et al.*, 1993). However, interpretation of preserved mangrove deposits is limited by a lack of understanding of the sediment dynamics of mangrove swamps. Further, there is a need to predict coastal change resulting from sea-level rise. Despite the obvious need, there are few published studies of sediment transport processes in tidal mangrove systems.

This paper describes aspects of sedimentary processes within a mesotidal mangrove creek and forest system in north Queensland, Australia. The system is of the 'riverine forest' type of mangrove, as defined by Lugo and Snedaker (1974). Throughout this paper, suspended sediment concentration is abbreviated to SSC.

Study Site and Methods

This study summarises a number of field experiments conducted between 1990 and 1992 on bedload and suspended-load sediment fluxes in Gordon Creek, near Townsville, Australia (Figure 1). The southern fringe of Cleveland Bay contains several mangrove creek systems, each subject to a mesotidal regime and seasonal freshwater input. Gordon Creek is a 3 km long mangrove creek, a tributary of Ross River, which discharges into the sea at Townsville (Figure 2). The creek is mostly between 5 m and 20 m wide, and the silty sand or lag gravel which forms the creek bed in the middle and lower reaches is exposed in places at low water. The sandier shoals contain current ripples and megaripples, and are bioturbated by burrowing crustaceans (*Callianasa* sp.).

The creek margins are formed of a muddy high-tidal mangrove forest flat, lying at an elevation of ca. +2.9 m Townsville Port Datum (or 1.2 m above mean sea level). The mangrove forest flat extends for up to 400 m away from the creek, and the floor of the dense forest has large aerial branching roots and stump-like pneumatophores, in a thick organic mud which is burrowed heavily by crustaceans. Beyond the mangroves are salt flats. These are only fully inundated on the largest tides of the year. The mangrove forest and salt flat together occupy approximately 1.5 km^2.

Field data was collected in the tropical dry season, which operates for ca. 9-10 months of the year, when freshwater input is generally absent. The study included measurements at one site in the creek and another site in the muddy mangrove forest (Figure 2). Equipment was deployed exclusively in the creek on neap tides, and was divided between creek and mangrove sites on spring tides in order to sample overbank flows.

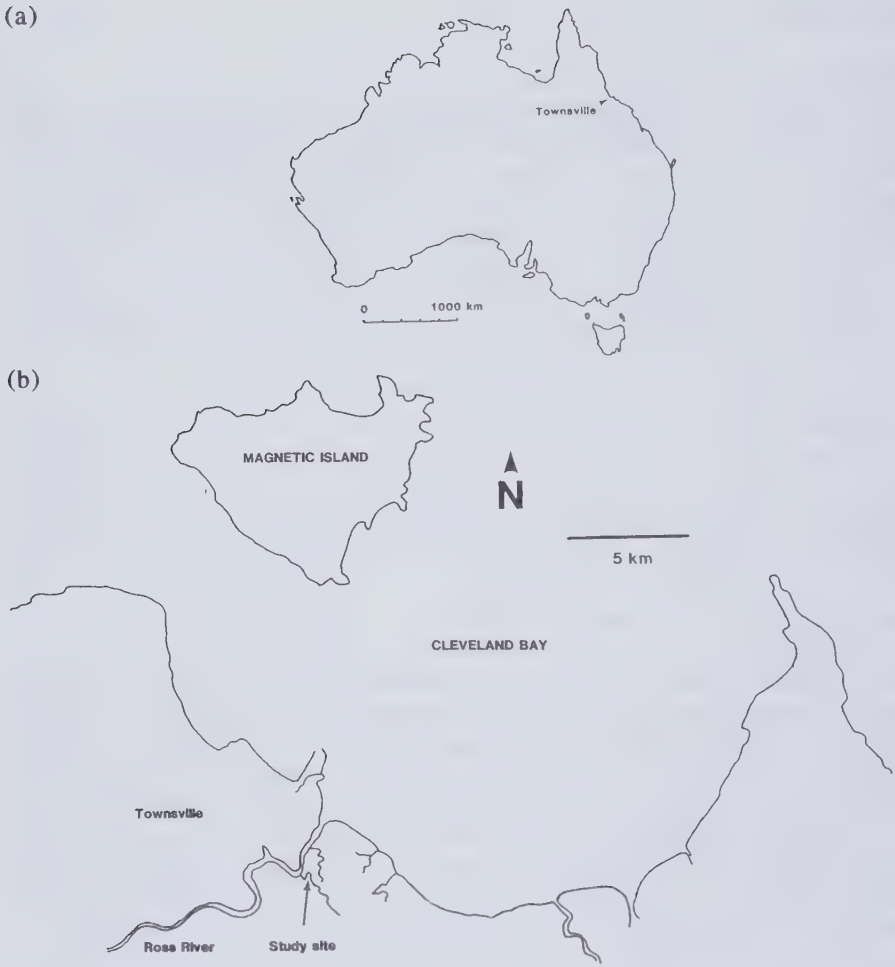

Figure 1. Location map showing a) Australia, b) Cleveland Bay and the study site (Gordon Creek).

Creek Site

At this site, the creek is 15-20 m in width and has a sandy bed formed into current ripples and larger megaripples, up to 4 m in length and 0.2 m high. Megaripple crests extend across the full width of the creek, and have the same orientation across the creek. The creek bed slopes gently upwards towards its south side forming an intertidal shoal ca. 20 m long and 10 m in width, and of grain size 0.4 mm. These sand accumulations in Gordon Creek are transient features formed

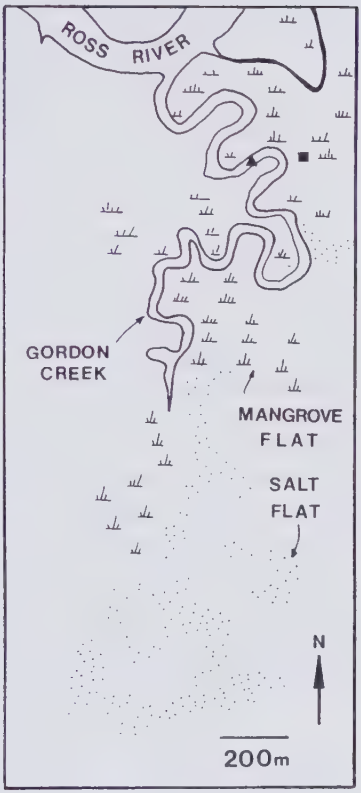

Figure 2. Plan of Gordon Creek showing distribution of mangrove forest flats and salt flats, and the locations of the two study sites, 'Creek Site' (filled triangle) and 'Mangrove Site' (filled square). Creek width has been increased for clarity.

locally (downstream from bank collapses) and the consistent megaripple orientations indicate that tidal re-circulation does not contribute to the shoals presence. The equipment deployed at this site is outlined below.

- 1 or 2 Interocean S4 current meters (measuring the average velocity every 60 s) measured currents at 0.5 m above the bed.

- 1 optical backscatter nephelometer measured suspended sediment concentrations (SSC) 0.5 m above the bed, taking one 10 s average every 2 minutes. A typical nephelometer calibration curve is shown in Figure 3. Due to potential changes in grain size, to which nephelometers are sensitive (Gibbs and Wolanski, 1992; Conner and De Visser, 1992) and which may occur even during a single tidal cycle, errors in the inferred SSC are estimated to be in the order of 20-40%.

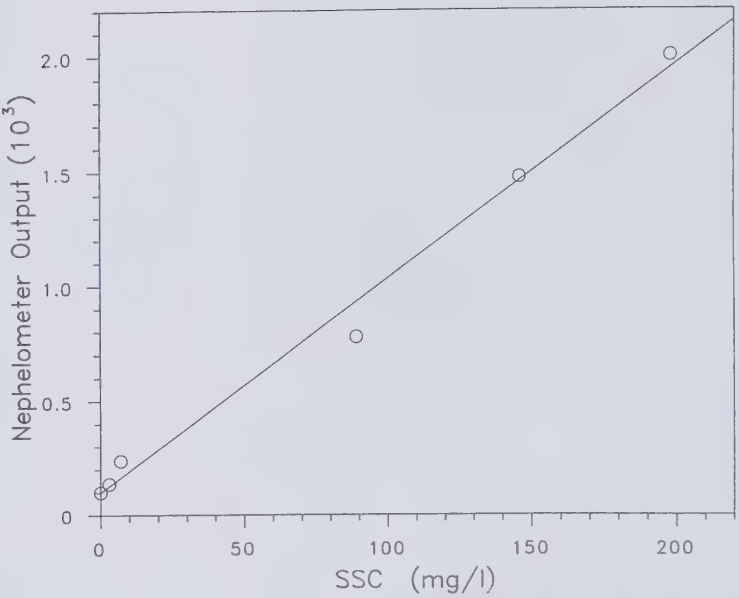

Figure 3. A typical calibration curve for nephelometers used in this study, plotting known SSC of a field sample (measured by filtration of a water sample) against raw nephelometer output (NO). The least squares linear regression is, SSC = (NO-99.5)/9.32 ($r^2 = 0.99$).

- Three electromagnetic bed-level sensors (Ridd, 1993) recorded bed level every 120 s, at 3 positions, 60 cm apart, on the intertidal shoal in the creek bed. In addition, a linear transect 15 m long and orientated axial with the creek, was surveyed daily to determine the position and shape of the megaripples. Together, this information allowed determination of the bedload flux associated with the migration of megaripples (details in Larcombe and Ridd, in press).

- On the largest spring tide, vertical profiles of SSC were measured in the creek at 15 minute intervals over the 10 h period of tidal influence. From a canoe, a direct reading nephelometer was lowered to the appropriate depth on a rod, and a 30 s average reading was recorded.

Mangrove Site

This site is amongst aerial Rhizophora roots ca. 100 m from the main creek (Figure 2). The sediment is comprised of a black, silty clay and is extensively bioturbated by crabs. The equipment deployed was:

- 1 or 2 Interocean S4 current meters, (measuring the average velocity every 60 s), installed at 0.2 m above the bed.

- 1 or 2 optical backscatter nephelometers, which measured suspended sediment concentrations (SSC) 0.12 m above the bed, taking a 10 s average every 2 minutes.

Results

A - Tidal Characteristics

The tide at Townsville is semi-diurnal and mesotidal, with mean spring and neap tidal ranges of 2.5 m and 0.6 m respectively. The elevation of the mangrove forest flats at the study site is ca. +2.9 m, resulting in only 165 overbank tides in 1992. A strong semi-diurnal inequality up to 1 m in high tide level (Figure 4) means that only alternate spring high tides inundate the mangrove forest and the salt flats beyond. On these large tides the ebb tide becomes accelerated so that ebb tidal currents are significantly stronger than the flood, similar to observations in mangrove creeks on Hinchinbrook Island, Queensland (Wolanski *et al.*, 1980). At neap tides, the mangroves are not inundated and the ebb is not enhanced.

The tidal currents at the creek site in Gordon Creek (Figure 5) are thus ebb-dominated at springs and slightly flood-dominated at neaps (Larcombe and Ridd, in press) with maximum velocities at spring tides of over 0.98 ms^{-1} (ebb) and

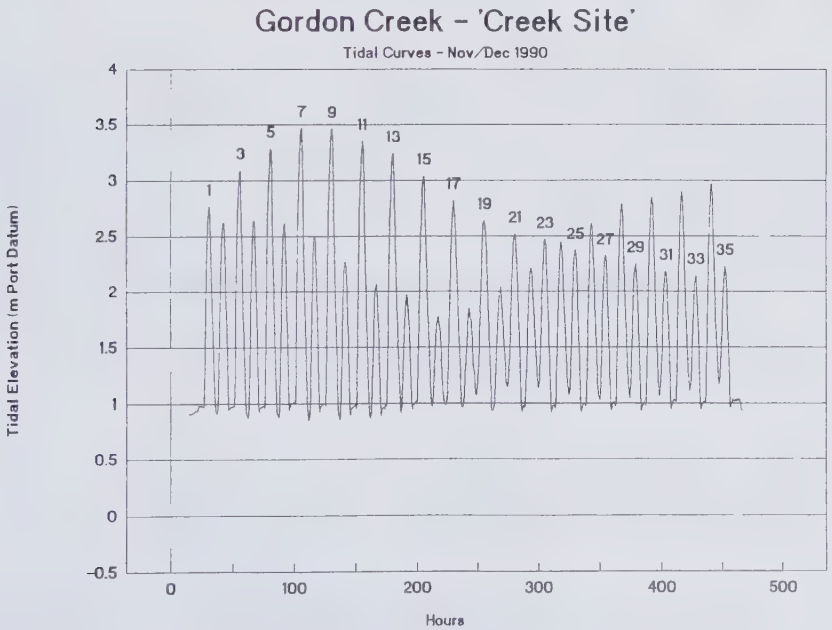

Figure 4. Tidal curve for the spring-neap period at the Creek Site.

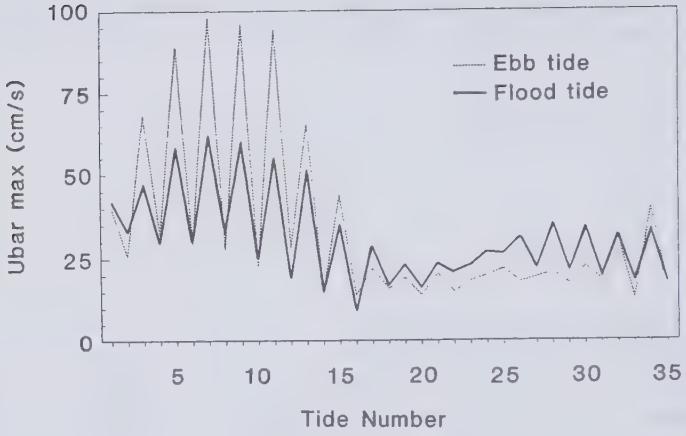

Figure 5. Tidal currents for the spring-neap period at the Creek Site.

0.68 ms^{-1} (flood). At the mangrove site, the tidal currents are nearly rectilinear, flooding towards ENE and ebbing to the W. Velocities of over 0.20 ms^{-1} occur at the mangrove site just before exposure during ebb. At the creek site, spring tides exhibit a phase lag between elevation and currents, with a landward current of 0.1-0.2 ms^{-1} at high tide which contributes volumes of water to produce high water further upstream. High water is delayed by ca. 30 minutes between Townsville Harbour and the mangrove site a distance of ca. 4 km.

In Gordon Creek, flood tides which do not inundate the swamp ('within-creek' tides) are relatively simple in nature, and have a gradual rise and fall in velocity (Figure 6). Where the mangrove flats are inundated ('overbank tides') there is a pronounced double peak in velocity on the flood tide, which is more pronounced the greater the inundation. The first peak coincides with a bankfull main creek immediately before inundation of the mangrove flats, and represents the maximum velocity attained in the creek whilst constrained by its banks. This velocity peak is predominantly a result of high surface slopes. The second peak represents maximum velocities attained in the creek with the flats inundated to a depth of 0.3-0.5 m. Where inundation of the mangrove forest flat has occurred, the ebb tide in the creek develops an extended period of high velocity.

B - Suspended Sediment Transport

(i) Suspended sediment transport ***at the Creek Site***

Figure 7 shows a set of SSC profiles taken during a large spring tide, taken at depths between 0.1 m below the surface and 0.3 m above the bed. The majority of SSC profiles are near-vertical with slightly higher concentrations near the bed,

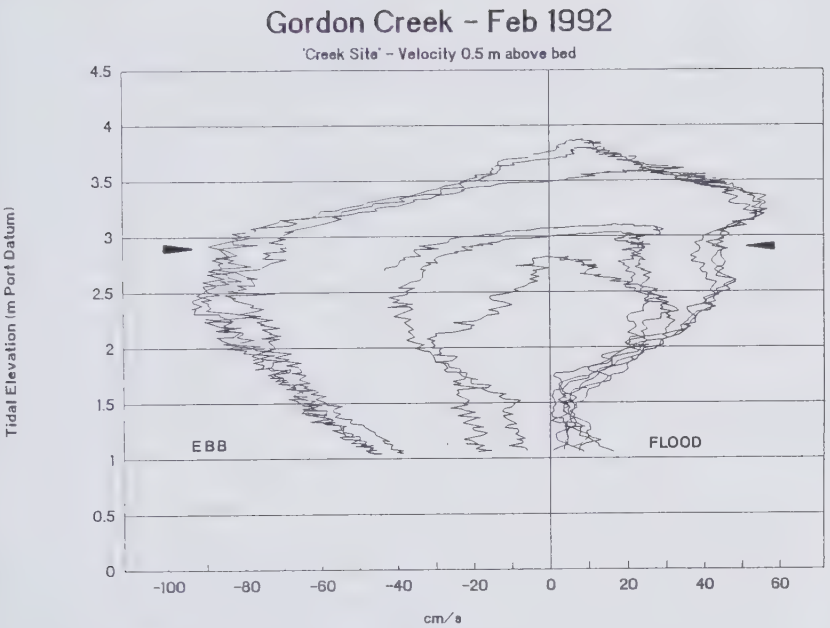

Figure 6. Velocity v Stage curves for 5 tidal cycles at springs. Arrows show the elevation of the mangrove forest flats. Note the distinct ebb-dominant overbank tides, which also have a complex flood tide signature.

indicating a water column well-mixed by the turbulent tidal currents. The flood tide SSC profiles rapidly increase in magnitude, increasing from a depth mean SSC of ca. 15 mg/L to ca. 120 mg/L in only 60 minutes, and more slowly decrease towards high water. In contrast, the ebb tide has a more gradual rate of SSC increase toward it's peak of ca. 80 mg/L, which decreases only slightly towards the end of the ebb flow. Complexity in the profiles is related to the overtopping of the creek banks and resultant inundation by the flood tide of the mangrove forest flats. There is a smaller effect upon exposure of the mangrove forest flats on the ebb.

- *On the flood tide*, immediately following inundation (at 1900 h), the mean SSC throughout the water column was more than doubled. On inundation, leaf litter, mangrove seed cases and other organic matter was floated off the surface of the forest flat. Where there are sharp meanders in the main creek, this material flowed across the forest flat and into the main creek again, producing a temporary surface layer of high SSC (1930 h), so that the water column in the main creek had a complex vertical SSC profile. For over 30 minutes the surface SSC was actually higher than near the bed.

  Closer to high water, the sediment became vertically mixed by turbulence, and the effects of the surface input of suspended sediment decreased. Water which had travelled up the centre of the creek showed a conventional downward

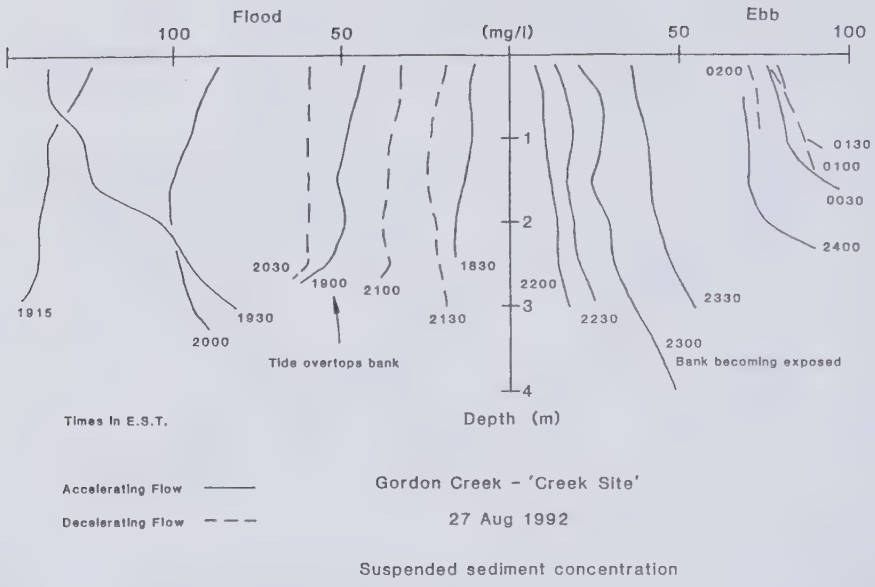

Figure 7. Suspended sediment profiles at the Creek Site for peak spring tide. All profiles are shown w.r.t. the water surface. Solid lines indicate accelerating flow, dashed lines indicate decelerating flow. The mangrove flat was inundated at ca. 1900 h and exposed at ca. 2310 h.

increase in SSC (2000 h), further indicating that the mangrove forest flat provided the material to raise the SSC in the surface water. The decrease in SSC from 1915 h to 2000 h, despite continuing flow acceleration, may be due to the arrival of less muddy marine water from Cleveland Bay, together with landward removal of material on the mangrove forest flat which was resuspended upon initial inundation.

- *On the ebb tide*, there was a slight increase in SSC in the upper 1-1.5 m of the water column as the mangrove flats became exposed (2300 h). This is probably related to minor low relief creeks across the forest flats which drain muddy water into the surface of the main creek. Maximum SSC's peaked 2 hours later (0030-0130 h) when the tide was ca. 1 m below the elevation of the mangrove forest flats. Muddy water continued to drain into the main creek late into the ebb tide, but drainage decreased in magnitude.

(ii) Suspended sediment transport *at the Mangrove Site*

Tidal currents over the mangrove forest flats are too weak to produce any bedload transport, and it is suspended transport of fine-grained sediment that dominants. There are few overbank tides withinin each lunar cycle (ca. 6 on each set of spring

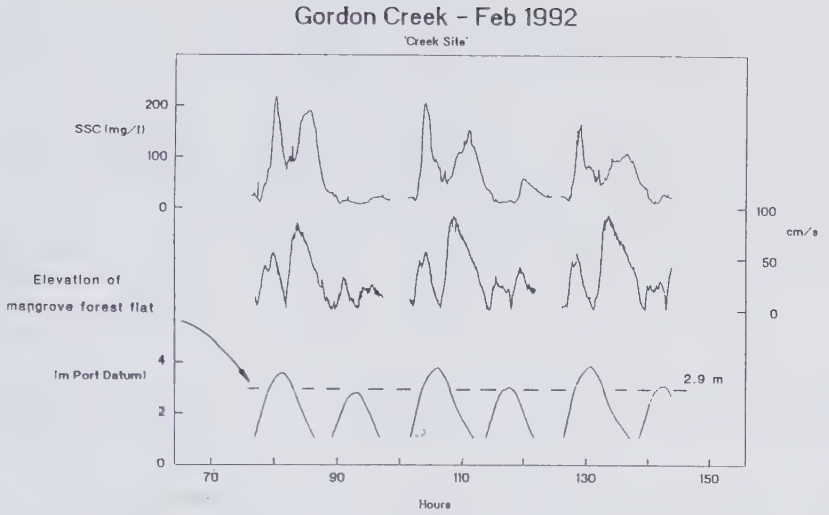

Figure 8. Time series of: a) Tidal elevation (m Port Datum); b) Tidal velocity (cms^{-1}); and c) Suspended sediment concentration (mg/L) for 6 flood-ebb cycles at spring tides at the Creek Site. Velocity and SSC data refer to 0.5 m above bed. The elevation of the mangrove forest flats is shown relative to the tidal curves.

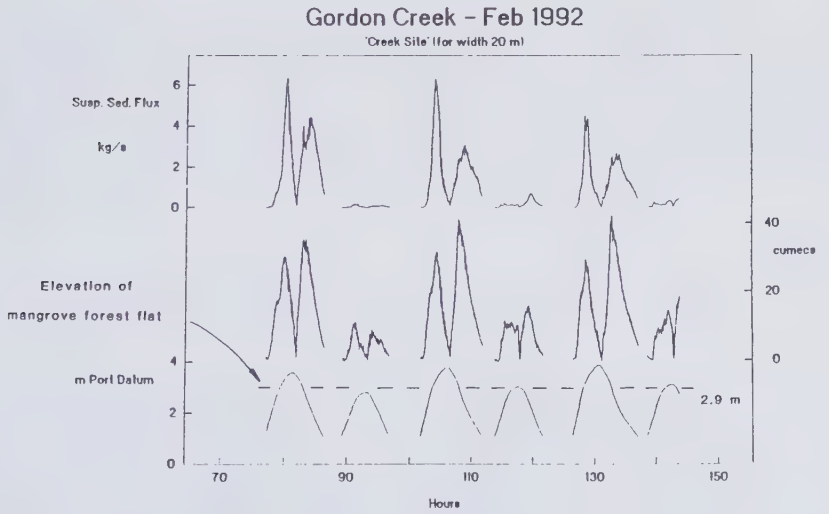

Figure 9. Time series of: a) Tidal elevation (m Port Datum); b) Tidal discharge (cumecs); and c) Suspended sediment flux (kgs^{-1}) for 6 flood-ebb cycles at spring tides at the Creek Site. Calculations assume a constant creek width of 20 m, and vertical and lateral uniformity in velocity and SSC.

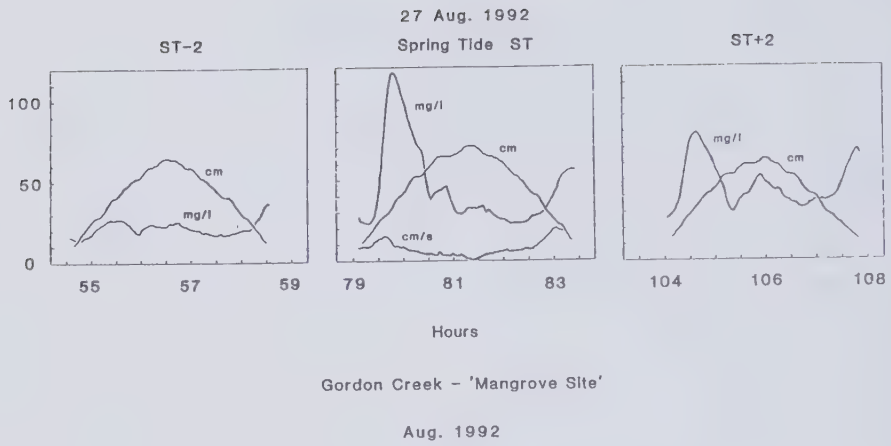

Figure 10. Time series of: a) Tidal elevation (m Port Datum); b) Tidal velocity (cms^{-1}); and c) Suspended sediment concentration (mg/L) for 3 overbank tides at the Mangrove Site. Current data was measured 0.2 m above bed, and SSC was measured 0.12 m above bed. Due to the low water depths, current data from the current meters was only reliable for the very high spring tide at 81 hours.

tides). Measured at 12 cm above bed, SSC's vary between 10 and 120 mg/L (Figure 10). A few features are common to most (but not all) of these tides:

- There is a lag of SSC with current velocity throughout the period of inundation, on accelerating and decelerating flows;
- After an initial increase, SSC's fall during tidal inundation, until the second half of the ebbing tide, where they increase again;
- SSC's generally have a higher peak concentration on the flood tide than on the ebb;
- The tidal currents are rectilinear in nature.

C - Bedload Sediment Transport

In the creek, transport of the megarippled fine-sand occurs when depth-averaged velocities exceed ca. 0.45 ms^{-1}, and significant bedload transport occurs in the form of megaripple migration at velocities above 0.55-0.6 ms^{-1}. Thus bedload transport occurs only on alternate spring tides (Figure 11) and overwhelmingly in the ebb direction (Larcombe and Ridd, in press). Instantaneous 'bedform transport rates' were ebb-directed at all times, attaining a peak of 0.29 kgs^{-1} per metre creek width late in spring tide ebb flows (Larcombe and Ridd, in review).

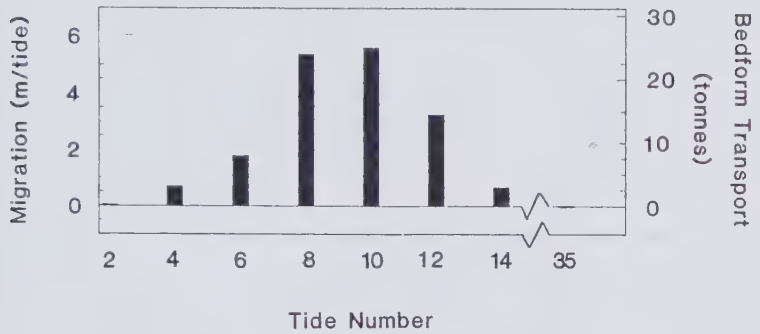

Figure 11. Net megaripple migration, with the approximate bedload transport equivalent in tonnes, for each flood ebb cycle for a spring neap period at the Creek Site. Net bedload transport was always seaward.

Discussion

i) Tides:

Tidal characteristics which, like Gordon Creek, are also controlled by the elevation of creek banks have been analysed by Bayliss-Smith *et al.* (1979) for tidal creeks in salt marshes, and modelled by Pethick (1980). Woodroffe (1985) noted similar differences between within-creek and overbank tides in a mangrove basin. In tidal mangrove environments, it is clear that the timing and relative velocity of flood and ebb tide velocity peaks are strongly related to the elevation of the mangrove forest flats.

ii) Suspended Sediment Transport

Sediment transport processes in this system are summarised in Table 1. The data from the creek site indicate that fine sediment is lifted off the mangrove forest flats and moved landward immediately following inundation of the flat by the flood tide. This process is responsible for the highest peak SSC's which occur, counter-intuitively, on the relatively weak flood tide (Figure 8). In the creek, SSC's reach a minimum ca. 10 minutes after high tide slack water, suggesting that settling takes place in the water column in the creek (there is also strong evidence for sediment settling onto the mangrove forest floor at high water). Net deposition in the mangrove forest may act to limit the quantity of sediment available for transport on the ebb tide.

TABLES 1. Summary of stages of flow and sediment transport in Gordon Creek for a spring tide flood-ebb cycle.

Tidal Height	*Main Creek*	*Mangrove Forest Flat*
EARLY RISING TIDE FLOW WITHIN CREEK < +2.9 m	Velocity <0.4 ms^{-1}. SSC profiles well-mixed, gradually increase from 15 to 120 mg/L. Negligible bedload transport	No transport.
LATE RISING TIDE TIDE NOW OVERBANK > +2.9m	Velocity < 0.7 ms^{-1}. Peak SSC (140 mg/L) and SS flux (6 kg s^{-1}) occurs 30 minutes after inundation of tidal flat. SSC profile locally complex due to transport off flats. SSC values fall as marine water arrives. Limited bedload transport, including slight re-working of megaripples.	Velocity slowly decreases from < 0.2 ms^{-1}. Flostation of organic matter and rapid resuspension of mud. SSG peaks at 80-120 mg/L and sediment transported into flats. Local lateral flow occurs across meander bends.
HIGH WATER ca. +3.2- +3.7 m	Velocity 0.1-0.2 ms^{-1} at HW. Some settling as SSC falls to minimum of ca. 10 mg/L at HW + 10 minutes.	Velocity < 0.5 ms^{-1}. SSC falls slowly to a minimum at HW + 60 minutes, inferring sediment accumulation.
EARLY FALLING TIDE TIDE STILL OVERBANK > +2.9 m	Velocity rapidly increasing to < 1 ms^{-1}. Slow SSC rise steepens sharply as flats are exposed. Seaward megaripple migration commences.	Velocity peak ca. 0.2 ms^{-1}. SSC continues to fall until resuspension threshold is exceeded ca. 60 mins before exposure. Muddy water flows back into main creek.
LATE FALLING TIDE FLOW WITHIN CREEK < +2.9 m.	Velocity slowly decreasing towards ca. 0.4 ms^{-1}. SSCs rises rapidly when flats are exposed with slight rise in SSC in upper 1 m. SSC raised by drainage from mangrove flat and maintained by high turbulence. SSC peaks > 2 hours after peak velocity. Bedload transport increases to peak when water depths < 1.5 m, late in the ebb tide.	Draining of muddy water into main creek, along shallow gullies, with some downcutting near the creek bank.
LOW WATER ca. +0.6 - +1 m.	Velocity drops rapidly to < 0.1 ms^{-1}. SSC remains at 0-5 mg/L. Deposition of mud drapes on moribund bedforms (neap tides).	Negligible final drainage from flats.

Flood tide SSC's have a negligible lag with respect to tidal velocity, but in contrast, the ebb SSC's lag in the creek velocity by 2 hours or more. This is interpreted as due to supply of sediment-laden water through shallow channels in the mudflat. This explanation is consistent with the observation that the SSC time-series data begin to rise markedly as the flats are exposed on the ebb tide, coincident with maximum velocities within the creek. This pattern further suggests that the supply of sediment to the ebb tide is limited.

Assuming a uniform SSC and velocity distribution across the creek cross-section, the product of current velocity and SSC was integrated for a number of flood and ebb tides. We acknowledge that this is a simplification of the true situation, because the pattern of across-creek SSC varies with the stage of the tide (particularly with overbank tides) and because tidal currents are stronger in the centre of the creek than at its margins (see also below), but it provides figures useful for later discussion. Further, measurements of SSC profiles indicate that errors in the flux calculations are probably small relative to the initial calibration errors of the nephelometers.

Figure 8 shows the time series of water and suspended sediment flux at the creek site, calculated for a creek width of 20 m. The total weight of suspended sediment transported past the creek site on overbank spring tides is calculated as 10-16 tonnes on each flood tide, and a similar amount on each ebb tide. No clear pattern of dominance of either flood or ebb sediment flux is revealed, and the differences in calculated sediment fluxes of flood and ebb tides are less than the errors in its measurement and calculation. Fluxes of suspended sediment on within-creek tides appear negligible.

Boon (1978) described the lateral variations in velocity in a 10.5 m wide creek, and found that an error of ±12% would result in mean water flux calculated from readings taken at only one station. In this study, such errors are compounded by errors in the measurement of SSC by nephelometers. Further, near high water on spring tides there is significant water and particulate transport through mangrove forest flats. The assumption that overbank water movement is negligible has been implicit or explicit in some other studies (e.g. Woodroffe, 1985b) but is clearly not valid for Gordon Creek where SSCs in overbank water can exceed 100mg/L and velocities may attain 20 cms^{-1}. This creek-normal flow makes calculations of water and sediment flux inaccurate (calculated water fluxes on the flood tides were between 25% less or greater than the ebb, and suspended sediment fluxes were similarly apparently variable). Further, the fact that turbid water is periodically present at the surface of the water column in the tidal creeks, related to dynamic processes in the mangrove forest flat, means that the use of simple models of SSC profiles (e.g. Rouse, 1937) to estimate suspended sediment fluxes is inappropriate in Gordon Creek, and probably also in similar mangrove systems.

The data from the mangrove site are interpreted as reflecting 3 sedimentary process phases on the mangrove forest flat:

1. During initial inundation, as depths increase, the flow accelerates across the flat, coincident with the velocity pulse in the creek. This induces some resuspension of material, thus sharply increasing SSC's;
2. Flows slacken around HW leading to some fallout of sediment from suspension (also evident at the creek site). Sediment settling continues throughout the first half of the ebb flow;
3. In the final period of inundation, accelerating ebb currents resuspend some sediment from the mangrove flat. A marked upward break in the SSC curve occurs up to 60 minutes before exposure on peak spring tides (e.g. Tide 7).

An alternative explanation for phase 3 is that muddier water is flowing out from higher in the mangroves, where circumstances may have somehow led to less sediment having been lost by settling. However, this would not explain the occasional occurrence of a higher peak SSC on the ebb tide rather than the flood, nor would it be consistent with observed erosion in some shallow channels within the mangrove forest flat; thus it is strongly implied that some resuspension occurs within the mangrove forest flat. Close to the edge of the mangrove flat, small gullies occur which drain water into the main creek. Some of these gullies show evidence of erosion, such as active downcutting, suggesting that small-scale erosion during the ebb tide also contributes to sediment supply to the main creek.

As (above) for the creek site, water and sediment fluxes were estimated for the mangrove site. A total of 13.4 kg of sediment per metre width of forest flat is brought past the sampling site on the highest spring flood tides (e.g. Spring Tide, Figure 10) half of which is retained within the swamp. The flow in the sampled part of the swamp is such that inflowing water returns along the same path, so the results suggest net landward movement of suspended sediment and net accumulation. There is only 5% difference in the calculated volumes of the flood and ebb tide water at the mangrove site, so while it is acknowledged that the sediment flux is derived from a simplified view of the processes, the strong inequality in the flux of suspended sediment appears real. (The authors have recently collected similar data from nearby Cocoa Creek, which shows a similar result).

These data are from one of the highest tides of the year, and are likely to represent an upper limit on the weight of sediment deposited by a single tide in the dry season. Smaller range, lower-velocity tides are likely to transport less sediment. Using a figure for net landward transport of 6.5 kg per m width per tide (ca. half the total flood flux), and using:

- the total number of all overbank tides for 1992 (165 tides)
- a mangrove flat 'length' (the integral of velocity) of 550 m
- an assumed initial sediment porosity of 50 % (Dyer, 1986),

we can calculate a notional annual sediment accumulation rate for dry season conditions of ca. 1.6 mm/yr. Given that these data are from a large tide, this value possibly represents an upper limit on accumulation rate for dry season conditions.

iii) Bedload Transport

The conclusion that the creek system flushes sand is consistent with the scarcity of sand in the creek and the presence of lag gravels in places along the creek bed. Megaripple migration data can be extrapolated to infer that the potential sand flushing rate for the dry season each year is ca. 180 m^3 or 400 tonnes. This rate will only be achieved given continuous sand supply to the creek, which is not the case. In the dry season, sand appears to be supplied only in discrete pulses, by bank collapses or when rapid meander cutoffs take place. A few months after the fieldwork for this study, the sand at the study site had almost been completely removed, and the quantity of sand had increased at the next downstream meander. No wet season data is yet available, although it is expected that bank collapses would be more frequent due to waterlogging of bank sediments. Some sand may be eroded from salt flats into the mangrove forest. In both cases, overall sand supply would probably be increased in wet season conditions.

Conclusions

This work and a related study (Larcombe and Ridd, in press) has inferred a net seaward flux of bedload sediment in Gordon Creek. It has also inferred that accumulation of fine sediment takes place on the mangrove forest flats by settling of sediment at high water spring tides. Both these effects are sedimentary consequences of the intimate relationship between the geomorphology of the creek-swamp system, and its hydrodynamics. In particular, the elevation of the mangrove forest flat affects the nature, magnitude and timing of the peak flood and ebb tidal currents.

This study measured dry season conditions in a highly seasonal environment. Further research is needed, particularly on wet season processes, to explain more fully the high sediment accumulation rates of preserved Holocene mangrove mud deposits along the North Queensland coast (ca. 6 mm/yr, Carter *et al.*, 1993), although our observations may allow a potential explanation for the lack of sand in many preserved mangrove deposits. The relative contribution to fine-grained sediment accumulation of the wet season and the influence of processes related to sea-level rise are as yet unresolved.

Acknowledgments. Simon Spagnol gave field assistance and helped in processing data from bed-level sensors and current meters. Mary Stafford-Smith kindly loaned a direct reading nephelometer, and Cheryl Ridd gave permission to use the R.V. Tirpitz. The Australian Research Council and James Cook University provided financial support. Two anonymous reviewers are thanked for their suggestions for improvements.

References

Alongi, D.M. Effect of mangrove detrital outwelling on nutrient regeneration and oxygen fluxes in coastal sediments of the Great Barrier Reef lagoon. *Estuarine Coastal Shelf Sci.*, 31, 581-598, 1990.

Bayliss-Smith, T.P. *et al*. Tidal flows in saltmarsh creeks. *Estuarine Coastal Mar. Sci.*, 9, 25-255, 1979.

Boon, J.D. Suspended-solids transport in a saltmarsh creek -an analysis of errors. In: *Estuarine Transport Processes*, edited by B.J. Kjerfve, University. S.C. Press, Columbia, S.C., pp.147-160, 1978.

Boto, K.G. and A.I. Robertson, The relationship between nitrogen fixation and tidal exports of nitrogen in a tropical mangrove system. *Estuarine Coastal Shelf Sci.*, 31, 51-540, 1990.

Carter, R.M., D.P. Johnson and K.G. Hooper, Episodic post-glacial sea-level rise and the sedimentary evolution of a tropical embayment (Cleveland Bay, Great Barrier Reef shelf, Australia). *Aust. J. Earth Sci.*, 40, 229-255, 1993.

Conner, C.S. and A.M. De Visser, A laboratory investigation of particle size effects on an optical backscatterance sensor. Mar. Geol., 108, 151-159, 1992.

Dyer, K.R. *Coastal and Estuarine Sediment Dynamics*. Wiley-Interscience, 342pp, 1986.

Flores-Verdugo, F. *et al*. Mangrove ecology, aquatic primary productivity, and fish community dynamics in the Teacapan-Agua Brava lagoon-stuarine system (Mexican Pacific). *Estuaries,* 13, 219-230, 1990.

Gibbs, R. and E. Wolanski, The effects of flocs on optical backscattering measurements of suspended material concentration. *Mar. Geol.*, 107, 289-291, 1992.

Larcombe, P. and P.V. Ridd, Megaripple dynamics and sediment transport in a mesotidal tropical mangrove creek - use of electromagnetic bed-level probes. *Sedimentology*, 1994 (In Press) .

Lugo, A.E. and S.G. Snedaker, The ecology of mangroves. In *Annual review of ecology and systematic,* edited by R.F. Johnston, P.W. Frank, P.W. and C.D. Michener, 5, 39-64, 1974.

Pethick, J.S. Velocity surges and asymmetry in tidal channels. *Estuarine Coastal Mar. Sci.*, 11, 331-345, 1980.

Ridd, P.V. A sediment level sensor for erosion and siltation detection. *Estuarine Coastal Shelf Sci.*, 35, 353-362, 1993.

Rouse, H. Modern conceptions of the mechanics of fluid turbulence. *Trans. Am. Soc. civ. Engnrs.*, 102, 436-505, 1937.

Vance, D.J., M.D.E. Haywood and D.J. Staples, Use of a mangrove estuary as a nursery area by postlarval and juvenile banana prawns, Penaeus merguiensis de Man, in northern Australia. *Estuarine Coastal Shelf Sci.*, 31, 689-701, 1990.

Wolankski, E., M. Jones and J.S. Bunt, Hydrodynamics of a tidal creek mangrove swamp system. *Aust J Mar Freshw Res.* 31, 431-450, 1980.

Woodroffe, C.D. Studies of a mangrove basin, Tuff Crater, New Zealand: II. Comparison of volumetric and velocity-area methods of estimating tidal flux. *Estuarine Coastal Shelf Sci.*, 20, 431-445, 1985.

Woodroffe, C.D. The impact of sea-level rise on mangrove shorelines. *Prog. in Phys. Geogr.*, 14, 483-520, 1990.

24

Uniform Bottom Shear Stress and Equilibrium Hyposometry of Intertidal Flats

C. T. Friedrichs and D. G. Aubrey

Abstract

Hypsometry is the distribution of horizontal surface area with respect to elevation. Recent observations of tidal flat morphology have correlated convex hypsometry with large tide ranges, long-term accretion and/or low wave activity. Concave hypsometry, in turn, has been correlated with small tide ranges, long-term erosion and/or high wave activity. The present study demonstrates that this empirical variation in tidal flat hypsometry is consistent with a simple morphodynamic model which assumes tidal flats to be at equilibrium if maximum bottom shear stress (τ) is spatially uniform. Two general cases are considered: (i) dominance of τ by tidal currents, where τ is equal to maximum tidally-generated shear stress (τ_T), and (ii) dominance by wind waves, where τ is equal to maximum wave-generated shear stress (τ_W). Analytic solutions indicate that a tidal flat which slopes linearly away from a straight shoreline does not produce a uniform distribution of τ_T or τ_W. If the profile is adjusted until either τ_T or τ_W is uniform, then domination by tidal currents favors a convex hypsometry, and domination by wind waves favors a concave hypsometry. Equilibrium profiles are also derived for curved shorelines. Results indicate that an embayed shoreline significantly enhances convexity and a lobate shoreline significantly enhances concavity — so much so that the potential effect of shoreline curvature on equilibrium hypsometry is of the same order as the effect of domination by τ_T or τ_W.

Mixing in Estuaries and Coastal Seas
Coastal and Estuarine Studies Volume 50, Pages 405-429
Copyright 1996 by the American Geophysical Union

Introduction

More than half of the world's non-Arctic coastlines are either macrotidal (spring range > 4 m) or mesotidal (spring range 2-4 m) (Davies, 1973). The study of equilibrium tidal flat morphology provides insight into the response of meso- and macrotidal coastlines to such external forcings as engineering works, periodic storm activity, and changes in relative sea level. Hypsometry, which measures cumulative horizontal basin area as a function of elevation, usefully represents broad aspects of tidal flat morphology in a concise and quantitative manner (e.g., Boon and Byrne, 1981). Recent observations (Dieckmann *et al.*, 1987; Kirby, 1992) relating characteristic tidal flat hypsometries to tide range, wind wave activity, and long-term accretion or erosion provide a base of empirical data with which to compare equilibrium hypsometries predicted by analytic theory.

Hypsometric analysis, which was formally introduced to geomorphology by Strahler (1952), is the study of the distribution of surface area of a land mass or basin with respect to elevation. Hypsometries are often presented as non-dimensional plots of relative elevation and relative surface area, allowing a comparison of hypsometry between systems having different scales. Strahler found distinctive hypsometries to be related to the erosional maturity of land regions formed in homogeneous strata. Boon (1975) and Boon and Byrne (1981) applied hypsometric analysis to the study of intertidal basins and used the hypsometry of intertidal storage areas to model patterns of asymmetric discharge in tidal channels near Wachapreague, Virginia.

Figure 1, modified from Boon and Byrne (1981), shows examples of basin morphologies and their associated hypsometries. In Figure 1 and throughout this paper, hypsometric plots display the cumulative horizontal basin area below a given contour. It is important to distinguish the hypsometry from the topographic profile, which is a plot of elevation versus horizontal distance along the gradient of the topography. In Figure 1, for example, all three topographies have linear profiles. Along a straight shoreline (Figure 1a) the profile and hypsometry are interchangeable. Along curved shorelines, however, the nonlinear transformation from profile to hypsometry causes a linear profile to produce a nonlinear hypsometry. If the profile is straight and the shoreline is embayed (Figure 1b), then the hypsometry will be convex. If the profile is straight and the shoreline is lobate (Figure 1c), then the hypsometry will be concave. Boon and Byrne (1981) emphasized the sensitivity of tidal flat hypsometry to shoreline curvature.

Recent observations of tidal flat hypsometry have related the form of the hypsometry to other factors including tidal range, exposure to wind wave activity and patterns of long-term accretion or erosion. In a study of tidal basins along the German Bight, Dieckmann *et al.* (1987) noted that hypsometries tend to be more concave for lower tidal range flats and more convex for higher tidal range flats (Figure 2a). In a study of macrotidal (spring range > 4 m) flats around Great Britain, Kirby (1992) related convexity to long-term accretion and concavity to long-term erosion (Figure 2b). At a few of the locations, Kirby in turn related accretion or erosion to protection from or

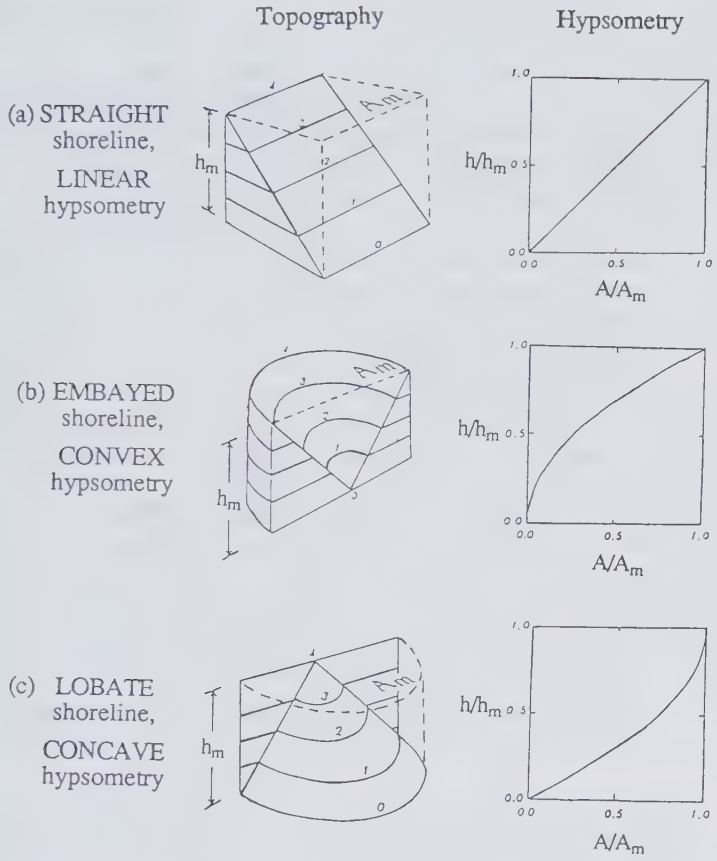

Figure 1. Block diagrams of topographies with linear profiles, along with their associated hypsometries (modified from Boon and Byrne, 1981): (a) Straight shoreline, (b) embayed shoreline, (c) lobate shoreline. h is elevation, h_m is maximum elevation, A is horizontal area, and A_m is maximum area.

exposure to wind waves. Figure 2b displays the examples of concave and convex hypsometries observed by Kirby along the Severn Estuary. Finally, in a study of sediment exchange off the wide macrotidal flats of western Korea, Wells and Park (1992) described a periodic increase in concavity associated with a seasonal increase in wave activity.

The hypsometric trends described above can be summarized by a qualitative ratio which indicates the relative importance of tidal currents and wind waves:

ratio of tidal to wave activity: high → CONVEX hypsometry
low → CONCAVE hypsometry

This correlation is consistent with observations from the German Bight if spatial variations in tidal range are assumed to be locally more important than spatial variations in wave activity. The same trend describes some of the flats in Great Britain if local variations in wave activity dominate variations in tidal activity. The ratio describes Korean flats, too, if temporal (rather than spatial) variations in wave activity are assumed to be most important.

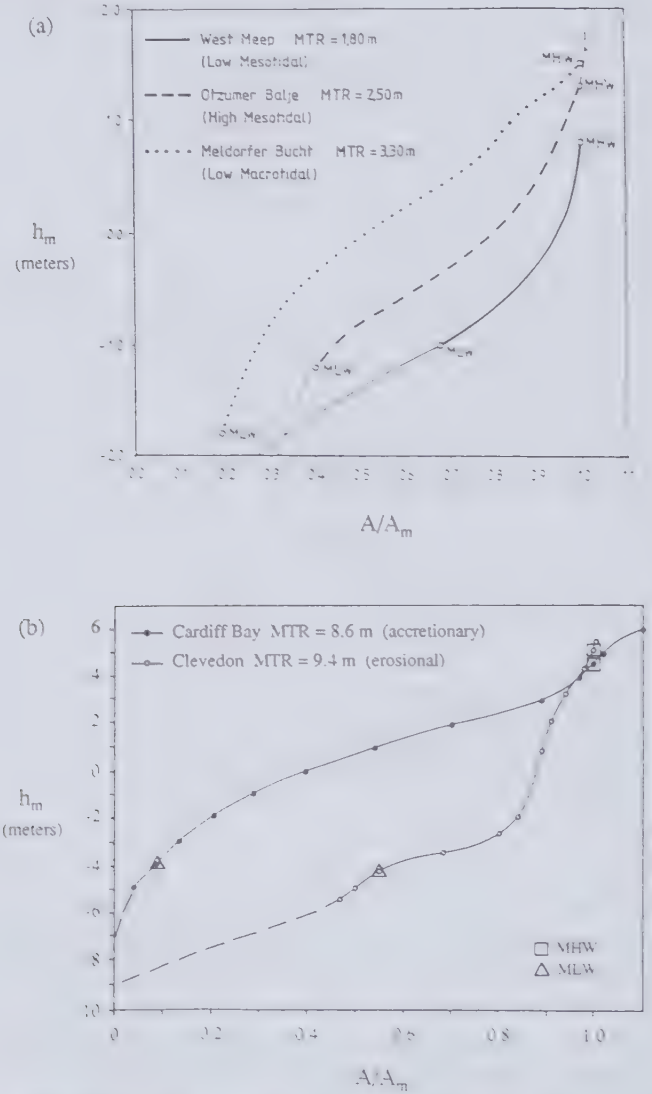

Figure 2. Hypsometries for tidal flats in (a) the German Bight (from Dieckmann *et al.*, 1987) and (b) the Severn Estuary (redrawn from Kirby, 1992). MTR is mean tide range, MHW and MLW are mean high and mean low water.

Morphodynamic Model

In this study it is assumed that a stable morphology will result when the distribution of maximum bottom shear stress (τ) is uniform across a tidal flat. This is a simplification of the more correct formulation that stable morphology results when there is a zero divergence in net sediment transport. Since common formulations for erosion, deposition and net transport are generally expressed as functions of bottom shear stress, often in the form of power relations (e.g., Dyer, 1986), the spatial distribution of bottom shear stress is a useful starting point before attempting to estimate sediment transport directly. Bottom shear stress can be derived from hydrodynamic relations more directly and with a greater degree of confidence.

A deviation of τ from its mean value across a flat is assumed to cause a local increase or decrease in the rate of sediment dispersal and to cause net erosion or deposition of sediment. This approach focuses on the diffusive nature of sediment transport and does not address the importance of asymmetries in the direction of bottom shear stress. The tidal and wind wave processes considered here are linearized so no asymmetries in direction of τ are generated. Clearly, asymmetries in τ can play a morphodynamic role. For example, Friedrichs *et al.* (1992) suggested that sheet-like intertidal flows tend to be flood dominant, which should enhance deposition. Nonetheless, if τ is considered to be symmetrical at first-order, then the spatial distribution of its magnitude alone should provide valuable insight into the morphology of stable tidal flats.

For tides in the absence of wind waves or for wind waves in the absence of tides, τ has been expressed as

$$\tau = \rho c_d U |U| , \qquad (1)$$

where ρ is the fluid density, c_d is a dimensionless drag coefficient, and U is maximum depth-averaged velocity during a complete wave or tidal period. The shallow-water approximation allows the decay of wave velocity with depth to be neglected. Bottom stress given by (1) is assumed to be dominated effectively by either waves or currents. Otherwise, wave-current interaction may play a role in determining the net stress field (e.g., Grant and Madsen, 1979). In this study, it is also assumed that ρ and c_d are constant in space. Under these conditions, uniform τ becomes equivalent to uniform U, and equilibrium morphologies can be defined by either τ or U.

Scaling of Problem: Southwest Coast of Korea

Before beginning a formal derivation of equilibrium hypsometry, it is useful to scale the problem in order to assess its applicability to real tidal flats. The tidal flats along the southwest coast of Korea (Wells *et al.*, 1990; Alexander *et al.*, 1991; Wells and Park, 1992) are chosen as a field example because of their open form and homogeneous composition, attributes which make them particularly amenable to first-order analytic modeling. Unlike many tidal flats bordering the North Sea, the

Korean flats lack extensive dendritic drainage systems, seaward barriers and landward salt marshes (Alexander *et al.*, 1991). The Korean intertidal sediments are predominantly poorly sorted mud, whereas sediments on flats in the North Sea often show a more well-defined shore-parallel gradation from mud to sand (Klein, 1985).

Along the southwest coast of Korea the mean tide range is about six meters and tidal flats extend locally more than 20 km out from the coast, although a more typical shore-normal flat length is about 5 km (Alexander *et al.*, 1991; Wells and Park, 1992). During calm summer weather, tidal currents are presumed to dominate bottom shear stress across the flats. Assuming a sinusoidal particle excursion, maximum tidal current speed is given by $U_T = \pi L/T$, where L is the horizontal distance from the low to high water line, and T is the tidal period. A semi-diurnal period then gives $U_T = 35$ cm s^{-1}, which is sufficient to mobilize unconsolidated sediment. Wells *et al.* (1990) measured maximum current speeds of ~ 40 cm s^{-1} across Korean tidal flats, consistent with the above estimate.

During the winter monsoon, Korean flats are exposed to intervals of large ocean swell (Wells and Park, 1992), and wave-generated shear stress is presumed to dominate. The amplitude of orbital velocity for a shallow water wave is given by linear theory to be

$$U_W = \frac{H}{2h} (gh)^{1/2}, \qquad (2)$$

where H is wave height, h is still water depth and g is the acceleration of gravity. At high tide, a swell of H = 2 m at the seaward edge of the flat (where h ≈ 6 m) gives $U_W = 120$ cm s^{-1}. Since $\tau \sim U^2$, shear stress generated by swell will be an order of magnitude larger than that generated by U_T, and U_W will effectively dominate the net field. Since maximum shear stress generated by waves (τ_W) has the potential to be much greater than maximum shear stress generated by tides (τ_T), one might expect a seasonal transition from tide- to wave-dominated hypsometry to be largely erosional, and a transition from wave- to tide-dominated hypsometry to be largely depositional.

In the following sections, U is used as a proxy for τ in deriving equilibrium flat morphologies. Under tidal currents, conservation of mass is used to determine the distribution of U_T, whereas under wind waves, conservation of energy is used to determine the distribution of U_W. In each section, U is first solved for a flat sloping linearly away from a straight shoreline. Profiles and hypsometries which result in a uniform distribution of U at equilibrium are then derived for both straight and curved shorelines. The uniqueness of the resulting equilibrium profiles and hypsometries will not be proven. The goal here is merely a description of simple profile forms across which U_T and τ_T are constant in space.

Tidal Currents

If the tidal excursion over the flat is much shorter than the tidal wave length, then it is reasonable to assume tidal elevation (η) pumps up and down uniformly across the tidal flat. Phase lags generated by momentum can contribute to velocity

asymmetries over tidal flats (Friedrichs *et al.*, 1992). However a kinematic approach is useful at first order when examining only the magnitude of tidal velocity. In the past, kinematic approaches have been used successfully in the study of velocity distributions along short channels in tidal marshes (Boon, 1975; Pethick, 1980).

The governing equation applied to tidal currents in the absence of wind waves is simply conservation of mass:

$$\frac{d\eta(t)}{dt} + \frac{\partial}{\partial x}\left\{h(x,t)\, u_T(x,t)\right\} = 0\,, \tag{3}$$

where h is local depth, and u_T is tidal velocity. Equation (3) also assumes tidal flow to be entirely one-dimensional, neglecting the role played by intertidal channels in concentrating the flow of water across the flats. Nonetheless, flow over tidal flats is often sheet-like, especially during the flood, even in the presence of intertidal channels (Wells and Park, 1992). Although one-dimensional, (3) does not require tidal currents to be perpendicular to the contours. Equation (3) only requires currents to flow at a constant angle to the bathymetry.

Integrating (3) to solve for u_T gives

$$u_T(x,t) = \frac{x_f(t) - x}{h(x,t)} \frac{d\eta(t)}{dt}\,, \tag{4}$$

where $x_f(t)$ is the boundary between the wetted and exposed portions of the flat, hereafter termed the tidal front (Figure 3). Channel depth is defined in terms of its time and space-dependent components:

$$h(x,t) = \eta(t) - Z(x)\,, \tag{5}$$

where Z(x) is the local elevation of the tidal flat profile. Equations (4) and (5) hold for any flat lacking along-shore variations. If $\eta(t)$ and Z(x) are specified, then h(x,t), $x_f(t)$ may be calculated, and a solution for u_T may be found from (4). Finally $U_T(x)$ is defined as the maximum value reached by u_T at each point in x during the tidal cycle.

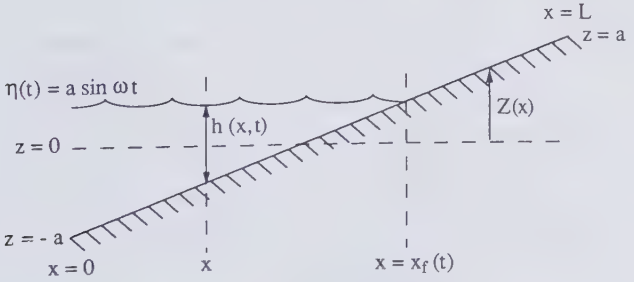

Figure 3. Schematic side view of a linearly sloping flat along a straight shoreline which is dominated by tidal currents. h is tidal elevation, h is local depth, x_f is the position of the tidal front, Z is the elevation of the profile.

Straight Shoreline, Linear Profile

Figure 3 displays a linearly sloping tidal flat with a distance L from the low to high water line. The tidal flat profile is given by

$$Z(x) = a\,(2x/L - 1)\,, \tag{6}$$

where x = 0 at the low water line, and Z = 0 at x = L/2. For a linear flat, evaluation of (4) is particularly straightforward. If the gradient of the flat is constant, then $(x_f - x)/h = L/2a$, and, with $\eta = a \sin \omega t$,

$$u_T(t) = \frac{L}{2a}\cos\omega t = \frac{L\omega}{2}\left(1-\frac{\eta^2}{a^2}\right)^{1/2}. \tag{7}$$

From (7) it is clear that maximum tidal velocity will occur when η^2 is at a minimum. For $x \le L/2$, η^2 is at a minimum when $\eta = 0$. Thus

$$U_T = L\omega/2 \quad \text{for} \quad x \le L/2, \tag{8}$$

and maximum tidal velocity occurs at mid-tide. For $x > L/2$, however, the smallest value of η which maintains water at x is (asymptotically) $\eta = Z$. So,

$$U_T(x) = \frac{L\omega}{2}\left(1-\frac{Z(x)^2}{a^2}\right)^{1/2} = L\omega\left(\frac{x}{L} - \frac{x^2}{L^2}\right)^{1/2} \quad \text{for} \quad x > L/2\,, \tag{9}$$

and maximum tidal velocity occurs at the tidal front. Thus (9) may be alternately expressed for $x > L/2$ as

$$U_T(x) = \frac{dx_f}{dt} \quad \text{when} \quad x = x_f > L/2\,. \tag{10}$$

Note that (8) - (9) indicate that U_T is independent of tidal amplitude.

Figure 4 shows U_T/U_{T0} as a function of x/L across a linearly sloping flat, where $U_{T0} = U_T(x=0)$. For $x/L \le 1/2$, U_T is constant, suggesting that (in the absence of wind waves) a linear profile is at morphologic equilibrium over the seaward half of the flat. If values are chosen appropriate to the southwest coast of Korea (M_2 tide, L ≈ 5 km) then $U_{T0} \approx 35$ cm s^{-1}, which is large enough to mobilize sediment. If the water flows at an angle to the shore, U_{T0} is potentially higher. For $x/L > 1/2$, however, there is a dramatic decrease in U_T as x/L approaches 1. Thus according to the morphodynamic model applied in this study, a linearly sloping flat with a stress field dominated by tidal currents alone is not at equilibrium for $x/L > 1/2$. Greater deposition (or less erosion) should occur on the landward half of the flat until U_T and τ_T become nearly uniform across the entire flat.

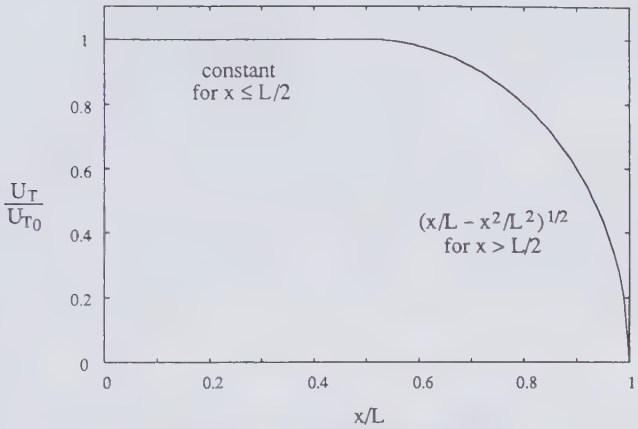

Figure 4. Maximum tidal velocity as a function of distance across a flat which slopes linearly away from a straight shoreline.

Straight Shoreline, Equilibrium Profile

A tidal flat profile is now derived which results in a uniform distribution of U_T across the entire flat. Figure 5 displays a profile which is linear for $x \leq L^*$ and non-linear for $x > L^*$. L^* is defined such that $Z = 0$ at $x = L^*$. The elevation of the lower tidal flat profile is given by

$$Z - (x) = a\,(x/L^* - 1) \quad \text{for} \quad x \leq L^*\,, \tag{11}$$

where L^* is also the length of the lower profile. From the linear profile case (see above) it follows that for $x \leq L^*$, $u_T = L^*\omega$ at mid-tide and, therefore, U_T is at least as large as $L^*\omega$. Also from the preceding section, it seems reasonable to assume that for $x > L^*$, U_T occurs at the tidal front. The next step is therefore to determine what Z is required to give

$$\frac{dx_f}{dt} = L^*\omega \quad \text{for} \quad x > L^*\,. \tag{12}$$

Following a particle at the tidal front:

$$\frac{dx_f}{d\eta} = \frac{dx_f}{dt}\,\frac{dt}{d\eta}\,, \tag{13}$$

where $dt/d\eta$ is found from $t = \omega^{-1}$ arcsin (η/a). Utilizing (12) and integrating (13) then yields

$$x_f - L^* = L^* \arcsin \eta/a\,. \tag{14}$$

At the tidal front, $x = x_f$, $h = 0$, and, from (5), $Z = \eta$. Eliminating η and x_f in (14) and solving for Z then gives

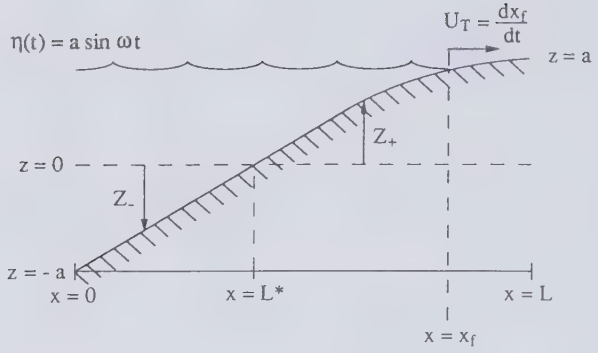

Figure 5. Schematic side view of an equilibrium flat along a straight shoreline which is dominated by tidal currents. Z_- is the elevation of the lower profile, Z_+ is the elevation of the upper profile, L* is the x location of Z = 0.

$$Z_+(x) = a \sin (x/L^* - 1) \quad \text{for} \quad x > L^* . \tag{15}$$

Since $Z_+ = a$ at x = L, from (15) it is clear that for an equilibrium flat along a straight shoreline,

$$L^*/L = (\pi/2 + 1)^{-1} . \tag{16}$$

The equilibrium profile given by (11) and (15) is illustrated in Figure 6a by the curve labeled "straight shoreline". Figure 6a indicates that the equilibrium profile for a current-dominated flat along a straight shoreline is convex relative to the linear profile. In Figure 6b, the curve labeled "straight shoreline" displays the corresponding hypsometry, which is identical to the profile for the straight shoreline case. Thus the results of this section indicate that tidal currents favor a convex hypsometry at equilibrium (at least along a straight shoreline), consistent with the general observational trends presented earlier.

Finally, (16) can be used to constrain the equilibrium length of a tidal flat in the absence of wind waves if there exists some characteristic magnitude of U_T at equilibrium. If $U_T = u_{eq}$, where u_{eq} is some (externally fixed) velocity at equilibrium, then (16), along with the relation $U_T = L^*\omega$, yields

$$L = (\pi/2 + 1)\, u_{eq}/\omega . \tag{17}$$

If $u_{eq} = 30$ cm s^{-1} during an M_2 tide, then (17) gives L = 5.5 km, where L is the length of the flat in the direction of maximum tidal velocity. Thus it is only necessary for the component of the flat perpendicular to the bathymetric contours to be of length L cos θ, where θ is the angle between the velocity and the shoreline. Also, intertidal flats may not extend all the way to high water, but rather may abut

salt marsh. If a flat along a straight shoreline extends from low water to mean water, for example, it need only have a length $L^* = u_{eq}/\omega$ parallel to the velocity direction. If $u_{eq} = 30$ cm s^{-1}, $\theta = 45^\circ$, and the flat in question lies below mean water, then the shore-normal component of the flat need only extend 1.5 km.

If a tidal flat abuts salt marsh, then its equilibrium hypsometry will be altered along with its horizontal extent. Intertidal marsh is generally concentrated in the upper portion of the intertidal zone with its lower extent limited by the frequency of submergence (Redfield, 1972; Frey and Basan, 1985). Since the convex portion of the "straight shoreline" hypsometry in Figure 6 is also limited to the upper part of the tidal range, overall tidal flat convexity will be reduced by the presence of salt marsh.

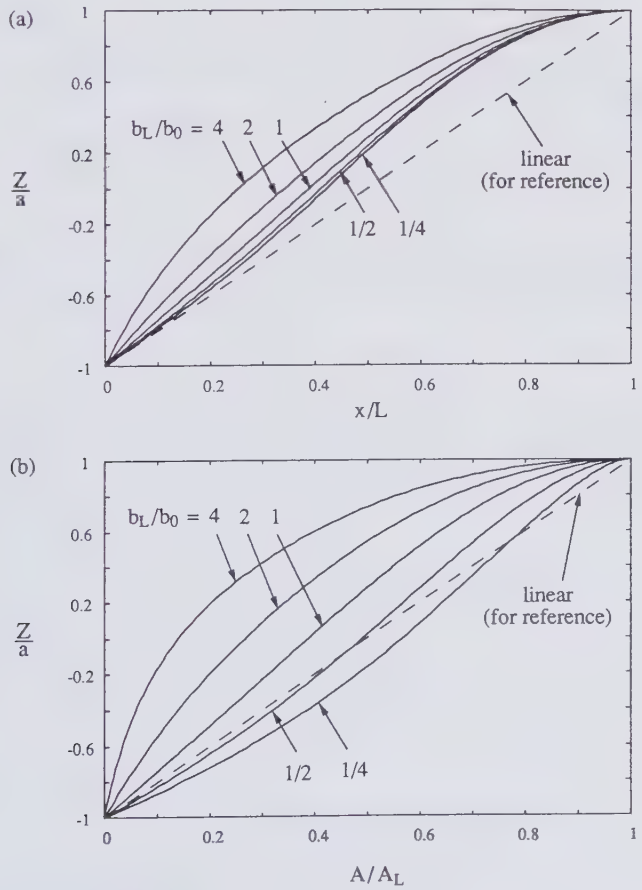

Figure 6. Equilibrium flats dominated by tidal currents. (a) profiles and (b) hypsometries. b_L/b_0 is the flat width (parallel to the shoreline) at $x = L$ divided by its width at $x = 0$. $b_L/b_0 > 1$ for an embayed shoreline, $b_L/b_0 = 1$ for a straight shoreline, and $b_L/b_0 < 1$ for a lobate shoreline.

Curved Shoreline, Equilibrium Flat

The effect of shoreline curvature on equilibrium profiles and hypsometries dominated by τ_T is now considered. Figure 7 provides plan views of "lobate" and "embayed" shorelines with tidal flats extending from x = 0 to x = L. A lobate shoreline has a shore-parallel width at x = L which is less than its width at x = 0, giving $b_L/b_0 < 1$. An embayed shoreline has $b_L/b_0 > 1$, and a straight shoreline has $b_L/b_0 = 1$.

For a curved shoreline which is radially symmetric, continuity is easily evaluated in polar coordinates:

$$\frac{d\eta}{dt} + \frac{1}{r}\frac{d}{dr}\left\{r\,h(r,t)\,u_T(r,t)\right\} = 0\,. \tag{18}$$

In this section tidal flow is assumed everywhere to be perpendicular to the bathymetry. Equation (18) integrates to

$$u_T(r,t) = \frac{r_f^{\,2} - r^2}{2\,r\,h(r,t)}\,\frac{d\eta}{dt}\,, \tag{19}$$

where r_f is the position of the tidal front. Keeping in mind that b is proportional to r (see Figure 7), (19) may be re-expressed as

$$u_T(r,t) = \frac{1}{2}\left(b(r_f)/b(r) + 1\right)\frac{r_f - r}{h(r,t)}\,\frac{d\eta}{dt}\,. \tag{20}$$

Transforming back to the x-coordinate, $r = r_0 \pm x$, $r_f = r_0 \pm x_f$, and $u_T(r,t) = \pm\, u_T(x,t)$, where $r_0 = r(x=0)$, and the $\pm$ corresponds to a shoreline that is embayed (+) or lobate (-). Then (20) becomes

$$u_T(x,t) = B(x_f,x)\,\frac{x_f - x}{h(x,t)}\,\frac{d\eta}{dt}\,, \tag{21}$$

where

$$B(x_f,x) = \frac{1}{2}\left(b(x_f)/b(x) + 1\right), \tag{22}$$

and

$$b(x)/b_0 = 1 + (b_L/b_0 - 1)\,x/L\,. \tag{23}$$

Equations (21) - (23) are valid for any radially symmetric flat, regardless of the precise form of the profile.

If shoreline curvature is negligible (i.e., $b_L/b_0 = 1$), then $b(x_f) = b(x)$, B = 1, and (20) is identical to (4). If the shoreline is lobate ($b_L/b_0 < 1$), then $b(x) \geq b(x_f) > 0$, and B is bounded by $1/2 < B \leq 1$. If the shoreline is embayed ($b_L/b_0 > 1$),

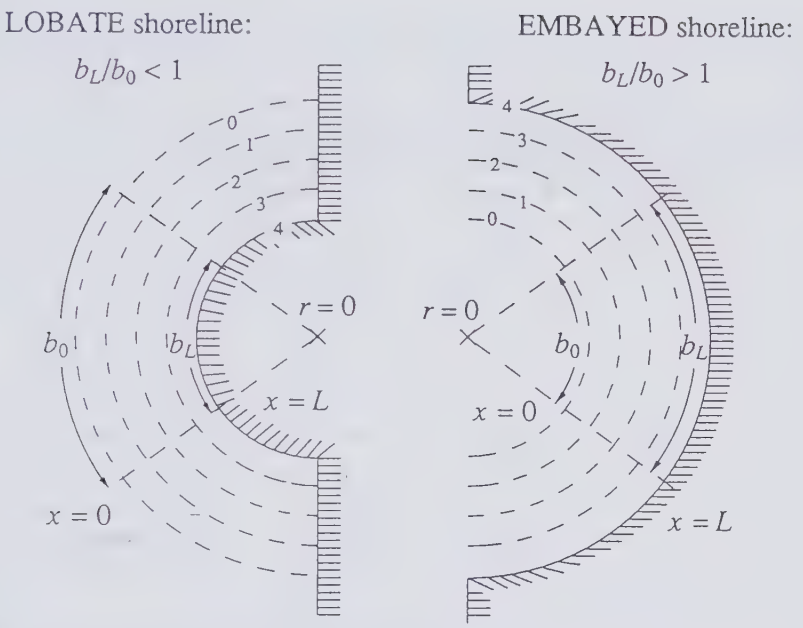

Figure 7. Schematic plan view of a lobate and an embayed shoreline. The contours 0 - 4 are arbitrary heights between low and high water.

then $0 < b(x) \leq b(x_f)$, and B is bounded by $1 \leq B < \infty$. Thus B is less sensitive to lobate shorelines and more sensitive to embayed shorelines.

The derivation of equilibrium tidal flat profiles along curved shorelines in the absence of wind waves closely follows that used for straight shorelines. By analogy to previous section, different relations are assumed to govern the equilibrium profile for $x \leq L^*$ and $x > L^*$. Also, as before it is assumed that $U_T = L^*\omega$ occurs simultaneously across all of $x \leq L^*$ when $x_f = L^*$. However, η is not assumed to be equal to zero when $x_f = L^*$. Rather, $\eta = z^*$ when $x_f = L^*$, where z^* may be less than or greater than zero, depending on the nature of the shoreline curvature. For $x > L^*$, it is again assumed that U_T occurs at the tidal front, i.e., $dx_f/dt = L^*\omega$.

In order to determine z^*, (21) is evaluated at $x = 0$ when $x_f = L^*$. Under these circumstances, (21) becomes

$$U_T = L^*\omega = B(L^*,0)\,\frac{L^*}{z^* + a}\,\frac{d\eta\,(z^*)}{dt}. \tag{24}$$

Using the expression $d\eta/dt = a\omega\,(1 - \eta^2/a^2)^{1/2}$, and solving for z^*/a then gives:

$$z^*/a = \frac{B(L^*,0)^2 - 1}{B(L^*,0)^2 + 1}. \tag{25}$$

If the shoreline is lobate, then $B < 1$, and z^* is negative. If the shoreline is embayed, then $B > 1$, and z^* is positive. Finally, if the shoreline is straight, $B = 1$, and $z^* = 0$.

The form of the tidal profile for $x \leq L^*$ is found by solving for $Z_-(x)$ in (21) with $h = \eta - Z_-$, $u_T = L^*\omega$, $x_f = L^*$, and $\eta = z^*$. Then (21) becomes

$$Z_-(x)/a = z^*/a - B(L^*,x)\,(1 - x/L^*)\left(1 - \frac{z^{*2}}{a^2}\right)^{1/2} \quad \text{for } x \leq L^*. \tag{26}$$

If the shoreline is straight, then $B = 1$, $z^* = 0$, and (26) is identical to (11).

For $x > L^*$, it is assumed that U_T occurs at the tidal front, i.e., $U_T = L^*\omega = dx_f/dt$. Proceeding as in previous section, integration of $dx_f/d\eta = dx_f/dt\ dt/d\eta$, followed by setting $x_f = x$ and $\eta = Z_+$ yields

$$Z_+(x)/a = \sin\left\{ (x/L^* - 1) + \arcsin z^*/a \right\} \quad \text{for } x > L^*. \tag{27}$$

If $z^* = 0$, (27) becomes equivalent to (15). Since $Z_+ = a$ at $x = L$, (27) can be used to derive L^* relative to L:

$$L^*/L = (\pi/2 + 1 - \arcsin z^*/a\ )^{-1}. \tag{28}$$

If $z^* = 0$, (28) reverts to (16).

Profiles given by (26) - (27) indicate that an embayed shoreline ($b_L/b_0 > 1$) significantly enhances the convexity of the equilibrium tidal profile, whereas a lobate shoreline ($b_L/b_0 < 1$) only slightly decreases the convexity of the profile (Figure 6a). This behavior is consistent with the function B, given by (22), which is also more sensitive to embayed shorelines.

Finally the profiles of Figure 6a are re-expressed as hypsometries, which are not equivalent to Z(x) if the shoreline is curved. Hypsometries are plots of elevation versus cumulative basin area, A, where $A(x) = \int b(x')\,dx'$. Integration of (23) yields:

$$\frac{A(x)}{A(L)} = \frac{2x/L + (b_L/b_0 - 1)\,(x/L)^2}{1 + b_L/b_0}. \tag{29}$$

If the shoreline is straight, then $b_L/b_0 = 1$, and (29) reduces to $A(x)/A(L) = x/L$. Equilibrium hypsometries for embayed shorelines are much more convex than the corresponding profiles (Figure 6b). Likewise, hypsometries for lobate shorelines are much less convex than the corresponding profiles — so much so that the equilibrium hypsometry for a current-dominated flat with $b_L/b_0 = 1/4$ is primarily concave. The enhanced variation of hypsometries relative to profiles stems from the nonlinear hypsometric function given by (29).

Wind Waves

The derivation for wave-dominated conditions parallels that described by Zimmerman (1973), who also examined the distribution of maximum bottom shear stress due to shoaling waves. The approach here differs in that Zimmerman did not apply the shallow water approximation nor did he consider waves shoaling across a linear profile.

The governing equation applied to wind waves in the absence of tidal currents is conservation of energy for monochromatic, remotely forced, forward propagating, shallow water surface waves:

$$\frac{d}{dx}\left\{E(x)\,C_g(x)\right\} = -D(x)\,, \tag{30}$$

where E is wave energy, $C_g = (gh)^{1/2}$ is the wave group velocity, g is the acceleration of gravity, and D is dissipation by bottom friction. In this section wind waves propagate perpendicular to the shoreline with no refraction across the flat. In evaluating (30) neither breaking waves nor wave energy reflected from the shoreline are considered. Thus this approach is inappropriate for energetic, steep beaches. However for gently sloping, highly dissipative tidal flats, the approach should be adequate for gaining useful physical insight. It is also assumed that the largest waves are most likely to occur around the time of high water. This is a reasonable assumption in enclosed intertidal basins because fetch will be smaller near low tide. It is also a reasonable assumption for open coasts if the intertidal slope continues some distance offshore. Then offshore dissipation will be greater at lower tide levels, reducing the height of waves impinging on the flats.

Wave energy in (30) is given by

$$E(x) = 1/8\ \rho\, g\, H(x)^2\,, \tag{31}$$

where ρ is the fluid density, and H is the wave height. Frictional dissipation in (30) is given by

$$D(x) = \frac{1}{T_W}\int_0^{T_W}\left\{\rho\, c_d\, u_W\, |u_W|\right\} u_W\, dt\,, \tag{32}$$

where T_W is the wave period, u_W is instantaneous wave velocity, and the quantity in brackets is instantaneous wave-generated bottom shear stress. If

$$u_W(x,t) = U_W(x)\,\sin\,(2\pi\, t/T_W)\,, \tag{33}$$

then substitution of (33) into (32) followed by integration gives

$$D(x) = \frac{4}{3\pi}\,\rho\, c_d\, U_W{}^3\,. \tag{34}$$

The above relations for E(x) and D(x), along with the relation $C_g = (gh)^{1/2}$, are substituted into (30), and (2) is used to eliminate H(x). The result is a non-linear ordinary differential equation for U_W:

$$\frac{1}{U_W^2}\frac{d}{dx}U_W + \frac{3}{4hU_W}\frac{dh}{dx} = -\frac{4c_d}{3\pi g^{1/2}h^{3/2}} . \tag{35}$$

Equation (35) can be rewritten as a linear O.D.E for U_W^{-1}:

$$\frac{d}{dx}U_W^{-1} - \frac{3}{4h}\frac{dh}{dx}U_W^{-1} = \frac{4c_d}{3\pi g^{1/2}h^{3/2}} . \tag{36}$$

The boundary condition on (36) is $U_W^{-1} = U_{W_0}^{-1}$ at x = 0, which may determined from H(x=0) via (2). Assuming h(x) is known, then (36) can be solved completely for U_W.

Straight Shoreline, Linear Profile

Figure 8 displays a linearly sloping tidal flat of length L, where L is the shore-normal distance from the low to high water line. The depth of the tidal flat profile is:

$$h(x) = (L - x)\, h_0/L , \tag{37}$$

where h_0 is the high-water depth at x = 0 and also is equal to the tidal range.

Substituting (37) into (36) yields

$$(L-x)\frac{d}{dx}U_W^{-1} + \frac{3}{4}U_W^{-1} = C_1 (L-x)^{-1/2} \tag{38}$$

with

$$C_1 = \frac{4c_d L^{3/2}}{3\pi g^{1/2}h_0^{3/2}} . \tag{39}$$

From the right hand side of (38), the particular solution for U_W^{-1} will have the form

$$\left\{U_W^{-1}\right\}_{part} = C_2 (L - x)^{-1/2} . \tag{40}$$

Substituting (40) into (38) yields $C_2 = 4/5\ C_1$. The homogeneous portion of (38) integrates to:

$$\left\{U_W^{-1}\right\}_{homo} = C_3 (L - x)^{3/4} . \tag{41}$$

Finally, the boundary condition at x = 0 gives $C_3 = U_{W_0}^{-1} L^{-3/4} - C_2 L^{-5/4}$.

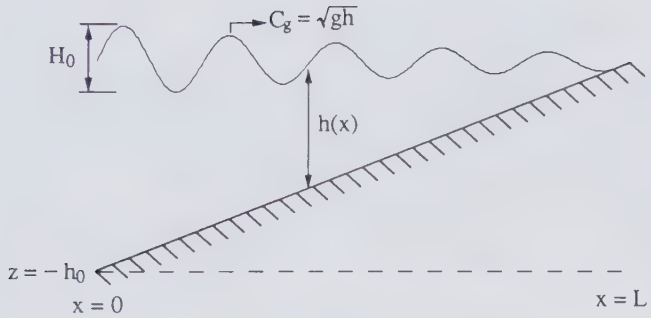

Figure 8. Schematic side view of a linearly sloping flat along a straight shoreline which is dominated by wind waves. H_0 is offshore wave height, C_g is wave velocity, h is local depth at high water, h_0 is high water depth at x = 0 and also equals the tidal range.

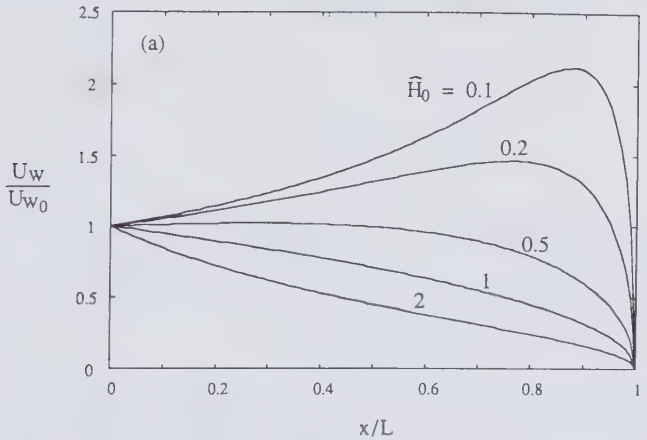

Figure 9. Maximum wave orbital velocity as a function of non-dimensional offshore wave height, $\hat{H}_0$, and of distance across a flat which slopes linearly away from a straight shoreline.

Combining the above equations yields:

$$U_W(x)/UW_0 = \left\{ \hat{H}_0 \ (1 - x/L)^{-1/2} + (1 - \hat{H}_0)\,(1 - x/L)^{3/4} \right\}^{-1} , \qquad (42)$$

where the non-dimensional forcing wave height, $\hat{H}_0$ is given by

$$\hat{H}_0 = \frac{16}{15\pi} c_d \frac{L}{h_0} \frac{U_{W_0}}{(gh_0)^{1/2}} = \frac{8}{15\pi} c_d \frac{L H_0}{h_0^2} . \qquad (43)$$

No value of $\hat{H}_0$ for a linearly sloping tidal flat results in a uniform distribution of U_W across the flat (Figure 9). Thus, according to the morphodynamic model applied here, a linearly sloping flat dominated by wind waves cannot be at equilibrium.

Straight Shoreline, Equilibrium Profile

A tidal flat profile is now derived which results in a uniform distribution of U_W across the entire flat. A similar solution was found previously by Bruun (1954) who assumed energy dissipation to be uniform across an equilibrium shoreface. However Bruun ignored the effect of shoreline curvature (see below).

Deriving an equilibrium profile with $U_W = U_{W0}$ everywhere is simpler than solving for $U_W(x)$. If U_W is constant, the first term in (35) is zero, and (35) may be rewritten as

$$h^{1/2}\,dh = -\frac{16}{9\pi}\,c_d\,U_{W_0}\,g^{-1/2}\,(L - x)\,. \tag{44}$$

Equation (44) integrates to

$$h(x)/h_0 = (1 - x/L)^{2/3}\,, \tag{45}$$

where

$$h_0 = \left(\frac{8}{3\pi}\,c_d\,U_{W_0}\,g^{-1/2}\,L\right)^{2/3}\,. \tag{46}$$

Equation (46) can be crudely checked by comparison to the Korean values. If (46) is solved for U_{W0}, then $c_d = 0.01$, $L = 5$ km, and $h_0 = 6$ m give $U_{W0} = 1.1$ ms^{-1}, which is a value that is certainly capable of mobilizing sediment. Using (2), this velocity is equivalent to a forcing wave height of $H_0 = 1.7$ m, which seems like a reasonable value for typical wave dominated conditions.

The equilibrium profile given by (45) is illustrated in Figure 10a by the curve labeled $b_L/b_0 = 1$. Figure 10a indicates that the equilibrium profile for a wave-dominated flat along a straight shoreline is concave relative to the linear profile. In Figure 10b, the curve labeled $b_L/b_0 = 1$ displays the corresponding hypsometry, which is identical to the profile for the straight shoreline case. Thus (45) indicates wind-waves favor a concave hypsometry at equilibrium (at least along a straight shoreline), which is consistent with the observations summarized in the Introduction.

Finally, (46) can be used to derive the equilibrium length for a flat under wave-dominated conditions. If H_0, h_0 and c_d are considered to be characteristic values, independent of the extent of the tidal flat, then (46) and (2) can be combined and solved for L:

$$L = \frac{3\pi}{4c_d}\,\frac{h_0^{\,2}}{H_0}\,. \tag{47}$$

Equation (47) seems qualitatively sensible in that it indicates that equilibrium tidal flat width decreases with increasing wave height, H_0, and increases dramatically with increasing tidal range, h_0. Equation (47) suggests that the position of the low

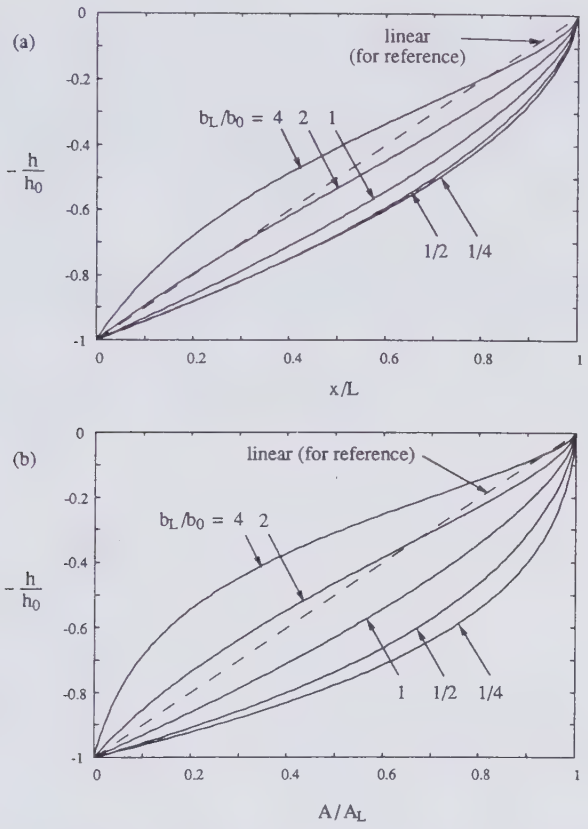

Figure 10. Equilibrium flats dominated by wind waves. (a) profiles and (b) hypsometries. $b_L/b_0 > 1$ for an embayed shoreline, $b_L/b_0 = 1$ for a straight shoreline, and $b_L/b_0 < 1$ for a lobate shoreline.

tide line should oscillate with seasonal variations in forcing wave height. This predicted oscillation is qualitatively consistent with the observations of Wells and Park (1992).

Equation (47) may also help explain the associations of small tidal ranges with concave hypsometry and of large tidal ranges with convex hypsometry illustrated in Figure 2a (Dieckmann *et al.*, 1987). If wave height is moderate and tidal range is small, (47) indicates that L will also be small. Before, U_T was found to be directly proportional to L. Thus if L is small, U_T will be small also. Under these conditions, U_W and τ_W will dominate U_T and τ_T, and the equilibrium profile will be concave. If tidal range is large and waves are moderate, then (47) indicates L will be much larger (since L is geometrically dependent on h_0). Since U_T is proportional to L, U_T will also be much larger. U_W and τ_W may no longer dominate U_T and τ_T, at least under fair weather conditions, and the equilibrium profile may be more convex.

Curved Shoreline, Equilibrium Profile

The effect of shoreline curvature on equilibrium profiles and hypsometries dominated by τ_W is now considered. For a curved shoreline which is radially symmetric (see Figure 7), conservation of energy is easily evaluated in polar coordinates:

$$\frac{1}{r}\frac{d}{dr}\left\{ r\,E(r)\,C_g(r)\right\} = -D(r)\,, \tag{48}$$

It is assumed that refraction has already caused the wind waves to propagate nearly perpendicular to the bathymetric contours by the time the waves reach the edge of the flat at $r_0 = r(x=0)$.

Evaluation of (48) is straightforward if $U_W = U_{W_0}$ across the entire profile. Using (2), (31), (34) and the relation $C_g = (gh)^{1/2}$, (48) integrates to

$$r\,h^{3/2} = \frac{4}{3\pi}\,c_d\,U_{W_0}\,g^{-1/2}\left| r_L^{\,2} - r^2\right|, \tag{49}$$

where $r_L = r(x=L)$. Since b is proportional to r (see Figure 7), (49) may be re-expressed as

$$h(r)^{3/2} = \frac{1}{2}\left(b(r_L)/b(r) + 1\right)\frac{8\,c_d\,U_{W_0}}{3\pi\,g^{1/2}}\left| r - r_L\right|. \tag{50}$$

Transforming back to the x-coordinate, (50) becomes

$$h(x)/h_0 = \left\{ B(L,x)/B(L,0)\right\}^{2/3}\,(1 - x/L)^{2/3}\,, \tag{51}$$

where

$$h_0 = \left(B(L,0)\frac{8}{3\pi}\,c_d\,U_{W_0}\,g^{-1/2}\,L\right)^{2/3}, \tag{52}$$

and

$$B(L,x) = \frac{1}{2}\left(b_L/b(x) + 1\right). \tag{53}$$

$B(L,x)$ is analogous to $B(x_f,x)$ in equation (22), and $b(x)$ above is identical to (23). If shoreline curvature is negligible (i.e., $b_L/b_0 = 1$), then $b_L = b(x)$, $B = 1$, and (51) - (52) become identical to (45) - (46).

Profiles given by (51) indicate that a lobate shoreline ($b_L/b_0 < 1$) only slightly increases the concavity of the profile, whereas an embayed shoreline ($b_L/b_0 > 1$) greatly decreases the concavity of the profile — so much so that the equilibrium profile for a flat with $b_L/b_0 = 4$ is primarily convex (Figure 10a). The greater sensitivity of the profile to embayed shorelines is similar to that under tidal currents

(see Figure 6a) which follows from a dependence of the equilibrium profile on the function B, which is also more sensitive to embayed shorelines.

Finally, the profiles of Figure 10a can be re-expressed as hypsometries (Figure 10b). Equilibrium hypsometries for lobate shorelines ($b_L/b_0 < 1$) are significantly more concave than the corresponding profiles, and hypsometries for embayed shorelines ($b_L/b_0 > 1$) are significantly less concave. In fact, the hypsometries for $b_L/b_0 \geq 2$ are primarily convex. The range of hypsometries in Figure 10b are qualitatively similar to the hypsometries observed by Kirby (1992) within the Severn Estuary (see Figure 2). Kirby included a location map, reproduced in Figure 11, which outlines the shoreline along the Severn. The shoreline at Cardiff Bay (which has a convex hypsometry) is strongly embayed, whereas the shoreline at Clevedon (which has a concave hypsometry) is straight to slightly lobate. Thus it is possible that shoreline shape has contributed to the hypsometric trends reported by Kirby.

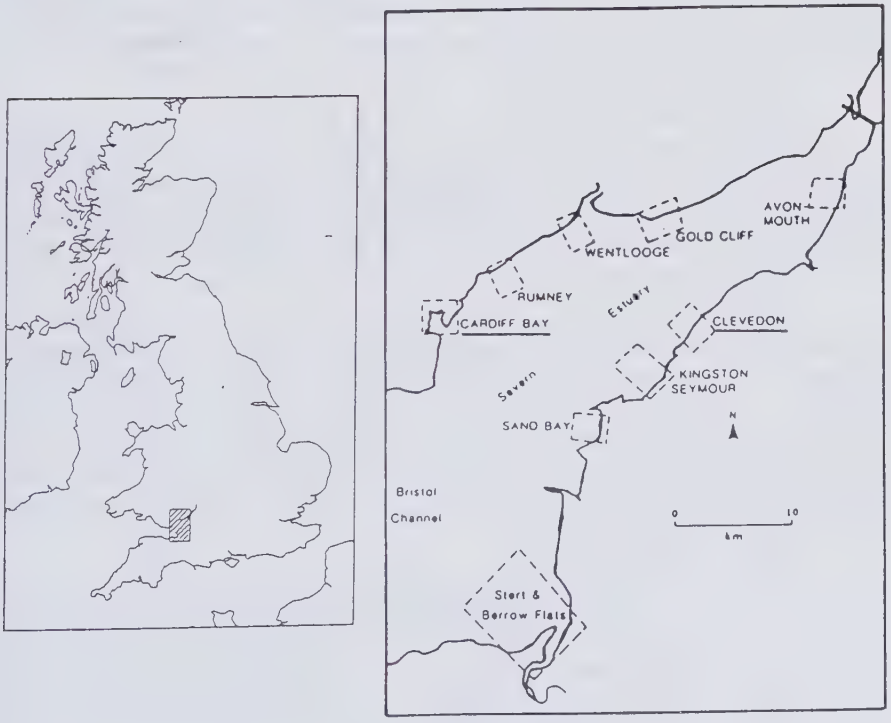

Figure 11. Location map showing flats along the Severn for which Kirby performed hypsometric analysis, modified from Kirby (1992). Cardiff Bay and Clevedon (underlined) have strongly convex and strongly concave hypsometries, respectively (see Figure 2).

Conclusions

Recent observations of tidal flat hypsometry have correlated convexity with large tide ranges, long-term accretion and/or low wave activity. Concavity, in turn, has been correlated with small tide ranges, long-term erosion and/or high wave activity. This study demonstrates that much of this empirically observed variation in tidal flat hypsometry is consistent with a simple morphodynamic model which assumes tidal flats to be at equilibrium if maximum shear stress is uniform in space. Assuming a constant drag coefficient, this condition is equivalent to a uniform distribution of maximum velocity.

In the absence of wind waves, maximum shear stress is a function of maximum tidal velocity, U_T. Assuming the intertidal excursion to be much shorter than the tidal wave length, continuity may be solved kinematically to determine U_T as a function of distance across the flat. For a flat which slopes linearly away from a straight shoreline, results show that U_T is constant across the seaward half of the flat. Therefore the lower portion of a linearly sloping flat is potentially at morphologic equilibrium. Across the landward half, however, a dramatic decrease in U_T is predicted, indicating disequilibrium.

For a straight waveless shoreline, the equilibrium profile has a linear slope over the seaward portion of the flat, and U_T occurs at mid-tide. Across the landward portion of the flat, U_T is assumed to occur at the tidal front. The equilibrium value for U_T is then proportional to the length of the tidal flat but is independent of tidal range. The resulting equilibrium profile is convex overall and demonstrates that tidal currents favor a convex hypsometry along a straight shoreline.

For a curved waveless shoreline, the equilibrium flat is derived in a similar manner. Results indicate that an embayed shoreline significantly enhances the convexity of the equilibrium profile, whereas a lobate shoreline only slightly decreases the convexity. The nonlinear transformation from profiles to hypsometries, however, causes the hypsometry of embayed and lobate shorelines to be much more or much less convex than the corresponding profiles — so much so that the effect of shoreline curvature on equilibrium hypsometry is potentially as strong as the effect of domination by tidal currents.

In the presence of wind waves, shear stress is often dominated by the maximum wave orbital velocity, U_W. Assuming dissipative shallow water waves impinging at high water, conservation of energy is utilized to determine U_W as a function of distance across the flat. For a flat sloping linearly away from a straight shoreline, the solution may be expressed in terms of a single dimensionless forcing wave height, $\widehat{H}_0$. No value of $\widehat{H}_0$ results in a uniform distribution of U_W, thus no part of a linearly sloping, wave-dominated flat is at equilibrium.

The equilibrium flat along a straight, wave-dominated shoreline is derived by setting U_W constant in the previously derived governing equation for U_W^{-1}. The resulting equilibrium profile has depth increasing as $x^{2/3}$, indicating wind waves favor a

concave hypsometry. Under domination by waves, the equilibrium profile length, L, is proportional to h_0^2/H_0, where h_0 is the tidal range and H_0 is the forcing wave height. This expression suggests L should increase dramatically with tidal range. Since $U_T \sim L$, the relative importance of tidal currents should also increase strongly with tidal range, favoring a transition from concave to convex hypsometry with increasing tidal range.

An equilibrium flat along a curved, wave-dominated shoreline is derived in a similar manner. Like the no-wave case, results indicate that an embayed shoreline significantly decreases the concavity of the profile — potentially to the point of convexity — whereas a lobate shoreline only slightly increases concavity. Again, the nonlinear transformation from profiles to hypsometries causes the hypsometries to be much more or much less concave than the profiles.

Acknowledgements. Special thanks are extended to J. Boon, R. Kirby, D. Lynch, O. Madsen, and J. Trowbridge who provided helpful comments on the manuscript. This work was supported by the National Science Foundation, under grant number OCE 91-02429. WHOI contribution No. 8294.

References

Alexander, C. R., C. A. Nittrouer, D. J. Demaster, Y.-A. Park and S.-C. Park, Macrotidal mudflats of the southwestern Korean coast: a model for interpretation of intertidal deposits. *J. Sediment. Petrol.*, 61, 805-824, 1991.

Boon, J. D., Tidal discharge asymmetry in a salt marsh drainage system. *Limnol. Oceanogr.*, 20, 71-80, 1975.

Boon, J. D., and R. J. Byrne, On basin hypsometry and the morphodynamic response of coastal inlet systems. *Mar. Geol.*, 40, 27-48, 1981.

Bruun, P., Coast erosion and the development of beach profiles. *U.S. Army Corps of Engineers*, Beach Erosion Board, Tech. Memo. 44, 79 pp, 1954.

Davies, J. L., *Geographical Variation in Coastal Development.* New York: Hafner, 204 pp, 1973.

Dieckmann, R., M. Osterthun and H. W. Partenscky, Influence of water-level elevation and tidal range on the sedimentation in a German tidal flat area. *Progress in Oceanogr.*, 18, 151-166, 1987.

Dyer, K. R., *Coastal and estuarine sediment dynamics.* New York: Wiley, 342 pp, 1986.

Frey, R. W., and P. B. Basan, Coastal salt marshes, in *Coastal Sedimentary Environments* edited by R. A. Davis, 225-302, Springer-Verlag, New York, 1985.

Friedrichs, C. T., D. R. Lynch and D. G. Aubrey, Velocity asymmetries in frictionally-dominated tidal embayments: longitudinal and lateral variability, in *Dynamics and Exchanges in Estuaries and the Coastal Zone. Coastal and Estuarine Studies*, edited by D. Prandle, American Geophysical Union, Washington, D.C., 40, 277-312, 1992.

Grant, W. D., and O. S. Madsen, Combined wave and current interaction with a rough bottom. *J. Geophys. Res.*, 84, 1797-1808, 1979.

Kirby, R., Effects of sea-level on muddy coastal margins, in *Dynamics and Exchanges in Estuaries and the Coastal Zone. Coastal and Estuarine Studies*, edited by D. Prandle, American Geophysical Union, Washington, D.C., 40, 313-334, 1992.

Klein, G. D., Intertidal flats and intertidal sand bodies, in *Coastal Sedimentary Environments*, edited by R. A. Davis, Springer-Verlag, New York, 187-218, 1985.

Pethick, J. S., Velocity surges and asymmetry in tidal channels. *Estuarine and Coastal Marine Science*, 11, 331-345, 1980.

Redfield, A. C., Development of a New England salt marsh. *Ecological Monographs*, 42, 201-237, 1972.

Strahler, A. N., Hypsometric (area-altitude) analysis of erosional topography. *Geological Soc. America Bull.*, 63, 1117-1142, 1952.

Wells, J. T., C. E. Adams, Y.-A. Park and E. W. Frankenberg, Morphology, sedimentology and tidal channel processes on a high-tide-range mudflat, west coast of Korea. *Mar. Geol.*, 95, 111-130, 1990.

Wells, J. T., and Y.-A. Park, Observations on shelf and subtidal channel flow: implications of sediment dispersal seaward of the Keum River estuary, Korea. *Est., Coastal and Shelf Sci.*, 34, 365-379, 1992.

Zimmerman, J. T. F., The influence of the subaqueous profile on wave induced bottom stress. *Netherlands J. Sea Res.* 6, 542-549, 1973.

Appendix - List of Symbols

a	tidal amplitude
A	cumulative horizontal basin area
A_L	A at x = L
A_m	maximum value of A
b	width of flat parallel to shoreline
b_0	b at x = 0
b_L	b at x = L
B	$B(x_1,x_2) = (b(x_1)/b(x_2) + 1)/2$
c_d	drag coefficient
$C_{1,2,3}$	constants
C_g	wind wave group velocity
D	energy dissipation by bottom friction
E	wave energy density
g	acceleration of gravity
h	still water depth or local elevation
h_0	h at x = 0
h_m	maximum value of h
H	wave height
H_0	H at x = 0

$\hat{H}_0$	non-dimensional H_0
L	shore-normal length of tidal flat
L*	shore-normal length of lower profile
r	shore-normal co-ordinate for radially symmetric flat
r_0	r at x = 0
r_f	r at $x = x_f$
r_L	r at x = L
t	time
T_W	wave period
u	velocity
u_{eq}	equilibrium velocity
u_T	depth-averaged tidal velocity
u_W	wave orbital velocity
U	maximum depth-averaged velocity
U_T	maximum depth-averaged tidal velocity
U_{T0}	U_T at x = 0
U_W	maximum wave orbital velocity
U_{W0}	U_W at x = 0
x	shore-normal co-ordinate
x_f	position of tidal front
z	vertical co-ordinate
z*	elevation of transition from lower to upper profile
Z	profile elevation
Z_+	upper profile elevation
Z_-	lower profile elevation
η	tidal elevation
θ	angle between velocity and shoreline
ρ	fluid density
τ	maximum bottom shear stress
τ_T	maximum tidal bottom shear stress
τ_W	maximum wave-generated bottom shear stress
ω	tidal frequency

25

Dispersion of Effluent from Sydney's New Deepwater Outfalls. Part 1: Ocean Processes

R. S. Lee and T. R. Pritchard

Abstract

An understanding of the complex shelf processes that effect the physical dispersion of waste in Sydney's coastal waters has resulted from studies which include satellite imagery, oceanographic experiments and analysis of data from an offshore Ocean Reference Station (ORS) operated by the Sydney Water Board. NSW continental shelf waters are influenced by flows from the *East Australian Current (EAC)*, *coastal-trapped waves (CTW)*, *tides* and *local wind* forcing. All four influences have a unique effect on the effluent field that emanates from deepwater outfalls in 60-80 metres of water, 3-4 km off the Sydney coast. Recent analysis of the Ocean Reference Station record and thermal satellite imagery indicates that EAC flows may directly influence Sydney's coastal waters for up to 75% of the time (Webb,1992), generally in the form of a marked warming of the water column and strong (up to 1 ms^{-1}) flows prevailing to the south. Coastal trapped waves are often apparent in the ORS record as 7-20 day weatherband oscillations and influence both the prevailing current pattern and the vertical density structure. LANDSAT imagery shows ebb jets from Sydney's estuaries extending 2-3 kilometres offshore and when EAC and CTW components are weak, a semi-diurnal internal tidal signal is often discernible in the ORS record. Strong winds associated with storm events at Sydney are generally from the south-east leading to a down welling which breaks down vertical structure and promotes transport of floatable matter to the coast.

Mixing in Estuaries and Coastal Seas
Coastal and Estuarine Studies Volume 50, Pages 430-438
Copyright 1996 by the American Geophysical Union

Introduction

In Australia much of the population is concentrated along the coastline, particularly in the south-east, with adjacent shelf waters being heavily used for recreation, commercial fishing, transport and waste disposal. Circulation by shelf currents changes local nutrient levels, water temperatures, pollutant dispersion, and may affect the uses for which water is suitable. Sydney's sewage waste has been discharged directly to the ocean since the turn of the century, with primary treatment occurring only in the last 20 years. Tunnels at North Head, Bondi and Malabar now

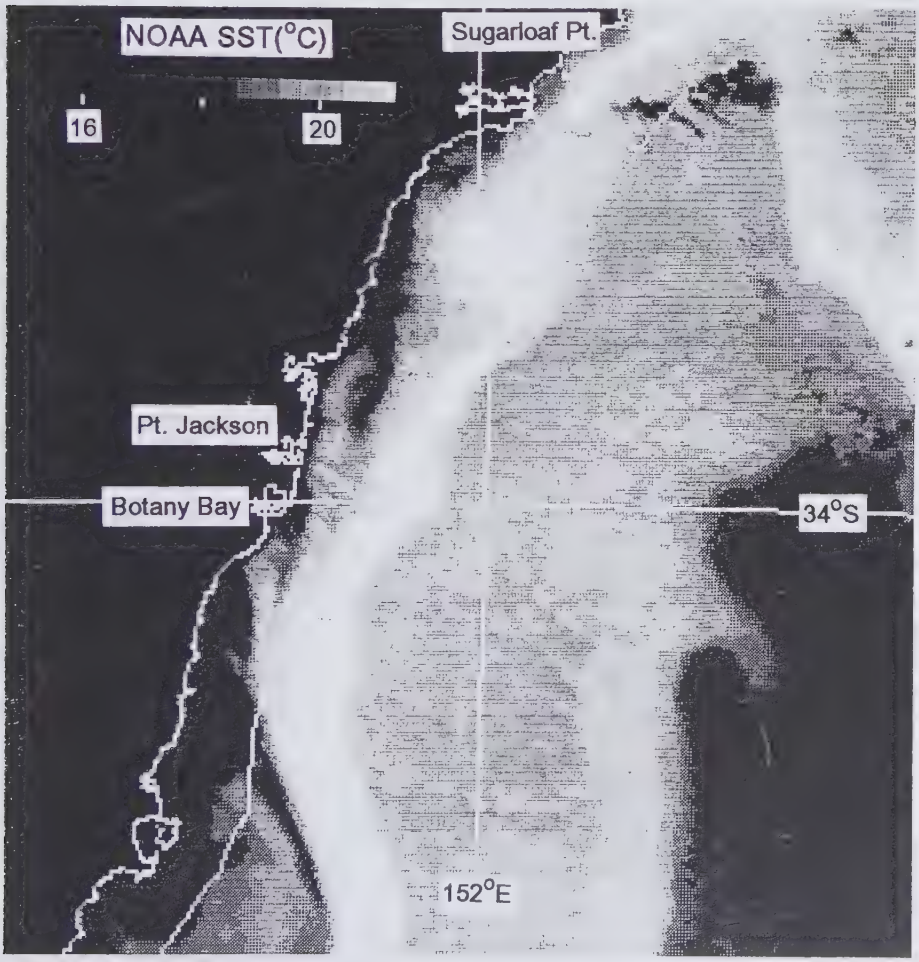

Figure 1. NOAA sea surface temperature image for 24 June 1991 showing backeddies south of Botany Bay and north of Port Jackson. The ORS registered the passage of the southern backeddy on 23 June 1991, as a reversal in the direction of the upper layer (15m) current.

transport sewage up to 3-4km off-shore and discharge in 60-80 metres of water from multiport diffusers. These deepwater outfalls were commissioned in 1990 and 1991.

A five year Sydney Deepwater Outfalls Environmental Monitoring Program is being implemented by the New South Wales Environment Protection Authority (NSW EPA). Oceanographic investigations, undertaken by the NSW EPA in-conjunction with NSW University and Australian Water and Coastal Studies Pty Ltd, have been designed to quantify the ambient shelf conditions in Sydney's coastal waters. These studies support the development of a suite of numerical models which aim to simulate the dispersion of sewage effluent from Sydney's new deepwater outfalls.

This paper (Part 1) identifies the major ocean processes influencing the dispersion of effluent from Sydney's new deepwater outfalls while plume characteristics are described by Pritchard, Lee and Davison in "Part 2: Observations of Plume Behaviour: Winter and Summer Examples".

Ocean processes affect the current structure and vertical density stratification in the water column and hence determine dispersion characteristics of effluent discharged into Sydney's coastal waters. An initial understanding of barotropic and baroclinic flows comes from studies which include satellite imagery, dispersion experiments and analysis of data from an offshore Ocean Reference Station (ORS). The ORS, maintained by the Sydney Water Board, has operated since mid 1989 and provides an invaluable time series record of near-surface wind, current (15m and 50m depths) and temperature structure at a mooring some 4.5 km offshore from Bondi in a water depth of about 65m.

NSW continental shelf waters are influenced by a combination of adjacent deep ocean circulation from the *East Australian Current, coastal-trapped waves* propagating northward along the continental shelf from Bass Strait, the effect of tides and local wind forcing. The strength of these influences is determined and directed by the continental shelf which extends 650km south of Sydney to Bass Strait, and some 1000km north to the Stradbroke Island group. Southward currents prevail near Sydney where the shelf is narrow (30km) and orientated 32^{O} east of true north.

East Australian Current

The characteristics of the East Australian Current (EAC) are well documented by Godfrey *et al.* (1980) and Tranter *et al.* (1986). It typically separates from the coast ~ 300km north of Sydney at Sugarloaf Point as a southward flowing jet of warm Coral Sea water, forming a turbulent eddy field as it intrudes into the cooler Tasman Sea.

The EAC influence on Sydney shelf waters has often been recognised (e.g. Cresswell, 1974) as an infrequent event affecting temperature stratification and inducing, or enhancing alongshore transport to the south. However, recent analysis of ORS data and thermal satellite imagery, indicated that EAC flows may directly influence Sydney's coastal waters for as much as 75% (Webb, 1992) of the time.

This figure is indicative of the EAC influence during the period August 1989 to June 1991, and may vary in the long term due to the large scale of this circulation. Direct EAC influences on the shelf off Sydney include encroachments of the main EAC flow and warm and cold core eddies which separate from the main flow as depicted in Figure 1. In this instance, a narrow jet separates from the main EAC flow near Sugarloaf Point, and continues south along the shelf break. This breakaway EAC flow may form large warm core (anti-clockwise) eddies which are typically about 150km in diameter. Alternatively the flow can form standing waves which frequently develop into a series of smaller cold core (clockwise) eddies which intrude shelf waters. EAC influences are limited when separation of the EAC occurs far to the north of Sydney and/or when a pool of cold Tasman Sea water blocks the flow of EAC water.

An unseasonal EAC encroachment onto the shelf off Sydney during the winter of 1991 enhanced the thermocline by 2°C for a period of two months and maintained prevailing southward barotropic flow, swamping the previous ambient conditions on the shelf. The initial effects of this encroachment are clearly illustrated by the ORS record shown in Figure 2. Operational models driven by this ORS data indicated that effluent discharged from the deepwater outfalls during the EAC encroachment remained submerged rather than rising to the surface, as it had prior to the encroachment.

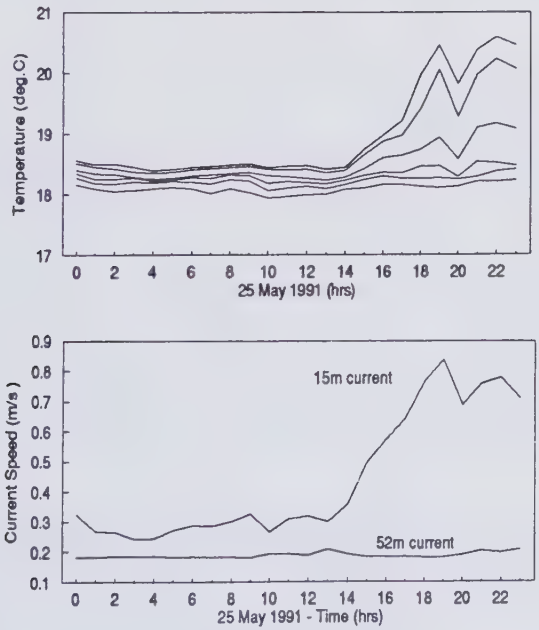

Figure 2. ORS thermistor (0 - 52m) and current speed records for initial EAC encroachment during winter 1991. This unseasonal encroachment maintained significant stratification for two months.

Remotely sensed thermal imagery has detected up-welling at the coast due to Ekman pumping of bottom waters associated with a major EAC flows at the shelf break. This localised vertical mixing and shoreward transport of bottom waters has the potential to transport submerged effluent fields from deepwater outfalls to Sydney beaches.

Coastally Trapped Waves

The Australian Coastal Experiment, which involved current observations along the east Australian coast during 1983-84, identified the passage of coastally trapped waves (CTW) out of Bass Strait and north along the continental shelf past Newcastle at a phase speed of around 3 ms^{-1} (Church *et al.*, 1986a,b; Church and Freeland, 1987; and Clarke, 1987). They found that the CTW signal accounted for 63% of the alongshelf currents at a near-shore location in the Sydney region, and was particularly apparent in the absence of EAC flows.

The time series record from the ORS often displays 7-20 day weatherband oscillations which have been attributed to the passage of CTWs that propagate from Bass Strait and southern NSW. CTW oscillations are clearly visible in the ORS record for November 1990 (Figure 3), with a direction offset between top (15m) and

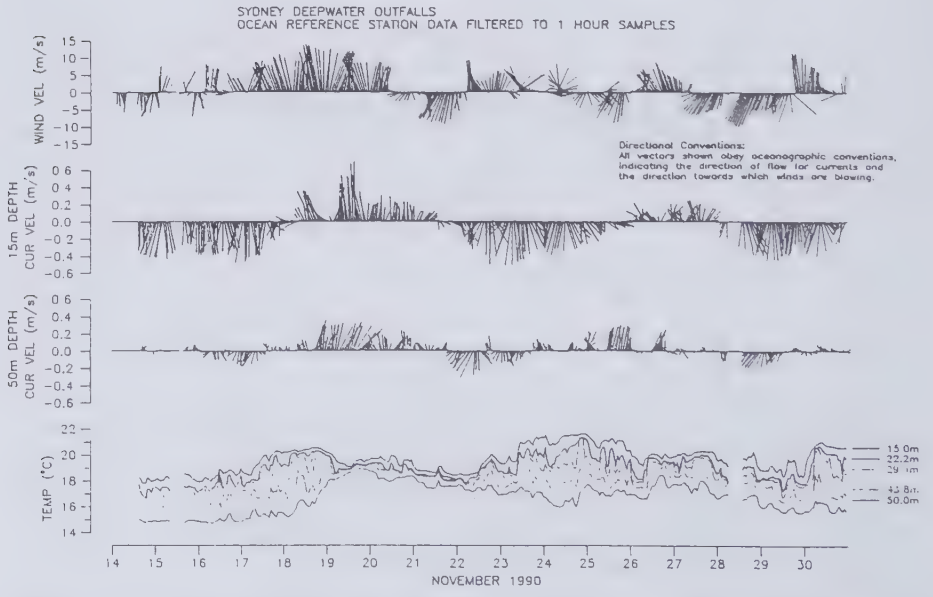
SYDNEY DEEPWATER OUTFALLS
OCEAN REFERENCE STATION DATA FILTERED TO 1 HOUR SAMPLES
WIND VEL (m/s)
15m DEPTH CUR VEL (m/s)
50m DEPTH CUR VEL (m/s)
TEMP (°C)
Directional Conventions:
All vectors shown obey oceanographic conventions, indicating the direction of flow for currents and the direction towards which winds are blowing.
15.0m
22.2m
29.4m
43.8m
50.0m
14 15 16 17 18 19 20 21 22 23 24 25 26 27 28 29 30
NOVEMBER 1990

Figure 3. A dominant coastal trapped wave signal is shown in the ORS record for November 1990.

bottom (50m) currents due to the bottom Ekman flux. This offset, together with the displacement of the thermocline, indicates downwelling to the coast with northbound flow (lowering the thermocline by up to 30 metres), and upwelling (with a corresponding rise of the thermocline) when flows are to the south.

Griffin and Middleton (1990, 1991, 1992) noted that this phenomenon occurred frequently in Mk0 ORS records (Aug '89-Apr '90) and during earlier current meter deployments (1984-85). Plume behaviour would clearly be influenced by such dramatic variations of current speed and direction, and thermocline position. Observations of near field plume behaviour on 9 April 1991 coincided with the passage of a CTW event (Lee, 1991). A current reversal to the south resulted in a 20 metre rise of the plume trapping depth combined with increased dilutions. Midway through the reversal, the plume surfaced through a 1.5°C thermocline as flow decreased to <0.05 ms^{-1}.

Griffin and Middleton (1991) have devised a prediction scheme of the CTW component for the inner shelf currents experienced off Sydney from real-time wind stress measurements along the southern NSW and Victorian coast. These predictions are however only comparable to observations during quiescent periods of EAC shelf activity, which, from subsequent analysis of EAC activity from the ORS, occurs up to 75% of the time.

Tides

Local tides on the Sydney shelf region induce generally weak flows of <0.05 ms^{-1} (Hamon, 1984), and are often neglected when considering all the components of the general shelf circulation (Lee and Jones, 1990). Analysis of LANDSAT satellite imagery has shown that ebb jets from enhanced tidal flows at the estuarine mouths of Port Jackson (Sydney Harbour) and Botany Bay extend some 3-4km offshore. An ebb jet may aggregate surface floatable matter from the deepwater outfalls along its front, which if accompanied by a steady onshore wind, could increase concerns for beach pollution. In general though, the weak surface tides of the region have a negligible impact on the shelf currents. However, as noted in Griffin *et al.* (1991), internal tides may be significant particularly when stratification is strong (typically summer).

The ORS record for 12-15 February 1991 clearly shows semi-diurnal internal tides affecting the temperature structure (Figure 4) ORS current data indicated peak onshore flow in the upper layer, coinciding with peak offshore flow in the bottom layer, occurred as the thermocline rose in response to the passage of the internal tide. The internal tide can displace the thermocline by some 20 metres, and in this instance, was preceded by short (20min) period internal waves of similar amplitude to the tidal wave.

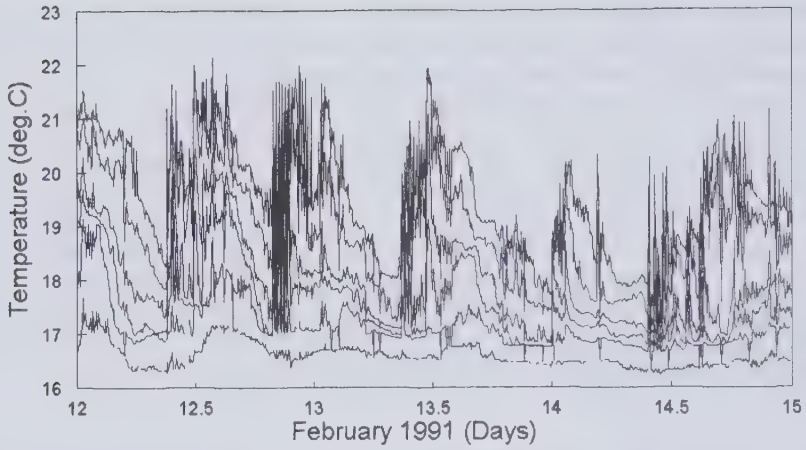

Figure 4. ORS thermistor record (15-50 metres) for 12-15 February 1991, during a period of internal tide activity.

Griffin and Middleton (1992) have shown that the coastal reflection of internal tides is sufficiently complete to imply that only a small fraction of the incident tidal energy is dissipated at the shoaling coast by breaking of the internal tide. This reflection is indicated in Figure 4 with a warming some time after the acute thermal response to the passage of the internal tide.

Local wind

ORS data acquired between July 1989 and April 1990, were analysed by Griffin and Middleton (1992). They indicate that weather-band variability of the thermocline displacement in Sydney's coastal waters is primarily due to local forcing by the alongshore component of the wind-stress. South-easterly winds favour downwelling while upwelling can be associated with north-easterly winds.

Upwelling and downwelling may affect the depth to which effluent rises and its subsequent transport across shelf. Both scenarios degrade the vertical density stratification thus affecting the extent of plume rise. Thermocline displacements rapidly relax when the wind stress is removed. Upwelling events may bring a submerged effluent field to the surface close to the coast. Downwelling events are associated with onshore transport of the surface layer which may include effluent or grease which has reached the surface from the deepwater outfalls.

Storm events present conditions which may result in beach pollution. Strong winds associated with storms lasting more than a day, erode the thermocline in the vicinity of the outfalls and promote the formation of surface effluent fields (Figure 5). A

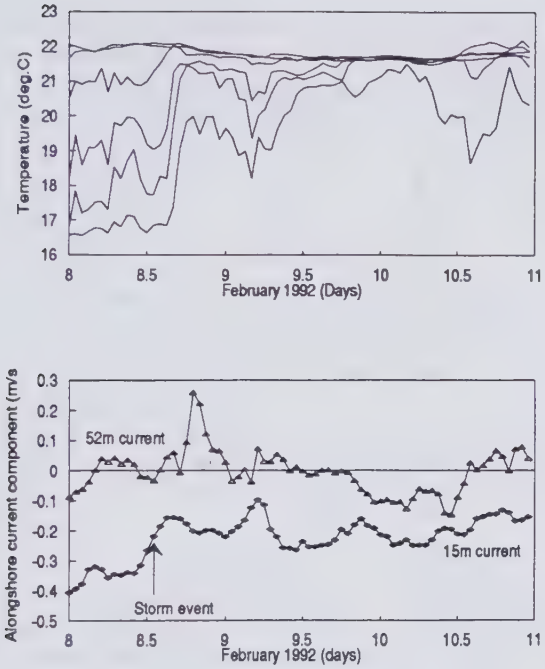

Figure 5. A storm event at the ORS over 8-10 February 1992 resulted in the quick reduction of a strong 6°C thermocline to < 1°C and a change in the current field. Beach sampling on 9 and 10 February 1992 revealed faecal coliform concentrations above criteria set for bathing waters.

surface effluent field may then be transported to shore by the south-easterly winds which often accompany storm events in Sydney. As winds subside, EAC influenced southward flows generally restore stratified conditions to Sydney's coastal waters.

Conclusions

The ocean processes described, account for much of the observed variability in temperature and current records. The position and strength of the thermocline and the current structure are expected to have a profound effect on the formation and subsequent dispersion of deepwater plumes. An understanding of the processes operating within and beyond the Sydney region is clearly necessary for the development of numerical models which aim to simulate the dispersion of effluent from Sydney's new deepwater outfalls.

Acknowledgments. This work was funded by the Environment Protection Authority of New South Wales as part of its Sydney Deepwater Outfalls Environmental Monitoring Program. The authors are grateful to Dr Robin Macdonald (EPA) who reviewed the manuscript. The provision of Ocean Reference Station data from by Sydney Water Board is also gratefully acknowledged.

References

Church, J.A., H.J. Freeland and R.L Smith, Coastal-trapped waves on the east Australian continental shelf. Part 1. Propagation of Modes, *J. Phys. Oceangr.*, 16, 1929-1943, 1986a.

Church, J.A., N.J. White, A.J. Clarke, H.J. Freeland and R.L Smith, Coastal-trapped waves on the east Australian continental shelf. Part II. Model Verification, *J. Phys. Oceangr.*, 16, 1945-1957, 1986b.

Church J.A., and H.J. Freeland, The energy source for the Coastal-trapped waves in the Australian Coastal Experiment, *J. Phys. Oceanogr.*, 17, 289-300, 1987.

Clarke A.J., The origin of the Australian Coastal Experiment Coastally Trapped Waves, *J. Phys. Oceanogr.*, 17, 1847-1859, 1987.

Cresswell, G.R., Ocean currents measured concurrently on and off the Sydney Area continental shelf, *Aust. J. Mar. Freshwat. Res.*, 25, 427-438, 1974.

Godfrey J.S., G.R. Cresswell, T.J. Golding and A.F. Pearce, The separation of the East Australian Current, *J. Phys. Oceanogr.*, 10, 430-440., 1980

Griffin D.A., M.A. Merrifield and J.H Middleton, An acoustic doppler current profiler survey of the nearshore current structure off Sydney, 26 November 1990, Unisearch Rep. R8567, 1991.

Griffin D.A., and J.H. Middleton, Current, water temperature and wind time-series, July 1989 - April 1990. A brief report on data from the Mk0 Ocean Reference Station, Unisearch Rep. R7410, 1990.

Griffin, D.A., and J.H. Middleton, Local and Remote wind forcing of New South Wales inner shelf currents and sea level, *J. Phys. Oceanogr.*, 21, 304-322, 1991.

Griffin, D.A., and J.H. Middleton, Upwelling and internal tides over the inner New South Wales Continental shelf, *J. Geophys. Res.*, 97, C9, 14389-14405, 1992.

Hamon, B.V., Tidal currents off Sydney, Marine Studies Centre Tech. Rep. 2/84, University of Sydney, 1984.

Lee, R.S., and I.S.F. Jones, The prediction of currents on the Sydney continental shelf, AMOS Newsletter, V3, 1, 2-12, 1990.

Lee, R.S., CTD surveying of the plume- Model Verification Experiment #3 - 9 April 1991, SPCC Rep. TR 91/11, 1991.

Middleton, J.H., Sydney Deepwater Outfalls Environmental Monitoring Program Commissioning Phase Volume 2- Physical Oceanography, EPA Report SPCC TR 92/43, 1991.

Tranter, D.J., D.J. Carpenter and G.S. Leech, The coastal enrichment effect of the east Australian Current eddy field, *Deep Sea Res.*, 3311/12, 1705-1728, 1986.

Webb, A. T., Sydney Deepwater Outfalls Environmental Monitoring Program Post-Commissioning Phase - East Australian Current influence on Sydney inner shelf currents, EPA report SPCC TR 92/36, 1992.

26

Dispersion of Effluent from Sydney's New Deepwater Outfalls. Part 2: Observations of Plume Behaviour: Winter and Summer Examples

T. R. Pritchard, R. S. Lee and A. Davison

Abstract

The plumes emanating from one of Sydney's new deepwater outfalls have been investigated using a combination of high resolution conductivity/temperature/depth (CTD) and radioisotope tracer techniques. Results presented illustrate typical winter (unstratified) and summer (stratified) scenarios. In the near field region, plume positions and effluent concentrations were estimated principally from observed salinity deficits (w.r.t. ambient ocean waters) while concentrations of introduced radioisotope tracers (Technetium-99m or Gold-198 and tritiated water) were mapped as they were advected with the plume into the far field region. Unstratified conditions during the May 1991 winter experiment resulted in the plume establishing in the top 20 m of the water column; initial effluent dilutions were about 1:700 to 1:1300. On this occasion, plumes from individual diffuser heads were observed to merge within 100 m of the diffusers at a depth of 55 m. Stratified conditions were encountered during the December 1992 summer experiment when the plume was observed at depths greater than 40 to 45 m with initial effluent dilutions of 1:200 to 1:300. Observations of the inactivation of enteric microorganisms within the submerged plume encountered during the December experiment indicated that sudden inactivation of faecal coliforms may be significant.

Mixing in Estuaries and Coastal Seas
Coastal and Estuarine Studies Volume 50, Pages 439-452
Copyright 1996 by the American Geophysical Union

Introduction

Three deepwater outfalls discharge most of Sydney's sewage waste some 3-4km off-shore from multiport diffusers in 60-80 m of water. Some of the oceanographic variables which determine plume position and effluent dilution have been described by Lee and Pritchard in Part 1: Ocean Processes.

A suite of models is being developed to simulate both near and far field behaviour of effluent plumes in Sydney's coastal waters. To verify these models, an experimental program has been implemented by the NSW Environment Protection Authority (EPA) in-conjunction with the Australian Nuclear Science and Technology Organisation, Australian Water and Coastal Studies Pty Ltd and the University of NSW Mathematics Oceanography Laboratories. This work forms part of the five year Sydney Deepwater Outfalls Environmental Monitoring Program.

A series of experiments was considered necessary to quantify plume characteristics under a wide range of ambient conditions. Results from experiments for two of the target scenarios are presented in this paper. That is, for typical unstratified winter conditions which were encountered on 17 May 1991 and for stratified summer conditions which were encountered on 18 December 1991. The experiments were undertaken in the vicinity of the Malabar deepwater outfall, located 4 km off-shore in 80 m of water (Figure 1). At the Malabar outfall, sewage effluent is discharged from up to 28 multiport diffusers spanning a shore normal distance of nearly 800 m. For both experiments, average effluent flow rates were about 400ML/day (4.63 $m^3 s^{-1}$).

Methods

Previous studies of the type described here are relatively scarce due to the high cost per measurement and the practical difficulties in locating and mapping highly diluted effluent from deepwater outfalls in dynamic environments. However, the thickness, position and dilution of some effluent fields have been determined using both CTD techniques (Washburn *et al.*, 1992, and Wallis, 1981) and introduced or artificial tracers, such as fluorescent dyes (Roberts and Wilson, 1990; Wright *et al.*, 1988; Toms and Botes, 1988; Bennet, 1981; and Wallis 1981) and radioisotopes (Davison *et al*, 1980).

High resolution CTD techniques were adopted principally for near field investigations using the plume's salinity and temperature signature. Radioisotope tracer techniques were employed for far field investigations due to their high sensitivity.

Washburn *et al.* (1992) used a T-S mixing curve to define progressive dilution for effluent discharged from outfalls in southern California. This was possible because of the large initial temperature and salinity differences between discharged effluent and ambient bottom waters (19 °C and 32 psu). However, in the Sydney region, the initial temperature difference between effluent and ambient bottom waters is small (2-5 °C) and the entrainment of cool bottom waters masks any positive temperature

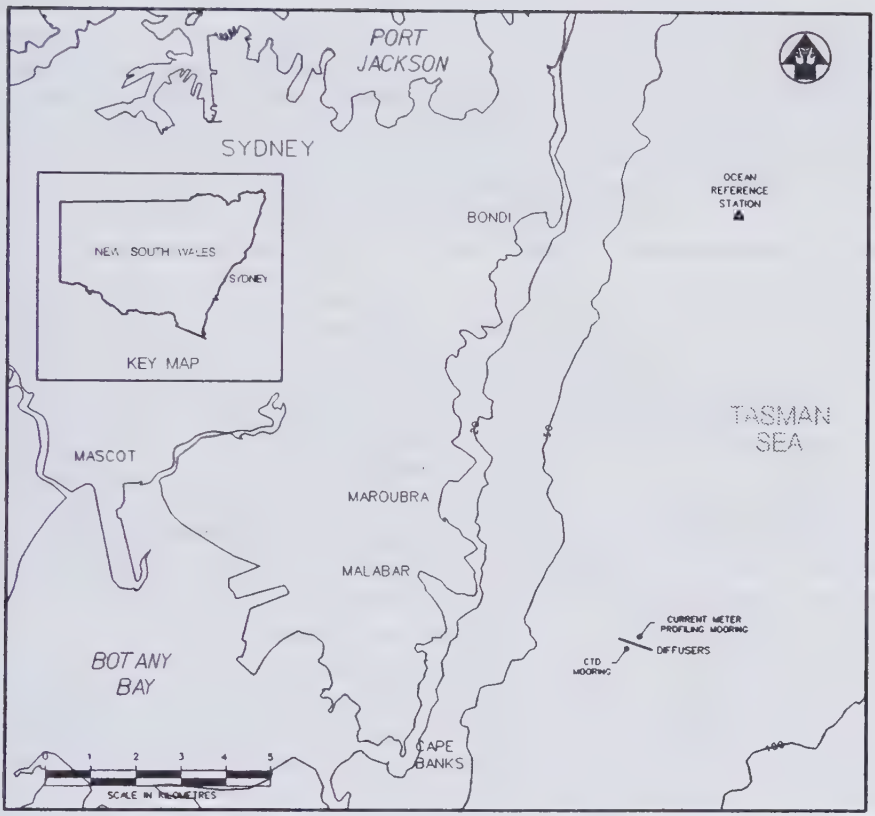

Figure 1. Locality of the Malabar deepwater outfall, the CTD and current meter moorings and the off-shore monitoring Ocean Reference Station.

anomaly that may exist close to the sea floor. Indeed, under stratified conditions, entrained bottom waters can label the rising plume with a negative temperature anomaly. Therefore, effluent concentrations were estimated from observed salinity deficits associated with the effluent (with respect to measured ambient salinity). Data from a Seabird Seacat CTD probe (conductivity resolution 0.0001 S/m; temperature resolution 0.001 °C and depth accuracy 0.5 m) were processed for differences in sensor response times, filtered for pressure reversals (due to excessive boat pitching) and values of temperature, salinity and density were derived from algorithms given by Fofonoff and Millard (1983). Vertical and horizontal CTD profiles were recorded both upstream (ambient) and downstream (impacted) from the outfall.

Radioisotope tracer techniques were selected for far field studies following comparative fluorometric trials. Technetium-99m (gamma energy 0.17 Me/V; half life 6.05 hour) was selected for one day experiments as it readily satisfies all

necessary safety requirements, provides high sensitivity to *in situ* measurement and has been successfully used as a conservative tracer for related applications (Hanna, 1983 & 1989). Gold-198 (gamma energy 0.42 MeV; half life 2.7 days) and Tritium (energy 0.018 MeV; half life 12.3 years) were used for later experiments in order to extend far field monitoring and provide a high sensitivity to indirect detection in discrete water samples collected for microbiological analyses. Gold-198 is adsorbed to mostly sub micron sewage particles while Tritium, a naturally occurring isotope of hydrogen, behaves as water. There was good agreement between both tracers in terms of average dilution and position within the water column.

Radioisotopes were injected into the effluent stream at Malabar Sewage Treatment Plant (STP), and tracer concentrations were monitored in the ocean using a triple detector system of scintillation counters at 10 metre depth intervals. Concurrent 'tow-yo' profiles were obtained from a second boat by raising and lowering a scintillation counter in transit across the plume to map the vertical and lateral extent of the labelled zone. The triple detector system integrated counts over periods of 10 seconds while the 'two-yo' system integrated counts over periods of 1 to 3 seconds. Hydraulic modelling of the outfall tunnel (Cathers and Peirson, 1991) indicated that the durations of tracer injections (2 to 6 hours) were sufficient to provide true estimates of effluent dilutions for the experiments reported here. All radioisotope data were corrected for natural background radiation, the relative sensitivity of sensors and radioactive decay before dilutions were calculated.

An investigation of the inactivation of microbiological sewage indicators in submerged effluent fields was also incorporated into the experiment. Twenty one samples were obtained from the STP to determine the average concentration of faecal coliforms in the effluent stream during isotope tracer injection. The patch of labelled effluent was then repeatedly sampled in the ocean over a period of about 7 hours as it advected away from the diffusers. All samples were stored in sterile containers at approximately 4°C and analysis commenced within 6 hours of collection. Analysis for faecal coliforms followed the American Public Health Association and Australian Standard methods with resuscitation as described by Rose *et al.* (1977).

Ambient currents and vertical density stratification were locally monitored throughout each experiment whilst the Sydney Water Board's Ocean Reference Station (Figure 1) continuously recorded temperatures through the water column and currents at depths of 15 m and 50 m. All current observations were made using Interocean S4 instruments. All position fixing was by Miniranger to an accuracy of ± 5 to 10 m.

No stratification- A Surfacing Plume - 17 May 1991

An unstratified water column with a top to bottom temperature difference of <0.05 °C, was maintained throughout the day providing optimum conditions for effluent to

surface. Current strengths observed in the vicinity of the outfall were relatively constant throughout the water column but gradually increased from 0.1 ms^{-1} to 0.2 ms^{-1} during the experiment. This flow prevailed generally to the south, with a 40-60° anti-clockwise offset in current direction from bottom to top due to bottom Ekman flux. Hence the effluent field within the surface layer travelled southwest for some 6km during the 12 hour experiment. Prevailing southeasterly winds of 7 ms^{-1} promoted on-shore transport, particularly of the effluent's floatable fraction.

Conductivity/Temperature Tracing

CTD profiles intersecting the rising plume in the immediate vicinity of the diffusers indicated salinity deficits up to 0.08psu while more distant profiles identified salinity deficits in plume waters as low as 0.02psu. However, typical salinity deficits of 0.05 to 0.035psu were measured throughout the day in the established plume corresponding to effluent dilutions of 700:1 to 1000:1. Initial CTD profiles showed the plume established in the top 30 m of the water column within 200 m of the diffusers although, with increasing currents, subsequent profiles indicated the plume occupying the entire water column significantly further downstream.

Plumes from individual diffuser heads (each with 7 active ports) appeared to merge approximately 100 m downstream at a depth of about 55 m. Dilutions calculated over the CTD track shown in Figure 2, indicate high dilutions between diffuser heads within 100m of the diffusers. Further downstream, the individual plumes appeared to have merged with average dilution of about 1:700. The signal was possibly punctuated by the CTD passing through the irregular lower boundary of the rising plume at the eastern end of the transect.

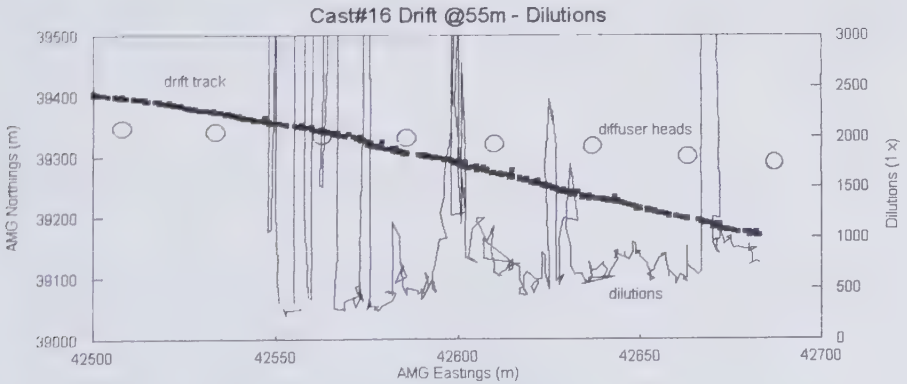

Figure 2. The track of the CTD, at a fixed depth of 55 m, is shown as it crosses the line of diffuser heads. Downstream dilution minima are located midway between diffuser heads within 100 m of the outfall. Ambient (upstream) salinities are stable.

Radioisotope Tracing

The radioisotope Technetium-99m was metered into the effluent stream at Malabar Sewage Treatment Plant (STP) for 2.5 hours, emerging from the diffuser system between 10:30 and 13:00. Measured mean tracer concentrations of 32 counts/second in the plume correspond to an initial dilution of 1:1260 at the time of ejection.

The 'tow-yo' detection system executed a longitudinal transect through the labelled plume shown in Figure 3. Initially the plume occupied the entire water column but, by 700 m downstream, it had lifted off the bottom and eventually became confined to the top 30 m of the water column. The labelled zone exhibited steep leading and trailing edges as seen in Figure 3.

A lateral transect across the established effluent field was completed by the triple detector system while the longitudinal transect (shown in Figure 3) was underway.

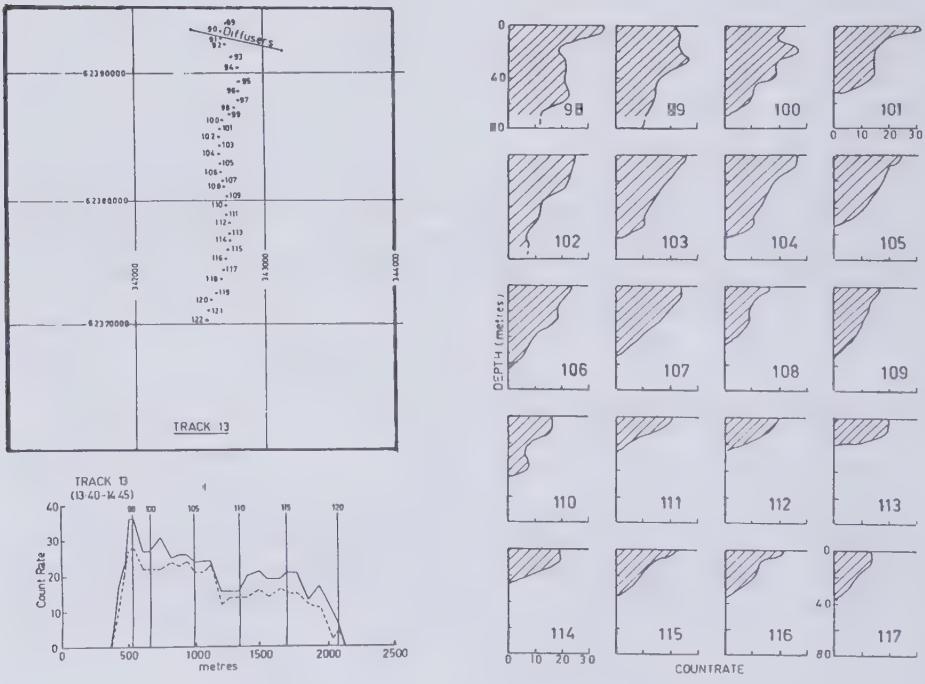

Figure 3. Radioisotope 'tow-yo' detector track extending nearly 1.5 km downstream from the diffuser system and showing vertical profiles obtained in transit. A north south transect has been constructed using the maximum count rate (solid line) and the mean count rate in the upper 20 m (dotted line) of the water column, determined from the vertical profiles.

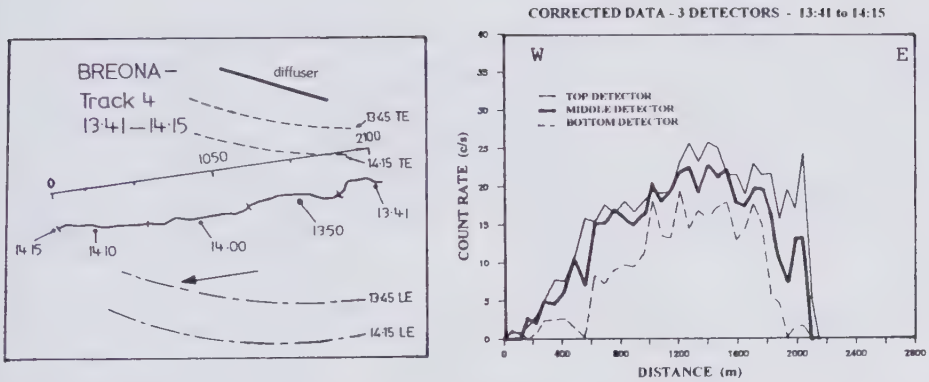

Figure 4. Profiles are given at depths of 10m, 20m and 30m along the east-west track taken by the triple detector system. The leading edge (LE) and trailing edge (TE) of the labelled zone were inferred from tracer observations (triple detector and 'tow-yo' profiling) and simultaneous local current profiling.

Figure 4 shows profiles from each of the sensors at depths of 10, 20 and 30 m. The relative difference between sensor profiles confirms the progressive increase in tracer concentration towards the ocean surface. It also shows increased tracer concentrations at the offshore end of the outfall where effluent flows are greatest (as designed) and where the southeast wind would be expected to promote the development of a front.

An areal dispersion pattern of the sewage field was constructed by combining 5 triple detector transects with some 140 'tow-yo' vertical profiles (Figure 5). Rapid lateral expansion of the effluent field occurs immediately after ejection while central contours converge to enclose a zone of maximum concentration. Subsequent lateral dispersion over a downstream interval of 1230 m was considerably less with a mean lateral dispersion coefficient of 9.5 $m^2 s^{-1}$ calculated between Section t1 and t2 in Figure 5. This value is similar to that expected for continental shelf waters and the length scale involved (Okubo, 1974).

Stratified conditions - A Submerged Plume - 18 December 1991

An East Australian Current (EAC) eddy encroachment was responsible for strong southward currents of 0.4 ms^{-1} in the upper layer. Baroclinic flows were observed with a strong pycnocline vertically separating an EAC influenced flow in the upper layer from weak diurnally/semi-diurnally rotating currents in a discrete lower layer at depths greater than 40 m. Observations from a nearby instrumented mooring (the Ocean Reference Station) showed that this scenario prevailed for the majority of this EAC shelf encroachment and hence results from the experiment are considered representative of plume behaviour during a summer EAC encroachment.

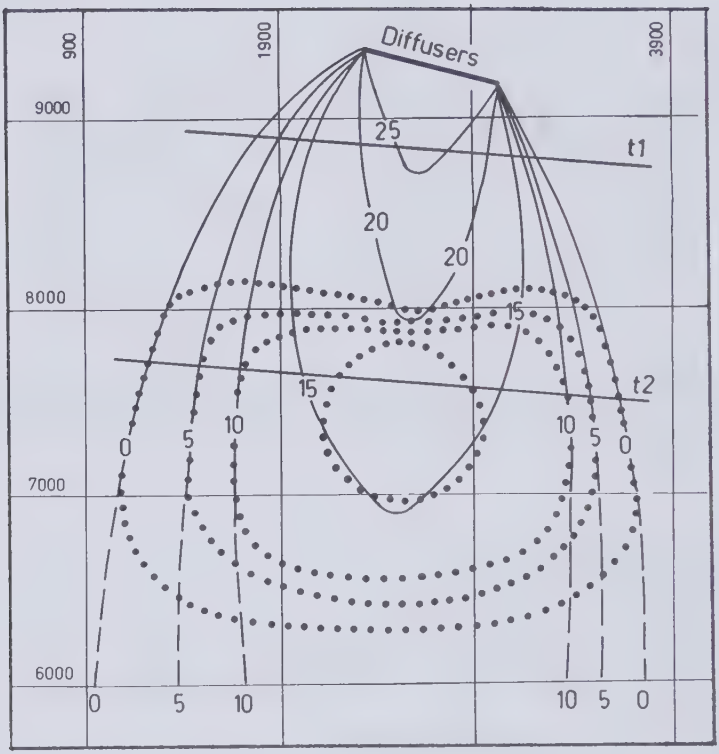

Figure 5. The areal dispersion pattern of the surfaced effluent field on 17 May 1991 constructed from radioisotope data. Contours represent the mean count rate (c/s) occurring in the surface 20m. Dotted contours represent tracer concentrations at a point in time.

Conductivity/Temperature Tracing

A comparison of CTD profiles shown in Figure 6, clearly identifies the plume by its (0.25psu) salinity deficit and its relatively cool temperature which was due to entrainment of cold bottom waters during initial dilution. At the impacted site, water temperatures of 15.4-15.8°C prevailed up to the plume's upper surface at 40-45 m whereas the ambient (control) vertical temperature profile exhibited a linear temperature gradient in the depth interval from 70m (15°C) to the surface (20°C). The temperature range of plume waters corresponded to ambient waters between depths of 60 and 68 m.

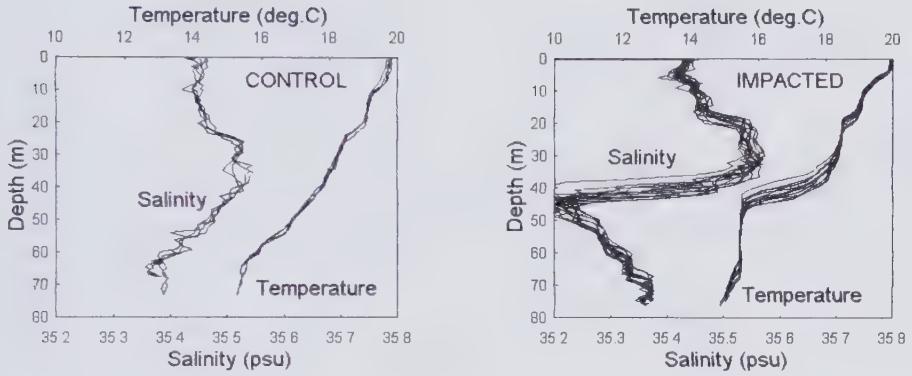

Figure 6. CTD profiles at the downstream mooring, and the upstream control on 18 December 1991.

Under stratified conditions such as these, the temperature signature of the dominant entrained water mass can be used to select the appropriate depth for the control salinity value from which dilutions are estimated. Near field dilutions of about 1:250-300 were estimated from CTD observations at this mooring, some 300 m downstream of the diffusers. During the experiment, a current reversal in the bottom waters (containing the plume) promoted a shallowing of the plume's discrete upper edge, and a deepening of its increasingly diffuse lower edge as depicted in Figure 7.

CTD 'tow-yo' dips and a drift along the centreline of the plume (Figure 8) identified an initial buoyant overshoot of the turbulent plume up to 100 m downstream of the diffusers. Other CTD drifts at a depth of 55m, indicated little difference between effluent dilutions estimated at 1 kilometre from the diffuser and those estimated at a distance of 150 m.

Radioisotope Tracing

The pair of radioisotopes tracers, Tritium and Gold-198 were used for the experiment on 18/12/92 to assess their potential to extend the ocean monitoring program and to facilitate a study of bacterial inactivation. Tritium was injected into the STP effluent stream for a period of 5.35 hours while Gold-198 was injected for 2.75 hours midway through the Tritium release. Real-time Gold-198 concentrations in the effluent field were measured using techniques developed for previous Technetium 99m experiments. Tritium concentrations were determined by liquid scintillation counting of samples which had been recovered from the effluent field either by Niskin Bottles or by pumping material to the surface. Dilution estimates based on-

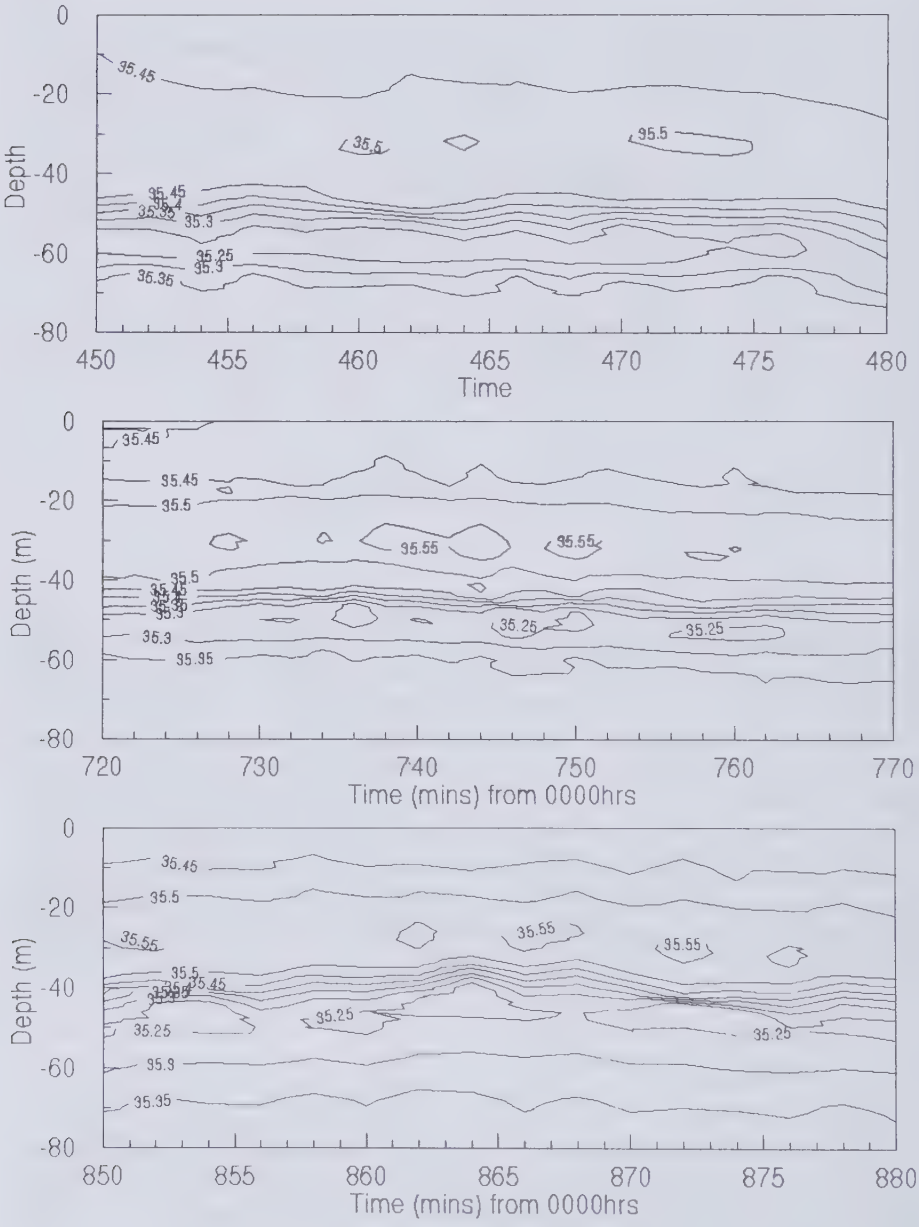

Figure 7. Contoured time series plots of the salinity field recorded at a mooring located 300 m downstream from the outfall cover the morning and afternoon periods of southward currents (450-460 and 850-880 minutes from midnight) and the interval of northward currents during the middle of the day (720-780 minutes from midnight).

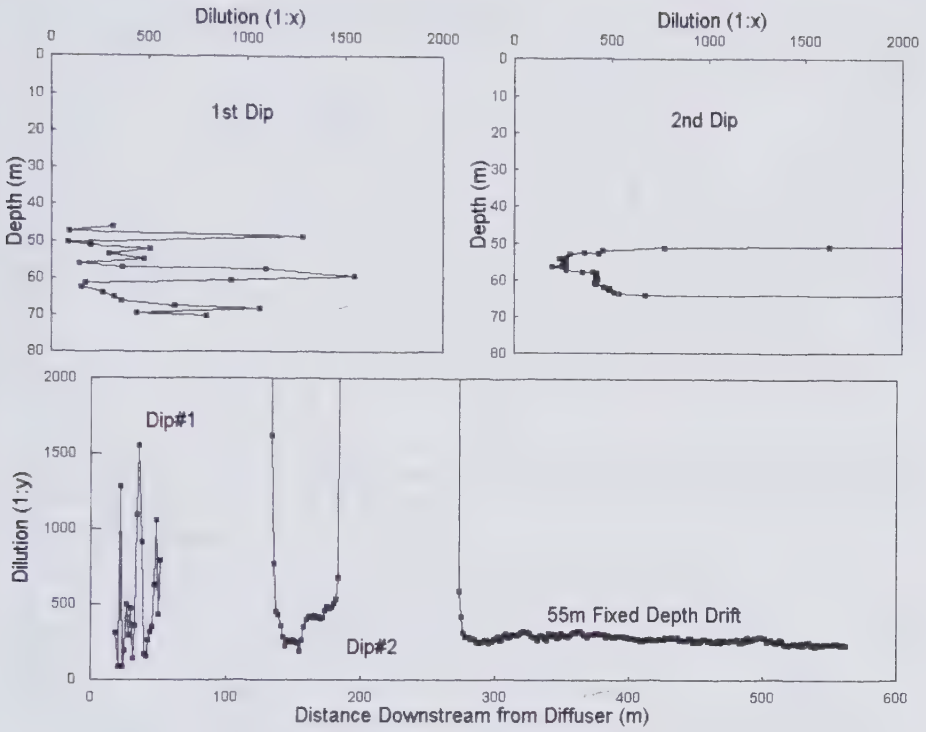

Figure 8. CTD casts including two 'tow-yo' dips within 200m of the diffuser system followed by a 55m fixed depth drift 270-570m downstream. An initial turbulent zone is evident in the first dip between 45 and 70m depth with minimum effluent dilutions of 1:100, while further downstream the second dip indicates the plume has become more homogeneous and dilute (1:300) occupying the depth interval from 50m to 65m. A subsequent centreline drift to 570m depicts minimal further dilution.

Tritium and Gold-198 concentrations were in good agreement with each other indicating a plume trapped below 45 m with dilutions in the range from 1:200 to 1:300.

Figure 9 shows the position and extent of the effluent field which had more than doubled in width 900 m downstream from the outfall. Maximum count rates rose rapidly on the eastern boundary of the effluent field due to the angle between the track line and the field centreline and partly due to the asymmetry in the discharge pattern (also observed during the May experiment).

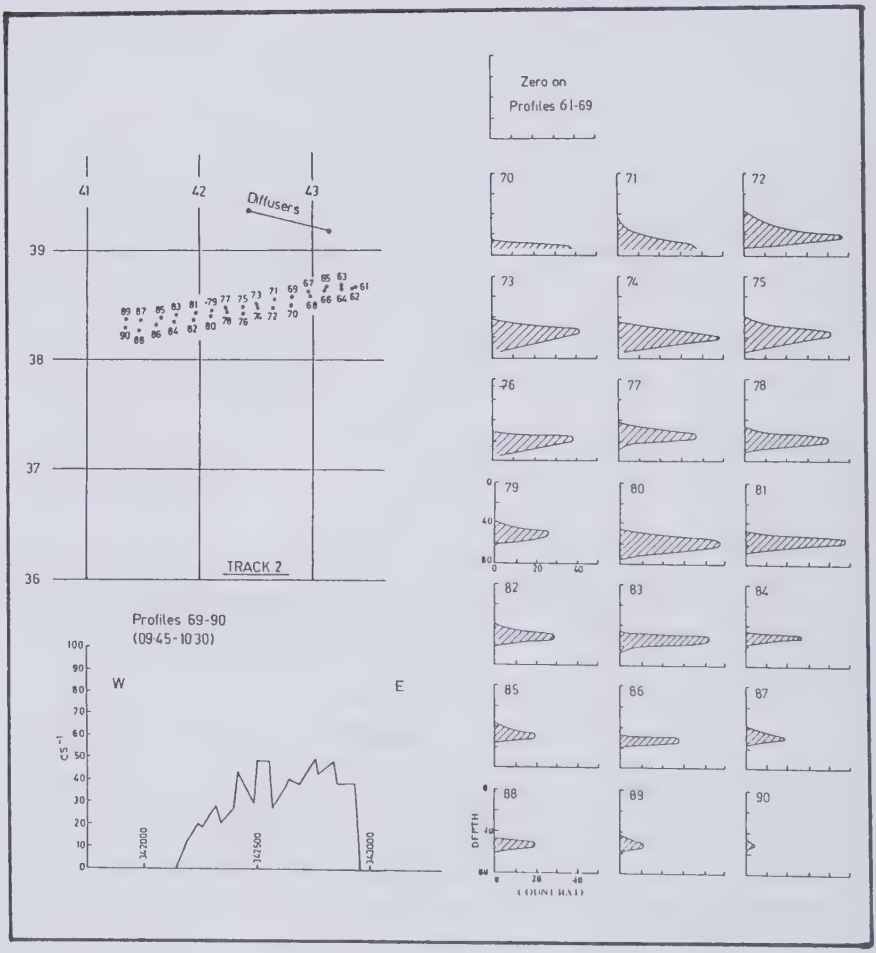

Figure 9. Radioisotope 'tow-yo' detector track extending across the effluent field and showing vertical profiles obtained in transit. An east west transect has been constructed using the maximum count rates observed during 'tow-yo' profiles.

Microbiological Studies

The models that have been developed to simulate the dispersion of effluent from Sydney's deepwater outfalls, can accommodate a time dependant decay factor to represent microbiological inactivation. Therefore, the program of model verification included observations of the inactivation of faecal indicator bacteria in submerged effluent plumes.

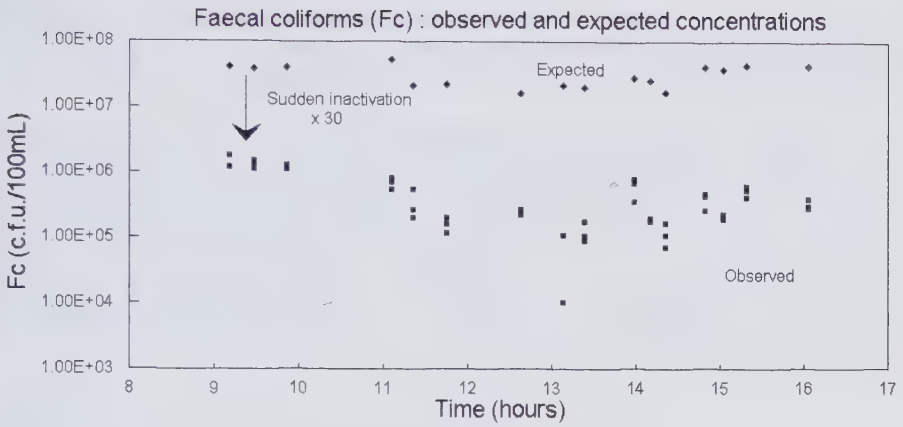

Figure 10. Faecal coliform densities, together with concentrations that would be expected due to physical dilution alone. Physical dilution was calculated from companion Tritium concentrations.

The relative importance of factors contributing to inactivation of indicator bacteria in deeply submerged effluent fields is poorly understood although temperature, nutrient levels, natural predation and lysis, and initial sewage characteristics are potentially significant. Other studies of microbiological inactivation in outfall environments indicate great variability between, and within, both field and laboratory studies. In this context, the microbiological results presented here are specific to the experiment conducted on 18 December 1992.

Reductions in concentrations of faecal coliforms observed in the ocean were greater than that expected due to physical dilution alone (Figure 10). Sudden inactivation appears to be significant with subsequent gradual inactivation (or removal by sedimentation/ flotation) taking place due to processes operating in the absence of bactericidal solar radiation. Previous microbiological studies conducted for the former cliff face outfalls by Caldwell Connell (1980) indicated that sudden inactivation was generally an order of magnitude less than that observed during the experiment reported here. Further experiments are therefore required to quantify sudden inactivation in deepwater outfall environments.

Conclusions

The combination of radioisotope and CTD techniques is capable of providing a comprehensive description of plume behaviour in the near and transition to far field regions for both surfacing and submerged effluent fields. CTD techniques and the various isotope tracers used for these studies appear to provide mutually consistent effluent dilution estimates. The high sensitivity of radioisotope tracers indicates that

these techniques are suitable to track effluent into the distant far field over a period of up to 36 hours. These studies also indicated that inactivation of indicator bacteria can be significant in the absence of bactericidal solar radiation.

Acknowledgments. This work was funded by the Environment Protection Authority of New South Wales as part of its Sydney Deepwater Outfalls Environmental Monitoring Program. Bacteriological analyses were completed by Mipro Pty Ltd and sample pick-ups were by SLSA Helicopters Pty Ltd. The work of staff and boat crews from the EPA, AWACS, ANSTO and the University of New South Wales is acknowledged. The authors are grateful to Dr Robin Macdonald (EPA) who reviewed the manuscript. The provision of real time data from the Sydney Water Board's Ocean Reference Station, is also gratefully acknowledged.

References

Bennet, N.J., Initial dilution: A practical study on the Hastings Long Sea Outfall. *Proc. Inst. Civ. Engrs.*, Part 1, 1981.

Caldwell Connell Engineers, Analysis of Oceanographic Data and Review of Ocean Outfall Design Concepts, Report for MWSDB, Sydney, July, 1980.

Cathers, B. and Peirson, W.L., Sydney Ocean Outfalls, Environmental Monitoring Program, Commissioning Phase, Model Verification Report 17 May 1991, AWACS Interim report No. 9/01/24, 1991.

Davison, A., Easey, J.F., Varjavandi, J.J. and Warner, K.M., Investigations into sewage grease behaviour in coastal waters. *Prog.Wat.Tech.*, Toronto, 12: 499-508, 1980.

Fofonoff, J. and Millard, A. Algorithms for computation of fundamental properties of seawater, UNESCO *Technical Papers in Marine Sciences* #44, 1983.

Hanna, G.L., Flow path and residence time studies in wastewater treatment lagoons. 10th Fed. Conv., Aust. Water and Waste Water Assoc., Sydney, 1983.

Hanna, G.L., An investigation of the flow and retention time in a two-meter deep waste sabilisation pond system. 13th Fed. Conv., Aust. Water and Waste Water Assoc., Canberra, 1989.

Okubo, A., Some speculations on oceanic diffusion diagrams, Rapports et Proces-verbaux des Reunions Conseil International Pour L'Exploration de la Mer, 167, 77-85, 1974.

Roberts, P.J.W. and Wilson, R. Field and Model Studies of Ocean Outfall. Hydr. Eng. Proc. Nat. Conf., HY Div/ASCE, San Diego. 1990.

Rose, R.E., Geldreich, E.E. and Litsky, W. A Layered Membrane Filter Medium for Improved Recovery of Stressed Faecal Coliforms. Symposium on The Recovery of Indicator Organisms (Sept '77) EPA 600/9-77-024, 1977.

Toms, G. and Botes, W.A.M., Measurements of initial dilution of a buoyant effluent. Water Research Commission, S.Africa, CSIR Report C/SEA 8766, 1988.

Wallis, I.G., Verification of Ocean Outfall Performance Predictions. *Proc. Am. Soc. Civ. Eng,* 107, EE2, 1981.

Washburn L, Jones, B.H., Bratkovich, A., Dickey, T.D. and Chen, M., Mixing, dispersion and resuspension in the vicinity of ocean wastewater plume, *J. Hyd. Eng.*,118(1), 38-58, 1992.

Wright, S.J., Mangarella, P.A. and Colonell, J.M., Outfall Plume Dilution in Stratified Fields. In Burgi P.(ed) *Proc.International Symposium on Model Correlation of Hydraulic Structures*. ASCE 1988, 148-157, 1988.

27

Monte Carlo Simulation of Sydney Deepwater Outfalls

T. Webb and D. Cox

Abstract

A stochastic model has been developed as part of the Environmental Monitoring Program for the Sydney Deepwater Outfalls. The model is based on an integral solution to the steady diffusion equations for a finite-width, finite-depth source. The coastal geometry, seabed, currents and sea water profile are very simply modelled, providing computation times more rapid than equivalent full numerical models and allowing use of a personal computer. Such computations are carried out hundreds of times, allowing statistics of pollutant indicator concentrations (faecal coliforms) to be estimated at sites distant from the outfalls. Verification against measured faecal coliform statistics from two beaches show that at least the high concentrations can be simulated using realistic measures of the physical processes. The model has been used to predict 90 percentile concentration contour maps for the sea surface and the sea bed.

Introduction

Effluent from Sydney's three major sewage treatment plants is discharged through deepwater ocean outfalls at Bondi, Malabar and North Head (Figure 1), commissioned in June 1991, September 1990 and December 1990. The outfalls are located between 2 and 3 km offshore in water 60-80 m depth and each comprises a line of vertical risers spaced 20-30 m apart. At the top of each of the risers is a rosette of between 4 and 8 ports from which the effluent is discharged in the form of

Mixing in Estuaries and Coastal Seas
Coastal and Estuarine Studies Volume 50, Pages 453-466
Copyright 1996 by the American Geophysical Union

buoyant jets. As part of an environmental monitoring program, a suite of numerical models is being developed with manifold objectives, one of which is to model the long term, far-field impact of the deepwater outfalls.

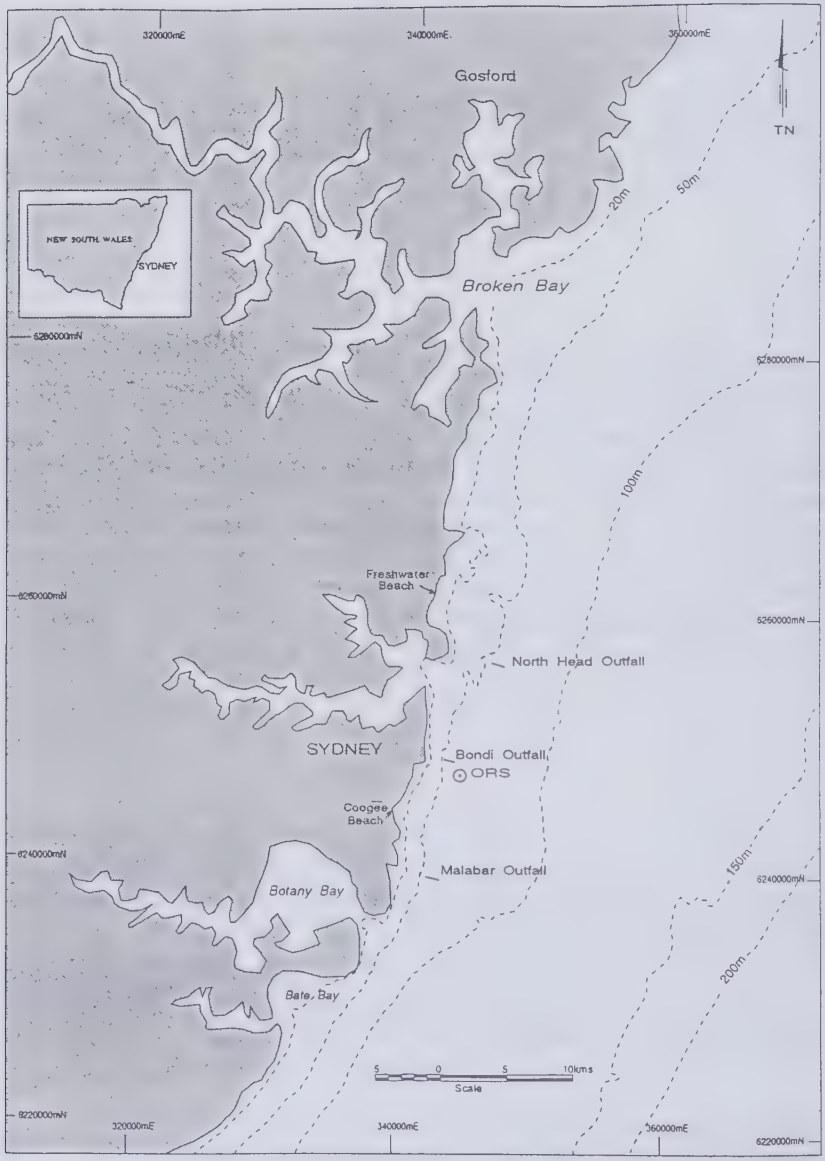

Figure 1. Location of Sydney deepwater outfalls, ocean reference station and beaches used for model verification.

The Problem

The dispersion mechanisms of wastewater effluent released from simple outfall diffusers are well understood from laboratory, theoretical and field studies. From models of buoyant jet behaviour, far-field dispersion, biological reactions etc., it is possible to develop an expression for the concentration C_{tgt} of a pollutant or tracer (we will be using faecal coliform bacteria) at an environmental target (such as a beach):

$$C_{tgt} = f\left(\begin{array}{ccc}\text{effluent/outfall} & \text{environmental} & \text{boundary} \\ \text{parameters,} & \text{parameters,} & \text{parameters}\end{array}\right) \quad (1)$$

where 'effluent/outfall parameters' include tracer concentration C_o, discharge flow rate Q, effluent density ρ_o, outfall depth D_o; 'environmental parameters' include density and density gradient ρ, $\partial\rho/\partial z$, current and current gradient, V, $\partial V/\partial z$, turbulent diffusivities K_x, K_y, K_z, biological decay reduction time t_{90}; and 'boundary parameters' include target location and geometry of the bed and coastline.

With each of these parameters well specified, a deterministic model can provide instantaneous values for C_{tgt}, and indeed, such models are being developed by others for the Sydney Deepwater Outfalls Environmental Monitoring Program (EMP) (Peirson, 1993), despite the fact that these outfalls are far from simple. The function *f* actually takes the form of a series of numerical models, principally one for the near-field (buoyant plume model) and one for the far-field (diffusion-advection model). That such an approach is bound to encounter difficulties is evidenced by a time series of measured faecal coliform concentrations at any site (Figure 2). Even plotting on a log scale cannot disguise the high temporal variability in the data.

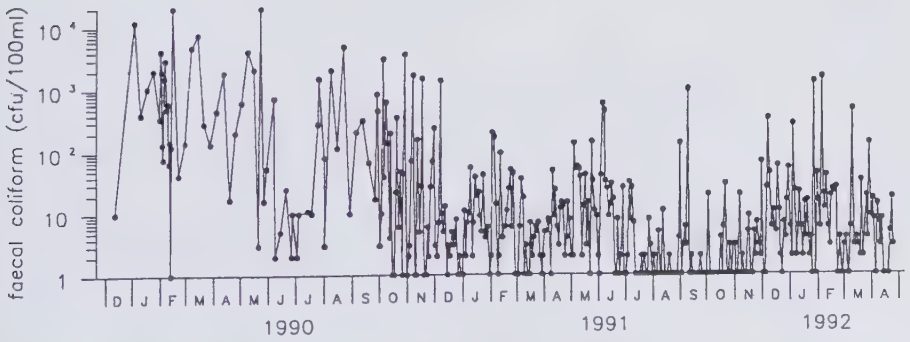

Figure 2. Measured faecal coliform concentration at a Sydney Beach. Although some pattern may be discerned, of more importance is the high variability. The data includes both wet and dry weather, but even excluding wet weather leaves a highly variable parameter (see Figure 5).

The cause of this variability is obvious when one examines time series of the effluent and environmental parameters (Figures 3 and 4). While there may be some underlying patterns in the data, the dominating feature is their variability — i.e. the parameters are stochastic, characterised by broad spectra. Consequently, deterministic models need to be run for very long simulation periods in order to develop reliable time series or statistics of C_{tgt}.

If only the statistics were required (e.g. for licence compliance checking), a stochastic model would suffice, but simple stochastic models cannot be developed for two reasons: firstly, the statistical distributions of the parameters are incompatible (e.g. it is not simple to find the result of multiplying a Gaussian and a log-normally distributed variable); secondly, the functional relations are by no means simple additions and multiplications, as evidenced by the effort being put into the deterministic numerical models.

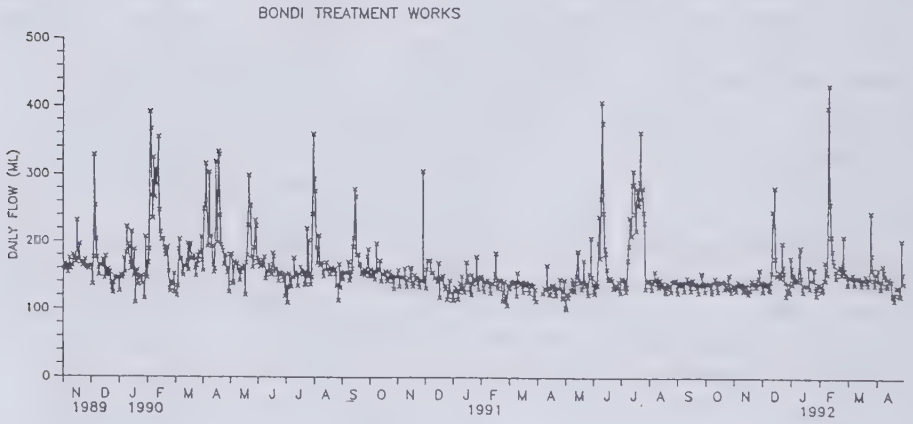

Figure 3. Effluent discharge rate from one of the Sydney outfalls. (The data are actually influent to the treatment works but there is little attenuation.) The hydrological response to storms is evident over a variable dry weather flow. The effluent faecal coliform concentration (not shown here) is even more variable.

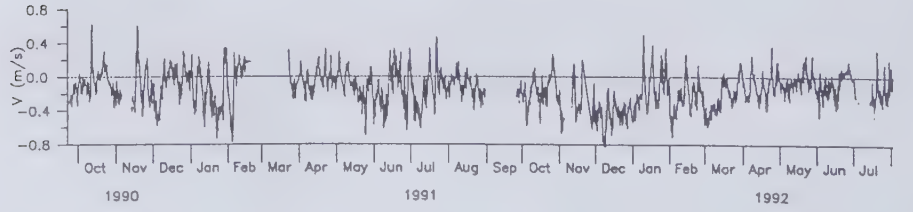

Figure 4. Alongshore component of current at the Ocean Reference Station, 15 m below the water surface. Other environmental parameters (e.g. other current components, temperature) show similar variability.

The Solution

As a compromise between the fully deterministic and fully stochastic approaches, we use a Monte Carlo simulation based on deterministic models simpler than the more complete numerical solutions. The essence of the simulation model is as follows:

Far-field model

The prime analytical component is an integral solution to the 3D diffusion equation featuring a finite-sized source, steady current, a reflecting sea surface, a reflecting, sloping sea bed and bacterial decay. In contrast to the integral models normally used in outfall design, the 'narrow plume' assumption (i.e. that alongstream diffusion can be ignored) is not employed. To account for persistence of tracer when the mean current has turned away from the target we view diffusion as a large scale phenomenon, so that much of the current variability is ascribed to diffusion, and only slowly varying currents are ascribed to the underlying mean current. In such a model, along-current diffusion is important and the narrow plume simplification is invalid. (This aspect is expanded by Webb, 1993.)

Sea-surface and seabed boundaries are accommodated using the imaginary reflecting source technique (only approximately true for the sloping seabed). Horizontal diffusion is based on measured rms currents, while vertical diffusion is estimated using vertical density and current gradients. Bacterial decay is modelled separately using multi-layer, 1st order kinetics with time constants based on field data.

Given this description, the conceptual model (Equation 1) can be developed using the superposition principle:

$$C_{tgt} = \sum_{i_{outf}} \sum_{i_{refl}} C_{i_{outf}\, i_{refl}} \tag{2}$$

where i_{outf} indexes the finite number of outfalls and i_{refl} indexes the reflections from the bed and sea surface (an infinite series that does converge). $C_{i_{outf}\, i_{refl}}$ represents the concentration at the target corresponding to a source (either original or one of the imaginary reflected sources) of a single outfall which, again by the superposition principle can be found by integrating instantaneous puffs from points within the source rectangle:

$$C_{i_{out} i_{refl}} = \int_0^{\infty} \int_{-\frac{d}{2}}^{\frac{d}{2}} \int_{-\frac{b}{2}}^{\frac{b}{2}} C_{puff\text{-}point}\, dy'\, dz'\, dt' \tag{3}$$

If we take $C_{puff\text{-}point}$ to be given by the Gaussian cloud (see e.g. Csanady, 1973), then the inner two integrals can be evaluated analytically (see Appendix A) to yield:

$$C_{i_{outf}\ i_{refl}} = \frac{q}{4\sqrt{2\pi}\ bd} \int_0^\infty \frac{1}{\sigma_x} \exp\left\{-\frac{(x-Ut)^2}{2\sigma_x^2}\right\} \cdot \left(\operatorname{erf}\left(\frac{b/2+y}{\sqrt{2}\sigma_y}\right) + \operatorname{erf}\left(\frac{b/2-y}{\sqrt{2}\sigma_y}\right)\right) \cdot \left(\operatorname{erf}\left(\frac{d/2+z}{\sqrt{2}\sigma_z}\right) + \operatorname{erf}\left(\frac{d/2-z}{\sqrt{2}\sigma_z}\right)\right) dt \qquad (4)$$

where $q = Q.C_0$ is source tracer flux, b and d are the source breadth and depth, x, y, z are the coordinates of the target relative to the source centre in the alongshore, offshore and vertical directions, U is the steady alongshore current, σ_x, σ_y, σ_z are diffusion standard deviations (functions of time), and t is the time since release of an instantaneous puff (disappears with the numerical integration). The result is reduced by an additional factor D to account for bacterial decay.

At the scale we have chosen to partition turbulence (days), horizontal diffusion times can be assumed short, and we use a linear time relation for σ_x and σ_y :

$$\sigma_x = u_{rms}t, \qquad \sigma_y = v_{rms}t \qquad (5)$$

For vertical diffusion, we use a constant diffusivity form where diffusivity is related to stratification (Munk and Anderson, 1948):

$$\sigma_z = \sqrt{2K_z t} \qquad (6)$$

$$K_z = \frac{1}{(1+3.3\,R_i)^{3/2}} K_{zo} \qquad (7)$$

where K_{zo} is the value of diffusivity in the absence of stratification and R_i is a gradient Richardson number:

$$K_{zo} = \lambda^2 \left|\frac{\partial U}{\partial z}\right| \qquad (8)$$

$$R_i = -\frac{g}{\rho} \frac{\frac{\partial \rho}{\partial z}}{\rho\left(\frac{\partial U}{\partial z}\right)^2} \qquad (9)$$

The density and velocity gradients are taken from the two current/temperature meters of the reference station and the mixing length λ (taken to be a fraction of depth) is used as a model tuning parameter.

The dieoff factor D is taken to comprise an initial instantaneous factor and a slowly acting 1st order decay derived from field experiments conducted during the outfall project design (Caldwell Connell Engineers, 1980). The latter are made depth dependent to account for the attenuation of light with water penetration, given that UV radiation is the main factor in faecal coliform decay. The initial dieoff is used as a second tuning parameter, although it is not allowed to take values outside the range deduced from field measurements (values up to 15 reported by Caldwell Connell, 1980; and even higher for the present outfalls — Pritchard, pers. comm.). Whether initial dieoff is a real biological process or due to sedimentation is beyond the scope of this study and for the impact on far-field concentrations it is enough that we have a tuning factor that accounts for processes that rapidly reduce populations.

Near-field model

The sources for the far-field model are defined by the flux of faecal coliform issuing from each of the three treatment works, together with the dimensions and position of the initial dilution zones (IDZ). Each IDZ is treated as rectangular with a characteristic field thickness, width and position (rise height and distance downstream from the diffuser).

The dimensions and position of the IDZ are estimated using results of laboratory studies by (Roberts *et al.* 1989), involving finite-length, multi-port diffusers with T-shaped risers discharging into a linearly stratified current[1]. These results showed that for diffusers with sufficiently closely spaced ports and low momentum flux, interaction between plumes from adjacent risers allowed the diffusers to be approximated as a line source. An assessment based on the geometry of a typical port (Webb and Cox, 1992) suggested that although the geometry was not identical to that of Roberts *et al*, there would indeed be considerable interaction, and hence the line diffuser model results could be used.

The influences of ambient current and density profile are based on the same data as the far-field model.

Simulations

The linked far and near-field models (Equation 2) are embedded in a shell that implements the Monte Carlo simulation. At each realisation (cycle of the loop), random number generators select values for the input parameters according to their distributions (joint distribution for pairs of parameters where the relationship is important). The cumulative frequency distribution of tracer concentration is assembled in the simulation loops.

---

[1]A similar laboratory study of the diffusers from the Sydney outfalls was being performed concurrently with the present study. The results are as yet unpublished (Couriel, 1993) and have not yet been reduced to a form suitable for inclusion in our model, although the plume interaction is confirmed.

Random number generators are required to simulate the statistical distributions of the model input parameters. Distribution types include normal (Gaussian), log-normal, log Pearson type III (LPIII) and gamma, whose parameters are estimated by matching measured data; e.g. the ocean current and temperature data were derived from the two current meters on an Ocean Reference Station located 3 km offshore at depths of approximately 15 m and 50 m. The current meter data records were filtered at ten days, the low frequency component being taken as 'current' and the high frequency component converted to rms to represent dispersion. At this partition frequency, the low frequency component of offshore current is small enough to be ignored. The distribution types for these and other parameters are summarised in Table 1.

TABLE 1. Parameter Distribution Types

Parameter	Distribution
current at top meter	normal with piecewise linear modification
conditional current at bottom meter	normal, linear relation for mean and s.d.
temperature at top meter	gamma
conditional bottom temperature	gamma, linear for mean, quadratic for s.d.
rms turbulent horizontal velocities	log-normal
dieoff t_{90}	log-normal
sudden decay	log-normal
effluent discharge rate	LPIII
effluent faecal coliform concentration	log-normal

An example of the fitted distributions is given for outfall discharge rates in Figure 5. The result of the simulations is the predicted statistical distribution of tracer concentration at a nominated target position.

The Test

Faecal coliform data for many beaches in the study region have been collected for over several years by the Water Board, with increased frequency since the construction of the outfalls. Post-commissioning data were selected on the basis of North Head outfall commissioning (taken to be 20-12-90) for the northern beaches, and Bondi outfall commissioning (01-06-91) for the southern beaches. (Malabar (01-09-90) was commissioned before both of the other sites.) Because of the difficulty in quantifying non-outfall sources, the data were further limited to those corresponding to dry weather on the basis of local rainfall records. The lag between a rainfall event and beach sample measurement is between one and two days, which should be well and truly long enough to minimise stormwater source effects when most of the catchments are small and the decay time for the tracer is typically less than one day. The sites chosen for calibration and verification are Coogee and Freshwater Beaches respectively.

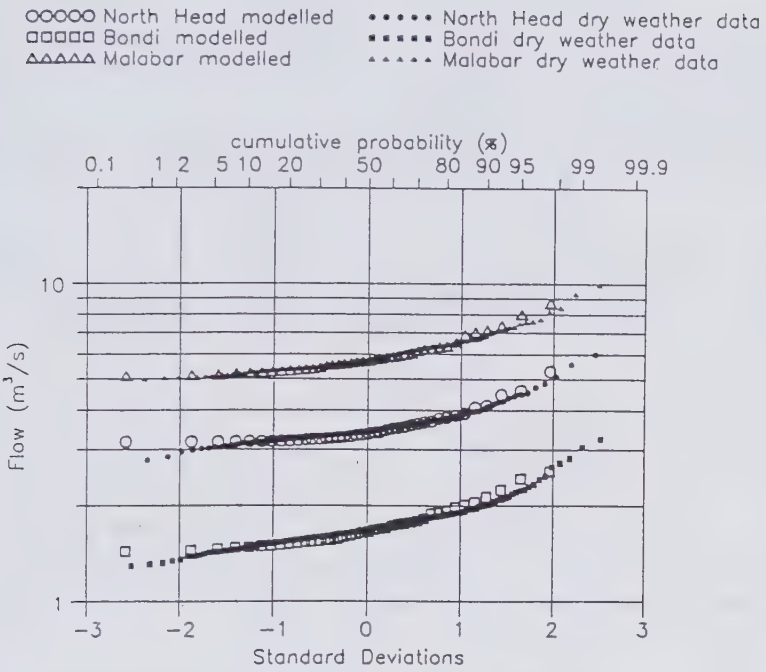

Figure 5. Measured and fitted distributions for outfall discharge rates. The modelled distribution types are Log-Pearson Type III. (Adapted from Webb and Cox, 1992)

Of the many parameters that could have been used for tuning, only two were selected - the mixing length λ for vertical diffusivity, and the values for sudden dieoff (D_{sud}).

Values selected to get as good match as possible for Coogee were kept for the verification check on Freshwater. Figure 6 shows the resulting comparison between model and field data.

The calibration/verification match seems acceptable for the upper portion of the distribution (above 50 percentile) and therefore predictions for 90 percentiles (values most commonly used in monitoring) should be reliable. However there is still some factor missing that influences the lower part of the distribution. (NB models based on the narrow plume assumption miss far more of the bottom of the distribution.) Whether the mismatch in this region is due to the model or the presence of alternate sources (they are not all eliminated by restricting data to dry weather) is yet to be determined.

Some comment is warranted regarding the values used for tuning and the sensitivity of the model to those parameters. Recognising that the top half of the distribution is the more important, and that the model does not appear to be able to reproduce the bottom half of the distribution, we choose as a two parameter merit function the absolute difference between modelled and measured 50 and 84 percentiles on the

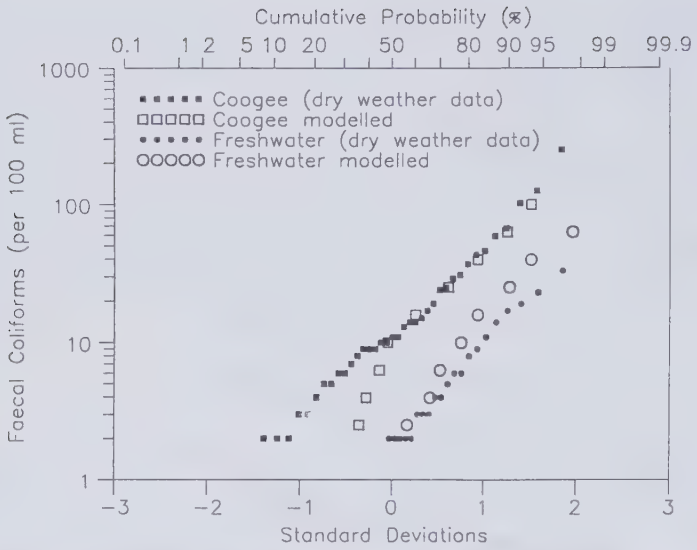

Figure 6. Predicted and measured faecal coliform cumulative probability distributions at two Sydney beaches. (Adapted from Webb and Cox, 1992).

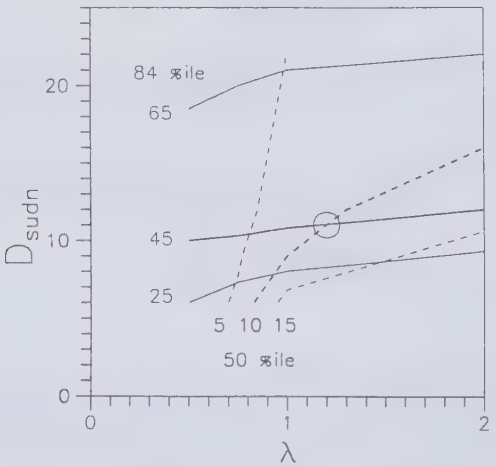

Figure 7. Tuning parameter selection. The model is deemed to be 'tuned' when the 50 and 84 percentile faecal coliform concentrations are both matched to their measured values of 10 and 45 cfu/100 mL — i.e. at the intersection of the thicker solid and dashed lines.

faecal coliform concentration distribution. By estimating the 50 and 84 percentiles at the target site corresponding to several values of the tuning parameters (λ and D_{sud}) we can interpolate the contours where the estimated percentiles match the measured values. The point at which those contours cross (Figure 7) gives the best model fit according to the merit function.

The value of λ found to get a good match (1.2) was a little higher than expected, (turbulent boundary layers have $\lambda \approx 0.4$), but may account for missing phenomena such as upwelling. The value of sudden decay (50 percentile of 11) is also a little higher than that found in the Caldwell Connell (1980) field experiments (50 percentile of 4), but there is still some contention about what values would be expected from the deepwater outfalls and there may be additional factors contributing to sudden decrease in faecal coliform population.

Given the simplicity of the underlying models (line diffusers, highly regularised bathymetry, uniform diffusion parameters, the steady snapshot assumption and others) it is remarkable that the tuning process works as well as it does. It remains to be seen how much better the more complete models now under development perform.

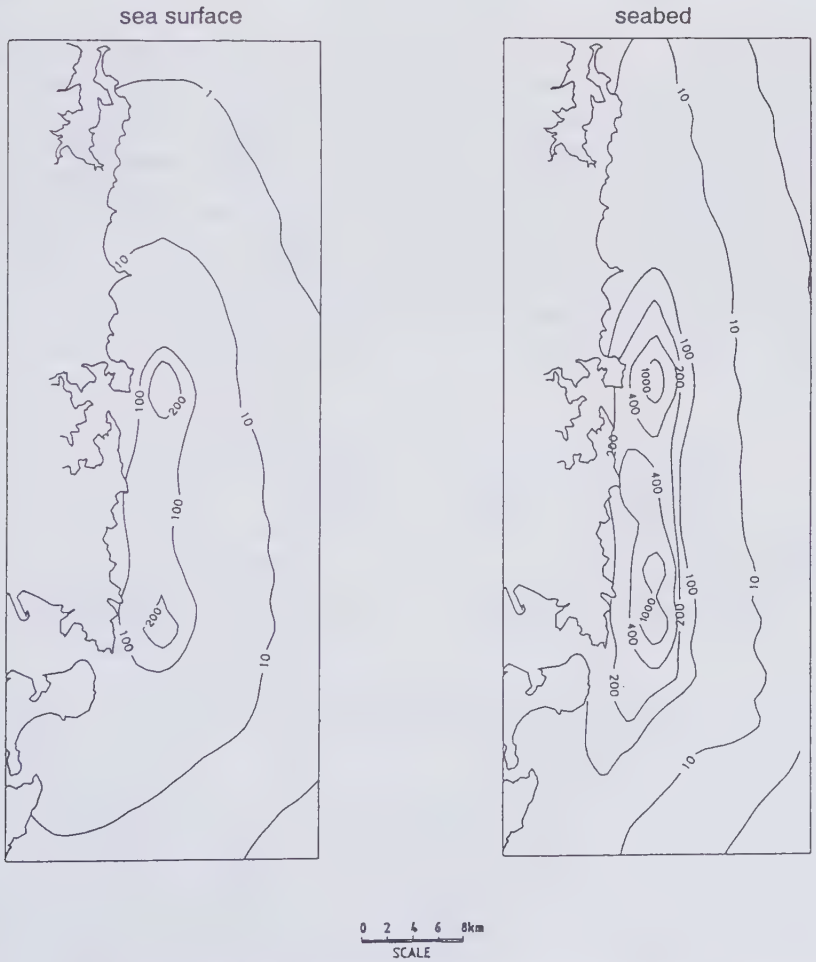

Figure 8. Predicted faecal coliform 90 percentiles at sea surface and seabed. (Adapted from Webb and Cox, 1992)

The Use

On the strength of the verification we have enough confidence to use the model to produce contour maps of 90 percentile values for C_{tgt} at various depths over the coastal waters of Sydney (Figure 8). If we take a 90 percentile of 200 counts/100 mL as a suitable standard for bathing waters, then the outfalls appear to be doing their intended job, at least for surface waters. Even on the seabed, it is only the region around the outfalls that is significantly impacted. Note that seabed values are much higher than those at the surface because the initial dilution zone is often trapped well below mid depth. Note also the asymmetry resulting from the sloping bed.

Acknowledgements. This work was carried out as part of the Sydney Deepwater Outfalls Environmental Monitoring Program (Webb and Cox, 1992) on behalf of the NSW Environment Protection Authority. The provision of data and assistance by The Environment Protection Authority, the Sydney Water Board, and Australian Water and Coastal Studies is gratefully acknowledged. The reviews of Professor I. Wood, University of Canterbury and Professor D. Wilkinson, University of New South Wales provided timely corrections and improvements. The advice of Dr R. Nunez-Vaz, Australian Defence Force Academy is also acknowledged. Finally the authors thank the reviewers who made several useful suggestions.

References

Caldwell Connell Engineers, Analysis of Oceanographic Data and Review of Ocean Outfall Design Concepts, Report for MWSDB, Sydney, July 1980.

Couriel, E.D. Sydney deepwater outfalls environmental monitoring program post-commissioning phase: near field physical modelling, *Australian Water and Coastal Studies Report* 93/01/06 (in prep), 1993.

Csanady, G.T. *Turbulent Diffusion in the Environment*, Reidel Pub. Co., Dordrecht, 1973.

Munk, W.H. and E.R. Anderson, Notes on a theory of the thermocline, *J. Mar. Res.*, 1, 276-295, 1948.

Peirson, W.L. Sydney deepwater outfalls, environmental monitoring program post-commissioning phase period 1: Numerical Modelling Report, *Australian Water and Coastal Studies Report* 92/01 (in prep), 1993.

Roberts, P.J.W., W.H. Snyder and D.J. Baumgartner. (3 papers) Ocean outfalls: (I) Submerged wastefield formation (II) Spatial evolution of submerged wastefield. (III) Effect of diffuser design on submerged wastefield. *ASCE J. Hyd. Eng.*, 115(1) (3 papers) 1-70, 1989.

Webb, A.T. and D.R. Cox. Sydney deepwater outfalls, environmental monitoring program post-commissioning phase, SDOSIM — a Monte Carlo simulation model, *Australian Water and Coastal Studies Report* 92/01/17, also published by Environment Protection Authority TR 92/52, 1992.

Webb, A.T. Why can't you use the narrow plume assumption in modelling large ocean outfalls, *Proc. 11th Australasian Conf. Coastal and Ocean Eng.*, Inst. Eng. Australia, Townsville, 1993.

Appendix A — Diffusion of Instantaneous Rectangular Source

We seek a solution to the three dimensional diffusion equation (uniform current (U) in x-direction; x, y, and z are principal diffusion directions):

$$U\frac{\partial C}{\partial x} - \frac{\partial K_x \frac{\partial C}{\partial x}}{\partial x} - \frac{\partial K_y \frac{\partial C}{\partial y}}{\partial y} - \frac{\partial K_z \frac{\partial C}{\partial z}}{\partial z} + \frac{\partial C}{\partial t} = 0, \tag{A1}$$

for a source of mass M released at t = 0, from x = 0, distributed over a rectangle defined by:

$$\left.\begin{aligned} -\frac{b}{2} \le y' \le \frac{b}{2}, \\ -\frac{d}{2} \le z' \le \frac{d}{2}. \end{aligned}\right\} \tag{A2}$$

For an infinite ocean the boundary conditions are:

$$C = 0 \quad \text{at} \quad x = y = z = \pm\infty \tag{A3}$$

The solution (δC) to A1 for a point source of mass $\delta M = \frac{M}{bd}\,\delta y\,\delta z$ released from the origin is given by the expanding Gaussian cloud with possibly anisotropic variances:

$$\delta C(x, y, z, t) = \delta M \frac{\exp\left(-\frac{(x-Ut)^2}{2\sigma_x^2}\right)}{\sqrt{2\pi}\sigma} \cdot \frac{\exp\left(-\frac{y^2}{2\sigma_y^2}\right)}{\sqrt{2\pi}\sigma} \cdot \frac{\exp\left(-\frac{z^2}{2\sigma_z^2}\right)}{\sqrt{2\pi}\sigma} \tag{A4}$$

where the only condition on the variances σ_x^2 etc. is that they satisfy: $\frac{d\sigma_x^2}{dt} = 2K_x$ etc.

Using the superposition principal expounded by Csanady (1973) and other texts, we can construct the finite source solution from incremental point sources distributed over the rectangle:

$$C(x,y,z,t) = \int_{-\frac{d}{2}}^{\frac{d}{2}} \int_{-\frac{b}{2}}^{\frac{b}{2}} \frac{M}{bd} \frac{\exp\left(-\frac{(x-Ut)^2}{2\sigma_x^2}\right)}{\sqrt{2\pi}\sigma_x} \cdot \frac{\exp\left(-\frac{(y-y')^2}{2\sigma_y^2}\right)}{\sqrt{2\pi}\sigma_y} \cdot \frac{\exp\left(-\frac{(z-z')^2}{2\sigma_z^2}\right)}{\sqrt{2\pi}\sigma_z} dy'\,dz' \tag{A5}$$

Assuming that the variances depend only on time (as implied in the condition mentioned below equation (A4)), the integrations in (A5) can be separated:

$$C(x,y,z,t) = \frac{M}{bd} \frac{\exp\left(-\frac{(x-Ut)^2}{2\sigma_x^2}\right)}{\sqrt{2\pi}\sigma_x} \int_{-\frac{b}{2}}^{\frac{b}{2}} \frac{\exp\left(-\frac{(y-y')^2}{2\sigma_y^2}\right)}{\sqrt{2\pi}\sigma_y} dy' \int_{-\frac{d}{2}}^{\frac{d}{2}} \frac{\exp\left(-\frac{(z-z')^2}{2\sigma_z^2}\right)}{\sqrt{2\pi}\sigma_z} dz' \tag{A6}$$

Finally, the integrals can be evaluated, giving:

$$C = \frac{M}{bd} \frac{\exp\left(-\frac{(x-Ut)^2}{2\sigma_x^2}\right)}{\sqrt{2\pi}\sigma_x} \frac{1}{2}\left(\operatorname{erf}\left(\frac{y+\frac{b}{2}}{\sqrt{2}\sigma_y}\right) - \operatorname{erf}\left(\frac{y-\frac{b}{2}}{\sqrt{2}\sigma_y}\right)\right) \frac{1}{2}\left(\operatorname{erf}\left(\frac{z+\frac{d}{2}}{\sqrt{2}\sigma_z}\right) - \operatorname{erf}\left(\frac{z-\frac{d}{2}}{\sqrt{2}\sigma_z}\right)\right) \tag{A7}$$

This function vanishes at $t = \pm\infty$ and hence the solution for continuous discharge can be found by integration (numerical) over the effective duration.

28

Study of Thermal Discharge with Satellite and Airborne Data

S. Onishi

Abstract

Analytical methods to locate the axis of thermal discharges and to estimate the area influenced by the discharge in coastal regions using satellite data are presented. At a site of a power station operating in Japan, the relationship between water temperatures predicted using satellite data (Landsat), field surveys and airborne remote sensing data are discussed. In the case of Landsat data, algorithms suggested by Gibbons *et al.* (1989) and RESTEC provide water temperatures approximately 3°C higher than measured values. Combined use of satellite and airborne data may be useful in routine monitoring to avoid problems caused by cloud cover etc.. However, data obtained from the 2 systems cannot be compared directly with each other. To establish a monitoring system combining the two different surveying methods, more investigations are required.

Introduction

Ecological effects of thermal discharges into the coastal zone from industrial sources have generated worldwide interest. To estimate these effects, field investigations are indispensable. From an idealistic viewpoint it is required that synoptic observations of the discharge are available. However, this goal is hindered by two serious obstacles: (1) the large spatial scale of the related phenomena and, (2) difficulty in visually distinguishing the effluent. However, we can take a synoptic view of the sea surface and visualize the discharge through data obtained

Mixing in Estuaries and Coastal Seas
Coastal and Estuarine Studies Volume 50, Pages 467-478
Copyright 1996 by the American Geophysical Union

from satellite scanners. Landsat imagery have been used to predict chlorophyll concentrations in coastal water with a high degree of accuracy (Bagheri and Dios, 1990; Lathrop and Lillesand, 1986; Tassan, 1987; Lavery and Pattiaratchi, 1990; Lopez-Garcia and Caselles, 1990; Pattiaratchi, 1992). Images of sea surface temperature, derived from the Landsat TM 6 band data have been used to study the behavior of river effluents and thermal discharges from power stations (Lathrop and Lillesand, 1987; Gibbons *et al.* 1989; Onishi and Kawai, 1992). However, one of the major problems of satellite remote sensing is that since satellites pass the same area only at fixed intervals, the observations may be hindered by cloud. The deficiencies of satellite remote sensing may be supplemented by the use of airborne scanners. For example, Davies and Mofor (1991) used data from a series of airborne remote sensing flights to survey the marine discharge of cooling water from a coastal power station to investigate its turbulent characteristics. However, the cost of airborne remote sensing is considered expensive for it's use in routine monitoring of discharges and their effects on the environment. From a practical point of view, proper use of both the satellite and airborne remote sensing is favourable for routine surveying of the discharges in coastal areas. From this point of view, this study presents an analytical method to estimate the water area influenced by thermal discharge from power plants, with satellite data. The significance of results obtained from the satellite, near-field survey and airborne remote sensing data are discussed.

Survey of Thermal Discharge with Satellite Data

Satellite Data

This study used digital data obtained by the Landsat Thematic Mapper (TM). The Landsat satellite circle the Earth every 98.9 minutes in a near polar orbit, 705 km high. From that perspective, it can view the same area every 16 days, at the same local time of day. The TM collects data by continually scanning the Earth from west to east with an oscillating mirror and records radiation in seven spectral bands shown in Table 1. The TM data has a resolution of 30 m^2 for bands 1 to 5 and 7 and 120 m^2 for band 6. For this study data from band 6 (thermal) was used.

TABLE 1. Range of Electro-Magnetic Wave Length of Landsat TM

Electro-Magnetic Wave Name	Band	Wavelength (μ m)	Resolution (μ m)
Visible Blue	1	0.45 - 0.52	30
Green	2	0.52 - 0.60	30
Red	3	0.63 - 0.69	30
Near Infrared	4	0.76 - 0.90	30
Middle Infrared	5	1.55 - 1.75	30
	7	2.08 - 2.35	30
Far Infrared	6	10.4 - 12.5	120

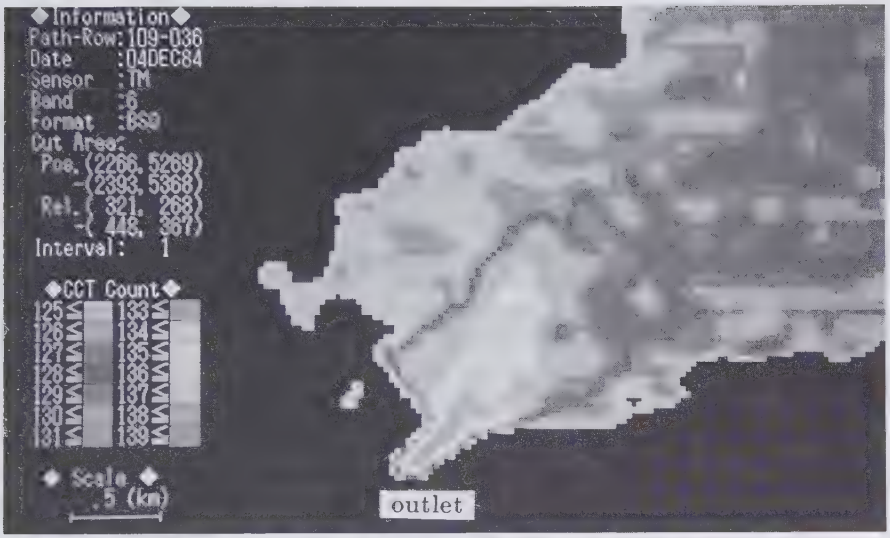

(a) TM-6 band image

(b) Thermal DN contour map

Figure 1. Thermal discharge from Mita power station (4 Dec. '84)

Radiation intensity gathered by the scanner is known as DN (Digital Number), which permit large volumes of data to be processed by a computer. The conversion of radiation intensity to digital data is based on separating the measured intensities into binary increments, based on byte word lengths with 0 representing the darkest or lowest level of reflectance and 255 the highest (brightest) reflectance, i.e., the radiometric resolution of the TM data is 256 gradations. The DN in the visible wavelength range, namely TM bands 1 to 3 relate to water color, which may vary with color and concentration of suspended solid particles as well as chemical and biological matter. The DN in band 6 relates to temperature. Algorithms for estimation sea surface temperature from the Landsat TM-6 band have been presented in the literature and as an example, Gibbons *et al.* (1989) showed that using the calibration constants of the sensor, uncorrected sea surface temperature may be predicted using the following set of equations.

$$T = \{K2 / \ln (K1/Ru)\} + 1 \quad (1)$$

where, T = uncorrected absolute temperature of sea surface water (°K),

$K1 = 60.776$ (mW cm^{-2} Sr^{-1} mm^{-1}), $K2 = 1260.56$ (°K),

Ru = the spectral radiance given by, $Ru = \alpha\ (DN) + \beta$ (2)

where, $\alpha = 0.005632$ (mW cm^{-2} Sr^{-1} mm^{-1} DN^{-1}),

$\beta = 0.1238$ (mW cm^{-2} Sr^{-1} mm^{-1}).

An Example of Visualization of Thermal Discharges from Power Plant

With the Landsat TM band 6 data, the influence of thermal discharge of the Mita power station, which is operating in Japan, was investigated. Figure 1(a) is derived from an infrared image obtained on 4 December, 1984 on which the area of influence of the discharge can be clearly identified. Figure 1(b) is a contour map of points having the same DN values, which may be converted to the corresponding isotherm map once the relationship between the DN and the water temperature is established.

Estimation of Effluent Axis

In environmental fluid dynamics, the distribution of water temperature along the plume axis is often analyzed to study its diffusive features. Equations (1) and (2) suggest that the axis of surface discharge may be detected by the measurements of the thermal DN instead of the water temperature. The discharge axis may be predicted using Landsat data as follows: Landsat data consisting of 512 pixel × 400 line elements can be saved in a personal computer. A P-L co-ordinate system, as

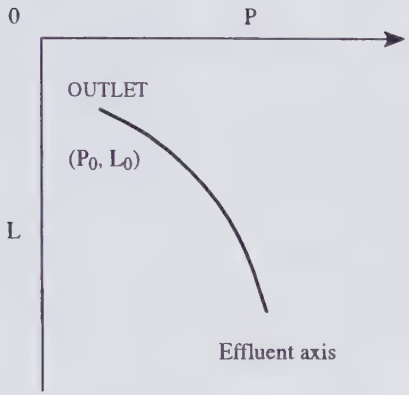

Figure 2. P-L co-ordinate system

indicated in Figure 2, is used and assumes that the axis is represented by the following equation:

$$L^* = a1\ P^* + a2\ P^{*2} + a3\ P^{*3} \tag{3}$$

L_* and P_* are defined as follows.

$$L_* = L - L_0 \quad , \quad P_* = P - P_0 \tag{4}$$

where, (L_0, P_0) is the coordinate of an origin to be selected at a outlet. Deviation of any element mesh from the curve of (3), δ_k and the sum of deviation square multiplied by proper weight function, S are presented by the following equations.

$$\delta_k = (L_k - l_0) - \{a_1\ (P_k - P_0) + a_2\ (P_k - P_0)^2 + a_3\ (P_k - P_0)^3\} \tag{5}$$

$$S \equiv \Sigma\ W_k\ \delta_k \tag{6}$$

where, W_k is the weighting function.

Under the condition that S becomes a minimum, the following equations hold:

$$\frac{\delta S}{\delta a_1} = -2\ \Sigma\ W_k\ (P_k - P_0)\ (L_k - L_0) + 2a_1\ \Sigma\ W_k\ (P_k - P_0)\ \Sigma\ W_k\ (P_k - P_0)^2 + 2a_2\ \Sigma\ W_k\ (P_k - P_0)^3 + 2a_3\ \Sigma\ W_k\ (P_k - P_0)^4 = 0 \tag{7a}$$

$$\frac{\delta S}{\delta a_2} = -2\ \Sigma\ W_k\ (P_k - P_0)^2\ (L_k - L_0) + 2a_1\ \Sigma\ W_k\ (P_k - P_0)\ \Sigma\ W_k\ (P_k - P_0)^3 + 2a_2\ \Sigma\ W_k\ (P_k - P_0)^4 + 2a_3\ \Sigma\ W_k\ (P_k - P_0)^5 = 0 \tag{7b}$$

$$\frac{\delta S}{\delta a_3} = -2\Sigma W_k (P_k - P_0)^3 (L_k - L_0) + 2a_1 \Sigma W_k (P_k - P_0) \Sigma W_k (P_k - P_0)^4 + 2a_2 \Sigma W_k (P_k - P_0)^5 + 2a_3 \Sigma W_k (P_k - P_0)^6 = 0 \quad (7c)$$

The above three equations can be rewritten as follows:

$$\Sigma \begin{bmatrix} W_k (P_k - P_0) & (L_k - L_0) \\ W_k (P_k - P_0)^2 & (L_k - L_0) \\ W_k (P_k - P_0)^3 & (L_k - L_0) \end{bmatrix} \Sigma \begin{bmatrix} W_k (P_k - P_0)^2 & W_k (P_k - P_0)^3 & W_k (P_k - P_0)^4 \\ W_k (P_k - P_0)^3 & W_k (P_k - P_0)^4 & W_k (P_k - P_0)^5 \\ W_k (P_k - P_0)^4 & W_k (P_k - P_0)^5 & W_k (P_k - P_0)^6 \end{bmatrix} \begin{bmatrix} a_1 \\ a_2 \\ a_3 \end{bmatrix} \quad (8)$$

When DN at the land surface is larger than that of the sea water at the outlet, and water temperatures in the mixing area of discharge decrease toward offshore, the mixing area of discharge may be detected by selecting the weighting function as follows (Figure 3(a)):

$$W_k = \begin{cases} 0 & (LMth^{\beta} < Uk) \\ (Uk - UBnd)\beta & (UBnd \le Uk \le UMth) \end{cases} \quad (9)$$

where, UMth is the maximum value of infrared DN in the water area near the outlet, UBnd is at the boundary of mixing area, β = constant (usually equal to 1). The value of UBnd is related to the definition of the boundary of mixing area. Here, it was assumed that UBnd = 0.1(UMth).

In winter, temperature of the land surface may be lower than that of the sea water, and the water temperature at the outlet, lower than that of the surrounding water. In such case the weighting function is selected as follows (Figure 3(b)):

$$W_k = \begin{cases} 0 & (Uk < UMth,\ UBand < Uk) \\ (UBand - Uk)\beta & (UMth \le Uk \le UBand) \end{cases} \quad (10)$$

By solving (7) or (8), we can yield the coefficients in (1). The axis in near field adjacent to the outlet was estimated for the case of Figure 1 and is shown on Figure 4. In the far field, the behavior of the discharge may be affected by oceanic currents and other turbulent processes and needs to be analyzed separately. Figure 5 shows the distribution of thermal DN as well as the uncorrected temperature along the predicted axis. The convergence of the discharge water temperature to that of surrounding sea water is clearly evident.

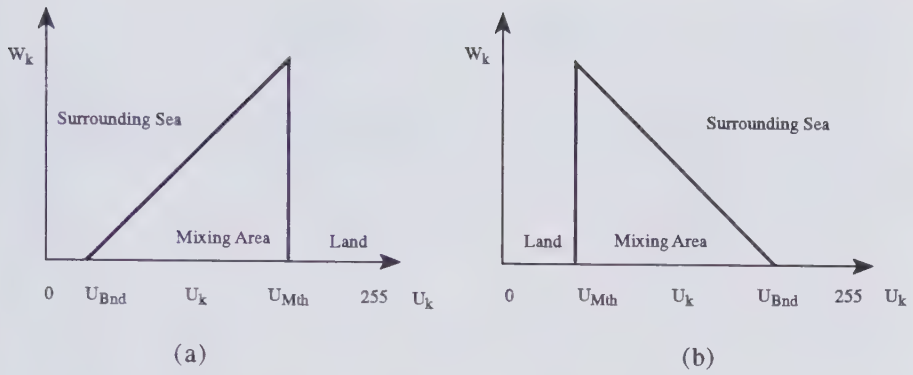

Figure 3. Weighting function

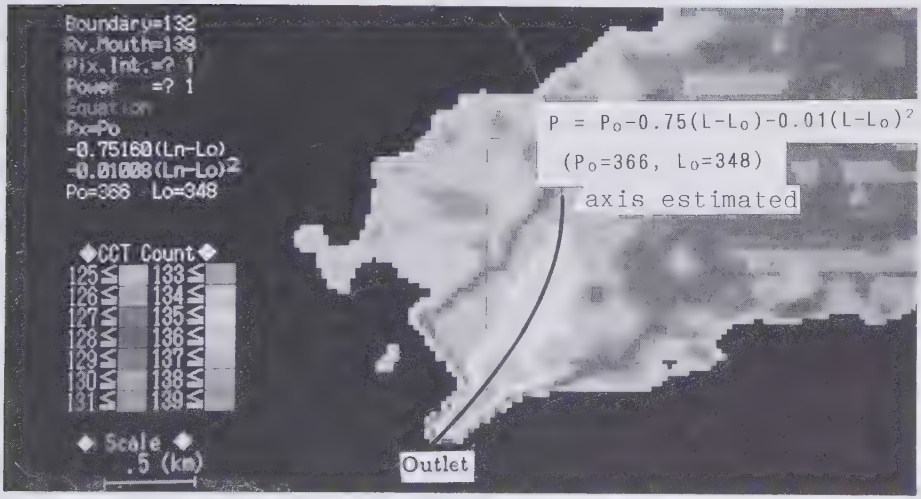

Figure 4. Estimated effluent axis

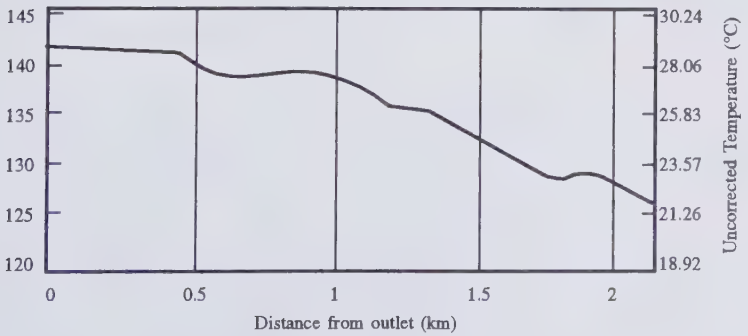

Figure 5. Thermal DN along the axis

Relation Between Water Temperature and DN

To investigate the relationship between the water temperature and DN measured by the Landsat TM, a near-simultaneous field survey was carried out in the Matsura power station located in approximately 520 km west of the Mita power station on 15 April and 8 October 1988.

The water temperatures at the sea surface were measured every 10 minutes at the station indicated in Figure 6. The DN obtained by Landsat and the water temperatures obtained by field survey at the time of the Landsat overpass at 10:20 am are presented in Table 2. The uncorrected water temperatures predicted by (1) and (2) are also given. It is seen that the temperature predicted by (1) and (2) are 3 °C or 2.3 °C higher than the observed values. In Japan, the algorithm suggested by RESTEC (Remote Sensing Technology Center of Japan) is often used, and it has been reported that the temperature calculated by using this method may also deviate by up to 3 °C through 4 °C from the actual values (RESTEC, 1985).

$$DN = 0.00093\ (T_S + 273.155)^2 - 3.20\ (T_S + 273.155) + 268.054 \qquad (11)$$

where, T_S(C) is water temperature at sea surface.

TABLE 2. Landsat RM-6 Band DN and Water Temperature

Date	TM band 6 DN	Water temperature (Observed)	Uncorrected temperature (Predicted by (1), (2))
15 Apr. 1988	118.0	15.0 (°C): 288.15 (°K)	18.0 (°C) 291.12 (°K)
8 Oct. 1988	134.0	22.1 (°C): 310.25 (°K)	24.4 (°C) 298.53 (°K)

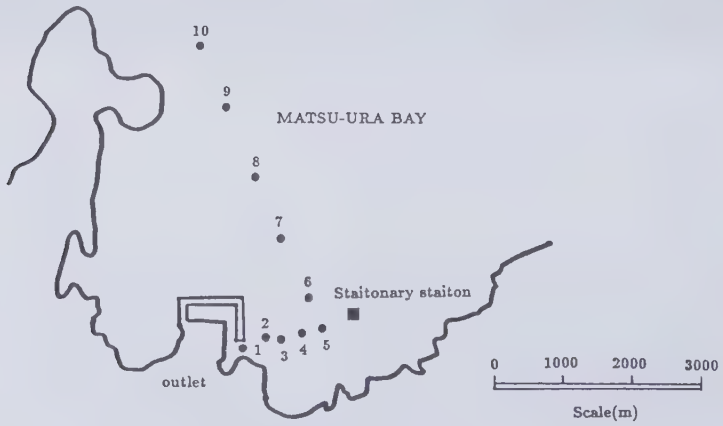

Figure 6. Measurement points of water temperature.

It has been known that such deviation is due to atmospheric effects (RESTEC, 1985; Gibbons *et al.*, 1989; Pattiaratchi, 1992). The atmospheric effects may change daily, therefore it is desirable to calibrate all satellite data using actual water temperatures measured simultaneously. Equation (11) suggests that the TM band 6 DN is represented by a quadratic equation of surface water temperature. For a range of T_S = 5°C through 30 °C, which are water temperatures usually recorded in this area, the relationship may be closely resembled by a linear equation. In the case presented in Table 2, such linear correlation is represented by the following equation.

$$T_S = 0.42\ (DN) - 34.7 \qquad (12)$$

Relation Between the DN Obtained with the Airborne Remote Sensing and Field Measurements

Landsat TM is useful for the observation of phenomena with large spatial scales. However, it can only observe a particular area only at 16 day intervals, and also the observations may often be hindered by clouds. Therefore from a practical view point, combined use of airborne and satellite remote sensing may be considered as being effective for monitoring the discharge effects on the surrounding water environment. To make such combined measurements the relationship between the two different surveying methods must be known. From this viewpoint, infrared radiation emitted from the water surface was measured from an altitude of approximately 2500m, on 29th January and 2nd February 1991 using band 11 of the Multi-Spectral Scanner S-1250 type, properties of which are presented in Table 3. With the aim of studying how the differences in tidal state may influence the thermal DN, observations of 29th January were undertaken during rising tide (from 9:10 am to 9:48 am) and those of 2nd February under a falling tide (from 4:50 pm to 5:25 pm). Sea surface temperature was measured using ET-5- type thermometers at the 10 stations indicated in Figure 4. The results obtained are listed in Table 4 and shown on Figure 5. In the figure it can be seen that the effect of tidal state on the airborne DN is insignificant.

The relationship between the measured water temperatures and the DN observed with the scanner on the aircraft is presented in Figure 7. In this figure, curves of T_S calculated by substituting the airborne DN for "DN" in equations (11) and (12), which are applied to the Landsat remote sensing, are also shown.

Since the instruments used and the observation altitude selected in the airborne observations differ from those in Landsat remote sensing, it is illogical to compare directly the calculated results with that observed with the airborne scanner. Nevertheless, it is considered being useful in practice to have some knowledge of the differences estimated through the airborne and satellite surveying methods.

TABLE 3. Properties of DS-1250 Type Scanner

Scanning angle	77 20'			
Scanning width	approximately 1.6 times flying altitude			
Temperature resolvability	0.2 C			
Optical resolvability	2.5 mrad			
Bandwidth (μm)	Band No.		Band No.	
	1	0.38- 0.42	7	0.65- 0.69
	2	0.42- 0.45	8	0.70- 0.79
	3	0.45- 0.50	9	0.80- 0.89
	4	0.50- 0.55	10	0.92- 1.10
	5	0.55- 0.60	11	8.00-14.00
	6	0.60- 0.65		

TABLE 4. Infrared DN Observed with Airborne Measurements and Water Temperature During Plant Operation

Rising tide condition (1991-1-29)			Falling tide condition (1991-2-2)		
Station	DN	Water Temperature (°C)	Station	DN	Water Temperature (°C)
st.1	140	19.2	st.1	125	19.2
st.2	142	19.2	st.2	115	18.7
st.3	113	17.7	st.3	107	17.0
st.4	102	13.7	st.4	105	16.2
st.5	103	13.7	st.5		
st 6	104	13.7	st 6	103	15.2
st 7	105	13.7	st 7	97	13.3
st 8	101	13.2	st 8	98	13.4
st 9	102	13.7	st 9	99	13.5
st 10	104	13.7	st 10	99	13.5

One can see that in range of the DN = 100 to 130 the water temperatures predicted by the airborne scanner band 11 are higher than those estimated by equations (11) or (12), for a given value of DN, and this differences tend to decrease with an increase of DN. However, further investigations are required to enable direct comparison between the two methods.

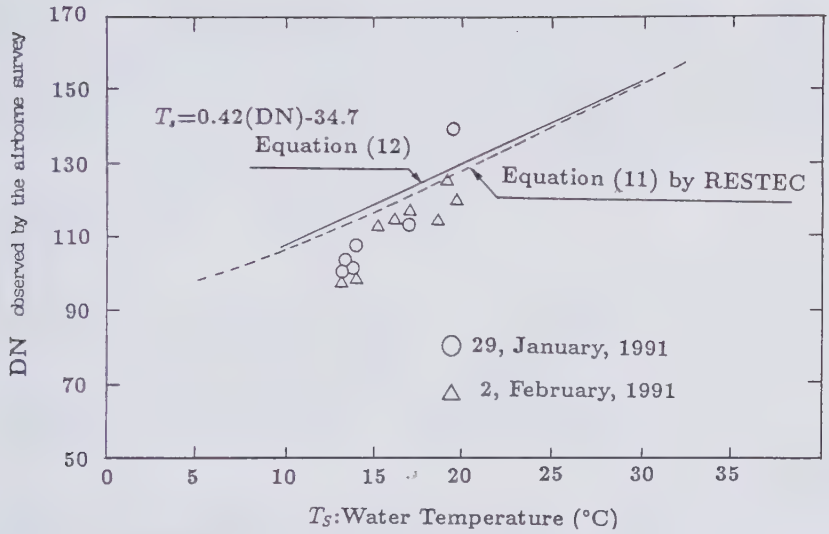

Figure 7. Relationships between Landsat TM-6 band DN, airborne DN and water temperature observed in field.

As discussed above, when satellite data is used to supplement airborne and field measurements, deviations in the results are obtained due to the differences in instruments, observation date, scanning altitude and atmospheric effects. Efforts to reduce this deviation are required before establishing a monitoring system to combine both the airborne and satellite surveying. One approach would be to develop statistical relationships between the two different methods through repeated observations such as those discussed here, in the same area.

Concluding Remarks

Thermal images of the sea surface obtained with the satellite data can present a qualitative view of thermal discharge from power plants. For quantitative understanding of its diffusive nature, the isotherm map is more effective and its estimation of the temperature distribution along the effluent axis is very helpful to hydraulic engineers. Here, analytical methods, from which the DN contour map is composed and the effluent axis can be located easily are presented. The relationship between the measured water temperature and the thermal DNs obtained through the Landsat and airborne remote sensing techniques were presented. For Landsat data, algorithms suggested by Gibbons *et al.* (1989) and RESTEC (1985) provide the uncorrected water temperatures of approximately 3 °C higher than the measured temperatures. It is considered that either of these algorithms may be used for monitoring the sea water environment at this particular site. Direct comparison between the two different sets of the observed water temperatures and the infrared

DNs obtained by the aircraft and the satellite is illogical, because of the differences of the instruments, observation altitude and other factors. To establish a monitoring system combining these two surveying methods, the author is continuing more observations in the same sea with the aim of finding some statistical relationship between the results obtained from two different methods.

References

Bagheri, S. and R.A. Dios. Chlorophyll a estimation in New Jersey's coastal waters using Thematic Mapper data. *Int. J. Remote Sensing. 11*, 289-300, 1990.

Davies, P.A. and L.A. Mofor. Remote sensing observations and analyses of cooling water discharges from a coastal powerstation, *Int. J Rem. Sensing*, 14, 253-273, 1991.

Gibbons, D.E., G.E. Wukelic, J.P. Leighton and M.J. Doyle. Application of Landsat Thematic Mapper data for coastal thermal plume analysis at Diablo Canyon. *Photogram. Eng. Rem. Sens. 55*, 903-909, 1989.

Lathrop, R.G. and T.M. Lillesand. Calibration of thematic mapper thermal data to assess water surface temperature mapping, Case study on the Great Lakes. *Rem. Sens. Environ.*, 22, 297 - 307, 1987.

Lathrop, R.G. and T.M. Lillesand. Calibration of thematic mapper thermal data to assess water quality in Green Bay and Central Lake Michigan. *Photogram Eng. Remote Sensing*, 51, 1407 - 1416, 1986.

Lavery, P.S. and B. Pattiaratchi. Multi-date algorithms for estimating water quality in estuaries from TM data. *Proc. 5th Aust. Rem. Sens. Conf.* Perth., p.789-792, 1990.

Lopez-Garcia, M. and V. Caselles. A multi-temporal study of chlorophyll concentration in the Albufera lagoon of Valencia, Spain, using TM data. *Int. J. Rem. Sens., 11*, 301-313, 1990.

Onishi, S. and H Kawai, Estimation methods of river effluent behavior through Landsat TM data, *J. Japan Civil Eng. Assoc.*, No. 452/2-20, 11-20, 1992.

Pattiaratchi, C. Coastal environmental mapping using Landsat data. *Proc. Central Sym. of Int. Space Year Conf.* Munich, 739-743, 1992.

Tassan, S. Evaluation of the potential of the Thematic Mapper for marine applications. *Int. J. Rem. Sens.*, 8, 1488-1478, 1987.

29

Distortion and Dispersion: Dilution of Solutes in Coastal Waters

R. Smith

Abstract

In moderately deep water the tidal flow has slightly different orientations at different depths. As the vertically averaged velocity rotates around a tidal ellipse, there is a phase lag of the upper waters behind the lower waters. Also, there is the effect of the Earth's rotation (the Ekman spiral). For any solute in the flow the concentration distribution undergoes substantial time-dependent horizontal displacements in different directions at different depths. As well as this distortion there is consequent shear-augmented mixing. It is well known that the long-term (tidally-averaged) effect of the shear upon solute dilution can be quantified in terms of a shear dispersion tensor. Attempts to define time-dependent shear dispersion usually result in time spans of negative apparent diffusivity and violent numerical instability. Here it is shown that a clear distinction between distortion and the consequent dispersion leads to a positive-definite time-dependent shear dispersion tensor. The neat formulae for the tensor coefficients makes it feasible to consider the nonlinear way different physical processes interact in modifying the solute dilution process. Details are presented for shear dispersion in off-shore waters as influenced by the Earth's rotation and by the aspect ratio of the tidal ellipse.

Introduction

In one of the most cited papers in the subject of fluid mechanics, G. I. Taylor (1953) showed that for steady pipe flow the cross-sectionally averaged concentration of a dilute

Mixing in Estuaries and Coastal Seas
Coastal and Estuarine Studies Volume 50, Pages 479-495
Copyright 1996 by the American Geophysical Union

solute at large times after discharge satisfies a diffusion equation and that the dominant contribution to the effective diffusivity depends on the velocity shear. Bowden (1965) applied Taylor's calculation procedures to long-term horizontal mixing in uni-directional tidal flows and showed that the vertically and tidally averaged concentration satisfies a diffusion equation, with a shear dispersion coefficient much greater than a turbulent eddy diffusivity.

The restrictions to large times or to tidal averages were removed by Gill & Sankarasubramanian (1971). They showed that the initial development of the shear dispersion process and the time dependence of a uni-directional flow could be accounted for in a diffusion equation with a time-dependent shear dispersion coefficient. Chatwin (1975) pointed out that following flow reversal the shear dispersion coefficient becomes negative. In such circumstances diffusion equation models for the solute concentration are violently unstable. If predictions of the cross-sectionally averaged concentration are required when the shear dispersion coefficient is negative then some other stable type of mathematical model must be used. For example, Smith (1982) advocated the use of the more complicated but stable delay-diffusion equations.

Yasuda (1982) suggested that the failure of the diffusion equation model was a consequence of the cross-sectional averaging. Near the free surface the faster flow carries regions of high concentration far forward above deeper-down slower-flowing regions of lower concentration. Thus, the straightforward vertical averaging is representative of neither region (except at large times or when averaged over a tidal period). For three different uni-directional flows Yasuda (1982, 1984) demonstrated numerically that when the horizontal displacement of different levels of the flow is removed the effective shear dispersion coefficient remains positive. Smith (1983, 1985) provided analytical confirmation that Yasuda's separation between dilution and distortion works for arbitrary time-dependent uni-directional flows.

The flow in coastal waters is not uni-directional. A tidal ellipse is commonly used to quantify the changing orientation of the velocity vector. Also, the rotation of the earth causes a difference in flow alignment at different depths (the Ekman spiral). For steady skewed shear flows Fischer (1978) gave the appropriate two-dimensional generalisation of Taylor's (1953) calculation procedures. At large times after discharge the horizontal dilution of the vertically averaged concentration can be represented by a positive definite shear dispersion tensor. For unsteady skewed flows Hamrick (1986) notes that the unsteady shear dispersion tensor can exhibit the change of sign objected to by Chatwin (1975). Accordingly, Hamrick (1986) only gives detailed results for the tidally averaged shear dispersion tensor.

The purpose of the present paper is to give a two-dimensional application of Yasuda's (1982) idea. Explicit account is made for the oscillatory horizontal distortion of the concentration distribution. Thus attention is focused upon the genuine dilution process, which is quantified in terms of a time-dependent positive-definite shear dispersion tensor. The resulting formulae for the tensor coefficients are finally used in a graphical presentation of how dilution in tidal waters is affected by the tidal frequency, vertical mixing time, Coriolis frequency and tidal aspect ratio.

The Dimensional Equations

For simplicity it will be assumed that the sea bed can be regarded as being locally flat ($z = -h$) and that the free surface does not move up and down significantly ($z = 0$). Thus, the tidal velocity will be modelled as being independent of the horizontal coordinates x, y and having zero vertical component:

$$u(z, t), \quad v(z, t), \quad w = 0. \tag{1}$$

The turbulent mixing process will be modelled in terms of eddy diffusivities with components $K_1(z, t)$, $K_2(z, t)$, $K_3(z, t)$ in the x, y, z coordinate directions. Thus, the solute concentration $c(x, y, z, t)$ is assumed to satisfy the three-dimensional advection-diffusion equation.

$$\partial_t c + u\partial_x c + v\partial_y c - K_1 \partial_x^2 c - K_2 \partial_y^2 c - \partial_z(K_3 \partial_z c) = 0. \tag{2}$$

On the bed and on the free surface the conditions of zero flux of solute are

$$K_3 \partial_z c = 0 \quad \text{on} \quad z = -h, 0. \tag{3}$$

For a sudden discharge with vertical solute mass distribution $q(z)$ the initial conditions are

$$c = q(z)\,\delta(x - x_0)\,\delta(y - y_0) \quad \text{at} \quad t = t_0. \tag{4}$$

Here, the zero subscripts indicate the starting time and horizontal position.

Vertical adjustment

If there is zero loss or gain of solute through the bed and free surface, then the total amount of solute in the entire flow constant $h\,\bar{q}$, where the over-bar indicates a depth average:

$$\bar{q} = \frac{1}{h}\int_{-h}^{0} q\,dz\ . \tag{5}$$

However, there can be vertical adjustment if the initial discharge distribution $q(z)$ is vertically non-uniform.

At any particular z level the total amount of solute will be represented:

$$\iint c(x, y, z, t)\,dx\,dy = \bar{q}\,\phi(z, t). \tag{6}$$

The vertical concentration profile function $\phi(z, t)$ satisfies the equation

$$\partial_t \phi - \partial_z (K_3 \partial_z \phi) = 0 \tag{7a}$$

with

$$K_3 \partial_z \phi = 0 \text{ on } z = -h, 0, \tag{7b}$$

and

$$\phi = q(z) / \overline{q} \text{ at } t = t_0. \tag{7c}$$

The vertical average value of the concentration profile function $\phi(z, t)$ has the fixed value of unity:

$$\overline{\phi} = 1 \text{ for } t \geq t_0. \tag{8}$$

Considerable simplifications are possible if at all times the vertical eddy diffusivity K_3 (z, t) has the same z-dependence as its tidal average $<K_3>$:

$$K_3 (z, t) = <K_3> I(t) \text{ with } <I(t)> = 1. \tag{9}$$

In this circumstance it is convenient to introduce vertical eigenmodes $\psi_m(z)$ with associated decay rates λ_m $(0 = \lambda_0 < \lambda_1 < \lambda_2 \mathbf{L})$:

$$\frac{d}{dz}\left(<K_3> \frac{d\psi_m}{dz} \right) + \lambda_m \psi_m = 0 \ , \tag{10a}$$

with

$$<K_3> \frac{d\psi_m}{dz} = 0 \text{ on } z = -h, 0, \tag{10b}$$

and

$$\overline{\psi_m^2} = 1. \tag{10c}$$

The eigenmode representation for $\varphi(z, t)$ is

$$\varphi(z, t) = 1 + \sum_{m=1}^{\infty} \left(\overline{\psi_m q} / \overline{q} \right) \psi_m(z) \exp\left(-\lambda_m \int_{t_0}^{t} I(t') \, dt' \right). \tag{11}$$

Thus, vertical uniformity is achieved on the vertical mixing time scale $1 / \lambda_1$.

Horizontal Displacement

The solute distribution will be carried by the non-uniform flow. To a first approximation the effective horizontal velocity will be the weighted average

$$\overline{u\phi},\ \overline{v\phi},\ 0. \tag{12}$$

At any particular z level the centroid position will be represented

$$x_0 + \int_{t_0}^{t} \overline{u\phi}\, dt' + X(z, t),\quad y_0 + \int_{t_0}^{t} \overline{v\phi}\, dt' + Y(z, t). \tag{13}$$

The centroid displacement functions X(z, t), Y(z, t) satisfy the equations

$$\partial_t(\varphi X) - \partial_z(K_3\, \partial_z\, (\varphi X)) = \left(u - \overline{u\phi}\right)\phi, \tag{14a}$$

$$\partial_t(\varphi Y) - \partial_z(K_3\, \partial_z\, (\varphi Y)) = \left(v - \overline{v\phi}\right)\phi, \tag{14b}$$

with $$K_3\, \partial_z\, (\phi X) = K_3\, \partial_z(\phi Y) = 0 \quad \text{on} \quad z = -h, 0, \tag{14c}$$

and $$\phi X = \phi Y = 0 \quad \text{at} \quad t = t_0. \tag{14d}$$

The relative horizontal displacements will be largest at z-levels where the flow is fastest.

The vertical average values of φX and φY are identically zero

$$\overline{\varphi X} = \overline{\varphi Y} = 0 \ \text{ for } t \geq t_0. \tag{15}$$

On the time scale of vertical mixing the memory of the initial vertical concentration distribution fades away and the centroid displacement functions asymptote to the form

$$\phi X \sim g_1(z, t),\quad \phi Y \sim g_2(z, t) \tag{16}$$

where $$\partial_t\, g_1 - \partial_z(K_3\, \partial_z\, g_1) = u - \bar{u}, \tag{17a}$$

$$\partial_t\, g_2 - \partial_z(K_3\, \partial_z\, g_2) = v - \bar{v}, \tag{17b}$$

with $$K_3\, \partial_z\, g_1 = K_3\, \partial_z\, g_2 = 0 \ \text{ on } \ z = -h, 0 \tag{17c}$$

and $$\overline{g_1} = \overline{g_2} = 0. \tag{17d}$$

If at all times $K_3(z, t)$ has the same z-dependence as its tidal average $\langle K_3 \rangle$, then the vertical eigenmodes $\psi_m(z)$ can be used to represent g_1, g_2. First it is necessary to represent the velocity components u, v:

$$u(z, t) = \bar{u}(t) + \sum_{m=1}^{\infty} u_m(t)\, \psi_m(z), \tag{18a}$$

$$v(z, t) = \bar{v}(t) + \sum_{m=1}^{\infty} v_m(t)\, \psi_m(z). \tag{18b}$$

The corresponding series representations for the asymptotic centroid displacement functions are

$$g_1(z, t) = \sum_{m=1}^{\infty} g_{1m}(t)\, \psi_m(z)\ , \tag{19a}$$

with
$$g_{1m}(t) = \int_0^{\infty} u_m(t-\tau) \exp\left(-\lambda_m \int_0^{\tau} I(t-\tau')\, d\tau'\right) d\tau\ , \tag{19b}$$

$$g_2(z, t) = \sum_{m=1}^{\infty} g_{2m}(t)\, \psi_m(z)\ , \tag{19c}$$

with
$$g_{2m}(t) = \int_0^{\infty} v_m(t-\tau) \exp\left(-\lambda_m \int_0^{\tau} I(t-\tau')\, d\tau'\right) d\tau\,. \tag{19d}$$

Since the higher eigenmodes have larger decay rates λ_m, the convergence rates of the series for g_1, g_2 are more rapid than the convergence rates of the series for u, v.

Eliminating the Distortion

In the early stages of solute dilution the magnitude of the relative horizontal displacements X, Y at z level can exceed the horizontal scale of the solute distribution at that level. It is only on the time scale of vertical mixing that the spreading due to shear dispersion begins to exceed the distortion between the different z-levels (Smith, 1983). Hence, as argued by Yasuda (1982), the vertically averaged concentration represents the deformation of the water particles more than the degree of mixing.

To remedy this situation, we replace the conventional horizontal coordinates x, y by the centroid-following coordinates ξ, η :

$$\xi = x - x_0 - \int_{t_0}^{t} \overline{u\phi}\, dt' - X(z, t) \tag{20a}$$

$$\eta = y - y_0 - \int_{t_0}^{t} \overline{v\phi}\, dt' - Y(z, t). \tag{20b}$$

Also, we shall attempt to build-in the vertical adjustment by representing the solute concentration:

$$c(x, y, z, t) = \overline{q}\, \phi(z, t)\, b(\xi, \eta, z, t). \tag{21}$$

The evolution equation satisfied by $b(\xi, \eta, z, t)$ can be written:

$$\partial_t(\varphi b) - \partial_z\left(K_3\, \partial_z(\varphi b)\right) - \left\{\varphi K_1 + \varphi K_3\, (\partial_z X)^2\right\} \partial_\xi^2 b$$

$$-2\varphi K_3\, \partial_z X \partial_z Y\, \partial_\xi\, \partial_\eta\, b - \left\{\varphi K_2 + \varphi K_3\, (\partial_z Y)^2\right\} \partial_\eta^2 b$$

$$+2\, \varphi K_3\, \partial_z X\, \partial_\xi\, \partial_z b + 2\, \varphi K_3\, \partial_z Y\, \partial_\eta\, \partial_z b = 0\ , \tag{22a}$$

with $$K_3\, \partial_z\, (\varphi b) = 0 \qquad \text{on} \quad z = -h,\ 0\,, \tag{22b}$$

and $$b = \delta(\xi)\, \delta(\eta) \quad \text{at} \quad t = t_0. \tag{22c}$$

It deserves comment that the absence from equation (14a) of the first derivative terms $\partial_\xi b$, $\partial_\eta b$ results from the definitions (14a, b) of the centroid displacement functions X. Y. As a consequence, the first moments of b with respect to ξ and η are identically zero (ie the centroid remains at the origin $\xi = \eta = 0$).

Diffusion Approximation

It is convenient to decompose $b(\xi, \eta, z, t)$ into a vertical average $\overline{b}$ and a perturbation b'

$$b = \overline{b} + b' \ \text{ with } \ \overline{\varphi b'} = 0. \tag{23}$$

The vertical average of equation (14a) is

$$\partial_t \bar{b} - \left\{ \overline{\varphi K_1} + \overline{\varphi K_3 (\partial_z X)^2} \right\} \partial_\xi^2 \bar{b} - 2 \overline{\varphi K_3 \partial_z X \partial_z Y} \; \partial_\xi \partial_\eta b$$

$$- \left\{ \overline{\varphi K_2} + \overline{\varphi K_3 (\partial_z Y)^2} \right\} \partial_\eta^2 \bar{b} = \text{ Terms involving } b' . \tag{24}$$

To derive a diffusion approximation we simply ignore the terms involving b':

$$\partial_t \bar{b} - \left\{ \overline{\varphi K_1} + D_{11} \right\} \partial_\xi^2 \bar{b} - 2 D_{12} \partial_\xi \partial_\eta \bar{b} - \left\{ \overline{\varphi K_2} + D_{22} \right\} \partial_\eta^2 \bar{b} = 0, \tag{25a}$$

with $$D_{11} = \overline{\varphi K_3 (\partial_z X)^2} \; , \; D_{12} = D_{21} = \overline{\varphi K_3 \partial_z X \partial_z Y} , \tag{25b,c}$$

$$D_{22} = \overline{\varphi K_3 (\partial_z Y)^2} . \tag{25d}$$

The coefficients D_{ij} of the shear dispersion tensor automatically satisfy the positive definiteness property

$$D_{11} D_{22} - D_{12}^2 \geq 0 \text{ with } D_{11} + D_{22} > 0. \tag{26}$$

So the disaster of explosive instabilities highlighted by Chatwin (1975), cannot arise.

In the work of G. I. Taylor (1953) the key feature was that the c' terms could not be neglected. What has been done here is to subsume the role of c' into the X, Y distortion terms. The residual vertical nonuniformity φ initially grows more slowly than c' and eventually decays more rapidly than c' Thus, b' is uniformly unimportant.

The relationships between the shear dispersion coefficients D_{ij} as calculated here and the traditional definitions (Taylor 1953, Gill & Sankarasubramanian 1971) are

$$\overline{X(u - \bar{u}\bar{\varphi})\varphi} = D_{11} + \frac{1}{2} \frac{d}{dt} \overline{\varphi X^2} , \tag{27a}$$

$$\frac{1}{2} \left\{ \overline{Y(u - \bar{u}\bar{\varphi})\phi} + \overline{X(v - \bar{v}\bar{\varphi})\varphi} \right\} = D_{12} + \frac{1}{2} \frac{d}{dt} \overline{\varphi XY} , \tag{27b}$$

$$\overline{Y(v - \bar{v}\bar{\varphi})\varphi} = D_{22} + \frac{1}{2} \frac{d}{dt} \overline{\varphi Y^2} . \tag{27c}$$

It is the time-derivative contributions that give rise to the time spans of negative apparent diffusion after flow reversal. It is also clear from equations (27a–c) why tidal averaging, as used by Bowden (1965) and Hamrick (1986) eliminates the disaster of negative diffusion (by integrating the d/dt contributions).

If at all times K_3 (z, t) has the same z-dependence as its tidal average $<K_3>$, then the asymptotic shear dispersion coefficients have the series representations

$$D_{11}(t) = I(t) \sum_{m=1}^{\infty} \lambda_m \, g_{1m}(t)^2 \tag{28a}$$

$$D_{12}(t) = D_{21}(t) = I(t) \sum_{m=1}^{\infty} \lambda_m \, g_{1m}(t) \, g_{2m}(t) \tag{28b}$$

$$D_{22}(t) = I(t) \sum_{m=1}^{\infty} \lambda_m \, g_{2m}(t)^2 \tag{28c}$$

Convergence is ensured by the comparatively rapid decay with m of g_{1m}, g_{2m} relative to the velocity series u_m, v_m.

Coriolis Effect

Smith (1982, section 8) gave a calculation of the influence of the earth's rotation upon longitudinal dispersion when the vertically averaged flow was uni-directional. This section extends those calculations to two dimensions.

The vertical eddy diffusivity K_3 (z, t) is modelled:

$$K_3 = k \; hu_* \, (1-\eta) \, \eta \tag{29a}$$

with

$$\eta = \eta_* + (1 + z/h)(1 - \eta_*) \tag{29b}$$

where k is von Kármáns constant (about 0.4), h is the water depth, $u_*(t)$ a turbulence velocity scale and η_* the dimensionless roughness height (about 0.001). The vertical eigenmodes are rescaled Legendre polynomials:

$$\psi_m(z) = (2m+1)^{1/2} \, P_m(2\eta - 1) \tag{30a}$$

$$\lambda_m = m(m+1)\frac{k}{h} < u_* >, \quad I(t) = \frac{u_*(t)}{< u_* >} \tag{30b, c}$$

Smith (1982) shows that if the vertical eddy diffusivities for both horizontal velocity components are equal to K_3, then the velocity eigenmodes can be represented in terms of the diffusion eigenmodes $\psi_m(z)$. In particular, if $\bar{u}$, $\bar{v}$ are specified then the coefficients u_m, v_m can be evaluated :

$$u_m(t) = \frac{(-1)^{m+1}\,(2m+1)^{1/2}}{(-\ln \eta_*)\, m(m+1)} \Big\{ \bar{u}(t)$$

$$- \int_0^\infty \left(\partial_t \bar{u} - f\bar{v}\right)\Big|_{t-\tau} \cos f\tau \exp\left(-\lambda_m \int_0^\tau I(t-\tau')d\tau'\right) d\tau$$

$$- \int_0^\infty \left(\partial_t \bar{v} + f\bar{u}\right)\Big|_{t-\tau} \sin f\tau \exp\left(-\lambda_m \int_0^\tau I(t-\tau')d\tau'\right) d\tau \qquad (31a)$$

$$v_m(t) = \frac{(-1)^{m+1}\,(2m+1)^{1/2}}{(-\ln \eta_*)\, m(m+1)} \Big\{ \bar{v}(t)$$

$$- \int_0^\infty \left(\partial_t \bar{v} + f\bar{u}\right)\Big|_{t-\tau} \cos f\tau \exp\left(-\lambda_m \int_0^\tau I(t-\tau')d\tau'\right) d\tau$$

$$+ \int_0^\infty \left(\partial_t \bar{u} - f\bar{v}\right)\Big|_{t-\tau} \sin f\tau \exp\left(-\lambda_m \int_0^\tau I(t-\tau')d\tau'\right) d\tau \qquad (31b)$$

The earth's rotation, as quantified by the Coriolis frequency f, gives rise to a dependence of u_m upon $\bar{v}$ and of v_m upon $\bar{u}$. This is a manifestation of the Ekman spiral (in the northern hemisphere the upper flow moves slightly to the right of the lower flow).

For a given tidal flow $\bar{u}(t)$, $\bar{v}(t)$ and a given turbulence model for $u_*(t)$ it is a straightforward numerical task to compute $I(t)$, λ_m, $u_m(t)$, $v_m(t)$, $g_{2m}(t)$, $g_{2m}(t)$ and finally the asymptotic shear dispersion coefficients $D_{ij}(t)$.

Constant Turbulence Model

To give some insight into the respective roles of the tidal frequency, vertical mixing time, Coriolis frequency and tidal aspect ratio, a greatly simplified flow and turbulence specification will be used. The flow has a single tidal frequency ω with peak velocity U in the x-direction and a tidal ellipse with aspect ratio r:

$$\bar{u} = U \sin \omega t, \qquad \bar{v} = -rU \cos \omega t. \qquad (32a, b)$$

A negative value of r gives a reversed (clockwise) rotation of flow around the tidal ellipse. The turbulence velocity scale u_* is assumed to be constant and related to the mean square bottom stress:

$$I(t) = 1 \quad \text{and} \quad \langle u_* \rangle = \frac{k\,U}{(-\ln \eta_*)} \left(\frac{1+r^2}{2} \right)^{1/2} \tag{33a, b}$$

The integrations (31a, b) can be performed explicitly, to yield the results

$$u_m = \frac{\langle u_* \rangle}{k} \left(\frac{2}{1+r^2} \right)^{1/2} \frac{(2m+1)^{1/2}\,(-1)^{m+1}}{\left[m^2\,(m+1)^2 + (\Omega - F)^2 \right] \left[m^2\,(m+1)^2 + (\Omega + F)^2 \right]}$$

$$\times \left\{ m(m+1) \left[m^2\,(m+1)^2 + \Omega^2 + F^2 - 2r\,\Omega F \right] \sin \omega t \right.$$

$$\left. - \left[\Omega\,(m^2\,(m+1)^2 + \Omega^2 - F^2) + rF\,(m^2 (m+1)^2 - \Omega^2 + F^2) \right] \cos \omega t \right\} \tag{34a}$$

$$v_m = \frac{\langle u_* \rangle}{k} \left(\frac{2}{1+r^2} \right)^{1/2} \frac{(2m+1)^{1/2}\,(-1)^{m+1}}{\left[m^2\,(m+1)^2 + (\Omega - F)^2 \right] \left[m^2\,(m+1)^2 + (\Omega + F)^2 \right]}$$

$$\times \left\{ - \left[r\,\Omega\,(m^2 (m+1)^2 + \Omega^2 - F^2) + F\,(m^2 (m+1)^2 - \Omega^2 + F^2) \right] \sin \omega t \right.$$

$$\left. - m(m+1) \left[r\,(m^2 (m+1)^2 + \Omega^2 + F^2) - 2\,\Omega F \right] \cos \omega t \right\} \tag{34b}$$

where the dimensionless parameters Ω, F characterise the vertical mixing time and the Coriolis parameter:

$$\Omega = \omega h / k \langle u_* \rangle \quad , \quad F = fh / k \langle u_* \rangle \tag{35a, b}$$

The further integrations (19b, d) to evaluate the centroid displacement coefficients g_{1m}, g_{2m} can likewise be performed explicitly:

$$g_{1m} = \frac{h}{k^2} \left(\frac{2}{1+r^2} \right)^{1/2} \frac{(2m+1)^{1/2}\,(-1)^{m+1} \left[(G_1 - r\,\Omega F G_4) \sin \omega t - (\Omega G_2 + rFG_3) \cos \omega t \right]}{\left[m^2\,(m+1)^2 + (\Omega + F)^2 \right] \left[m^2\,(m+1)^2 + (\Omega + F)^2 \right]} \tag{36a}$$

$$g_{2m} = \frac{h}{k^2}\left(\frac{2}{1+r^2}\right)^{1/2}$$

$$\frac{(2m+1)^{1/2}\,(-1)^{m+1}\left[-(r\,\Omega G_2 + F\,G_3)\sin\omega t - (\Omega G_2 + rFG_3)\cos\omega t\right]}{\left[m^2(m+1)^2 + (\Omega - F)^2\right]\left[m^2(m+1)^2 + (\Omega + F)^2\right]} \tag{36b}$$

with

$$G_1 = m^2(m+1)^2 - \Omega^2 + F^2 \tag{36c}$$

$$G_2 = 2\,m(m+1) \tag{36d}$$

$$G_3 = m(m+1)\frac{\left[m^2(m+1)^2 - 3\Omega^2 + F^2\right]}{m^2(m+1)^2 + \Omega^2} \tag{36e}$$

$$G_4 = \frac{\left[3m^2(m+1)^2 - \Omega^2 + F^2\right]}{m^2(m+1)^2 + \Omega^2} \tag{36f}$$

There are four categories of contributions to the centroid displacement: 1) in phase with the parallel tidal velocity, 2) out-of-phase with the parallel tidal velocity, 3) in phase with the perpendicular tidal velocity, 4) out-of-phase with the perpendicular tidal velocity. In the numerators of equations (36a, b) these respective categories of terms can be identified via the multiplicative factors 1, Ω, F, ΩF.

Since the summation formulae (28a-c) for the shear dispersion coefficients involve symmetric products of the centroid displacement functions, we can expect twelve categories of terms which can be labelled by symmetric double indices k, l, ranging from 1 to 4. The formulae for D_{ij} are denoted

$$D_{11} = \frac{2h < u_* >}{(1+r^2)\,k^3}\left\{\left[\Gamma_{11} - 2r\Omega F\,\Gamma_{14} + r^2\Omega^2F^2\Gamma_{44}\right]\sin^2\omega t\right.$$

$$+2\left[-\Omega\Gamma_{12} - rF\,\Gamma_{13} + r\,\Omega^2F\,\Gamma_{24} + r^2\Omega F^2\,\Gamma_{34}\right]\sin\omega t\cos\omega t$$

$$\left.+\left[\Omega^2\,\Gamma_{22} + 2r\,\Omega F\,\Gamma_{23} + r^2F^2\Gamma_{33}\right]\cos^2\omega t\right., \tag{37a}$$

$$D_{12} = D_{21} = \frac{2h < u_* >}{(1+r^2)\,k^3} \Big\{ -F\Big[\Gamma_{13} - r\,\Omega\,\Gamma_{12} + r\,\Omega\,F^2\Gamma_{34} + r^2\Omega^2 F\,\Gamma_{24}\Big] \sin^2 \omega t$$

$$+\Big[\Omega F(\Gamma_{14}+\Gamma_{23})(1+r^2) - r\,\Gamma_{11} + r\,\Omega^2\Gamma_{22} + rF^2\Gamma_{33} - r\,\Omega^2F^2\Gamma_{44}\Big] \sin \omega t \cos \omega t$$

$$+\Big[-\Omega^2 F\,\Gamma_{24} + r\,\Omega\Gamma_{12} - r\,\Omega F^2\Gamma_{34} + r^2 F\,\Gamma_{13}\Big] \cos^2 \omega t\Big\}, \qquad (37b)$$

$$D_{22} = \frac{2h < u_* >}{(1+r^2)\,k^3} \Big\{\Big[F^2\Gamma_{33} + 2r\Omega F\,\Gamma_{23} + r^2\Omega^2\Gamma_{22}\Big] \sin^2 \omega t$$

$$+2\Big[-\Omega F^2\Gamma_{34} + rF\,\Gamma_{13} - r\,\Omega^2 F\,\Gamma_{24} + r^2\Omega\,\Gamma_{12}\Big] \sin \omega t \cos \omega t$$

$$+\Big[\Omega^2F^2\,\Gamma_{44} - 2r\,\Omega F\,\Gamma_{14} + r^2\,\Gamma_{11}\Big] \cos^2 \omega t\,. \qquad (37c)$$

Here the dimensionless coefficients Γ_{kl} are defined by the summations

$$\Gamma_{kl} = \sum_{m=1}^{\infty} \frac{(2m+1)\,m(m+1)\,G_k\,G_l}{\Big[m^2(m+1)^2 + (\Omega - F)^2\Big]^2 \Big[m^2(m+1)^2 + (\Omega + F)^2\Big]^2} \qquad (38)$$

Figure 1 gives graphs of the coefficients Γ_{kl} as functions of Ω^2 for several values of F^2. The general tendency for the size of the coefficients to reduce with increasing Ω^2 or F^2 can be related to lack of coherence between the velocity at different levels in the flow when the mixing time is large or rotation is dominant.

The lengthy formulae (37a-c) encompass the time-dependence of the shear dispersion coefficients D_{ij}, the aspect ratio of r of the tidal ellipse, the velocity phase lags associated with the vertical mixing time and the Ekman spiral of the flow direction. As an illustrative example amidst this wide range of regimes, Figure 2 shows the time dependence of D_{ij} for the particular case

$$\Omega = 1,\ F = 1 \quad \text{with } k = 0.4. \qquad (39)$$

For a semi-diurnal tide with $< u_* > = 0.01$ ms^{-1} this would correspond to a water depth of 27m at latitude 30°. For the southern hemisphere the reversed sign of F can be accommodated by a reversal sign of r and of D_{12}. From Figure 2 we observe that when the phase lags associated with the rotation of the tidal ellipse and with the Ekman spiral are additive (rF positive) there is on average a reduction in the magnitude of the shear dispersion, and an increased phase lag of the dispersion behind the tidal current.

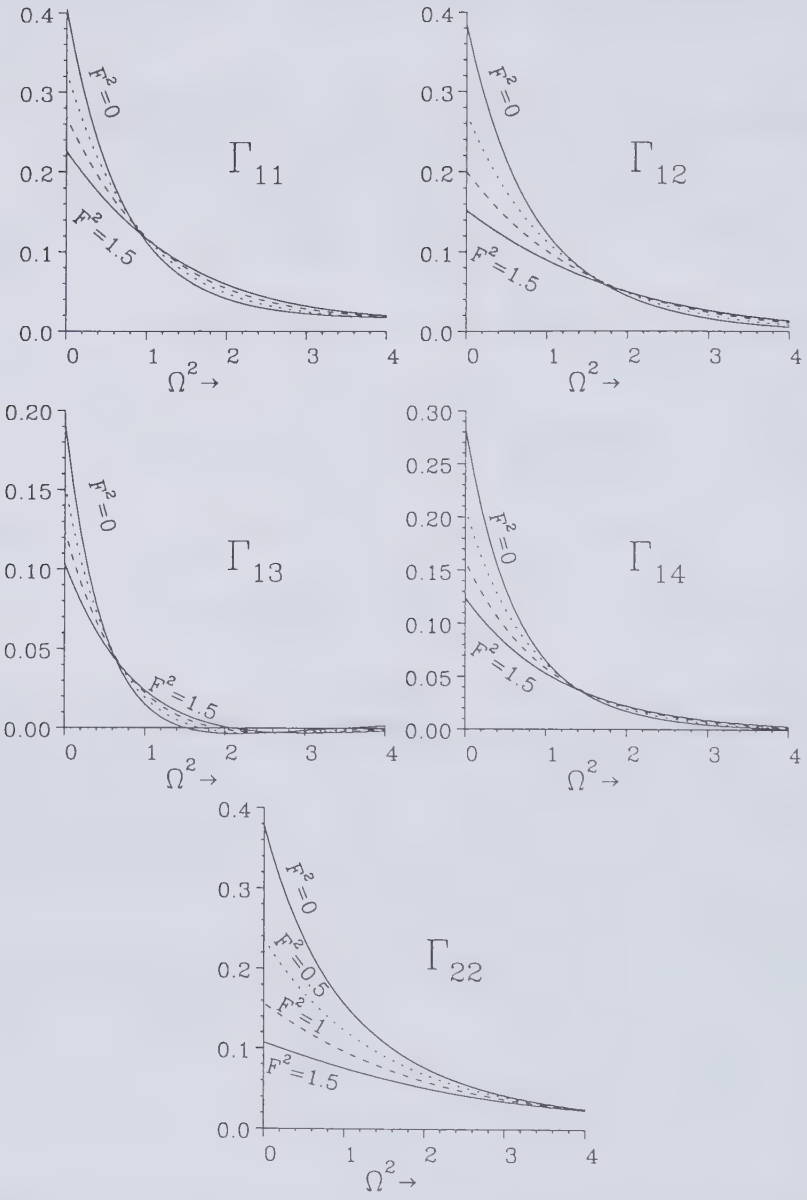

Figure 1. Dispersion response coefficients Γ_{kl} where the numbering k, l of the indices indicates the combinations of 1) in-phase velocity, 2) out-of-phase parallel velocity, 3) in-phase perpendicular velocity, 4) out-of-phase perpendicular velocity.

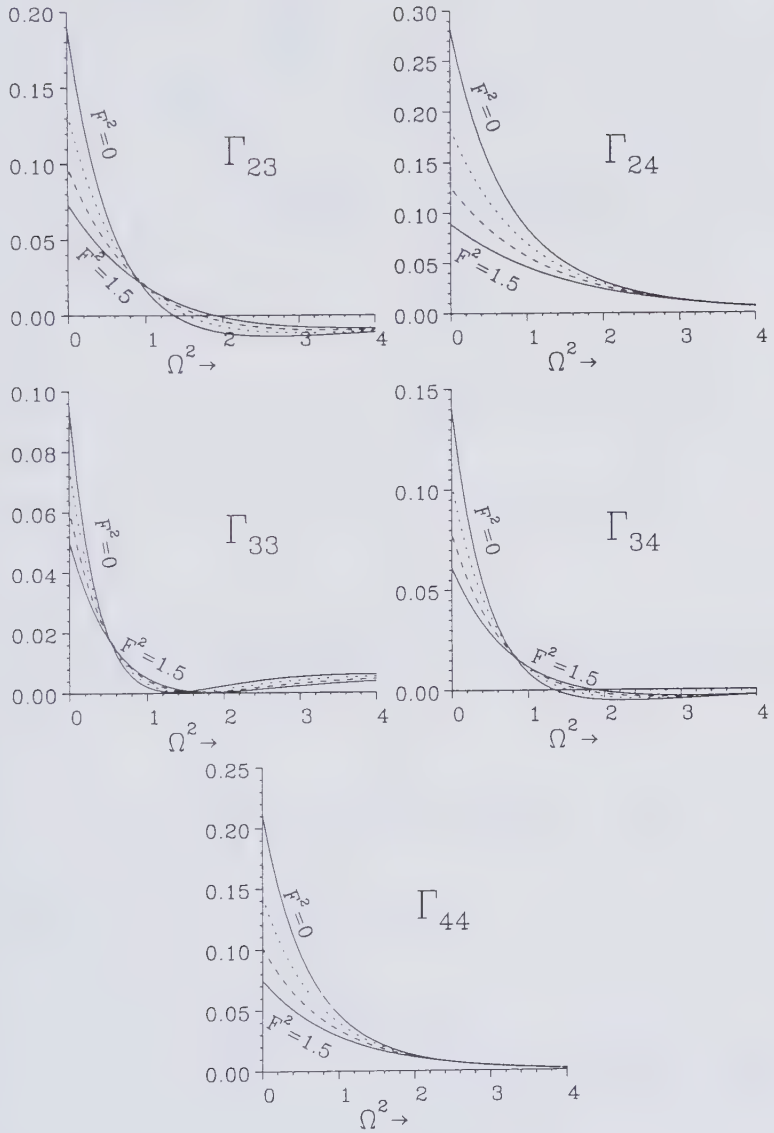

Figure 1 (Continued). Dispersion response coefficients Γ_{kl} where the numbering k, l of the indices indicates the combinations of 1) in-phase velocity, 2) out-of-phase parallel velocity, 3) in-phase perpendicular velocity, 4) out-of-phase perpendicular velocity.

A more visual representation of the shear disperion tensor is shown in Figure 3. The arrows indicate the direction and magnitude of the vertically averaged tidal current. The ellipses give the relative size and shape that a recently discharged dye spot would have

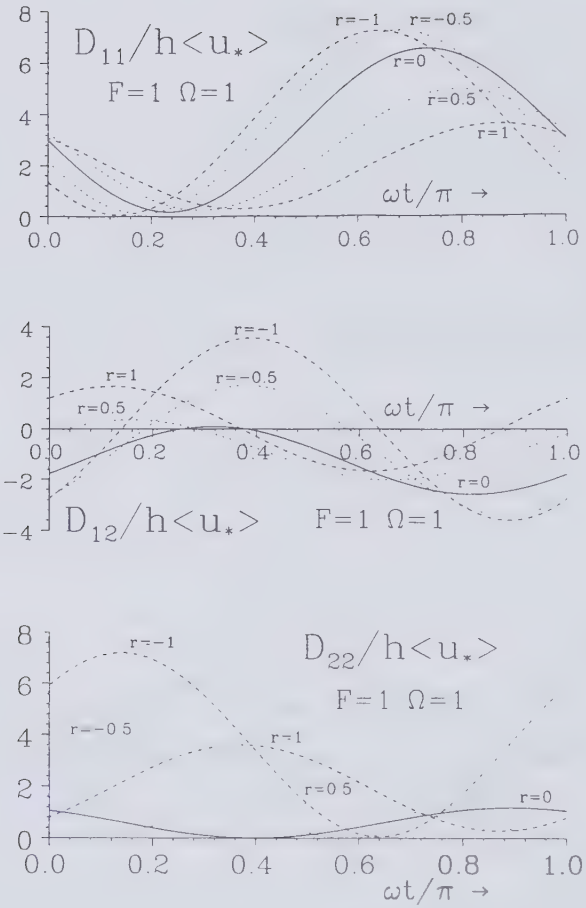

Figure 2. Time-dependence of the shear dispersion coefficients D_{ij} for several values of the tidal aspect ratio r.

evolved to if it were subject only to shear dispersion (ie with the generally smaller turbulent diffusivities K_1, K_2 neglected):

$$x^2 D_{22} - 2\,xh\,D_{12} + h^2 D_{11} = 2(t - t_0)(D_{11} D_{22} - D_{12}^2). \qquad (40)$$

In the rectilinear case r = 0 the effect of the Earth's rotation is particularly noticable: the dispersion ellipse has its principal axis systematically rotated to the right of the tidal flow in the northern hemisphere.

Acknowledgement. I am grateful to the Royal Society, Loughborough University and NERC not only for travel funds but also for research support.

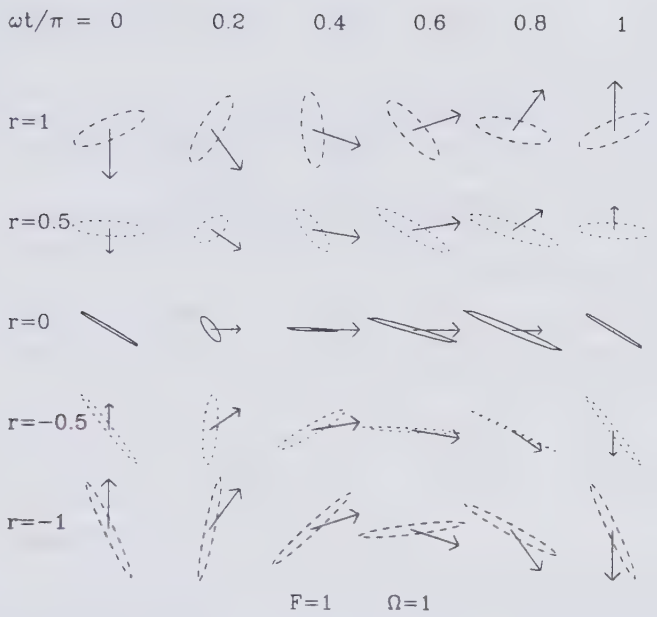

Figure 3. Relationship between the tidal velocity vector and the instantaneous shear dispersion tensor when the parameters characterising the vertical mixing time and the Coriolis effect have the values $\Omega = F = 1$.

References

Bowden, K.F. Horizontal mixing in the sea due to a shearing current. J. Fluid Mech 43: 321–352, 1965.

Chatwin, P.C. On the longitudinal dispersion of passive contaminants in oscillating flow in tubes. J. Fluid Mech. 71: 513-527, 1975.

Fischer, H.B. On the tensor form of the bulk dispersion coefficient in a bounded skewed shear flow. J. Fluid Mech. 83: 2373-2375., 1987

Gill, W.N. & Sankarasubramanian, R. Dispersion of a non-uniform slug in time-dependent flow. Proc. Roy. Soc. Lond A 322: 101-117, 1971.

Hamrick, J.M. Long-term dispersion in unsteady skewed free surface flow. Estuarine, Coastal Shelf Sci. 23: 807-845, 1986.

Smith, R. Contaminant dispersion in oscillating flows J. Fluid Mech. 114: 378-398, 1982.

Smith, R. The contraction of contaminant distributions in reversing flows. J. Fluid Mech. 129: 137-152, 1983.

Smith, R. When and where to put a discharge in an oscillatory flow. J. Fluid Mech. 153:479-499, 1985.

Taylor, G.I. Dispersion of soluble matter in solvent flowing slowly through a tube. Proc. Roy. Soc. Lond A 219: 186-203, 1953.

Yasuda, H. Longitudinal dispersion due to the boundary layer in an oscillatory current - theoretical analysis in the case of an instantaneous line source. J.Oceanogr. Soc.Japan 38:385-394, 1982.

Yasuda, H. Longitudinal dispersion of matter due to the shear effect of steady and oscillatory currents. J. Fluid Mech. 148: 383-403, 1984.

30

Capillarity Correction to Periodic Solutions of the Shallow Flow Approximation

D. A. Barry, S. J. Barry and J.-Y. Parlange

Abstract

The shallow flow expansion is used to derive equations describing the flow of fluid in an unconfined aquifer. The expansion, which is carried out to second order, is combined with an approximation accounting for the influence of the capillary fringe to give a model that describes the motion of the phreatic surface as it is affected by the capillarity of the porous medium. The results are derived for the case of an aquifer in contact with a reservoir, with the fluid in the reservoir undergoing a steady periodic motion. A linearised solution of the second-order theory is shown to agree well with an "exact" numerical solution. It is demonstrated using the linearised solution that the porous medium capillarity affects the time-averaged mean square height of the phreatic surface of the aquifer in the second-order term, but leaves the first-order term unchanged.

Introduction

Coastal aquifers will respond to the ocean as a result of wave or tidal action, or to variability of recharge. The beach profile also depends on the aquifer configuration. For example, the relative height the water table below the beach affects the amount of erosion of the beach face (e.g., Sato, 1991; Heaton, 1992). In the absence of boundary effects, the evaporative loss of water from the aquifer depends on the depth

Mixing in Estuaries and Coastal Seas
Coastal and Estuarine Studies Volume 50, Pages 496-510
Copyright 1996 by the American Geophysical Union

of the water table, which in turn depends on the recharge rate. These effects tend to damp out water table fluctuations. However, near a fluctuating boundary condition such as that imposed by tidal variations, water table movement is dominated by the fluctuations. Previously developed models consider these fluctuations, but do not take into account the effect of the capillary fringe. This effect will be explored below.

Studies of shallow coastal aquifers commonly simplify the governing flow model by invoking the Dupuit assumption of vertical equipotentials in the fluid. The resulting model does not include capillary effects. Therefore, results of such models will be appropriate so long as the capillary fringe length scale is significantly less than any other length scale entering the problem (Parlange *et al.*, 1984). It would appear that this assumption is reasonable in that theoretical predictions and experimental results compare quite well. However, to determine precisely the cause of this result, in this paper we relax the length scale assumption on the capillary fringe. We examine the behaviour of the water level in coastal aquifers (i.e., subject to a periodic boundary condition) utilising a model that includes the effect of the capillary fringe. Note that our purpose is not to model the complex phenomena observed at the zone of interaction (e.g., wave action or sediment transport) between the coastal aquifer and the ocean; rather, it is to quantify directly the effect of the capillary fringe in a physically realistic way. In particular, we focus on the effect of the capillary fringe as it alters the phreatic surface of the aquifer.

The paper is structured as follows: The governing equations modelling the behaviour of the phreatic surface are derived, up to second order, using the shallow flow expansion. Then, an approximation for the time-averaged mean square of true phreatic surface height is presented using the results from the expansion. The second-order theory is then solved, approximately, using a linearisation of the governing equations. An explicit expression for the mean square height is then derived and compared with the analogous case based on the assumption of no capillary fringe.

Derivation of the Governing Equations

We consider isothermal flow of an incompressible fluid in a structurally rigid porous medium. The simplified problem definition is given schematically in Figure 1. The flow domain is assumed to be uniform in the direction normal to the page, i.e., a two-dimensional vertical slice model is analysed. In Figure 1, the ocean is supposed to impose a periodic variation on the boundary of the aquifer, which is located at $x = 0$ (symbol definitions are collected in the notation list). This simplified model isolates the effect of the periodic boundary condition on the free surface of the aquifer, and so mimics the behaviour of a coastal aquifer. The height of the free surface, defined as the position where the fluid pressure is atmospheric, is given by $h(x,t)$. In the region $z > h$, there exists a capillary zone where the fluid pressure is less than

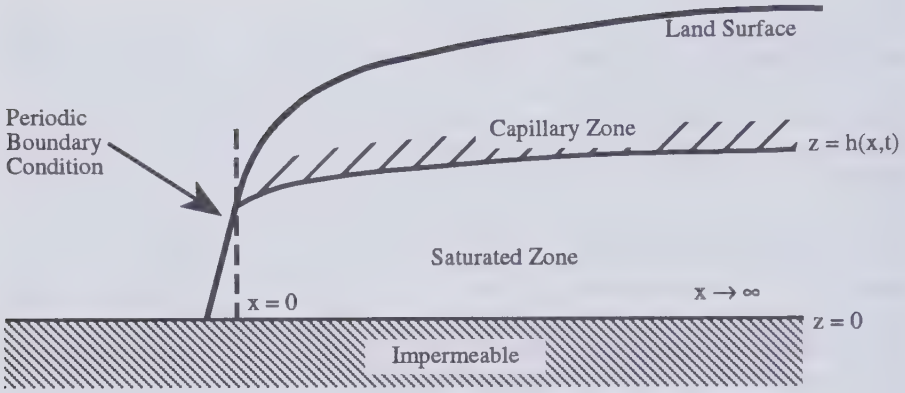

Figure 1. An unconfined aquifer subject to a periodic boundary condition.

atmospheric. The aquifer will be assumed be infinitely long. The fluid potential, ϕ ($= z + p/\rho g$), in the saturated zone then satisfies Laplace's equation since we assume the fluid to be incompressible and the porous medium inelastic (e.g., Bear and Verruijt, 1987), i.e.,

$$\frac{\partial^2 f}{\partial x^2} + \frac{\partial^2 f}{\partial z^2} = 0, \qquad x > 0,\ h > z > 0. \tag{1}$$

A zero-flux condition,

$$\frac{\partial \phi}{\partial z} = 0, \quad z = 0, \tag{2}$$

applies at the impermeable base of the aquifer, while at the phreatic surface we have (e.g., de Marsily, 1986):

$$\phi = h, \qquad z = h, \tag{3}$$

(which simply states that $\psi = 0$ on the phreatic surface), together with the kinematic boundary condition

$$n_e \frac{\partial \phi}{\partial t} = K\left[\left(\frac{\partial \phi}{\partial x}\right)^2 + \left(\frac{\partial \phi}{\partial z}\right)^2\right] + q - (K + q)\frac{\partial \phi}{\partial z}, \qquad z = h. \tag{4}$$

Note that in (1) and (4) we have assumed the hydraulic conductivity, K, in the aquifer to be homogeneous and isotropic. Also, at this point, q is left unspecified although its meaning is clear. It is a source term representing supply of fluid to the free surface from the unsaturated zone. The source could be recharge or, alternatively, supply of capillary fluid.

The Shallow Flow Expansion

In this section we derive an approximation for the free surface height, h, using the shallow flow expansion. The shallow flow expansion was developed by Friedrichs (1948) to derive the shallow water theory. It was subsequently applied by Dagan (1967) to the case of a phreatic aquifer. Following Dagan (1967) (c.f., Bear, 1972) then, (1) to (4) can be expanded using

$$X = x\sqrt{\varepsilon}, \tag{5}$$

$$T = \frac{t\varepsilon K}{n_e}, \tag{6}$$

$$q = K\varepsilon q_1, \tag{7}$$

$$\phi = \phi_0 + \varepsilon\phi_1 + \varepsilon^2\phi_2 + \cdots \tag{8}$$

and

$$h = h_0 + \varepsilon h_1 + \varepsilon^2 h_2 + \cdots, \tag{9}$$

where ε is a perturbation parameter. The precise meaning of the small parameter, ε, in (5)-(9), is unimportant in the expansions because terms of various orders are matched. Nonetheless, the meaning of ε will be discerned below.

The substitution of (5), (6), (8) and (9) into (1) and (2) yields:

$$\phi_0 = c_0(X,T), \tag{10}$$

$$\phi_1 = c_1(X,T) - \frac{z^2}{2}\frac{\partial^2\phi_0}{\partial X^2} \tag{11}$$

and

$$\phi_2 = c_2(X,T) - \frac{z^2}{2}\frac{\partial^2 c_1}{\partial X^2} + \frac{z^4}{24}\frac{\partial^2\phi_0}{\partial X^2}, \tag{12}$$

where c_0, c_1 and c_2 are functions to be determined. To find these functions we first expand (3) and find, on $z = h_0$,

$$\phi_0 = h_0, \tag{13}$$

$$\phi_1 = h_1, \tag{14}$$

and

$$\phi_2 = h_2 + h_0 h_1 \frac{\partial^2 h_0}{\partial X^2}. \tag{15}$$

Equations (13)-(15) can now be used to find the unknown functions in (10)-(12). This operation gives ϕ_0, ϕ_1, and ϕ_2 in terms of h_0, h_1, h_2 and z. Finally, these expressions are used in the expansion of (4), with the following results:

$$\frac{\partial h_0}{\partial T} = \frac{\partial}{\partial X}\left(h_0 \frac{\partial h_0}{\partial X}\right) + q_1 \tag{16}$$

and

$$\frac{\partial h_1}{\partial T} = \frac{\partial^2 \left(h_0 h_1\right)}{\partial X^2} + \frac{1}{3}\frac{\partial^2}{\partial X^2}\left(h_0^3 \frac{\partial^2 h_0}{\partial X^2}\right). \tag{17}$$

Equation (16) is the familiar Boussinesq (1903) equation with the source term, q_1. It is interesting to note that q_1 does not enter into the expression (17) defining h_1, and so the latter is identical to the result obtained by Stagnitti *et al.* (1983) and Parlange *et al.* (1984), who ignored capillary effects. In the following, both (16) and (17) are needed to determine an expression for the time-averaged mean-square water table height.

Behaviour of the Time-Averaged Free-Surface Height

As it stands, the model equations are incomplete as boundary conditions have not been imposed. The boundary is assumed to extend vertically upwards from the point x = 0 in Figure 1, on which the periodic condition

$$\phi(0,z,t) = h(0,t) = \gamma\,[1 + \alpha \cos(\omega t)]\,, \tag{18}$$

is applied. On physical grounds we see that $\alpha \leq 1$. We require also that the solution remain bounded as $x \rightarrow \infty$, or

$$\frac{\partial \phi}{\partial x} = \frac{\partial h}{\partial x} = 0, \qquad x \rightarrow \infty. \tag{19}$$

Drawing on results derived by Knight (1981), Parlange *et al.* (1984) showed that for the periodic boundary condition (18), the time average of h^2, denoted by $\langle h^2 \rangle$, is

$$\langle h^2 \rangle = \langle h_0^2 \rangle + \frac{2}{3} \varepsilon \langle h_0^2 \left(\frac{\partial h_0}{\partial X} \right)^2 \rangle + O(\varepsilon^2), \tag{20}$$

where

$$\langle h_0^2 \rangle = \gamma^2 \left(1 + \frac{\alpha^2}{2} \right). \tag{21}$$

Equation (21) is valid for (16) so long as q_1 has the same period as (18). It shows that the mean square free surface height within the aquifer is always greater than γ^2, although the time-averaged mean height of the forcing at the boundary is γ. This result, which can be derived easily directly from the Boussinesq equation and (18), has the following simple interpretation (Knight, 1981): The effective transmissivity of the aquifer depends on the height of the phreatic surface, so higher water levels on the boundary will result in more water entering the aquifer. The averaged height of water in the aquifer must therefore be greater than that on the boundary so that, on average, the flux at the boundary is zero. Alternatively, it shows that the free surface within the aquifer must be asymmetric. Field data confirm this asymmetry (e.g., Lanyon *et al.*, 1982).

The major contribution of (20) is that $\langle h^2 \rangle$ is determined exactly to $O(\varepsilon)$ by knowledge of h_0 alone, i.e., the solution satisfying (17) for h_1 is not needed. However, although not presented here, (17) was used to obtain (20). For that reason, its derivation (and the consequence that it is independent of q_1) was sketched above. It is common to use (16), or variations of it, to model the behaviour of coastal aquifers (e.g., Nielsen, 1990). Equation (20) shows that estimates of $\langle h^2 \rangle$ based solely on (21) will have an error of $O(\varepsilon)$. In the following this error will be quantified. Before doing so, it is necessary to derive an explicit expression for q_1 that will model the effect of the capillary fringe.

The Capillary Correction

In a recent paper, Parlange and Brutsaert (1987) (cf. Parlange *et al.*, 1990; Fink, 1990) considered the linearised version of (16) and derived an estimate of q_1 based on that linearisation. If (16) is taken as the point of departure, it is possible to use the approach of Parlange and Brutsaert (1987) to derive (in dimensional form)

$$n_e \frac{\partial h_0}{\partial t} = K \frac{\partial}{\partial x} \left(h_0 \frac{\partial h_0}{\partial x} \right) + B \frac{\partial^2}{\partial t \partial x} \left(h_0 \frac{\partial h_0}{\partial x} \right), \tag{22}$$

where B is approximated by

$$B \simeq \int_{-\infty}^{0} \theta - \theta_r \, d\psi. \tag{23}$$

Thus, B represents, for example, the average depth of water held in the capillary zone above the phreatic surface, or the average suction required to remove the capillary water from the unsaturated zone.

Equation (22) is a nonlinear model that incorporates the effect of capillarity on h_0. Observe that because the final term on the right-hand side of (22) is periodic if h_0 is periodic, the time average given in (21) remains unchanged by capillarity, as might be expected. Clearly, however, capillarity will influence the first-order term on the right-hand side of (20).

In order to estimate $\langle h^2 \rangle$ in (20), we must solve (22) subject to the following conditions resulting from (18) and (19):

$$h_0(0,t) = \gamma[1 + \alpha \cos(\omega t)] \tag{24}$$

and

$$\frac{\partial h_0}{\partial x} = 0, \qquad x \to \infty. \tag{25}$$

Equations (24) and (25) are the boundary conditions which the solution to (22) must satisfy. Clearly, an initial condition is needed to complete the specification of the problem, and any initial condition could be invoked. As time progresses, however, "memory" of the initial condition will be lost and, eventually, a quasi-steady state will be attained. Regardless of the initial condition, the behaviour of the system will be influenced wholly by the boundary condition (24). Therefore, in what follows we look for the periodic solution only, i.e., the solution that applies after a long time when all transient effects due to the initial condition have decayed.

Estimation of h_0

The solution of (22)-(25) is required to determine $\langle h^2 \rangle$ in (20). In general, such a solution will be obtained numerically. However, the numerical solution will not give ε. This parameter can be determined from an analytical solution satisfying (22)-(25). In this section an approximate analytical solution is calculated.

Motivated by the boundary condition (24), we seek an approximate solution in the form;

$$h_0(x,t) = \gamma[1 + \alpha h_{0,1}(x,t) + \alpha^2 h_{0,2}(x,t) + \ldots], \tag{26}$$

i.e., α is treated as a perturbation parameter. Clearly, (26) will be accurate for $\alpha \ll 1$. Upon substituting (26) into (22)-(25) we find that the $O(\alpha)$ terms give the following problem defining $h_{0,1}$:

$$n_e \frac{\partial h_{0,1}}{\partial t} = K\gamma \frac{\partial^2 h_{0,1}}{\partial x^2} + B\gamma \frac{\partial^3 h_{0,1}}{\partial t \partial x^2}, \tag{27}$$

$$h_{0,1}(0,t) = \cos(\omega t) \tag{28}$$

and

$$\frac{\partial h_{0,1}}{\partial x} = 0, \qquad x \to \infty. \tag{29}$$

Equations (27)-(29) have the obvious solution:

$$h_{0,1} = \exp(-x\lambda P)\cos(\omega t - x\lambda Q), \tag{30}$$

where

$$\lambda = \sqrt{\frac{n_e \omega}{2K\gamma}}, \tag{31}$$

$$\begin{bmatrix} P \\ Q \end{bmatrix} = \sqrt{\frac{1}{\sqrt{1+\omega^{*2}}} \begin{bmatrix} + \\ - \end{bmatrix} \frac{\omega^*}{1+\omega^{*2}}} \tag{32}$$

and

$$\omega^* = \frac{\omega B}{K}. \tag{33}$$

Stagnitti *et al.* (1983) point out that the problem defined by (27)-(29) was solved by Steggewentz (1933) for the case of no capillary term, i.e., B = 0. Setting B = 0 in (30) yields

$$h_{0,1}\big|_{B=0} = \exp(-x\lambda)\cos(\omega t - x\lambda). \tag{34}$$

Equation (34) agrees with the corresponding result reported by Lewandowski and Zeidler (1978), Parlange *et al.* (1984) and Nielsen (1990).

We proceed now to the calculation of $h_{0,2}$. The $O(\alpha^2)$ expressions resulting from the use of (26) in (22)-(25) are

$$n_e \frac{\partial h_{0,2}}{\partial t} = K\gamma \frac{\partial^2 h_{0,2}}{\partial x^2} + B\gamma \frac{\partial^3 h_{0,2}}{\partial t \partial x^2} + \frac{\gamma}{2}\left(K + B\frac{\partial}{\partial t}\right)\frac{\partial^2 h_{0,1}^2}{\partial x^2}, \tag{35}$$

$$h_{0,2}(0,t) = 0 \tag{36}$$

and

$$\frac{\partial h_{0,2}}{\partial x} = 0, \qquad x \to \infty. \tag{37}$$

The solution for $h_{0,2}$ satisfying (35)-(37) can be shown to be:

$$h_{0,2} = \frac{1}{4}[1 - \exp(-2x\lambda P)] + \frac{1 + 6\omega^{*2}}{2(1 + 9\omega^{*2})}\left[\exp(-\sqrt{2}x\lambda P_1)\cos(\beta_1) - \exp(-2x\lambda P)\cos(\beta)\right]$$
$$+ \frac{\omega^*}{2(1 + 9\omega^{*2})}\left[\exp(-\sqrt{2}x\lambda P_1)\sin(\beta_1) - \exp(-2x\lambda P)\sin(\beta)\right], \tag{38}$$

where

$$\begin{bmatrix} P_1 \\ Q_1 \end{bmatrix} = \sqrt{\frac{1}{\sqrt{1 + 4\omega^{*2}}}\begin{bmatrix} + \\ - \end{bmatrix}\frac{2\omega^*}{1 + 4\omega^{*2}}}, \tag{39}$$

$$\beta = 2\omega t - 2x\lambda Q \tag{40}$$

and

$$\beta_1 = 2\omega t - \sqrt{2}x\lambda Q_1. \tag{41}$$

Setting B = 0 in (39) yields

$$h_{0,2}\Big|_{B=0} = \frac{1}{4} - \frac{\exp(-2x\lambda)}{4} + \frac{1}{2}\left[\exp(-\sqrt{2}x\lambda)\cos(2\omega t - \sqrt{2}x\lambda) - \exp(-2x\lambda)\cos(2\omega t - 2x\lambda)\right], \tag{24}$$

in agreement, again, with the results reported by Parlange *et al.* (1984) and Nielsen (1990). Note that, by comparison with (34) and (42), (30) and (38) indeed represent a correction to the standard Boussinesq solution, i.e., the same basic form is obtained except that the various parameters become functions of ω^*.

With $h_{0,1}$ and $h_{0,2}$ now evaluated in (30) and (38), respectively, (26) can be used to evaluate h_0 analytically. This expression will be used shortly to determine ε in (20). Before doing so, however, the validity of (26) as an approximation for h_0 needs to be evaluated. For this purpose a numerical solution for (22)-(25) was developed. The details of this numerical solution are presented in the Appendix.

The "exact" numerical solution and the analytical approximation, (26), are compared in Figure 2. Because the approximation is exact for $\alpha = 0$, we took the extreme value of $\alpha = 1$ in order to check (26). Note that checking $\alpha = -1$ is unnecessary since it changes only the phase of the boundary condition (24).

Because the initial condition is unimportant, $h_0(x,0)$, calculated using (26), was used as the initial condition for the numerical solution. The results in Figure 2 show that the analytical approximation is satisfactory, even for this extreme case.

These results suggest further that (26) is suitable for estimating $\langle h^2 \rangle$ in (20). Using the expansion for h_0 in (26) gives

$$\frac{\langle h^2 \rangle}{\gamma^2} = \frac{\langle h_0^2 \rangle}{\gamma^2} + \frac{\alpha^2 n_e \gamma \omega \exp(-2x\lambda P)}{3K\left(1+\omega^{*2}\right)}. \tag{43}$$

For B = 0 ($\omega^* = 0$, P = 1), (43) reduces to the analogous expression reported by Parlange *et al.* (1984). In addition, (43) indicates that the perturbation parameter, ε, is given by (using dimensional quantities)

$$\varepsilon = \frac{\alpha^2 n_e \gamma \omega K}{6\left(K^2 + B^2\omega^2\right)}. \tag{44}$$

Equation (44) contains an interesting result, not reported previously. It predicts that the coefficient of the exponential in the second-order term of (43) will be maximised for a particular value of ω ($\approx$ K/B). Thus, the second-order term is a maximum for this value of ω at x = 0.

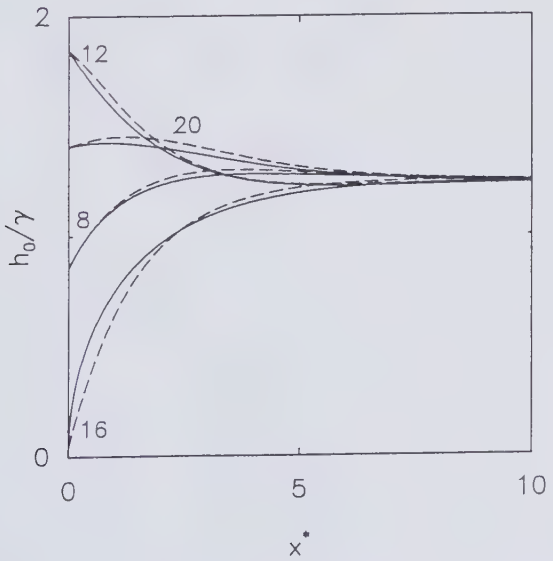

Figure 2. Comparison of "exact" numerical solution (Appendix) - lines - satisfying (22)-(25) and the analytical approximation (26) - dashes - for $\alpha = 1$ and $\omega^* = 1$. Labels on the curves give values of t^*.

Discussion and Conclusions

The main result of this study is contained in (43), which gives the time-averaged mean square height of the free surface in the aquifer. Only a few reports of appropriate laboratory experiments are available in the literature, and these are usually analysed using the Boussinesq equation, i.e., (22) with B = 0. For this reason the experiments were carried out using porous media composed of coarse materials so that the capillary effect on the free surface would be minimised. For example, Smiles and Stokes (1976) used a Hele-Shaw model while Parlange *et al.* (1984) used 0.5 cm diameter gravel. It is, therefore, not surprising that Parlange *et al.* (1984), who neglected capillary effects in their analysis, found that the experimental results were predicted quite well. Clearly, neither of these data sets can usefully be analysed using (43). Thus, at present we cannot provide experimental evidence to confirm our results. This is unfortunate because, paradoxically, the theory predicts that the correction term in (43) reduces in magnitude as B increases, and so the first term, $\langle h_0^2 \rangle$, dominates. It is clear physically why this is so: Due to capillarity, water can be stored in the unsaturated zone and it becomes easier for the groundwater to follow the fluctuations imposed at x = 0.

It is possible to show, approximately, the effect of the capillarity correction by inserting typical parameter values in (43). To simplify matters we set x = 0. Then, the only place where non zero values of the capillarity parameter, B, enter is in the denominator of the final term, through ω^*. If $\omega^* << 1$, then capillarity has negligible influence. Typical parameter values for a sandy beach with ocean tidal forcing are (e.g., Bear and Verruijt, 1987) K = 10 m d^{-1}, ω = 2 d^{-1} and B = 0.5 m, yielding ω^* = 0.1. On the other hand, parameters relevant for a lake undergoing seasonal variations in its water level that is connected with a relatively low permeability aquifer might be ω = 2 yr^{-1}, K = 0.01 m d^{-1}, B = 2 m, giving $\omega^* \approx 1.1$. This range of values suggests, not surprisingly, that the capillarity effect is important only in relatively low conductivity, small grained media.

Equation (43) also shows that the decay length of the fluctuations in the porous medium due to the fluctuating water body is of order $l_f = 2(\lambda P)^{-1}$. For a coastal aquifer, we take as the depth of the aquifer, γ, the magnitude of the tidal fluctuation, since the fresh water aquifer is underlain by the salt wedge which, for the purpose of an order of magnitude calculation, may be taken as being stationary. To compute λ we take the values used above with n_e = 0.35 and γ = 1.7 m. Thus, tidal fluctuations on a sandy beach are approximately l_f = 13.3 m, with B = 0.5 m or 13.9 m with no capillary effect, B = 0. If, on the other hand, γ is taken as the entire depth of the aquifer, say 15 m, then l_f = 39.6 m, with B = 0.5 m or 41.4 m with B = 0. The actual range probably lies between these limits. Some data on beach water table fluctuations at a Wollongong (New South Wales, Australia) beach is available from the study of Lanyon *et al.* (1982, Table 4). A 1.7 m tidal range decays to 0.15 of this value over a distance of 23 m. Similar calculations can be performed for the lake example discussed above. The same parameter values are used along with n_e = 0.45 and γ = 15 m yielding l_f = 20.4 m or 22.1 m with B = 0. These representative cases

show that the decay length of the fluctuations at the boundary are little affected by capillarity.

Finally, these results suggest that, because the effect of capillarity is relatively small, the Boussinesq solution (neglecting capillarity) will be good in situations where the parameters are curve fitted with ad hoc parameters.

References

Barry, D.A., Parlange, J.-Y., and Starr, J.L. Numerical analysis of the precursor effect, *Soil Sci.*, 143, 309-317, 1987.

Barry, D.A., Starr, J.L., Parlange, J.-Y., and Braddock, R.D. Numerical analysis of the snow-plow effect, *Soil Sci. Soc. Am. J.*, 47, 862-868, 1983.

Bear, J. *Dynamics of fluids in porous media*, American Elsevier, New York, 1972.

Bear, J., and Verruijt, A. *Modeling groundwater flow and pollution*, D. Reidel, Dordrecht, 1987.

Boussinesq, J. Recherches theoretiques sur l'ecoulemant des nappes d'eau infiltrées dans le sols et sur debit de sources, *C. R. Hebd. Seances Acad. Sci.*, 10, 7-78, 1903.

Crank, J., and Nicolson, P. A practical method for numerical evaluation of solutions of equations of the heat-conduction type, *Proc. Camb. Philos. Soc.*, 43, 50-67, 1947.

Dagan, G. Second-order theory of shallow free-surface flow in porous media, *Q. J. Mech. Appl. Math.*, 20, 517-526, 1967.

de Marsily, G. *Quantitative hydrogeology*, Academic Press, San Diego, 1986.

Fink, J.P. Curious behavior of a groundwater flow model. *Water Resour. Res.*, 26, 1833-1836, 1990.

Friedrichs, K.O. On the derivation of the shallow water theory (Appendix to a paper by J. J. Stoker), *Comm. Appl. Math.*, 1, 81-85.

Heaton, K. Local effects of groundwater table variations on on-shore off-shore sediment transport. Honours thesis, Dept Civil & Environ. Eng., Univer. West. Aust., 1992.

Knight, J.H. Steady periodic flow through a rectangular dam, *Water Resour. Res.*, 17, 1222-1224, 1981.

Lanyon, J.A., Elliot, I.G., and Clarke, D.J. Groundwater-level variation during semidiurnal spring tidal cycles on a sandy beach, *Aust. J. Mar. Freshwater Res.*, 33, 377-400, 1982.

Lewandowski, A., and Zeidler, R.B. Beach ground-water oscillations, *Proc. 16th Coastal Eng. Conf.*, Am. Soc. Civ. Eng., New York, II, 2051-2065, 1978.

Nielsen, P. Tidal dynamics of the water table in beaches. *Water Resour. Res.*, 26, 2127-2134, 1990.

Parlange, J.-Y., and Brutsaert, W. A capillary correction for free surface flow of groundwater, *Water Resour. Res.*, 23, 805-808, 1987.

Parlange, J.-Y., Brutsaert, W., Fink, J.P., and El-Kadi, A.I. A capillary correction for free surface flow revisited, *Water Resour. Res.*, 26, 1691-1692, 1990.

Parlange, J.-Y., Stagnitti, F., Starr, J.L., and Braddock, R.D., Free-surface flow in porous media and periodic solution of the shallow-flow approximation, *J. Hydrol.*, 70, 251-263, 1984.

Sato, M. Underground water table and beach face erosion, in B. L. Edge (ed.), *Proc. 22nd Coastal Eng. Intl. Conf.*, Am. Soc. Civil Eng., New York, 2644-2657, 1991.

Stagnitti, F., Parlange, J.-Y., Starr, J.L., Chu, B.T., and Braddock, R.D. Water level variations in aquifers caused by ocean tides, *Proc. 6th Aust. Conf. on Coastal & Ocean Eng.*, Gold Coast, Qld. 13-15 July, 216-219, 1983.

Steggewentz, J.H. De invloed van de getijbeweging van zeeen en getijrivieren op de stijghoogte van het groundwater. Thesis, Delft University of Technology, Holland, 1933.

Thomas, L.H., Elliptic problems in linear difference equations over a network, Watson Scientific Computing Lab., Columbia Univ., New York, NY, 1949.

Appendix

A numerical solution satisfying (22), (24), (25) and an arbitrary initial condition is developed here. If we define the dimensionless free surface height, h^*, as

$$h^* = h/\gamma \tag{A1}$$

then, in dimensionless form, the problem to be solved is

$$\frac{\partial h^*}{\partial t^*} = \frac{\partial^2 h^{*2}}{\partial x^{*2}} + \frac{\partial^3 h^{*2}}{\partial t^* \partial x^{*2}} \tag{A2}$$

subject to

$$h^*(0,t^*) = 1 + \alpha \cos\left(\omega^* t^*\right), \tag{A3}$$

$$\frac{\partial h^*}{\partial x^*} = 0, \qquad x^* \to \infty \tag{A4}$$

and

$$h^*(x^*,0) = h^*_{in}(x^*). \tag{A5}$$

In the numerical solution, (A4) is applied at a finite distance, with that distance chosen so that the effect of the finite domain size is negligible. Equations (A2)-(A5) are now transformed using the substitution $u = h^{*2}$. The resulting equations are then solved using the approach of Crank and Nicolson (1947), i.e., we take centred finite difference approximations to both the spatial and temporal derivatives about the point $[j\Delta x^*, (n + 1/2)\Delta t^*]$, where $x^* = j\Delta x^*$, $j = 0, \ldots, N$ and $t^* = n\Delta t^*$, $n = 0, \ldots, M$. The method yields the following system of equations to be solved

$$\mathbf{A}(r)^{n+1}\mathbf{u}^{n+1} = \mathbf{A}(s)^n\mathbf{u}^n + \mathbf{b}, \tag{A6}$$

where

$$\mathbf{u}^n = \left[u_1^n, u_2^n, \ldots, u_{N-1}^n, u_N^n\right]^T, \tag{A7}$$

$$\mathbf{A}(s)^n = \begin{bmatrix} D_1 & -s & 0 & \cdots & & 0 \\ -s & D_2 & -s & 0 & & \\ 0 & \ddots & \ddots & \ddots & & \vdots \\ \vdots & & \ddots & \ddots & \ddots & \\ & \cdots & 0 & -s & D_{N-1} & -s \\ 0 & & \cdots & 0 & -2s & D_N \end{bmatrix}, \tag{A8}$$

$$\mathbf{b} = \left[\left\{1 + \alpha \cos\left(j\omega^* \Delta t^*\right)\right\}^2 s + \left\{1 + \alpha \cos\left((j+1)\omega^* \Delta t^*\right)\right\}^2 r, 0, \cdots, 0\right]^T \quad \text{(A9)}$$

$$\begin{bmatrix} r \\ s \end{bmatrix} = \frac{1}{\Delta x^{*2}} \left(\frac{\Delta t^*}{2} \begin{bmatrix} + \\ - \end{bmatrix} 1 \right). \quad \text{(A10)}$$

and

$$D_i = 2s + \frac{1}{\sqrt{u_i^n}}, i = 1, \ldots, N \quad \text{(A11)}$$

Equation (A6) defines a nonlinear system of equations to be solved on successive time lines, j, j + 1, etc., with the j = 0 time line determined from the initial condition (A5). Fixed-point iteration was used to solve (A6) at each time line, i.e., the coefficient matrix $\mathbf{A}^{j+1}$ was linearised by setting the unknown terms on the diagonal to the values computed at the previous time step. The resulting linear system was then solved using the efficient Thomas (1949) algorithm. The updated estimates contained in **u** were substituted into $\mathbf{A}^{j+1}$ and the procedure repeated until convergence (defined as when each element in successive estimates of **u** differed by less than 10^{-12}). The calculations then proceeded to the next time step.

A consistency analysis shows this scheme has an error term of $O(\Delta x^{*2}, \Delta t^{*2})$. The scheme is similar to those used by Barry *et al.* (1983, 1987), where further details of its properties can be found.

Notations

- **A** coefficient matrix in the finite-difference solution (Appendix)
- **b** forcing term in finite-difference solution (Appendix)
- B coefficient in capillary correction term, L
- c_i i = 0, 1, 2, arbitrary functions, L
- D_i i=1, ..., N, defined by (A11)
- g magnitude of gravitational acceleration, LT^{-2}
- h height of the free surface, L
- h^* dimensionless free surface height, (A1)
- h_{in}^* arbitrary function of x^*, (A5)
- h_i i = 1, 2, ..., functions appearing in the expansion of h, L
- $h_{0,i}$ i = 1, 2, ..., functions appearing in the expansion of h_0
- j spatial counter used in the finite-difference solution (Appendix)
- K hydraulic conductivity, LT^{-1}
- l_f fluctuation length scale, L
- M maximum number of temporal steps in the finite-difference grid (Appendix)

n	temporal counter used in the finite-difference solution (Appendix)
n_e	effective porosity
N	maximum number of spatial steps in the finite-difference grid (Appendix)
p	fluid pressure offset such that $p = 0$ is atmospheric pressure, $ML^{-1}T^{-2}$
P	function of ω^*, (32)
P_1	function of ω^*, (39)
q	flux of fluid supplied to the saturated zone, LT^{-1}
q_1	flux of fluid supplied to the saturated zone (dimensionless form)
Q	function of ω^*, (32)
Q_1	function of ω^*, (39)
r	factor used in finite-difference solution (Appendix)
s	factor used in finite-difference solution (Appendix)
t	time, T
t^*	tK/B, dimensionless time variable
T	scaled time, L
u	function of h^* (Appendix)
$\mathbf{u}$	vector used in finite-difference solution (Appendix)
x	distance from the location of the forcing boundary condition, L
x^*	$x\sqrt{\frac{2n_e}{B\gamma}}$, dimensionless position variable
X	scaled position, L
z	distance above the impermeable base of the aquifer, L
α	the semi-tidal amplitude (maximum possible relative fluid fluctuation at $x = 0$)
γ	mean water depth at $x = 0$, L
Δx^*	spatial grid size used in the finite-difference solution
Δt^*	temporal grid size used in the finite-difference solution
ε	perturbation parameter
θ	volumetric moisture content
θ_r	residual volumetric moisture content
ρ	fluid density, ML^{-3}
ϕ	$z + \psi$, piezometric head, L
ϕ_i	$i = 1, 2, \ldots$, functions appearing in the expansion of ϕ, L
ψ	pressure head, $p/\rho g$, L
ω	frequency, T^{-1}
ω^*	dimensionless frequency, (33)
$\cdot^T$	transpose of $\cdot$
$\langle\cdot\rangle$	time average of $\cdot$

List of Contributors

D. G. Aubrey
Woods Hole Oceanographic Institution
Woods Hole, MA 02543
USA

K. Black
Victorian Institute of Marine Sciences,
14 Parliament Place
East Melbourne, Vic 3002
AUSTRALIA

D.A. Barry
Department of Environmental
Engineering
The University of Western Australia
Nedlands, WA, 6907
AUSTRALIA

S.J. Barry
Department of Environmental
Engineering
The University of Western Australia
Nedlands, WA, 6907
AUSTRALIA

M.L. Barton
Plymouth Marine Laboratory
Plymouth PL1 3DH
UNITED KINGDOM

P.J. Bills
Department of Applied Mathematics
The University of Adelaide
Adelaide, SA, 5000
AUSTRALIA

M. Breton
IFREMER
Laboratoire Hydrodynamique et
Sédimentologie
B.P. 70, F 29280
Plouzane
FRANCE

D. Cox
Water Research Laboratory, University
of New South Wales
Manly Vale, NSW 2093
AUSTRALIA

N. D'Adamo
Department of Environmental Protection
Marine Impacts Branch
Perth, WA, 6000
AUSTRALIA

A. Davison
Australian Nuclear Science and
Technology Organisation
Lucas Heights, NSW, 2234
AUSTRALIA

C.T. Friedrichs
School of Marine Science
Virginia Institute of Marine Science
College of William and Mary
Gloucester Point
VA 23062-1346
USA

P. Garreau
IFREMER
Laboratoire Hydrodynamique et
Sédimentologie
B.P. 70, F 29280
Plouzane
FRANCE

A. Graham
Department of Oceanography
The University
Southampton SO9 5NH
UNITED KINGDOM

I. Grabemann
GKSS Forschungszentrum Geesthacht GmbH
21502 Geesthacht
GERMANY

A.J. Hall
Institute of Oceanographic Sciences,
Wormley, Godalming
Surrey, GU8 5UB
UNITED KINGDOM

J.B. Hinwood
Department of Mechanical Engineering
Monash University
Clayton, VIC 3168
AUSTRALIA

P.E. Holloway
Department of Geography and Oceanography
Australian Defence Force Academy
Canberra, ACT 2600
AUSTRALIA

Z.Z. Ibrahim
Department of Environmental Sciences,
Universiti Pertanian Malaysia,
43400 UPM Serdang,
MALAYSIA

T. Ishimaru
Tokyo University of Fisheries
Konan 4-5-7
Minanto-ku
Tokyo 108
JAPAN

D.A. Jay
Geophysics Program AK-50
University of Washington
Seattle, WA 98195
USA

C.F. Jago
School of Ocean Sciences
University of Wales Bangor
Marine Science Laboratories
Menai Bridge
Gwynedd LL59 5EY
UNITED KINGDOM

S.E. Jones
School of Ocean Sciences
University of Wales Bangor
Marine Science Laboratories
Menai Bridge
Gwynedd LL59 5EY
UNITED KINGDOM

B. King
Australian Institute of Marine Science
PMB No 3
Townsville MC, QLD 4810
AUSTRALIA

H. Kühle
ZEWU Hamburg
2100 Hamburg 90
GERMANY

B. Kunze
GKSS Forschungszentrum Geesthacht GmbH
21502 Geesthacht
GERMANY

P. Larcombe
Marine Geophysical Laboratory
James Cook University
Townsville, QLD 4811
AUSTRALIA

R.S. Lee
NSW Environment Protection Authority
Sydney, 2000
AUSTRALIA

R.E. Lewis
ICI Group Environmental Laboratory
Brixham, Devon,
UNITED KINGDOM

G. Lessa
Coastal Studies Unit
Department of Geography
University of Sydney
Sydney, NSW, 2006
AUSTRALIA

D. Mills
Department of Environmental Protection
Marine Impacts Branch
Perth, WA, 6000
AUSTRALIA

A. Müller
GKSS Forschungszentrum Geesthacht
GmbH
21502 Geesthacht
GERMANY

J.D. Musiak
Geophysics Program AK-50
University of Washington
Seattle, WA 98195
USA

P. Nielsen
Civil Engineering
University of Queensland
St. Lucia
AUSTRALIA

B.J. Noye
Department of Applied Mathematics
The University of Adelaide
Adelaide, South Australia.5000
AUSTRALIA

S. Onishi
Civil Engineering Department, Science
University of Tokyo
Yamazaki Noda city, Chiba
JAPAN

J -Y. Parlange
Agricultural and Biological Engineering
Department
Cornell University
Ithica NY 14853-5701
USA

C. Pattiaratchi
Centre for Water Research
The University of Western Australia
Nedlands, WA 6907
AUSTRALIA

A. Pearce
Commonwealth Scientific and Industrial
Research Organisation
Division of Oceanography
Marmion, WA 6020
AUSTRALIA

T.R. Pritchard
NSW Environment Protection Authority
Sydney, NSW 2000
AUSTRALIA

J.R. Pennock
Marine Environmental Sciences
Consortium
Dauphin Island
Alabama 36528
USA

S. Peene
Coastal & Oceanographic Engineering
Department
336 Weil Hall, University of Florida,
Gainesville, Florida 32611
USA

P.V. Ridd
Marine Geophysical Laboratory
James Cook University
Townsville, QLD 4811
AUSTRALIA

M. Rosenberg
Victorian Institute of Marine Sciences,
Melbourne, VIC 3000
AUSTRALIA

J. Salomon
IFREMER
Laboratoire Hydrodynamique et
Sédimentologie
B.P. 70, F 29280
Plouzane
FRANCE

T. Saino
Ocean Research Institute
University of Tokyo
Minami-dai 1-15-1
Nakano-ku
Tokyo 130
Japan

W.W. Schroeder
Marine Science Program
The University of Alabama and
Marine Environmental Sciences
Consortium
Dauphin Island
Alabama 36528
USA

Y. P. Sheng
Coastal & Oceanographic Engineering
Department
336 Weil Hall
University of Florida, Gainesville,
Florida 32611
USA

J.H. Simpson
School of Ocean Sciences
University of Wales Bangor
Marine Science Laboratories
Menai Bridge
Gwynedd LL59 5EY
UNITED KINGDOM

R. Simons
Civil and Environmental Engineering,
University College
London
UNITED KINGDOM

N.P. Smith
Harbor Branch Oceanographic
Institution
5600 Old Dixie Highway
Fort Pierce
Florida 34946
USA

R. Smith
Department of Mathematical Sciences
Loughborough University
LE11 3TU
UNITED KINGDOM

D.W.F. Standingford
Department of Applied Mathematics
The University of Adelaide
Adelaide, SA 5000
AUSTRALIA

J.A. Stephens
Plymouth Marine Laboratory
Plymouth PL1 3DH
UNITED KINGDOM

G. Symonds
Geography and Oceanography,
Australian Defence Force Academy,
Canberra, ACT 2601
AUSTRALIA

S.A. Thorpe
Department of Oceanography
The University
Southampton SO9 5NH
UNITED KINGDOM

R.J. Uncles
Plymouth Marine Laboratory
Plymouth PL1 3DH
UNITED KINGDOM

J. van de Kreeke
Rosenstiel School of Marine and Atmospheric Science
Division of Applied Marine Physics
4600 Rickenbacker Causeway
Miami, Florida 33149
USA

A. Webb
Department of Civil and Maritime Engineering
Australian Defence Force Academy,
Canberra, ACT 2601
AUSTRALIA

W.J. Wiseman, Jr.
Department of Oceanography and Coastal Sciences
Louisiana State University
Baton Rouge, LA 70803
USA

E. Wolanski
Australian Institute of Marine Science
PMB No 3
Townsville MC, QLD 4810
AUSTRALIA

A. Wyllie
Department of Land Administration,
Remote Sensing Applications Centre,
Perth, WA 6000
AUSTRALIA

T. Yamamoto
Department of Civil and Ocean Engineering
Ehime University
Matsuyama 790
JAPAN

T. Yanagi
Department of Civil and Ocean Engineering
Ehime University
Matsuyama 790
JAPAN

E. Yassuda
Coastal & Oceanographic Engineering Department
336 Weil Hall, University of Florida,
Gainesville, Florida 32611
USA

H. Yasuda
Chugoku National Industrial Research Institute
2-2-2 Hiro-Suehiro
Kure-City, 737-01
JAPAN

ISBN 0-87590-264-2